Applications of Cavity Ring-Down Spectroscopy in Environmental Physics: Rayleigh Scattering Cross-sections and Airborne Measurements of Peroxy Radicals

Dissertation zur Erlangung des akademischen Grades des Doktor der Naturwissenschaften an der Universität Bremen

(Dr.rer.nat.)

Vorgelegt von

Yangzhuoran Liu

Institut für Umweltphysik

Fachbereich für Physik und Elektrotechnik

Universität Bremen

Bremen

Deutschland

Abstract

This doctoral thesis aims at the improvement of the airborne measurement of peroxy radicals by focusing on two applications of **c**avity **r**ing-**d**own **s**pectroscopy (CRDS): the determination of the EM radiation extinction cross-section of gas molecules, and the determination of gas molecule concentrations with the knowledge of the EM radiation extinction and the EM radiation extinction cross-sections. The experimental part of the work is based on the use of the **Pe**roxy **R**adical **C**hemical **E**nhancement and **A**bsorption **S**pectrometer (PeRCEAS) instrument which combines the **pe**roxy **r**adical **c**hemical **a**mplification (PERCA), for the amplified conversion of peroxy radicals in NO_2, with a sensitive NO_2 detection by CRDS.

For the first CRDS application, three setups were used for the determination of Rayleigh scattering cross-sections $\sigma_{Rayl.}$ of atmospheric gases at 408 nm. Thus, the EM radiation extinction by N_2, O_2, Ar, CO, CO_2, N_2O, CH_4, and synthetic air (SA) was measured using step pressure changes and pressure ramps in optical cavities. The experimentally determined $\sigma_{Rayl.}$ were compared with calculated values based on literature refractive index (n) and King correction factors. The calculated and measured $\sigma_{Rayl.}$ agreed within 0.6 %, 2.4 %, 1.2 %, 2.2 %, and 1.5 % for CO_2, N_2, O_2, SA, and Ar, respectively, at $\sim$ 408 nm. The measured $\sigma_{Rayl.}$ for N_2O and CH_4 confirmed the improved accuracy of the most recently published determinations of their refractive indexes. The CO $\sigma_{Rayl.}$ experimentally determined for the first time in this work at 408 nm, is 4.1 % higher than the calculated value resulting from extrapolation, suggesting the need for improved knowledge of the refractive index and King correction factors in the blue spectral region.

The second CRDS application is a pre-requisite for the acquisition of airborne peroxy radical data and involves the deployment of PeRCEAS on an airborne platform for the measurement of the total sum of peroxy radicals which react with NO (RO_2^*) during the EMeRGe (Effect of Megacities on the transport and transformation of pollutants on the Regional and Global scales) project. The retrieved RO_2^* were then compared with the results of four atmospheric models and with calculations based on photostationary steady state (PSS) assumptions. The box model and the PSS calculations are constrained to the airborne measurements. Three case studies/scenarios were investigated: 1) close to Rome and Manila's major population centres, 2) long-range transported air masses from megacities in the Western Pacific, and 3) over a very populated area in Taiwan during different take-off and landing scenarios.

Generally, models agree with measurements within their uncertainties, but they face difficulties with short-term variations. Notably, in Rome, models underestimated measurements by up to 80% at lower altitudes close to the boundary layer, while in Manila the box model underestimated 30% of the observations. In the Taiwan cases, the models showcased a 2 to 5 times underestimation in capturing short-term RO_2^* variability in more polluted, aerosol-rich conditions. A re-evaluation method, adjusting the ratio of different peroxy radicals in the RO_2^* calculations, reduced differences between the box model and PSS results by up to 40%. Overestimations by the PSS calculations were linked to high NO levels, organic nitrate formation, and aerosol-induced radical losses unaccounted for in current calculations. The findings underscore the capabilities of the models investigated and highlight the necessity for the speciation of radical measurements to improve the understanding of the short-term variability of RO_2^* in complex polluted areas.

Keywords: cavity ring-down spectroscopy, PeRCEAS instrument, Rayleigh scattering, peroxy radicals, airborne measurements, atmospheric models, EMeRGe project.

Table of content

List of abbreviations and acronyms

Abbreviation	Meaning
BAHAMAS	Basic Halo measurement and sensor system
CFC	Chlorofluorocarbon
CL	Chain length
CRDS	Cavity ring-down spectroscopy
DAQ	Data acquisition
DUALER	Dual channel airborne peroxy radical chemical amplifier
eCL	Effective chain length
EM	Electromagnetic
EMeRGe	Effect of Megacities on the transport and transformation of pollutants on the Regional and Global scales
FWHM	Full-width half maximum
GI	Gas of interest
HALO	High altitude and long range
HWHM	Half-width half maximum
IUP	Institute for Environmental Physics ("Institut für Umweltphysik" in German)
MFC	Mass flow controller
NMHC	Non-Methane Hydrocarbon
OMO	Oxidation Mechanism Observations
OVOC	Oxygenated Volatile Organic Compound
P	Pressure
PBL	Planetary Boundary Layer
PERCA	Peroxy radical chemical amplification
PeRCEAS	Peroxy radical chemical enhancement absorption spectrometer
PSS	Photostationary steady state
PXI	PCI extensions for instrumentation
RH	Relative humidity
RO_2^*	The total sum of peroxy radicals which react with NO
SA	Synthetic air
T	Temperature
TTL	Transistor - Transistor logic
VOC	Volatile Organic Compound
σ	Cross-section
τ	Ring-down time

1   Introduction: motivation and objectives

Our understanding of atmospheric physics and chemistry has made much progress in the past two centuries in particular since the 1950s. These advances have been driven in part by scientific curiosity and also by the need to understand how the atmosphere is changing as a result of human activity. The human population has grown from around 1 billion since 1800 to 8 billion today. This growth began with the Industrial Revolution and has been made possible by the use of fossil fuels as a major source of power. The increasing population and associated industrial activity have led to increasing releases of i) chemical precursors (e.g. nitrogen monoxide, NO, nitrogen dioxide NO_2, ammonia, NH_3, and sulfur dioxide, SO_2) of short-lived climate pollutants (aerosol and ozone, O_3), ii) persistent organic pollutants, which accumulate in the food chain, iii) ozone depleting species (e.g. chlorofluorocarbons, CFCs, brominated fire retardants and methyl bromide, CH_3Br), and iv) long-lived greenhouse gases (e.g. carbon dioxide, CO_2, methane, CH_4, nitrous oxide, N_2O, etc.). In addition, there have been large land use changes. This has led to a) smog and air pollution from local to global scales (Manisalidis et al., 2020), b) the loss of stratospheric ozone (World Meteorological Organization, 2022), and c) climate change (IPCC, 2023). As is well known, these changes impact the health of humans, the ecosystem and its services, and the loss of biodiversity.

The improvement in our understanding of atmospheric chemistry and physics has in large part been a result of the following research activities: a) the development of techniques to measure meteorological parameters and atmospheric composition, and b) the development of atmospheric models, accurately describing the chemical, physical, and biological processes, which determine conditions in the atmosphere and at the earth's surface. Atmospheric modelling began with the objective of numerical weather prediction, it has now evolved to include climate and chemistry modelling.

In this doctoral research, the scientific involvement extended to the development of measurement techniques, experimental exploration of atmospheric composition, and the analysis of model simulations within the troposphere. A significant aspect of the experimental research encompassed active participation in the development of instrumentation employing cavity ring-down spectroscopy, CRDS. This relatively novel spectroscopic technique has brought about a revolutionary transformation in the measurement of molecular absorption and scattering. Specifically, the focus of CRDS applications centred on two primary areas: the detection of atmospheric gases and the investigation of Rayleigh scattering by molecules. CRDS, a highly sensitive optical spectroscopic technique utilised for the measurement of trace gases, isotopes, and other molecular species, has a high-grade historical development as follows: Considered one of the pioneers of CRDS, Kastler, 1962 employed a Fabry-Perot etalon to extend the path length and thus enhance absorption. Later, Hansch et al., 1972 introduced intra-cavity laser absorption spectroscopy. A significant advancement came in 1980 when Herbelin et al. recognised the connection between the decay rate of electromagnetic (EM) radiation inside a high-finesse cavity and its extinction due to absorption and scattering by

molecules. This understanding subsequently led to the invention of CRDS by O'Keefe and Deacon in 1988. CRDS has since been employed for various applications, both in laboratory settings and in atmospheric studies.

Within this PhD, CRDS has been used in two specific areas of application: a) the precise and accurate measurement of Rayleigh scattering cross section of atmospheric gases; and b) the detection of NO$_2$. This work is grounded in the previous development of CRDS at the Institute of Environmental Physics in Bremen (Institut für Umwelt Physik, IUP-Bremen), Germany, which is detailed in the following:

    I.   CRDS in the measurement of peroxy radicals

Peroxy radicals in the troposphere comprise the hydroperoxyl radicals, HO$_2$, and organic peroxy radicals, RO$_2$, where R stands for an organic group. They are short-lived free radicals, which play an important role as key intermediates in the oxidation reactions in tropospheric chemistry (Monks, 2005 and reference herein). Due to their high reactivity, the peroxy radicals are present at low mixing ratios in the atmosphere and consequently require accurate and sensitive observational techniques. In this context, the airborne measurement of peroxy radicals is particularly challenging.

The IUP-Bremen has developed the Peroxy Radical Chemical Enhancement and Absorption Spectrometer (PeRCEAS) instrument. PeRCEAS combines the Peroxy Radical Chemical Amplification (PERCA) and the CRDS detection of NO$_2$ in an instrument designed to make airborne measurements of the total sum of peroxy radicals, RO$_2^*$. The latter is the sum of HO$_2$ and those RO$_2$ which have at least one H atom in the R group and react with NO to produce NO$_2$. The RO$_2^*$ are converted and amplified after passing through the instrument inlet. This is achieved by mixing the ambient airflow with flows of NO and CO. A chain reaction ensues and the RO$_2^*$ are converted into an amount of NO$_2$, which is related to the length of the chain reaction. The airflow then passes into the CRDS detector, which measures the decay time of an EM radiation pulse of a laser at approximately 408 nm to 1/e th of its initial value by the absorption and/or scattering of gas-phase molecules inside a high finesse optical cavity (i.e. the cavity ring-down time). This decay time is attributed to the extinction by NO$_2$, and all gas molecules in the CRDS cavity, where the absorption of NO$_2$ is dominant (see further details in chapter 2).

PeRCEAS was designed to be deployed on board the High Altitude and Long Range Research Aircraft, HALO (HALO-SPP, 2023), and has been characterised and optimised for participation in various HALO research campaigns (Horstjann et al., 2014; George et al., 2020).

With respect to point I, the aim of this PhD was the participation in the development and characterisation of the PeRCEAS instrument, the preparation and conducting of measurements during the airborne campaigns of the EMeRGe (Effect of Megacities on the transport and transformation of pollutants on the Regional and Global scales) project

taking place in Europe in 2017 and in East Asia in 2018 (www.iup.uni-bremen.de/emerge) (Andrés Hernández et al., 2022; George, 2022).

II.   CRDS in the study of Rayleigh scattering cross-sections

The CRDS has been recently used for the accurate determination of the wavelength-dependent Rayleigh scattering cross-section, $\sigma_{Rayl.}(\lambda)$, of different molecules in the UV and UV-VIS (Naus and Ubachs, 2000; Sneep and Ubachs, 2005; Ityaksov et al., 2008; Thalman et al., 2014, 2017). Using the knowledge of the gas refractive index, n, and the correction of the depolarisation known as the King correction factor, F_k, $\sigma_{Rayl.}$ of gas molecules can be calculated. This calculation is normally referred to as n-based calculation or $\sigma_{Rayl.}$ for a n-value.

In the investigation at IUP-Bremen, CRDS measurements of the target molecule NO_2 were conducted to determine its change in concentration, as a result of the chemical amplification. Measurements of the extinction of NO_2 and the absorption cross-section for NO_2 determined as part of the PeRCEAS calibration (George, 2022) were consistent with scattering by NO_2 having a negligibly small error on the determination of NO_2 concentration. From the literature (e.g. Vandaele, 2002), the Rayleigh scattering cross-section $\sigma_{Rayl.}$ n-value for most gases at 408 nm is typically several orders of magnitude smaller than the absorption cross-section of NO_2. This implies that any interference of the PeRCEAS measurement by changing the mixture of gases during the chain reaction in the air sampled would be negligible. However, due to the wavelength dependency of n and F_k, both parameters are usually determined experimentally at specific wavelength ranges and then extrapolated to particular wavelength ranges. In some cases, the extrapolated $\sigma_{Rayl.}$ values have been shown to have significant inaccuracies (Wilmouth and Sayres, 2019, 2020; He et al., 2021).

As part of the verification of the PeRCEAS instrument, the extinction of the flowing mixtures used in PerCEAS inflight measurements (typically 9 % carbon monoxide, CO, and 9 % nitrogen, N_2, in synthetic air, SA (see further details in section 4.10) at 408 nm were compared in the laboratory. The high sensitivity of the CRDS detectors in PeRCEAS enabled the difference in the extinction to be measured for the two mixtures of gases. The difference between the two extinction decay times was $\sim$ 4 times higher than the noise of the ring-down time signal. Since CO, N_2, and SA do not absorb at this wavelength, the extinction must be dominated by the scattering of the three molecules. The results of these experiments thus indicated that scattering by NO_2, as expected, has a negligible impact on the determination of NO_2 concentrations and that the CRDS detector is suitable for the determination of the $\sigma_{Rayl.}$ for atmospheric gases, which do not absorb at 408 nm.

In the literature, the values available for many atmospheric gases are extrapolations from measurements at shorter or longer wavelengths. At the start of this PhD, there were no experimental data for the CO scattering cross section in the blue spectral region.

With respect to point II, the goal of this PhD was the experimental determination of $\sigma_{Rayl.}$ for a set of atmospheric molecules at 408 nm, as discussed in Chapter 4, to analyse the extent of potential interferences when gas mixtures in the PeRCEAS were changed, potentially affecting the accuracy of PeRCEAS measurements.

III. Measurements of PeRCEAS during airborne campaigns and comparison with model simulations

Before EMeRGe, IUP-Bremen participated with the PeRCEAS measurements in the airborne campaign of the OMO (Oxidation Mechanism Observations, https://www.mpic.de/3599603/OMO) project (Lelieveld et al., 2018). Most of the measurements were carried out in the upper troposphere. From the simultaneous HO_2 measurements and comparison with EMAC model calculations by other groups the assumed 1:1 HO_2 to RO_2 ratio for the PeRCEAS retrieval in the air masses sampled in the lower troposphere was confirmed (George, 2022).

To assess the current understanding of the production and loss of the RO_2^* in the air masses observed during the EMeRGe campaigns, atmospheric models simulating the RO_2^*, were planned.

With respect to point III, the goal of the present PhD was to contribute to the retrieval and analysis of RO_2^* measurements following the completion of the campaigns and to evaluate the performance of the RO_2^* available simulations within EMeRGe in reproducing the measurements.

Research objectives

From the considerations above, the research objectives of this doctoral research are summarised as follows:

1. The experimental study of the Rayleigh scattering cross-section, $\sigma_{Rayl.}$, of atmospheric gases at 408 nm. The gases nitrogen, N_2, oxygen, O_2, synthetic air, SA, argon, Ar, carbon monoxide, CO, carbon dioxide, CO_2, nitrous oxide, N_2O and methane, CH_4 are selected for the experiments. The following tasks have to be undertaken to achieve this objective:

   - Design, installation, and characterisation of CRDS setups required to determine $\sigma_{Rayl.}$;
   - Undertaking of the measurements to determine $\sigma_{Rayl.}$;
   - Determination of the accuracy and reproducibility of the experiments by using different procedures (step pressure changes and continuous pressure changes);

- Comparison of $\sigma_{Rayl.}$ values at 408 nm for the gases, listed above, with literature values and assessment of any consequences for PeRCEAS measurements.

2. Acquisition of an accurate data set of airborne RO_2^* from the measurements of air masses made during the EMeRGe project in Europe and East Asia. The following tasks have to be undertaken to achieve this objective:

   - Participation in further development and characterisation of PeRCEAS for the airborne measurement of RO_2^* before and after the EMeRGe campaigns;
   - Participation in the deployment and maintenance of PeRCEAS on HALO during the EMeRGe campaigns;
   - Participation in the retrieval of the RO_2^* measurements from the PeRCEAS measurements.

3. The investigation of the capabilities of state-of-the-art models to predict the RO_2^* airborne measurements made during the EMeRGe campaigns. The following tasks were undertaken to achieve this objective:

   - Selection of suitable atmospheric models and relevant PSS calculations;
   - Selection of case studies for comparison among modelled, calculated, and measured RO_2^* made during the EMeRGe campaign;
   - Acquisition of results from atmospheric models and calculations of RO_2^* through cooperation with other scientists involved in the EMeRGe project;
   - Preparation of data for RO_2^* and chemical precursors for comparison;
   - Analysis and interpretation of similarities and differences between measurements and simulations.

Furthermore, the presentation and publication of results in scientific congresses and peer-reviewed journals is an overall objective of the work.

2 Relevant experimental and theoretical background

In this chapter, fundamental physical and chemical knowledge of relevance to the scientific objectives of this doctoral research is provided.

2.1 EM radiation scattering

The scattering of EM radiation occurs as a result of the interaction of atoms and molecules with photons. As a result of the inhomogeneity of materials, fluctuation in the optical properties of the material medium, specifically the refractive index also causes scattering. When the EM radication passes from one medium to another, it is refracted. In Figure 1, an example of a homogeneous piece of material is illuminated by plane waves. If the volume dV_1 scatters EM radiation with an angle of ϑ, then all the other directions of EM radiation scattered by volume dV_2 (where ϑ is not 0) will have a destructive inference with the EM radiation field of dV_1. Since the material is completely homogeneous, all volumes in the material dV would have the same scatter behaviour, aka. only scattering in the forward direction can occur, i.e. the coherent forward scattering which is the origin of the index of refraction.
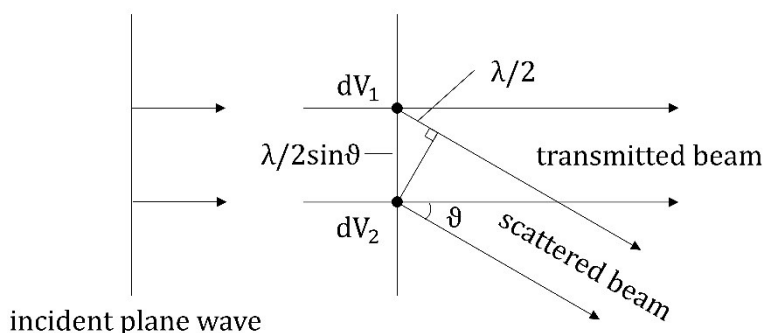
Figure 1: EM radiation scattering cannot occur in completely homogeneous matter (Boyd, 2008).

Generally, when an incident beam interacts with a medium, the EM radiation is partially absorbed and partially scattered by the medium particles. When the incident EM radiation's electric field interacts with molecules, it can induce oscillating electric dipoles within the molecules. The induced dipoles will radiate, triggering a secondary EM radiation field. The position of molecules is not correlated, the secondary wave of the various particles cannot interfere with one another and the intensities may be added directly. The strength of scattering depends on the wavelength of the EM radiation and the size of the particles. The probability of scattering is inversely proportional to λ^4 where λ is the wavelength of the EM radiation. The EM radiation scattering and in general the EM scattering can be elastic, i.e. that does not gain or lose energy during the scattering and therefore remains at the same λ (e.g. Rayleigh and Mie scattering), or inelastic such as the Raman, Compton and Brillouin scattering.

Raman scattering results from the interaction of EM radiation with the vibrational modes of the molecules constituting the scattering medium. Raman scattering can equivalently be described as the scattering of EM radiation from optical phonons. Brillouin scattering

is the scattering of EM radiation from sound waves, that is, from propagating pressure (and thus density) waves. Brillouin scattering can also be considered as the scattering of EM radiation from acoustic phonons. Rayleigh scattering (or Rayleigh-centre scattering) is the scattering of EM radiation from no propagating density fluctuations. Formally, it can be described as scattering from entropy fluctuations. (Boyd, 2008)

2.1.1 Rayleigh scattering

Lord Rayleigh explained why the sky is blue and why the sunset is red in his famous paper of 1899 (Rayleigh, 1899). He used the theory of electromagnetism to show that the scattering of molecules alone was sufficient to explain the observed brightness of the sky. Lord Rayleigh derived a frequency-dependent expression for the total scattering cross-section of a molecule as a function of the refractive index, molecular gas density and a factor that considers non-spherical molecules. Later on, with the development of the theory, two corrections were applied to the original expression. First, the correction for the local field effect which is known as the Lorentz-Lorenz correction (Lorenz, 1869; Lorentz, 1878; Jackson, 1998) and second, the correction related to the non-spherical molecules and the effect of depolarisation. This was studied by Strutt (Strutt R.J., 1918, 1920) and later introduced by King as a correction factor for the cross-section values, the so-called King correction factor (King, 1923).

According to the theory, the Rayleigh scattering of the molecules is expected to be significantly smaller than their absorption. Consequently, the extinction of EM radiation because of Rayleigh scattering in regions where there is no absorption is also very small. The detection and investigation of Rayleigh scattering in the laboratory were difficult before the measurements made by Naus and Ubachs, 2000, which directly from extinction.

Rayleigh scattering by gas phase molecules is an adequate approximation for wavelengths of incident EM radiation, which are much larger than the size of particles. This is because the electric field of the incident EM radiation is assumed to be homogeneous relative and not disturbed by the presence of the molecule. Therefore, the dipole secondary radiate may be applied. That means if the particle size is larger, the scattering will have to include higher-order multipole terms for triggering the secondary EM radiation field. To describe the Rayleigh scattering, both the radiation of the oscillating dipole and the magnitude of the induced dipole is needed.

The oscillating electric dipole radiation is described in classic electrodynamic theory (Jackson, 1998):

$$I_{rad}(\vartheta') = \left(\frac{\omega^4}{32\varepsilon_0\pi^2 c^3} p_{max}^2 \right) sin^2 \vartheta' \qquad\qquad E\,2\text{-}1$$

Where $I_{rad}(\vartheta')$ is the intensity distribution of the emitted radiation by a dipole, ϑ' is the angle between the axis of the dipole and the direction of observations, ω is the angular

frequency of the radiation, p_{max} is the maximum value of the dipole and ε_0 is the permittivity of a vacuum. Permittivity is a measure of the electric polarisability of a dielectric. Therefore, the permittivity of a vacuum is defined as the absolute dielectric permittivity of a classical vacuum. As shown in Figure 2, the intensity distribution of dipole radiation, in the direction of the dipole axis is zero.
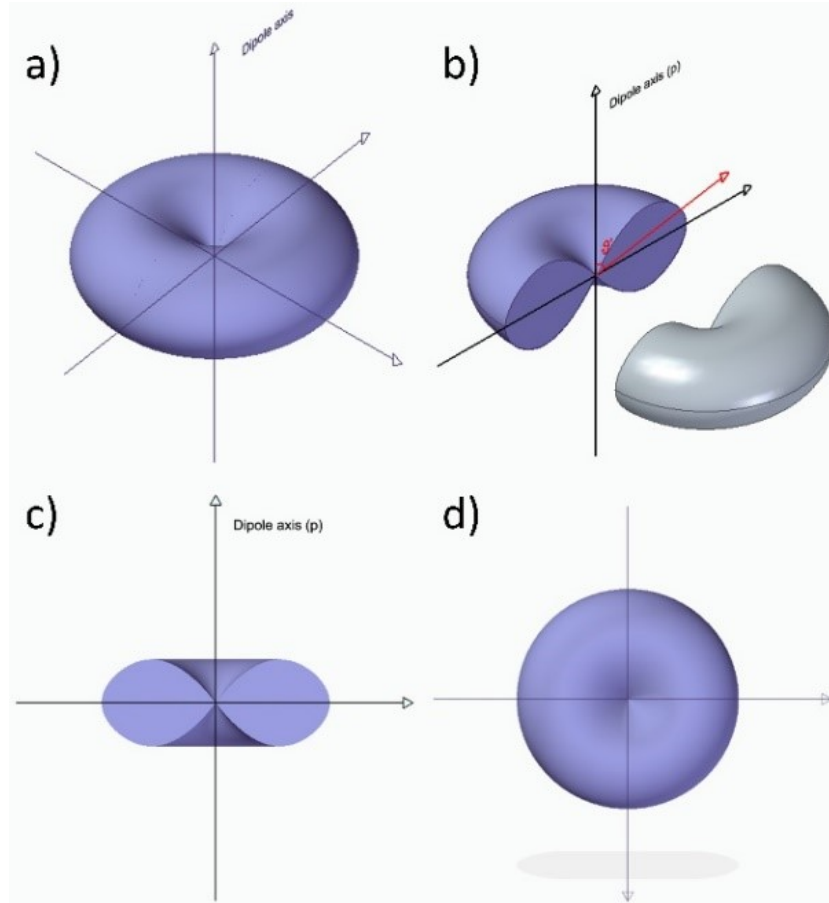
Figure 2: 3D model for the intensity distribution of dipole radiation a) in the coordinate system; b) the vertical section along the dipole axis; c) the intensity distribution in the plane of the dipole (side); d) the intensity distribution in the plane perpendicular to the dipole (top).

The total power which is radiated by the dipole is obtained by integrating the intensity distribution over all directions:

$$P_{rad} = (\frac{\omega^4}{32\varepsilon_0\pi^2c^3}p_{max}^2)\int_{\varphi=0}^{2\pi}\int_{\vartheta'=0}^{\pi}sin^3\,\vartheta'd\vartheta'd\varphi = \frac{1}{4\pi\varepsilon_0}\frac{\omega^4}{3c^3}p_{max}^2 \qquad E\,2\text{-}2$$

For linear dielectric matter, the macroscopic polarisation P induced in a matter by a field E is given by:

$$P = \varepsilon_0\chi_e E \qquad\qquad E\,2\text{-}3$$

where E is the macroscopic field, χ_e is the electric susceptibility (which is a dimensionless proportionality constant that indicates the degree of polarisation of dielectric material in

response to an applied electric field), and ε_0 is the electric permittivity in vacuum. The induced dipole for a single particle at a linear matter at microscopic perspective is:

$$p = \alpha_{SI} E_{local}$$
$$E\ 2\text{-}4$$

E_{local} is then the electric field of the particle, here including the influence of nearby induced dipoles. α_{SI} is the molecular polarisability in S.I. units $[F \cdot m^2]$. Volume polarisability is often used with the dimension of volume (Hohm and Kerl, 1990):

$$\alpha_{vol} \equiv \frac{\alpha_{SI}}{4\pi\varepsilon_0}$$
$$E\ 2\text{-}5$$

For a less dense medium, the effect from nearby particle dipoles may be ignored, therefore the macroscopic polarisation is given as $P = pN = \alpha_{SI} E_{local} N$, where N is the number concentration in m^{-3}. Then, the molecular polarisability α_{SI} can be rewritten as $\alpha_{SI} = \varepsilon_0 \chi_e / N$. Since the electric permittivity is $\varepsilon = \varepsilon_0 (1 + \chi_e)$, α_{SI} can be rearranged as:

$$\alpha_{SI} = \frac{\varepsilon_0}{N}\left(\frac{\varepsilon}{\varepsilon_0} - 1\right) = \frac{\varepsilon_0}{N}(n^2 - 1)$$
$$E\ 2\text{-}6$$

The speed of EM wave propagation is $c = \frac{1}{\sqrt{\varepsilon\mu}}$, where μ is the electric permeability. Then the speed of an EM wave in a vacuum, c_0, over the speed of an EM wave in a medium, c_m, is the refractive index $n = \frac{c_0}{c_m}$. The magnetic susceptibility (χ_e) is very small in the case of optical frequencies, i.e. $\varepsilon = \varepsilon_0$. The electric permeability μ will be the same in a vacuum and a medium.

The Lorentz-Lorenz relation for molecular polarisability is required to include the influence of the nearby particles.

$$\alpha_{SI} = \frac{3\varepsilon_0}{N}\left(\frac{n^2 - 1}{n^2 + 2}\right)$$
$$E\ 2\text{-}7$$

Since for most of the gases $n \approx 1$, the error made by this approximation is proven to be small, for example in the air α (polarisability per particle) has an error of about 0.05 % (Bucholtz, 1995).

2.1.2 Scattering cross-section

The relationship between the intensity of the incident radiation and its electric field:

$$I_{inc.} = \frac{1}{2} c\varepsilon_0 E_{max}^2$$
$$E\ 2\text{-}8$$

Combining equations E 2-4, E 2-7, and E 2-8 leads to the induced dipole p_{max}.

$$p_{max} = \frac{3\varepsilon_0}{N}\left(\frac{n^2-1}{n^2+2}\right)\sqrt{\frac{2I_{inc.}}{c\varepsilon_0}}$$

E 2-9

The power of the EM radiation scattered from a single particle at an EM radiation field with an intensity of $I_{inc.}$, i. e. P_{sc} can be calculated by inserting p_{max} into E 2-2:

$$P_{sc} = I_{inc.}\frac{3}{2\pi}\frac{\omega^4}{c^4}\frac{1}{N^2}\left(\frac{n^2-1}{n^2+2}\right)^2$$

E 2-10

The surface area σ receives the same power which is scattered by particles. This is known as scattering cross-section, aka. $\sigma = P_{sc}/I_{inc.}$:

$$\sigma = \frac{3}{2\pi}\frac{\omega^4}{c^4}\frac{1}{N^2}\left(\frac{n^2-1}{n^2+2}\right)^2 = \frac{24\pi^3}{\lambda^4 N^2}\left(\frac{n^2-1}{n^2+2}\right)$$

E 2-11

Where $\omega = 2\pi v = \frac{2\pi c}{\lambda}$, N in [molecule $\cdot$ m^{-3}], λ in [m]. This gives the scattering cross-section the unit of [m$^2 \cdot$ molecule^{-1}]. Since the refractive index n depends on the wavelength of the driving EM radiation, the refractive index is a collective effect and the Lorentz-Lorenz relation E 2-7 shows the molecular polarisability for a single molecule, the equation E 2-11 is independent of the density and could be rewritten (using E 2-5 and E 2-7) in terms of the molecular volume polarisability:

$$\sigma = \frac{128\pi^5\alpha_{vol}^2}{3\lambda^4}$$

E 2-12

α_{vol} has the unit [m^3] and λ has the unit in [m]. It is clear that in E 2-12 the scattering cross-section is independent of the density of the molecules.

The theoretical calculation of the Rayleigh scattering cross-section σ_λ based on the refractive index of the gas at a given wavelength λ is given by (Rayleigh, 1899; Strutt R.J., 1920; King, 1923; Owens, 1967; Bates, 1984; Bucholtz, 1995):

$$\sigma_\lambda = \frac{24\pi^3}{\lambda^4 N^2}\left(\frac{n_\lambda^2-1}{n_\lambda^2+2}\right)F_K(\lambda)$$

E 2-13

where λ is the wavelength of EM radiation, N is the number density of the gas, n_λ is the wavelength-dependent refractive index, and $F_K(\lambda)$ is the King correction:

$$F_K(\lambda) = \frac{6+3\rho_n(\lambda)}{6-7\rho_n(\lambda)} = \frac{3+6\rho_p(\lambda)}{3-4\rho_p(\lambda)}$$

E 2-14

where $\rho_n(\lambda)$ and $\rho_p(\lambda)$ are the depolarisation ratio for natural EM radiation and polarised EM radiation at the given wavelength.

2.2 Cavity Ring-Down Spectroscopy (CRDS)

2.2.1 Principle of the Cavity Ring-Down Spectroscopy (CRDS) technique

The principle of cavity ring-down spectroscopy is based on the measurement of the rate of decay of laser EM radiation in an optical resonator with a long lifetime of photons (Demtröder, 2014). Optical resonators also named optical cavities have been used in many forms for spectroscopy, commonly as an analysis method of determining the wavelength of resonant EM radiation. Herbelin et al. (1980) brought the idea of using the rate of decay of a finesse cavity for optical measurements which was applied to the measurement of mirror reflectivity. The connection between the extinction of EM radiation in the cavity and the absorption by molecules was later made by O'Keefe and Deacon (O'Keefe and Deacon, 1988), who developed cavity ring-down spectroscopy (CRDS). Since then, CRDS methods have been applied to different absorption ranges from around 200 nm to 10µm by using various excitation and detection setups (Berden et al., 2000; van Zee and Looney, 2002; Wheeler et al., 1998). The principle of CRDS is described as follows. A laser pulse of short duration is redirected into a stable but non-confocal cavity which consists of (at least) two highly reflecting (R > 99.9 %) concaved mirrors. The majority of the incident laser pulse will be reflected out of the cavity, and a small fraction (1 - R) of the power will enter the cavity for the first round. Inside the cavity, at each mirror, a small fraction (1 - R) of the circulating power will be coupled out, while the remaining fraction is reflected back into the cavity. The first pulse leaking out of the cavity will have an intensity:

$$I_0 = (1 - R^2)I_{in} \qquad \qquad E\ 2\text{-}15$$

The xth pulse has the intensity:

$$I_x = I_0 R^{2(x-1)} = I_0 e^{(2(x-1)lnR)} \qquad \qquad E\ 2\text{-}16$$

This intensity will leak out of the cavity after the laser pulse in $\frac{2d(x-1)n}{c}$ seconds, where d is the length of the cavity, n is the refraction index and c is the speed of EM radiation. The data acquisition system has a response time that will give discrete pulses to blend into a continuous signal as a function of time t:

$$I_t = I_0 e^{(-\frac{c}{d}|lnR|t)} \qquad \qquad E\ 2\text{-}17$$

The decay rate between each pulsed EM radiation for an empty cavity cell β_λ^0 or the decay time:

$$\tau_\lambda^0 = 1/\beta_\lambda^0 \qquad \qquad E\ 2\text{-}18$$

is the background signal of cavity ring-down measurement. β_λ^0 is determined by the cavity mirror reflectivity and the length of the cavity that is dependent on the wavelength of the EM radiation:

$$\beta_\lambda^0 = \frac{c}{d}|lnR_\lambda| \qquad\qquad E\ 2\text{-}19$$

Additional losses inside the cavity result in a faster decay rate, caused by the attenuation of the EM radiation (absorption and scattering) on molecules. Any gas will cause extinction through Rayleigh scattering, the total extinction (κ_λ) is the sum of the loss through absorption (α_λ) and the loss through scattering ($\alpha_\lambda^{scat.}$). For the total extinction:

$$\kappa_\lambda = \alpha_\lambda^{absorp.} + \alpha_\lambda^{scat.} = N(\sigma_\lambda^{absorp.} + \sigma_\lambda^{scat.}) \qquad\qquad E\ 2\text{-}20$$
$$\sigma_\lambda^{tot.} = \sigma_\lambda^{absorp.} + \sigma_\lambda^{scat.} \qquad\qquad E\ 2\text{-}21$$

According to the Beer-Lambert law, the extinction in a medium is expressed as the extinction over distance. In a first approximation, this can be rewritten as extinction over time, neglecting the refractive index:

$$I_z = I_0e^{(-\kappa_\lambda z)} = I_0e^{(-N\sigma_\lambda^{tot.}z)} \equiv I_0e^{(-\kappa_\lambda ct)} = I_0e^{(-N\sigma_\lambda^{tot.}ct)} \qquad\qquad E\ 2\text{-}22$$

If the additional losses (absorption of EM radiation and Rayleigh scattering on molecules) also follow the Beer-Lambert law, the decay will remain exponential over time. Then the total losses can be combined:

$$I_t = I_0e^{(-\frac{c}{d}(|lnR_\lambda|+N\sigma_\lambda l)t)} \qquad\qquad E\ 2\text{-}23$$

l is the length inside the cavity filled with absorbing molecules, σ_λ is the wavelength-dependent cross-section. The decay rate of the ring-down signal with (β_λ) or without (β_λ^0) the presence of additional absorbers, is given by:

$$\beta_\lambda = \frac{c}{d}(|lnR_\lambda| + N\sigma_\lambda l) \qquad\qquad E\ 2\text{-}24$$
$$\beta_\lambda^0 = \frac{c}{d}|lnR_\lambda| \qquad\qquad E\ 2\text{-}25$$

Assuming that the absorber fills the entire cavity ($l = d$), it is possible to derive a simple equation combining E 2-24 and E 2-25, which represents the extinction in terms of cavity decay rates:

$$N\sigma_\lambda = \frac{\beta_\lambda - \beta_\lambda^0}{c} \qquad\qquad E\ 2\text{-}26$$

2.2.2 Advantages and limitations of CRDS

For CRDS in general, a typical ring-down cavity is a stable, linear resonator with two identical mirrors. The geometry stability criterion must be fulfilled by the cavity (Kogelnik and Li, 1966):

$$0 < \left(1 - \frac{d}{R_c}\right)^2 < 1 \qquad\qquad\qquad E\ 2\text{-}27$$

Where d is the length of the cavity, R_c is the radius of the curvature of the mirrors. A stable cavity means the EM radiation remains close to the centre of the cavity while the beam enters along its axis. According to E 2-27, the equation could be rewritten as $0 < d < 2R_c$, the length becomes the criterion for a stable cavity.

As shown in E 2-26, the determination of the extinction cross-section from the known concentration of molecules (or vice versa) does not depend on the intensity of the EM radiation and all the information is obtained from the decay rate (or loss rate), β_λ, which is basically the ring-down time, τ_λ. Thus, CRDS is independent of the fluctuations of the EM radiation source. A long effective path length can be created by using high reflectivity mirrors up to 99.999%. In such a way, a cavity of 80 cm in length can lead up to 100 km effective path length. The very long effective path length ensures a very high sensitivity making it possible to detect weak absorption in the range of $2 \times 10^{-9} \text{cm}^{-1}$ (Naus et al., 1997).

In summary, the CRDS technique enables high sensitivity with very small cavity volumes. This makes the technique particularly suitable for volume-constrained measurement setups.

However, the use of CRDS still faces limitations for the determination of the absolute cross-sections of narrow line features. The decay rate of the EM radiation inside the cavity should ideally obey the Beer-Lambert law and be exponential. Then considering the decay of EM radiation purely depends on the cavity mirrors (see E 2-23), this will lead to a mono-exponential decay in a cavity filled with gas. If the decay function is not exponential in reality, the decay rate, β_λ, cannot be derived from the fitting procedure. In addition, it is very challenging to obtain mathematically a fitting procedure for a random sum of exponentials. A multi-exponential decay could be caused by different mechanisms, one of the most common being laser bandwidth-induced effects. As shown in Figure 3 when the bandwidth of the exciting laser is not negligible to the width of the spectral line of a molecule, the various wavelength components within the bandwidth profile are subject to different rates of absorption. The frequency components will then produce a sum of exponentials. Then the overall non-exponential decay is:

$$I_t = \int_\lambda I_\lambda e^{(-\beta_\lambda t)} d\lambda \qquad\qquad\qquad E\ 2\text{-}28$$
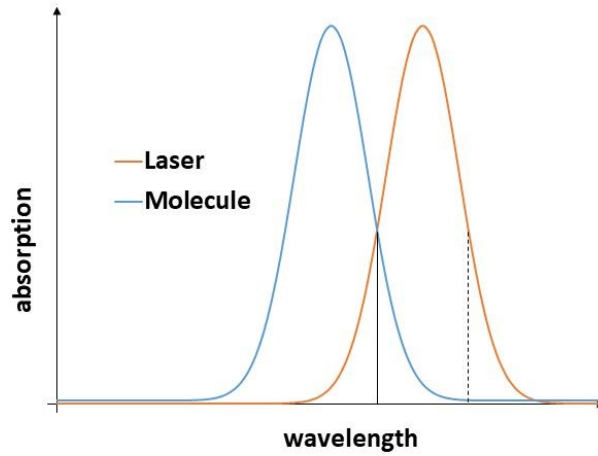
Figure 3: Example of a multi-exponential decay in CRDS.

This effect is common in spectroscopy and called "slit-function". In the case of CRDS, the correction is especially complex because of its non-linear properties. This problem has been noted in the literature (Jongma et al., 1995; Zalicki and Zare, 1995; Hodges et al., 1996; van Zee et al., 1999). If both the laser profile and the absorption profile have a Gaussian shape, the shift of bandwidth does not affect the integrated intensity ($\int_\lambda \sigma_\lambda d\lambda$). Even so, the peak absorption is underestimated and the result is sensitive to the laser line shape. Therefore, the invariance from the assumption is not of practical use.

2.2.3 Retrieval of the Rayleigh scattering cross-section from CRDS

The extinction coefficient, $\alpha(\lambda)$, in an optical cavity is defined as:

$$\alpha(\lambda) = \frac{N}{V} \times \sigma(\lambda) = \frac{n(\lambda)}{c_0} \times \left(\frac{1}{\tau(\lambda)} - \frac{1}{\tau_0(\lambda)} \right) \qquad \text{E 2-29}$$

where $\frac{N}{V}$ is the gas number density [$\text{molec.} \cdot \text{cm}^{-3}$], λ is the wavelength, $\sigma(\lambda)$ is the extinction cross-section [$\text{cm}^2 \cdot \text{molec.}^{-1}$] at the wavelength λ, $n(\lambda)$ is the refractive index of the molecule, c_0 is the speed of EM radiation in vacuum, $\tau(\lambda)$ and $\tau_0(\lambda)$ are the cavity ring-down times of the filled and the empty cavity, respectively. In the absence of absorption, it is assumed that $\sigma(\lambda) = \sigma_{\text{Rayl.}}(\lambda)$. Rearranging E 2-29 leads to:

$$\frac{1}{\tau} = \sigma_{Rayl.}(\lambda) \cdot \frac{c_0}{n} \cdot \frac{N}{V} + \frac{1}{\tau_0} \qquad \text{E 2-30}$$

where τ is measured by CRDS, $\frac{N}{V}$ can be calculated from the measured temperature and pressure of the cavity, and n is close to 1 for most gases. σ_λ can be retrieved from the slope of the number concentration of molecules as a function of the decay rate (inverse of the ring-down time, τ).

2.3 Peroxy radicals in the troposphere

The peroxy radicals in the atmosphere comprise hydroperoxyl radicals, HO_2, and organic peroxy radicals, RO_2, where R stands for an organic group. They are reactive species that play an important role in the chemistry of the atmosphere. For the research presented in this dissertation, the role of peroxy radicals in the troposphere is the main focus, but above the tropopause, they also participate in catalytic cycles which deplete the ozone in the stratosphere and the mesosphere.

Peroxy radicals are produced by photochemical and chemical reactions which oxidise CO, CH_4, and volatile organic compounds, VOC, which include non-methane hydrocarbons, NMHC and oxygenated NMHC (e.g. alcohols, aldehydes and, organic acids) emitted into the troposphere.

Examples of oxidising agents in the troposphere are OH, O_3, halogen atoms (chlorine, Cl, bromine Br, and iodine, I) and at night the nitrate radical, NO_3. The most important is the hydroxyl radical, OH, which is produced as follows. The photolysis of O_3 in the troposphere occurs at wavelengths below 1180 nm. At longer wavelengths the ground state of oxygen atoms $O(^3P)$ and molecules $O_2(X^3\Sigma_g^-)$ are produced. However, in the ultraviolet spectral region excited oxygen atom $O(^1D)$ is produced. In the UVA region from 310 to 411 nm, the quantum yield for the production of $O(^1D)$ in the photolysis of O_3 is small ~ 0.04, but in the UVB region from 280 to 310 nm, it is around 0.9. (Matsumi and Kawasaki, 2003)

$$O_3 \xrightarrow{h\nu \ (\lambda < 1180 \ nm)} O(^3P) + O_2(X^3\Sigma_g^-) \qquad\qquad R\ 2\text{-}1$$

$$O_3 \xrightarrow{h\nu \ (310 < \lambda < 411 \ nm)} O(^1D) + O_2(X^3\Sigma_g^-) \qquad\qquad R\ 2\text{-}2$$

$$O_3 \xrightarrow{h\nu \ (280 < \lambda < 310 \ nm)} O(^1D) + O_2(a^1\Delta_g) \qquad\qquad R\ 2\text{-}3$$
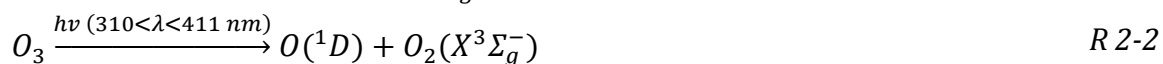
In the troposphere, once $O(^1D)$ is formed there is a competition between quenching by nitrogen N_2 and oxygen O_2 molecules and its reaction with H_2O to produce OH:

$$O(^1D) + N_2 \rightarrow O + N_2 \qquad\qquad R\ 2\text{-}4$$

$$O(^1D) + O_2 \rightarrow O + O_2 \qquad\qquad R\ 2\text{-}5$$

$$O(^1D) + H_2O \rightarrow 2OH \qquad\qquad R\ 2\text{-}6$$

OH is removed by its rapid reaction with CO, CH_4 and NMHC. The reaction of OH with CO in the presence of O_2 produces HO_2 and CO_2. The reaction between CO and OH is complex. This reaction is considered to proceed via the generation of an activated HOCO* intermediate, which can dissociate to HO + CO or H + CO_2, and be collisionally stabilised to yield thermalised HOCO. The H atoms and HOCO react rapidly to form HO_2 and CO_2:

$$OH + CO \rightleftharpoons HOCO^* \qquad\qquad R\ 2\text{-}7$$

$$HOCO^* \rightarrow H + CO_2 \qquad\qquad R\ 2\text{-}8$$

$$HOCO^* \xrightarrow{M} HOCO \qquad\qquad\qquad R\ 2\text{-}9$$
$$HOCO + O_2 \rightarrow HO_2 + CO_2 \qquad\qquad\qquad R\ 2\text{-}10$$
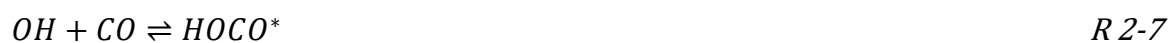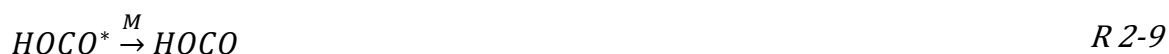
As these reactions are fast, this can be considered as a bimolecular reaction in the presence of O_2 (Demore, 1984; Miyoshi et al., 1994).

$$HO + CO \xrightarrow{O_2} HO_2 + CO_2 \qquad\qquad\qquad R\ 2\text{-}11$$

The sum of HO_2, RO_2, OH, and RO is often referred to as RO_2^* in relation to measurement techniques which do not speciate these radicals.

RO_2^* influence the equilibrium cycle between the NO and NO_2 and actively participate in the catalytic cycles responsible for both the production and depletion of ozone in the troposphere. In tropospheric chemistry, the photolysis of NO_2 is the only known source of the tropospheric ozone, $O(^3P)$ produced from NO_2 photolysis reacts with O_2 and produces O_3. The NO produced from the NO_2 photolysis react with O_3 and produce NO_2. The NO and NO_2 reach a quasi-stationary equilibrium due to the fast reaction cycle. The amount of O_3 does not change in the absence of peroxy radicals, i.e. there is an ozone null cycle:

$$NO_2 \xrightarrow{h\nu\ (\lambda<420\ nm)} O(^3P) + NO \qquad\qquad R\ 2\text{-}12$$
$$O(^3P) + O_2 \xrightarrow{M} O_3 \qquad\qquad\qquad R\ 2\text{-}13$$
$$NO + O_3 \rightarrow NO_2 + O_2 \qquad\qquad\qquad R\ 2\text{-}14$$

In the presence of peroxy radicals, they react with NO and for conditions where $[NO] \cdot k(HO_2 + NO) > [O_3] \cdot k(HO_2 + O_3)$, NO_2 is produced:

$$HO_2 + NO \rightarrow OH + NO_2 \qquad\qquad\qquad R\ 2\text{-}15$$
$$RO_2 + NO \rightarrow RO + NO_2 \qquad\qquad\qquad R\ 2\text{-}16$$

The extra NO_2 produced changes the NO to NO_2 ratio and eventually results in O_3 production through R 2-12 and R 2-13.

For other conditions where $[NO] \cdot k(HO_2 + NO) < [O_3] \cdot k(HO_2 + O_3)$, RO_2^* react with ozone leading to ozone depletion:

$$HO_2 + O_3 \rightarrow OH + 2O_2 \qquad\qquad\qquad R\ 2\text{-}17$$
$$RO_2 + O_3 \rightarrow RO + 2O_2 \qquad\qquad\qquad R\ 2\text{-}18$$
$$OH + O_3 \rightarrow HO_2 + O_2 \qquad\qquad\qquad R\ 2\text{-}19$$

RO_2^* are produced in the troposphere and lower stratosphere mainly through:

1. The oxidation of CO with OH is shown in R 2-11.
2. The oxidation of CH_4 with OH:

$$OH + CH_4 \rightarrow CH_3 + H_2O \qquad\qquad R\,2\text{-}20$$
$$CH_3 + O_2 \xrightarrow{M} CH_3O_2 \qquad\qquad R\,2\text{-}21$$

3. The oxidation of aldehydes with OH, e.g. HCHO:

$$OH + HCHO \rightarrow CHO + H_2O \qquad\qquad R\,2\text{-}22$$
$$CHO + O_2 \rightarrow HO_2 + CO \qquad\qquad R\,2\text{-}23$$

4. The oxidation of peroxides with OH, e.g. H_2O_2 and CH_3O_2H:

$$OH + H_2O_2 \rightarrow HO_2 + H_2O \qquad\qquad R\,2\text{-}24$$
$$OH + CH_3O_2H \rightarrow CH_3O_2 + H_2O \qquad\qquad R\,2\text{-}25$$

5. Photolysis of aldehydes, e.g. HCHO:

$$HCHO \xrightarrow{h\nu\ (<340\ nm)} H_2 + CO \qquad\qquad R\,2\text{-}26$$
$$H_2 + OH \rightarrow H_2O + H \qquad\qquad R\,2\text{-}27$$
$$H + O_2 \xrightarrow{M} HO_2 \qquad\qquad R\,2\text{-}28$$
$$HCHO \xrightarrow{h\nu\ (<340\ nm)} H + CHO \qquad\qquad R\,2\text{-}29$$

The products from R 2-29 will then follow R 2-28 and R 2-23 to produce HO_2.

6. The ozonolysis of alkenes, e.g. C_2H_4 (Kan et al., 1981):

$$C_2H_4 + O_3 \rightarrow CH_2OOOCH_2 \qquad\qquad R\,2\text{-}30$$
$$CH_2OOOCH_2 \rightarrow HCHO + CH_2OO' \qquad\qquad R\,2\text{-}31$$

CH_2OO' is called the "Criegee intermediate", and will go through complex pathways of decomposition forming H, HCHO, and OH with a total radical yield of ~ 0.45 (Atkinson and Aschmann, 1993; Paulson and Orlando, 1996).

7. The oxidation of organic species (RH) by the nitrate radical (NO_3) which is a significant radical source during night-time (Platt et al., 1981; Heikes and Thompson, 1983; Wayne et al., 1991; Heintz et al., 1996; Geyer et al., 2001; Geyer et al., 2003):

$$NO_3 + RH \rightarrow HNO_3 + R \qquad\qquad R\,2\text{-}32$$
$$R + O_2 \xrightarrow{M} RO_2 \qquad\qquad R\,2\text{-}33$$

The sinks of peroxy radicals are mainly the following:

1. The direct radical-radical reactions of HO_2 and RO_2 leading to non-radical productions (e.g. CH_3O_2):

$$HO_2 + OH \rightarrow H_2O + O_2 \qquad\qquad R\,2\text{-}34$$

$$HO_2 + HO_2 \xrightarrow{M} H_2O_2 + O_2 \qquad\qquad R\,2\text{-}35$$

$$HO_2 + CH_3O_2 \rightarrow CH_3O_2H + O_2 \qquad\qquad R\,2\text{-}36$$

$$CH_3O_2 + CH_3O_2 \rightarrow 2CH_3O + H_2O \qquad\qquad R\,2\text{-}37$$

The peroxides produced from R 2-35 and R 2-36 might be washed out of the troposphere leading to RO_2^* loss or get oxidised by OH through R 2-24 and R 2-25, leading to RO_2^* formation. The photolysis of peroxides produces OH and RO_2^* precursor, which leads to the production of RO_2^*.

$$H_2O_2 \xrightarrow{h\nu} 2OH \qquad\qquad R\,2\text{-}38$$

$$CH_3O_2H \xrightarrow{h\nu} HCHO + H + OH \qquad\qquad R\,2\text{-}39$$

$$H + O_2 \xrightarrow{M} HO_2 \qquad\qquad R\,2\text{-}40$$

2. The reaction of the OH produced from R 2-15, R 2-17, R 2-38, R 2-39 with NO and NO_2:

$$OH + NO \xrightarrow{M} HONO \qquad\qquad R\,2\text{-}41$$

$$OH + NO_2 \xrightarrow{M} HNO_3 \qquad\qquad R\,2\text{-}42$$

The HONO produced from R 2-41 will either be washed out or photolysis and produce OH (R 2-43). The HNO_3 consume OH and effectively acts as RO_2^* sink during the radical interconversion.

$$HONO \xrightarrow{h\nu\,(\lambda\,\le\,400\,nm)} OH + NO \qquad\qquad R\,2\text{-}43$$

3. The radical heterogeneous uptake on particles in the submicrometer range. Previous studies (Mozurkewich et al., 1987; Hanson et al., 1992; Gershenzon et al., 1995; Bedjanian et al., 2005; Remorov et al., 2002; Thornton and Abbatt, 2005; Taketani et al., 2008, 2009, 2010) showed the HO_2 update by aerosol for single component particles depends on the phase and relative humidity of the particle. The HO_2 heterogeneous loss rate is then given as:

$$L_{Het.}(HO_2) = \frac{\omega \cdot ASA \cdot \gamma}{4} \cdot [HO_2] \qquad\qquad E\,2\text{-}31$$

where ω is the mean molecular speed of HO_2; ASA is the total aerosol surface area; γ is the aerosol uptake coefficient; and $[HO_2]$ is the concentration of HO_2.

2.3.1 Peroxy radicals and Peroxy Radical Chemical Amplification (PERCA)

The measurement of peroxy radicals in the atmosphere is difficult due to their high reactivity and short lifetime. Highly sensitive detection instruments are required for which enough accuracy in the pptv (part per trillion volume) range.

The Peroxy Radical Chemical Amplification (PERCA) is an indirect measurement technique for peroxy radicals, first reported by Cantrell and Stedman, 1982. Specifically, it detects the sum of HO_2 and RO_2 which react with NO to produce NO_2, where R is an organic group collectively known as RO_2^* in the sampled air.

The PERCA method exploits a chain reaction which consumes NO and CO, and in which OH and HO_2 are chain carriers.

$$HO_2 + NO \rightarrow OH + NO_2 \qquad\qquad R\,2\text{-}15$$
$$HO + CO \xrightarrow{O_2} HO_2 + CO_2 \qquad\qquad R\,2\text{-}11$$

NO is oxidised by the chain carrier HO_2 in reaction R 2-15, forming OH and NO_2. CO is then oxidised by the second chain carrier OH. The complex reactions between OH and CO in the presence of O_2 are represented in a simplified manner by reactions R2-11. HO_2 is converted and amplified into NO_2. Similarly, RO_2 will react with NO and CO in the chain reaction. For example, the simplest RO_2, CH_3O_2:

$$CH_3O_2 + NO \rightarrow CH_3O + NO_2 \qquad\qquad R\,2\text{-}44$$
$$CH_3O + O_2 \rightarrow CH_2O + HO_2 \qquad\qquad R\,2\text{-}45$$

The produced HO_2 from R 2-44 then follow the chain reactions through R 2-15 and R2-11. The chain length (CL) of the chain reaction defines the number of NO_2 produced by one HO_2. The CL is not infinite because the reaction cycle eventually ends due to a series of loss reactions in the reactor as shown below (CH_3O_2 is taken as an example for RO_2 radical-radical reaction):

$$RO_2 + wall \rightarrow nonradical\ products \qquad\qquad R\,2\text{-}46$$
$$OH + wall \rightarrow nonradical\ products \qquad\qquad R\,2\text{-}47$$
$$OH + NO \xrightarrow{M} HONO \qquad\qquad R\,2\text{-}41$$
$$OH + NO_2 \xrightarrow{M} HNO_3 \qquad\qquad R\,2\text{-}42$$
$$HO_2 + NO \xrightarrow{M} HNO_3 \qquad\qquad R\,2\text{-}48$$
$$HO_2 + NO_2 \xrightarrow{M} HO_2NO_2 \qquad\qquad R\,2\text{-}49$$
$$HO_2 + HO_2 \xrightarrow{M} H_2O_2 + O_2 \qquad\qquad R\,2\text{-}35$$
$$HO_2 + RO_2 \rightarrow ROOH + O_2 \qquad\qquad R\,2\text{-}50$$
$$CH_3O_2 + CH_3O_2 \rightarrow 2CH_3O + H_2O \qquad\qquad R\,2\text{-}37$$
$$HO_2 + OH \rightarrow H_2O + O_2 \qquad\qquad R\,2\text{-}34$$
$$OH + OH \xrightarrow{M} H_2O_2 \qquad\qquad R\,2\text{-}51$$

$$RO + NO \xrightarrow{M} RONO \qquad\qquad R\,2\text{-}52$$
$$RO_2 + NO \rightarrow RONO_2 \qquad\qquad R\,2\text{-}53$$

When NO and CO are introduced into the system at high concentrations, the reactions of radicals with NO and CO are dominant instead of undergoing radical-radical reactions. The losses of radicals primarily occur through wall loss reactions. The effective amplification factor specific to each PeRCEAS instrument, known as the effective chain length (eCL), is determined experimentally through a series of calibrations and is determined by the setup and experimental conditions. The eCL is always smaller than the theoretical CL due to the impact of radical losses within the instrument, which affects the conversion and amplification rate of radicals into NO_2. The NO_2 concentration is then measured by a NO_2 detector.

The concentration of OH in the atmosphere is typically two orders of magnitude lower than the concentration of HO_2. Similarly, the concentration of RO is much smaller than the concentration of RO_2. Overall and to a good approximation $[RO_2^*] = [HO_2] + \Sigma[RO_2]$ where RO_2 measured as RO_2^* are those RO_2, which have at least one H atom in the R group and react with NO to produce NO_2 A PERCA instrument operates by alternately introducing CO/NO and N_2/NO into the reaction area (i.e. the inlet). This causes a modulation between the correspondingly amplified signal and the background signal which allows for accurate measurements. When CO is added to the top of the inlet, a chain reaction occurs, leading to an amplified signal detected by the NO_2 detector. On the other hand, when N_2 is added to the top of the inlet, the reaction of OH with CO does not take place, RO_2 and HO_2 react with the added NO and OH is produced. The OH terminations reactions with NO, NO_2 and possibly the wall occur and OH decays rapidly before reaching the second addition point where in this case CO is added. Only NO_2 in the ambient air and O_3 which reacts with the added NO in the inlet is measured in this background flow or mode.

Theoretically, the peroxy radical concentration in the air sampled can be calculated from the difference in NO_2 concentration between the amplified and background signal. The RO_2^* is then determined using E 2-32:

$$[RO_2^*] = \frac{\Delta[NO_2]}{eCL} \qquad\qquad E\,2\text{-}32$$

In E 2-32, $\Delta[NO_2]$ is measured by the NO_2 detector and the eCL is determined in the laboratory by sampling known concentrations of HO_2 and RO_2.

2.3.2   Airborne measurement of peroxy radicals by PERCA and CRDS: PeRCEAS

The PeRCEAS instrument combines the PERCA with the CRDS technique in a dual channel instrument to measure the RO_2^*. The sampled air is first sampled through an orifice into the **Du**al channel **A**irborne peroxy radical Chemica**l** Amplifi**er** (DUALER) inlet (as shown in Figure 4) which was developed and reported by Kartal et al., 2010. Then the air will

reach the two independent reactors and then reach two CRDS NO_2 detectors (more details in section 3.1) which are mounted in a rack. The prototype of the instrument was first reported by Horstjann et al., 2014, and further development and optimisation for the instrument which was used for this study is reported by George et al., 2020.
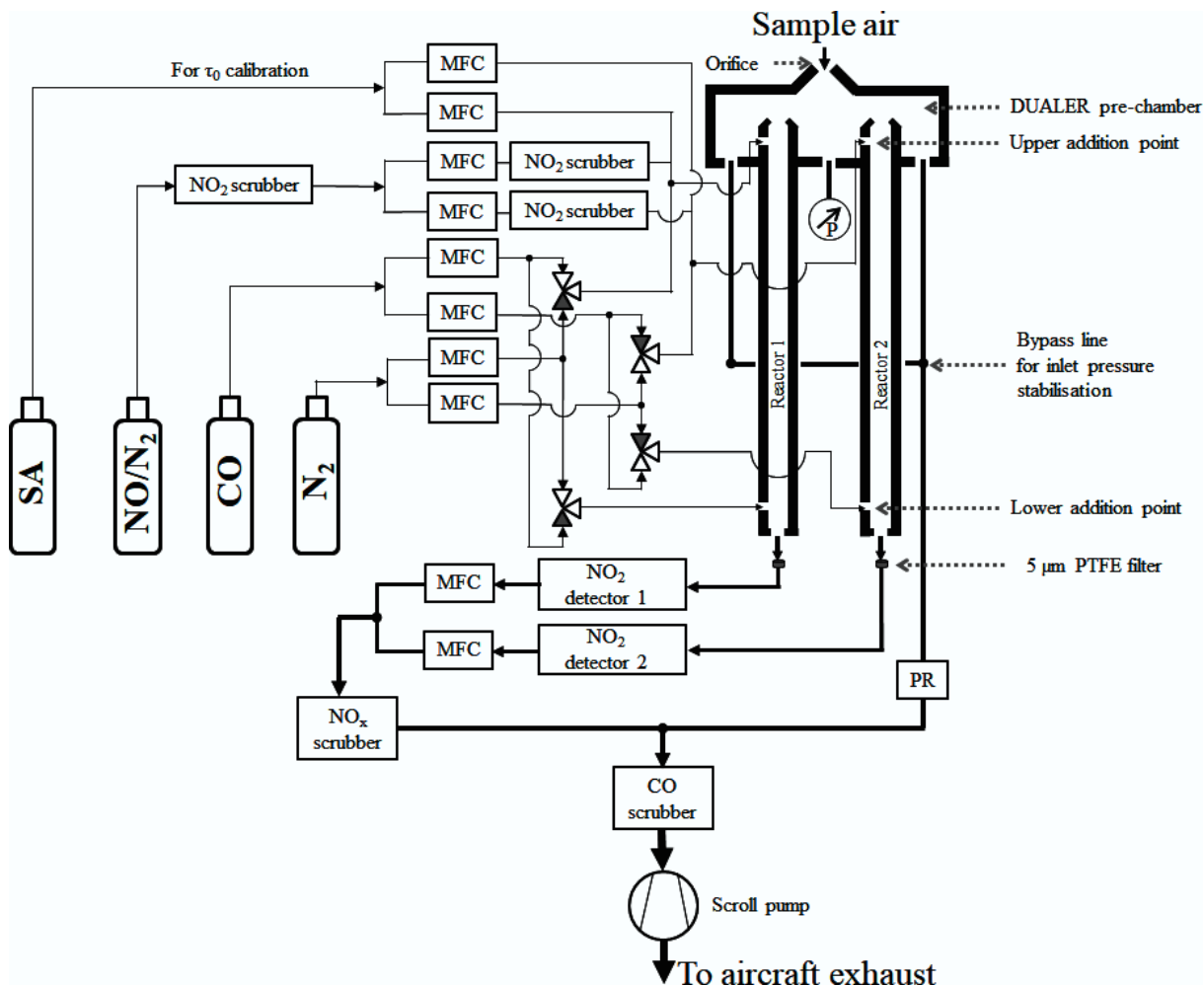
Figure 4: Schematic diagram of PeRCEAS instrument. MFC: mass flow controllers; PR: pressure regulator; P: pressure sensor; T/RH: temperature/relative humidity sensor; NO/N₂: a mixture of NO in N₂; SA: synthetic air. (George et al., 2020)

3. Methodology

This chapter provides a detailed explanation of the experimental setups used for determining the Rayleigh scattering cross-section, the EMeRGe campaign, PeRCEAS deployment, and the associated modelled and calculated RO_2^* employed in this study.

3.1 Experimental methodology for determinations of Rayleigh scattering cross-sections

In this work, CRDS is deployed for the determination of the Rayleigh scattering cross-section of molecules at 408 nm. The suitability of this highly sensitive measurement technique to detect small intensity losses caused by scattering (e.g. around $2.13 \times 10^{-6} cm^{-1}$ for O_2 at atmospheric pressure) is investigated. Different gases are introduced into the cavity equipped with highly reflective CRDS mirrors. The lasers used in these experiments have a peak wavelength of approximately 408 nm, which is calibrated using a pen-ray lamp as a calibration source. The procedure for the accurate determinations of the peak wavelength of each laser is described in section 3.1.2. During the measurement, the pulsed laser beam is reflected by mirrors into the CRDS cavity and then reflected multiple times in the v-shaped cavity. Two beams exit the cavity, with one directed to a photodiode detector and the other to a camera for monitoring the shape of the laser modes. The two different cavity setups used in the Rayleigh scattering experiments are described in the following sections.

3.1.1 Experimental setups

3.1.1.1 Setup A

Measurement setup A for the determination of Rayleigh scattering cross-section uses the NO_2 detector from PeRCEAS instrument, which is also a standalone independent instrument. As shown in Figure 5, the NO_2 detector comprises a continuous wave multimode diode laser (Stradus 405, wavelength ≈ 408 nm at max output power 100 mW, Vortran Laser Technology Inc.), and an optical V-shape cavity with three highly reflective mirrors (radius of the curvature, roc = 100 cm; reflectivity, R = 99.995 %; diameter, d = 0.5"; AT Films, USA). The EM radiation transmitted through the end mirrors of the cavity is directed to a Silicon (Si) photodiode detector (type HCA-S, spectral range 320 - 1000 nm, active diameter 0.8 mm, bandwidth 2 MHz, gain 1 MV/A, Femto Messtechnik GmbH) and to a beam camera (BM-USB-SP907-OSI, Ophir Spiricon Europe GmbH). The V-shaped cavity used in this setup has a length of 39 cm. The ring-down times are recorded at 1 Hz frequency by averaging (10^6 sample·s^{-1}) a non-linear least-squares fit (Levenberg-Marquardt algorithm) by a customised LabVIEW program.

Methodology
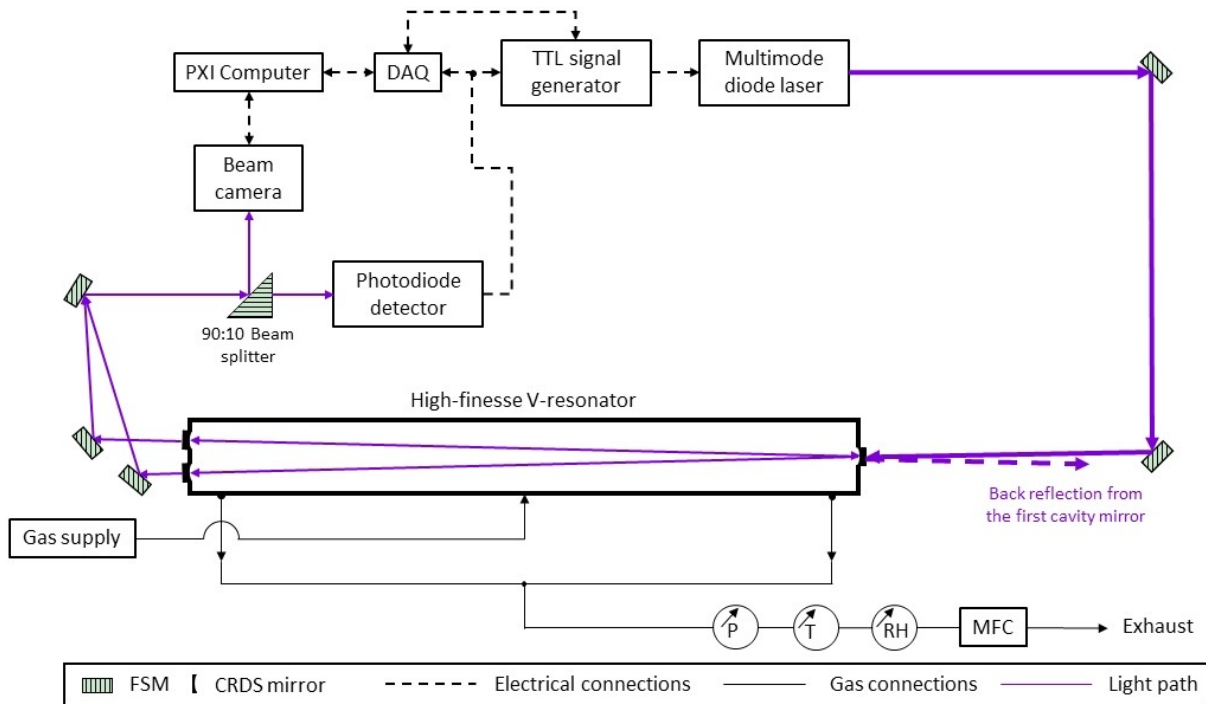
Figure 5: Schematic diagram of CRDS setup A used for the $\sigma_{Rayl.}$ determination in this work. PXI: PCI extensions for instrumentation; DAQ: data acquisition system; TTL: transistor to transistor logic; FSM: front silvered aluminium mirror; P: pressure sensor; T: temperature sensor; RH relative humidity sensor; MFC: mass flow controller.

Figure 6 shows an example of a typical residuum trace along the decay time. The data are measured by a data acquisition system (PXI-6132, National Instrument) DAQ card, saved and analysed with a PXI-computer (PXI-8105, National Instrument). The laser base plate is kept at 298 K using a Peltier element (type CP-031, Te Technology Inc.) and Peltier temperature controller (type MPT 10000, Wavelength Electronics) ensuring a constant operating temperature ($\sim 21\,°C$). The laser output is modulated using a customised TTL switch-off (at 0.1 V measured by photodiode) signal generator (Stachl Elektronik GmbH). Gas is added in the centre of the cavity and then equally distributed to the two ends close to the mirrors to a common exhaust. The pressure- (HXC001A6V-1714, ± 0.1 % accuracy of the measurement value $\sim \pm 1$ hPa, Sensor Technics), temperature- (AS22100, ± 0.4 % accuracy of the measurement value $\sim \pm 0.1\,°C$, Analog Devices), and relative humidity- (HIH-4000-1311, ± 3.5 % accuracy of the measurement value $\sim \pm 0.03$ %, Honeywell) sensors are installed at the outflow of the cavity. These sensor data are measured with DAQ (PXI-6129 DAQ card, National Instrument) at a sample rate of 1 Hz.
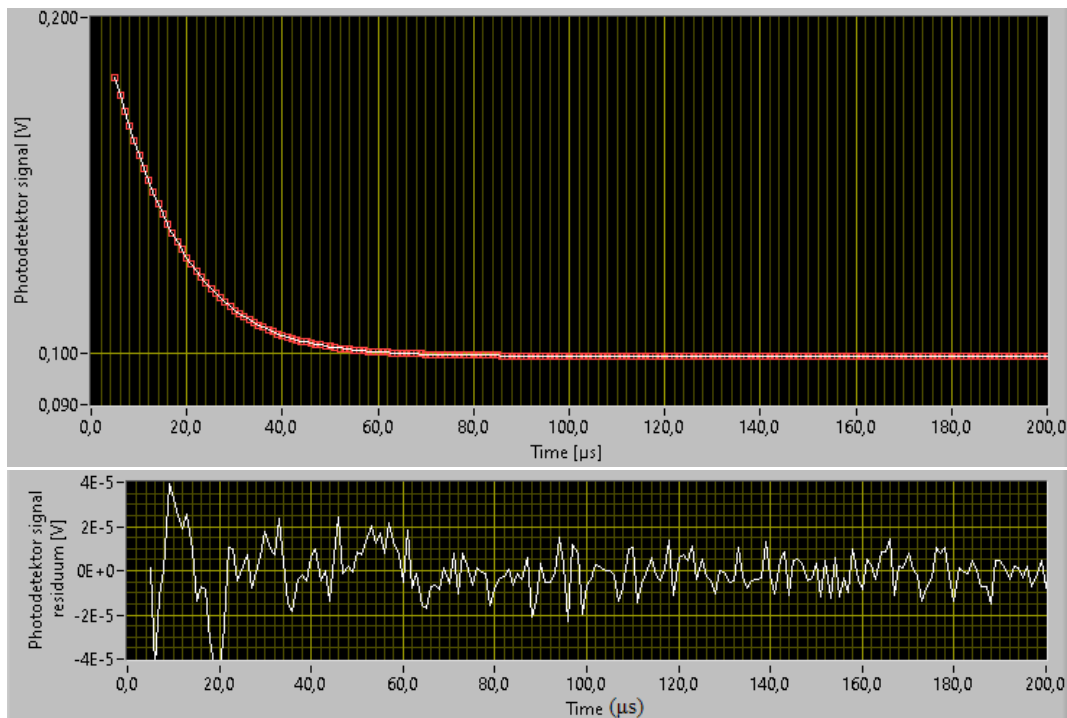
Figure 6: A screenshot example of applying a custom LabVIEW program to perform the Levenberg-Marquardt algorithm of 1s averaged τ residuum for online monitoring. The upper plot is the laser pulse decay measurements (red dot) and the corresponding fit (yellow line) over time; the lower plot is the corresponding residuum between measurements fits fit over time.

The setup depicted in Figure 7 is suitable to operate with a continuous flow of the measurement gas through the cavity at discrete pressure using a pressure regulator (type 640A, MKS Instruments Inc.). This cavity was designed for airborne measurements, i.e. controlled under pressure conditions.
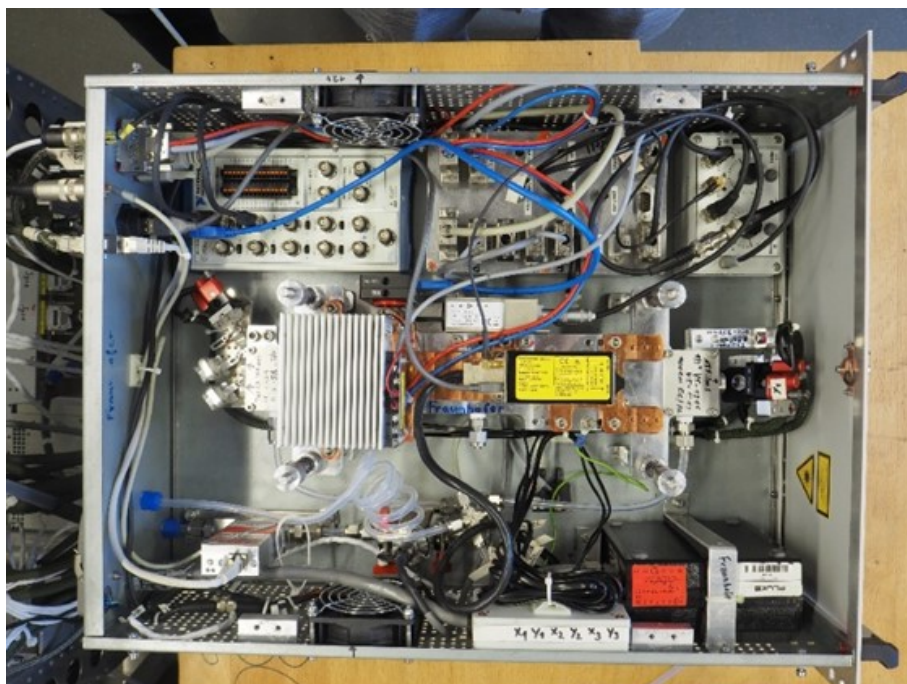
Figure 7: Top view of Rayleigh scattering cross-section measurement setup A: NO_2 detector used in PeRCEAS

3.1.1.2 Setup B

The Rayleigh scattering cross-section measurement setup B is a customise-designed CRDS V-shaped cavity similar to the cavity in setup A but with a concaved mirror of 200 cm focus in the front (reflectivity, R = 99.995 %; diameter, d = 0.5"; AT Films, USA) and two identical concaved mirrors with 100 cm focus in the back. Gas is added equally from both ends of the cavity close to the mirrors and distributed evenly to the middle and exit of the cavity. The pressure- (626A, ± 0.15 % accuracy of the measurement value ~ ± 1 hPa, MKS Instruments Inc.), humidity and temperature- (HMP 238, ± 0.04 % accuracy of the measured temperature ~ ± 0.1 °C; ± 1 % accuracy of the measured RH ~ ± 0.01 %, Vaisala) sensors of the cavity are installed after the gas exited the cavity with two T-piece KF connections in series.
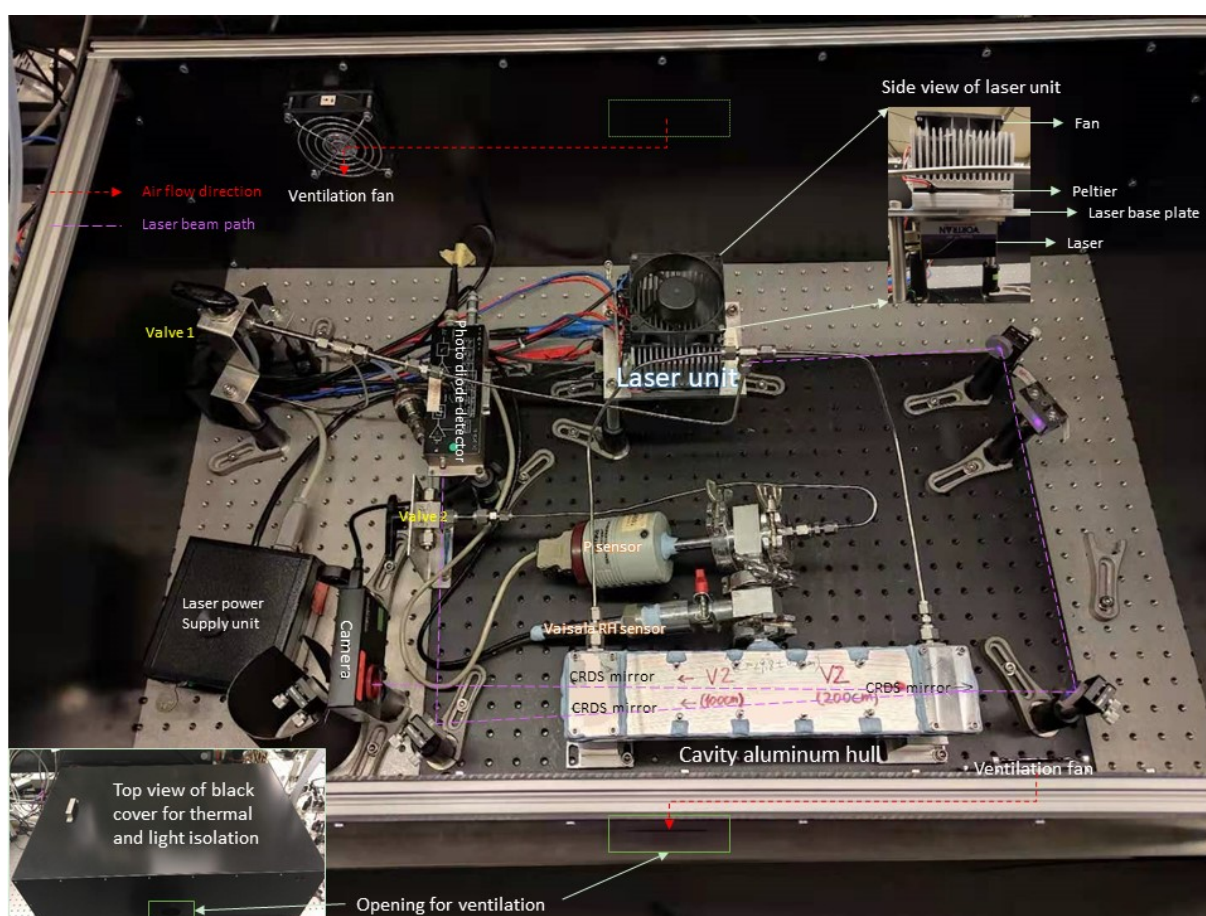
Figure 8: Top view of Rayleigh scattering cross-section measurement setup 2: Optics, laser, mirror, cavity, and the photodiode.

The detector is attached to a Peltier element with a temperature controller to keep a constant temperature (~ 23 °C) as shown in Figure 8. Unlike setup A, the laser base plate is not attached to the cavity hull but is separately fixed at the optical bench. A 1/8" tube is added before the cavity as an additional gas addition, which makes small gas addition possible for continuous pressure ramp measurements in a small volume. The laser output is modulated using a digital switch-off (at 0.1 V measured by the photodiode, OE-200-SI, spectral range 320 – 1060 nm, active diameter 1.2 mm, bandwidth 0.4 MHz, gain 5 MV/A, Femto Messtechnik GmbH) signal generator (DG 535, Stanford Research Systems, Inc.).

The V-shaped cavity used in this setup has a length of 32 cm. This cavity setup is suitable for operation with a continuous flow of the scattering gas through the cavity at a discrete pressure and a continuous flow of the measurement gas accumulating inside the cavity and creating a continuous pressure variation. A custom-made black cover is used for optimising EM radiation isolation and temperature stabilisation. As depicted in Figure 8, two fans are installed on diagonal sides of the cover with the same flow direction. An additional housing with a different opening position as the fan is installed outside the layer of the fan to prevent EM radiation interference via fan opening. In addition, all the tubes and electric cables are connected to the outside through a special opening at the back cover. The opening is covered by light-proof cloths with wire and cable wrapped.

In the experiments involving setup A, two detector setups were employed and will be denoted as setup 1 (Abbé) and setup 2 (Fraunhofer), respectively. Setup B is associated with only the customised detector setup, which will be referred to as setup 3.

3.1.2 Determination of the laser wavelength

The accurate determination of Rayleigh scattering cross-sections requires a high degree of precision, with one of the key challenges being the determination of the peak wavelength of the laser used for the experiment. In this work, two instruments were employed for cross-comparison, a wavelength meter (Bristol 621, SN: 6081. 350 nm $< \lambda <$ 1100 nm, with an accuracy of ± 0.2 ppm) and a spectrometer (AvaSpec-ULs2048x64 ENV11, SN: 1803001U1, Avantes BV. Grating, 1200 lines/mm, from 295 to 535 nm, with slit size of 200 μm, 0.74 ± 0.04 (2σ) nm spectral resolution). The wavelength meter features a self-calibration function that does not require additional calibration, while the spectrometer requires calibration prior to the comparison.

The Vortran Stradus 405 laser used in the experiments has a peak emission wavelength of 405 ± 5 nm. Natural Hg has several emission lines, and three strong emission lines (I-line: 365.0153 nm, H-line: 404.6563 nm, and G-line: 435.8328 nm) are well described (Burns et al., 1950). These emission lines make a Hg(Ar) pen ray lamp an ideal calibration source for the spectrometer. To ensure stable and correct emission from the Hg lamp, the calibration is started after at least 30 minutes of warm-up time, and the optical fibre must point directly (perpendicular) to the Hg lamp. Figure 9 shows the measured spectrum by the spectrometer at its full wavelength range of the Hg lamp. Since the H-line is close to the peak emission (408 nm) of the laser, it is used for the fitting correction. The correction for the spectrometer is + 0.517 nm. The spectrometer is calibrated before each measurement of the laser peak emission wavelength.

Methodology
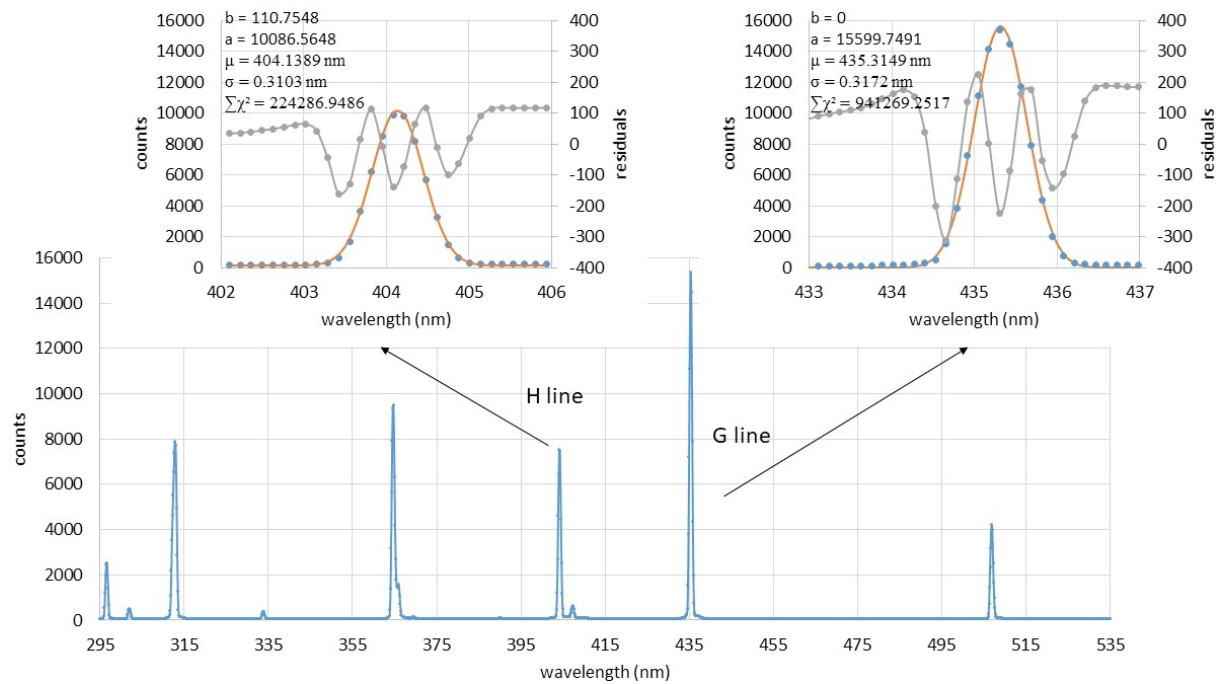
Figure 9: Avantes AvaSpec-ULs2048x64 ENV11 (SN: 1803001U1) calibration measurements using Hg(Ar) lamp, sample rate 1ms then averaged for 1s. Each blue point is a total averaged value for the selected time. The zoom-in plot shows the Gaussian fit (orange) for the H-line and G-line peak emission of the Hg lamp, where counts are the intensity of the EM radiation, b is the offset, a is the height of the curve's peak, μ is the centre of the peak, σ is the Gaussian root mean square width, and χ is the difference between the fit and the measurement values. The residual of the fit is shown in grey.

Secondly, the wavelength meter and the spectrometer are installed to measure the laser wavelength simultaneously. The wavelength meter detects the back-reflected beam from the first cavity mirror, and the spectrometer detects one of the outgoing beams from the V-shaped cavity while the other one is directed to the photodiode sensor, as illustrated in Figure 10.
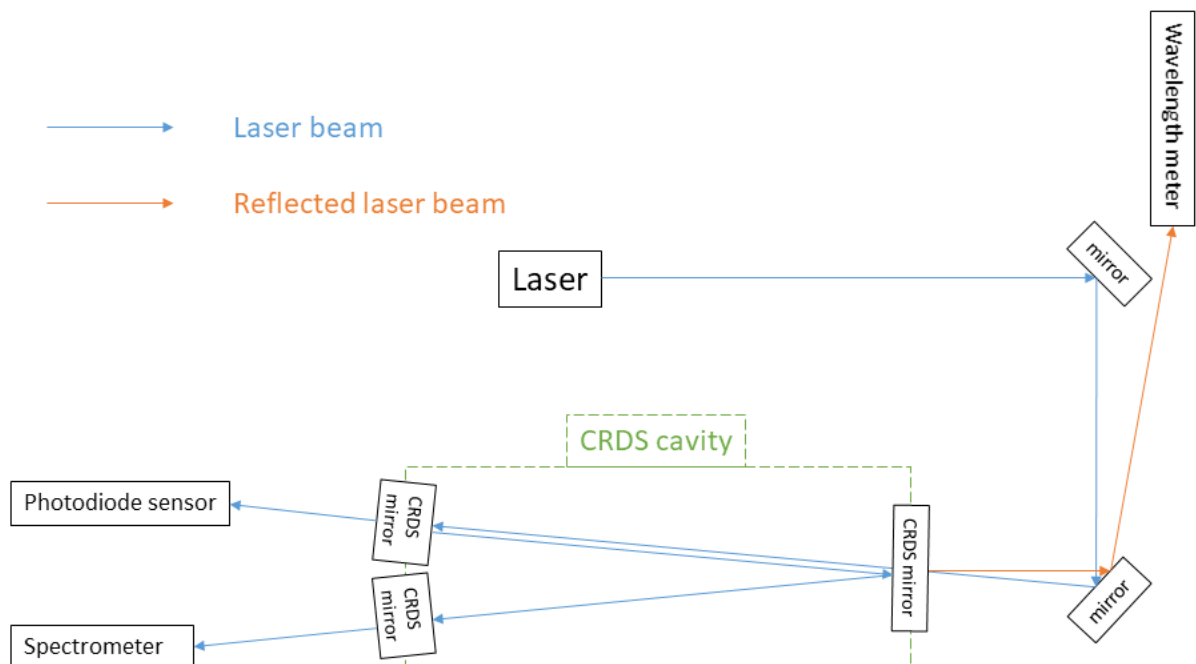
Figure 10: Scheme of the setup used for the simultaneous measurement of the laser wavelength by a spectrometer and a wavelength meter

27

Methodology

According to the specification of the wavelength meter, the EM radiation input power should be between 100 µW and 10 mW. After several tests prior to calibrations, the possible series of measurements were made at 10 mW, 20 mW, and 30 mW laser output power. In this way, the laser power does not exceed the tolerance of the spectrometer, while its sensitivity is sufficient for detection. Each step takes approximately 60 minutes and all the instruments have a minimum warm-up time of 60 minutes before calibration begins. The results obtained from the wavelength meter are utilised for comparison with the spectrometer results under laser power output of 10 mW, 20 mW, and 30 mW due to the limitations of the wavelength meter.

Table 1: Bristol 621 wavelength meter measurement results without and with the threshold comparison for the laser of setup 3 (VL03145D15)

	All points			Applying a threshold of 408.4nm		
Laser power output	10mW	20mW	30mW	10mW	20mW	30mW
Averaged Wavelength	408.50	408.10	408.07	407.99	408.02	408.07
Error (2σ)	14.67	1.80	0.24	0.16	0.14	0.09

The results of the raw calibration of the wavelength meter are shown in Figure 11. The values at 10 mW and 20 mW have significantly more noise. Therefore, a threshold is set that includes 97% of the measurements to calculate a realistically measured wavelength over time (Figure 11 right-hand side). Table 1 summarises the results of the setup threshold compared to all points.
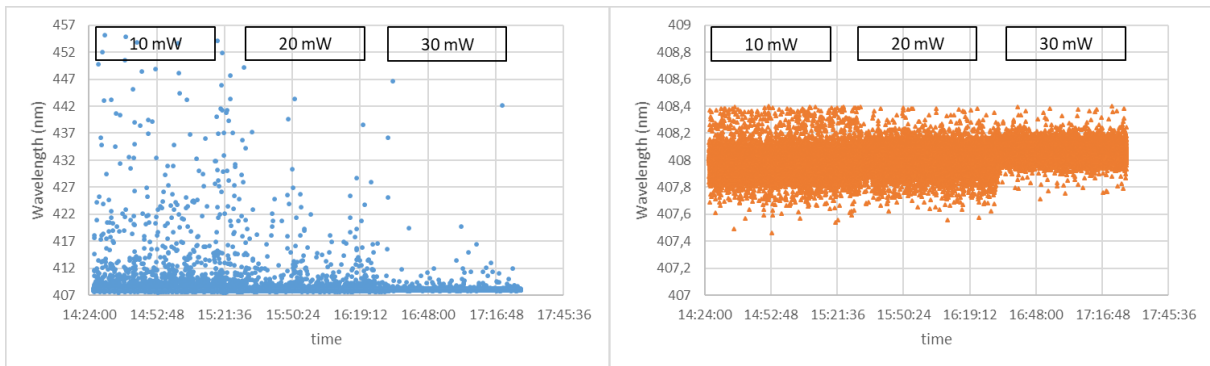
Figure 11: Bristol 621 measurements of the variation of the laser wavelength of setup 3 (VL03145D15) when varying the laser power between 10-30mW. On the left side is the original data, and on the right side is the data applying the threshold of 408.4nm.

To obtain the wavelength from the spectrometer at different laser powers, a Gaussian fit is applied to the spectral measurements obtained within 60 minutes. The corresponding spectrometer measurement results are corrected by using the Hg-lamp calibration. Figure 12 shows for the laser of setup 3 the averaged wavelength value over 60 minutes corrected with the calculated values at 10 mW, 20 mW, and 30 mW, respectively.

#	Laser power (mW)	b	a	μ (nm)	σ (nm)	Σχ²
a)	10	0.0009	0.1605	407.7095	0.3043	0.0004
b)	20	0.0011	0.1348	407.7402	0.3558	0.0002
c)	30	0.0009	0.1317	407.7656	0.3713	0.0001
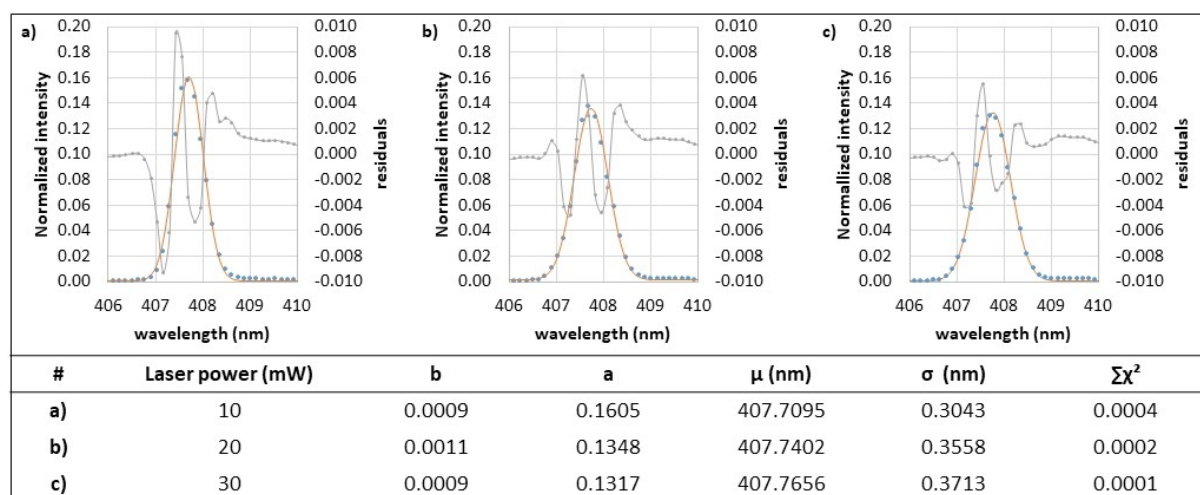
Figure 12: Spectrometer measurements of the laser wavelength of setup 3 at different power outputs. Blue filled circles are the values of normalised intensity of averaging typically 60-mins of measurement with a 1-second sample interval of the spectrometer. The orange solid lines are the Gaussian fit of the blue measurement filled circles. b is the offset, a is the height of the curve's peak, μ is the centre of the peak, σ is the Gaussian root mean square width, and χ is the difference between the fit and the measurement values

The results of the wavelength measurements of the Vortran Stradus 405 laser are summarised in Table 5. The agreement between the wavelength meter and spectrometer at 3 different laser powers is within the experimental error.

Table 2: comparison results from Bristol 621 wavelength meter with Avantes AvaSpec-ULs2048x64 ENV11 (SN: 1803001U1) for the laser of setup 3 (VL03145D15). The errors of the spectrometer measurements are given as half-width half maximum, HWHM.

Laser power setup (mW)	wavelength meter measurements (nm)	Spectrometer measurement peak wavelength (nm)	Correlation between the wavelength meter and the spectrometer
10	407.99 ± 0.16 (2σ)	407.71 ± 0.36 (HWHM)	$y = 0.9993x$, $R = 0.90$
20	408.02 ± 0.14 (2σ)	407.74 ± 0.42 (HWHM)	
30	408.07 ± 0.09 (2σ)	407.77 ± 0.44 (HWHM)	

In this study, all measurements for determining the Rayleigh scattering cross-section are conducted using a laser output of 100 mW. The comparison shown above at 10 mW, 20 mW, and 30 mW shows good agreement between the spectrometer and the wavelength meter. This validates the measurement results from the spectrometer at 100 mW presented in the following. The fitted spectral plots for the different lasers used in the experiments are shown in Figure 13. These are used to calculate the theoretical values of the Rayleigh cross-section of the molecules investigated. The shape of the laser emission line was stable within 98.5 % of the normalised intensity during the 60 minutes measurements.
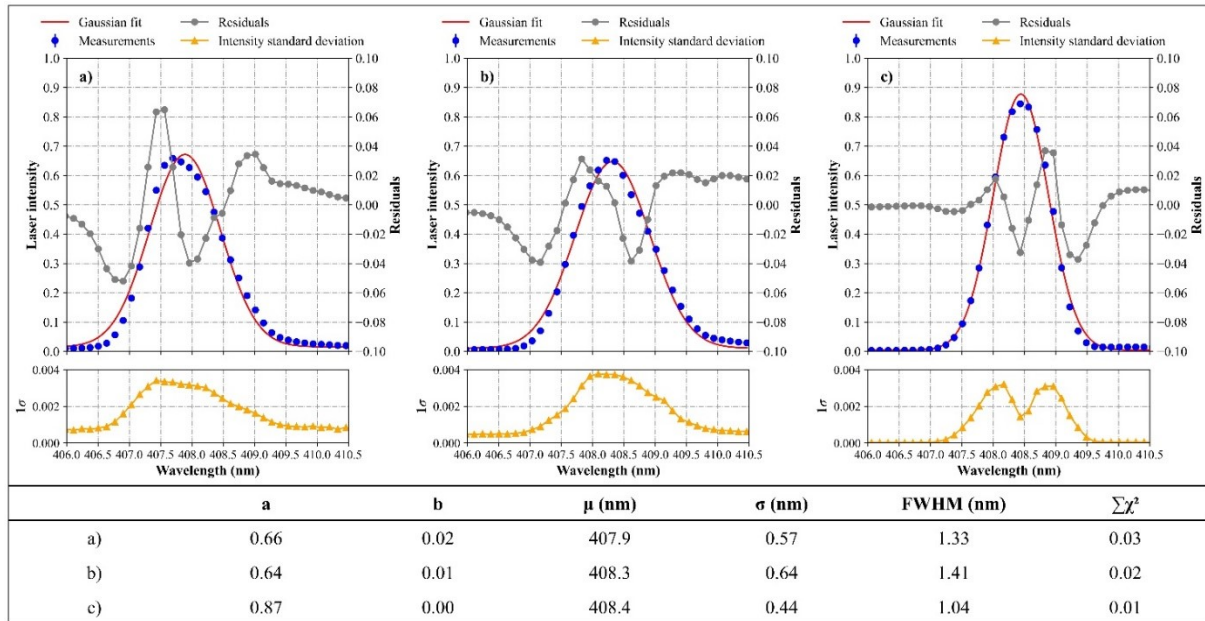
Figure 13: The determination of the wavelength of the maximum intensity for the lasers used in this study using the spectrometer. The corresponding lasers are a) laser of setup 1(VL04156E01), b) laser of setup 2 (VL1036S09), and c) laser of setup 3 (VL03145D15). The counts at each wavelength λ are normalised to the total intensity measured during 60 min (blue measurement points). The parameters of the Gaussian fit applied (red line), i.e. a: height of the curve, b: offset of the curve, µ: centre of the peak, σ: Gaussian root mean square width, FWHM: full-width half maximum, and χ: difference between fitted and measured values. The residual of the fit is shown in grey and the 1σ standard deviation of the normalised intensity is shown in yellow.

The free spectral range of an optical cavity, υ_r, is given by Hecht, 2017:

$$\upsilon_r = \frac{c}{2nL} \qquad\qquad E\ 3\text{-}1$$

where L is the length of the cavity, n is the refractive index of the medium, and c is the speed of EM radiation. Since the CRDS optical cavities used in this study have a length between 32 cm (setup 3) and 39 cm (setup 1 and 2) the free spectral range of the CRDS cavity is much smaller compared to that of the diode laser cavity. Therefore, it is expected that all the longitudinal modes from the laser can couple to the CRDS cavity. This is also shown in Figure 13 where the output of the laser is measured after the optical cavity. The effect of multiple longitudinal modes on the refractive index is accounted for by convoluting the $\sigma_{Rayl.}$, theoretical values with the corresponding laser spectral output.

3.1.3   Pressure control of the optical cavity

The number concentration of the molecules in the cavity is calculated using the ideal gas law and precise pressure measurement. The sensors used were calibrated by using a commercial calibration-free absolute pressure sensor (GDH 12AN, Greisinger GmbH) with analogue output as a reference. The pressure sensors are symmetrically connected to a chamber containing the reference unit in which different pressure levels are generated. The readings from both instruments are recorded.
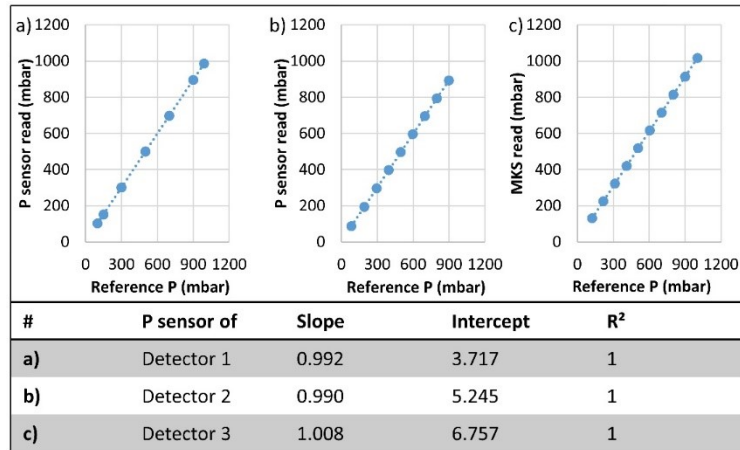
Figure 14: Calibrations of the pressure sensors used in this work. a) P sensor used in setup 1; b) P sensor used in setup 2; c) pressure sensor used in setup 3.

The pressure sensor calibrations and correction factors used in this work are shown in Figure 14. The measurement of pressure in the setups had ± 1 % accuracy and linearity in the range of 100 - 1000 hPa. The pressure measurements in later sections are corrected using this calibration.

3.1.4   Measurement procedures

In this work, the determination of the Rayleigh scattering cross-section is performed using three distinct measurement procedures that depend on the specific characteristics of the setups. These procedures include continuous flow, ramp and inverse ramp experiments, which are all detailed in the following sections.

3.1.1.3 Measurement procedure 1: continuous mode

Measurement procedure 1 consists of the so-called continuous flow experiments with discrete pressure steps, i.e. the investigated gases are passed at a constant flow through the cavity, which is kept at pressures below ambient. The number densities are changed stepwise by changing the pressure using a pressure regulator and a membrane pump.
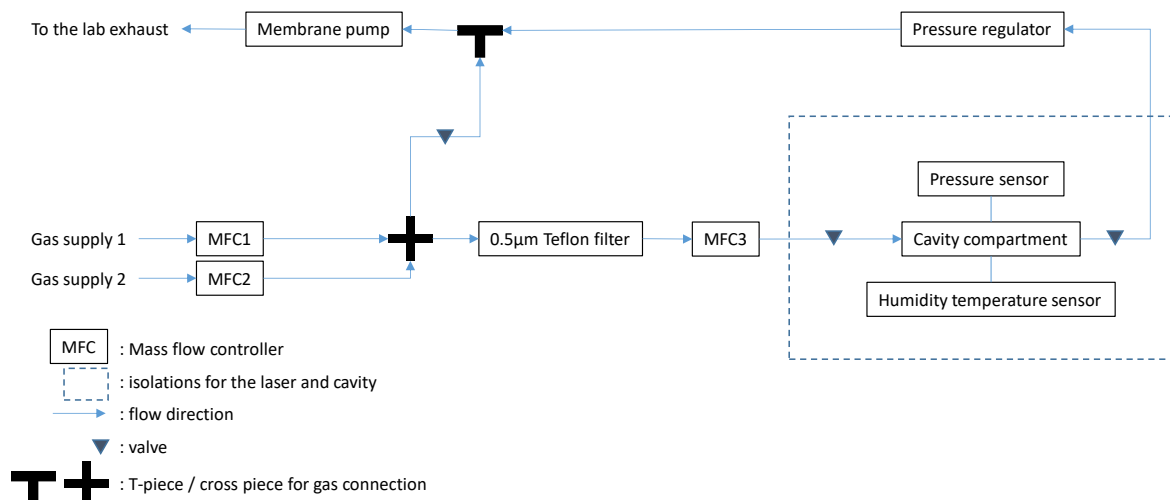
Figure 15: Gas flow sketch of the measurement procedure 1 with continuous flow.

Figure 15 illustrates the gas flow scheme for measurement procedure 1. The gas of interest is added using the mass flow controllers MFC1 and/or MFC2. Normally, the MFC3 is kept at a constant rate to maintain the flow through the cavity, and the total feed gas flow (MFC1 and/or MFC2) is kept constant. An excess gas supply to the flow into the cavity is required to prevent contamination from the lab air. A 0.5µm Teflon filter upstream of MFC3 removes small particles such as dust or aerosols. Prior to the experiment, the cavity is flushed with the gas of interest and the pressure is varied between 300 hPa and 1000 hPa with 100 hPa steps every 10s several times until the ring-down time and the cavity relative humidity of the cavity are stabilised. During the experiment, a pressure regulator controls the pressure steps. Each pressure step is typically held for 2 to 10 minutes to ensure the stability of the flow dynamics inside the cavity.

3.1.1.4 Measurement procedure 2: ramp mode

Measurement procedure 2, known as ramp experiments. In the pressure ramp mode, the cavity is flushed with the gas of interest at a flow rate of $1000 \text{ cm}^3 \cdot \text{min}^{-1}$ at 300 hPa until the ring-down time and the relative humidity are stable. The exit line is then closed until the standard deviation (1σ) of the τ signal remains < 0.007 µs for 1 hour. The pressure ramp is then initiated by gas addition using a constant flow (typically at $20 \text{ cm}^3 \cdot \text{min}^{-1}$) which then gradually increases the pressure as a function of time.
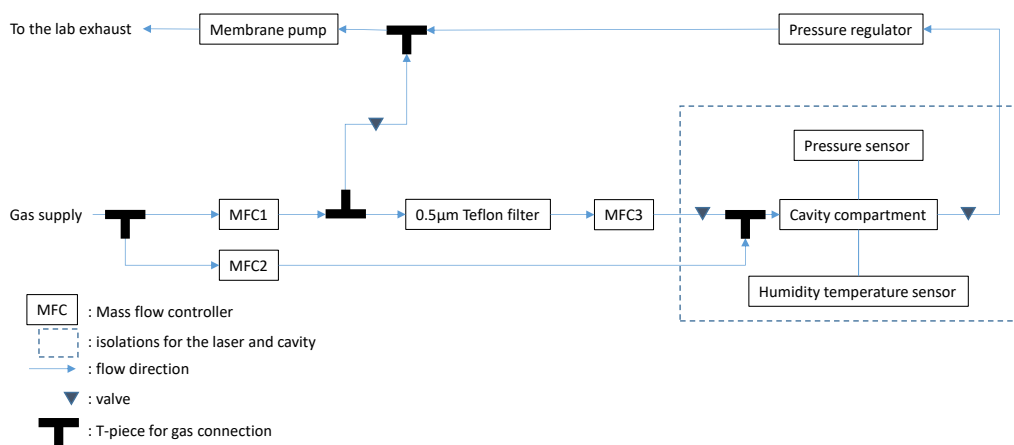
Figure 16: Gas flow sketch for the Rayleigh scattering experiments for the measurement procedure 2.

The gas flow schematic for procedure 2 is depicted in Figure 16. The cavity is flushed with the gas of interest using a mass flow controller (MFC1) following the same procedure as mentioned in procedure 1 to obtain a stable ring-down time signal and relative humidity. Next, the supply and exhaust flow to the cavity is stopped by switching off the two valves of the cavity. In practice, the supply flow is cut off shortly before the exhaust flow to prevent accidental pressure increases inside the cavity. The pressure inside the cavity is then increased by adding gases through MPC2.

3.1.1.5 Measurement procedure 3: inverse ramp mode

The pressure ramp can also start from overpressure to reduced pressure in a controlled manner. The flow sketch of procedure 3 is shown in Figure 17. The cavity is flushed with

the gas of interest at a given flow with MFC1 and MFC3 open. When the ring-down time signal and the relative humidity in the cavity are stable, the gas supply is adjusted to 1300 hPa, and MFC1 and MFC3 are closed simultaneously. A continuous pressure-decreasing ramp is generated by venting the gas in the cavity by using MPC2. Unless stated otherwise, the results of the ramp experiments are performed using the increased pressure procedure.
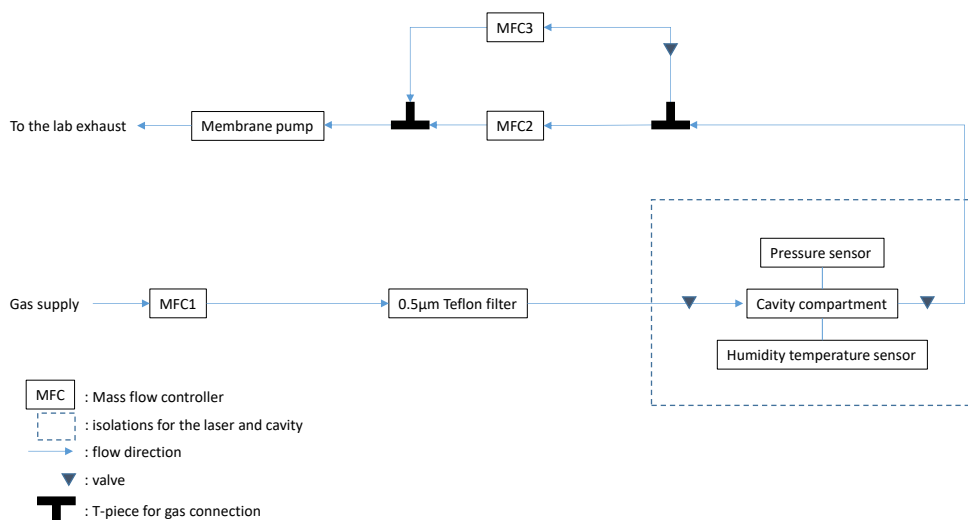
Figure 17: Gas flow sketch for the measurement procedure 3.

Prior to the pressure ramp experiments, all the PeRCEAS NO_2 detectors were pressure tested. A leak rate of less than 0.61 ± 0.03 hPa/min was determined for the cavities in the PeRCEAS NO_2 detectors by averaging the pressure change over 15 minutes starting at 325 hPa. Such a leakage rate will not affect the measurements for measurement procedure 1, as the molecules inside the cavity are rapidly refreshed by the molecules of the incoming gas flow. However, a leak-free cavity is essential for ramp experiments to avoid errors, as the molecules from the outside will inevitably enter the cavity and accumulate inside. Therefore, the ramp procedure was applied only to setup 3, which had leak rates below 0.02 ± 0.03 hPa/min after averaging the pressure change over 10 hours starting at 290 hPa.
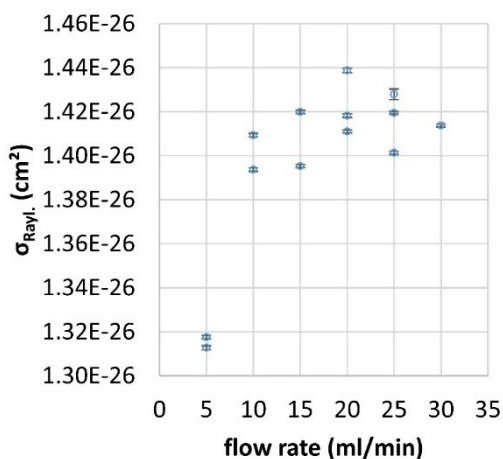
Figure 18: Synthetic air Rayleigh scattering cross-section retrieved for different flow rates using the ramp procedure with setup 3.

In order to determine the appropriate flow rate required for the ramp experiments, a sensitivity study was conducted to assess its effect on the results. Synthetic air was added to a cavity at different flow rates, and the cross-section was determined. The results showed that a flow rate of at least 10 ml/min is required to obtain reproducible cross-section measurements, as depicted in Figure 18. An adequate flow rate ensures a homogeneous distribution of gas inside the cavity during the ramp procedure. Therefore, a flow rate of 20 ml/min was selected for adding gas to the cavity during ramp experiments.

3.2 EMeRGe campaign and PeRCEAS deployment

The EMeRGe campaign aims to investigate the local, regional, and inter-regional pollution transport originating from major population centres (MPCs) in Europe and Asia, and their impact on atmospheric chemistry and dynamics during two intensive operational periods (IOPs) (Andrés Hernández et al., 2022). The main objective is to improve the existing knowledge of the chemical and physical changes that occur in the atmospheric outflows originating from MPCs and their regional to global impact. To achieve this objective, the campaign aims to identify emission signatures in MPC plumes, assess the chemical processing of MPC pollution outflows, and determine the relative importance of MPCs as sources of pollution of the IOPs. The campaign primarily utilises the unique research platform, HALO, in synergy with observational data sets from ground-based networks and satellite measurements, supported by the modelling of the EMeRGe campaign. The HALO payloads for EMeRGe comprise a set of instruments for the measurements of trace gases and aerosol particles are summarised in Table 3.

The EMeRGe in EU field experiments were conducted during the summer from 10 - 28 July 2017, with a total of 53 HALO flight hours across 7 measurement flights. London, Paris, Benelux, Ruhr region, Po Valley, Rome, Madrid, and Barcelona were taken as target MPCs. All of the HALO flights were operated from the DLR base airport at Oberpfaffenhoffen, and the EMeRGe international team provided additional coordinated aircraft, satellite and ground-based observation and modelling studies. Two flights were carried out by the Facility for Airborne Atmospheric Measurements (FAAM, FAAM, 2022) from the UK Natural Environment Research Council, with one flight on 13-07-2017, being the so-called blind intercomparison exercise. More details about the results from the blind intercomparison exercise could be found at Schumann, 2021. The flight information and targeted regions for each flight are summarised in Table 4, with E-EU-01 and 02 are test flights which were not taken into consideration. The flight tracks for EMeRGe in Europe are depicted in Figure 19.

Methodology

Table 3: HALO instrument payload for EMeRGe. VOC: volatile organic compound; PERCA: Peroxy Radical Chemical Amplification; CRDS: Cavity Ring-Down Spectroscopy; HVS: High Volume Sampler; GC-C-IRMS: Gas Chromatography - Combustion - Isotope Ratio Mass Spectrometry; PTR-MS: Proton Transfer Reaction - Mass Spectrometer; AT-BS: Adsorption Tube and Bag air Sampler; TD-GC-MS: Thermal Desorption - Gas Chromatography and Mass Spectrometry; CI-ITMS: Chemical Ionisation - Ion Trap Mass Spectrometry; GC-MS: Gas Chromatography-Mass Spectrometry analysis; PAN: Peroxyacetyle nitrate; $\delta^{13}C(CH_4)$: Isotopic signature of methane; PFC: Perfluorinated carbon chemicals; DOAS: Differential Optical Absorption Spectrometry; ToF-AMS: Time of Flight – Aerosol Mass Spectrometry; SP2: Single Particle Soot Photometry; CCNC: Cloud Condensation Nucleus Counting; MI: Multi Impactro for aerosol off-line analysis; CPC: Condensation Particle Counting; DMA: Differential Mobility Analysis; OPC: Optical Particle Counting; PSAP: Particle Soot Absorption Photometry. KIT: Karlsruhe Insitute of Technology; DLR-IPA: Institute of Atmospheric Physics of DLR; MPIC: Max Planck Institute for Chemistry; FZJ: Forschungszentrum Jülich; DLR-FX: Flight experiments, DLR.

Measurements	Instrument Acronym	Institute	Instrumental Technique	References
Trace gas in-situ measurements				
$RO_2^* = HO_2 + \Sigma RO_2$	PeRCEAS	Uni-Bremen	PERCA, CRDS	(George et al., 2020)
VOC/C isotope ratios	MIRAH	Uni-Wuppertal	HVS, GC-C-IRMS	(Wintel et al., 2013)
VOC	HKMS	KIT	PTR-MS	(Brito and Zahn, 2011)
O_3	FAIRO	KIT	UV photometry, Chemiluminescence	(Zahn et al., 2012)
O_3, CO	AMTEX	DLR-IPA	UV photometry, UV-Vis fluorimetry	(Gerbig et al., 1996)
NO, NOy	AENEAS	DLR-IPA	Chemiluminescence, gold converter	(Ziereis et al., 2004)
SO_2, HCOOH	CI-ITMS	DLR-IPA	CI-ITMS	(Speidel et al., 2007)
CO_2, CH_4 PAN 3. $\delta^{13}C(CH_4)$	CATS	DLR-IPA	CRDS GC-MS 3. GC-IRMS	1. (Chen et al., 2010) 2. (Volz-Thomas et al., 2002) 3. (Fisher et al., 2006)
PFC tracer	PERTRAS	DLR-IPA	AT-BS, TD-GC-MS	(Ren et al., 2015)
Trace gas remote sensing measurements				
NO_2, HONO, BrO, CH_2O, $C_2H_2O_2$, $C_3H_4O_2$, SO_2, IO	Mini-DOAS	Uni-Heidelberg	DOAS, UV-NIR, 2D optical spectrometer	(Hüneke et al., 2017)
NO_2, CH_2O, $C_2H_2O_2$, H_2O, SO_2, BrO, O_3	HAIDI	Uni-Heidelberg	DOAS, $3 \times 2D$ imaging spectrometers	(General et al., 2014)
Aerosol measurements				
Particle composition	C-ToF-AMS	MPIC Mainz Uni-Mainz	ToF-AMS, OPC	(Schulz et al., 2018)
BC, CCN, microscopic properties	CCN-Rack	MPIC Mainz	SP2 CCNC, MI	(Holanda et al., 2020) (Wendisch et al., 2016)
Particle size distribution, number concentration	AMETYST	DLR-IPA	CPC, OPC, PSAP, DMA	(Andreae et al., 2018)
Other parameters				
Spectral actinic flux density (up/down) photolysis frequencies	HALO-SR	FZJ	CCD spectro-radiometry	(Bohn and Lohse, 2017)
Basic aircraft data	BAHAMAS	DLR-FX	various	(Mallaun et al., 2015)

Methodology

Table 4: Details of HALO flights in IOPs of EMeRGe in EU. The flight naming: E stands for EMeRGe, EU for Europe, and the flight number.

Flight	Date	Start/End time (UTC)	Targeted MPCs and regions	Other objectives
E-EU-03	11-07-2017	10:00/16:30	Rome and Po Valley	Mineral dust from Northern Africa, Fires in Southern Italy
E-EU-04	13-07-2017	10:40/15:00	Central Europe	HALO-FAAM blind comparison, Canada fires
E-EU-05	17-07-2017	10:30/18:30	London, Benelux, and Ruhr region	FAAM flight over London
E-EU-06	20-07-2017	09:00/17:30	Rome and Po Valley	Mineral dust from Northern Africa, fires in Southern Italy and Croatia
E-EU-07	24-07-2017	09:45/18:15	Po Valley, South France, and Barcelona	Dust transport from Northern Africa, fires in Southern Europe
E-EU-08	26-07-2017	07:45/15:20	London, Benelux, Ruhr region, Paris, English Channel, and Central Europe	PFC tracer releases London and Wuppertal
E-EU-09	28-07-2017	10:00/18:30	Po Valley, South France, Madrid, and Barcelona	Fires in Southern France and Portugal

The EMeRGe in Asia field experiments were carried out during the spring inter-monsoon period from 10 March - 09 April 2018, with a total of 127 HALO flight hours across 18 measurement flights. Bangkok, Manila, Taipei, Tainan, the Peral River Delta region, the Yangtze River Delta region, and South Japan were taken as target MPCs. Flights E-AS-01 to E-AS-03 were the transfer flights from the DLR base airport at Oberpfaffenhofen to the Tainan airport, where all the IOPs measurement flights were operated for the mission. Flights E-AS-14 to E-AS-16 were the transfer flights back to the Oberpfaffenhofen airport base. The flight information and the targeted regions for IOPs of EMeRGe in Aisa are summarised in Table 5. The corresponding flight tracks are depicted in Figure 20.
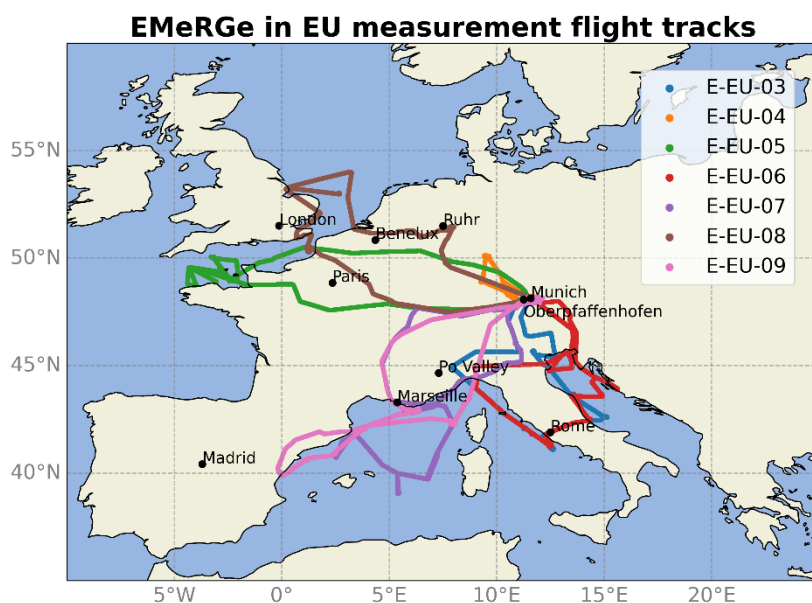
Figure 19: Flight tracks of the 7 measurement flights carried out during the EMeRGe campaign in Europe.

Table 5: Details of HALO flights in IOPs of EMeRGe in Aisa. The flight naming: E stands for EMeRGe, AS for Asia, and the flight number. YRD: Yangtze River Delta; PRD: Pear River Delta.

Flight	Date	Start/End time (UTC)	Targeted MPC and regions	Other objectives
E-AS-04	17-03-2018	01:09/09:45	Outflow from China over East China Sea	
E-AS-05	19-03-2018	00:24/08:28	Outflow from Shanghai and YRD region	Impact of outflow from YRD on Taipei in the afternoon
E-AS-06	19/20-03-2018	23:47/06:37	Manila	Tracer experiment
E-AS-07	22-03-2018	00:46/09:31	Taipei, Tainan, and outflow from China over East China Sea	Tracer experiment
E-AS-08	24-03-2018	01:00/09:26	Outflow from China over East China Sea and Taiwan	
E-AS-09	26-03-2018	00:24/09:26	Outflow from China over East China Sea and Taiwan	
E-AS-10	27/28-03-2018	23:53/08:32	Manila and PRD region	Tracer experiment
E-AS-11	30-03-2018	00:02/09:26	Outflow from YRD and Fukuoka	
E-AS-12	03-04-2018	00:25/06:25	Taipei and Tainan	
E-AS-13	04-04-2018	00:26/09:24	Outflow from Japan	Long-transported biomass burning in higher altitudes
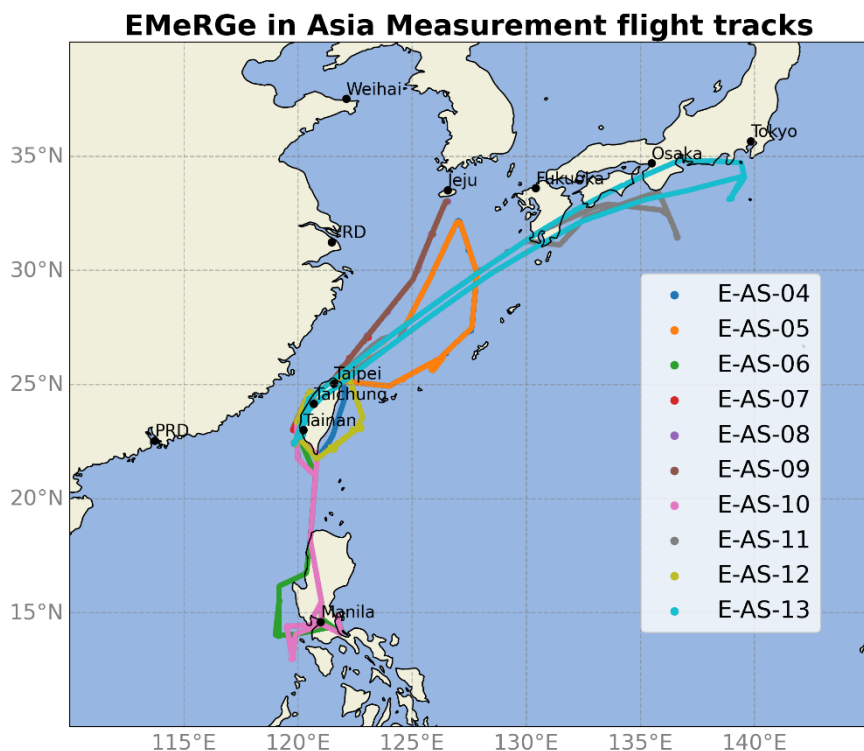
Figure 20: Flight tracks of the 10 measurement flights carried out during the EMeRGe campaign in Asia. YRD: Yangtze River Delta, PRD: Pearl River Delta.

3.3 Modelling and calculated data used for comparison

This chapter provides background information about the four state-of-the-art models and the calculation method chosen for the comparison with the RO_2^* airborne measurements during the EMeRGe campaign. Additionally, the background information of the two trajectory models used as analysis tools was presented in this section.

3.3.1 WRF/CMAQ model

The WRF/CMAQ model used in this study was developed under the project Japan's study for reference air quality modelling (J-STREAM) (Chatani et al., 2018). It used the Weather Research and Forecasting (WRF) model version 3.7.1 (Skamarock et al., 2008) coupled with the Community Multiscale Air Quality (WRF/CMAQ) version 5.0.2 (US EPA Office of Research and Development, 2014; Byun and Schere, 2006). The model at the stage of this study had two horizontal domains, D1: Asia 220×170 grids with a resolution of 45 km and D2: Japan 154×160 grid with a resolution of 15 km. In this study, D1 was used for the EMeRGe in Asia. The vertical domain consisted of 27 layers between 1013.15 hPa and 50 hPa. Land use was based on data from the Biodiversity center of Japan (Center of Japan, Ministry of the Environment Natural Environment Bureau Biodiversity, 2023). The National Center for Environmental Prediction (NCEP) Final Operational Global Analysis (FNL, ds083.3) data (six-hourly; $0.25 \degree \times 0.25°$ resolution) (National Centers for Environmental Prediction/National Weather Service/NOAA/U.S. Department of Commerce, 2015) and real-time, global, sea surface temperature (RTG_SST_HR) analyses (Gemmill et al., 2007) were used as the initial and boundary conditions and grid nudging. The grid nudging was switched on for all levels of wind with a coefficient of $1 \times 10^{-4}(s^{-1})$, and all levels of temperature and water vapour with a coefficient of $5 \times 10^{-5}(s^{-1})$, in D1 domain. The Kain-Frisch scheme (Kain and Fritsch, 1993) was used as the convective parameterisation scheme. The Thompson scheme (Thompson et al., 2008) was used for the microphysical parameterisation. The Mellow-Yamada-Nakanishi-Niino (MYNN) level-3 scheme (Nakanishi and Niino, 2006) was applied for the Planetary Boundary Layer (PBL) parameterisation. The Noah Land-Surface model (Ek et al., 2003) was used for the surface physics calculations, and the MYNN Surface-Layer scheme (Olson, 2021) was used for surface layer physics. The sea surface temperature data was based on the Group for High Resolution Sea Surface Temperature (GHRSST) data (24 hourly; 1×1 km resolution) (Piolle, 2020). The Rapid Radiative Transfer Model for General circulation models (RRTMG) (Pincus et al., 2015) was used to simulate the shortwave and longwave radiations. The Statewide Air Pollution Research Center, version 07 (SAPRC-07) scheme (Carter, 2010) was used to simulate the chemistry of trace gases, and the 6th generation WRF/CMAQ aerosol module (AERO6) (Simon and Bhave, 2012) was used as aerosol chemistry mechanism. Anthropogenic emissions were taken from the Hemispheric Transport of Air Pollution (HTAP) version 2.2 (monthly 2010; $0.1° \times 0.1°$ resolution) (Janssens-Maenhout et al., 2015), and the Global Fire Emission Database (GFED) version 4.1 (Daily and three-hourly, $0.25° \times 0.25°$ resolution) (van der Werf et al., 2017) was used for biomass burning emissions. The Model of Emissions of Gases and Aerosols from Nature (MEGAN) version 2.1 (Guenther et al., 2012) was used for biogenic emissions. The Grell-Dévényi convection parameterising ensemble (Grell and Dévényi, 2002) was used for cumulus modelling. The WRF/CMAQ model has provided the simulation output of 8 measurement flights from E-AS-05 to E-AS-12 with a temporal resolution of 15 s (E-AS-08 to 12) and 30 s (E-AS-05 and 07). The RO_2^* in this model is defined as:

$$RO^*_{2\,WRF/CMAQ} = HO_2 + CH_3O_2 + RO_2C + CH_3COO_2 + RCOO_2 + BZCOO_2 \\ + MACOO_2$$

<div style="text-align:right">E 3-2</div>

where HO_2 is the hydroperoxyl radical; CH_3O_2 is the methylperoxy radical; RO_2C is the peroxy radical operator representing NO to NO_2 and NO_3 to NO_2 conversions, and the effects of peroxy radical reactions on acyl peroxy and other peroxy radicals, CH_3COO_2 is the acetyl peroxy radicals, $RCOO_2$, is the peroxy propionyl and higher peroxy acyl radicals, $BZCOO_2$ is the peroxyacyl radical formed from aromatic aldehydes, and $MACOO_2$ is the peroxyacyl radicals formed from methacrolein (CH_2CCH_3CHO) and other acroleins.

The WRF/CMAQ model simulations for EMeRGe in Asia were provided by Prof. Yugo Kanaya, JAMSTEC, Kanagawa, Japan (yugo@jamstec.go.jp).

3.3.2   WRFchem model

The WRFchem model development is based on a study for Megacity Aerosol Composition by Satellite: a tool to study anthropogenic Emissions, Climate changes and human Health (MACSECH) project which contains two parts, the EMeRGe and the Dynamics-Aerosol-Chemistry-Cloud Interactions in West Africa (DACCIWA) campaigns (Deroubaix et al., 2022). The model used for EMeRGe campaign is based on the Weather Research and Forecasting model coupled with chemistry (WRFchem) (Grell et al., 2005; Fast et al., 2006; Powers et al., 2017). The model provided a horizontal resolution at 10 km and a vertical domain consisting of 40 layers between 1013.15 hPa and 50 hPa. There are two models used to define the initial and boundary conditions namely: the fifth-generation European Centre for Medium-Range Weather Forecasts (ECMWF) climate Reanalysis (ERA5) (Hersbach et al., 2020) which is denoted as WRFchem(ERA5); the Global Forecast System (GFS) (National Oceanic and Atmospheric Administration, 2023) which is denoted as WRFchem(GFS). The results will be discussed separately in the later sections. The WRF Single Moment 6-Class (WSM6) scheme (Hong and Lim, 2006) was used for microphysical parameterisation. The Carlson-Boland viscous sub-layer with the surface physics was calculated by the Noah land surface model. PBL physics was calculated by the Yonsei University scheme (Hong et al., 2006). The low frequency spectral nudging was used above the 12th vertical level to enable the PBL variability to be resolved by WRF (Deroubaix et al., 2022). The Kain-Frisch scheme was used for the convection parameterisation scheme. The Rapid Radiative Transfer Model (RRTM) (Mlawer et al., 1997) was used to simulate the shortwave and longwave radiations. The Model for Ozone and Related chemical Tracers, version 4 (MOZART-4) mechanism (Emmons et al., 2010) was used to simulate the chemistry of trace gases. The Georgia Tech/Goddard Global Ozone Chemistry Aerosol Radiation and Transport (GOKART) model (Chin et al., 2000) was used as the aerosol chemistry mechanism, the mineral dust, and the sea salt simulations. The Copernicus Atmosphere Monitoring Service (CAMS) reanalysis based on the global reanalysis dataset of the atmospheric composition produced by the ECMWF (Inness et al., 2019) was used for the simulation of anthropogenic emissions. The Global Fire Assimilation System (GFAS) (Heil et al., 2010) was used for biomass burning

emissions. The MEGAN version 2.1 (Guenther et al., 2012) was used for biogenic emissions. The WRFchem model has provided the simulation output of 14 measurement flights for EMeRGe in EU from E-EU-03 to E-EU-08, and for EMeRGe in Asia from E-AS-04 to E-AS-10 and E-AS-12 with a temporal resolution of 60 s. The RO_2^* in this model is defined as:

$$\begin{aligned} RO_{2\,WRFchem}^* = {} & HO_2 + CH_3O_2 + ISOOH + ACETO_2 + DICARBO_2 + ENEO_2 \\ & + EO_2 + HMPROPO_2 + ISOPAO_2 + ISOPBO_2 + ISOPNO_3 \\ & + MVKO_2 + MALO_2 + MBONO_3O_2 + MBOO_2 + MCO_3 \\ & + MDIALO_2 + MEKO_2 + NTERPO_2 + PHENO_2 + PO_2 \\ & + TERPO_2 + TERP_2O_2 + TOLO_2 + XO_2 + XYLENO_2 \\ & + XYLOLO_2 \end{aligned} \qquad \text{E 3-3}$$

where HO_2 is the hydroperoxyl radical; CH_3O_2 is the methylperoxy radical; ISOOH is the product from isoprene + OH oxidation; $ACETO_2$ is $CH_3COCH_2O_2$, the product from acetone (CH_3COCH_3) and HO_2; $DICARBO_2$ is $C_5H_5O_4$, acylperoxy radical formed from aromatic oxidation, via unsaturated dicarbonyl chemistry; $ENEO_2$ is $C_4H_9O_3$, lumped hydroxyperoxy radical from OH + large alkenes; EO_2 is $HOCH_2CH_2O_2$, hydroxyperoxy radical from OH + ethene chemistry; $HMPROPO_2$ is $C_4H_7O_4$, peroxy radical from HMPROP (hydroxymethylpropanal, OH + 2-methyl-3-buten-2-ol [MBO] product) oxidation; $ISOPAO_2$ is $HOC_5H_8O_2$, beta-isomer of isoprene peroxy radical; $ISOPBO_2$ is $HOC_5H_8O_2$, delta-isomer of isoprene peroxy radical; $ISOPNO_3$ is $C_5H_8NO_5$, peroxy radical from isoprene NO_3 oxidation; $MVKO_2$ is $CH_2CHCOCH_2O_2$, peroxy radical formed from methyl vinyl ketone (MVK) oxidation; $MALO_2$ is $C_4H_3O_4$, acylperoxy radical from OH reaction with butenedial (BIGALD1), a product of aromatic oxidation; $MBONO_3O_2$ is $C_5H_{10}NO_6$, peroxy radical from NO_3 + MBO; $MBOO_2$ is $C_5H_{11}O_4$, peroxy radical from OH+MBO; MCO_3 is $CH_2CCH_3CO_3$, peroxy radical from OH abstraction reaction with methacrolein (MACR); $MDIALO_2$ is $C_4H_5O_4$, peroxy radical from OH addition to BIGALD1; $MEKO_2$ is $C_4H_7O_3$, peroxy radical formed from methyl ethyl ketone (MEK) oxidation; $NTERPO_2$ is $C_{10}H_{16}NO_5$, peroxy radical from NO_3 + terpene chemistry; $PHENO_2$ is $C_6H_7O_6$, bicyclic peroxy radical from phenol; PO_2 is $C_3H_6OHO_2$, propene-derived peroxy radical; $TERPO_2$ is $C_{10}H_{17}O_3$, peroxy radical from terpenes + OH; $TERP_2O_2$ is $C_{10}H_{15}O_4$, peroxy radical from lumped terpene product oxidation; $TOLO_2$ is $C_7H_9O_5$, bicyclic peroxy radical from toluene; XO_2 is $C_5H_9O_5$, peroxy radical from unsaturated hydroxyhydroperoxide (ISOPOOH), isoprene-derived epoxide (IEPOX), unsaturated hydroperoxyaldehyde, from isoprene chemistry (HPALD); $XYLENO_2$ is $C_8H_{11}O_5$, bicyclic peroxy radical from OH+xylenes chemistry; $XYLOLO_2$ is $C_8H_{11}O_6$, bicyclic peroxy radical from OH + dimethyl phenol from xylenes oxidation (XYLOL) chemistry.

The WRFchem model simulations for EMeRGe were provided by Dr. Andrien Deroubaix, Institute of Environmental Physics, University of Bremen, Bremen, Germany (Adrien.Deroubaix@iup.physik,uni-bremen.de).

3.3.3 MECO(n) model

MECO(n) is short for MESSy-fied ECHAM and COSMO/MESSy models nested n times which was developed by the Institut for Atmospheric Physics of DLR (German Aerospace Center). The Modular Earth Submodel System (MESSy) (Jöckel et al., 2005) is a software and a framework for the assembly of Earth System Models (ESMs). The European Centre – Hamburg (ECHAM) model evolved originally from ECMWF (Roeckner et al., 2003; Roeckner et al., 2004). The Consortium for Small-scale Modeling (COSMO) (Doms and Baldauf, 2013) is a collaboration of meteorological institutes and research organisations in Europe and the Climate Limited-Area Modeling (CLM) community extended the COSMO model to be able to run long-term simulations, the resulting modelling system is called COSMO-CLM (Rockel and Geyer, 2008). The MECO(n) model system (Kerkweg and Jöckel, 2012b; Hofmann et al., 2012; Mertens et al., 2016; Kerkweg et al., 2018; Kerkweg and Jöckel, 2012a) consists of the global chemistry-climate model ECHAM/MESSy Atmospheric Chemistry (EMAC) model and the regional chemistry-climate model COSMO-CLM/MESSy. MECO(n) model provided three different horizontal resolutions: CM50, 50 km horizontal resolution, 131×121 horizontal grid boxes, timestep length = 240 s; CM12, 12 km horizontal resolution, 245×221 horizontal grid boxes, timestep length = 120 s; CM7, 7 km resolution, 330×310 horizontal grid boxes, timestep length = 60 s. The model refinements were applied with 40 terrain following vertical levels from the surface up to around 20 km. Aqueous-phase chemistry in clouds and wet deposition are simulated with the combined explicit scavenging (SCAV) submodel (Tost et al., 2006; Tost et al., 2007; Tost et al., 2010). The big leaf approach (Wesely, 1989) was used for the dry deposition of chemical species. The Module Efficiently Calculating the Chemistry of the Atmosphere (MECCA) submodel (Sander et al., 2011) was used to simulate the chemical kinetics. Mainz Isoprene Mechanism ver.1 (MIM1) (Pöschl et al., 2000) was used for the isoprene and selected NMHCs chemistry simulation. The long-lived greenhouse gases (CO_2, CH_4, and N_2O) and chlorofluorocarbon (CFC) concentrations were taken from the Representative Concentration Pathways (RCPs) (Moss et al., 2010) 8.5 emissions scenario. The emissions from biomass burning and agricultural waste burning use the RCPs emission inventory (except for the biomass burning missions in 2017). The Emissions Database for Global Atmospheric Research (EDGAR) (Janssens-Maenhout et al., 2019) 4.3.1 monthly resolution for the year 2010 was used for the anthropogenic emissions. The emissions of NOx from soils and biogenic VOC are calculated from the meteorological conditions following the empirical model of global soil-biogenic NOx emissions (Yienger and Levy, 1995) and a global model of natural VOC emissions (Guenther et al., 1995). The modelling of global lightning distributions in GCM (Price and Rind, 1994) was used for the lightning NOx emissions. The RO_2^* in this model is defined as:

$$RO_2^*{}_{MECO(n)} = HO_2 + CH_3O_2 + ISOOH + CH_3COO_2 + CH_3COCH_2O_2 \\ + C_2H_5O_2$$

$$E\ 3\text{-}4$$

where HO_2 is the hydroperoxyl radical; CH_3O_2 is the methylperoxy radical; ISOOH is the product from isoprene + OH oxidation; CH_3COO_2 is the product from CH_3CHO and HO_2; $CH_3COCH_2O_2$ is the product from acetone and HO_2; $C_2H_5O_2$ is the product from ethan + OH oxidation.

The MECO(n) model results for EMeRGe were provided by Dr. Mariano Mertens, Institute for Atmospheric Physics, DLR, Oberpfaffenhofen, Germany (mariano.mertens@dlr.de). The provided data has the resolution CM12 for EMeRGe in EU and CM7 for EMeRGe in Asia.

3.3.4   Box model setups

The box model is a gas-phase chemistry mechanism operating freely, constraining the measurements without considering aerosol mechanisms. The detailed setups are described as follows: A chemistry mechanism was developed for box (Poisson et al., 2001) and global (Kanakidou and Crutzen, 1999; Poisson et al., 2000) modelling studies, initially coupled to the global 3-D climatological tropospheric transport model (CTM) MOGUNTIA (Model Of the Global Universal Tracer Transport In the Atmosphere) (Zimmermann, 1988). The chemistry model scheme which was developed for the box modelling study is then further developed and updated (Poisson et al., 2000; Myriokefalitakis et al., 2008; Myriokefalitakis et al., 2020) by the Environmental Chemical Processes Laboratory (ECPL), Department of Chemistry, University of Crete. The MOGUNTIA chemical scheme was implemented in the global 3-D CTM chemistry Transport Model, version 5 (TM5) (Krol et al., 2005) in the massively parallel version (TM5-MP) (Williams et al., 2017) which has a resolution of $1° \times 1°$ globally. The mass-conserving tracer transport (Bregman et al., 2003) was applied in the box model. The meteorological field was taken from the ECMWF ERA-Interim reanalysis (Dee et al., 2011) with an update frequency of 3 h. The slopes scheme (Russell and Lerner, 1981) was used as the advection scheme and a comprehensive mass flux scheme (Tiedtke, 1989) is used for the deep and shallow cumulus convection parameterisation. The dry and wet deposition scheme was taken from the atmospheric aerosol distribution in European Community Earth System Model (EC-Earth) v3.2.0 (de-Bruine et al., 2018). The Community Emissions Data System (CEDS) (Hoesly et al., 2018) was used for the anthropogenic emissions and the gridded historic global inventories (van Marle et al., 2017) developed for Coupled Model Intercomparison Project Phase 6 (CIMP6) (Eyring et al., 2016) was used for the biomass burning simulation. The box model runs by constraining all the available trace gas measurements, photolysis frequencies, and the basic aircraft data from the EMeRGe campaign. In cases where the measurements are unavailable, the model employs interpolation methods to estimate the values based on nearby values. When this isn't feasible, the model runs with its chemical mechanism and the scheme setups as described. The RO_2^* in this model is defined as:

$$RO^*_{2\,box} = HO_2 + CH_3O_2 + C_2H_5O_2 + TERO_2 + MEKO_2 + C_2O_3 + HYPO_2$$
$$+ AROO_2 + HYEO_2 + ACO_2 + C_4H_9O_2 + MVKO_2 + ISOPO_2 \qquad E\ 3\text{-}5$$
$$+ MACRO_2 + NH_2O_2 + C_3H_7O_2p + C_3H_7O_2s$$

where HO_2 is the hydroperoxyl radical; CH_3O_2 is the methylperoxy radical; $C_2H_5O_2$ is the product from ethan + OH oxidation; $TERO_2$ is $C_{10}H_{17}O_3$, peroxy radical from terpenes + OH; $MEKO_2$ is $C_4H_7O_3$, peroxy radical formed from MEK oxidation; C_2O_3 is CH_3COO_2, the product from CH_3CHO and HO_2; $HYPO_2$ is $C_3H_6OHO_2$, propene-derived peroxy radical; $AROO_2$ peroxy radical from lumped aromatics product oxidation; $HYEO_2$ is $C_2H_5OO_2$, hydroxyethylperoxy radicals; ACO_2 is $CH_3COCH_2O_2$, peroxy radical from acetone; $C_4H_9O_2$ is the peroxy radical from butyl; $MVKO_2$ is $CH_2CHCOCH_2O_2$, peroxy radical formed from MVK oxidation; $ISOPO_2$ is $HOC_5H_8O_2$, isoprene peroxy radical; $MACRO_2$ is $CH_3COCHO_2CH_2OH$, peroxy radical from OH addition to methacrolein; NH_2O_2 is the amino peroxy radical; $C_3H_7O_2p$ is $CH_3CH_2CH_2O_2$, the primary isomer of propylperoxy radical; $C_3H_7O_2s$ is $CH_3CHO_2CH_3$, the secondary isomer of propylperoxy radical.

The box model simulations for EMeRGe were provided by Dr. Maria Kanakidou, Environmental Chemical Processes Laboratory (ECPL), Department of Chemistry, University of Crete, Heraklion, Greece (mariak@uoc.gr).

3.3.5 FLEXTRA model

The Flexible kinematic Trajectories (FLEXTRA) 5.0 model (Stohl et al., 2001; Stohl et al., 1995) was used to calculate the air mass back trajectories during the EMeRGe campaign. The model employs the ECMWF ERA5 reanalysis meteorological data at a 0.25° horizontal resolution. The trajectories were calculated every 10 mins of flight time and 10 days in the past. Post-processed scalar information of FLEXTRA (SCALTRA) provides additional information over the boundary layer conditions.

The FLEXTRA model results for EMeRGe were provided by Dr. Mihalis Vrekoussis, Laboratory for Modeling and Observation of the Earth System (LAMOS), Institute of Environmental Physics, University of Bremen, Bremen, Germany (mvrekous@uni-bremen.de).

3.3.6 HYSPLIT model

The Hybrid Single-Particle Lagrangian Integrated Trajectory (HYSPLIT) model (Stein et al., 2015) was developed by the National Oceanic and Atmospheric Administration (NOAA) Air Resources Laboratory (ARL). The model is widely used for atmospheric trajectory and dispersion calculations. The model was used to calculate the transport and dispersion of CO emissions over 6 days during the EMeRGe campaigns over IOPs. The model used the meteorology data from the operation ECMWF where it concatenates the initial state and the first eleven hours of the forecast from successive forecasts datasets (0-12UTC daily). The meteorological data featured a time step of 1 hour and 137 vertical levels and was horizontally interpolated onto a 0.1° latitude-longitude grid for use with

the HYSPLIT model. The CO emissions were taken from the EDGAR HTAP V2 (Janssens-Maenhout et al., 2015) emission inventory (monthly gridmaps $0.1° \times 0.1°$ for the year 2010). The CO outputs from the model indicate the enhancements in the plumes which means that the CO accumulated in the background is not included. The model provides the CO mixing ratio of the whole 6 days accumulation period and the different individual age periods of 0 - 3 hrs, 3 - 6 hrs, 6 - 12 hrs, 12 - 24 hrs, 24 - 48 hrs, 48 - 72 hrs, 72 - 96 hrs, and 96 - 144 hrs. Furthermore, the model also provides the average age of CO contributions through arithmetic contributions. For the EMeRGe in EU, the available source regions include Berlin, Benelux, London, Milan, Munich, Paris, Rome, and Spain. For the EMeRGe campaign in Asia, the available source regions include Beijing, Manila, Osaka, Pearl River Delta, Seoul, Taipei, and Yangtze River Delta.

The HYSPLIT model results for EMeRGe were provided by Dr. Robert Baumann, Institute of Atmospheric Physics, DLR, Oberpfaffenhofen, Munich, Germany (robert.baumann@dlr.de).

3.3.7 Radical photostationary steady state (PSS) expression

The peroxy radicals are short-lived in most environments, therefore, the RO_2^* concentration is expected to be in a photostationary steady state (PSS) where the production and loss rate of RO_2^* is balanced.

Under this assumption, an analytical expression is used for the calculation of the RO_2^* based on the works of George, 2022; George et al., 2023. The calculations are adjusted and constrain the HALO onboard measurements. The main production reactions of RO_2^* considered in this work are:

$$O_3 \xrightarrow{hv\ (\lambda < 320\ nm)} O(^1D) + O_2 \qquad\qquad R\ 3\text{-}1$$

$$O(^1D) + H_2O \rightarrow 2OH \qquad\qquad R\ 3\text{-}2$$

$$O(^1D) + O_2 \rightarrow O(^3P) + O_2 \qquad\qquad R\ 3\text{-}3$$

$$O(^1D) + N_2 \rightarrow O(^3P) + N_2 \qquad\qquad R\ 3\text{-}4$$

$$HONO \xrightarrow{hv\ (\lambda < 400\ nm)} OH + NO \qquad\qquad R\ 3\text{-}5$$

$$H_2O_2 \xrightarrow{hv} 2OH \qquad\qquad R\ 3\text{-}6$$

$$OH + O_3 \rightarrow HO_2 + O_2 \qquad\qquad R\ 3\text{-}7$$

$$OH + CO + O_2 \rightarrow HO_2 + CO_2 \qquad\qquad R\ 3\text{-}8$$

$$OH + CH_4 + O_2 \rightarrow CH_3O_2 + H_2O \qquad\qquad R\ 3\text{-}9$$

$$HCHO + 2O_2 \xrightarrow{hv\ (\lambda < 340\ nm)} 2HO_2 + CO \qquad\qquad R\ 3\text{-}10$$

$$CH_3CHO + 2O_2 \xrightarrow{hv\ (\lambda < 340\ nm)} CH_3O_2 + HO_2 + CO \qquad\qquad R\ 3\text{-}11$$

$$CH_3C(O)CH_3 + 2O_2 \xrightarrow{hv\ (\lambda < 340\ nm)} 2CH_3O_2 + 2CO \qquad\qquad R\ 3\text{-}12$$

$$CH_3C(O)CH_3 + 2O_2 \xrightarrow{hv\ (\lambda < 340\ nm)} CH_3C(O)O_2 + CH_3O_2 \qquad\qquad R\ 3\text{-}13$$

$$CHOCHO + 2O_2 \xrightarrow{hv} 2HO_2 + 2CO \qquad\qquad R\ 3\text{-}14$$

$$OH + HCHO + O_2 \rightarrow HO_2 + CO + H_2O \qquad\qquad R\ 3\text{-}15$$

$$OH + CH_3CHO + O_2 \xrightarrow{M} CH_3C(O)O_2 + H_2O \qquad \text{R 3-16}$$
$$OH + CH_3C(O)CH_3 \rightarrow CH_3C(O)CH_2 + H_2O \qquad \text{R 3-17}$$
$$OH + CH_3OH + O_2 \rightarrow CH_2O + HO_2 + H_2O \qquad \text{R 3-18}$$
$$OH + CHOCHO + O_2 \rightarrow HO_2 + 2CO + H_2O \qquad \text{R 3-19}$$

Reactions R 3-3 and R 3-4 do not produce OH or RO_2^* directly, but will influence the OH yield by reacting with $O(^1D)$ will be used in the later calculations. There are second channels for reactions R 3-10 and R 3-11 that do not produce proxy radicals therefore, the reactions are not listed.

The loss process reactions of RO_2^* considered in this calculation are:

$$HO_2 + HO_2 \xrightarrow{M} H_2O_2 + O_2 \qquad \text{R 3-20}$$
$$HO_2 + CH_3O_2 \rightarrow CH_3OOH + O_2 \qquad \text{R 3-21}$$
$$CH_3O_2 + CH_3O_2 \rightarrow CH_3OH + HCHO + O_2 \qquad \text{R 3-22}$$
$$OH + HO_2 \rightarrow H_2O + O_2 \qquad \text{R 3-23}$$
$$OH + OH \xrightarrow{M} H_2O_2 \qquad \text{R 3-24}$$
$$OH + OH \rightarrow H_2O + O(^3P) \qquad \text{R 3-25}$$
$$OH + NO \xrightarrow{M} HONO \qquad \text{R 3-26}$$
$$OH + NO_2 \xrightarrow{M} HNO_3 \qquad \text{R 3-27}$$
$$OH + HONO \rightarrow H_2O + NO_2 \qquad \text{R 3-28}$$
$$CH_3O + NO \xrightarrow{M} CH_3ONO \qquad \text{R 3-29}$$
$$HO_2 + NO_2 \rightarrow HO_2NO_2 \qquad \text{R 3-30}$$
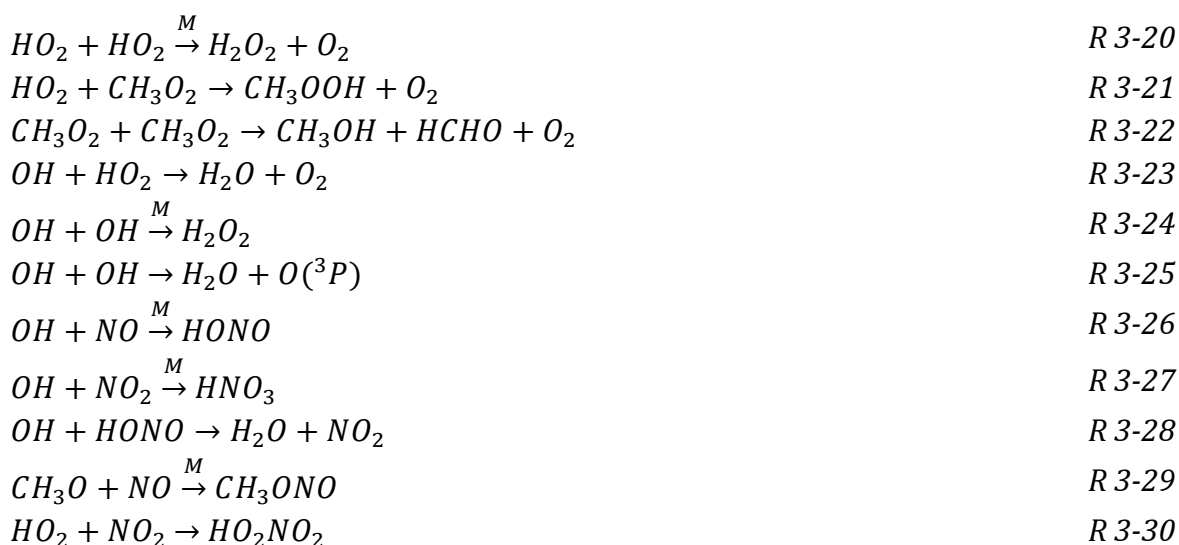
The OH, RO and RO_2^* participate in radical interconversion reactions:

$$HO_2 + NO \rightarrow OH + NO_2 \qquad \text{R 3-31}$$
$$HO_2 + O_3 \rightarrow OH + 2O_2 \qquad \text{R 3-32}$$
$$CH_3O_2 + NO \rightarrow CH_3O + NO_2 \qquad \text{R 3-33}$$
$$CH_3O_2 + CH_3O_2 \rightarrow 2CH_3O + O_2 \qquad \text{R 3-34}$$
$$CH_3O + O_2 \rightarrow CH_2O + HO_2 \qquad \text{R 3-35}$$
$$OH + O_3 \rightarrow HO_2 + O_2 \qquad \text{R 3-7}$$
$$OH + CO + O_2 \xrightarrow{M} CO_2 + HO_2 \qquad \text{R 3-8}$$
$$OH + CH_4 + O_2 \rightarrow CH_3O_2 + H_2O \qquad \text{R 3-9}$$
$$OH + HCHO + O_2 \rightarrow HO_2 + CO + H_2O \qquad \text{R 3-15}$$
$$OH + CH_3CHO + O_2 \xrightarrow{M} CH_3C(O)O_2 + H_2O \qquad \text{R 3-16}$$
$$OH + CH_3C(O)CH_3 \rightarrow CH_3C(O)CH_2 + H_2O \qquad \text{R 3-17}$$
$$OH + CH_3OH + O_2 \rightarrow CH_2O + HO_2 + H_2O \qquad \text{R 3-18}$$
$$OH + CHOCHO + O_2 \rightarrow HO_2 + 2CO + H_2O \qquad \text{R 3-19}$$
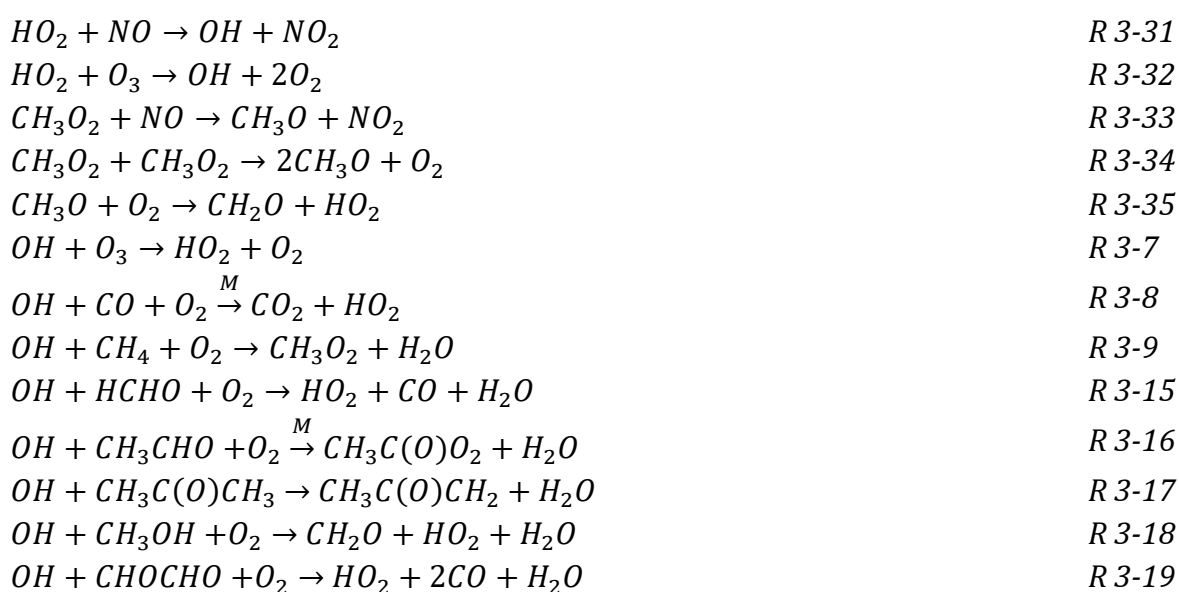
Based on the PSS assumption the relation between the production/loss rate of RO_2^* and the concentraiton of RO_2^* start with the balance between the production ($P_{RO_2^*}$) and loss ($L_{RO_2^*}$) rates:

$$P_{RO_2^*} = L_{RO_2^*} \qquad\qquad E\ 3\text{-}6$$

$P_{RO_2^*}$ is the sum of all the RO_2^* produced from reactions R 3-1 to R 3-14 for which measurements are available, specifically involving the photolysis of O_3, HONO, HCHO, $CH_3C(O)CH_3$, and CHOCHO:

$$
\begin{aligned}
P_{RO_2^*} = \ & 2 \cdot j(R\ 3\text{-}1) \cdot [O_3] \\
& \cdot \left(\frac{k(R\ 3\text{-}2) \cdot [H_2O]}{k(R\ 3\text{-}2) \cdot [H_2O] + k(R\ 3\text{-}3) \cdot [O_2] + k(R\ 3\text{-}4) \cdot [N_2]} \right) \\
& + j(R\ 3\text{-}5) \cdot [HONO] + 2 \cdot j(R\ 3\text{-}10) \cdot [HCHO] + 2 \cdot j(R\ 3\text{-}11) \\
& \cdot [CH_3CHO] + 2 \cdot (j(R\ 3\text{-}12) + j(R\ 3\text{-}13)) \cdot [CH_3C(O)CH_3] + 2 \\
& \cdot j(R\ 3\text{-}14) \cdot [CHOCHO]
\end{aligned}
\qquad E\ 3\text{-}7
$$

where j is the photolysis rate of the corresponding reactions; k is the reaction constant for the corresponding reactions; [X] is the concentration from the measurements. For simplicity of the calculation, the production of $CH_3C(O)O_2$ from R 3-13 is treated as CH_3O_2. The effective yield of OH in the reaction of $O(^1D)$ with H_2O is defined as β for simplicity:

$$\beta = \frac{k(R\ 3\text{-}2) \cdot [H_2O]}{k(R\ 3\text{-}2) \cdot [H_2O] + k(R\ 3\text{-}3) \cdot [O_2] + k(R\ 3\text{-}4) \cdot [N_2]} \qquad E\ 3\text{-}8$$

$L_{RO_2^*}$ consists of 2 parts, the radical-radical reactions concerning reactions R 3-20 to R 3-22, and the radical losses through HONO and HNO_3 formation. R 3-6 leads to:

$$
\begin{aligned}
(2 \cdot j(R\ 3\text{-}1) & \cdot [O_3] \cdot \beta + j(R\ 3\text{-}5) \cdot [HONO]) \cdot (1 - \rho) + 2 \cdot j(R\ 3\text{-}10) \cdot [HCHO] \\
& + 2 \cdot j(R\ 3\text{-}11) \cdot [CH_3CHO] + 2 \cdot (j(R\ 3\text{-}12) + j(R\ 3\text{-}13)) \\
& \cdot [CH_3C(O)CH_3] + 2 \cdot j(R\ 3\text{-}14) \cdot [CHOCHO] \\
& = \delta \cdot [RO_2^*] \cdot (k(R\ 3\text{-}31) \cdot [NO] + k(R\ 3\text{-}32) \cdot [O_3]) \cdot \rho + 2 \\
& \cdot k(R\ 3\text{-}21) \cdot \delta \cdot (1 - \delta) \cdot [RO_2^*]^2 + 2 \cdot k(R\ 3\text{-}22) \\
& \cdot \left((1 - \delta) \cdot [RO_2^*] \right)^2 + 2 \cdot k(R\ 3\text{-}20) \cdot (\delta \cdot [RO_2^*])^2
\end{aligned}
\qquad E\ 3\text{-}9
$$

Where $(1 - \rho)$ accounts for the effective yield of HO_2 and RO_2 production through radical initiated reactions R 3-2, R 3-5, R 3-7, R 3-8, R 3-9, and R 3-15 (where only the measured VOCs are considered). ρ is then accounting for the radical termination through the reactions from R 3-26 to R 3-28 over the radical undergoes OH to peroxy radical conversion. δ is the ratio of the HO_2 to RO_2^* (i.e. $[HO_2] = \delta \cdot [RO_2^*]$, $[CH_3O_2] = (1 - \delta) \cdot [RO_2^*]$).

$$\rho = (k(R\ 3\text{-}26) \cdot [NO] + k(R\ 3\text{-}27) \cdot [NO_2] + k(R\ 3\text{-}28) \cdot [HONO])$$
$$/(k(R\ 3\text{-}7) \cdot [O_3] + k(R\ 3\text{-}8) \cdot [CO] + k(R\ 3\text{-}9) \cdot [CH_4]$$
$$+ k(R\ 3\text{-}10) \cdot [HCHO] + k(R\ 3\text{-}11) \cdot [CH_3CHO] + k(R\ 3\text{-}12)$$
$$\cdot [CH_3C(O)CH_3] + k(R\ 3\text{-}18) \cdot [CH_3OH] + k(R\ 3\text{-}19)$$
$$\cdot [CHOCHO] + k(R\ 3\text{-}26) \cdot [NO] + k(R\ 3\text{-}27) \cdot [NO_2]$$
$$+ k(R\ 3\text{-}28) \cdot [HONO])$$

$$E\ 3\text{-}10$$

Equation E 3-9 is quadratic in terms of $[RO_2^*]$, and therefore, the calculated RO_2^* is determined as one of the solutions (with positive values) to this quadratic equation:

$$[RO_2^*]_c = \frac{-(-L_{RO_2^*}) - \sqrt{L_{RO_2^*}^2 - 4 \cdot (-2 \cdot k_{RO_2^*}) \cdot P_{RO_2^*}}}{2 \cdot (-2 \cdot k_{RO_2^*})} \qquad E\ 3\text{-}11$$

As defined previously,

$$k_{RO_2^*} = k(R\ 3\text{-}21) \cdot \delta \cdot (1 - \delta) + k(R\ 3\text{-}22) \cdot (1 - \delta)^2 + k(R\ 3\text{-}20) \cdot \delta^2 \qquad E\ 3\text{-}12$$

$$P_{RO_2^*} = (2 \cdot j(R\ 3\text{-}1) \cdot [O_3] \cdot \beta + j(R\ 3\text{-}5) \cdot [HONO]) \cdot (1 - \rho) + 2 \cdot j(R\ 3\text{-}10)$$
$$\cdot [HCHO] + 2 \cdot j(R\ 3\text{-}11) \cdot [CH_3CHO] + 2 \cdot (j(R\ 3\text{-}12) \qquad E\ 3\text{-}13$$
$$+ j(R\ 3\text{-}13)) \cdot [CH_3C(O)CH_3] + 2 \cdot j(R\ 3\text{-}14) \cdot [CHOCHO]$$

$$L_{RO_2^*} = \delta \cdot (k(R\ 3\text{-}31) \cdot [NO] + k(R\ 3\text{-}32) \cdot [O_3]) \cdot \rho \qquad E\ 3\text{-}14$$

δ was set to 0.5 in $k_{RO_2^*}$ and in the PSS calculation as a weighted rate coefficient of RO_2^* self-reactions, assuming that $HO_2 = RO_2$ in RO_2^*.

4. Results and Discussion Part I: Rayleigh scattering cross-sections experimental determination at 408 nm

The Rayleigh scattering cross-sections, $\sigma_{Rayl.}$, of selected gases have been determined experimentally with the three CRDS detectors and two different setups mentioned in sections 3.1.1 and 3.1.4.

In this study, the $\sigma_{Rayl.}$ of nitrogen, N_2, oxygen, O_2, argon, Ar, carbon monoxide, CO, carbon dioxide, CO_2, nitrous oxide, N_2O, methane, CH_4 molecules and synthetic air (SA) are determined. The theoretical $\sigma_{Rayl.}$ values are calculated using n-based calculation equation E 2-13 based on the refractive index values, n and the correction of the depolarisation ratio, $F_K(\lambda)$. The comparison among the $\sigma_{Rayl.}$ measurements of this work, the available $\sigma_{Rayl.}$ measurements from other publications at the nearby wavelength, and the n-based $\sigma_{Rayl.}$ values will be discussed in a later section. An example of the determination of $\sigma_{Rayl.}$ for O_2 with the CRDS measurements is shown in Figure 21. A 1st order linear fit is applied to the loss rate, $1/(\tau \cdot c)[cm^{-1}]$ (where τ is the ring-down time, c is the speed of EM radiation) and the corresponding number density N of the molecules of interest [molec.$\cdot cm^{-3}$]. According to equation E 2-30, the slope of the fit is the Rayleigh scattering cross-section $[cm^2]$. The offset value of the empty cell results from the combined effect of the mirror cleanliness, the alignment of the CRDS mirrors of the cavity, and the molecule absorption on the surfaces of the CRDS mirror.
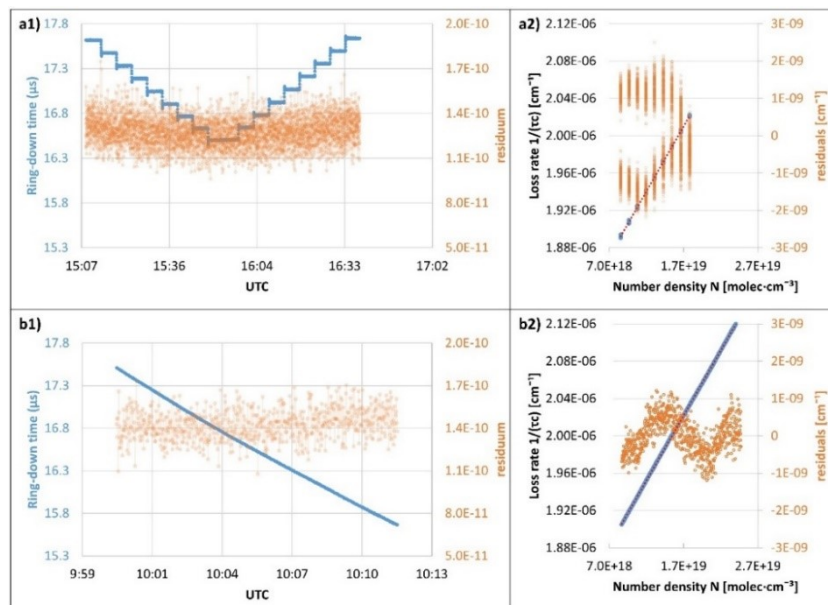
Figure 21: Example of CRDS measurement for the $\sigma_{Rayl.}$ determination of O_2 at 408.4 nm using setup 3. Panel a) shows the continuous mode with discrete pressure changes 300 → 700 → 300 hPa with 50 hPa pressure differences, 90 min total measurement duration (5 min each step), 4115 signal points; Panel b)shows ramp mode with continuous pressure change from 350 hPa to 1000 hPa, 11 min measurement duration, 695 signal points. The measurements are depicted as blue filled circles in panel 1)for ringdown time signal over time and in panel 2) for loss rate over number density. The orange filled circles in panel 1) represent the residuum of the ring-down time signal from the non-linear least-squares fit, while the orange filled circles in panel 2) represent the residuals of the loss rate measurements to the loss rate fit. The red dashed lines in panel 2) represent the linear fit. The slope of the fitted lines corresponds to the determined $\sigma_{O_2(Rayl.)}$.

Table 6: Configurations of the pulse generator used to improve the performance of setup 2.

Conf1	original setup
Conf2	Replace the Stachl pulse generator with signal generator DG535, Stanford Research Systems, Inc.
Conf3	Replace the power supply of the Stachl pulse generator to the VOLTCRAFT lab power supply
Conf4	Replace the Stachl pulse generator with Stanford Research Systems DG535 and clean the cavity mirrors thoroughly

Several optimisations have to be made during the experiment to improve the stability of different setups. In the early experiments of the $\sigma_{N_2(Rayl.)}$ determination, the results of setup 2 show around 5 times lower reproducibility compared to setup 1 both using continuous mode. As mentioned in section 3.1.1, setups 1 & 2 are equipped with a customised TTL pulse generator from the company Stachl, which uses the 12V power supply from the dedicated power distribution of the detector. The Stachl pulse generator has sufficient accuracy and low noise for the PeRCEAS detector, which is intended for the measurement of NO_2 extinction in 10^{-19} cm^2 order of magnitude. The noise of this pulse generator was proven not to be adequate for the determination of the $\sigma_{Rayl.}$ in the 10^{-26} cm^2 order of magnitude. Therefore, a cleaner power supply and/or a more accurate pulse generator were required to improve accuracy. To address this issue, the pulse generator system of setup 2 was replaced, and four different configurations of tests were conducted, as shown in Table 6.
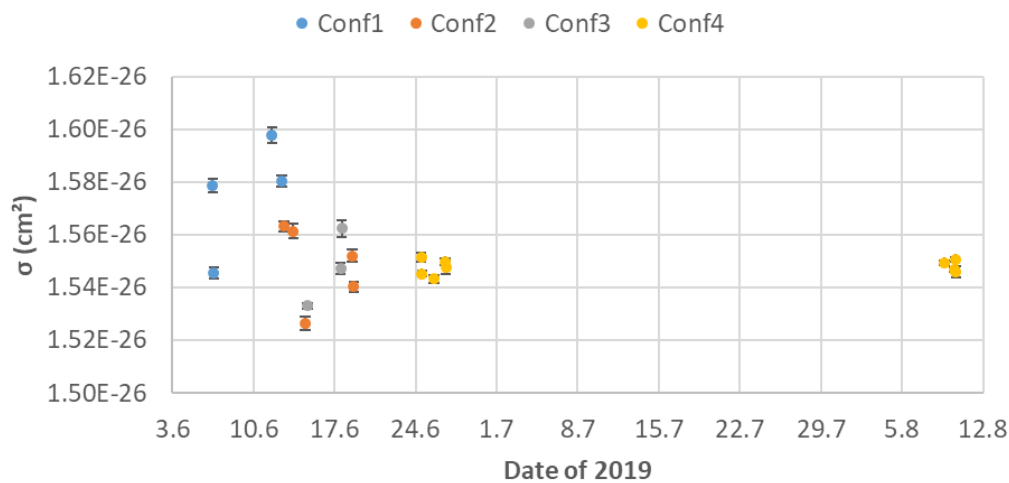
Figure 22: Retrieved $\sigma_{N_2(Rayl.)}$ with the configurations of setup 2 described in Table 6.

The test results depicted in Figure 22 indicate a significant improvement in reproducibility ($\sim$ 10 times lower standard deviation) after replacing the pulse generator system setup 2. This confirms that the original setup of the pulse generator was not accurate enough to provide a stable pulse for the measurement. The effect from the power supply seems not to be significant after cleaning the mirrors. Consequently, all measurements with setup 2 were performed using Conf4.

4.1 N₂ $\sigma_{(Rayl.)}$ determination

All three setups were used to determine the N_2 Rayleigh scattering cross-section at 408 nm. Measurement procedure 1 (section 3.1.4.1) is used for all three setups; measurement procedure 2 (section 3.1.4.2) and procedure 3 (section 3.1.4.3) are applied for setup 3. The gas used in this study were from Air Liquide Alphagaz™ 1 N_2 (purity of ≥ 99.999 mol %) and Alphagaz™ 2 N_2 (high purity N_2, HPN_2, purity of ≥ 99.9999 mol %). For more details about the N_2 gas supply please check appendix A 1. The different conditions for the experiments with measurement procedure 1 are summarised in Table 7.

Table 7: Measurement conditions for the determination of $\sigma_{N_2(Rayl.)}$ using measurement procedure 1.

Name	Setup	Pressure range (hPa)	Step duration (mins)	Step P difference (hPa)
Condition 1	1	300-500	10	100
Condition 2	1	300-500	10	50
Condition 3	2	300-500	10	50
Condition 4	2	300-700	10	100
Condition 5	3	300-700	5	50

The measured $\sigma_{N_2(Rayl.)}$ are compared with the $\sigma_{N_2(Rayl.)}$ calculated with E 2-13 and E 2-14 from the measured refractive index and depolarisation ratios. The N_2 refractive index, n_{N_2}, in the wavelength range of 254 nm ≤ λ ≤ 468 nm is given by Bates, 1984; Sneep and Ubachs, 2005 based on the measurements of Peck and Khanna, 1966 and Abjean, 1970 scaled to 15 °C and 1013.15 hPa:

$$\left(n_{N_2} - 1\right) \times 10^8 = 5677.465 + \frac{318.81874 \times 10^{12}}{1.44 \times 10^{10} - \tilde{v}^2} \qquad \text{E 4-1}$$

Based on the measurements by Alms et al., 1975, Bridge and Buckingham, 1966 and calculations by Oddershede and Svendsen, 1982, the dispersion relation for the wavelength dependent King correction factor of N_2, $F_k N_2(\tilde{v})$, is given by Bates, 1984:

$$F_k N_2(\tilde{v}) = 1.034 + 3.17 \times 10^{-12} \cdot \tilde{v}^2 \qquad \text{E 4-2}$$

where $\tilde{v}$ is the wavenumber ($\tilde{v} = 1/\lambda$) in cm^{-1}.

Then the corresponding n-based $\sigma_{N_2(Rayl.)}$ values and the refractive index of N_2 for different setups are calculated by convoluting the calculated $\sigma_{N_2(Rayl.)}$ and n with the Gaussian fit of the laser spectrum at its full-width half maximum (FWHM). Note here that the convoluted n values are needed in E 2-29. An example of the convolution is shown in Figure 23. The calculated results of $\sigma_{N_2(Rayl.)}$ and n are shown in Table 8, as "n-based $\sigma_{Rayl.}$" and "n (refractive index)".
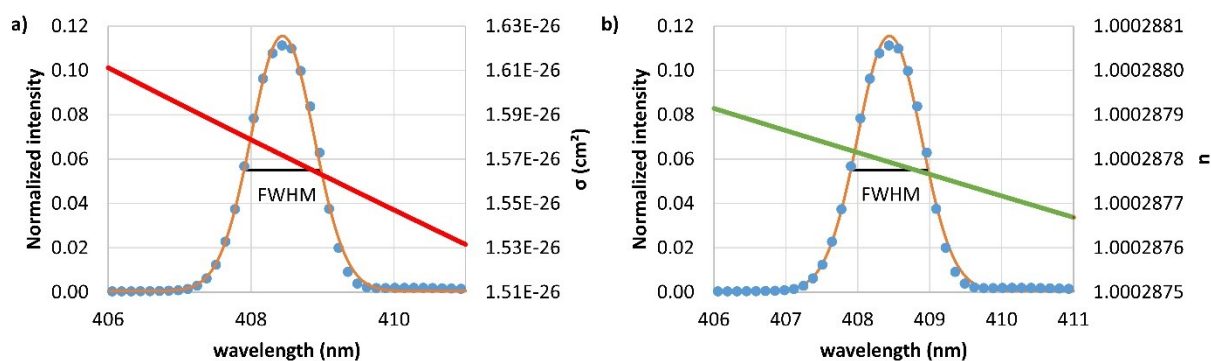
Figure 23: a) Convolution of the calculated $\sigma_{N_2(Rayl.)}$ (red filled circles) or b) the calculated refractive index n_{N_2} (green filled circles)) with the Gaussian fit (orange line) of the spectrum of setup 3 at FWHM, aka, from 407.9 nm to 409.0 nm. The blue filled circles are the original measurements of the spectrometer.

Table 8 summarises the $\sigma_{N_2(Rayl.)}$ retrieved for all setups with two procedures. All the measurements for the ramp mode are retrieved at a pressure range between 350 hPa and 1000 hPa. The mean values for different conditions for the same setup agree within the experimental error: conditions 1 & 2 for setup 1, conditions 3 & 4 for setup 2, and condition 5 and ramp mode for setup 3. The pressure range and the step P difference do not have a significant effect on the determination of the $\sigma_{N_2(Rayl.)}$. Therefore, the results are grouped by the laser peak emissions of the setups, and the later discussion for the other molecules will not be differentiated between pressures. The differences between the measured and calculated values for the continuous mode of setup 1, 2, as well as the ramp mode of setup 3, were found to be - 1.12 %, - 1.35 %, - 3.22 %, and - 3.63 %, respectively. The differences between the measured and calculated $\sigma_{N_2(Rayl.)}$ are calculated as: $\frac{\sigma_{meas.} - \sigma_{n-based}}{\sigma_{n-based}} \times 100 \%$. The $\sigma_{HPN_2(Rayl.)}$ agrees within the standard deviation of $\sigma_{N_2(Rayl.)}$ for all setups and measurement modes.

Table 8: Measurement results for the determination of $\sigma_{N_2(Rayl.)}$. The calculated values of n-based $\sigma_{Rayl.}$ are included for reference. The error is reported as the 2σ standard deviation of the mean values. C: condition. N₂ and HPN₂ results are both included.

mode	Continuous mode						Ramp mode	
Setup	1			2			3	
Group	C 1	C 2	overall	C 3	C 4	overall	C 5	overall
n-based $\sigma_{Rayl.}$ ($\times 10^{-26} cm^2$)	1.580			1.572			1.574	
n	1.00028782			1.00028780			1.00028779	
Mean ($\times 10^{-26} cm^2$)	1.564	1.562	1.562	1.552	1.554	1.552	1.521	1.515
2σ std. dev. ($\times 10^{-26} cm^2$)	0.020	0.017	0.018	0.003		0.003	0.016	0.014
Median ($\times 10^{-26} cm^2$)	1.563	1.560	1.561	1.552	1.554	1.553	1.522	1.511
Number of measurements	3	13	16	4	1	5	14	11

The reproducibility was studied during the series of measurements for setups 1 & 2 (see Figure 24). The mean value obtained for setup 1 is reasonably good, but the increase in the standard deviation between the experiments in January (1.559 ± 0.011 cm²) and May (1.563 ± 0.020 cm²) was due to a potential HCl contamination of the mirrors in setup 1

related with experiments carried out between January and May 2019. This affected the stability of the setup but the mean values are still valid.
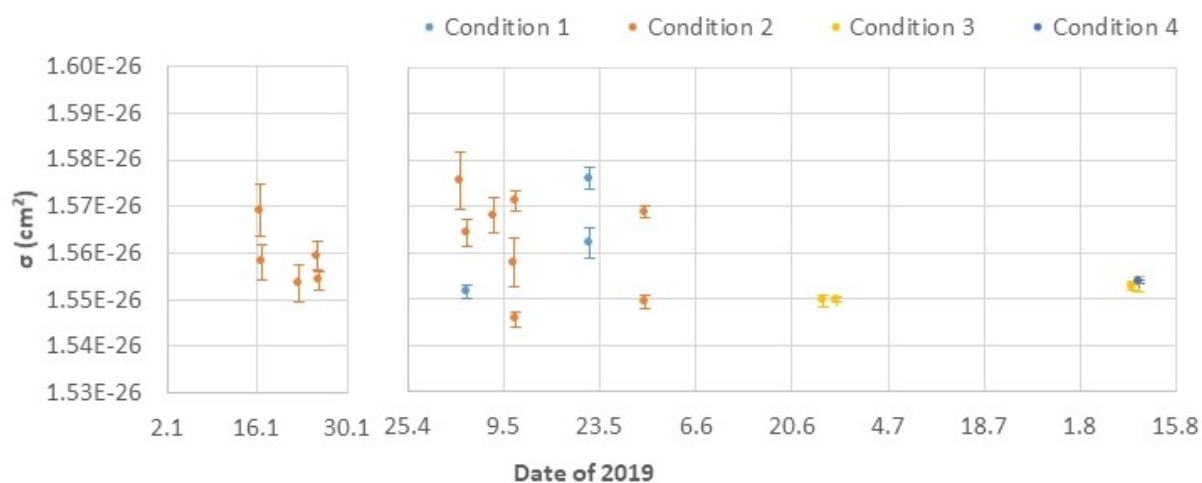
Figure 24: Reproducibility of the $\sigma_{N_2(Rayl.)}$ determined by with setup 1 & 2 in continuous mode. The error bars represent the 2σ standard deviation of the mean values.

The experiments are designed in a way to keep as much as possible the conditions controlled. In reality, it is necessary to check the quality of the data and make the necessary screening. In this work, the cavity temperature, frequency of the laser switch-off, and the τ_0 of an empty cell are selected as key indicators for the quality control and screen of the experiments before elaborating the final results. An example of measurement quality control for N_2 with setups 1 & 2 is shown in Figure 25. The temperature of the cavity was kept under 25 °C for this work and the temperature varied for each experiment less than 0.5 °C so that the lasers worked with minimum temperature interferences from the ambient environment. As mentioned in section 3.1.1, the laser output is modulated with a switch-off threshold at 0.1 V. The switch-off frequencies primarily depend on the CRDS mirror cleanliness, molecules inside the cavity, the degree of alignment of the cavity, and the CPU power of the PXI computer. Therefore, the frequency can be used as an indirect indicator of the signal quality. When a retrieved $\sigma_{Rayl.}$ has obvious low or high values or higher standard deviations compared to the results from the other measurements of the same setup, the experiment will be reviewed. The τ_0 is directly affected by the cleanliness of the CRDS mirrors and the alignment of the cavity. $\tau_0(N_2)$ decreased gradually up to 15 % over the series of measurements (over 3 weeks) without cleaning the CRDS mirror. This decrease might be related to a gradual gas saturation of the CRDS mirror surface. The τ signal decrease with continuous N_2 flow in the cavity during one measurement (90 mins) is < 0.3 μs (2 %). The τ_0 recovers after cleaning the CRDS mirrors at the best alignment. In the presented example in Figure 25, the retrieved $\sigma_{N_2(Rayl.)}$ do not correlate with the variations observed in the selected indicators. The data control procedures are similar for all the molecules measured by all the setups and conditions as presented in the following sections. Therefore, the corresponding plots for all the other molecules will be shown in the Appendix.
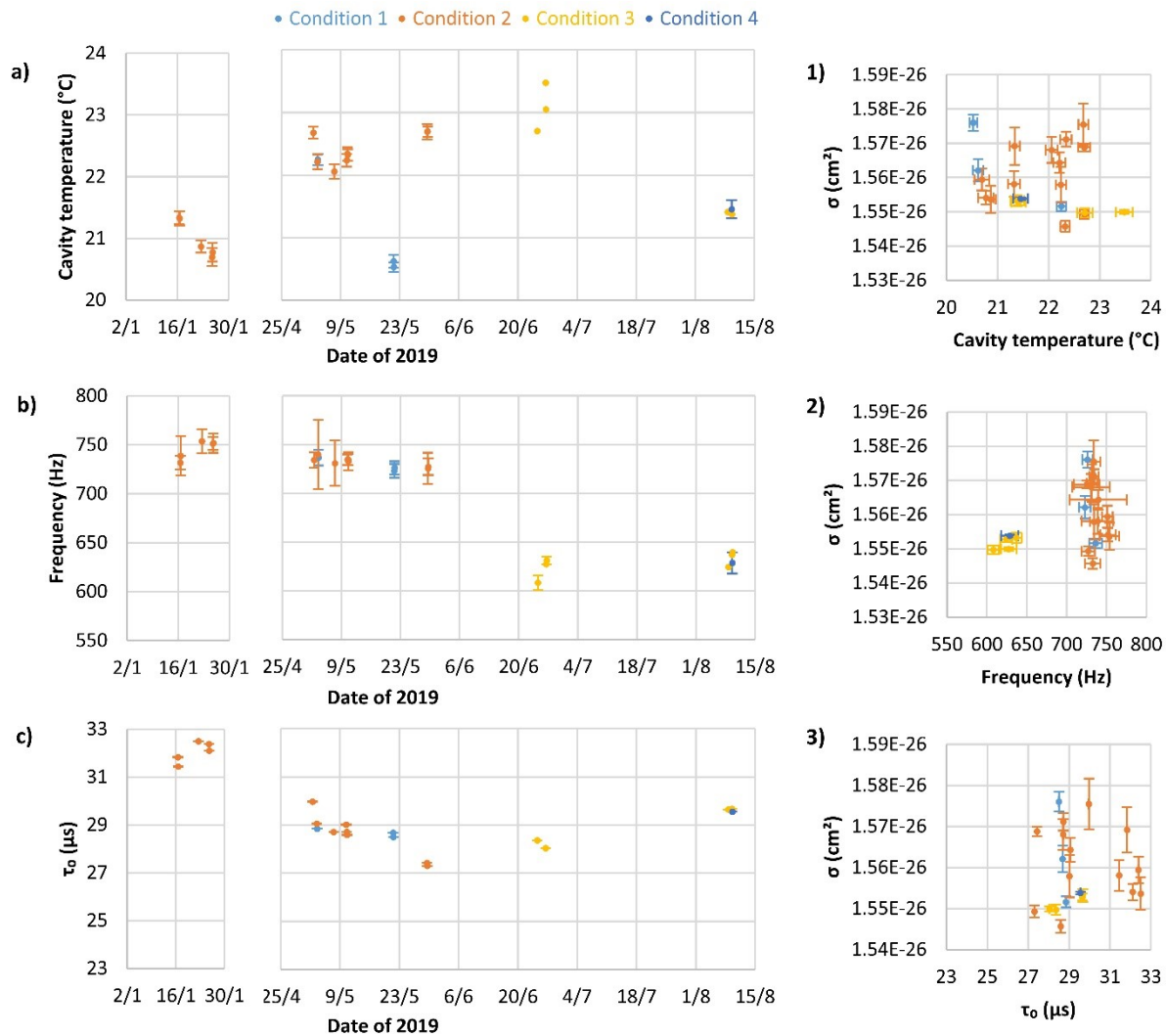
Figure 25: Variability of the experimental quality control indicators during the determination of $\sigma_{N_2(Rayl.)}$ for setup 1&2 over the time of the measured a) cavity temperature, b) frequency of the laser, and c) τ_0 of the cavity. The numbers 1), 2) and 3) are the $\sigma_{N_2(Rayl.)}$ relative to the measured parameters a), b), and c), respectively.

When flowing N_2 through the cavity, a continuous and significant decrease in the τ signal at constant temperature and pressure is observed before a stable signal is reached. The ring downtime decreases further within a few days and does not recover till the CRDS mirrors are cleaned. Please note here that within these few days the cavity has continuous N_2 flow during the measurement period (8 hours) and the system is shut down during the night. The decreasing rate of τ reduces non-linearly with constant N_2 flow through the cavity. To minimise the time required for cavity stabilisation, N_2 was filled inside the cavity at 300 hPa overnight without N_2 flow continuously before the ramp mode experiment. A stable τ signal was reached typically 6 hours after closing the cavity. Such a procedure ensures a stable system ready for a ramp experiment on the following morning.
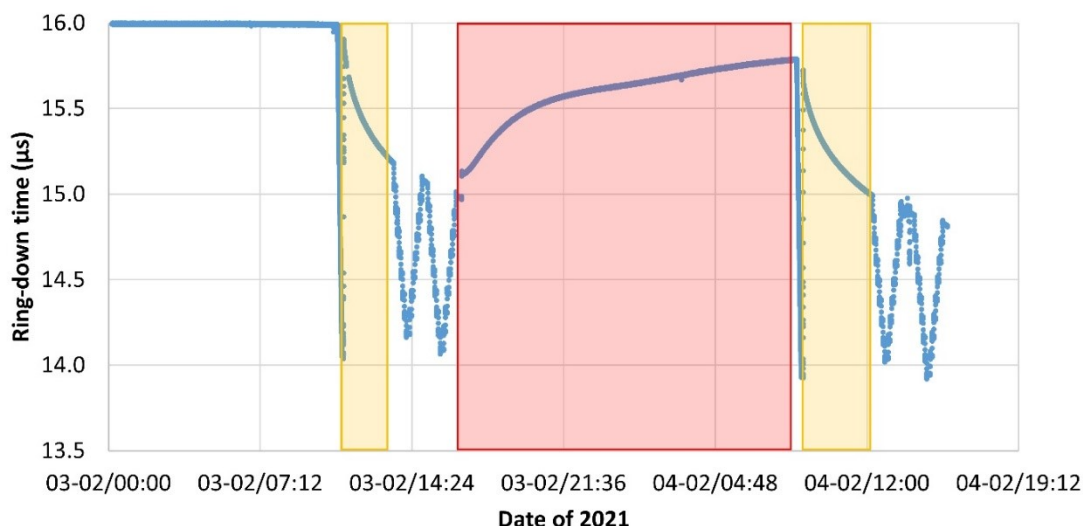
Figure 26: Long-term change of the ring downtime signal of setup 3 from 03-02-2021 to 04-02-2021 when the cavity is filled with N_2. The blue filled circles are the τ signal. In yellow are highlighted the τ signal drops with N_2 flowing continuously through the cavity and in red the τ signal increases when the cavity is flushed and filled with N_2.

Figure 26 shows a representative example of the τ variation during the experiment. At the beginning of the plot, stable τ was observed after 8 hours of stabilisation. As soon as N_2 start to flow into the cavity (marked in yellow, pressure and temperature are stable), the τ signal drops continuously over the day. When the N_2-filled cavity is closed under pressure, the τ recovers over the night (marked in red). Since all system tubes have been replaced with stainless steel except for the exhaust, the possibility of permeation of gases (especially water) is very low. Another possible source of humidity is the lab air through the leak of setup 3 at the rate of 0.02 hPa/min. The error in the determination of $\sigma_{Rayl.}$ related to this water will be discussed in the error analysis in section 4.11.4. The leak of the cavity does not explain the τ signal increase overnight. One hypothesis to explain this behaviour is that impurities from the N_2 ($\geq$ 99.999 mol % Alphagaz™ 1, AirLiquide S.A.) gas may stick to the cavity mirror when continuous N_2 flows through the cavity. This will reduce the reflectivity of the CRDS mirrors and explain the continuous τ drop. According to this, the τ should reach a stable value when the mirror is fully saturated with impurities. However, this is not observed even after more than 48 hours of continuous flow. In contrast, when the cavity is closed, no more impurities enter the cavity. The impurities on the cavity mirror surface have a higher concentration than in the cavity air. Consequently, the impurities diffuse from the mirror surface to the cavity air gradually over time. The mirror reflectively is gained back gradually until a balance is reached. This explains why the τ increased and stabilised overnight. This hypothesis was tested experimentally. As setup 3 has better tightness than setups 1 & 2 and is more sensitive, it should be more suitable to identify a possible effect coming from impurities in the added gases. Higher purity N_2 gas ($\geq$ 99.9999 mol% Alphagaz™ 2 from AirLiquide S.A.) with lower hydrocarbon impurities than the N_2 gas used in the previous experiments was tested. The higher N_2 purity did not affect the τ drop over time or the value of the retrieved $\sigma_{N_2(Rayl.)}$. Other potential NOx-related impurities in N_2 are difficult to determine by the manufacturer and cannot be ruled out. During the weekly period, the τ decreases significantly ($\sim$ 8 %). Therefore, the cavity mirrors are cleaned weekly.

4.2 O_2 $\sigma_{(Rayl.)}$ determination

The oxygen used in this study is from Air Liquide oxygen N48 which has a purity of ≥ 99.998 mol % with Ar ≤ 10 ppmv. For more details about the gas supply please check appendix A 1. The Rayleigh scattering cross-section of oxygen, $\sigma_{O_2(Rayl.)}$, has been determined from CRDS measurements made with all three setups using continuous mode and setup 3 using ramp mode at 408 nm. The refractive index of O_2, n_{O_2}, is given by Bates, 1984; Sneep & Ubachs, 2005 for wavelength from 288 nm to 546 nm at 0 °C and 1013.15 hPa as:

$$\left(n_{O_2} - 1\right) \times 10^8 = 20564.8 + \frac{2.480899 \times 10^{13}}{4.09 \times 10^9 - \tilde{v}^2} \qquad \text{E 4-3}$$

The O_2 King correction factor of wavelength dependent, $F_k O_2(\tilde{v})$, was given by Bates, 1984 as:

$$F_k O_2(\tilde{v}) = 1.09 + 1.385 \times 10^{-11} \cdot \tilde{v}^2 + 1.448 \times 10^{-20} \cdot \tilde{v}^4 \qquad \text{E 4-4}$$

where $\tilde{v}$ is the wavenumber ($\tilde{v} = 1/\lambda$) in cm^{-1}.

Table 9: Measurement conditions for the determination of $\sigma_{O_2(Rayl.)}$ using continuous mode.

Name	Setup	Pressure range (hPa)	Step duration (mins)	Step P difference (hPa)
Condition 1	1	300-500	10	50
Condition 2	2	300-500	10	50
Condition 3	3	300-500	2	50
Condition 4	3	300-700	2	100
Condition 5	3	300-700	5	50

The continuous mode conditions for the determination of $\sigma_{O_2(Rayl.)}$ are summarised in Table 9. The calculated $\sigma_{O_2(Rayl.)}$ are similar convolutions as shown in Figure 23 and are presented in Table 10 as "n-based $\sigma_{Rayl.}$". The $\sigma_{O_2(Rayl.)}$ results indicate that the pressure range and the step pressure difference do not affect the determination of the $\sigma_{Rayl.}$ when using continuous mode. In the experiment of O_2, different step times are introduced for the experiments with setup 3. All of the $\sigma_{O_2(Rayl.)}$ results are summarised in Table 10. Additional information about the quality control plots is shown in appendix A 2 and A 3.

The $\sigma_{O_2(Rayl.)}$ retrieved from setup 3 using continuous mode at different conditions agree within the experimental errors. Conditions 3 & 4 using a shorter step time (2 mins) give a higher standard deviation compared to condition 5. This indicates that the system needs more time for pressure stabilisation after each change in the cavity pressure. Although the stability of the signal is reduced, therefore, the larger standard deviation of $\sigma_{O_2(Rayl.)}$, the mean $\sigma_{O_2(Rayl.)}$ does not change significantly. The measurements with different step times are not grouped separately but considered in the overall mean calculation of $\sigma_{Rayl.}$ for the continuous mode. The determined results using continuous and ramp modes agree

within their experimental errors for setup 3. The differences between the measured and calculated values for the continuous mode of setup 1, setup 2, setup 3 and ramp mode of setup 3 are - 2.10 %, - 1.90 %, - 0.57 %, and - 0.44 %, respectively.

Table 10: Measurement results for the determination of $\sigma_{O_2(Rayl.)}$. The calculated vlues of n-based $\sigma_{Rayl.}$ and n (refractive index) are included in the reference. The error is reported as the 2σ standard deviation of the mean values. C: condition.

mode	Continuous mode						Ramp mode
Setup	1	2	3				
Group	C 1	C 2	C 3	C 4	C 5	overall	overall
n-based $\sigma_{Rayl.}$ ($\times 10^{-26} cm^2$)	1.406	1.400	1.399				
n	1.00027675	1.00027673	1.00027672				
Mean ($\times 10^{-26} cm^2$)	1.377	1.374	1.393	1.390	1.393	1.391	1.393
2σ std. dev. ($\times 10^{-26} cm^2$)	0.012	0.008	0.010	0.006	0.003	0.006	0.004
Median ($\times 10^{-26} cm^2$)	1.377	1.371	1.396	1.389	1.393	1.392	1.394
Number of measurements	2	7	3	11	9	23	6

In contrast to N_2, the τ signal of O_2 does not decrease with constant O_2 flow through the cavity over time. The τ variation is generally ≤ 1.2 % over one hour. The long-term $\tau_0(O_2)$ variation is less than 0.2 μs (~ 5 %) over 1 week without cleaning the CRDS mirrors. A possible explanation is that the continuous O_2 flow into the cavity can clean the cavity mirrors gradually. A cleaner surface will cause less EM radiation attenuations, i.e. higher τ signal.

4.3 SA $\sigma_{(Rayl.)}$ determination

Synthetic air used in this study was from the company Air Liquide ALPHAGAZ™ 1 Air (synthetic air, SA, ≥ 99.999 mol %) and ALPHAGAZ™ 2 Air (high purity synthetic air, HPSA, ≥ 99.9999 mol %) with 20.5 mol. % O_2 mixed in N_2. Alphagaz™ 1 Air is the mixture of Alphagaz™ 1 N_2 and Alphagaz™ 1 O_2. Alphagaz™ 1 N_2 does not contain Ar, but Alphagaz™ 1 O_2 has Ar ≤ 10 ppm, therefore, the mixture of SA has ≤ 2.1 ppm Ar. In the case of Alphagaz™ 2 Air, both Alphagaz™ 2 N_2 and Alphagaz™ 2 O_2 do not contain Ar. For more details about the gas supply please check appendix A 1. For a known mixture of gas, the $\sigma_{Rayl.}$ can be calculated as (Bates, 1984):

$$\sigma_{SA(Rayl.)} = f(N_2) \cdot \sigma_{N_2(Rayl.)} + f(O_2) \cdot \sigma_{O_2(Rayl.)}$$
E 4-5

where $f(N_2)$ and $f(O_2)$ are the fraction of the mixture. $\sigma_{N_2(Rayl.)}$ and $\sigma_{O_2(Rayl.)}$ are calculated using equations E 4-1 to E 4-4.

The refractive index, n, of a known mixture of gas, can be calculated in the case of SA (Bates, 1984):

$$(n_{SA} - 1) = f(N_2) \cdot (n_{N_2} - 1) + f(O_2) \cdot (n_{O_2} - 1)$$
E 4-6

The results are presented in Table 11, all the ramp mode experiments took the pressure range between 300 hPa and 1300 hPa. As the $\sigma_{SA(Rayl.)}$ are often stable and reproducible, SA is used as a reference gas during this study whenever a comparison is needed after modification of the setups or the gases. The results presented in this section do not include the SA measurements made for short tests. The differences between the measured and calculated values for the continuous mode of setup 1, setup 2, setup 3 and ramp mode of setup 3 are - 2.78 %, - 2.83 %, - 2.25 %, and - 0.79 %, respectively. The results obtained by setup 3 in continuous and ramp modes agree within the experimental error. The $\sigma_{HPSA(Rayl.)}$ agrees within the standard deviation of $\sigma_{SA(Rayl.)}$ for all setups and measurement modes. Additional information about the quality control plots is shown in appendix A 5 and A 6.

Table 11: Measurement results for the determination of $\sigma_{SA(Rayl.)}$. The calculated vlues of n-based $\sigma_{Rayl.}$ and n (refractive index) are included in the reference. The error is reported as the 2σ standard deviation of the mean values. SA and HPSA results are both included.

mode	Continuous mode		Ramp mode	
Setup	1	2	3	
n-based $\sigma_{Rayl.}$ ($\times 10^{-26} cm^2$)	1.544	1.538	1.536	
n (refractive index)	1.00027902	1.00027900	1.00027899	
Mean ($\times 10^{-26} cm^2$)	1.501	1.495	1.502	1.524
2σ std. dev. ($\times 10^{-26} cm^2$)	0.005	0.009	0.018	0.014
Median ($\times 10^{-26} cm^2$)	1.500	1.495	1.499	1.523
Number of measurements	11	14	7	11

The $\sigma_{SA(Rayl.)}$ values (appendix A 5) between 24-06-2019 and 07-08-2019 show larger variability than in the other periods where the peak-to-peak difference of setup 1 is less than 0.01×10^{-26} [cm^2] and of setup 2 is around 0.015×10^{-26} [cm^2]. The N_2 measurements carried out with setup 2 in that period showed a similar variability (also see Figure 24). This might be explained by stability changes related to set-up changes for the measurement of other gases in between. The τ_0 decreased ~ 4 µs (~ 12 %) after the HCl experiments with setup 1 agreed with the observed τ_0 at the same period measuring with N_2. The τ_0 variations for SA are normally below 0.2 µs (~ 0.6 %) over 2 weeks for all three setups. The changes of τ_0 remained < 3 % for SA during 10 months. The cavity seemed to be damaged and contaminated during the previous HCl tests, leading to higher τ noise for condition 2 and deviations in the $\sigma_{SA(Rayl.)}$ determined. Interestingly, SA does not show the fast temporal decrease of the τ signal from N_2 (see section 4.1) despite N_2 being the bulk constituent.

4.4 Ar $\sigma_{(Rayl.)}$ determination

The Ar used in this study was from Air Liquide Alphagaz™ Ar (purity ≥ 99.999 mol %). For more details about the gas supply please check appendix A 1. The Rayleigh scattering cross-section of argon, $\sigma_{Ar(Rayl.)}$, has been determined at 408 nm with CRDS measurements made with three setups using continuous mode and setup 3 using ramp mode. The refractive index of Ar, n_{Ar}, was measured by Peck and Fisher, 1964 at the

wavelength range from 467.9 nm to 2056.8 nm. A dispersion relation valid from 303 nm to 2000 nm is given by Sneep and Ubachs, 2005 scaled at 1013.15 hPa and 15 °C:

$$(n_{Ar} - 1) \times 10^8 = 6432.135 + \frac{286.06021 \times 10^{12}}{14.4 \times 10^9 - \tilde{v}^2} \qquad \qquad E\ 4\text{-}7$$

where $\tilde{v}$ is the wavenumber ($\tilde{v} = 1/\lambda$) in cm^{-1}.

Argon is assumed to be spherical, the depolarisation is taken to be zero, therefore, the King correction factor of Ar, $F_k Ar = 1$.

Table 12: Measurement results for the determination of $\sigma_{Ar(Rayl.)}$. The calculated values of n-based $\sigma_{Rayl.}$ are included for reference. The error is reported as the 2σ standard deviation of the mean values.

mode	Continuous mode			Ramp mode
Setup	1	2		3
n-based $\sigma_{Rayl.}$ ($\times 10^{-26} cm^2$)	1.358	1.353		1.351
n (refractive index)	1.00027162	1.00027161		1.00027160
Mean ($\times 10^{-26} cm^2$)	1.348	1.337	1.324	1.327
2σ std. dev. ($\times 10^{-26} cm^2$)	0.013	0.008	0.014	0.017
Median ($\times 10^{-26} cm^2$)	1.347	1.333	1.322	1.326
Number of measurements	11	9	48	13

The results of the experimental determined $\sigma_{Ar(Rayl.)}$ are tabulated in Table 12. All the ramp experiments have the same pressure range from 300 hPa to 800 hPa. In the setup 1 continuous mode experiments, a needle valve was used in the beginning and then replaced by a mass flow controller, MFC. The results indicate that using a mass flow controller will stabilise the system faster in terms of flow dynamics and speed up the process of reaching the stable τ signal at each pressure change. Note that only some of the Ar experiments used a needle valve instead of an MFC for controlling the flow rate control in the continuous mode. Setup 1 was used for the continuous measurements mode in two periods before and after the HCl experiment (as mentioned in sections 4.1 and 4.3). The mean $\sigma_{Ar(Rayl.)}$ retrieved before and after HCl experiments are $(1.347 \pm 0.006) \times 10^{-26}$ cm^2 and $(1.351 \pm 0.015) \times 10^{-26}$ cm^2, respectively, where the $\sigma_{Ar(Rayl.)}$ agree within the experimental error but the standard deviation after HCl experiments is more than two times higher. Similar effects are observed in the case of N$_2$ and SA. The $\sigma_{Ar(Rayl.)}$ determined in continuous and ramp modes agree within the experimental error for setup 3. The continuous mode results for setup 3 show a higher standard deviation because 29 out of 48 measurements are using 2 mins step time. As mentioned in section 4.2, a shorter step time will increase the standard deviation of the $\sigma_{Rayl.}$ retrieval because the system was just reaching stable before changing to another pressure level. The differences between the measured and calculated values for the continuous mode of setup 1, setup 2, setup 3 and ramp mode of setup 3 are - 0.74 %, - 1.21 %, - 2.01 %, and - 1.84 %, respectively. Additional information about the quality control plots for Ar is shown in appendix A 8 and A 9.

The τ signal for Ar drops continuously when the flowing gas inside the cavity is at constant pressure and temperature. The effect is similar to the case of N_2. During the measurements of Ar in continuous mode (5 weeks), the change in τ_0 was up to 18 %. The τ signal decrease with continuous Ar flow in the cavity during a 100 mins measurement is < 0.4 μs (1.5 %).

4.5 CO_2 $\sigma_{(Rayl.)}$ determination

The CO_2 used in this study was from Air Liquide CO_2 N48 (purity ≥ 99.998 mol %). For more details about the gas supply please check appendix A 1. The Rayleigh scattering cross-section of carbon dioxide, $\sigma_{CO_2(Rayl.)}$, has been determined at 408 nm with CRDS measurements made with setup 3 using continuous and ramp mode. The refractive index of CO_2, n_{CO_2}, is given by Sneep and Ubachs, 2005 based on the measurements of Bideau-Mehu et al., 1973 for wavelength between 180.7 nm and 1694.5 nm scaled to 1013.15 hPa and 15 °C:

$$
\begin{aligned}
\left(n_{CO_2} - 1\right) &\times 10^8 \\
&= 1.1427 \times 10^{11} \\
&\times \left(\frac{5799.25}{128908.9^2 - \tilde{v}^2} + \frac{120.05}{89223.8^2 - \tilde{v}^2} + \frac{5.3334}{75037.5^2 - \tilde{v}^2} \right. \\
&\left. + \frac{4.3244}{67837.7^2 - \tilde{v}^2} + \frac{1.218145 \times 10^{-5}}{2418.136^2 - \tilde{v}^2} \right)
\end{aligned}
\qquad E\text{ 4-8}
$$

Alms et al., 1975 measured the depolarisation of CO_2. Sneep and Ubachs, 2005 give the fitted dispersion relation for wavelength dependent King correction factor of CO_2, $F_k CO_2(\tilde{v})$, based on these measurements and the model function presented by Bates, 1984:

$$
F_k CO_2(\tilde{v}) = 1.1364 + 2.53 \times 10^{-11} \tilde{v}^2
\qquad E\text{ 4-9}
$$

where $\tilde{v}$ is the wavenumber ($\tilde{v} = 1/\lambda$) in cm^{-1}.

Table 13: Measurement results for the determination of $\sigma_{CO_2(Rayl.)}$ using setup 3. The calculated values of n-based $\sigma_{Rayl.}$ are included for reference. The error is reported as the 2σ standard deviation of the mean values.

mode	Continuous mode	Ramp mode
Setup	3	
n-based $\sigma_{Rayl.}$ ($\times 10^{-26} cm^2$)	3.988	
n (refractive index)	1.00043479	
Mean ($\times 10^{-26} cm^2$)	3.989	3.975
2σ std. dev. ($\times 10^{-26} cm^2$)	0.019	0.064
Median ($\times 10^{-26} cm^2$)	3.992	3.982
Number of measurements	26	7

The experimentally determined results of $\sigma_{CO_2(Rayl.)}$ are tabulated in Table 13. All the continuous mode experiments are made between 300 hPa and 700 hPa, with 50 hPa pressure step differences, and 5 mins step duration. All the ramp mode experiments have a pressure range from 300 hPa to 1200 hPa. The $\sigma_{CO_2(Rayl.)}$ mean value for both modes

agrees within the experimental error. Due to higher $\sigma_{CO_2(Rayl.)}$, the τ signal for all the CO_2 experiments remains below 11 µs. The τ_0 variation < 0.8 µs (7 %) over two weeks. The differences between the calculated and retrieved values from the setup 3 measurements in continuous and ramp modes are + 0.04 %, and - 0.32 %, respectively. The τ signal decrease with continuous CO_2 flow in the cavity during 90 minutes of measurement is < 0.08 µs (0.7 %). Additional information about the quality control plots is shown in appendix A 10.

4.6 CO $\sigma_{(Rayl.)}$ determination

The CO used in this study was from Air Liquide CO N47 (purity ≥ 99.997 mol %). For more details about the gas supply please check appendix A 1. A dispersion relation of the refractive index of CO, n_{CO}, is given by Sneep and Ubachs, 2005 based on the measurement of Smith et al., 1976 for the wavelength range between 168 nm and 288 nm at 1013.15 hPa and 15 °C:

$$(n_{CO} - 1) \times 10^8 = 22851 + 45.6 \times \frac{10^{12}}{71427^2 - \tilde{v}^2} \qquad \text{E 4-10}$$

where $\tilde{v}$ is the wavenumber ($\tilde{v} = 1/\lambda$) in cm^{-1}.

Since CO is a diatomic molecule, the depolarisation is not zero. Measurements of the depolarisation ratio of CO, ρ_{CO_p}, were made by Bogaard et al., 1978 at 488.0 nm, $\rho_{CO_p}(488.0\,nm)$ = 0.0521, at 514.5 nm, $\rho_{CO_p}(514.5\,nm)$ = 0.0519, and Bridge and Buckingham, 1966, at 632.8 nm, $\rho_{CO_p}(632.8\,nm)$ = 0.0480. A study using ab initio calculations has shown that the dispersion in the depolarisation ratio can be neglected (Oddershede and Svendsen, 1982), therefore, the depolarisation ratio of CO at 408 nm is taken as $\rho_{CO_p}(408\,nm)$ = 0.0520. The King correction factor for CO, $F_k CO$, is calculated using equation E 2-14.

Table 14: Measurement results for the determination of $\sigma_{CO(Rayl.)}$ using setup 3. The calculated values of n-based $\sigma_{Rayl.}$ are included for reference. The error is reported as the 2σ standard deviation of the mean values.

mode	Continuous mode	Ramp mode
Setup	3	
n-based $\sigma_{Rayl.}$ ($\times 10^{-26} cm^2$)	2.027	
n (refractive index)	1.00032979	
Mean ($\times 10^{-26} cm^2$)	1.938	1.953
2σ std. dev. ($\times 10^{-26} cm^2$)	0.011	0.021
Median ($\times 10^{-26} cm^2$)	1.935	1.952
Number of measurements	14	6

As a toxic and flammable gas, the CO Rayleigh cross-section was first tried to be measured as a diluted mixture for safety reasons. The measurement was undertaken under the CO lower explosion limit, namely, at 9% CO in synthetic air, and the $\sigma_{CO(Rayl.)}$ was calculated from the measurement of the CO mixing ratio using the equation similar to E 4-5, replacing the N_2 and O_2 to N_2, O_2 and CO. The results are highly dependent on the quality of the gas

mixing process as well as the accuracy of the flow controller. This approach was shown not to be suitable in the experiments carried out using setup 1. The retrieved $\sigma_{CO(Rayl.)}$ at 408 nm using a CO mixture differed between - 11 % and + 12 % from the theoretical value and small changes in the gas mixture had a significant effect on the results. Therefore, the direct measurement of pure CO gas is necessary. Since setups 1 and 2 are not airtight enough, for safety reasons, the pure CO measurements were carried out by setup 3 using continuous and ramp modes. The continuous mode measurements are made in the 300 - 700 hPa pressure range with 5 mins pressure steps, and 50 hPa pressure differences. Ramp mode measurements are taken in the pressure range from 300 hPa to 1000 hPa. The summarised results are tabulated in Table 14. The $\sigma_{CO(Rayl.)}$ mean values for both measurement modes agree within the experimental error. A τ_0 variation < 1 μs (6 %) was observed over two weeks. The τ signal decrease with continuous CO flow in the cavity during a 90 mins measurement is < 0.2 μs (2 %). Generally, the gas supply comes from a dedicated gas storage location using stainless steel tubes more than 30 m in length to the lab. During the experiment with CO, the gas supply line was shortened to 1 m in length. The experimentally retrieved $\sigma_{CO(Rayl.)}$ values do not change significantly with the length of the supply line. The differences between the measured and calculated values for the continuous mode and ramp mode of setup 3 are - 4.41 %, and - 3.67 %, respectively. Additional information about the quality control plots is shown in appendix A 11.

4.7 N_2O $\sigma_{(Rayl.)}$ determination

The N_2O used in this study was from Air Liquide N_2O N25 (purity ≥ 99.5 mol %). For more details about the gas supply please check appendix A 1. The dispersion relation of the refractive index of N_2O, n_{N_2O}, is given by Sneep and Ubachs, 2005 based on the measurement made by Alms et al., 1975 scaled to 1013.15 hPa and 15 °C:

$$\left(n_{N_2O} - 1\right) \times 10^8 = 46890 + 4.12 \times 10^{-6}\tilde{v}^2 \qquad\qquad E\ 4\text{-}11$$

The dispersion relation of the N_2O wavelength dependent King correction factor, $F_k N_2 O(\tilde{v})$, is given by He et al., 2021 based on the measurement of Alms et al., 1975:

$$F_k N_2 O(\tilde{v}) = \frac{3.3462 + 70.8 \times 10^{-12}\tilde{v}^2}{2.7692 - 47.2 \times 10^{-12}\tilde{v}^2} \qquad\qquad E\ 4\text{-}12$$

A new dispersion relation of n_{N_2O} is suggested by He et al., 2021 combining their latest measurement for a wavelength range of 307 nm – 725 nm:

$$\left(n_{N_2O} - 1\right) \times 10^8 = 22095 + \frac{1.66291 \times 10^{14}}{6.75226 \times 10^9 - \tilde{v}^2} \qquad\qquad E\ 4\text{-}13$$

where $\tilde{v}$ is the wavenumber ($\tilde{v} = 1/\lambda$) in cm^{-1}.

The $\sigma_{N_2O(Rayl.)}$ at 408 nm is determined by setup 2 using continuous mode and setup 3 using continuous and ramp mode. The ramp mode measurements are made between 350 hPa and 1000 hPa pressure. The results of the experimentally retrieved and calculated $\sigma_{N_2O(Rayl.)}$ are summarised in Table 15. Additional information about the quality control plots is shown in appendix A 13 and A 14.

Table 15: Measurement results for the determination of $\sigma_{N_2O(Rayl.)}$. The calculated values of n-based $\sigma_{Rayl.}$ are included for reference. The error is reported as the 2σ standard deviation of the mean values.

mode	Continuous mode	Ramp mode	
Setup	2	3	
n-based $\sigma_{Rayl.}$ ($\times 10^{-26} cm^2$) (Sneep and Ubachs, 2005)	5.531	5.517	
n-based $\sigma_{Rayl.}$ ($\times 10^{-26} cm^2$) (He et al., 2021)	5.471	5.464	
n (refractive index)	1.00049123	1.00049122	
Mean ($\times 10^{-26} cm^2$)	5.428	5.478	5.485
2σ std. dev. ($\times 10^{-26} cm^2$)	0.035	0.010	0.008
Median ($\times 10^{-26} cm^2$)	5.431	5.476	5.484
Number of measurements	15	13	4

The τ signal decreased < 0.2 μs (~ 0.9 %) when continuously flowing N_2O during a 100 min measurement. The τ_0 of N_2O decreased < 3 μs (~ 10 %) over two weeks for setup 2 and < 1 μs (~ 7 %) over one week for setup 3. For the $\sigma_{N_2O(Rayl.)}$ experiments with setup 3, the CRDS mirrors were cleaned weekly and the τ_0 recovered after each cleaning. The differences between the measured and calculated values based on Sneep and Ubachs, 2005 for the continuous mode with setups 2 & 3 and the ramp mode with setup 3 are -1.87 %, - 0.71 %, and - 0.58 %, respectively. Using the new proposed n_{N_2O} dispersion relation, the difference between the measured and calculated $\sigma_{N_2O(Rayl.)}$ for the continuous mode with setups 2 & 3 and ramp mode with setup 3 are -0.79 %, + 0.25 %, and +0.38%, respectively. The $\sigma_{N_2O(Rayl.)}$ results from this work at 408 nm agree with the findings of He et al., 2021.

4.8 CH_4 $\sigma_{(Rayl.)}$ determination

The CH_4 used in this study was from Air Liquide CH_4 N45 (purity ≥ 99.995 mol %). For more details about the gas supply please check appendix A 1. The refractive index of CH_4, n_{CH_4}, is given by Sneep and Ubachs, 2005 based on the measurements of Hohm, 1993:

$$\left(n_{CH_4} - 1\right) \times 10^8 = 46890 + 4.12 \times 10^{-6}\tilde{v}^2 \qquad E\ 4\text{-}14$$

Wilmouth and Sayres, 2020 proposed a different dispersion function of n_{CH_4} for the wavelength range 250 nm – 650 nm based on their measurement at 264 nm - 297 nm and 333 nm – 363 nm:

$$\left(n_{CH_4} - 1\right) \times 10^8 = 4869.8 + \frac{4.1023 \times 10^{14}}{1.133 \times 10^{10} - \tilde{v}^2} \qquad E\ 4\text{-}15$$

He et al., 2021 give two dispersion functions of n_{CH_4} based on their measurements at a wavelength range between 307 nm and 725 nm.

For 307 nm – 400 nm:

$$\left(n_{CH_4} - 1\right) \times 10^8 = 5476 + \frac{4.1579 \times 10^{14}}{1.1568 \times 10^{10} - \tilde{\nu}^2} \qquad \qquad E\ 4\text{-}16$$

and for 320 nm – 725 nm:

$$\left(n_{CH_4} - 1\right) \times 10^8 = 3603.09 + \frac{4.40362 \times 10^{14}}{1.1741 \times 10^{10} - \tilde{\nu}^2} \qquad \qquad E\ 4\text{-}17$$

where $\tilde{\nu}$ is the wavenumber ($\tilde{\nu} = 1/\lambda$) in cm^{-1}.

The King correction factor for CH_4, $F_k CH_4 = 1$, the depolarisation ratio is negligible according to Bridge and Buckingham, 1966; Sneep and Ubachs, 2005; Wilmouth and Sayres, 2020.

Table 16: Measurement results for the determination of $\sigma_{CH_4(Rayl.)}$ and the corresponding differences between the mean values and the n-based calculations.

mode	Continuous mode	Ramp mode	
Setup	1	3	
n-based $\sigma_{Rayl.}$ ($\times 10^{-26} cm^2$) (Sneep and Ubachs, 2005)	4.434	4.411	
n-based $\sigma_{Rayl.}$ ($\times 10^{-26} cm^2$) (Wilmouth and Sayres, 2020)	3.420	3.403	
n-based $\sigma_{Rayl.}$ ($\times 10^{-26} cm^2$) (He et al., 2021) 307 - 400 nm	3.465	3.448	
n-based $\sigma_{Rayl.}$ ($\times 10^{-26} cm^2$) (He et al., 2021) 320 – 725 nm	3.425	3.407	
n (refractive index)	1.00043133	1.00043127	
Mean ($\times 10^{-26} cm^2$)	3.403	3.447	3.450
2σ std. dev. ($\times 10^{-26} cm^2$)	0.021	0.018	0.050
Median ($\times 10^{-26} cm^2$)	3.401	3.448	3.456
Number of measurements	4	19	9
Differences between the measured mean value and the n-based $\sigma_{Rayl.}$ in (%)			
(Sneep and Ubachs, 2005)	-23.25	-21.85	-21.78
(Wilmouth and Sayres, 2020)	-0.51	1.30	1.39
(He et al., 2021) 307 – 400 nm	-1.80	-0.02	0.07
(He et al., 2021) 320 – 725 nm	-0.64	1.17	1.26

The $\sigma_{CH_4(Rayl.)}$ has been determined at 408nm with setup 1 using continuous mode and by setup 3 using continuous and ramp modes. All the ramp mode measurements with setup 3 are made from 350 hPa to 900 hPa pressure. The results of the measurement, the calculated $\sigma_{CH_4(Rayl.)}$, and the differences between the mean measured $\sigma_{CH_4(Rayl.)}$ and n-based values are summarised in Table 16. The continuous and ramp mode results agree within the experimental errors for setup 3. The $\sigma_{CH_4(Rayl.)}$ results show > 20 % differences to the n-based values calculated by using the refractive index dispersion suggested by Sneep and Ubachs, 2005. Comparably much smaller differences with < 2 % are observed for the other 3 cases. The τ decreases with continuous CH_4 flow through the system is < 0.15 µs (0.14 %) over one 90 mins measurement. The decreased τ signal of setup 3

recovered by itself overnight when the cavity was closed and filled with CH_4. The variation of τ_0 remained < 0.6 µs (5 %) over 3 weeks. Additional information about the quality control plots is shown in appendix A 15 and A 16.

4.9 Comparison with other studies

Direct retrieval of $\sigma_{Rayl.}$ from measurements using CRDS have been made for N_2, O_2, SA, and Ar at 405.8 nm (Thalman et al., 2014); and for O_2, CO_2, N_2O, and CH_4 at 404 nm (He et al., 2021). The calculated n-based $\sigma_{Rayl.}$ based on various literature values, the available CRDS direct measurements, and the results from this work in the wavelength range between 403 nm and 410 nm are plotted in Figure 27. The values provided in the present study are consistent with previous measurements for O_2, Ar, CO_2, and SA. The obtained $\sigma_{Rayl.}(\lambda)$ agree on average within 0.6 % with the calculated n-based $\sigma_{Rayl.}(\lambda)$ for CO_2, N_2O, and CH_4, respectively. The obtained $\sigma_{Rayl.}(\lambda)$ agree on average within 2.4 %, 1.2 %, 2.2 %, 1.5 %, and 4.1 % for N_2, O_2, SA, Ar and CO, respectively. For CH_4 and N_2O, the retrieved $\sigma_{Rayl.}(\lambda)$ values provide independent experimental evidence and thus confirm the revised values of $n(\lambda)$ reported by Wilmouth and Sayres, 2020 and He et al., 2021 as part of their CRDS and BBCES studies of the $\sigma_{Rayl.}(\lambda)$ for these greenhouse gases in this wavelength range. He et al., 2021 reported CH_4 absorption cross sections $\approx 1 \times 10^{-27}$ cm^2 around 408 nm. This would imply a ≈ 3 % contribution of the absorption in the total extinction measured to retrieve the Rayleigh cross sections in this study. For the case of N_2, the commonly accepted n-based $\sigma_{Rayl.}(\lambda)$ (Bates, 1984; Sneep and Ubachs, 2005) overestimate the experimental $\sigma_{Rayl.}$ at around 408 nm. This overestimation of $\sigma_{Rayl.}(\lambda)$ of N_2 requires further investigation in other λ ranges.
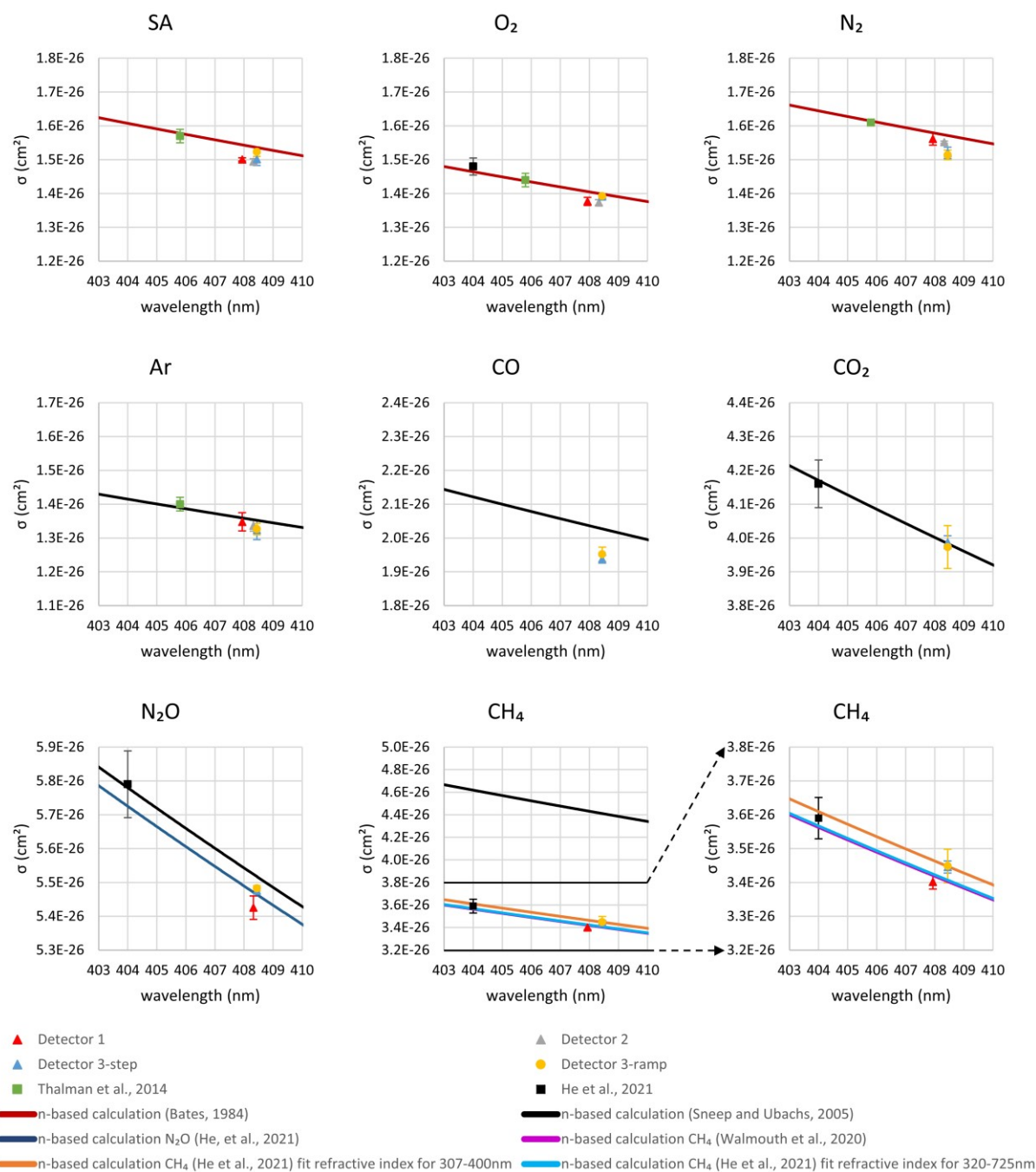
Figure 27: Rayleigh scattering cross-sections, $\sigma_{Rayl.}$, for N_2, O_2, Ar, CO, CO_2, N_2O and CH_4 available in the literature in the range $403 \leq \lambda \leq 410$ nm and the measurements made in this study. The $\sigma_{Rayl.}$ experimentally obtained in this study are shown as follows: triangles for continuous measurements (red, grey and blue for setup 1, 2 and 3, respectively) and yellow filled circles for the ramp measurements. Previous CRDS measurements: from Thalman et al. (Thalman et al., 2014) and He et al. (He et al., 2021) are also indicated in squares (green and black, respectively). The continuous lines show the calculations of $\sigma_{Rayl.}$ using equation E 2-13 from Bates, (in dark red) (Bates, 1984), Sneep and Ubachs (in black) (Sneep and Ubachs, 2005), He et al. N_2O (dark blue) (He et al., 2021), He et al. CH_4 with fitted refractive index based on measurement for $307 - 400$ nm (in orange), $320 - 725$ nm (in cyan) (He et al., 2021) and Wilmouth and Sayres (in magenta) (Wilmouth and Sayres, 2020).

4.10 CO and N₂ EM radiation extinction for CRDS NO₂ detector

As mentioned in the introduction section, during the performance tests of PeRCEAS, significant differences in EM radiation extinction were observed between 9 % CO in SA and 9 % N₂ in SA, as depicted in Figure 28. One of the primary motivations for

experimentally determination of $\sigma_{Rayl.}$ was to understand if the significant differences could be attributed to differences in the $\sigma_{Rayl.}$ from the respective gas molecules.
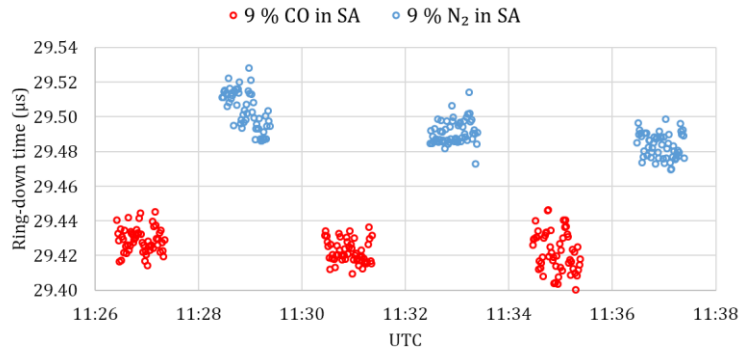
Figure 28: Ring-down time signal for 9 % CO (in red filled circles) and 9 % N_2 in (blue filled circles) mixing with SA using CRDS NO_2 detector (peak emission at 408.3 nm).

Based on E 2-30, the ring-down time of the NO_2 detector filled when 9 % CO and 9 % N_2 mixed with SA are calculated as:

$$\frac{1}{\tau_1} = \sigma_{1(Rayl.)} \cdot c_0 \cdot \frac{N}{V} + \frac{1}{\tau_0} \qquad\qquad E\ 4\text{-}18$$

$$\frac{1}{\tau_2} = \sigma_{2(Rayl.)} \cdot c_0 \cdot \frac{N}{V} + \frac{1}{\tau_0} \qquad\qquad E\ 4\text{-}19$$

Where τ_1 and τ_2 are the ring-down time measurements of 9 % CO and 9 % N_2 mixed with SA, respectively; $\sigma_{1(Rayl.)}$ and $\sigma_{2(Rayl.)}$ are the respective total $\sigma_{Rayl.}$ of the CO and N_2 9 % mixture in SA; c_0 is the speed of EM radiation in vacuum; $\frac{N}{V}$ is the number concentration; τ_0 is the ring-down time in an empty cavity. Subtract E 4-18 by E 4-19:

$$\frac{1}{\tau_1} - \frac{1}{\tau_2} = \left(\sigma_{1(Rayl.)} - \sigma_{2(Rayl.)}\right) \cdot c_0 \cdot \frac{N}{V} \qquad\qquad E\ 4\text{-}20$$

According to Bates, 1984, the total $\sigma_{Rayl.}$ of the mixtures can be calculated as:

$$\sigma_{1(Rayl.)} = 9\% \cdot \sigma_{CO(Rayl.)} + 91\% \cdot \sigma_{SA(Rayl.)} \qquad\qquad E\ 4\text{-}21$$

$$\sigma_{2(Rayl.)} = 9\% \cdot \sigma_{N_2(Rayl.)} + 91\% \cdot \sigma_{SA(Rayl.)} \qquad\qquad E\ 4\text{-}22$$

The left-hand side of equation E 4-20 is equal to $79 \pm 5\ [s^{-1}]$ from the measurements. Based on the experimental determined $\sigma_{(Rayl.)}$ results from the previous sections, the right-hand side of the equation is equal to $53 \pm 29\ [s^{-1}]$ and $56 \pm 26\ [s^{-1}]$ for $\sigma_{(Rayl.)}$ measured by the continuous mode and ramp mode, respectively. The results from both sides of the equation are in agreement within their associated errors for setup 3. The agreement validates that the observed differences in EM radiation extinction can be attributed to the Rayleigh scattering of different molecules.

4.11 Error analysis and limit of detection

4.11.1 Error related to the determination of the laser wavelength

The multimode output of the laser was investigated by measuring the shape of the comb of multimode lasers using an in comparison a low spectral resolution of the spectrometer, having FWHM resolution of 0.74 ± 0.02 nm. The FWHM values of the multimode laser assuming a Gaussian profile were determined for setups 1, 2, and 3, and were found to be 1.33, 1.41, and 1.04 nm, respectively, which were larger than the FWHM of the spectrometer (see Figure 13 in section 3.1.2). The bias in the measurement of n-based $\sigma_{Rayl.}(\lambda)$ is assessed by assuming that E 2-13 was accurate and using the value for $n(\lambda)$ and $F_k(\lambda)$ determined, e.g. CO_2. The $n(\lambda)$ CO_2 dispersion relation for the calculation of n-based $\sigma_{Rayl.}(\lambda)$ was determined by the measurement between 180.7 nm to 1694.5 nm including the measurement at 410.9 nm (Bideau-Mehu et al., 1973). The convoluted value of n-based $\sigma_{Rayl.}(\lambda)$ was then compared across the FWHM of each laser, and the maximum possible bias was found to be ≤ 0.6 % for the FWHM spectral range around the maximum intensity of the multimode laser emission.

4.11.2 Error related to the pressure and temperature measurements

In section 3.1, it was stated that the pressure sensors used in setups 1 and 2 have an accuracy of ± 0.1 %, while for setup 3, the accuracy is ± 0.15 % of the output reading, corresponding to ± 1 hPa. The calibration process with the absolute pressure sensor Greisinger GDH 12AN resulted in an accuracy and linearity of ± 1% in the range of 100 - 1000 hPa. Considering the contribution of the pressure accuracy to the overall accuracy of the retrieved $\sigma_{Rayl.}$ values, it ranges between < 0.8 % and 1.1 %.

Concerning the T sensors, the accuracies are ± 1 °C for setups 1 & 2 and ± 0.1 °C for setup 3. The T accuracy contributes between < 0.4 % and 0.04 % to the accuracy of the $\sigma_{Rayl.}$ values retrieved.

4.11.3 Error related to absorption cross-section

The molecules O_2, N_2, CO, CO_2, Ar, and N_2O are not expected to have spectral absorption features at the wavelength (408 nm) measured. According to the MPI-Mainz spectral atlas database (Keller-Rudek et al., 2013), no absorption cross-sections of these molecules have been measured in the spectral range of 400 - 410 nm (Keller-Rudek et al., 2023). However, for the case of CH_4, the works of Karkoschka, 1994 and He et al., 2021 indicate that the absorption cross-section of CH_4 from 406 to 410 is in the order of magnitude of $\approx 2 \times 10^{-28}$ cm^2 and 1×10^{-27} cm^2, respectively (see appendix A 17). This would imply a ≤ 3 % contribution in the total extinction measured in this work to retrieve the Rayleigh cross sections.

4.11.4 Error related to water during the determination of $\sigma_{(\text{Rayl.})}$

During the stabilisation period before the ramp experiment in determining $\sigma_{\text{Rayl.}}$, a small amount of water (typically < 1 %) is accumulated by the small leak and permeation from the ambient air into the cavity. This water can be detected by using the RH sensor when the ramp procedure starts, as this part of the water is brought into the cavity, diffused, and detected by the RH sensor. Assuming that the cavity is only filled with the gas of interest (GI) and water, it is possible to calculate the $\sigma_{\text{Rayl.}}$ for a known mixture of gas using equation E 4-5:

$$N_{mix} \cdot \sigma_{mix} = N_{GI} \cdot \sigma_{GI} + N_{H_2O} \cdot \sigma_{H_2O} \qquad E\ 4\text{-}23$$

Where N_{mix}, is the number concentration of the mixture, $N_{mix} = N_{GI} + N_{H_2O}$, N_{GI} and N_{H_2O} are the number concentrations of the gas of interest and water, respectively. σ_{mix}, σ_{GI}, and σ_{H_2O} are the Rayleigh scattering cross-section for the mixture, gas of interest, and water, respectively. Then the ring-down time of the mixture gas, according to E 2-30 is:

$$\frac{1}{\tau} = c \cdot \sigma_{mix} \cdot N_{mix} + \frac{1}{\tau_0} \qquad E\ 4\text{-}24$$

Combine E 4-23 with E 4-24:

$$\frac{1}{\tau} = c \cdot (N_{GI} \cdot \sigma_{GI} + N_{H_2O} \cdot \sigma_{H_2O}) + \frac{1}{\tau_0} \qquad E\ 4\text{-}25$$

During the ramp experiment, N_{mix} is changing, differentiate with N_{mix} to E 4-25 yields:

$$\frac{d}{dN_{mix}}\left(\frac{1}{\tau}\right) = \frac{d}{dN_{mix}}(c \cdot (N_{GI} \cdot \sigma_{GI} + N_{H_2O} \cdot \sigma_{H_2O}) + \frac{1}{\tau_0})$$

$$\rightarrow \frac{d}{dN_{mix}}\left(\frac{1}{\tau}\right) = c \cdot \frac{d}{dN_{mix}}(N_{GI} \cdot \sigma_{GI} + (N_{mix} - N_{GI})\sigma_{H_2O})$$

$$\rightarrow \frac{d}{dN_{mix}}\left(\frac{1}{\tau}\right) = c \cdot \frac{d}{dN_{mix}}(N_{GI} \cdot \sigma_{GI} + N_{mix} \cdot \sigma_{H_2O} - N_{GI} \cdot \sigma_{H_2O}), \text{ apply product rule:}$$

$$\rightarrow \quad \frac{d}{dN_{mix}}\left(\frac{1}{\tau}\right) = c \cdot (N_{GI}\frac{d(\sigma_{GI})}{dN_{mix}} + \sigma_{GI}\frac{d(N_{GI})}{dN_{mix}} + N_{Tot}\frac{d(\sigma_{H_2O})}{dN_{mix}} + \sigma_{H_2O}\frac{d(N_{mix})}{dN_{mix}} - N_{CO}\frac{d(\sigma_{H_2O})}{dN_{mix}} - \sigma_{H_2O}\frac{d(N_{GI})}{dN_{mix}})$$

Since the total N change is only caused by adding the gas of interest, and the amount of water inside the cavity is considered constant during the ramp experiment and $N_{GI} \approx N_{mix}$, aka. $\frac{d(N_{GI})}{dN_{mix}} \approx 1$; $\frac{d(N_{H_2O})}{dN_{mix}} \approx 0$; σ_{CO} and σ_{H_2O} are constants.

$$\frac{d}{dN_{mix}}\left(\frac{1}{\tau}\right) = c \cdot \left(0 + \sigma_{GI} + 0 + \sigma_{H_2O} - 0 - \sigma_{H_2O}\right) = c \cdot \sigma_{GI} \qquad E\ 4\text{-}26$$

The derivation demonstrates that the change in the $\frac{1}{\tau}$ with respect to the N_{mix} is directly proportional to σ_{GI}. The initial trace amount of water inside the cavity has a negligible effect on the determination of $\sigma_{Rayl.}$ by the ramp experiment.

4.11.5 Limit of detection of the CRDS setups

The limit of detection (LOD) for the lowest signal is given by (Gold, 2019):

$$L_D = 3.3\sigma_0$$

$E\ 4\text{-}27$

Where σ_0 is the standard deviation of the replicate measurements.

Table 17: Limit of detection for the CRDS determination of $\sigma_{Rayl.}$ in this work, defined as 3.3 times the standard deviation of the ring-down time signal of each CRDS detector. Where % is the LOD divided by the rind-down time signal of an empty cell.

LOD	Unit	N₂	O₂	SA	Ar	CO	CO₂	N₂O	CH₄
Setup 1	($\times 10^{-9}$ cm^{-1})	1.53	2.03	1.65	1.08				1.40
	(%)	0.08	0.05	0.07	0.12				0.10
Setup 2	($\times 10^{-9}$ cm^{-1})	0.48	1.00	0.60	0.89			0.78	
	(%)	0.28	0.11	0.19	0.14			0.21	
Setup 3	($\times 10^{-9}$ cm^{-1})	3.28	4.48	3.23	3.69	3.97	7.66	6.43	6.53
	(%)	0.07	0.04	0.06	0.07	0.06	0.04	0.05	0.05

In our case standard deviation of ring-down at a stable pressure (the number concentration fixed). The detection limits of the CRDS detector for the corresponding molecules are calculated and summarised in Table 17.

4.11.6 Error estimation of $\sigma_{(Rayl.)}$ retrieval

The $\sigma_{(Rayl.)}$ is retrieved by fitting a linear relationship between the loss rate and the number concentration of the gas of interest inside the cavity. This involves analysing the ring-down time signal for the loss rate and measuring the pressure and temperature for the number concentration. To accurately account for errors in both the loss rate and number concentration, the orthogonal distance regression method proposed by Boggs and Donaldson, 1989 is utilised. This approach ensures that both sources of error are appropriately considered when determining the slope of the linear relationship.

5. Results and Discussion Part II: Airborne peroxy radicals: measurements and modelling

As explained in section 2.3, peroxy radicals play many important roles in atmospheric chemistry, particularly of interest for this doctoral dissertation in the troposphere. They are reactive free radicals and thus have highly variable concentrations, which are strongly dependent on a series of photochemical and chemical producing and removing reaction mechanisms. Measurements of RO_2^* can therefore be used to test the capability of models to simulate their atmospheric concentrations.

The PeRCEAS was deployed on the HALO aircraft during the EMeRGe research campaigns. These included two measurement campaigns: one over Europe in July 2017, and another over East Asia in March and April 2018 (refer to section 3.2 for more details).

Once the RO_2^* and the other trace gas, aerosol and meteorological data products from the EMeRGe became available, the investigation was made into how well a set of atmospheric models simulate RO_2^* and other trace gases. This study involved the comparison of the measured RO_2^* with that simulated by four different models and one calculation of RO_2^*, which assumes that the RO_2^* achieved a photostationary state. To achieve this objective, a collaboration was initiated with the group of modellers involved in the EMeRGe project. They supplied simulations from the different models described in sections 3.3.1 to 3.3.4.

Three case studies were investigated, which represent three types of air mass and conditions, observed during the EMeRGe EU and Asia campaigns: a) urban pollution from MPCs close to the sources, b) long-range transported air masses, and c) pollution measured over Taiwan, observed during the flights after take-off and before landing. The goal was to evaluate the capability of the different models to reproduce the fast photochemistry which determines the RO_2^* atmospheric concentrations in different environments.

5.1 EMeRGe case study 1: Rome and Manila

Among the pollution plumes from MPCs investigated within the EMeRGe project, those from Rome (Europe) and Manila (Asia) were chosen for the comparisons presented here. This is because the photochemical conditions experienced during the HALO research flights around both MPCs were similar.

In Europe, two flights, E-EU-03 (11-07-2017) and E-EU-06 (20-07-2017), with similar flight tracks and times, targeted the outflow from Rome as part of the EMeRGe in Europe campaign. In Asia, the EMeRGe flights E-AS-06 (20-03-2018) and E-AS-10 (28-03-2018) had similar flight tracks and times and targeted the measurement of pollution plumes emitted from Manila. Figure 29 and Figure 30 show 2D and 3D plots of these four research flights, colour-coded using the measurements of RO_2^* mixing ratios.

The HALO flights traverse Rome from the Southwest to the Northeast and Manila from East to West. The FLEXTRA backward trajectories indicate that the air masses sampled by the instruments during the legs along the East Coast of Italy had been transported over Rome. The two HALO research flights close to Manila sampled air masses along the East Coast of the Philippines, which had been transported via Manila.

These four flights by HALO thus measured air masses, which have emissions from Rome and Manila that have been transported and transformed en route. The flight legs of the four flights comprise shuttles at three different and selected altitudes. These shuttles enable the urban pollution plumes to be captured downwind. In the subsequent sub-sections, the measured RO_2^* values are compared with the modelled RO_2^* and the calculated RO_2^* assuming PSS (see section 3.3.7).
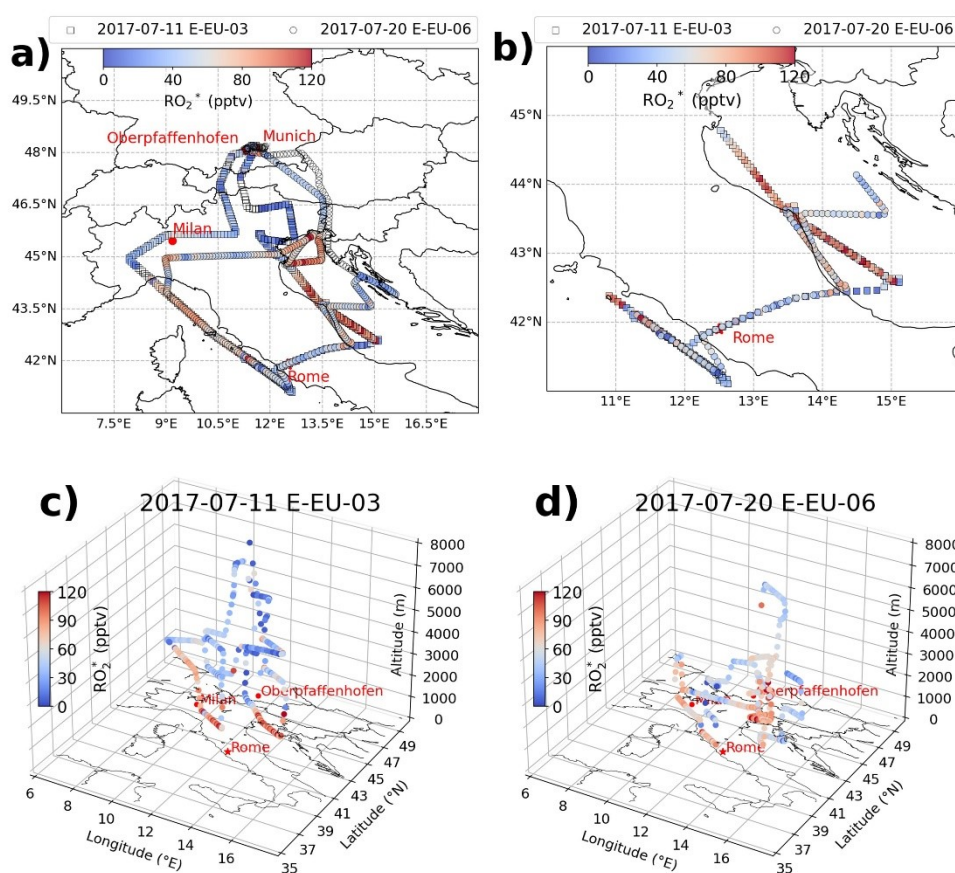
Figure 29: Flight tracks from EMeRGe, colour-coded by 60 s interval RO_2^* measurements for the target region Rome during E-EU-03 and E-EU-06 flights in Europe. Panel a) depicts the entire flight tracks; panel b) provides a detailed view focusing on the region around Rome; panels c) and d) present 3-D visualisations for E-EU-03 and E-EU-06, respectively.
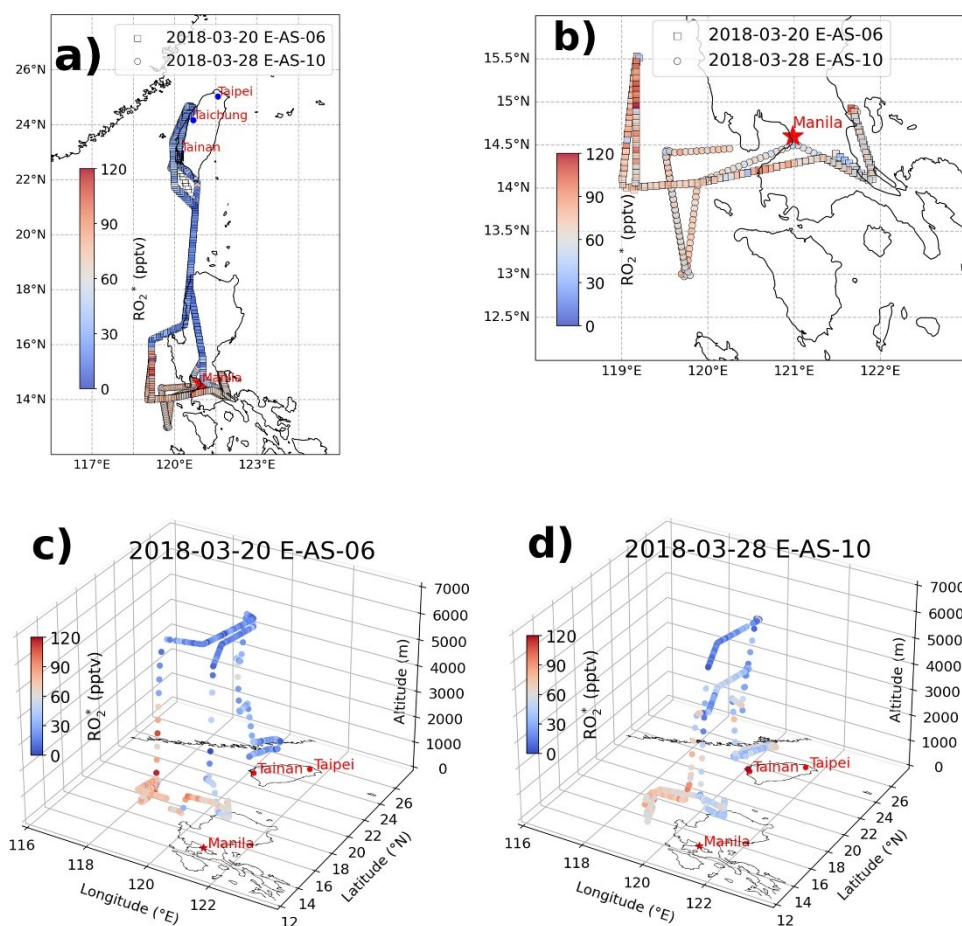
Figure 30: Flight tracks from EMeRGe, colour-coded by 60 s interval RO_2^* measurements for the target region Manila during E-AS-06 and E-AS-10 flights in Asia. Panel a) depicts the entire flight tracks; panel b) provides a detailed view focusing on the region around Manila; panels c) and d) present 3-D visualisations for E-AS-06 and E-AS-10, respectively.

5.1.1 Rome

The modelled RO_2^* values presented here, with the exception of those from the MECO(n) model, were converted into 60 s average values, to match the resolution of the PeRCEAS RO_2^* measurements. MECO(n) used the CM12 horizontal resolution (i.e. 0.1°x0.1° which is ≈ 12 km), and a temporal resolution of 120 s for EMeRGe in EU flight legs, as explained in section 3.3.3.

The PSS RO_2^* calculated results are also included in the comparison. The PSS RO_2^* analytical expression assumes a balance between peroxy radical production and loss rates and is constrained by using the measurements of trace gases made onboard HALO, as described elsewhere (George, 2022; George et al., 2023).

The flight legs of relevance in E-EU-03 and E-EU-06 are divided into 3 flight leg parts:

1) From take-off and southwards along the west coast side of Italy;
2) across the Rome region, where the urban plumes are expected and included the sampling upwind and downwind of Rome;
3) northwards along the east coast side of Italy.

In the following sections, the measurements from the flight leg part 2) are selected to be representative of air masses emitted from nearby urban emissions.

5.1.1.1 E-EU-03

Figure 31 shows the time series of the measured and simulated RO_2^* in E-EU-03. Specifically, these comprise the RO_2^* measured, RO_2^* calculated assuming PSS, and the RO_2^* simulated by the chemical models WRFchem(ERA5), WRFchem(GFS), MECO(n), and the box model. In addition, the following are also shown (with errors when available/applicable from HALO database):

a) ancillary observation provided by the BAsic HAlo Measurement And sensor System (BAHAMAS), such as the flight altitude, the airspeed, the height above the PBL and water vapour, H_2O,
b) the trace gases O_3, HCHO, NO, and NO_2, which were measured by the FAIRO, HKMS, AENEAS, and mini-DOAS instruments on HALO, respectively;
c) $jO(^1D)$ measured by HALO – SR;
d) the CO enhancements from the HYSPLIT trajectory models.

In spite of the PeRCEAS instrument inlet and reactor being designed to operate at a selected and constant pressure below the ambient pressure, pressure changes at the inlet occur when changing altitudes. Consequently, after a flight altitude change, it takes some time to stabilise the flows and this leads to pressure fluctuations in the CRDS detector. The latter interferes with the CRDS decay signal. Consequently, the RO_2^* measurements impacted by these pressure fluctuations have been excluded from the time series and the comparisons of measured and modelled RO_2^*. A comparison of the original RO_2^* measurements and those which have had RO_2^* influenced by pressure fluctuations, is provided in appendix A18.

The airspeed, during this HALO flight, reached values up to 190 m/s. As a result, the spatial resolution of measurements made onboard HALO was less than 11.4 km per minute, which is finer than that offered by all the models.

The modelled RO_2^* shown in Figure 31 agree with the measured RO_2^* within error at altitudes above 1200 m. Similarly, the modelled values for many other species and parameters presented in Figure 31 show reasonable agreement with measurements at altitudes above 1200 m. The exceptions are a) NO, which is underestimated by all the models by up to a factor of 10 and b) the modelled O_3 mixing ratios in the MECO(n) model, which overestimates the measurements by up to 40 %.

According to the SCALTRA modelled height over the PBL, HALO flew above the PBL. However, the lowest sampling altitudes are probably close to or even in the PBL. In addition, the vertical layer setup, used in the models, makes the region close to the PBL more challenging to simulate accurately.
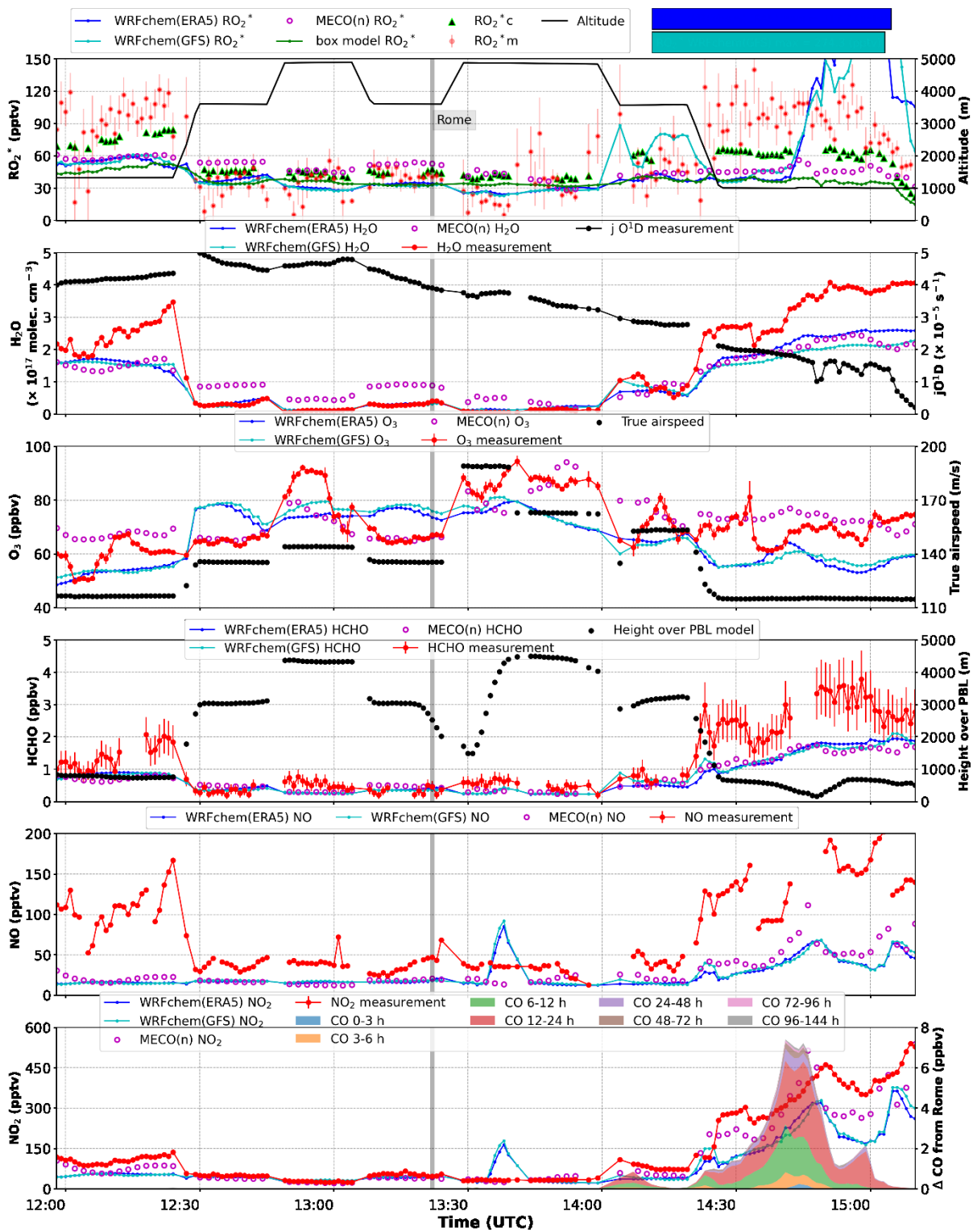
Figure 31: Time series of the RO_2^* measured by PeRCEAS and simulated by WRFchem(ERA5), WRFchem(GFS), MECO(n), box model, and calculated values using PSS expression for E-EU-03 selected region. Altitude, water concentration, and true airspeed are measured by BAHAMAS. The mixing ratios for O_3, HCHO, NO, and NO_2 were measured by AMTEX, HKMS, AENEAS, and mini-DOAS, respectively. $jO(^1D)$ are measured by HALO – SR. The height above PBL and the CO enhancement due to the Rome outflow are modelled by SCALTRA and HYSPLIT, respectively. The temporal resolution is normalised to 60 s for all the measurements and models except MECO(n) has a temporal resolution of 120 s. The highlighted section denotes the location of Rome. Additionally, modelled results for water concentration, O_3, HCHO, NO, and NO_2 mixing ratio have been plotted using the WRFchem(ERA5), WRFchem(GFS), and MECO(n) models. The box model constrains the measurements, therefore, is not featured in the plots.

74

The measurements made during the flight leg part a) of this research flight between 12:00 and 12:30 UTC at a flight altitude of $\sim$ 1200 m ($\sim$ 1000 m above PBL) are shown in Figure 31. The models underestimate the measurements of RO_2^* by up to 50 %. According to the FLEXTRA 36 hrs back trajectory model, the air masses sampled at these locations originated from Corsica and Sardinia Islands at altitudes close to or lower than the height of the PBL. This implies that fresh emissions of radical precursors mix into these air masses.

As mentioned above, for the flight leg part b) between 12:30 and 14:00 UTC where the flight is clearly above the PBL, the modelled and measured RO_2^* were in reasonable agreement. This probably implies the dominance of older long-range transported air masses which are more accurately described by the models.

Similarly, the models and calculations underestimated up to 70 % of the RO_2^* measurements for the flight leg part c) between 14:40 and 15:10 UTC at an altitude of $\sim$ 1000 m. The HYSPLIT model indicates enhanced CO by 8 ppbv in these air masses, which originated from Rome. This is corroborated by the FLEXTRA back trajectory model, which indicates that the air masses originating from pollution in Rome below 1000 m were sampled.

To summarise the comparison of the measurements and modelling of this flight, the differences between the modelled and measured RO_2^* and trace gases are most pronounced when the probed air masses originate within the PBL. During these flight leg parts, the variations of short-lived species such as NO can be significant. The models, which are not constrained by measurements underestimate NO, and RO_2^* precursors such as HCHO at $\leq$ 1200 m. They thus also underestimate RO_2^*.

In Figure 32, plots of measured versus modelled or calculated RO_2^* mixing ratios for the E-EU-03 flight are shown. The RO_2^* data are colour-coded using the corresponding measured or modelled NO mixing ratio. The lower values of NO are associated with a better agreement between measured and modelled RO_2^*. Figure 32 panel a) – e) are used to investigate the capability of the models to simulate the RO_2^* measurements.

Figure 32 panels a) and b), have cyan solid lines, which show the linear regressions between the measured and the WRFchem modelled RO_2^*. The outliers have been removed manually before determining the slope and the Pearson correlation coefficient of the linear regression. In panels c), d) and e) the red solid lines are the linear regression obtained between measured and modelled data for the MECO (n), box model, and PSS calculations of RO_2^*. The linear correlation and the correlation coefficient are displayed only when the correlation coefficient is greater than 0.4. Additional information on scatter plots featuring colour coding with different species is provided in appendix A 19. At lower altitudes where the measured NO > 100 pptv, the models using the inventories often underestimate the measured NO and RO_2^* precursors. Thus they also underestimate the RO_2^*.
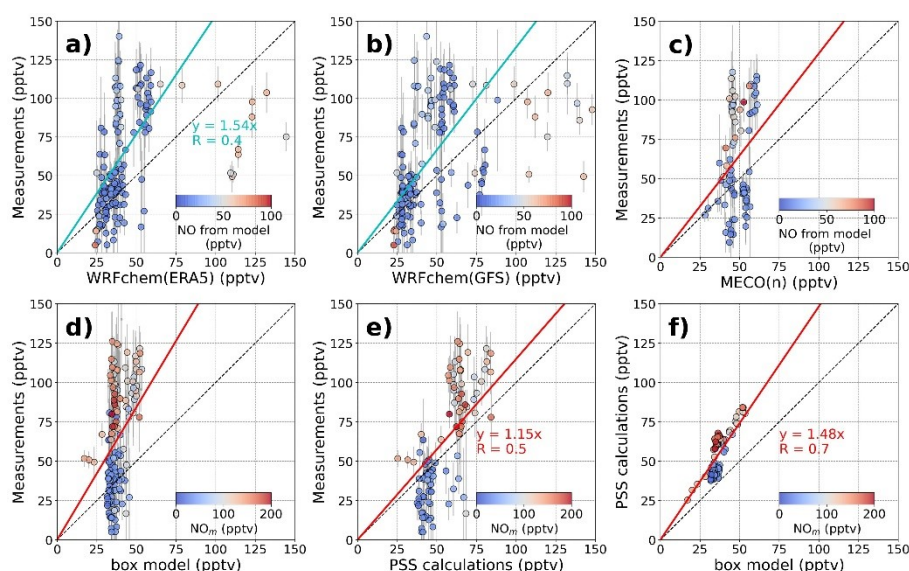
Figure 32: Scatter plots of PeRCEAS RO_2^* measurements and the modelled RO_2^* results from a) WRFchem(ERA5), b) WRFchem(GFS), c) MECO(n), d) box model, and e) calculation assuming PSS for E-EU-03 selected region. In f), the RO_2^* simulated by the box model and the PSS calculation are plotted against one another and compared. All the plots are colour-coded with corresponding NO from models or measurements. The 1:1 line is represented by black dashed lines, and the linear regressions are the red solid lines. The cyan solid lines are the linear regression fit after manually removing the outliers of WRFchem RO_2^* values. The temporal resolution for the plotted data is 60 s except for MECO(n) model, for which the temporal resolution is 120 s. All the linear regressions and their slopes are forced through the origin. Slopes and correlation coefficients are not depicted when the correlation coefficient is less than 0.4.

As explained by George et al., 2023, when NO is < 50 pptv in the probed air, the calculations made using the PSS assumptions overestimate the RO_2^* measurements. This difference is tentatively attributed to missing RO_2^* loss processes, involving the reactions of OH with HO_2 and OH with OH (R 2-34 and R 2-51). In contrast, these reactions and thus their rates are used in the box model. The box model estimates of RO_2^* agree best with the measurements when NO mixing ratios are below 50 pptv, i.e. cleaner air.

In polluted air mass sampled below 1200 m, where the sum of the measured OVOCs (oxygenated volatile organic compounds) mixing ratio exceeds approximately 7 ppbv, the models underestimate the RO_2^* measurements up to 50 %. In such pollution plumes, the oxidation and/or photolysis of OVOCs, coupled with the ozonolysis of alkenes, are potentially significant sources of RO_2^* which might not be considered adequately in the simulations. As not all the OVOCs, present in air masses, were measured during the EMeRGe campaigns, the PSS analytical expression is expected to underestimate the sources of RO_2^* and thus the RO_2^* mixing ratios. The RO_2^* measurements were underestimated by up to 25 % at high NO values in the box model. The box model and the PSS calculations have similar RO_2^* radical production reactions involving the photolysis of the precursors of the RO_2^*. Unlike the PSS expression, the box model includes reactions involving compounds, having organic groups, which are larger than CH_3. Nevertheless, the chemical mechanism does not adequately reproduce the production and loss of organic peroxy radicals larger than CH_3O_2 in polluted air masses and underestimates RO_2^* measurements.

In the box model for the E-EU-03 flights HO_2 and CH_3O_2 comprise > 92 % of RO_2^* (see appendix A 21). It can be concluded that an inadequate description of the production of organic peroxy radicals in the box model is the most likely explanation for the differences between the measured and the modelled RO_2^*.

5.1.1.2 E-EU-06

Following the same methodology applied to flight E-EU-03, Figure 33 presents the time series of RO_2^* measurements from the flight E-EU-06 in the selected region. In addition, the RO_2^*. from the four available models and the PSS calculation, selected data provided by BAHAMAS, and the trace gases measurements from the instrument payload onboard HALO are plotted.

Figure 34 panels a) to e) show the scatter plots between measured and modelled RO_2^*, colour-coded by NO mixing ratio. The linear regression between the measured and the two WRFchem modelled RO_2^*, after the outliers are removed, are the cyan lines shown in a) and b). In panels c) to f) the linear regressions are shown as red solid lines. The linear correlation and the correlation coefficient are displayed only when the correlation coefficient is greater than 0.4. Additional information on scatter plots featuring colour coding with different species is provided in appendix A 20.

The analysis of the measured, modelled, and calculated RO_2^* for E-EU-06 is similar to that for E-EU-03. The modelled RO_2^* and trace gas measurements generally agree with RO_2^* and trace gas measurements presented in the figure within the measurement uncertainties for altitudes above flight altitudes of 1000 m. Similar to the analysis of the E-EU-03, the exceptions for E-EU-06 are the O_3 mixing ratios modelled in MECO(n) and the downwind air masses from Rome at 1600 m altitude. According to the SCALTRA model, the flight was expected to be within or close to the PBL at the lowest altitudes of the shuttles and along the Western and Eastern Italian coast during the E-EU-06 flights. Downwind from Rome, RO_2^* of up to 92 pptv was observed at 1600 m altitude level, where relatively large mixing ratios for the precursors such as HCHO, CH_3CHO, and CH_3COCH_3 were observed, i.e. 4 ppbv, 750 pptv, and 3 ppbv, respectively.
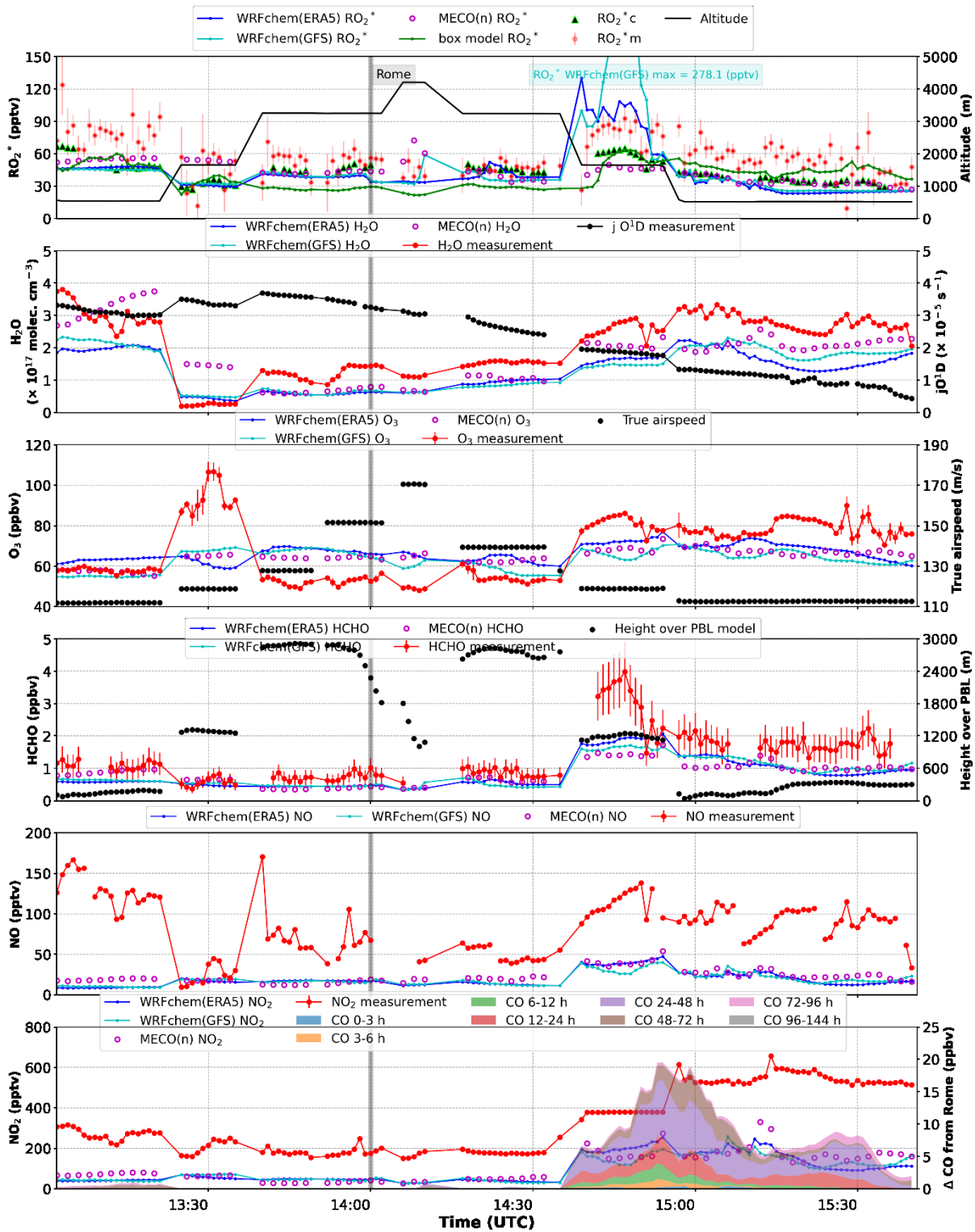
Figure 33: Time series of the RO_2^* measured by PeRCEAS and simulated by WRFchem(ERA5), WRFchem(GFS), MECO(n), box model, and calculated values using PSS expression for E-EU-06 selected region. Altitude, water concentration, and true airspeed are measured by BAHAMAS. The mixing ratios for O_3, HCHO, NO, and NO_2 were measured by AMTEX, HKMS, AENEAS, and mini-DOAS, respectively. $jO(^1D)$ are measured by HALO – SR. The height above PBL and the CO enhancement due to the Rome outflow are modelled by SCALTRA and HYSPLIT, respectively. The temporal resolution is normalised to 60 s for all the measurements and models except MECO(n) has a temporal resolution of 120 s. The highlighted section denotes the location of Rome. Additionally, modelled results for water concentration, O_3, HCHO, NO, and NO_2 mixing ratio have been plotted using the WRFchem(ERA5), WRFchem(GFS), and MECO(n) models. The box model constrains the measurements, therefore, is not featured in the plots.

Figure 34: Scatter plots of PeRCEAS RO_2^* measurements and the modelled RO_2^* results from a) WRFchem(ERA5), b) WRFchem(GFS), c) MECO(n), d) box model, and e) calculation assuming PSS for E-EU-06 selected region. In f), the RO_2^* simulated by the box model and the PSS calculation are plotted against one another and compared. All the plots are colour-coded with corresponding NO from models or measurements. The 1:1 line is represented by black dashed lines, and the linear regressions are the red solid lines. The cyan solid lines are the linear regression fit after manually removing the outliers of WRFchem RO_2^* values. The temporal resolution for the plotted data is 60 s except for MECO(n) model, for which the temporal resolution is 120 s. All the linear regressions and their slopes are forced through the origin. Slopes and correlation coefficients are not depicted when the correlation coefficient is less than 0.4.

The models (except for the two variants of WRFchem) and PSS calculated RO_2^* underestimate the measurement consistently in air masses affected by recent emissions of pollutants in the boundary layer. This is the case for flight leg part a) of the flight legs between 13:10 and 13:25 UTC and b) after 14:35 UTC. According to the FLEXTRA 36 hrs back trajectories, air masses in flight leg part a) likely originated from Sicily below 1000 m. The air masses in flight leg part b) originated below 2000 m downwind of Rome. An enhancement of CO was expected in the outflow of Rome according to HYSPLIT, primarily in air masses having an age of 24 to 72 hrs. According to FLEXTRA 24 hrs backwards trajectories, the air masses are not only transported from Rome but also from the West coast of Italy. The true airspeed of the aircraft during the measurements is less than 171 m/s, corresponding to a maximum spatial resolution of approximately 10.3 km per minute. This spatial resolution is thus similar to that of the WRFchem models but is finer than that of the other models. Both the PSS calculation and the box model, which are constrained by precursor measurements, consistently underestimate the RO_2^* measurements in flight leg part b) of the research flight. In contrast, WRFchem does not show this underestimation. This difference is possibly explained by the presence of unmeasured OVOCs. The oxidation of such gases would provide a missing source of RO_2^*.

In summary for the Rome cases, within the PBL, the RO_2^* mixing ratios measured vary from 60 to 120 pptv mainly depending on the variability of the precursor OVOCs and reactants NOx. Above the PBL, RO_2^* remain between 30 and 60 pptv depending on the origin of the air masses and are reproduced by the models and calculations within their uncertainties. Within the PBL, models relying on emission inventories fail to capture well

short-term variations, e.g. those produced by the presence of cloud. This is in contrast to the box model and PSS calculations, which are constrained to the onboard measurements.

At lower altitudes, particularly where the Rome plumes are expected, the measurements of RO_2^* are underestimated typically by the models/calculations by up to 80 %. The box model underestimates the PSS RO_2^* by up to 50 %.

For cases where the measured sum of OVOCs mixing ratios is high (e.g. > 7 ppbv), the PSS RO_2^* underestimate the RO_2^* measured by up to 50 %. This indicates potential missing sources of RO_2^* such as the oxidation and/or photolysis of OVOCs and the ozonolysis of alkenes. These species are not measured and, therefore, are not included in the PSS calculations.

The PSS RO_2^* overestimation of the measurements when NO < 50 pptv and $RO_2^* < 60$ pptv might be explained in part by the absence of the reaction of OH with HO_2 in the calculation of PSS RO_2^*.

5.1.2 Manila

In Asia, additional simulations from the WRF/CMAQ model are available for the EMeRGe flights (for more details, refer to section 3.3.1). As a result, there are five available models for the following studies. The two selected flights, E-AS-06 and E-AS-10, were divided for analysis into 4 flight leg parts:

1) take-off and flying southwards towards Manila over the South China Sea at altitudes above 6000 m;
2) the selected and designated Manila region where the urban plumes are expected, which includes upwind and downwind profiling legs below 2000 m;
3) flying northwards towards Taiwan at altitudes above 4000 m;
4) sample profiles close to the surface on the west coast of Taiwan.

According to UN Glossary of Environmental Statistics, long-range transport of air pollutants is defined as the "Atmospheric transport of air pollutants within a moving air mass for a distance greater than 100 kilometres." (EEA Glossary). Therefore, flight leg parts 1) and 3) of the flights were conducted over the ocean at elevated altitudes, where encountering air masses which have long-range transport is anticipated. Flight leg part 2) flights are representative of the urban plumes from Manila. The upwind and downwind scenarios legs provide insight into the changing composition of trace gases introduced by the Manila MPC.

An analysis of flight leg part 4) of the flight will be provided in section 5.3, which addresses the measurement of air masses during landing in Taiwan. It should be noted that the box model RO_2^* outputs for the selected flights have occasionally errors when the constrained measurements are missing. These data are manually removed and not considered in the

analysis. For a detailed comparison of the original and considered data, please refer to appendix A 26 and A 31.

5.1.2.1 E-AS-06

Figure 35 presents the time series of measurements, calculations, selected aircraft data measured by BAHAMAS, and the trace gases measurements from HALO instruments onboard during the E-AS-06.

During flight leg part 1) of E-AS-06, all the models and PSS calculated RO_2^* agree with the measurements within their respective errors. Air masses are characterised as long-range transported aged air masses coming from the western side of the flight track over the South China Sea and South Asia above 5000 m altitudes.

The flight leg part 2) covers the up- and downwind regions of Manila. Measurements were taken at altitudes above the simulated height of the PBL and between 1300 and 2000 m, where fresh plumes were expected downwind Manila. The 60 s RO_2^* measurements range from 35 ± 6 pptv to 140 ± 65 pptv. According to the HYPSLIT model, up to 20 ppbv CO enhancement from a plume of Manila origin occurs at the three flight levels downwind of Manila as a consequence of air masses ranging from 12 to 24 hrs and 24 to 48 hrs age. The FLEXTRA back trajectory model further indicates that the air sampled between 02:10 and 03:50 UTC likely originated from Manila. The true airspeed of the aircraft during these measurements is up to 120 m/s, translating to a spatial resolution of approximately 7.2 km per minute which is similar to or better than that of the models.
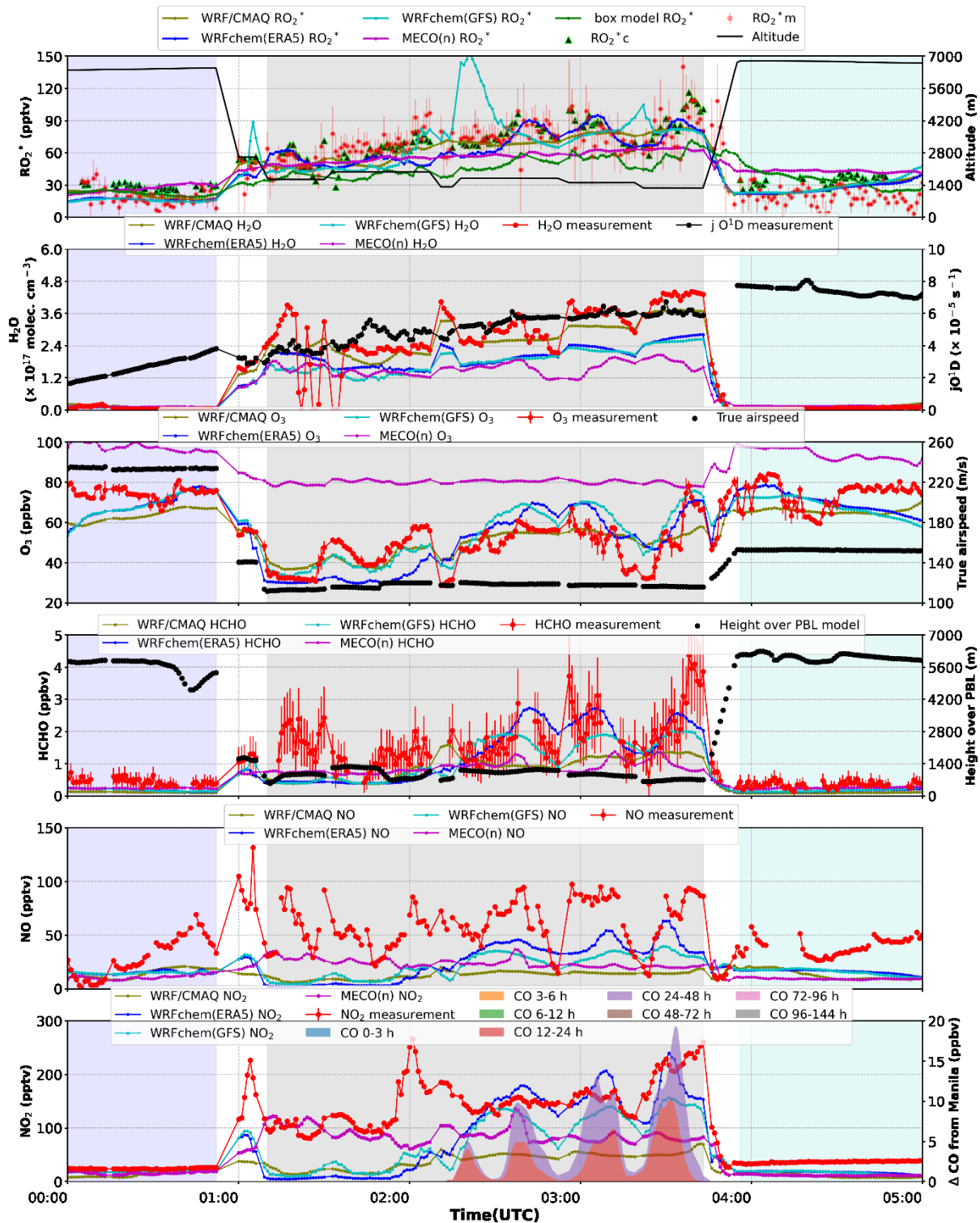
Figure 35: Time series of the RO$_2^*$ *measured by PeRCEAS and simulated by WRF/CMAQ, WRFchem(ERA5), WRFchem(GFS), MECO(n), box model, and calculated values using the PSS expression for E-AS-06 section 1)-3). Altitude, water concentration, and true airspeed are measured by BAHAMAS. The mixing ratios for O₃, HCHO, and NO, and NO₂ were measured by AMTEX, HKMS, AENEAS, and mini-DOAS, respectively. jO(¹D) are measured by HALO – SR. The height above PBL and CO enhancement due to the Manila outflow are modelled by SCALTRA and HYSPLIT, respectively. The temporal resolution is normalised to 60 s for all the measurements and models. The regions highlighted in blue, grey, and cyan mark sections 1), 2), and 3) of this flight, respectively. Additionally, modelled results for water concentration, O₃, HCHO, NO, and NO₂ mixing ratio have been plotted using the WRF/CMAQ, WRFchem(ERA5), WRFchem(GFS), and MECO(n) models. The box model constrains the measurements, therefore, is not featured in the plots.*

82

With the exception of the MECO(n) and the box models, there is a reasonable agreement with the RO_2^* measurements within the given uncertainties. The MECO(n) model underestimates the measurements by ∼ 15 % upwind Manila and ∼ 30 % downwind. The box model, on the other hand, underestimates the measurements consistently by up to 40 %. With regard to other trace species presented in Figure 35, O_3 is constantly and significantly overestimated by MECO(n) while NOx is underestimated by all the models. The short-term variations of NO and HCHO are captured at best by the WRF/CMAQ and WRFchem models, especially downwind of Manila. The consistency in their performance can be attributed to shared features, including the utilisation of WRF model ver 3.7.1, MEGAN ver. 2.1 for biogenic emission inventories, the RRTM for radiation modeling, Noah land surface model, and the Kain-Fritsch convection simulation. These shared features ensure precise dispersion representation of emission inventories near the source.

The conditions in flight leg part 3) are similar to those in flight leg part 1), where long-ranged transported air masses are sampled. These originate from the South China Sea and South Asia, at altitudes above 6000 m. The lowest RO_2^* are measured in this region and have an average mixing ratio of ∼ 14 pptv. In general, the models and calculated RO_2^* results agree with the measurements within the uncertainties.
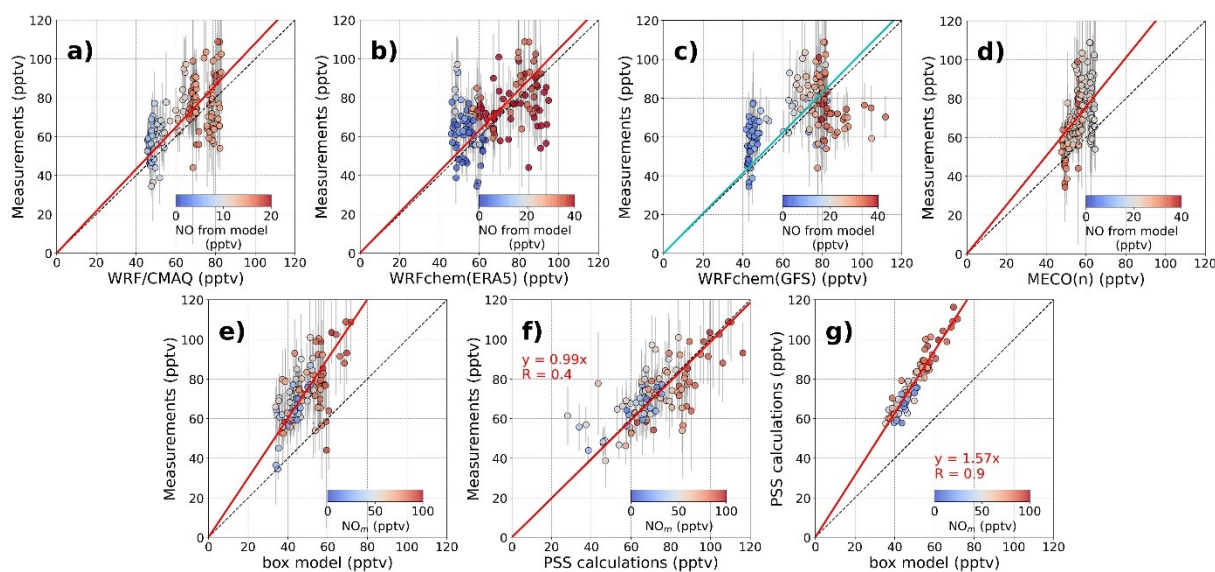
Figure 36: Scatter plots of PeRCEAS RO_2^* measurements and the modelled RO_2^* results from a) WRF/CMAQ, b) WRFchem(ERA5), c) WRFchem(GFS), d) MECO(n), e) box model, and f) calculation using PSS expression for E-AS-06 section 2). In g), the RO_2^* simulated by the box model and the PSS expression are compared. All the plots are colour-coded with corresponding NO from models or measurements. The 1:1 line is represented by black dashed lines, while the linear fit is denoted by red solid lines. The cyan solid lines are the linear fit for manually removing the clear outliers of WRFchem RO_2^*. The temporal resolution for the plotted data is normalised to 60 s. All the correlations are forced through the origin. Slopes and correlation coefficients are not depicted when the correlation coefficient is less than 0.4.

In Figure 36 and Figure 37, scatter plots summarise the relationships between the RO_2^* measurements, modelled and PSS calculation results for E-AS-06 flight leg part 2) and parts 1) & 3), respectively. The linear correlation and the correlation coefficient are displayed only when the correlation coefficient is greater than 0.4. Additional information

on scatter plots featuring colour coding with different species is provided in appendix A 25.

For flight leg part 2), the PSS calculations seem to reproduce the RO_2^* measurements best. The WRF/CMAQ model and WRFchem models also show reasonable agreement and linearities with the measurements.
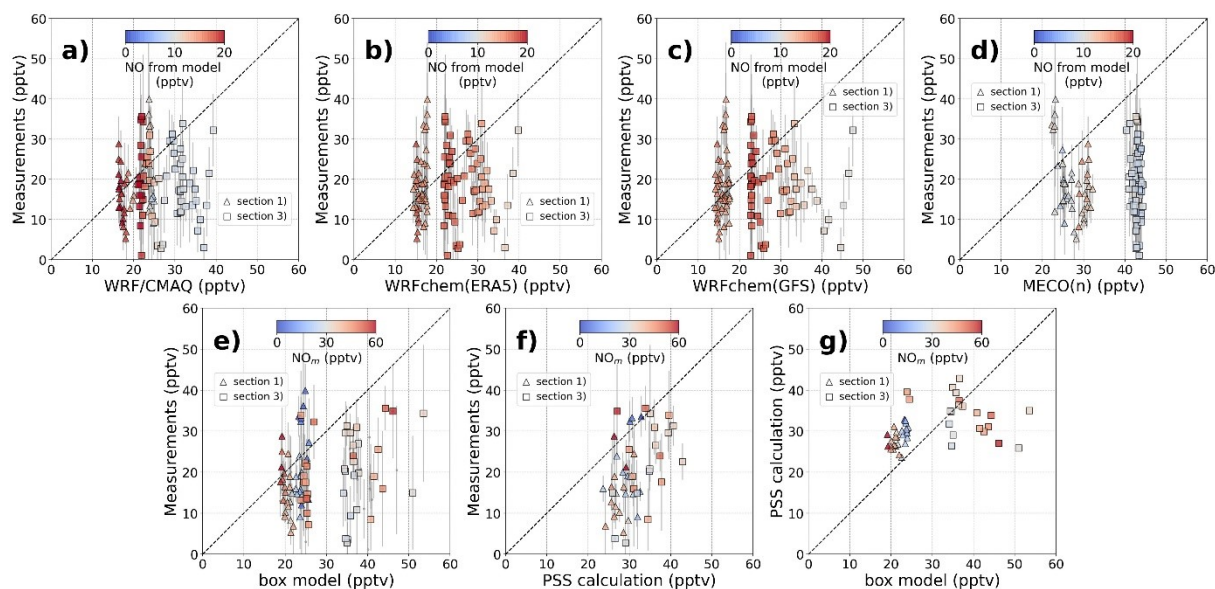
Figure 37: Scatter plots of PeRCEAS RO_2^* measurements and the modelled RO_2^* results from a) WRF/CMAQ, b) WRFchem(ERA5), c) WRFchem(GFS), d) MECO(n), e) box model, and f) calculation using PSS expression for E-AS-06 section 1) as triangles and 3) as squares. In g), the RO_2^* simulated by the box model and the PSS expression are compared. All the plots are colour-coded with corresponding NO from models or measurements. The dashed black lines denote the 1:1 line. The temporal resolution for the plotted data is normalised to 60 s.

All the models and PSS calculations agree with the measurements for section 1), but overestimate the measurements for ∼ 30 % (WRF/CMAQ, WRFchem), ∼ 50 % (MECO(n)), and ∼ 40 % (box model and PSS calculation), respectively in section 3). The models underestimate the NO by up to 90 % in this section and the radical losses are expected to be underestimated.

5.1.2.2 E-AS-10

Similarly to E-AS-06, the time series of the measured and PSS calculated RO_2^*, selected aircraft data measured by BAHAMAS and trace gases measurements from HALO onboard instruments for E-AS-10 are presented in Figure 38. During flight leg parts 1) and 3) of this flight at altitudes of about 4000 m over the Pacific and the South China Sea all the models and calculations agree with the RO_2^* measurement within the uncertainties. RO_2^* measurements are generally below 60 pptv with the lowest mean values during the whole flight. According to the 36 hrs HYSPLIT back trajectory model, the air masses are expected to be long-range transported over the South China Sea and South Asia.
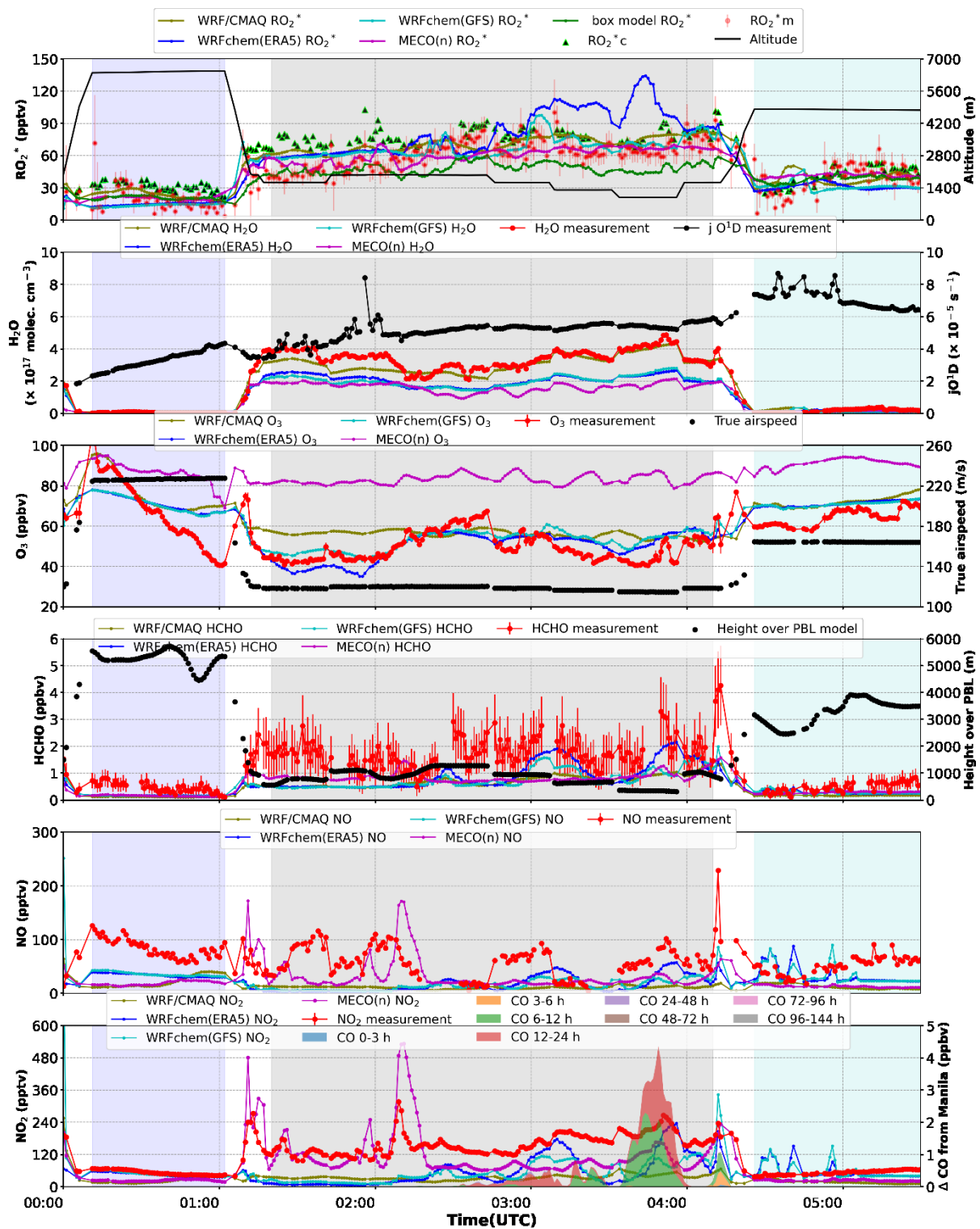
Figure 38: Time series of the RO_2^* measured by PeRCEAS and simulated by WRF/CMAQ, WRFchem(ERA5), WRFchem(GFS), MECO(n), box model, and calculated values using PSS expression for E-AS-10 section 1)-3). Altitude, water concentration, and true airspeed are measured by BAHAMAS. The mixing ratios for O_3, HCHO, and NO, and NO_2 were measured by AMTEX, HKMS, AENEAS, and mini-DOAS, respectively. jO(^{1}D) are measured by HALO – SR. The height above PBL and CO enhancement due to the Manila outflow are modelled by SCALTRA and HYSPLIT, respectively. The temporal resolution is normalised to 60 s for all the measurements and models. The regions highlighted in blue, grey, and cyan mark sections 1), 2), and 3) of this flight, respectively. Additionally, modelled results for water concentration, O_3, HCHO, NO, and NO_2 mixing ratio have been plotted using the WRF/CMAQ, WRFchem(ERA5), WRFchem(GFS), and MECO(n) models. The box model constrains the measurements, therefore, is not featured in the plots.

In flight leg part 2), HALO flew between 980 and 2000 m, staying at least 300 m above the PBL height, as simulated by SCALTRA. The RO_2^* mixing ratios vary between 33 ± 8 pptv and 100 ± 31 pptv. The HYSPLIT model indicated a significant CO enhancement due to the outflow from Manila around 4 UTC, primarily evident in fresh air masses less than 24 hrs old at an altitude of around 1000 m. This interpretation is supported by the FLEXTRA back trajectory model, suggesting that air sampled at these CO enhanced regions contains air masses from Manila, at an altitude below 2000 m. The true airspeed of the aircraft during the measurements up to 120 m/s, corresponds to spatial resolution of 7.2 km per minute, which is on par or higher than the models. Models with higher spatial resolution do not necessarily improve the agreement with RO_2^* measurements.

Concerning trace gas measurements, the MECO(n) model consistently exhibits a tendency to overestimate the mixing ratio of O_3. Notably, the two versions of WRFchem models generally capture the HCHO short-term variations, especially downwind of Manila. NO and NO2 are generally underestimated by the models, but the short-term variations are reasonably well captured.

The RO_2^* measurements upwind of Manila are 40 – 60 % overestimated by the models with the exception of the box model. In contrast, downwind of Manila, the WRFchem(ERA5) model overestimates the measurements by up to a factor of 2 whereas the box model underestimates the measurements by ~ 20 %.
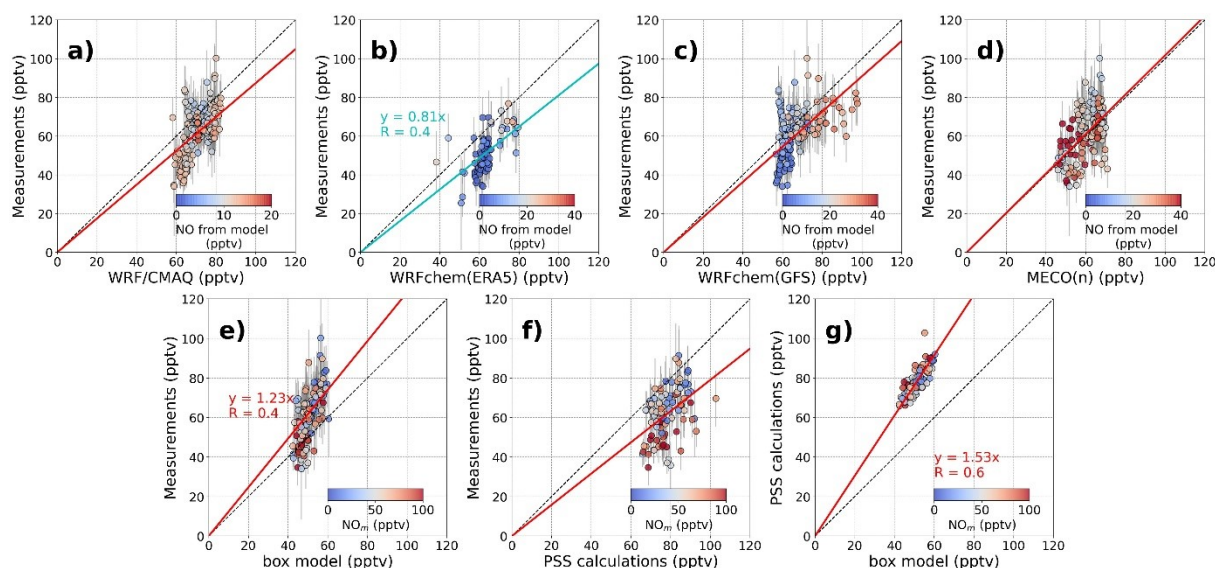
Figure 39: Scatter plots of PeRCEAS RO_2^* measurements and the modelled RO_2^* results from a) WRF/CMAQ, b) WRFchem(ERA5), c) WRFchem(GFS), d) MECO(n), e) box model, and f) calculation using PSS expression for E-AS-10 section 2). In g), the RO_2^* simulated by the box model and the PSS expression are compared. All the plots are colour-coded with corresponding NO from models or measurements. The 1:1 line is represented by black dashed lines, while the linear fit is denoted by red solid lines. The cyan solid lines are the linear fit for manually removing the clear outliers of WRFchem RO_2^*. The temporal resolution for the plotted data is normalised to 60 s. All the correlations are forced through the origin. Slopes and correlation coefficients are not depicted when the correlation coefficient is less than 0.4.

The relationships between the RO_2^* measurements and the RO_2^* estimated by models and calculations are shown in the scatter plots in Figure 39 for flight leg part 2) and Figure 40 for flight leg parts 1) and 3) of E-AS-10. The linear correlation and the correlation

coefficient are displayed only when the correlation coefficient is greater than 0.4. Additional information on scatter plots featuring colour coding with different species is provided in appendix A 30.

For flight leg part 2), the WRF/CMAQ and MECO(n) models show reasonable agreement and linearities with the measurements. The box model in this flight shows the underestimation of the measurements by around 20 %, and the PSS calculated results overestimate the measurements by around 20 %. The PSS calculations tend to overestimate results most significantly when NO levels are higher than 80 pptv. In an environment with a high level of NO where OVOCs are present, the formation of organic nitrate is likely. As the radical loss process involving organic nitrate formation is not considered in the PSS calculations, this may be a possible explanation for the overestimation of the measured RO_2^*.

Similar uncertainties arise in the PSS calculation observed under cloudy conditions upwind of Manila around 2:00 UTC as in E-AS-06.
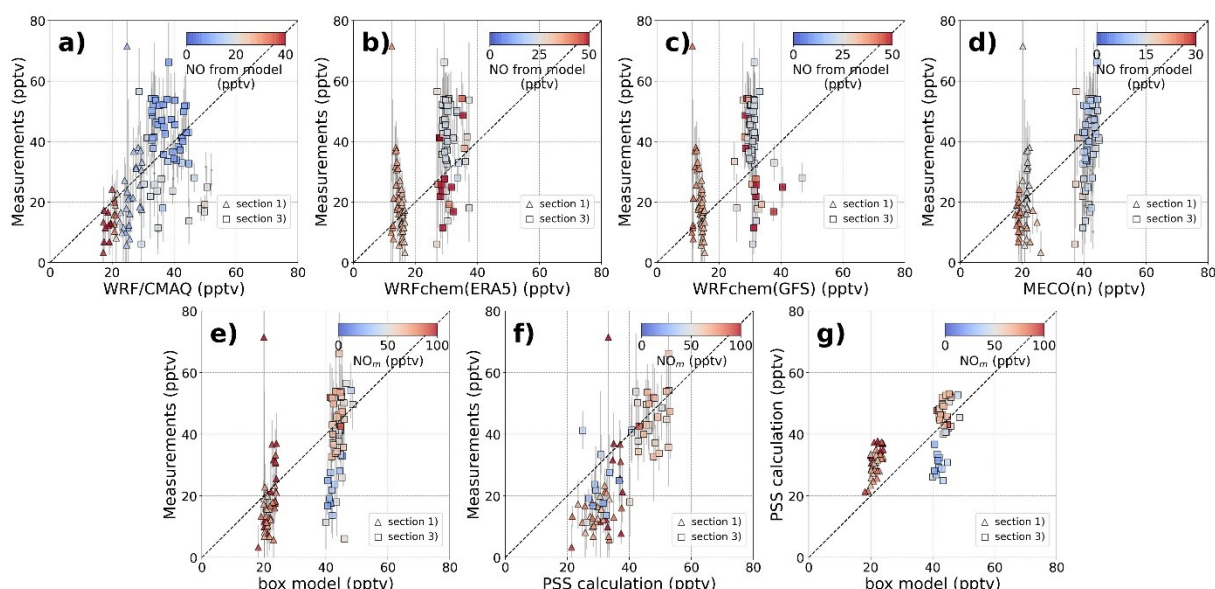
Figure 40: Scatter plots of PeRCEAS RO_2^* measurements and the modelled RO_2^* results from a) WRF/CMAQ, b) WRFchem(ERA5), c) WRFchem(GFS), d) MECO(n), e) box model, and f) calculation using PSS expression for E-AS-10 section 1) and 3). In g), the RO_2^* simulated by the box model and the PSS calculation are compared. All the plots are colour-coded with the corresponding NO from models or measurements. The 1:1 line is represented by black dashed lines, while the linear fit is denoted by red solid lines. The temporal resolution for the plotted data is normalised to 60 s. All the correlations are forced through the origin. Slopes and correlation coefficients are not depicted when the correlation coefficient is less than 0.4.

For flight leg parts 1) and 3), all the models and PSS calculations exhibit RO_2^* results of $\sim$ 20 pptv and $\sim$ 40 pptv, respectively, each with a standard deviation of $\sim$ 10pptv.

Summary for the Manila cases, for air masses influenced by emissions of precursors within the PBL, $RO_2^* \sim 50$ pptv was measured upwind and ~ 70 pptv downwind of Manila. The box model RO_2^* underestimates the measured RO_2^* by around 30 %. The PSS RO_2^* calculations tend to overestimate the observations when NO levels are higher than 80

pptv. and OVOCs are present. This overestimation might be the result of the formation of organic nitrate, which is not considered in the PSS calculations.

Generally speaking, the models using the inventories simulate the trace gases and peroxy radical precursors within their respective uncertainties except for the NOx and HCHO. Consequently, they fail to capture the short-term variations of RO_2^* and other gases. In particular, the O_3 simulated by MECO(n) is remarkably higher than the measurements. This may imply that emissions are not adequately taken into account.

5.2 EMeRGe case study 2: long-range transported air masses

The investigation of processed air masses probed relatively far from emission sources was investigated during the E-AS-08 flight over the East China Sea. The distance of HALO from the coast is approximately 400 km. Figure 41 shows the CO enhancement due to emission plumes from the Yangtze River Delta (YRD) and Beijing, as calculated by HYSPLIT. According to these simulations, the East China Sea receives the long-range transport of plumes mostly having their origin in the YRD, but with a significant contribution from Beijing emissions. The relevant measurements were made at three different altitudes above the East China Sea.
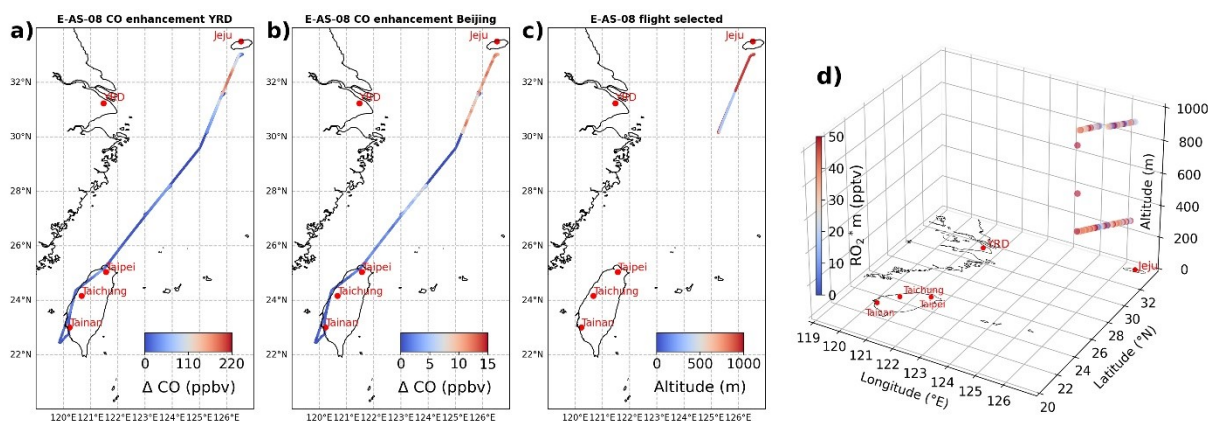
Figure 41: CO enhancement mixing ratio for E-AS-08 flight track by forward dispersion calculations using HYSPLIT for transportation from a) Yangtze River Delta (YRD) and b) Beijing. c) and d) are the top view colour-coded with altitude and the 3-D plot of the selected region colour-coded with RO_2^* measurements, respectively.

As shown in Figure 42, the region of the selected measurements is dominated by cloudy conditions with lower insolation. Consequently, the RO_2^* production from the photolysis of precursors is reduced significantly. The HALO measurements investigated between altitudes of 300 and 1000 m have RO_2^* values with an average of 35 ± 19 pptv. The relationship between the RO_2^* measurements, PSS calculations, and the modelling RO_2^* are presented in scatter plots in Figure 43. Additional information on scatter plots featuring colour coding with different species is provided in appendix A 35.

These show no simple linear relationship between measurement and modelled simulations. The CO enhancement results from the HYSPLIT model as well as the FLEXTRA back trajectory model imply that the aircraft was likely sampling the aged air masses from the Yangtze River Delta and Beijing at this selected region. At the lower

altitude level, HALO travelled through or above cloudy locations at ~ 330 m. The true airspeed during measurements is up to 111 m/s. This corresponds to a spatial resolution of 6.7 km/min, which is still comparable to or higher than the spatial resolution of the models.
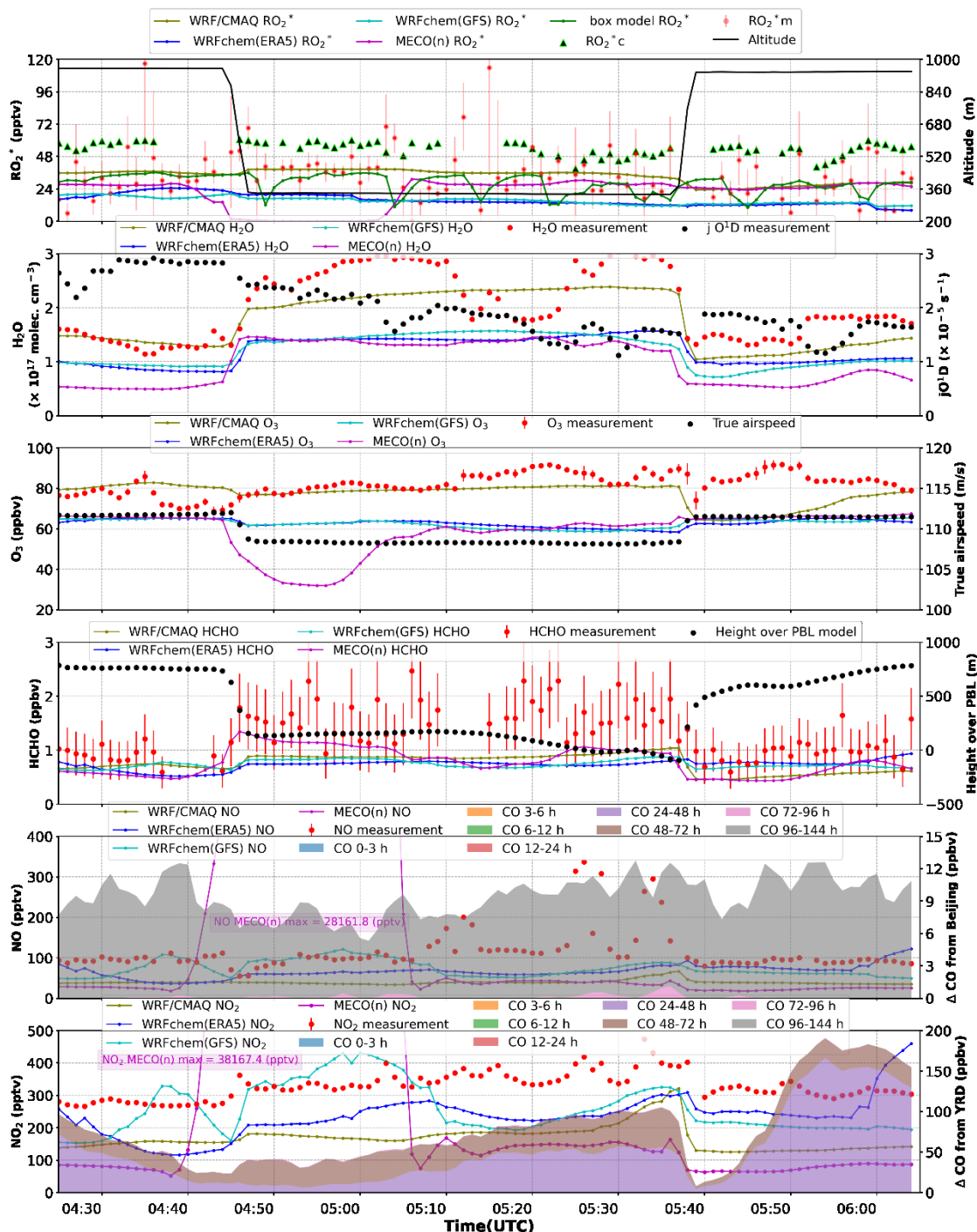
Figure 42: Time series of the RO_2^* measured by PeRCEAS and simulated by WRF/CMAQ, WRFchem(ERA5), WRFchem(GFS), MECO(n), box model, and PSS calculation for E-AS-08. Altitude, water concentration, and true airspeed are measured by BAHAMAS. The mixing ratios for O_3, HCHO, and NO & NOy are measured by AMTEX, HKMS, and AENEAS, respectively. jO(¹D) are measured by HALO – SR. The height above PBL is modelled by SCALTRA. CO enhancements due to the Beijing and YRD outflows are modelled by HYSPLIT. The temporal resolution is normalised to 60 s for all the measurements and models. Additionally, modelled results for water concentration, O_3, HCHO, NO, and NO_2 mixing ratio have been plotted using the WRF/CMAQ, WRFchem(ERA5), WRFchem(GFS), and MECO(n) models. The box model constrains the measurements, therefore, is not featured in the plots.

The PSS RO_2^* overestimate the measured values within the pollution plume by up to 20 %. The models mostly underestimate the measured RO_2^* and the other trace gases (e.g. HCHO, NO, and NO_2) used for this study. In contrast, maximum NO, NO_2, CO and minimum O_3 mixing ratios simulated by MECO(n) were observed between 04:40 and 05:10 UTC. As a result, MECO(n) simulated small RO_2^* to approximately zero. Consequently, MECO(n) results were omitted from the correlation plot analysis from this part.

As previously explained in both cases of air masses upwind of Manila, measurement uncertainties in the remote sensing instruments, particularly under cloudy conditions might lead to significant uncertainties in the PSS calculations.
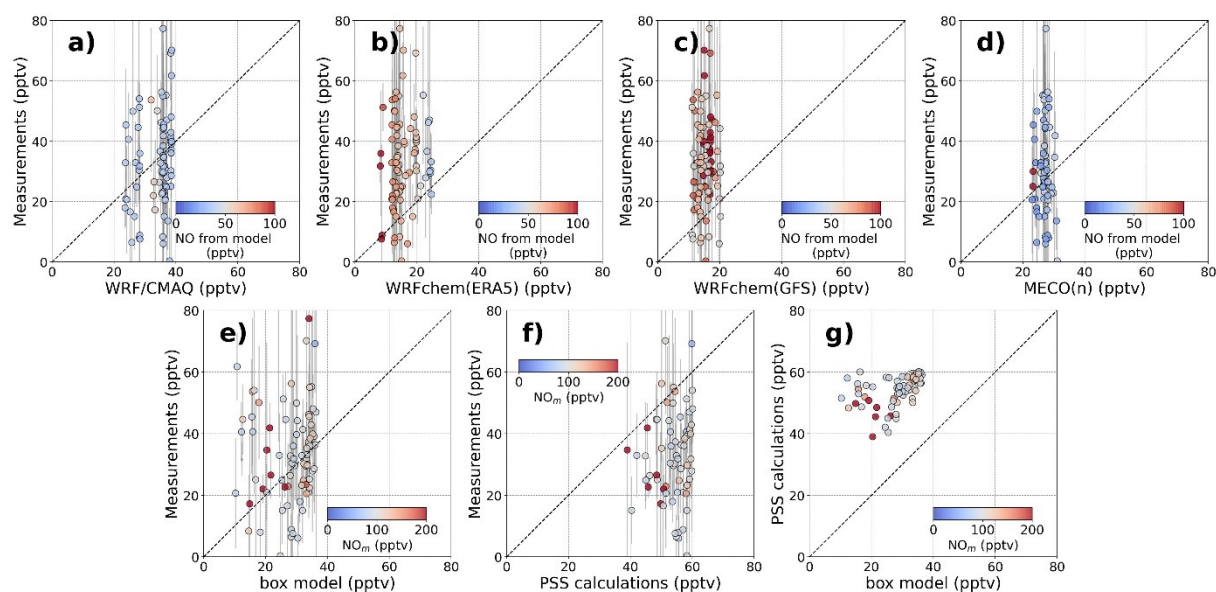
Figure 43: Scatter plots of PeRCEAS RO_2^* measurements and the modelled RO_2^* results from a) WRF/CMAQ, b) WRFchem(ERA5), c) WRFchem(GFS), d) MECO(n) where RO_2^* modelling results with 0 are not included, e) box model, and f) calculation using PSS expression for the E-AS-08 at the selected region. In g), the RO_2^* simulated by the box model and the PSS calculation results are compared. All the plots are colour-coded with corresponding NO from models or measurements. The dashed black lines denote the 1:1 line. The temporal resolution for the plotted data is normalised to 60 s.

Additionally, this measurement region is particularly cloudy and the total aerosol concentration measurement is 800 $[cm^{-3}]$ on average, whereas the typical total aerosol concentration for Manila flight leg parts 1) and 3) are below 30 $[cm^{-3}]$. Radical losses by aerosol uptake and heterogeneous reactions on the aerosol surface are therefore expected.

In summary, the RO_2^* observations in aged and long-range transported air masses from the Yangtze River Delta and Beijing within the PBL averaged below 35 pptv. The models generally underestimate the RO_2^* observations and cannot reproduce the variability observed. In addition the measurements of other involved species in the radical chemistry, such as OVOC precursors, in particular HCHO, and NO, are not well simulated. This might imply the necessity of revision of the dispersion patterns used in the models.

The PSS calculation constrained to the on-board measurements tends to overestimate the RO_2^* measurements by approximately 30 %. This overestimation may be linked to cloudy

conditions, which introduce significant uncertainties in the measurements obtained from remote sensing instruments, further affecting the precision of PSS calculations. Moreover, these air masses were characterised by high aerosol load, averaging around 800 $[cm^{-3}]$. which indicate potential radical aerosol uptake and heterogeneous reactions on the aerosol surface which are not accounted for in the current PSS calculations.

5.3 EMeRGe case study 3: flights over Taiwan – take-off and landing

During the EMeRGe campaign in Asia, the use of the airport in Tainan as the operations base for HALO flights, combined with strict air traffic regulations resulted in the flight tracks having similar routes following take-off and landing. The resultant set of atmospheric composition and meteorological measurements provides an opportunity to investigate the concentrations and mixing ratios of the atmospheric species and peroxy radical mixing ratios, measured in the different air masses above the same or very similar surface regions. In addition, comparing the PeRCEAS measurements with modelling results provides insight into the capability of the available models to simulate the total peroxy radicals concentrations and mixing ratios.
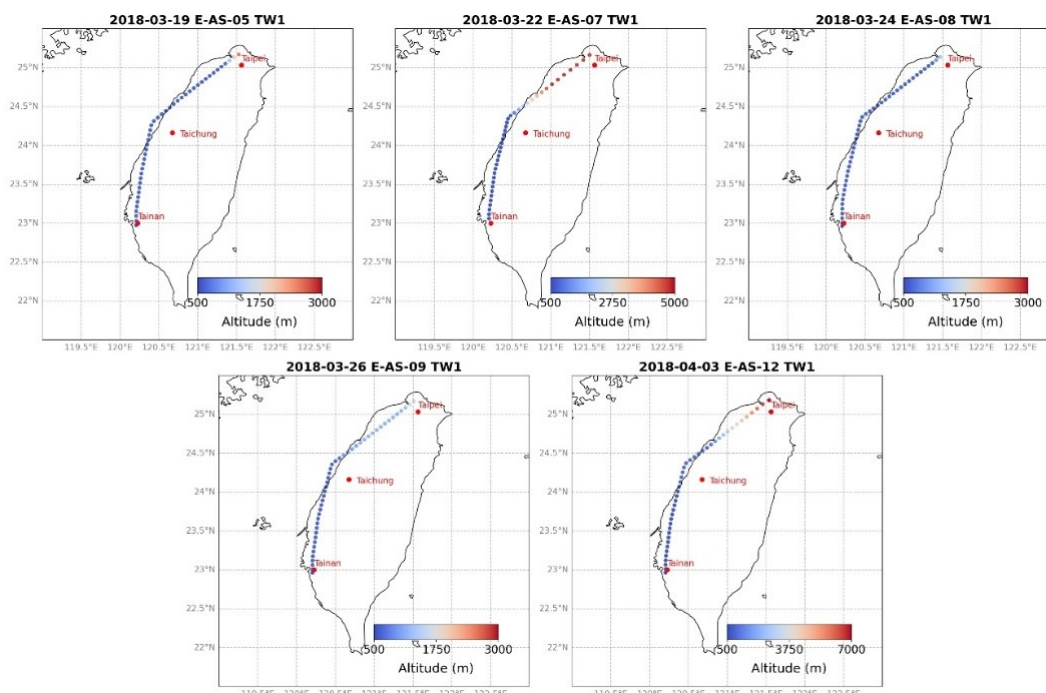
Figure 44: Flight tracks over Taiwan selected for the peroxy radical measurement and model comparison colour-coded with the altitude measured by BAHAMAS in 60 s temporal resolution. TW1 refers to take-off phases of the flight.

Figure 20 and Table 5 in section 3.2 summarise the 10 research flight tracks flown by the HALO aircraft during the EMeRGe campaign in Asia. Five of these flights (E-AS-05, E-AS-07 to E-AS-09, and E-AS-12) have nearly identical flight paths over Taiwan, for approximately 1 hour after the take-off. Nine of these flights (E-AS-05 to E-AS-13) have nearly identical flight paths over Taiwan, for approximately 1 to 3 hours before landing. For this reason, these flights provide interesting measurements of the composition of the atmosphere on the coast of Taiwan along the flight tracks during the campaign. For ease

of reference in the following, the take-off and landing flight legs are denoted as "TW1" and "TW2", respectively.

The RO_2^* retrieved from PeRCEAS has a temporal resolution of 60 seconds. Consequently, as for the previous case studies, the models were resampled and averaged such that they coincided with the 60s resolution of the PeRCEAS instrument. In appendix A 57 to A 126 for TW1 and A 147 to A 272 for TW2 time series of the following measurements are provided:

a) the measured and simulated mixing ratios of RO_2^*;
b) the mixing ratios of the trace gases NO, NO_2, NOy, CO, O_3, HCHO, CH_3CHO, CH_3CO CH_3, HONO, and SO_2;
c) the concentration of water vapour;
d) the concentration of black carbon;
e) the photolysis frequency for $jO(^1D)$.
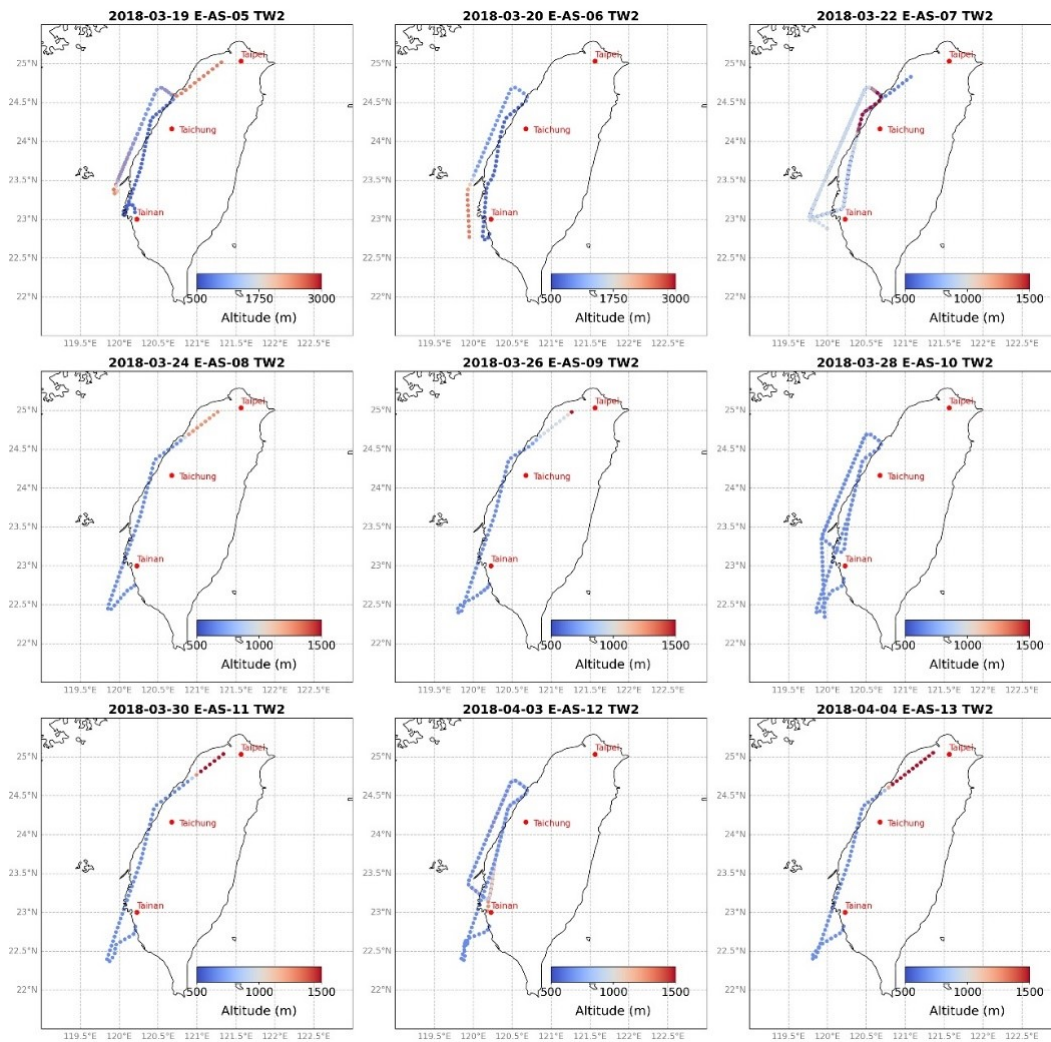
Figure 45: Flight tracks over Taiwan selected for the peroxy radical measurement and model comparison colour-coded with the altitude measured by BAHAMAS in 60 s temporal resolution. TW2 refers to the landing phases of the flight.

Figure 44 and Figure 45 provide summaries of the flight tracks and the flight altitudes for the TW1 and TW2 cases. The altitudes plotted are 60 s averages. As part of the comparison between measurements and models at specific locations, the measurement and model data were grouped according to their respective coordinates. For a consistent spatial resolution when comparing measured and modelled data, the measurements were binned at intervals of 0.1 ° latitude.
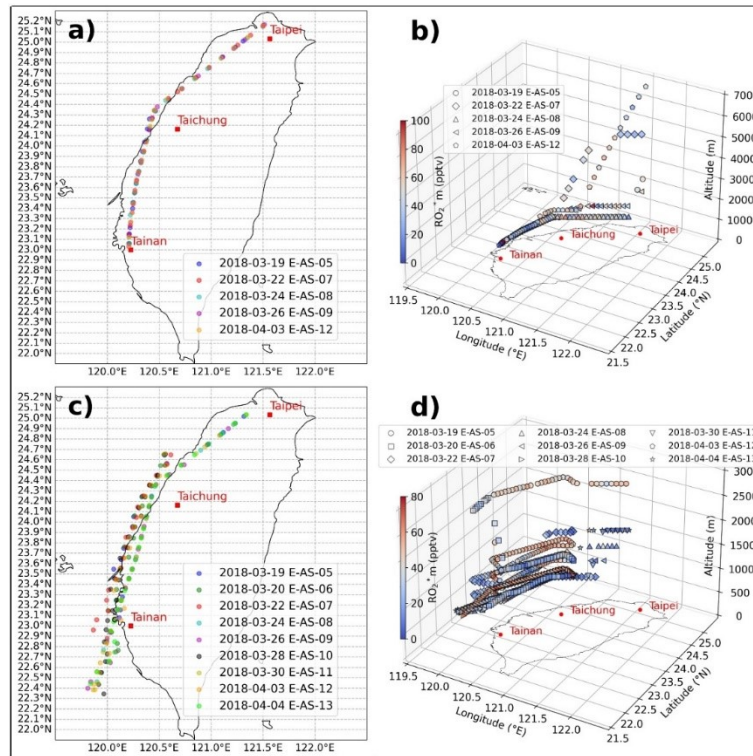
Figure 46: Flight tracks for the selected flights for TW1 and TW2. a) and c) represent the top view of the locations after binned over 0.1° latitude; b) and d) are the corresponding 3D plots in 1 min temporal resolution colour-coded with RO_2^* measurements.

Figure 46 shows the flight tracks for the TW1 and TW2 groups of flight legs, after 0.1° binned and their respective 3D plots. For the TW1, measurements were taken at four flight altitudes around 600 m, 1000 m, 1200 m, and above 4500 m. In TW2, measurements were taken at five flight altitudes around 600 m, 900 m, 1300 m, 1500 m, and 2500 m. The 60s averaged flight track measurements, spaced at 0.1 ° intervals along the latitude for each flight, provide comprehensive coverage without gaps. This binned resolution effectively captures both the temporal and spatial details of the measurements. In the following sections, the investigation of the TW1 and TW2 flight legs will be discussed separately in detail.

5.3.1 Take-off (TW1)

As explained above, the TW1 case comprises all comparable HALO post take-off measurements during the EMeRGe campaign in Asia. Figure 47 shows the altitude measured, the modelled height of the PBL, and the modelled height over the PBL at the position of the aircraft provided by SCALTRA. The area investigated during the TW1 is divided into two types of flight legs:

i) from take-off to 24.4 °N latitude the aircraft flights along the coast below 640 m except for E-AS-12, which reaches around 970 m;

ii) from 24.4 °N to 25.2 °N the aircraft heads towards Taipei over land and starts to ascend before leaving the island.
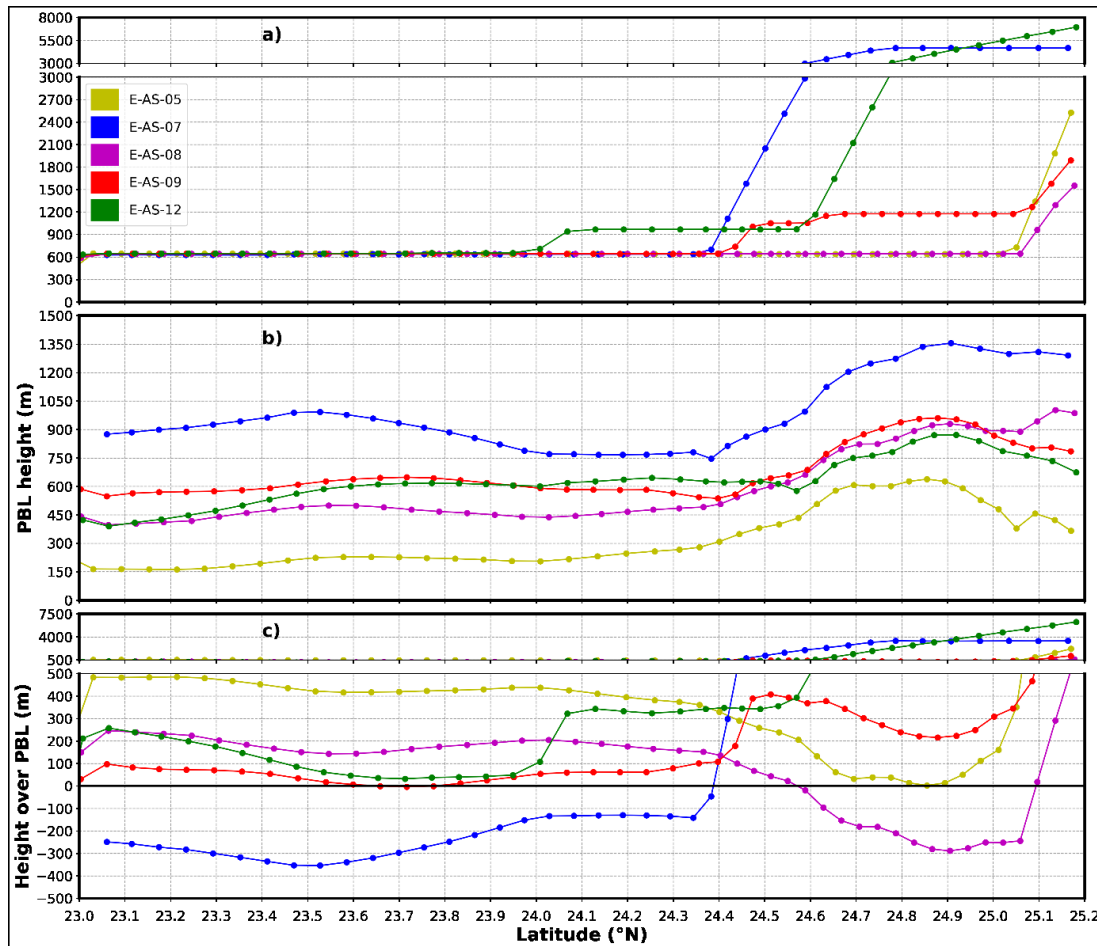
Figure 47: HALO altitude and modelled PBL height of the five flights selected for TW1 with a temporal resolution of 60 s. a) vertical profile of the flight along the latitude, b) PBL height modelled by SCALTRA along the latitude, and c) HALO height over the modelled PBL. The PBL height information is provided by SCALTRA. The black solid line in c) denotes 0 m.

The modelled PBL height is different from flight to flight. As shown in Figure 47 c), E-AS-07 was below, and E-AS-09 and E-AS-12 were close to the modelled PBL height during flight leg part i) of the TW1. During flight leg part ii), E-AS-05 was close to and E-AS-08 was within the PBL. The FLEXTRA 12 hrs backward trajectory model, at flight leg part i) of TW1 shows that the flights sampled air masses below 1000 m before ascending to around 24.4 °N. These air masses originated from the boundary layer of Taiwan. For TW1, ~ 60 % of the RO_2^* measurements were made above the PBL. The other measurements of gases and aerosols are shown in the appendix (A 39 to A 56).

During flight leg part ii), HALO in the flights E-AS-05 and E-AS-08 flow at a near constant altitude and sampled air masses below 1000 m from Taiwan. The measurements from E-AS-08 showed enhanced concentrations of total aerosol, NO and NOy. During E-AS-09, air masses from 1000 to 2000 m above Taiwan were sampled. In the last flight leg part of the

flights E-AS-07 and E-AS-12, HALO ascended to higher altitudes and sampled air masses from mainland China (Fujian) at altitudes of 4000 to 5000 m and 5000 to 6000 m, respectively.

In Figure 48, individual RO_2^* measurements were taken and binned at 0.1° latitude intervals, spanning from 23.0 °N to 25.2 °N. Figure 48 a) shows the 1 min averaged and 0.1° binned RO_2^* measurements made by PeRCEAS. The mean of each binned interval is calculated as the mean of the measurements of all individual flights and is plotted at each 0.05 ° of the 0.1 ° interval. That means, for example, that all the measurements between 23.0 °N and 23.1 °N are shown at 23.05 °N in the navy blue coloured square. The navy blue colour envelopes represent 1σ error around the mean, which includes the propagation of the individual measurement error for RO_2^*. The data is further grouped into two categories, i.e. above and below the PBL height, as modelled by SCALTRA. Specifically, measurements taken at altitudes greater than the modelled PBL height + 100 meters are defined to be "above the PBL" in Figure 48 b). In contrast, measurements at altitudes lower than this threshold are categorised as "within the PBL" in Figure 48 c).
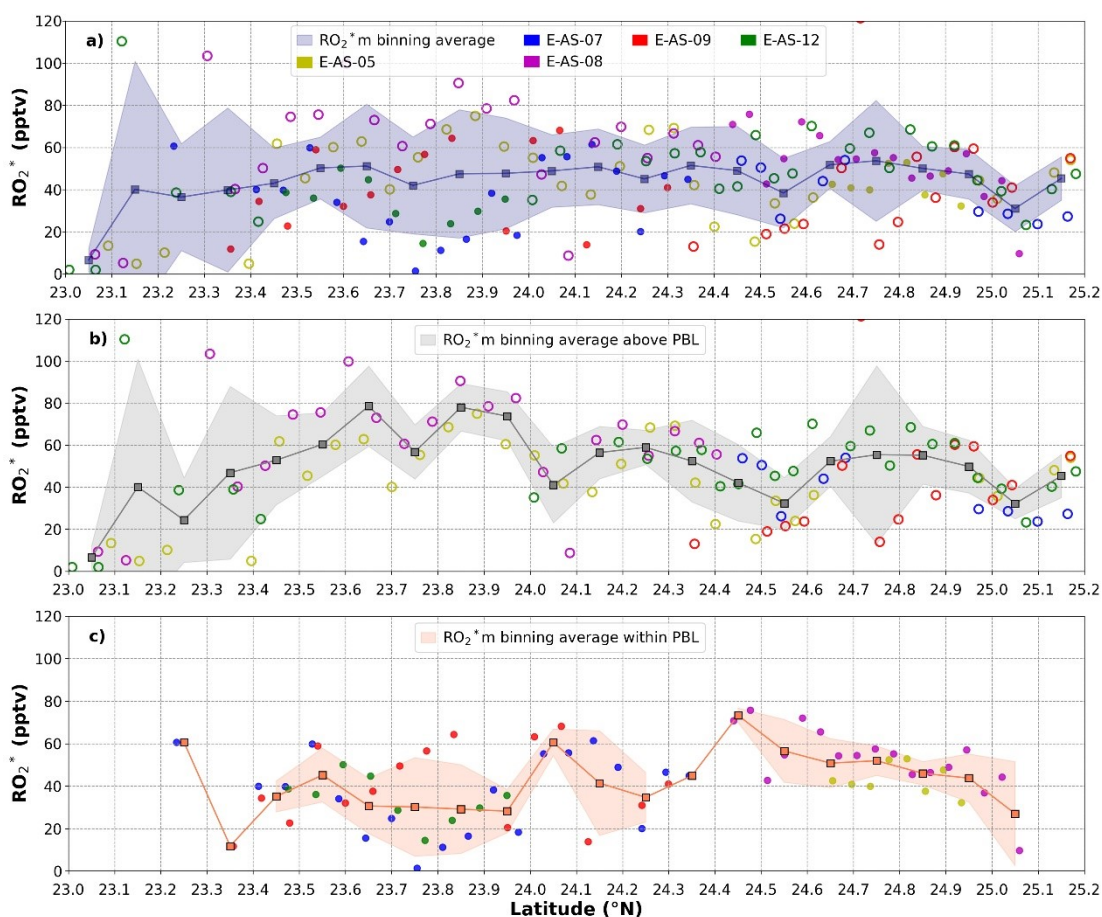
Figure 48: Plots of RO_2^* as a function of latitude for the TW1 group of flights at 60 s temporal resolution during EMeRGe in Asia. Panel a) shows the binned and averaged RO_2^* measurements colour-coded for each selected flight. Panel b) shows the binned and averaged RO_2^* above the PBL, as modelled by SCALTRA. Panel c) shows binned and averaged RO_2^* within the PBL, as modelled by SCALTRA. Symbols used: filled circles represent measurements within the modelled PBL, and circles indicate measurements above it. The colour-coded 1σ envelopes represent the standard deviation of the binned and averaged dataset. For clarity, individual measurement error bars are not depicted in the plots.

The average RO_2^* measurement is 44 ± 24 pptv for TW1. Over 60% of the RO_2^* measurements for the TW1 flight legs were made above the PBL and yielded an average mixing ratio of 50 ± 22 pptv. The most significant differences are observed in flight leg part i), where the sampled air masses are presumed to originate from Taiwan island areas along the flight track, particularly near the western cities and industrial regions. However, at flight leg part ii), significantly higher RO_2^* are observed in the air masses within the PBL which remain similar to the mixing ratios measured above.

Differences between the two categorised groups of measurements (above and within the PBL) are evident when sampling occurs around 600 m altitude in flight leg part i), with the exception of flight E-AS-09. The mixing ratios of measured radical precursors (HCHO, CH_3CHO, and CH_3COCH_3) and photolysis conditions are similar across all five flights, regardless of whether they were taken above or within the PBL. Peaks in NOx mixing ratios were observed for flights E-AS-07 and E-AS-12 around latitudes from 23.6 °N to 23.9 °N, correlating with low RO_2^* measurements. Notably, flight E-AS-07 shows a total aerosol concentration at least five times higher than that observed in other flights at the same location. This flight also recorded peak mixing ratios of NO (4ppbv), NOy (16ppbv), CO (350ppbv), and SO_2 (3 ppbv). These elevated levels of trace gases and aerosols and a possible overall more rapid RO_2^* loss rate may explain the lower RO_2^* measurements observed, due to the radical losses in the aerosol surface. At flight leg part ii), the difference in measurements taken above and within the PBL is less than 10%. The air sampled in this section is anticipated to come from north of the flight measurement location over the ocean.

The mean RO_2^* are calculated and modelled together with the 1σ standard deviation of the averages shown as the coloured envelopes in Figure 49 for the WRF/CMAQ, WRFchem(ERA5), WRFchem(GFS), MECO(n), box models, and calculations using PSS assumptions, respectively. In these figures, individual modelling results are separately marked above or within the modelled PBL height + 100 m by SCALTRA. The averaged results are 18 ± 9 pptv (WRF/CMAQ model), 9 ± 9 pptv (WRFchem(ERA5) model), 10 ± 9 pptv (WRFchem(GFS) model), 18 ± 12 pptv (MECO(n) model), 29 ± 15 pptv (box model), 36 ± 11 pptv (PSS calculation).

The PSS calculated RO_2^* have some missing values due to the availability of all required measurements at the beginning of the TW1 flight legs. Both the box model results and the PSS calculations, which are constrained to the in-situ measurements made on board HALO, show the best agreement with the RO_2^* measurements and are within the 1σ envelope. The WRF/CMAQ model, the two WRFchem models, and the MECO(n) model, all of which use selected emission inventories as input, underestimate the averaged RO_2^* measurements for TW1 flight leg part i), by approximately 60 to 80 %. The degree of this underestimation varies from flight to flight but is typically less than 15 pptv.
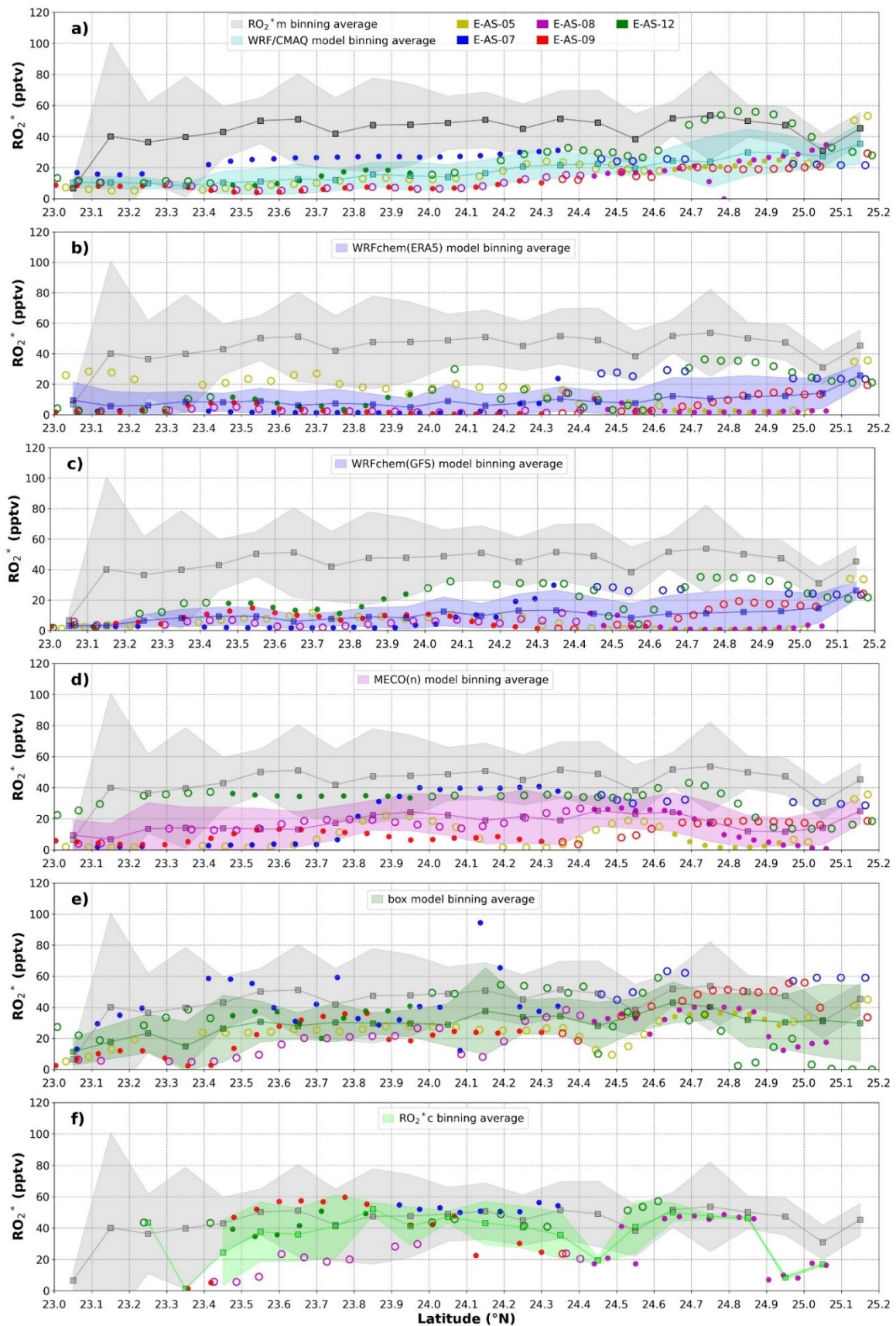
Figure 49: Comparison of the selected flights between 0.1° binned and averaged RO_2^* measured from PeRCEAS and a) results from the WRF/CMAQ model, b) results from WRFchem(ERA5) model,c) results from WRFchem(GFS) model, d) results from MECO(n) model, e) results from the box model, and f) results from calculations using PSS expression over TW1. The corresponding colour-coded 1σ envelope, are the measured and modelled RO_2^* averages for each latitude interval, respectively. Symbols used: filled circles represent measurements within the modelled PBL by SCALTRA, and hollow circles indicate measurements above it.

The differences are evident when comparing modelling and measurement results for $jO(^1D)$, NO, HCHO, and CH_3CHO. For example, models tend to overestimate $jO(^1D)$ up to 40 %. For NO, the modelled results are between 50 % and 500 % higher than the measurements. In contrast, HCHO measurements are underestimated by the models by 50 % to 100 %. Similarly, underestimations for CH_3CHO range from 50 % to 200 % in the model simulations.

In TW1 flight leg part ii), where the flights operate at different altitudes, the agreement between the modelled and the measured RO_2^* results improve. The models tend to overestimate $jO(^1D)$, though the differences remain below 15 %. As for NO, the models overestimate by 20 % to 50 % (except for a few peaks). HCHO measurements are commonly underestimated by the models, with the range lying between 20 % to 50 %. Similarly, differences for CH_3CHO range from 20 % to 60 % underestimation by the models.

Both the box model simulation and the PSS calculation of RO_2^* are constrained to the measurements made of trace gases and meteorological parameters onboard HALO. They do not consider the halogen in their RO_2^* calculations since there are no related measurements available. In those cases, the underestimation of the observations could be attributed to the missing halogen sources.

One possible additional explanation for the underestimation of RO_2^* could be the presence of a sufficient amount of halogens in the atmosphere. Halogens and interhalogens (X_2 where X= Cl, Br, or I and XY where Y= Cl, Br, or I) are known to be released from the ocean. In addition, there are also organic methyl halides and dihalomethanes (CH_3Cl, CH_3Br, CH_3I and CH_2CL_2, CH_2Br_2, CH_2I_2) that are released on land and from the ocean. A potential daytime source of halogen atoms in the lower troposphere is the photolysis of halogens and interhalogens in the visible and UV. Cl reacts with aliphatic hydrocarbons to generate an R radical. Cl, Br, and I also potentially add to unsaturated hydrocarbons, e.g. natural emissions from terpenes and anthropogenic emissions of alkynes and alkenes. The resulting halogen atom, X or Y then oxidises the hydrocarbons, RH, leading to the production of organic peroxy radicals RO_2, as shown in reactions R 5-1 to R 5-4 and R 2-31(Simpson et al., 2015):

$$X_2 \xrightarrow{h\nu} 2X \qquad\qquad\qquad R\ 5\text{-}1$$
$$XY \xrightarrow{h\nu} X + Y \qquad\qquad\qquad R\ 5\text{-}2$$
$$X + RH \rightarrow R + HX \qquad\qquad\qquad R\ 5\text{-}3$$
$$Y + RH \rightarrow R + HY \qquad\qquad\qquad R\ 5\text{-}4$$
$$R + O_2 \xrightarrow{M} RO_2 \qquad\qquad\qquad R\ 2\text{-}31$$

The reactions of XO or YO with NO are known to change the ratio of NO to NO_2. The unconstrained models do contain halogen chemistry. Inaccurate estimates of halogen inventories may in part play a role in the underestimate of RO_2^*. However, an analysis outside the scope of this study would be required to quantify, whether missing halogen

chemistry is playing a role in the difference between measured and unconstrained model RO_2^*.

A further point to consider is the true airspeed at the 600 – 800 m levels was around 110 m/s for all the flights. This implies that each in-situ measurement represents $\sim$ 6.6 km along the flight paths. This resolution is finer than the spatial resolution of all the models, presenting a challenge for these models to capture accurately the short-term local variations of the RO_2^*.

Overall it can be concluded that inaccuracies in the inventories used by the models will have a large impact on the simulations of the RO_2^*.

5.3.2   Landing (TW2)

The measurements made during nine landings during the EMeRGe campaign in Asia were analysed for the TW2 group of flights. Figure 50 shows the measured flight altitude of HALO and the corresponding modelled PBL heights. Most TW2 flights flew at around 600 m and 900 m altitude levels.
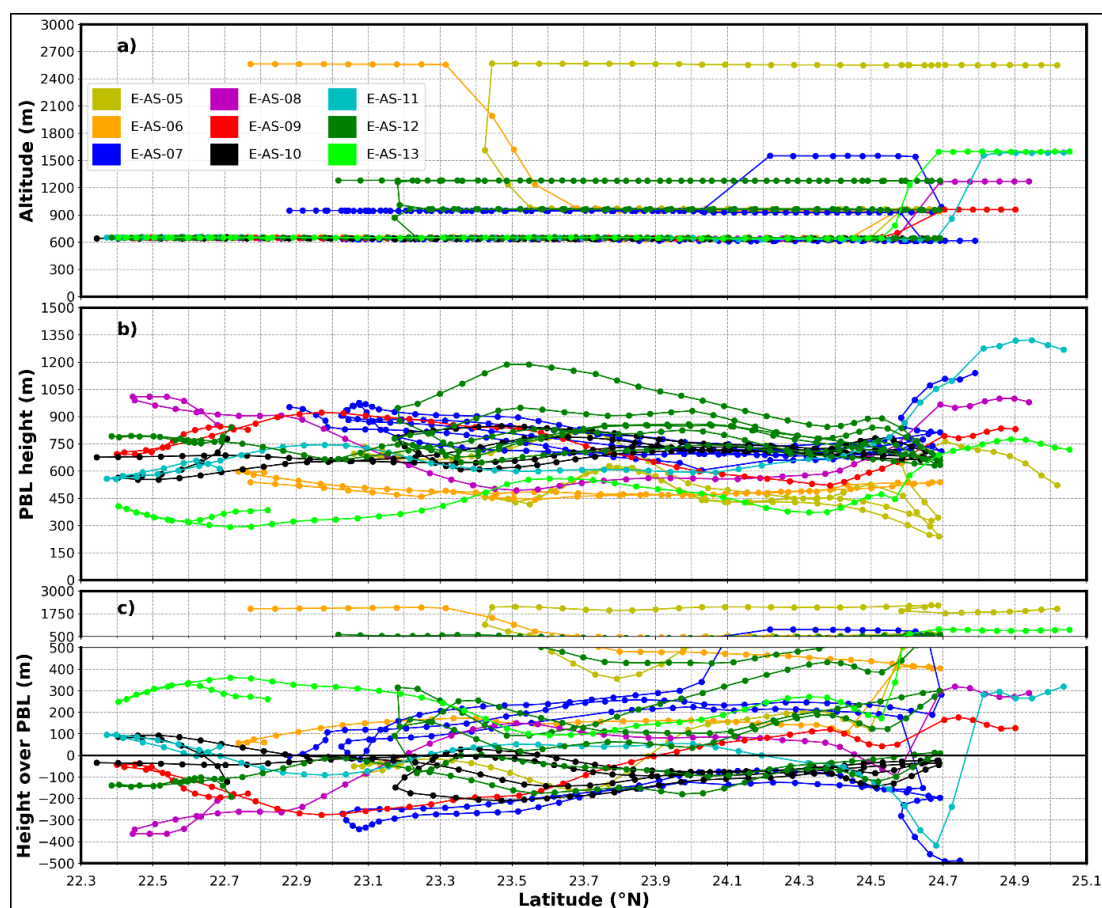
Figure 50: HALO altitude and modelled PBL height for the nine flights selected for TW2 with a temporal resolution of 60 s. Panel a) vertical profile of the flight along the latitude, panel b) PBL height modelled by SCALTRA along the latitude, and panel c) HALO above the PBL.

The comparisons of the photolysis rates, the composition of the air masses, the aerosols probed (see A 128 to A 146 in appendix) as well as the HYSPLIT (see appendix A 273 to A

281) and FLEXTRA model results indicate that there are three main sources of pollution observed in TW2 flights:

a) Urban pollution from the city of Tainan. Generally related to elevated mixing ratios of trace gases and aerosols between 22.5 °N and 23.3 °N over the coast. This urban plume is at its best captured during the E-AS-08, a clear and highly polluted flight day.
b) The Mailiao and Taichung power plants led to recurrent plumes of aerosols, NO, NOy, and SO_2 plumes at the coast between 23.7 °N and 24.5 °N approximately. This is well captured in E-AS-05.
c) Urban pollution from Taipei around 25 °N. Elevated mixing ratios of organic and inorganic aerosol and trace gases such as NOy and VOCs are generally observed

Individual RO_2^* measurements binned and averaged at 0.1° latitude intervals between 22.3 °N and 25.1 °N. Figure 51 presents plots for TW2 flight legs, similar to those of TW1 shown in Figure 48. These are depicted with 1σ envelopes and are classified based on whether the measurements were taken above or within the PBL. The average RO_2^* measurement is 35 ± 17 pptv for TW2. Less than 45 % of the RO_2^* measurements were taken above the PBL with an average value of 31 ± 16 pptv. On average the RO_2^* measured within the PBL (37 ± 16 pptv) and above the PBL (31 ± 16 pptv) are equivalent. This indicates that the polluted air masses probed over the PBL were of similar radical precursor composition to that within the PBL. The observed mixing ratios of most of the trace gases selected and the aerosol concentration over the PBL were higher in TW2 than in TW1 (see A41-A56 for TW1 and A131-A146 for TW2 in the appendix).

Given that the landing phase of the flights comprised in TW2 occurred at different local times of the day, the photolysis conditions differed significantly. E-AS-12 took place approximately 3 hours before other flights and had at least two times higher averaged $jO(^1D)$ than those of the other flights. More active photochemical processing of the probed air masses in comparison with the other four flights might be the cause of the RO_2^* observed during E-AS-12 being in the upper part of the envelope.
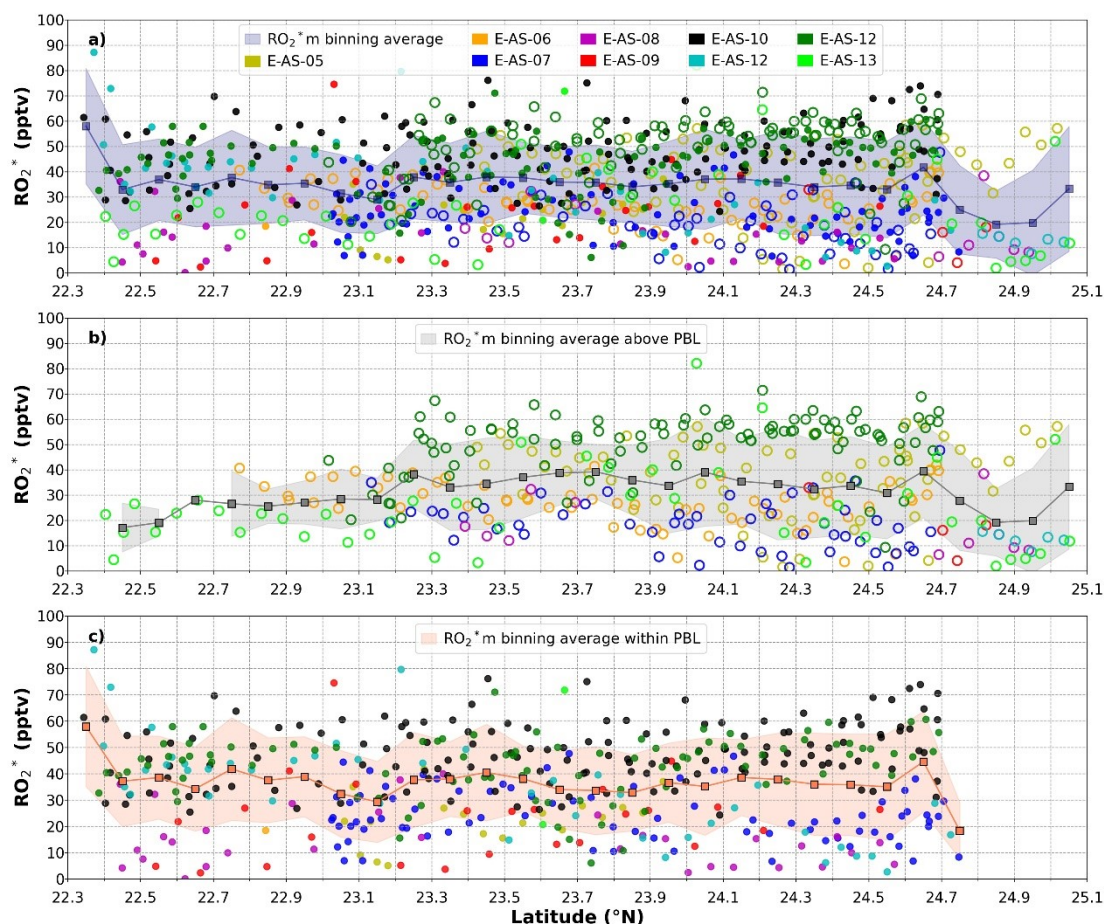
Figure 51: Plots of RO_2^* as a function of latitude for the TW2 group of flights at 60 s temporal resolution during EMeRGe in Asia. Panel a) shows the binned and averaged RO_2^* measurements colour-coded for each selected flight. Panel b) shows the binned and averaged RO_2^* above the PBL, as modelled by SCALTRA. Panel c) shows binned and averaged RO_2^* within the PBL, as modelled by SCALTRA. Symbols used: filled circles represent measurements within the modelled PBL, and circles indicate measurements above it. The colour-coded 1σ envelopes represent the standard deviation of the binned and averaged dataset. For clarity, individual measurement error bars are not depicted in the plots.

The composition of air masses measured during the E-AS-07 and E-AS-10 flights varied significantly, with each flight corresponding to the lower and upper limits of the RO_2^* envelope, respectively. E-AS-07, conducted later in the day, exhibited lower $jO(^1D)$ levels that decreased significantly over the course of the flight. This flight also had elevated aerosol concentrations, particularly above the PBL at 900 m altitude. In this altitude range, a distinct plume enriched in NO_y, CO, SO_2, and O_3 was observed, spanning latitudes between approximately 23.5 °N and 24.1 °N. Given the location, it is likely that this plume originated from Taichung and was transported above the PBL without much diffusion of pollutants out or into it. In contrast, E-AS-10 stayed within the PBL throughout the flight, resulting in lower trace gas and aerosol mixing ratios. This suggests that the air mass was less influenced by elevated emissions or long-range transport, i.e. a less complex chemical environment.

Figure 52 presents the comparison of the 0.1 ° latitude binned PeRCEAS measurements, the simulations of the WRF/CMAQ, WRFchem(ERA5), WRF/CHEMRE(GFS), MECO(n), box models, and the calculations using the PSS assumptions, respectively.
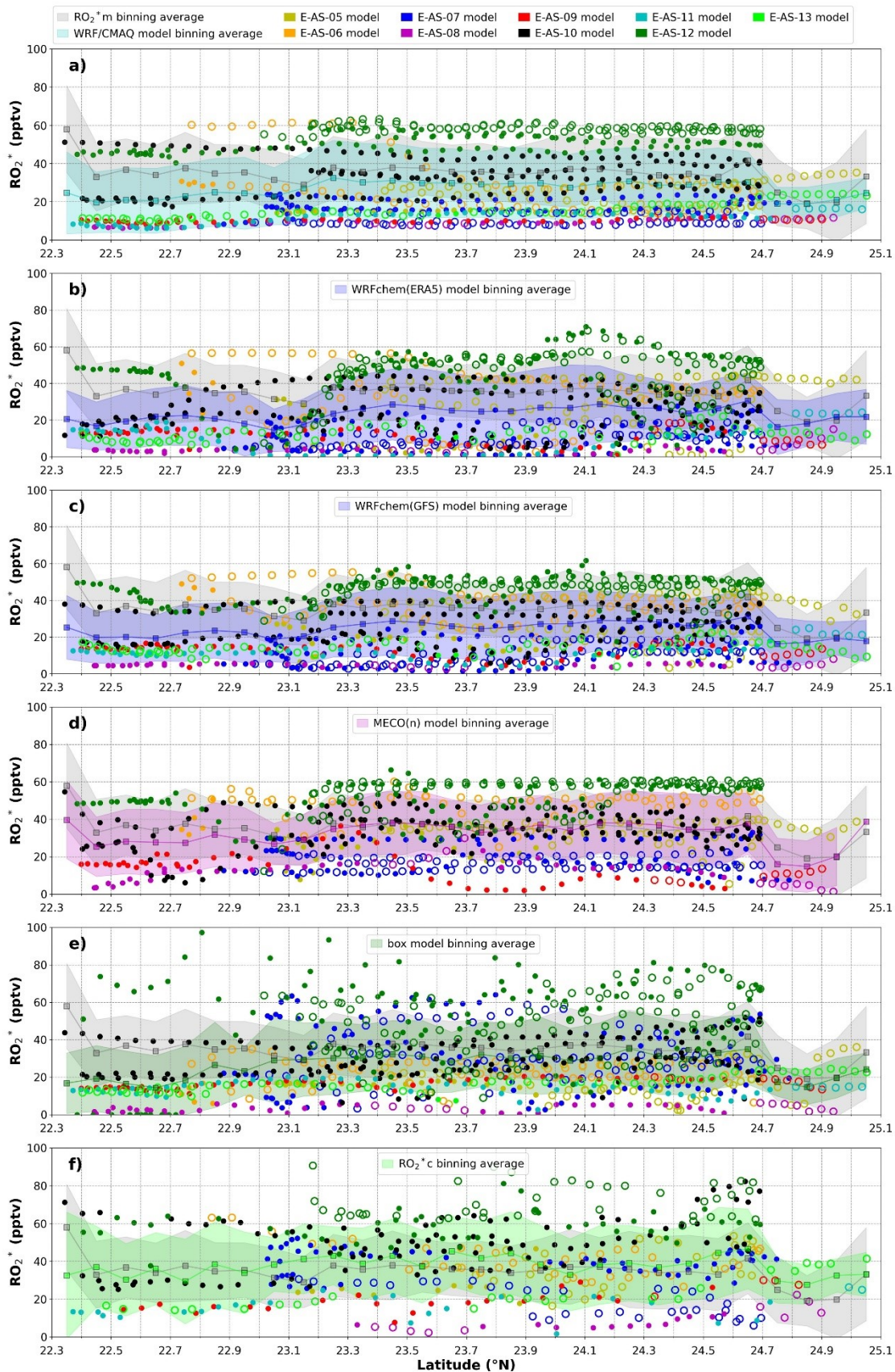
Figure 52: Comparison of the selected flights between 0.1° binned and averaged RO_2^* measured from PeRCEAS and a) results from the WRF/CMAQ model, b) results from WRFchem(ERA5) model,c) results from WRFchem(GFS) model, d) results from MECO(n) model, e) results from the box model, and f) results from calculations using PSS expression over TW2. The corresponding colour-coded 1σ envelopes are the measured and modelled RO_2^* averages for each latitude interval, respectively. Symbols used: filled circles represent measurements within the modelled PBL by SCALTRA, and hollow circles indicate measurements above it.

Similar to TW1, individual modelling results are separately marked as being above or within the PBL height + 100 m by modelled SCALTRA. The averaged results are 26 ± 17 pptv (WRF/CMAQ model), 23 ± 17 pptv (WRFchem(ERA5) model), 24 ± 15 pptv (WRFchem(GFS) model), 32 ± 16 pptv (MECO(n) model), 26 ± 18 pptv (box model), 38 ± 20 pptv (PSS calculation).

The overlap between the 1σ envelope of the binned and averaged measured and modelled RO_2^* significantly improves compared to the TW1 case. Here, all the models and the calculated RO_2^* lie within the envelopes of the binned average of the measurements. Changes in the complexity of the air masses (e.g. due to different content of aerosols or contact with surface emissions) might affect the insolation and the photochemical activity of the air masses with respect to the standard assumptions of the models.

As can be seen in the figures, the flights E-AS-05 and E-AS-12 RO_2^* are best simulated by the models investigated. These are flights with a comparatively longer time above the PBL and higher insolation conditions than the rest. In addition, the air masses probed during E-AS-12 were less polluted than on other days as indicated by the significantly lower mixing ratio of NO, NOy, BC, and OVOC.

Figure 53 shows latitudinally binned and averaged RO_2^* measurements for five selected flights of TW1 and nine selected flights of TW2, with each data point representing a latitudinal average. The mean RO_2^* measurement over latitude for TW1 is presented with a propagated 1σ error of 44 ± 24 pptv, and for TW2 35 ± 17 pptv. The average total peroxy radical expected at these locations around Taiwan is around 39 ± 21 pptv.
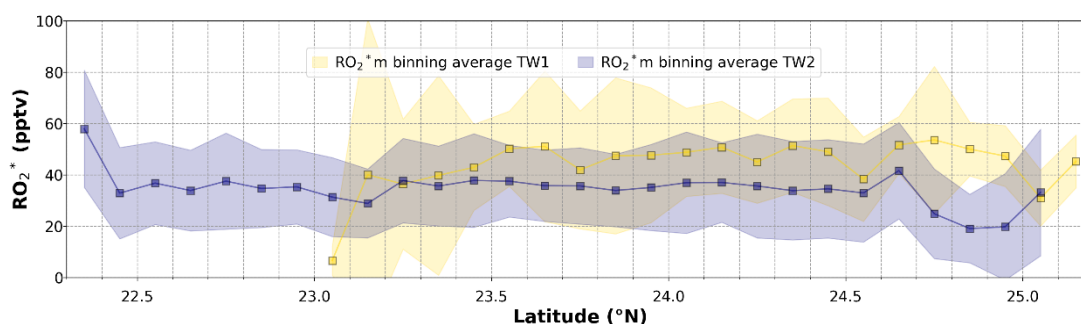
Figure 53: Binned and averaged RO_2^* measurement over latitude for 5 selected flights of TW1 and nine selected flights of TW2. The corresponding envelopes are the 1σ standard deviation of the binned and averaged.

In summary, around 60 % of the TW1 (take-off) scenarios are taken above the PBL. At altitudes higher than 1000 m, the air masses are transported from mainland China. The averaged RO_2^* measurements of TW1 is 44 ± 24 pptv, where the measurements above the PBL are ~ 20 % higher than within the PBL in air masses originating from western cities and industrial regions of Taiwan. The box model and PSS calculations constrained to the HALO measurements provide the best agreement and are within the 1σ envelope of the RO_2^* retrieved from PeRCEAS. The rest of the models fail to capture the short-term RO_2^* variability, which is partly underestimated by 60 to 80 %. The models which rely on inventories generally overestimate NO and underestimate OVOC by up to 70 % for TW1.

In addition, the dominant foggy conditions with a high content of aerosols and pollution are challenging for the modelling of fast photochemistry at low spatial resolution.

Around 45 % of the TW2 (landing) scenarios are taken above the PBL. The TW2 averaged RO_2^* measurement is 35 ± 17 pptv, without significant differences within and above the PBL. This indicates the probing of polluted air masses of similar radical precursor composition up to 1300 m approximately above the PBL. Pollution plumes from Tainan, Mailiao and Taichung power plants, and Taipei are identified based on the trajectory models and HALO measurements. The models agree within 1σ with the mean RO_2^* observed. but are generally not able to capture short-term variations of RO_2^* and their precursors as expected in such a complex polluted atmosphere.

The averaged RO_2^* in Taiwan based on the take-off and landing location is around 39 ± 21 pptv. This value can be used as a reference in photochemical simulations of polluted plumes of similar composition and atmospheric conditions.

5.4 Comparison of PSS calculation and box model RO_2^*

Although the box model and PSS calculations are both constrained to the measurements, the box model systematically underestimates the RO_2^* PSS values by about 50% (Figure 32 f). As discussed in section 3.3.7, one of the assumptions for the PSS calculation postulates a constant radical ratio, δ (= HO_2/RO_2^*), of 0.5. The PeRCEAS instrument does not separate the measurement of the different types of peroxy radicals but measures them as a total. The use of δ values, derived from the box model, in the RO_2^* PSS calculation enables the difference between the box model and PSS calculated RO_2^* to be investigated.

Changing the value of δ has impacts on: 1) The PSS calculations, where radical-radical reactions play a significant role in determining losses; 2) The eCL measured for PeRCEAS during calibration. The eCL values determined in the calibration use δ values generated in the laboratory of either 0.5 in the photolysis of mixtures of H_2O and CH_4 mixtures where $HO_2 = CH_3O_2$, or 1 for the photolysis of H_2O and CO for HO_2. For the EMeRGe campaigns, the δ = 0.5 calibrated eCL is used for the RO_2^* measurement retrievals.

Table 18: eCL obtained experimentally for the measurement conditions during EMeRGe campaign. δ = HO_2/RO_2^*.

Inlet P (mbar)	EU (Inlet 1)			Asia (Inlet 2)		
	δ	eCL	Simple Linear relationship between eCL and δ	δ	eCL	Simple Linear relationship between eCL and δ
350				1	48	eCL = 31δ + 17
				0.5	32.5	
300	1	48	eCL = 18δ + 25.5	1	37	eCL = 16δ + 21
	0.5	35.5		0.5	29	
200	1	43.5	eCL = 25δ + 23	1	30	eCL = 14δ + 16
	0.5	34.5		0.5	23	

To investigate the effect of δ on the differences observed between the box model and PSS calculations, the PSS RO_2^* values were re-calculated using the δ values from the box model. A linear relationship was assumed between the eCL and δ, which is a simple

approximation because the eCL calibrations are made using the photolysis of H_2O and thus only generate two values of δ, i.e. 0.5 or 1. Using the δ values from the box model, the eCL was calculated assuming a linear relationship between eCL and the δ values.

E-EU-03

The experimentally determined eCL used during the campaign, as well as the linear relationships used for the re-evaluating of the RO_2^* measurements are presented in Table 18. Plots with the measured RO_2^* calculated for different δ values are presented in Figure 54 for E-EU-03.
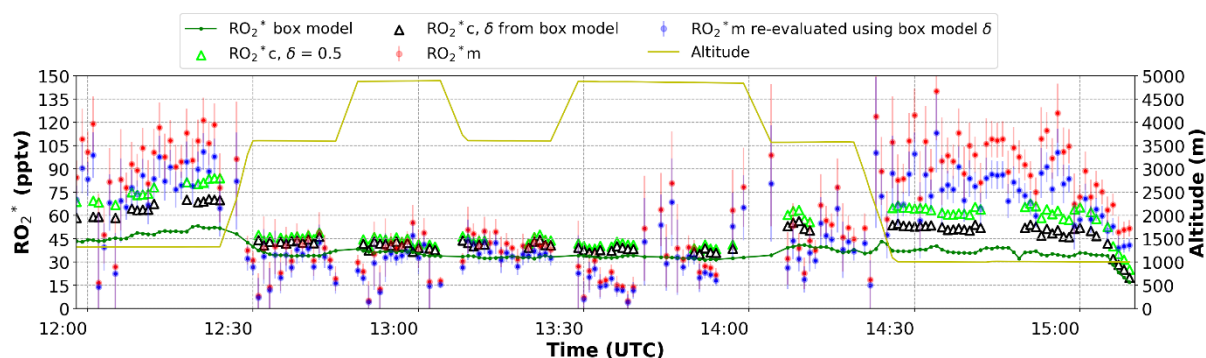
Figure 54: Time series of the RO_2^* box model (green line), PSS calculation with δ = 0.5 (lime triangle), PSS calculation with δ from box model (black triangle), measurement original (red circles), and re-evaluated measurement using δ from box model (blue circles) for E-EU-03 selected region.

Figure 55 shows improved correlations of E-EU-03 between the box model and the measurements, the PSS calculation and the measurements, and the PSS calculation and the box model. Following the re-evaluation and the re-calculation, the overall difference between the box model and the measurements was reduced from 69 % to 48 %. Similarly, the overall difference between the PSS calculation and the measurements dropped from 15 % to 7 %, and between the PSS calculation and the box model, it decreased from 48 % to 29 %.

As mentioned in section 3.3.7, the reaction rate coefficient of the total radical production within the PSS is dependent on the value of δ. When δ = 0, the reaction rate coefficient = k, corresponding to pure RO_2. When δ = 1 the reaction rate coefficient, k(R 2-35), represents pure HO_2. The pure HO_2 radical-radical losses are ∼ 10 times higher than the pure RO_2 radical-radical losses at the measurement conditions. Given that the mean δ derived from the box model is > 0.7, the rate of radical-radical loss reaction is higher than when δ = 0.5. As a result, the re-calculated RO_2^* is up to 20 % lower than the original calculation for the altitude level < 1200 m.
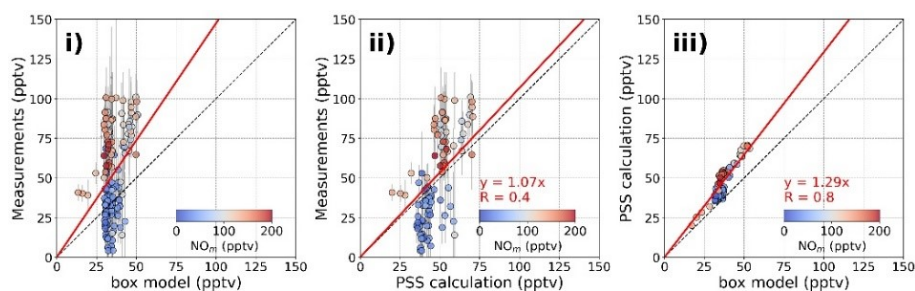
Figure 55: Scatter plots for i) box model vs. re-evaluated measurement RO_2^*; ii) PSS re-calculated RO_2^* vs. re-evaluated measurement RO_2^*; iii) box model vs. PSS re-calculated RO_2^* for the E-EU-03 selected region. All the plots are colour-coded with measurements of NO. δ adopted from the box model. The 1:1 line is represented by black dashed lines, while the linear fit is denoted by red solid lines. All the correlations are forced through the origin. Slopes and correlation coefficients are not depicted when the correlation coefficient is less than 0.4.

A higher δ is associated with a higher eCL for the PeRCEAS instrument (as the eCL obtained experimentally showed in Table 18) as a consequence of the balance between HO_2 and RO_2 terminating reactions and wall losses. The re-evaluated RO_2^* measurements reduced by 14 - 22 % with respect to the original measurements. The re-calculated PSS RO_2^* is 6 - 25 % smaller than the original results which lead to the PSS calculation underestimating the measurement from up to 80 % to up to 50 %.
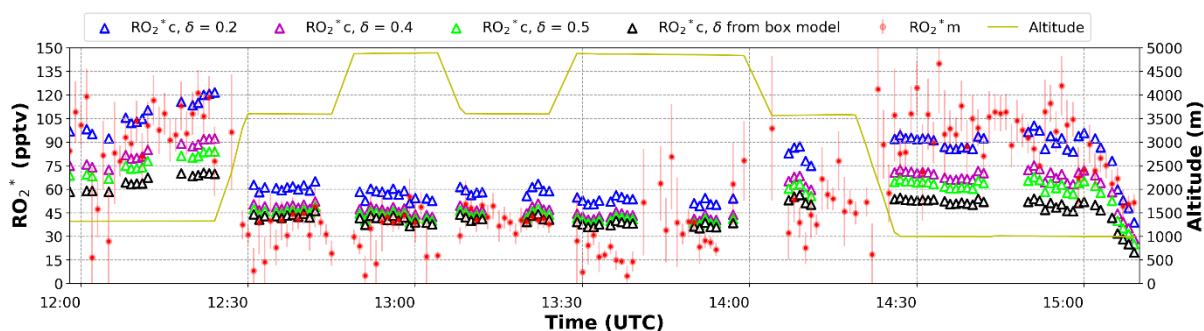
Figure 56: Time series of PSS calculated O_2^* with different δ for E-EU-03 selected.

A sensitivity study of E-EU-03 for the calculated RO_2^* has been made by using δ = 0.2 and 0.4 as shown in Figure 56. The differences between the calculated RO_2^* with δ = 0.2 and the measurement narrows to 10 % for altitudes under 1200 m. This observation suggests that in highly polluted air masses, where a higher variety of radical precursors are expected, RO_2 radicals could account for around 80 % of the RO_2^*. The accurate conversion of the RO_2^* measured for different δ requires specific eCL calibrations in the lab.

E-EU-06

The box model has an average δ of around 0.6 (refer to appendix A 22), close to the 0.5 used for the PSS calculations and the eCL for RO_2^* measurement retrieval for E-EU-06. The RO_2^* retrieved from the box model and the PSS calculations agree reasonably for the E-EU-06 selected regions. This is also the case for the comparison between the RO_2^* measured and RO_2^* calculated assuming PSS and that simulated by the box model. HO_2 and CH_3O_2 account for 83 % of the total peroxy radical output from the box model, while RO_2^* larger than CH_3O_2 is not considered in the PSS calculations.

Similar to the approach used to investigate the E-EU-03 RO_2^*, the δ values from the box model were used in the RO_2^* PSS calculation and a re-evaluation of the RO_2^* measurements (results in appendix A 23 and A 24). After re-evaluating and recalculating the RO_2^*, the agreement between the box model, the measurements, and the PSS calculations of RO_2^* improved overall. Specifically, the difference between the box model and the measurements of RO_2^* was reduced from 41 % to 12 % and between the PSS calculations and the measurements of RO_2^* was reduced from 38 % to 19 %. Though the difference between the PSS calculation and the box model increased by ∼ 6 %, the scatter of data points became more compact, indicating less dispersion compared to the initial results.

The re-calculated RO_2^* is on average 10 % smaller than originally estimated. The re-evaluated RO_2^* measurements were smaller by 14 - 22 % than the original measurements. With these corrections in place, the box model RO_2^*, re-calculated RO_2^*, and re-evaluated RO_2^* measurements agree within the measurement uncertainties.

E-AS-06

The box model underestimates the measurements by ∼ 50 %. The box model and the PSS calculation both are constrained to the measurements onboard HALO but the box model underestimates the results of the PSS calculation by a factor of 50 %. The δ simulated by the box model is 74 %. Similar to the Rome cases, the PSS and measured values were re-calculated by applying the δ from the box model (see δ details for E-AS-06 in appendix A 27 and the results in A 28 and A 29). It is important to note that around 1:20 - 1:30 UTC when HALO is flying upwind of Manila and passes under cloudy conditions (based on the water concentration, $jO(^1D)$ measurements and the flight report), significant uncertainties may arise in the PSS calculations due to measurement uncertainties from the remote sensing instruments.

For section 2), the PSS re-calculated RO_2^* are ∼ 6 - 20 % lower than the original results and still higher than the box model values by ∼ 25 %. The re-evaluated measurement results are ∼ 10 – 22 % lower than the original values, and the overall underestimation by the box model drops from ∼ 80 % to ∼ 40 %.

E-AS-10

The PSS calculated values are higher than the box model results by ∼ 50 % overall. The average δ used by the box model is around 0.73 The re-calculated and re-evaluated RO_2^* by applying the δ from the box model (see appendix A 32) results are depicted in A 33 (time series plots) and A 34 (correlation scatter plots).

The PSS re-calculated RO_2^* shows a decrease of ∼ 7 - 19 % relative to the original results. This re-calculation reduced the difference with the box model results from ∼ 40 % to ∼ 15 %. The box model results agree with the re-evaluated measurements within their uncertainties. The PSS re-calculated RO_2^* still overestimated the re-evaluated measurements, specifically between 01:10 and 02:00 UTC. At this time cloudy conditions

dominated which might increase the uncertainties associated with the use of remote sensing instrument data as stated by George, 2022. Such uncertainties remain unaddressed in the δ reanalysis.

E-AS-08 long-range transported air masses

To analyse the source of differences with the box model, a δ reanalysis has been applied using $\delta = 0.71$ as in the box model (see appendix A 36 - A 38). However, the differences are less than 10 % compared to the original results. Given that the sampled air masses are long-transported and aged the modelling results should rely on the adequacy of the dispersion of the air masses in the models which should dominate over the emission inventories and emissions patterns.

In summary, the effect of the δ ratio ($= \frac{HO_2}{RO_2^*}$) in the systematic underestimation of the RO_2^* observations and PSS calculations by the box model were investigated. Different δ values than 0.5 as used for the experimental retrieval and PSS calculations can lead to significant differences in the final results due to changes in the radical-loss reactions. In a first approach, re-evaluation of the RO_2^* measurements using the δ from the box model reduce the differences in RO_2^* from up to 40 % to minimal or no difference.

These results emphasise the uncertainties related to the ratio of different peroxy radicals in the air masses sampled as $\delta = 0.5$ may not be appropriate for all the conditions investigated. Thus, speciation of the peroxy radical measurement becomes a critical consideration for future investigations. The differences between the results of the box model and the PSS are partly reduced if the $\delta = 0.7$ calculated by the model is used for the PSS.

6. Summary and Conclusion

The research described in this dissertation has exploited CRDS in two application areas. These address two scientific objectives: a) the accurate measurement in the laboratory of the Rayleigh scattering cross sections of atmospheric gases in the blue spectral region; and b) the improvement of our understanding of the formation and loss of tropospheric peroxy radicals RO_2^* (= HO_2 + ΣRO_2, where R is an organic group having an H atom and the RO reacts with O_2 to form HO_2). The latter was achieved by making airborne measurements of RO_2^*, by the PeRCEAS instrument, which uses CRDS to determine the modulated and the chemically amplified NO_2 proxy for RO_2^*. Consequently, the doctoral thesis has addressed the following topics:

1. The experimental determination of Rayleigh scattering cross-sections at 408 nm for selected atmospheric gases using CRDS. Accurate knowledge of Rayleigh scattering is of fundamental interest and required for atmospheric radiative transfer calculations. The gases selected in this study were bulk and trace atmospheric gases of relevance for the measurements of RO_2^* by the PeRCEAS instrument. These gases would determine the cavity ring-down times measured in PeRCEAS in the absence of the absorption by NO_2.

2. The PeRCEAS measurements of RO_2^* during the airborne measurement campaigns of the EMeRGe project. One focus was therefore accurate in-situ airborne measurement of RO_2^*. The payload of the HALO research aircraft during the EMeRGe research campaigns included PeRCEAS and a set of instruments to measure trace gases which can be classified as precursors and reactants of RO_2^*, photolysis frequencies, and meteorological parameters. Having measured RO_2^* during EMeRGe, a collaboration with atmospheric modelling groups enabled the comparison of PeRCEAS measurements of RO_2^* with the simulated RO_2^* from a set of atmospheric models provided by the modelling groups, as well as calculations of RO_2^* using photostationary steady state (PSS) assumptions. The atmospheric models used are i) atmospheric models using inventory emission data (MECO(n), WRF/CMAQ, WRFchem) and ii) a box model constrained to the HALO measurements. A series of case studies were selected to test the capability of the models to simulate RO_2^* in different scenarios. In this context the investigation focused on a) the city plumes of Rome and Manila as examples of air masses close to the emissions from European and Asian major population centres, b) the long-range transport of plumes from Beijing and the Yangtze River Delta at the China Sea, and c) the complex pollution plume over Taiwan measured during repeated take-off and landing procedures.

The main achievements of this research are summarised in the following two sections.

6.1 Rayleigh scattering cross-section measurements

Some key activities and achievements during the measurement of the gas Rayleigh scattering cross sections, $\sigma_{Rayl.}$ at 408 nm are as follows:

- Three CRDS detectors were designed and built for this study and also used in PeRCEAS. Two measurement modes (i.e. the continuous and pressure ramp modes) were developed to determine $\sigma_{Rayl.}$.

- The CRDS detectors were used to investigate the effect of set-up changes and different modes of operation on the determination of $\sigma_{Rayl.}$ values. Using the same detector for both modes of operation confirmed the values determined for $\sigma_{Rayl.}$ were within the experimental error. A systematic error in the ramp experiments related to the interference of ambient humidity in the laboratory was identified but is estimated to be < 1 % of the total error.

- The $\sigma_{Rayl.}$ of N_2, O_2, SA, Ar, CO, CO_2, N_2O, and CH_4 measured at 408 nm by CRDS were accurately determined.

- The $\sigma_{Rayl.}$ of O_2, Ar, CO_2, and SA at 408 nm, determined in this study are shown to be consistent with previous literature measurements within 2.2 %, 1.5 %, 0.6 %, and 2.2 %, respectively.

- This study reports the first measurement of $\sigma_{Rayl.}(CO)$ at 408 nm. The currently available n-based calculation of $\sigma_{Rayl.}$ underestimates the experimental values and therefore requires revision.

- The use of the commonly accepted n-values to calculate $\sigma_{Rayl.}(N_2)$ underestimate the retrieved $\sigma_{Rayl.}(N_2)$ values determined in this study. Consequently, there is a need for further studies of the $\sigma_{Rayl.}(N_2)$ investigation in other wavelength ranges. N_2 is a bulk constituent of air. Accurate radiative transfer calculations require accurate knowledge of the retrieved $\sigma_{Rayl.}(N_2)$.

One unresolved experimental issue is also noted: The ring-down time signal decreased steadily during the period of measurements using N_2 and Ar. This decrease was reproducible and significantly higher than for other gases. The ring-down time was recovered after cleaning the mirrors. The effect of humidity and impurities was investigated but the reason for the decrease remains unclear. There are two potential explanations: a) the deposition of an unknown impurity or impurities in the gases on the cavity mirrors, or b) a gradual gas saturation of the CRDS mirror surface in the coated layer of N_2 or Ar.

Overall this part of the doctoral dissertation highlights the potential of CRDS as an absolute measurement technique for determining highly accurate Rayleigh scattering cross-sections of molecules. These results have been published by Liu et al., 2023.

6.2 Investigation of the capabilities of state-of-the-art models to reproduce the airborne measurements obtained during the EMeRGe campaigns

Part of this study involved active participation in the preparation and operation of the PeRCEAS instrument in the airborne campaigns of the EMeRGe project. Airborne measurements of RO_2^* were made on board the HALO platform in Europe and Asia. After the acquisition and calibration of experimental data, case studies were selected for investigation. The RO_2^* data simulated for these case studies by four different models and calculations using PSS assumption were gathered and prepared for comparison with the experimental measurements of RO_2^*, trace gases, photolysis frequencies, and meteorological parameters. The comparison of observations with simulations provides valuable insight into the capability of current atmospheric models to simulate RO_2^* in different types of air masses. The main achievements are the following:

a) Studies on city plumes: Rome and Manila cases.

a1) City plume of Rome: Within the PBL, RO_2^* mixing ratios range from 60 to 120 pptv, influenced by OVOC and NOx variability. Above the PBL, RO_2^* levels (30 - 60 pptv) depend on air mass origin and agree with models. However, within the PBL, emission-based models failed to capture short-term variations (i.e. cloud), unlike box models and PSS calculations constrained by onboard measurements. At lower altitudes, especially in Rome plumes, models underestimate RO_2^* (up to 80%), with the PSS RO_2^* also underestimating (up to 50%). Cases with high OVOCs (> 7 ppbv) suggest potential missing sources in PSS calculations, not accounting for OVOC oxidation or photolysis and alkene ozonolysis. The PSS RO_2^* overestimation at low NO (< 50 pptv) and RO_2^* (< 60 pptv) might be linked to the absence of OH reacting with HO_2 in PSS RO_2^* calculations.

a2) City plume of Manila: Within the PBL influenced by precursor emissions, the RO_2^* upwind is $\sim$ 50 pptv and downwind $\sim$ 70 pptv near Manila. The box model underestimates by $\sim$ 30%, and PSS RO_2^* tends to overestimate when NO > 80 pptv with OVOCs presented. This overestimation may result from unconsidered organic nitrate formation in PSS calculations. Models, using inventories, simulate trace gases and peroxy radical precursors within uncertainties except for NOx and HCHO, leading to a failure in capturing short-term RO_2^* variations. MECO(n) simulates remarkably higher O_3 than measurements, suggesting inadequate emission consideration.

b) Studies on long-ranged transported air masses:

In aged and long-range transported air masses from the Yangtze River Delta and Beijing within the PBL, average RO_2^* observations are below 35 pptv. Models generally underestimate RO_2^* and fail to reproduce observed variability, especially for OVOC precursors (e.g. HCHO) and NO, suggesting a need for dispersion pattern revision in models. PSS calculations, constrained to on-board measurements,

overestimate RO_2^* by around 30%, possibly due to cloudy conditions introducing uncertainties in remote sensing measurements and affecting PSS precision. These air masses have high aerosol loads (~ 800 cm^{-3}), suggesting potential radical aerosol uptake and heterogeneous reactions not considered in current PSS calculations.

c) Complex pollution over Taiwan: take-off (TW1) and landing (TW2) scenarios:

There are large differences between the estimates of RO_2^* from the model using inventories and measurements in TW1. The simplest explanation is that the inventories used in the model in the morning may be not sufficiently accurate e.g. the NOx and OVOCs underestimated by the models. The box model and the PSS calculation which constrained the measurements are closer to the RO_2^* measurements.

For TW2, the trace gases and radical precursors simulated by the models using the inventories agree reasonably well with the measurements. It is probably not a coincident that all the modelled and measured RO_2^* also agree reasonably well. However, the models do not capture well the short-term variations of the RO_2^* precursors and reactants. It is important to note that these conclusions come from the comparison with airborne RO_2^* observations which are also subject to limitations. In that respect, the speciated measurement of radicals would notably improve the knowledge of production and loss mechanisms in radical chemistry.

The averaged RO_2^* in Taiwan, based on take-off and landing locations, is approximately 39 ± 21 pptv, serving as a valuable reference for photochemical simulations of similarly composed and atmospheric conditions polluted plumes.

d) The comparison of PSS calculation with the box model RO_2^*:

This part of the study shows that a better understanding of the speciation (δ ratio) of RO_2^* in future measurements and modelling studies would be beneficial. It is likely to reduce the differences between the measured and modelled RO_2^*.

Overall, the results obtained in this part of the thesis highlight that the accuracy and resolution of the inventories for radical precursors and trace gases involved in radical formation and loss mechanisms limit the abilities to reproduce the short-term RO_2^* variability observed close to the polluted areas. In particular, inaccuracies in the simulation of the NOx and HCHO variabilities determine the inaccuracy of the RO_2^* simulations. Similarly, the accuracy in the photolysis rates and the dispersion patterns used for the simulation of long-range transported pollution plumes is of crucial importance.

List of Publications and Scientific Conferences Attended

Peer reviewed:

Liu, Y., Andrés Hernández, M. D., George, M., and Burrows, J. P.: Experimental determination of Rayleigh scattering cross-sections at 408 nm, Applied Physics B, 129, https://doi.org/10.1007/s00340-023-08025-8, 2023.

George, M., Andrés Hernández, M. D., Nenakhov, V., Liu, Y., Burrows, J. P., Bohn, B., Förster, E., Obersteiner, F., Zahn, A., Harlaß, T., Ziereis, H., Schlager, H., Schreiner, B., Kluge, F., Bigge, K., and Pfeilsticker, K.: Airborne observations of peroxy radicals during the EMeRGe campaign in Europe, Atmos. Chem. Phys., 23, 7799–7822, https://doi.org/10.5194/acp-23-7799-2023, 2023.

Andrés Hernández, M. D., Hilboll, A., Ziereis, H., Förster, E., Krüger, O. O., Kaiser, K., Schneider, J., Barnaba, F., Vrekoussis, M., Schmidt, J., Huntrieser, H., Blechschmidt, A.-M., George, M., Nenakhov, V., Harlass, T., Holanda, B. A., Wolf, J., Eirenschmalz, L., Krebsbach, M., Pöhlker, M. L., Kalisz Hedegaard, A. B., Mei, L., Pfeilsticker, K., Liu, Y., Koppmann, R., Schlager, H., Bohn, B., Schumann, U., Richter, A., Schreiner, B., Sauer, D., Baumann, R., Mertens, M., Jöckel, P., Kilian, M., Stratmann, G., Pöhlker, C., Campanelli, M., Pandolfi, M., Sicard, M., Gómez-Amo, J. L., Pujadas, M., Bigge, K., Kluge, F., Schwarz, A., Daskalakis, N., Walter, D., Zahn, A., Pöschl, U., Bönisch, H., Borrmann, S., Platt, U., and Burrows, J. P.: Overview: On the transport and transformation of pollutants in the outflow of major population centres – observational data from the EMeRGe European intensive operational period in summer 2017, Atmos. Chem. Phys., 22, 5877–5924, https://doi.org/10.5194/acp-22-5877-2022, 2022.

Georg, M., Andrés-Hernández, M. D., Nenakhov, V., Liu, Y., and Burrows, J. P.: Airborne measurement of peroxy radicals using chemical amplification coupled with cavity ring-down spectroscopy: the PeRCEAS instrument, Atmos. Meas. Tech 13, 2577–2600, https://doi.org/10.5194/amt-13-2577-2020, 2020.

Conference presentations:

Oral presentation: "Comparison of Airborne Peroxy Radical Measurements with MECO(n) model simulation during EMeRGe in Europe" in EGU General Assembly-Online in May 2020.

Poster presentation: "Peroxy radical airborne observations during EMeRGe over Rome and Manila" in EGU General Assembly in April 2019.

Appendix

A 1: Air Liquide gas supply consistent data

Gas supplier Air Liquide	ALPHAGAZ™ 1 N₂	ALPHAGAZ™ 2 N₂	O₂ N48	ALPHAGAZ™ 1 Air	ALPHAGAZ™ 2 Air	ALPHAGAZ™ 1 Ar	CO N47	CO₂ N48	N₂O N25	CH₆ N45
Purity (Vol.%)	≥ 99.999	≥ 99.9999	≥ 99.998	≥ 99.999	≥ 99.9999	≥ 99.999	≥ 99.997	≥ 99.998	≥ 99.5	≥ 99.995
Impurities (ppmv)										
H₂		≤ 0.1					< 1	≤ 0.5	≤ 1	≤ 1
H₂O	< 2	≤ 0.5	< 2	< 2	≤ 0.5	≤ 2	< 3	≤ 3	<10	≤ 5
CO	≤ 0.5	≤ 0.1	< 0.2	≤ 1	≤ 0.1	≤ 0.5		≤ 1	<5	
CO₂	≤ 0.5	≤ 0.1	< 0.2	≤ 1	≤ 0.1	≤ 0.2	< 1		<200	≤ 1
NOx		≤ 0.02			≤ 0.01					
N₂			< 5				< 10	≤ 8	≤ 4000	≤ 15
O₂	≤ 2	≤ 0.1				≤ 2	< 5	≤ 2	≤ 1000	≤ 5
Ar			≤ 10	≤ 2.1			< 7			
C₂H₆										≤ 15
Hydrocarbons	≤ 0.2	≤ 0.1	< 0.2	≤ 0.1	≤ 0.05	≤ 0.2	< 2	≤ 2		≤ 5
Halogenated hydrocarbons		≤ 0.001								
SO₂					≤ 0.01					
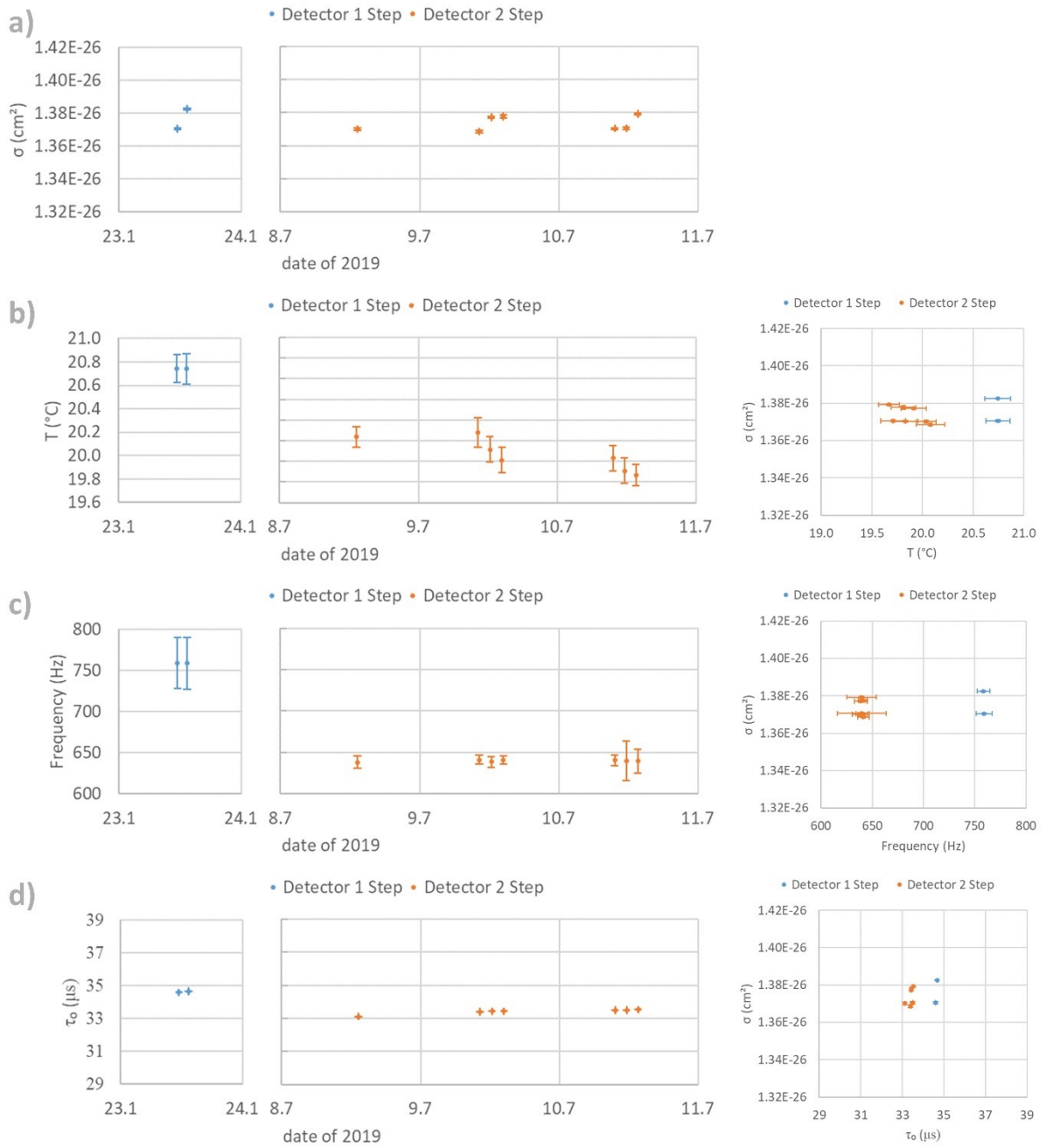
A 2:Variability of parameters selected for $\sigma_{O_2(Rayl.)}$ determination with setup 1 & 2 continuous mode: a) $\sigma_{O_2(Rayl.)}$ variation over time; b) cavity temperature averaged over measurement time and $\sigma_{O_2(Rayl.)}$; c) laser frequency averaged over measurement time and $\sigma_{O_2(Rayl.)}$; d) τ_0 variation over time and $\sigma_{O_2(Rayl.)}$.
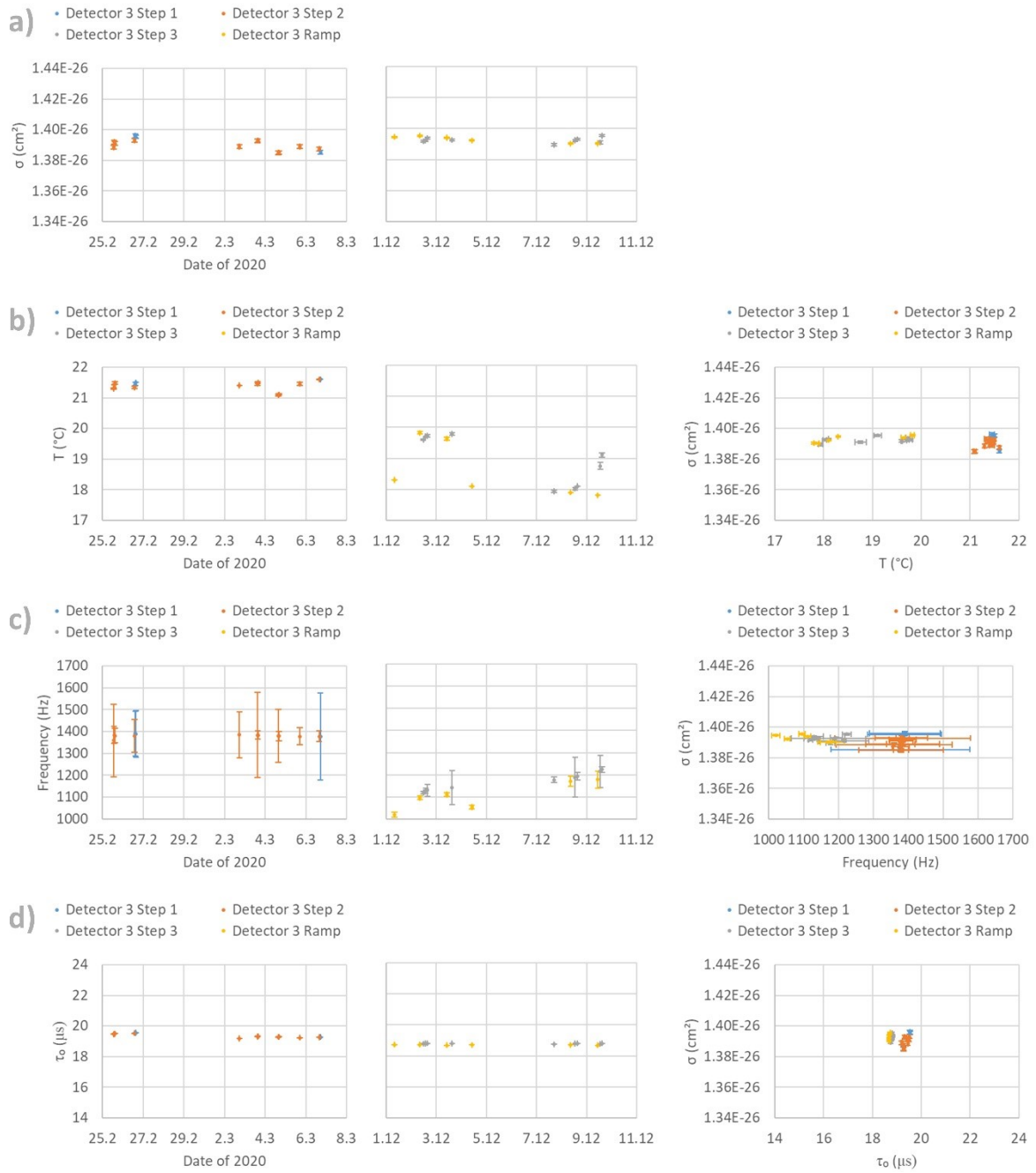
A 3: Variability of parameters selected for $\sigma_{O_2(Rayl.)}$ determination with setup 3 continuous and ramp mode: a) $\sigma_{O_2(Rayl.)}$ variation over time; b) cavity temperature averaged over measurement time and $\sigma_{O_2(Rayl.)}$; c) laser frequency averaged over measurement time and $\sigma_{O_2(Rayl.)}$; d) τ_0 variation over time and $\sigma_{O_2(Rayl.)}$. The conditions are tabulated in Table 9 (conditions 3,4, and 5).

Appendix

A 4: Measurement conditions for the determination of $\sigma_{SA(Rayl.)}$ using continuous mode.

Name	Setup	Gas	Pressure range (hPa)	Step duration (mins)	Step P difference
Condition 1		SA	300-500	10	50
Condition 2	1	SA	300-500	10	100
Condition 3		HPSA	300-500	10	50
Condition 4		SA	300-500	10	50
Condition 5		SA	300-500	10	50
Condition 6	2	SA	200-400	10	100
Condition 7		HPSA	300-500	10	50
Condition 8		HPSA	200-400	10	50
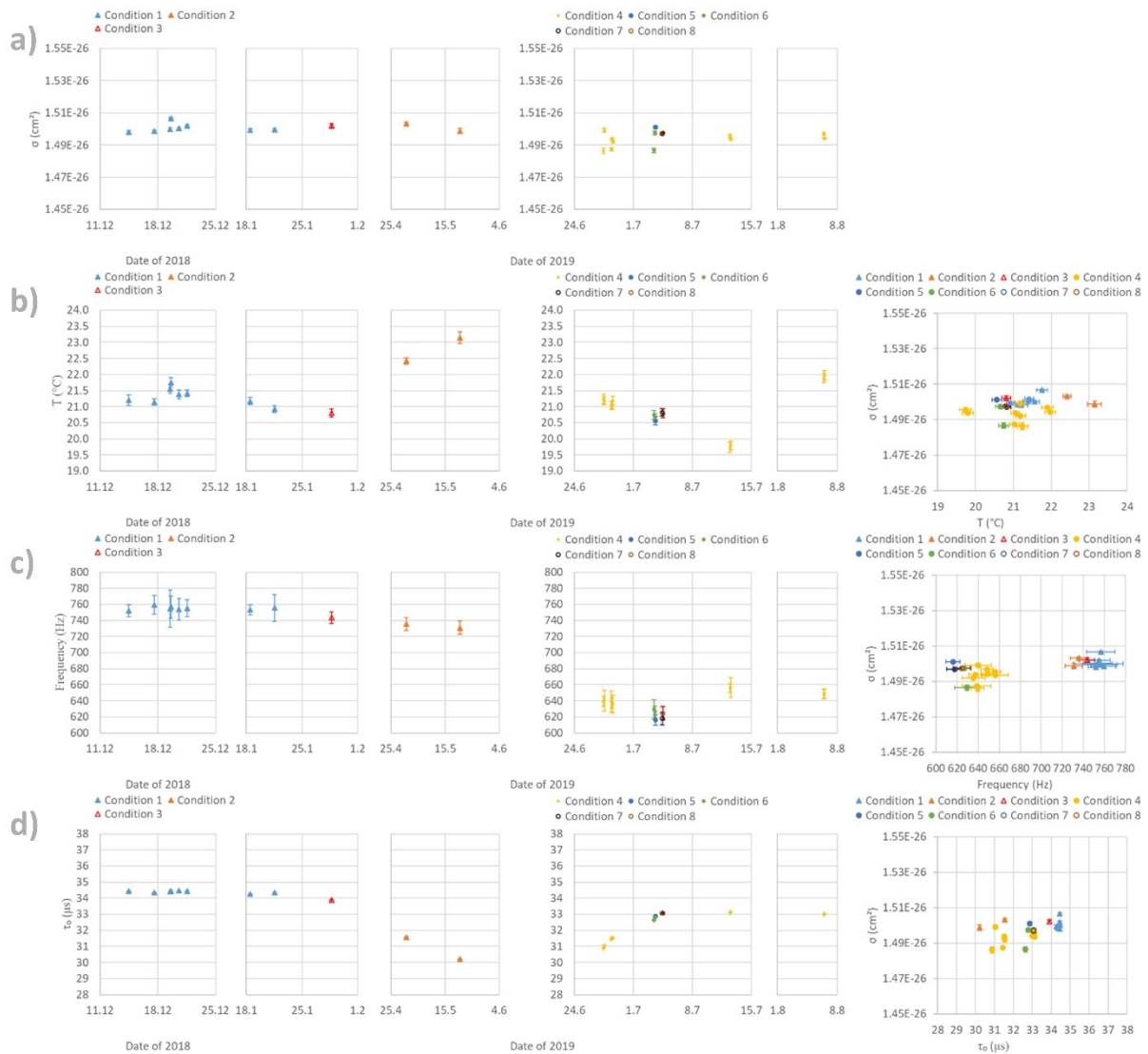
A 5: Variability of parameters selected for $\sigma_{SA(Rayl.)}$ determination with setup 1 & 2 continuous mode: a) $\sigma_{SA(Rayl.)}$ variation over time; b) cavity temperature averaged over measurement time and $\sigma_{SA(Rayl.)}$; c) laser frequency averaged over measurement time and $\sigma_{SA(Rayl.)}$; d) τ_0 variation over time and $\sigma_{SA(Rayl.)}$. The conditions are tabulated in appendix A 4.
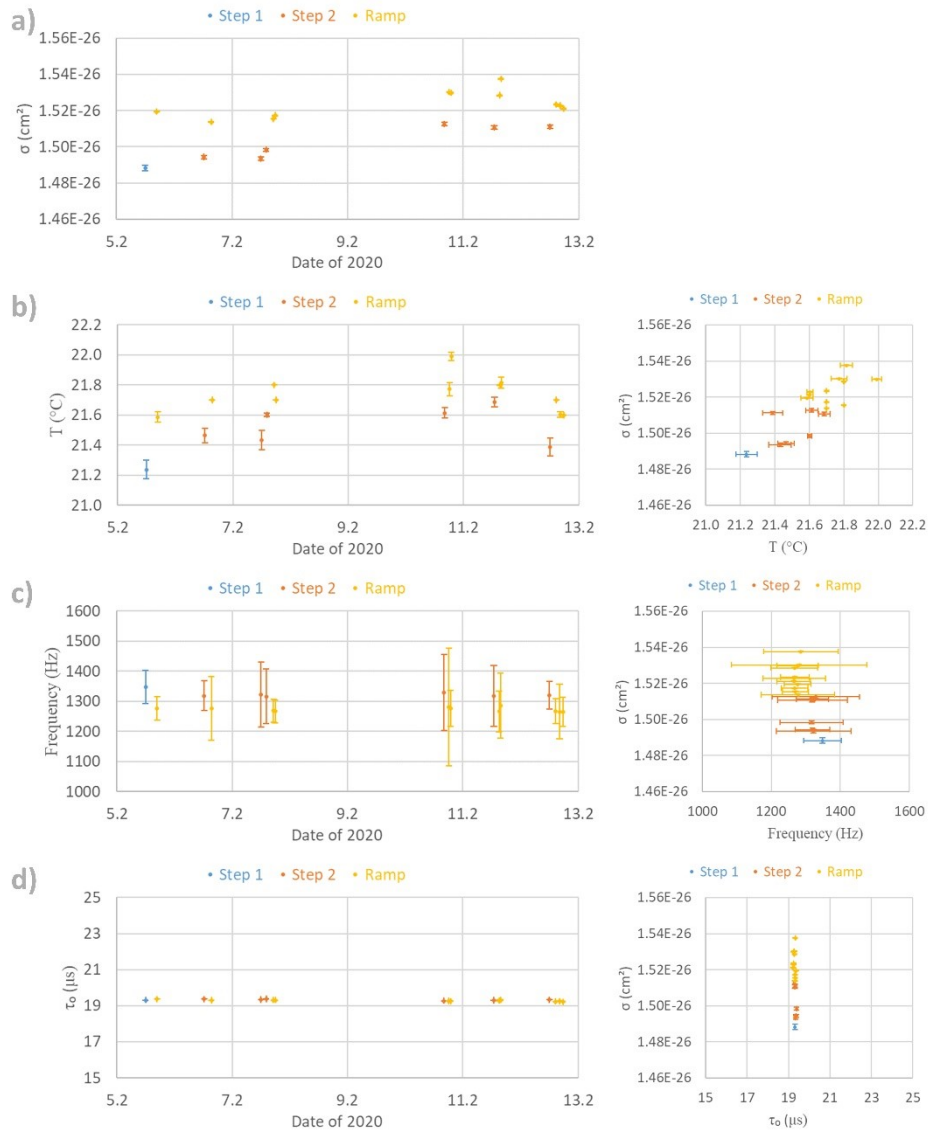
A 6: Variability of parameters selected for $\sigma_{SA(Rayl.)}$ determination with setup 3 continuous and ramp mode: a) $\sigma_{SA(Rayl.)}$ variation over time; b) cavity temperature averaged over measurement time; c) laser frequency averaged over measurement time; d) τ_0 variation over time. The conditions are tabulated in appendix A 4.

A 7: Measurement conditions for the determination of $\sigma_{Ar(Rayl.)}$ using continuous mode. NV: needle valve; MFC: mass flow controller.

Name	Setup	Pressure range (hPa)	Step duration (mins)	Step P difference	Flow control
Condition 1	1	300-500	10	50	NV
Condition 2		300-500	10	50	MFC
Condition 3	2	300-500	10	50	MFC
Condition 4	1	300-500	10	100	MFC
Condition 5	2	300-500	10	100	MFC
Condition 6	3	300-500	10	50	MFC
Condition 7		300-500	10	100	MFC
Condition 8		300-500	2	50	MFC
Condition 9		300-500	2	100	MFC
Condition 10		300-700	10	100	MFC
Condition 11		300-700	2	100	MFC
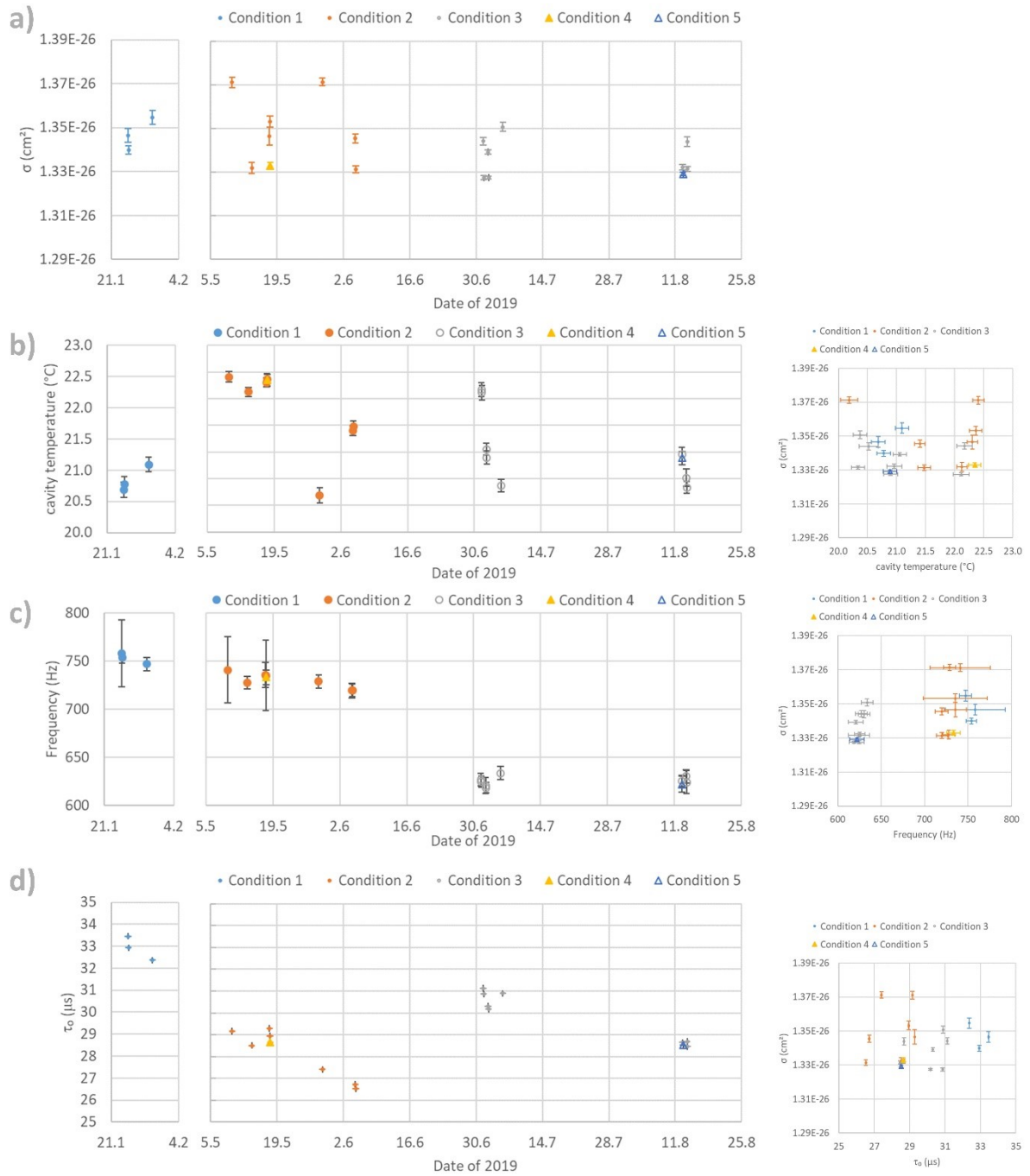
A 8: Variability of parameters selected for $\sigma_{Ar(Rayl.)}$ determination with setup 1 & 2 continuous mode: a) $\sigma_{Ar(Rayl.)}$ variation over time; b) cavity temperature averaged over measurement time and $\sigma_{Ar(Rayl.)}$; c) laser frequency averaged over measurement time and $\sigma_{Ar(Rayl.)}$; d) τ_0 variation over time and $\sigma_{Ar(Rayl.)}$. The conditions are tabulated in appendix A 7.
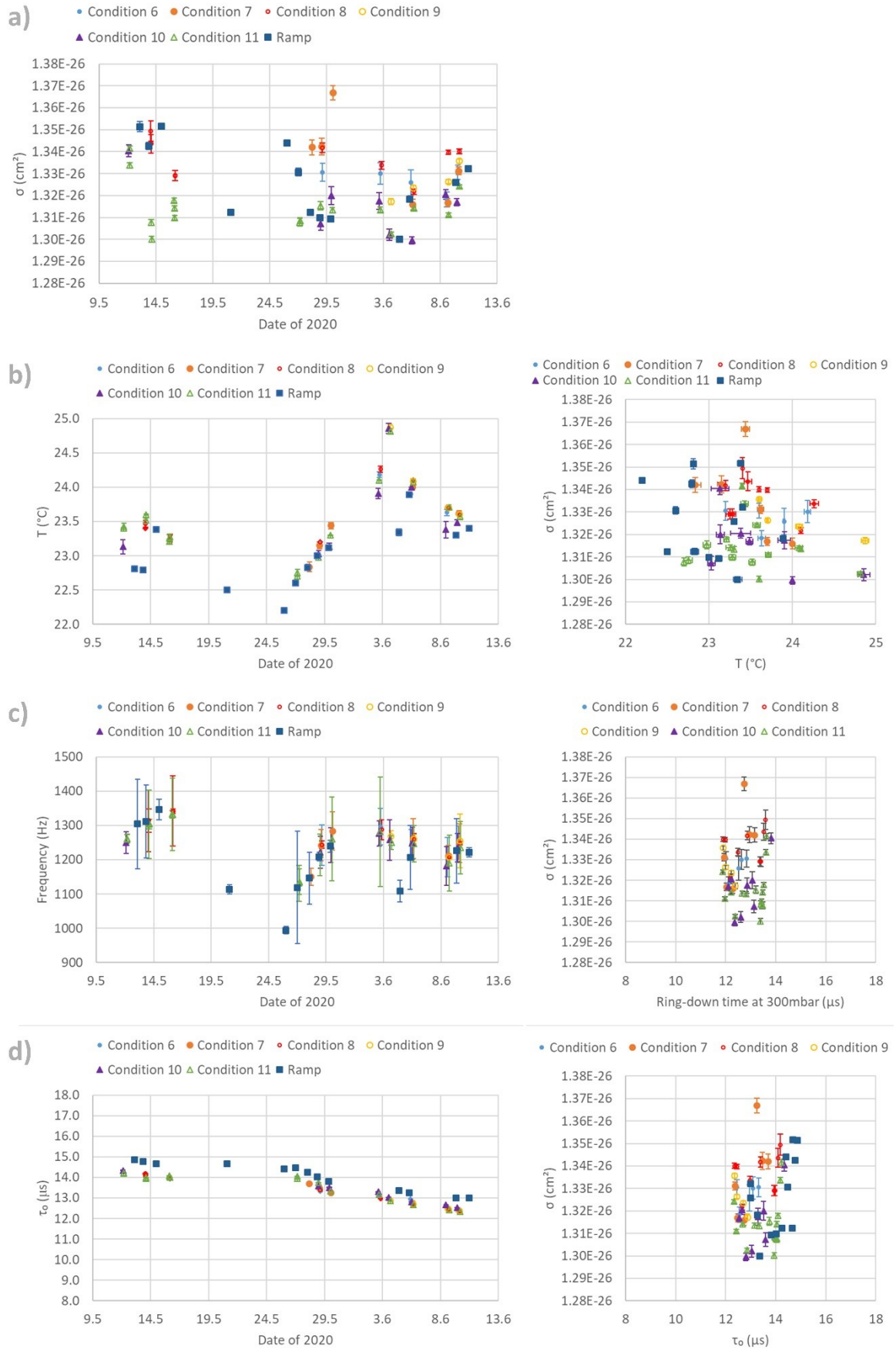
A 9: Variability of parameters selected for $\sigma_{Ar(Rayl.)}$ determination with setup 3 continuous and ramp mode: a) $\sigma_{Ar(Rayl.)}$ variation over time; b) cavity temperature averaged over measurement time and $\sigma_{Ar(Rayl.)}$; c) laser frequency averaged over measurement time and $\sigma_{Ar(Rayl.)}$; d) τ_0 variation over time and $\sigma_{Ar(Rayl.)}$. The conditions are tabulated in appendix A 6.
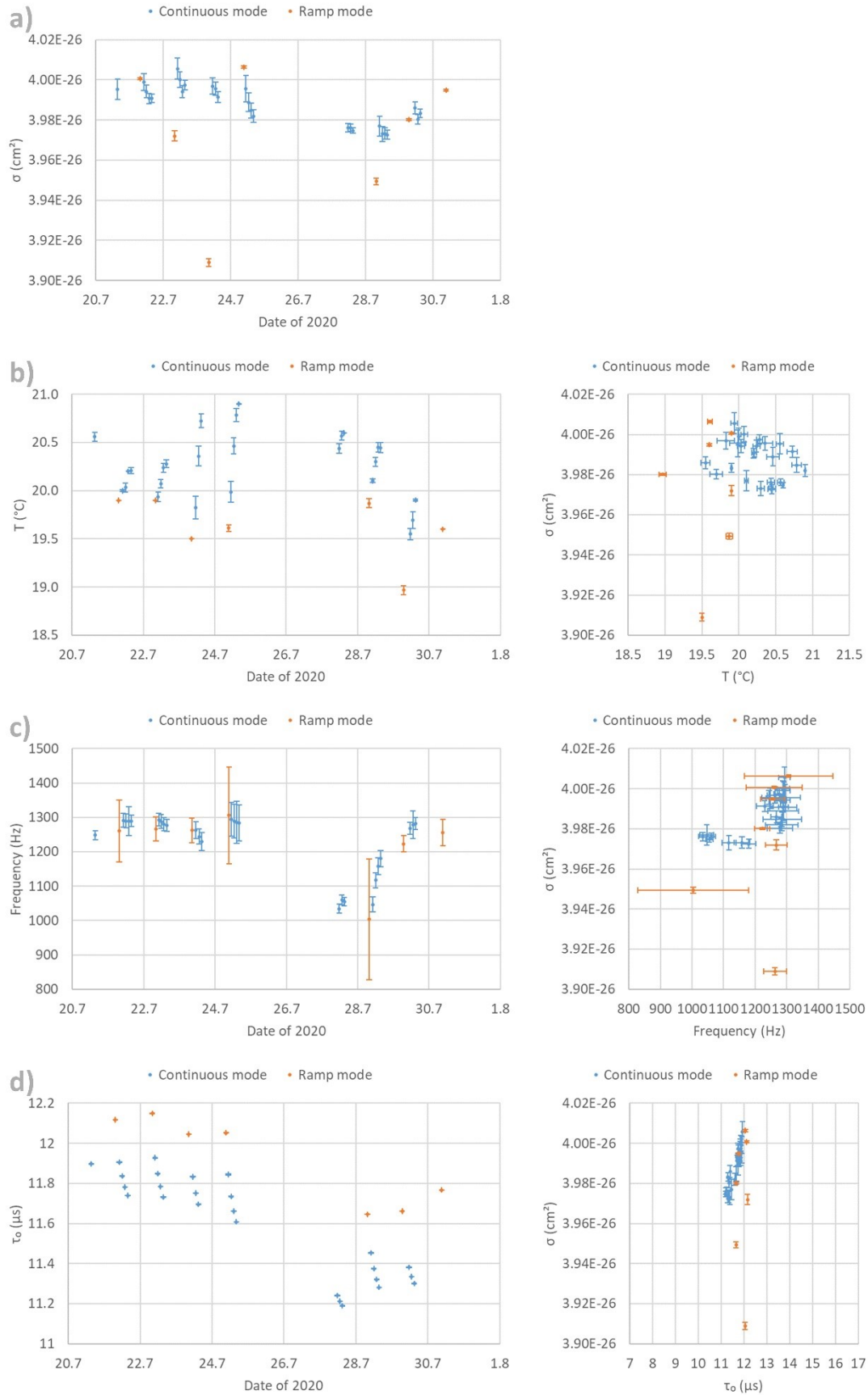
A 10: Variability of parameters selected for $\sigma_{CO_2(Rayl.)}$ determination with setup 3 continuous and ramp mode: a) $\sigma_{CO_2(Rayl.)}$ variation over time; b) cavity temperature averaged over measurement time and $\sigma_{CO_2(Rayl.)}$; c) laser frequency averaged over measurement time and $\sigma_{CO_2(Rayl.)}$; d) τ_0 variation over time and $\sigma_{CO_2(Rayl.)}$.
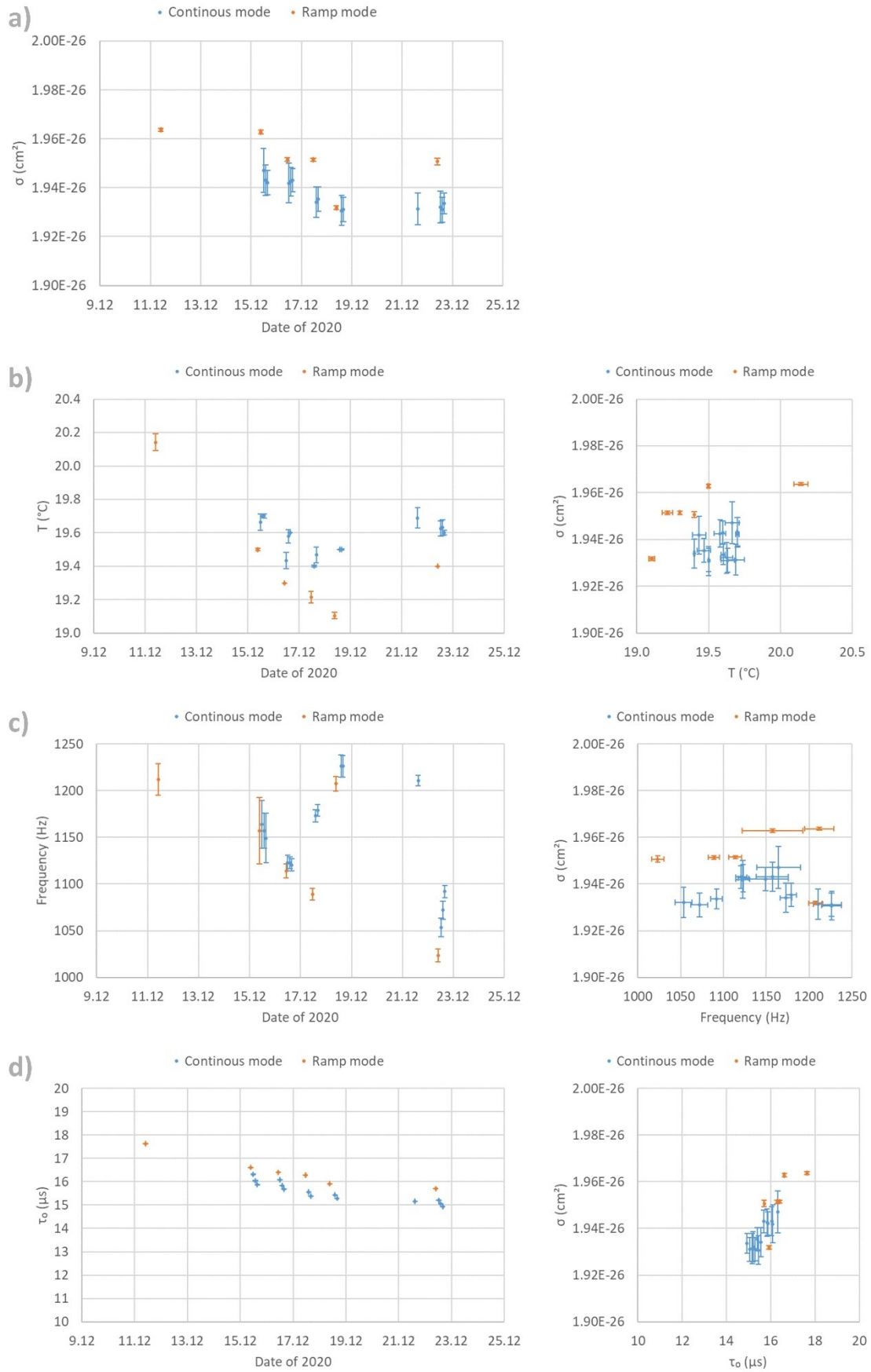
A 11: Variability of parameters selected for $\sigma_{CO(Rayl.)}$ determination with setup 3 continuous and ramp mode: a) $\sigma_{CO(Rayl.)}$ variation over time; b) cavity temperature averaged over measurement time and $\sigma_{CO(Rayl.)}$; c) laser frequency averaged over measurement time $\sigma_{CO(Rayl.)}$; d) τ_0 variation over time and $\sigma_{CO(Rayl.)}$.

A 12: *Measurement conditions for $\sigma_{N_2O\,(Rayl.)}$ determination using continuous mode.*

Name	Setup	Pressure range (hPa)	Step duration (mins)	Step P difference (hPa)	remarks
Condition 1	2	300-500	10	50	Gas supply line 40 m
Condition 2	2	300-500	10	100	
Condition 3	2	300-700	10	100	shorter connection (gas bottle in the lab)
Condition 4	3	300-700	5	50	
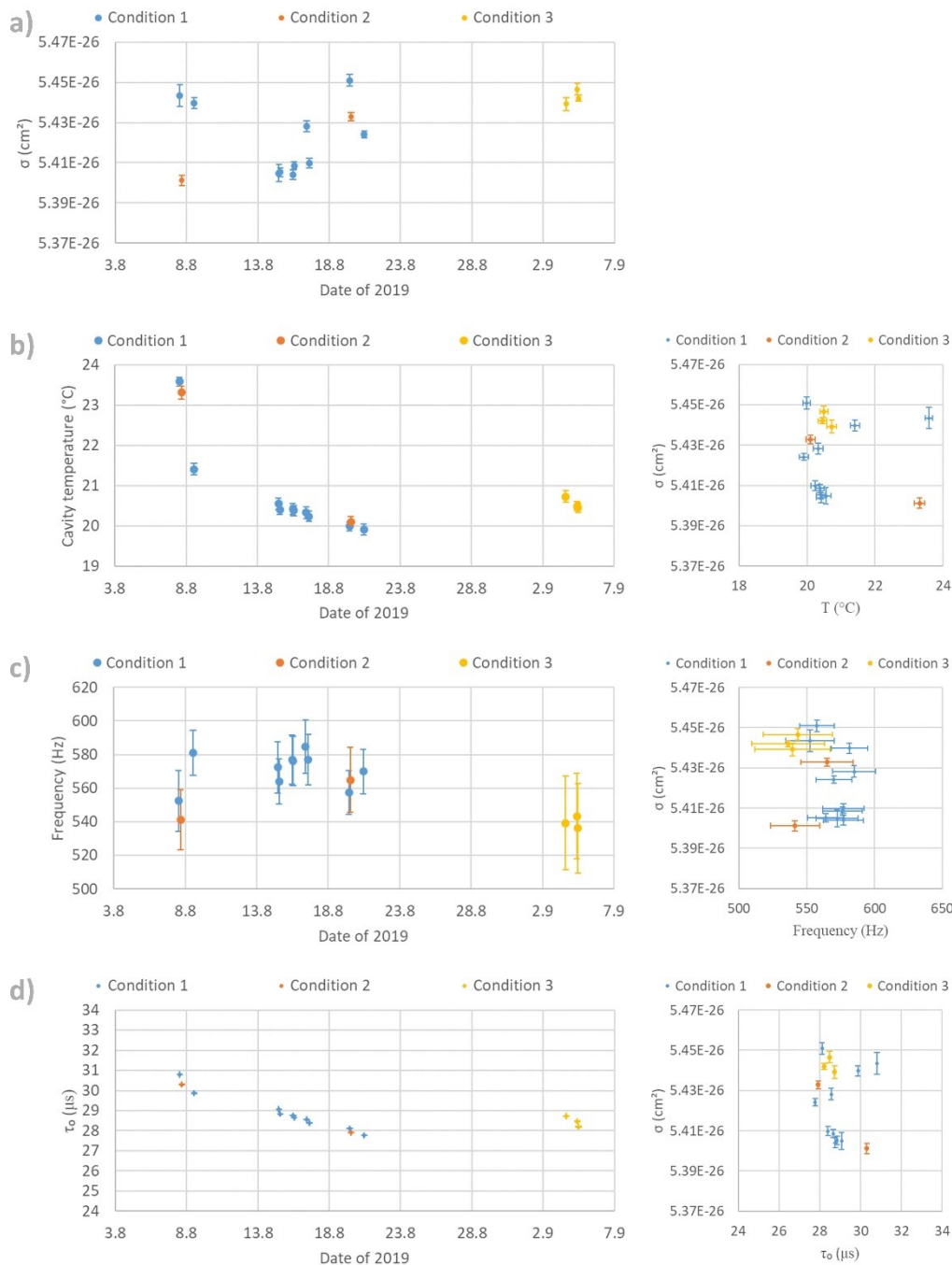
A 13: *Variability of parameters selected for $\sigma_{N_2O(ayl.)}$ determination with setup 2 continuous mode: a) $\sigma_{N_2O(Rayl.)}$ variation over time; b) cavity temperature averaged over measurement time and $\sigma_{N_2O(ayl.)}$; c) laser frequency averaged over measurement time and $\sigma_{N_2O(ayl.)}$; d) τ_0 variation over time and $\sigma_{N_2O(ayl.)}$. The conditions are listed in A 12.*
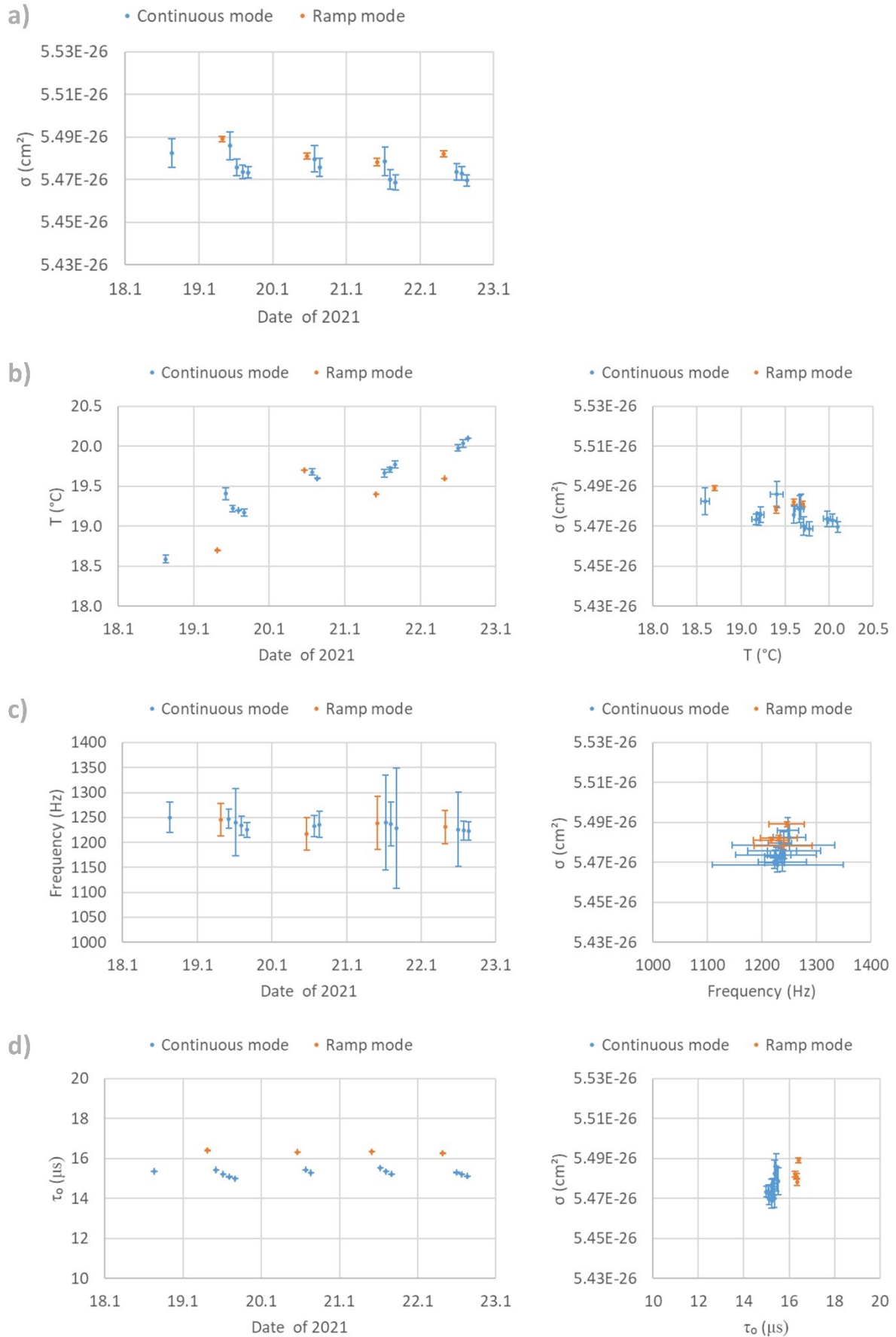
A 14: Variability of parameters selected for $\sigma_{N_2O(Rayl.)}$ determination with setup 3 continuous and ramp mode: a) $\sigma_{N_2O(Rayl.)}$ variation over time; b) cavity temperature averaged over measurement time and $\sigma_{N_2O(Rayl.)}$; c) laser frequency averaged over measurement time and $\sigma_{N_2O(Rayl.)}$; d) τ_0 variation over time and $\sigma_{N_2O(Rayl.)}$.
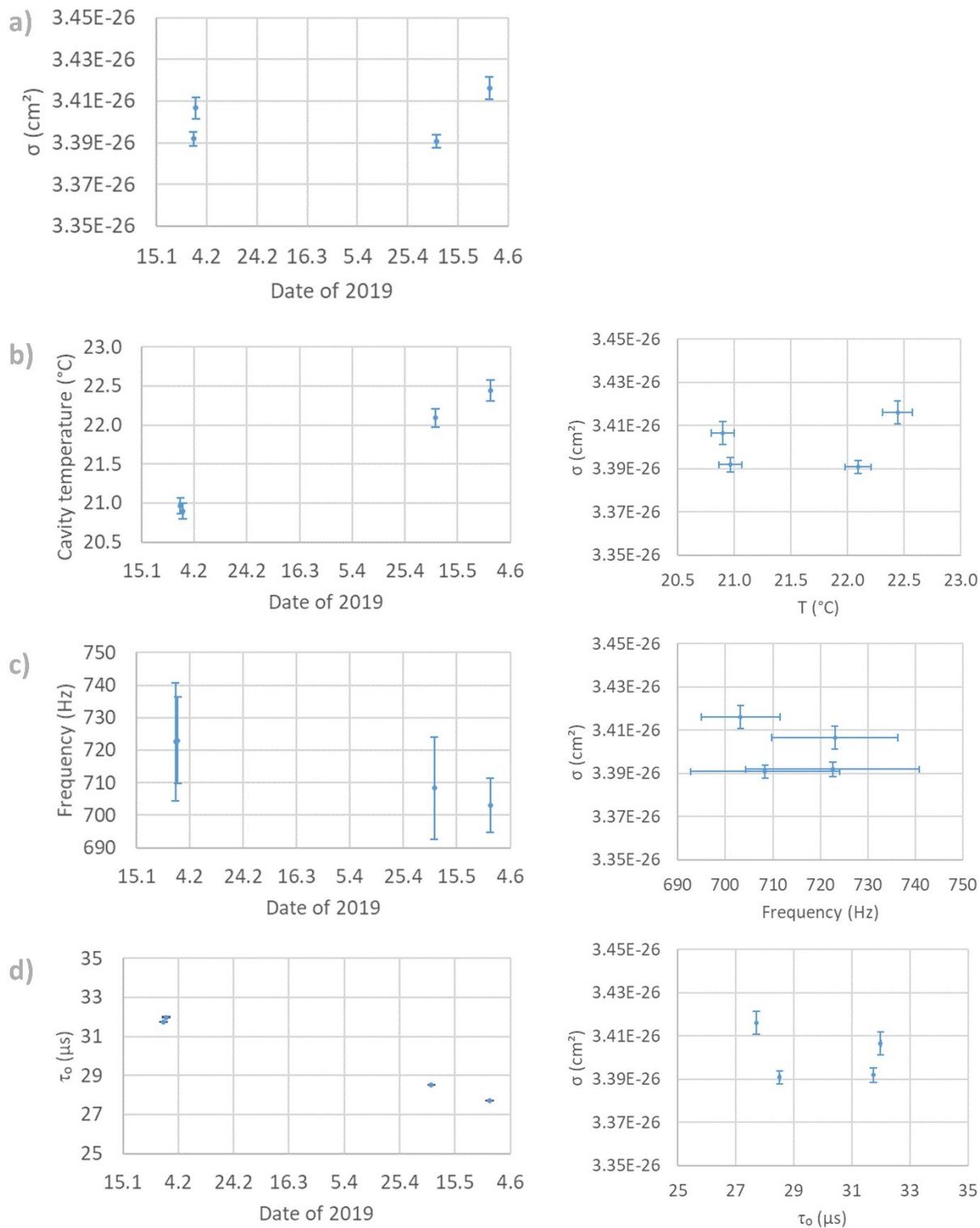
A 15:Variability of parameters selected for $\sigma_{CH_4(Rayl.)}$ determination with setup 1 continuous mode: a) $\sigma_{CH_4(Rayl.)}$ variation over time; b) cavity temperature averaged over measurement time and $\sigma_{CH_4(Rayl.)}$; c) laser frequency averaged over measurement time and $\sigma_{CH_4(Rayl.)}$; d) τ_0 variation over time and $\sigma_{CH_4(Rayl.)}$.
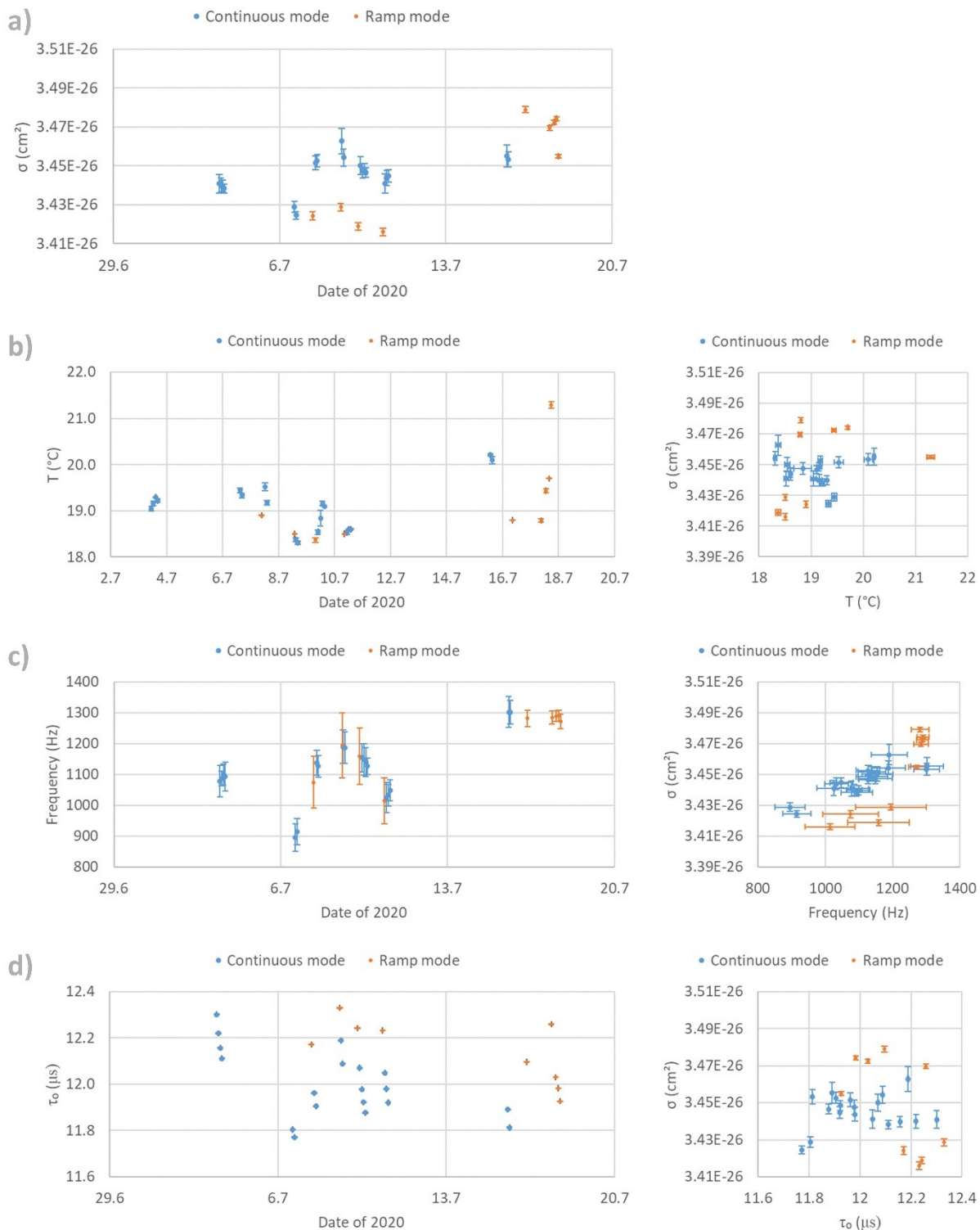
A 16: Variability of parameters selected for $\sigma_{CH_4(Rayl.)}$ determination with setup 3 continuous and ramp mode: a) $\sigma_{CH_4(Rayl.)}$ variation over time; b) cavity temperature averaged over measurement time and $\sigma_{CH_4(Rayl.)}$; c) laser frequency averaged over measurement time and $\sigma_{CH_4(Rayl.)}$; d) τ_0 variation over time and $\sigma_{CH_4(Rayl.)}$.
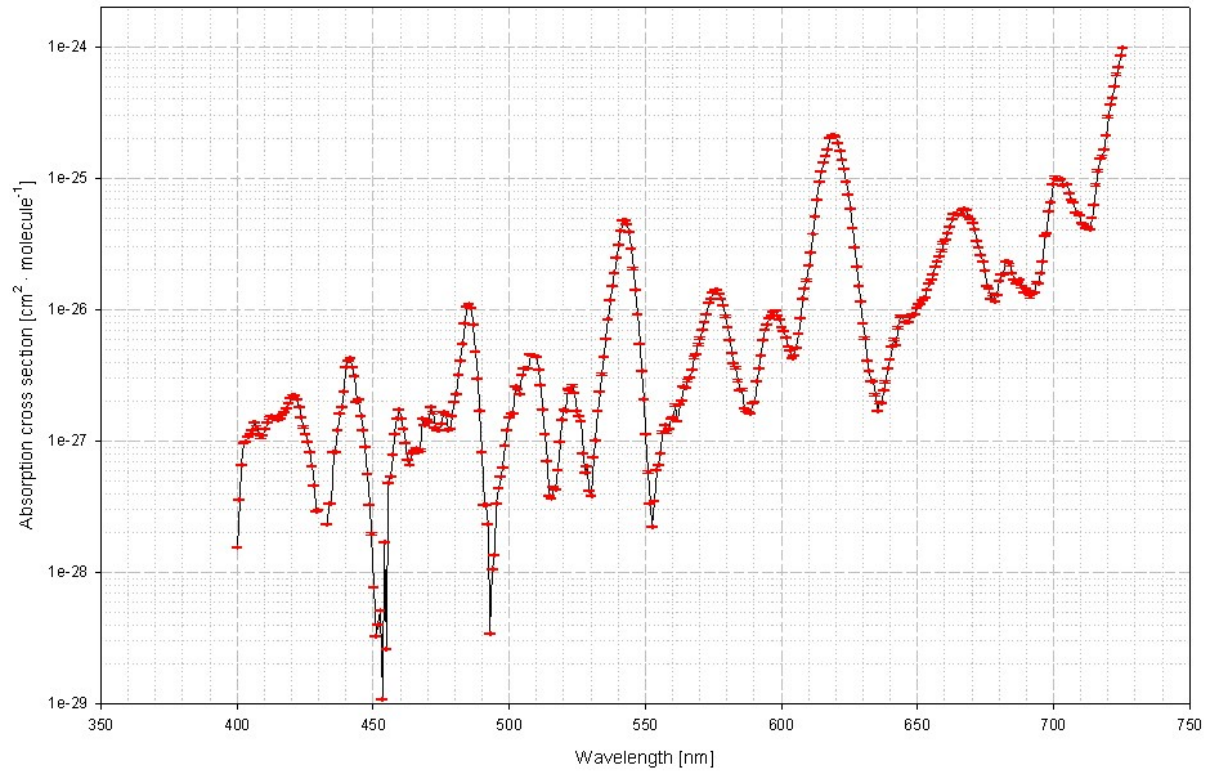
A 17: Absorption cross section of methane at room temperature. (He et al., 2021).
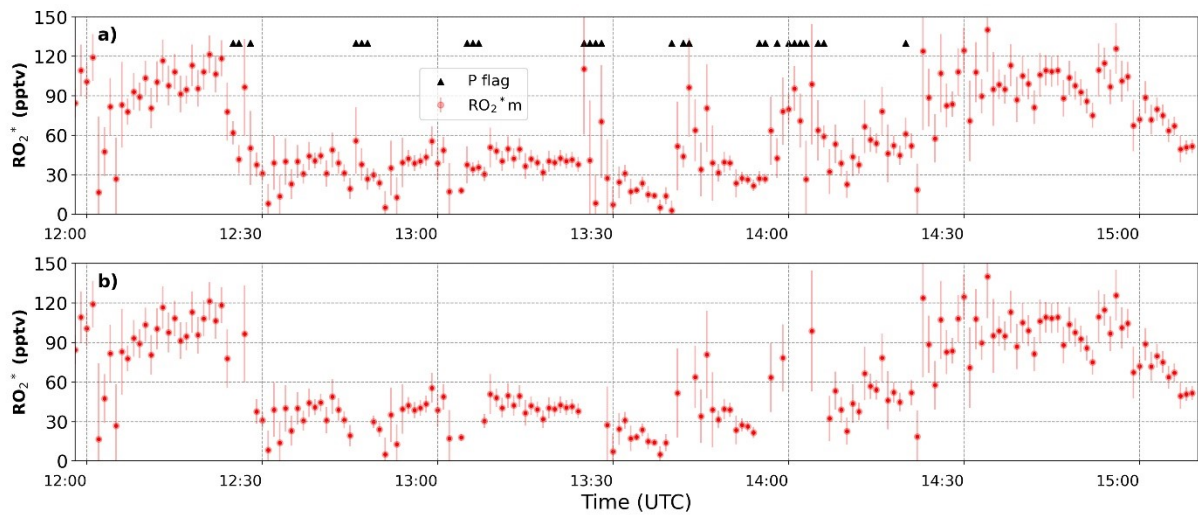
A 18: Time series of the RO_2^* measurements of E-EU-03. Panel a) shows all RO_2^* measurements, with P flags marked at the corresponding time; b) RO_2^* measurements where P flags marked in a) are removed, resulting in a plot of the remaining measurement points. P flag: pressure flag represents the RO_2^* measurements retrieval affected by the pressure variations in the inlet.
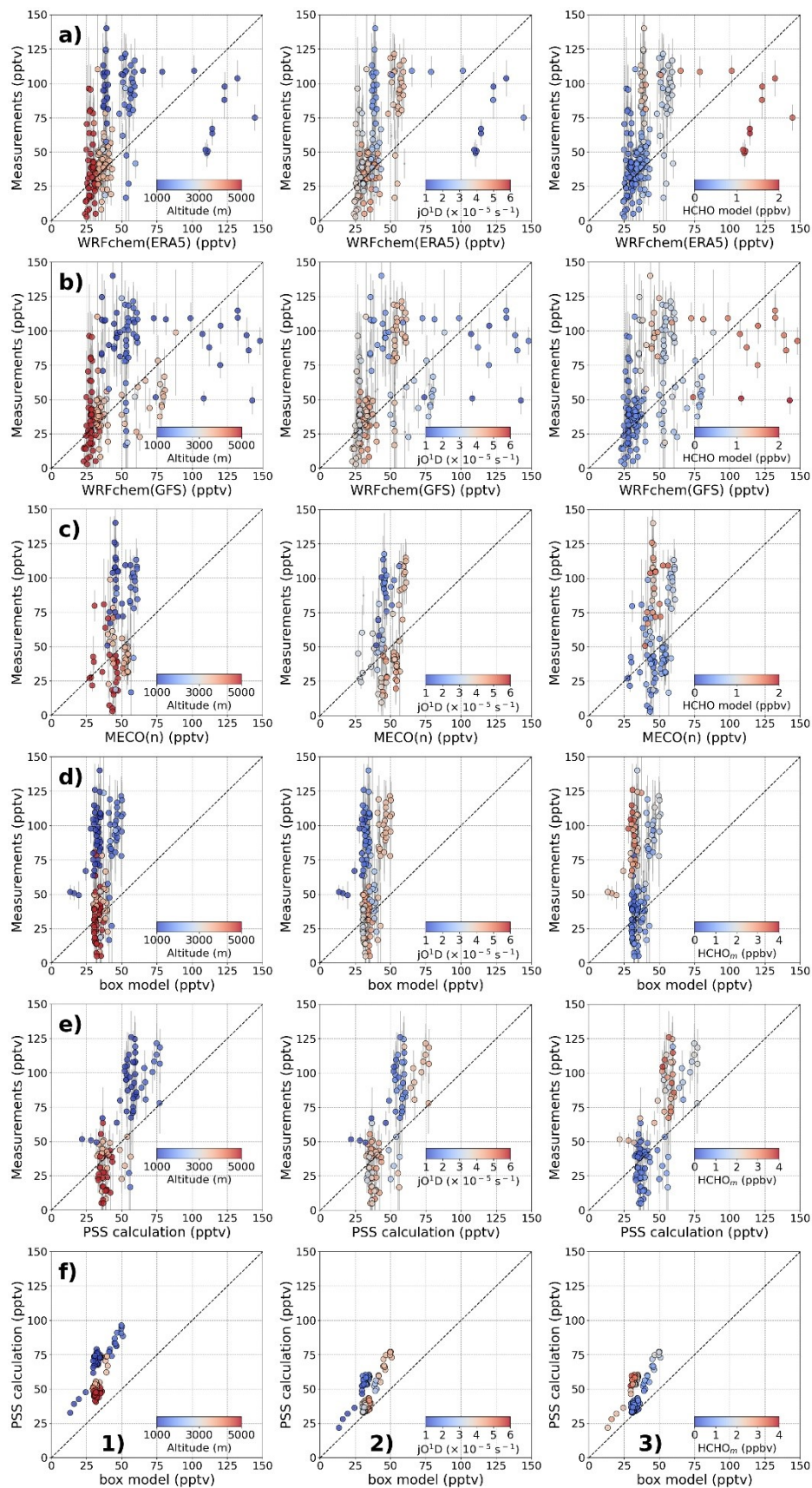
A 19: Scatter plots between RO$_2^*$ PeRCEAS measurements and the modelling results from a) WRFchem(ERA5), b) WRFchem(GFS), c) MECO(n), d) box model, and e) PSS calculation for E-EU-03 selected. f) is the RO$_2^*$ simulated by the box model and the PSS expression are compared. All the plots are colour-coded with measured or modelled 1) altitude, 2) jO^{1}D, and 3) HCHO mixing ratio. The black dashed line is the 1:1 line in the scatter plot. The temporal resolution for the plotted data is normalised to 60 s except for MECO(n) with a temporal resolution of 120 s.
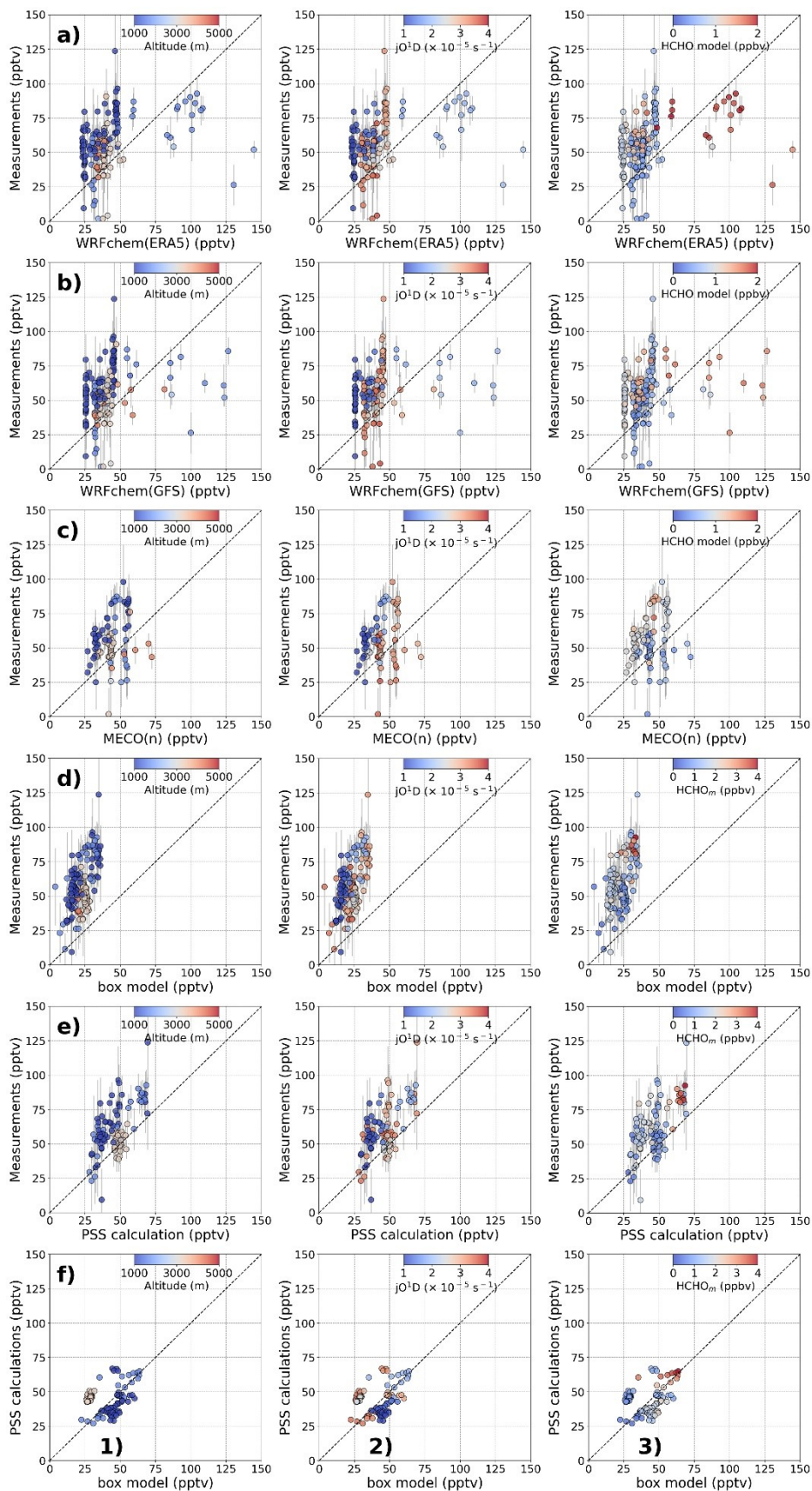
A 20: Scatter plots between RO_2^* PeRCEAS measurements and the modelling results from a) WRFchem(ERA5), b) WRFchem(GFS), c) MECO(n), d) box model, and e) PSS calculation for E-EU-06 selected. In f), the RO_2^* simulated by the box model and the PSS expression are compared. All the plots are colour-coded with measured or modelled 1) altitude, 2) jO^1D, and 3) HCHO mixing ratio. The black dashed line is the 1:1 line in the scatter plot. The temporal resolution for the plotted data is normalised to 60 s except for MECO(n) with a temporal resolution of 120 s.
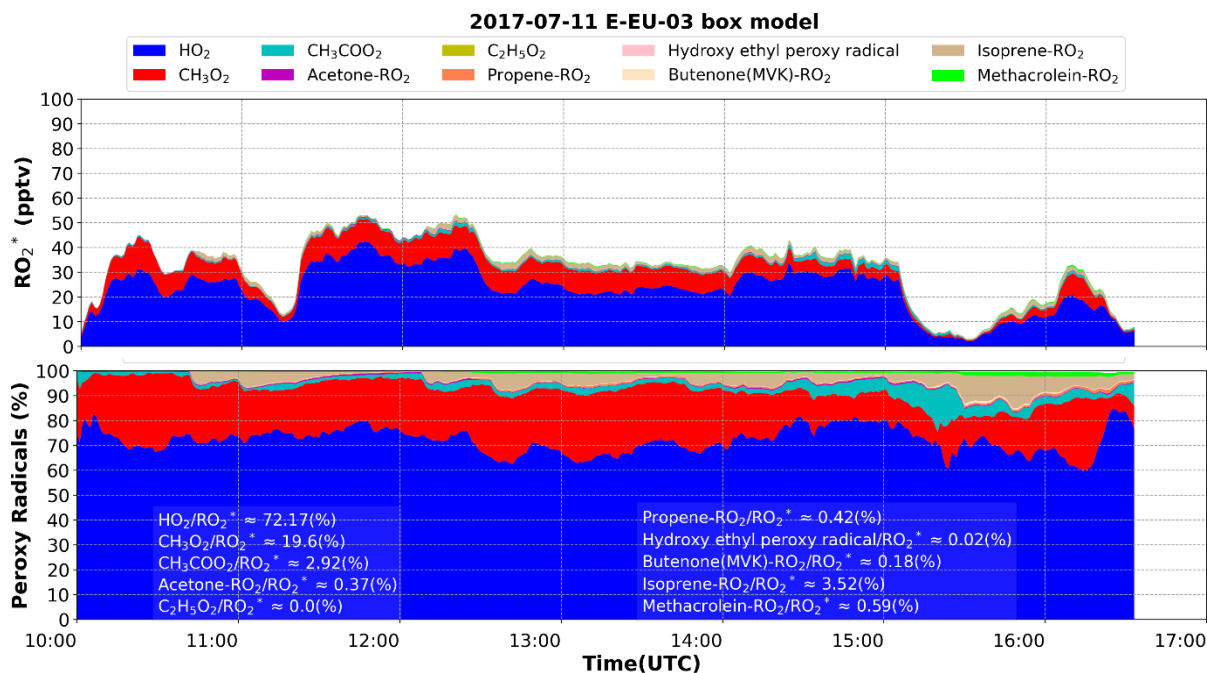
A 21: Time series of differentiation of peroxy radicals using the box model for the E-EU-03 flight. The top panel displays stacked results of peroxy radicals with outputs exceeding 0.1 pptv. The bottom panel illustrates specific radicals contributing more than 0.1 pptv to the total radical composition, expressed as a percentage. Percentages represent the average contribution of each specific radical to the total radical count.
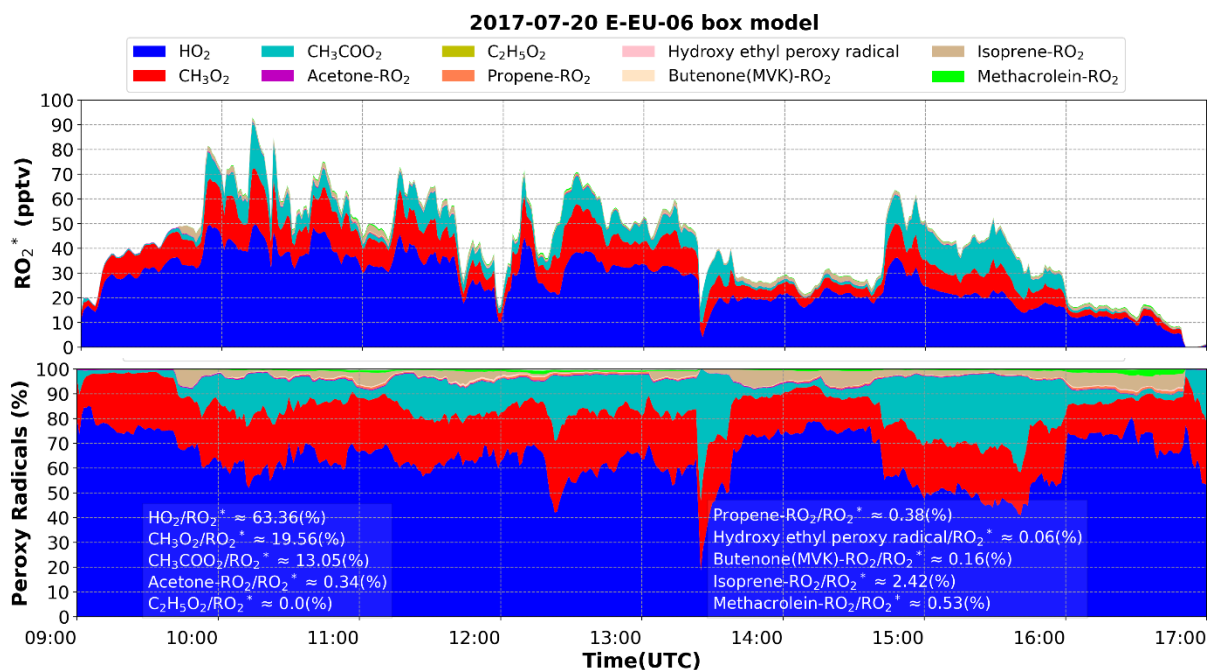
A 22: Time series of differentiation of peroxy radicals using the box model for the E-EU-06 flight. The top panel displays stacked results of peroxy radicals with outputs exceeding 0.1 pptv. The bottom panel illustrates specific radicals contributing more than 0.1 pptv to the total radical composition, expressed as a percentage. Percentages represent the average contribution of each specific radical to the total radical count.
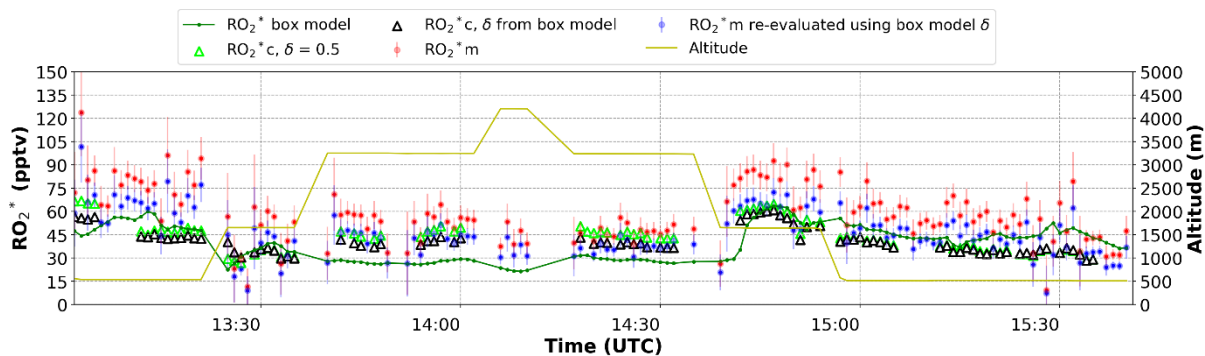
A 23: Time series of the RO_2^* box model (green line), PSS calculation with $\delta = 0.5$ (lime triangle), PSS calculation with δ from box model (black triangle), measurement original (red filled circles), and re-evaluated measurement using δ from box model (blue filled circles) for E-EU-06 selected region.
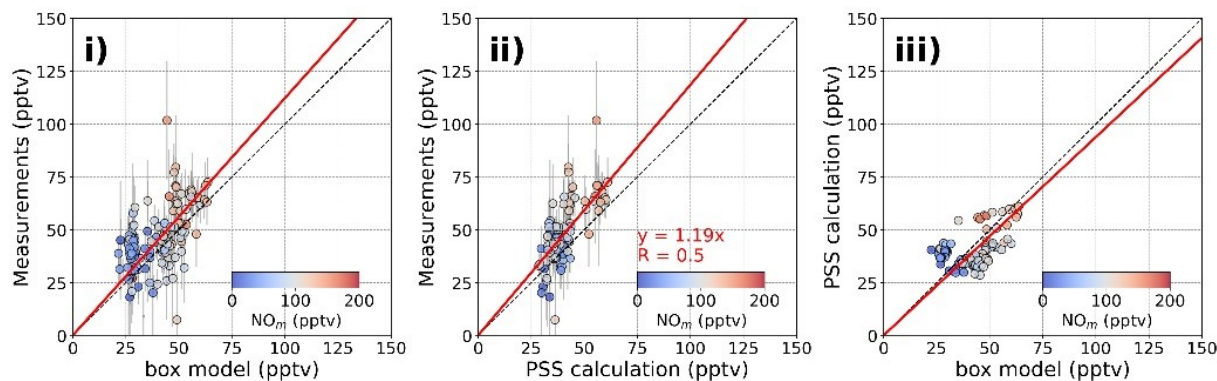
A 24: Correlation scatter plots for i) box model vs. re-evaluated measurement RO_2^*; ii) PSS re-calculated RO_2^* vs. re-evaluated measurement RO_2^*; iii) box model vs. PSS re-calculated RO_2^* for the E-EU-06 selected region. All the plots are colour-coded with measurements of NO. δ adopted from the box model. The 1:1 line is represented by black dashed lines, while the linear fit is denoted by red solid lines. All the correlations are forced through the origin. Slopes and correlation coefficients are not depicted when the correlation coefficient is less than 0.4.
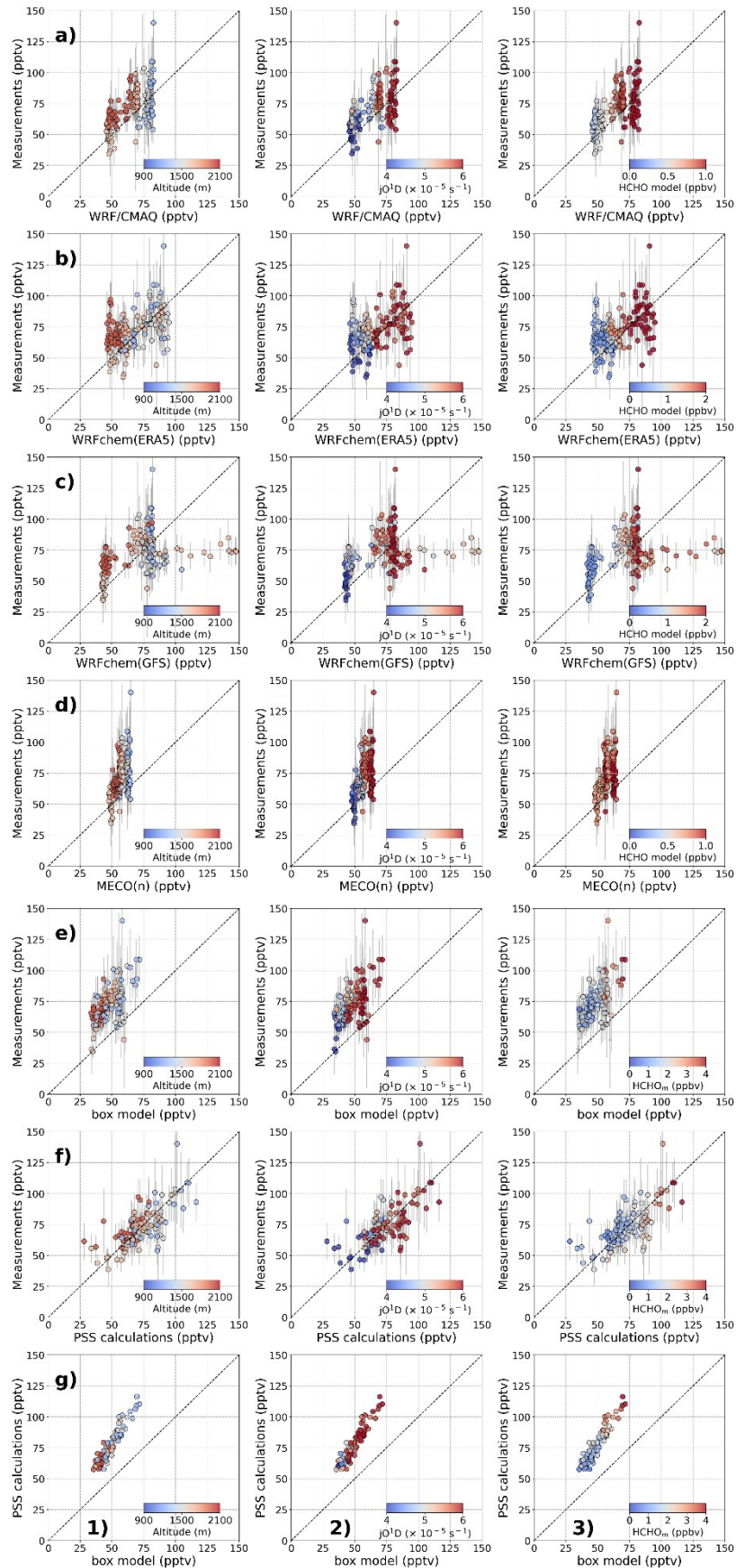
A 25: Relationship between RO_2^* PeRCEAS measurements and the modelling results from a) WRF/CMAQ, b) WRFchem(ERA5), c) WRFchem(GFS), d) MECO(n), e) box model, and f) PSS calculation for E-AS-06 over Manila. In g), the RO_2^* simulated by the box model and the PSS expression are compared. All the plots are colour-coded with measuremed or modelled 1) altitude, 2) jO^1D, and 3) HCHO mixing ratio. The black dashed line is the 1:1 line in the scatter plot. The temporal resolution for the plotted data is normalised to 60 s.
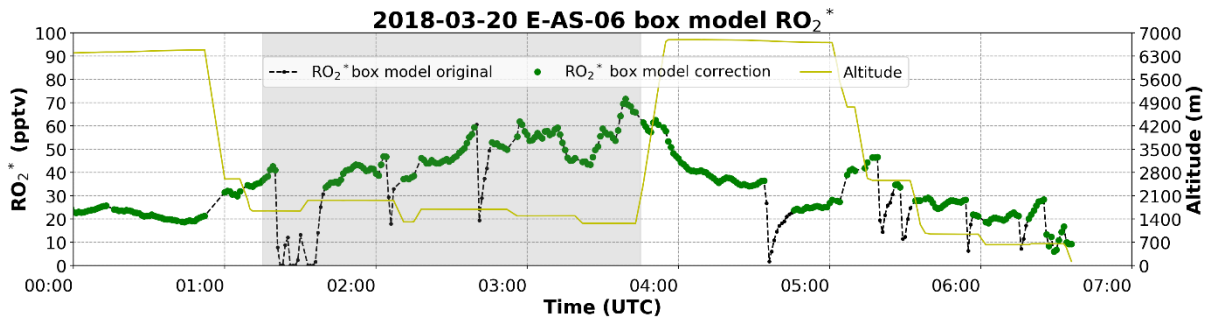
A 26: Time series of box model interpolation correction for E-AS-06. The black dashed line refers to the original box model RO_2^* output, the green filled circles refer to the corrected results. The highlighted section denotes the region traversed before and after passing over Manila.
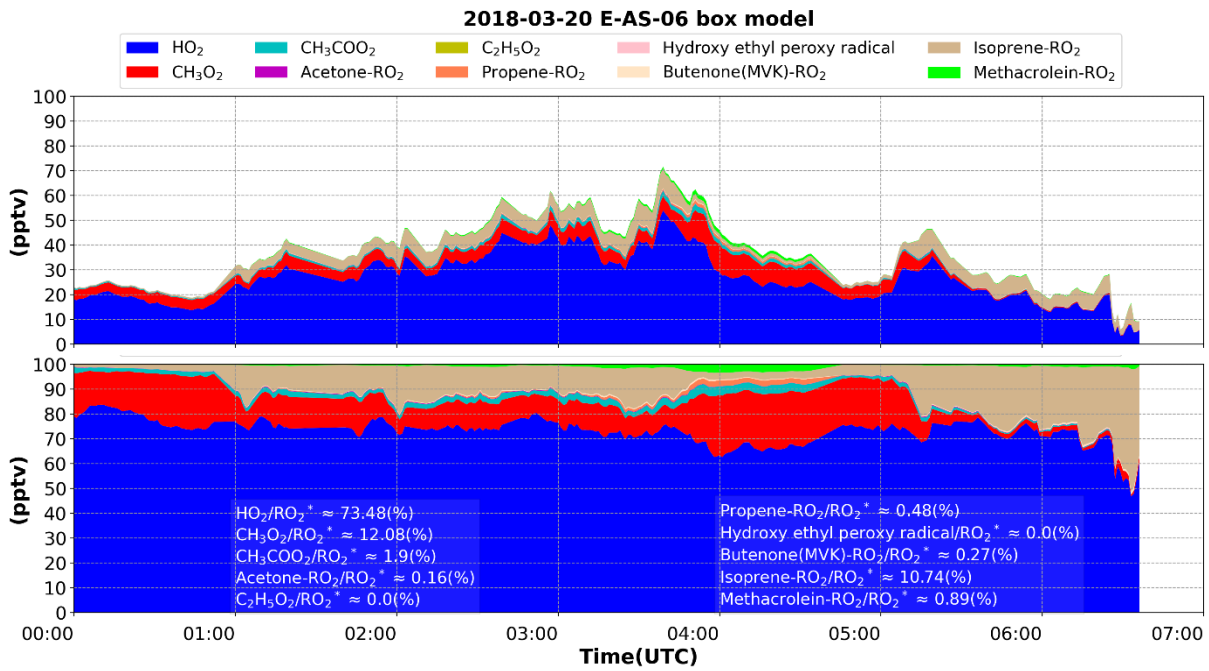
A 27: Time series of differentiation of peroxy radicals using the box model for the E-AS-06 flight. The top panel displays stacked results of peroxy radicals with outputs exceeding 0.1 pptv. The bottom panel illustrates specific radicals contributing more than 0.1 pptv to the total radical composition, expressed as a percentage. Percentages represent the average contribution of each specific radical to the total radical count.
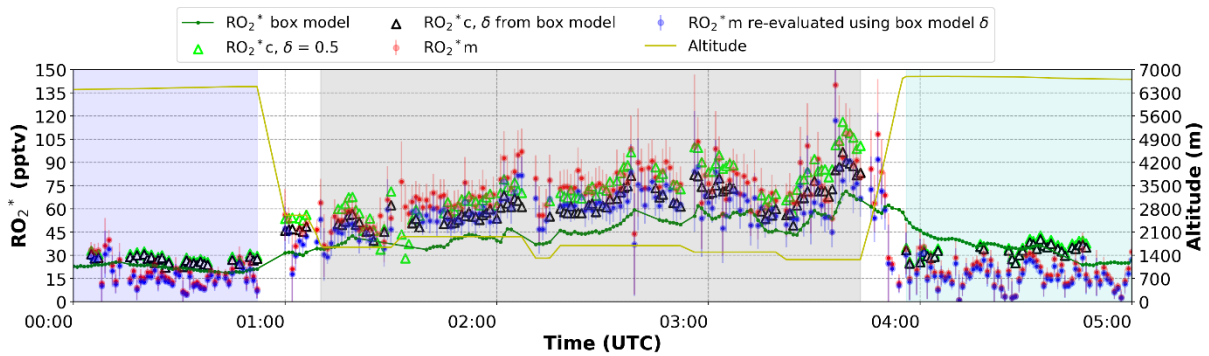
A 28: Time series of the RO_2^* box model (green line), PSS calculation with $\delta = 0.5$ (lime triangle), PSS calculation with δ from box model (black triangle), measurement original (red filled circles), and re-evaluated measurement using δ from box model (blue filled circles) for E-AS-06 sections 1)-3). The regions highlighted in blue, grey, and cyan mark sections 1), 2), and 3) of this flight, respectively.

133
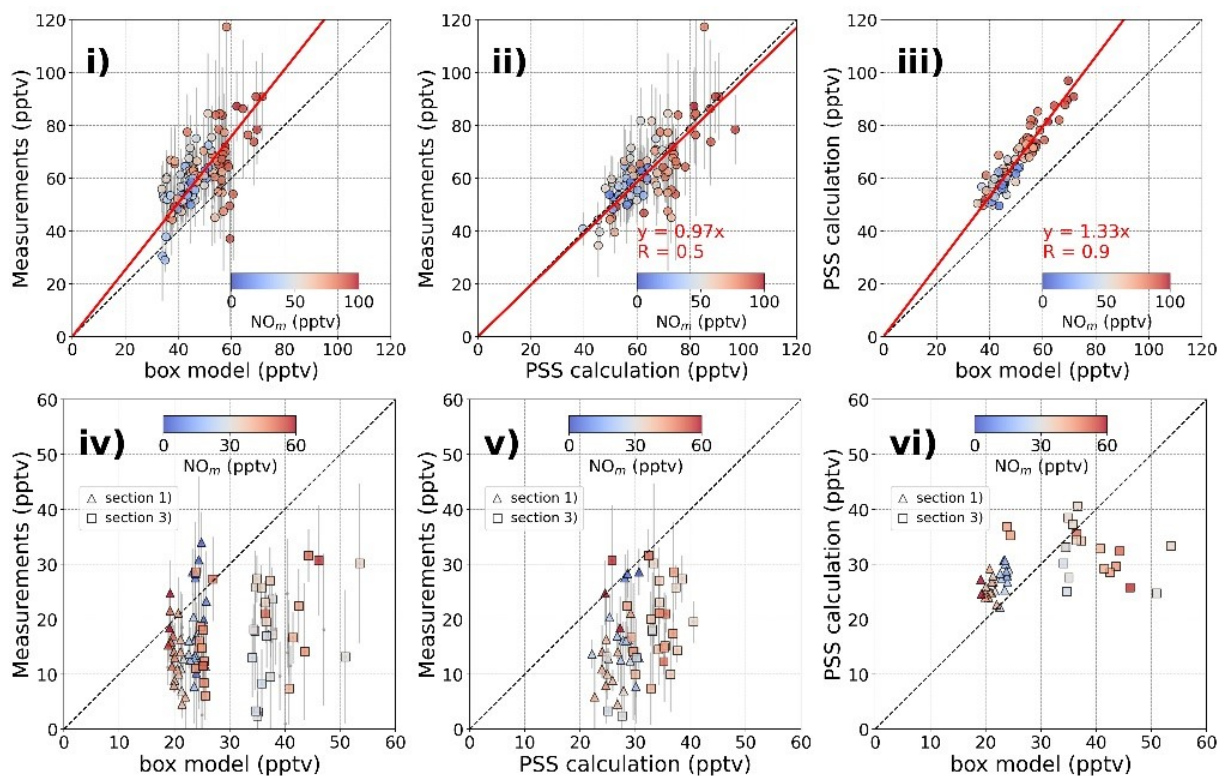
A 29: Correlation scatter plots for E-AS-06 i) box model vs. re-evaluated measurement RO_2^*; ii) PSS re-calculated RO_2^* vs. re-evaluated measurement RO_2^*; iii) box model vs. PSS re-calculated RO_2^* for section 2). iv) - vi) are the same correlations for sections 1) as triangles and 3) as squares. All the plots are colour-coded with measurements of NO. δ adapted from the box model. The 1:1 line is represented by black dashed lines, while the linear fit is denoted by red solid lines. All the correlations are forced through the origin. Slopes and correlation coefficients are not depicted when the correlation coefficient is less than 0.4.
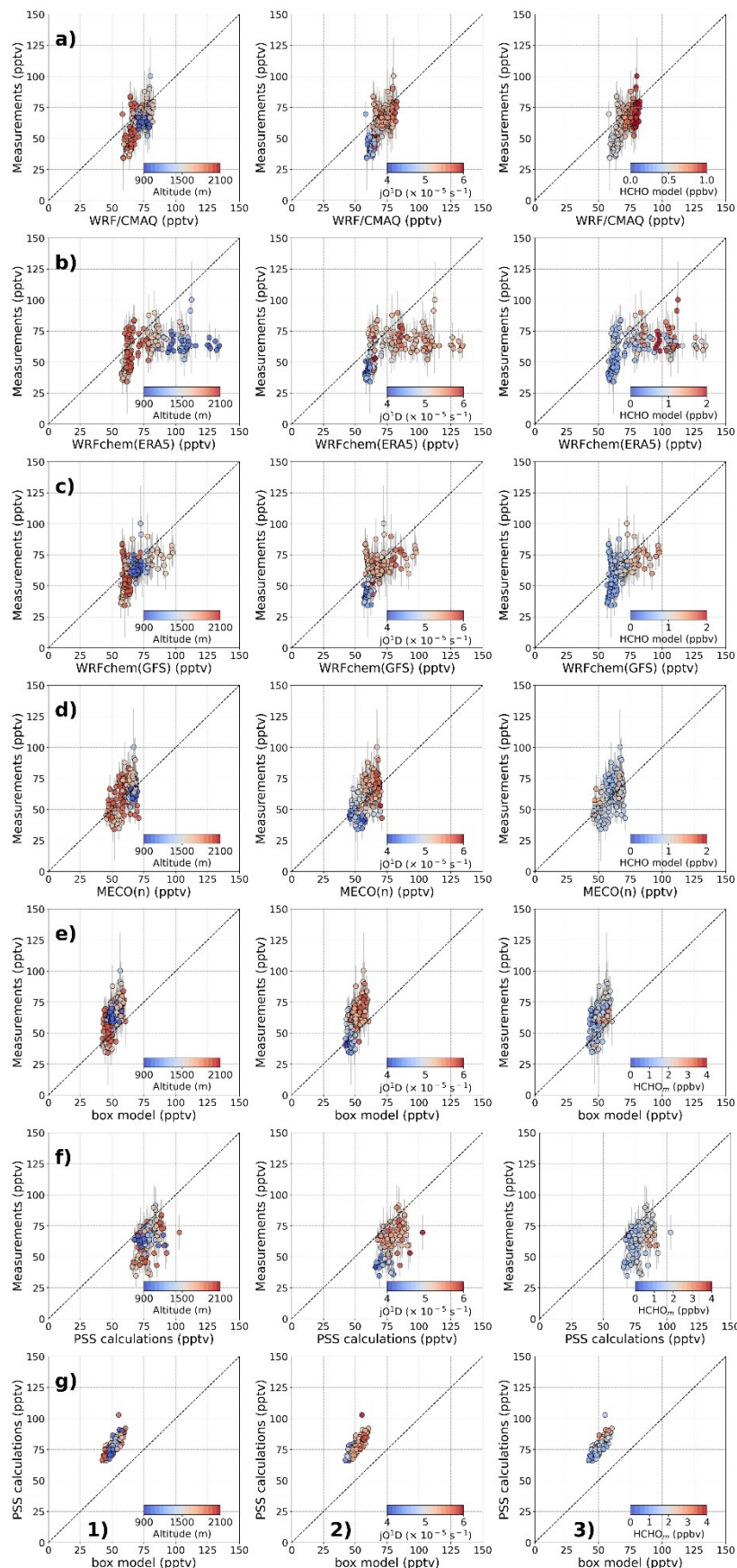
A 30: Relationship between RO_2^* PeRCEAS measurements and the modelling results from a) WRF/CMAQ, b) WRFchem(ERA5), c) WRFchem(GFS), d) MECO(n), e) box model, and f) PSS calculation for E-AS-10 over Manila. In g), the RO_2^* simulated by the box model and the PSS expression are compared. All the plots are colour-coded with measured or modelled 1) altitude, 2) jO^1D, and 3) HCHO mixing ratio. The black dasehd line is the 1:1 line in the scatter plot. The temporal resolution for the plotted data is normalised to 60 s.
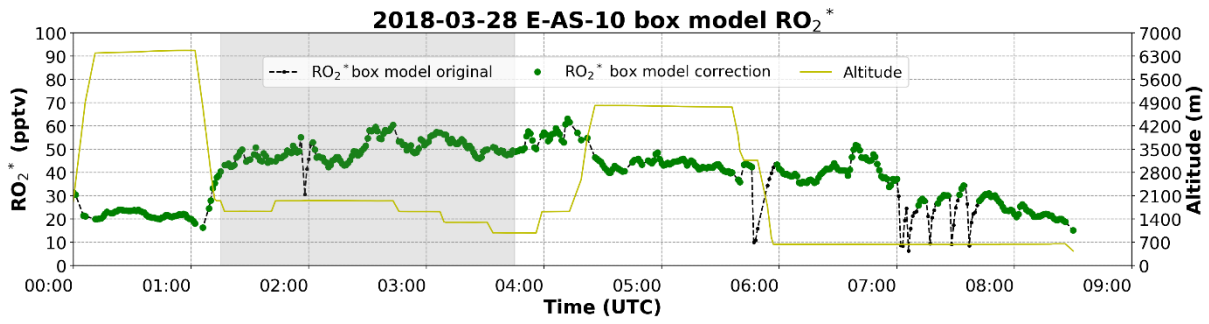
A 31: Time series of box model interpolation correction for E-AS-10. The black dashed line refers to the original box model RO_2^* output, the green filled circles refer to the corrected results. The highlighted section denotes the region traversed before and after passing over Manila.
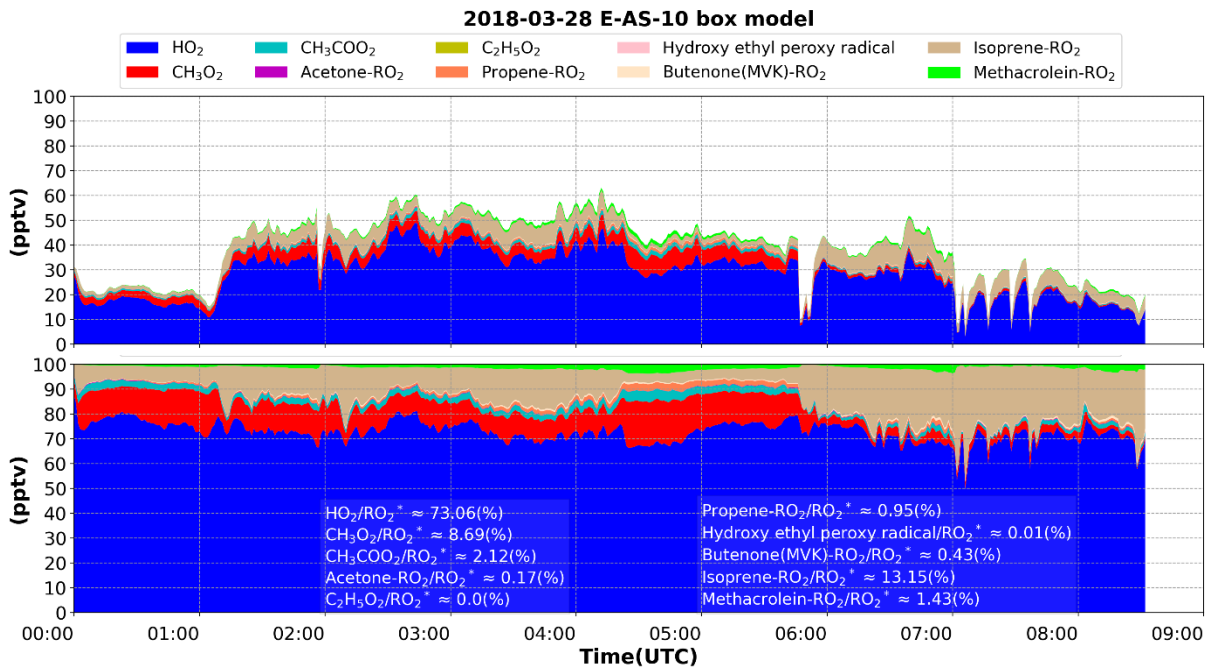
A 32: Time series of differentiation of peroxy radicals using the box model for the E-AS-10 flight. The top panel displays stacked results of peroxy radicals with outputs exceeding 0.1 pptv. The bottom panel illustrates specific radicals contributing more than 0.1 pptv to the total radical composition, expressed as a percentage. Percentages represent the average contribution of each specific radical to the total radical count.
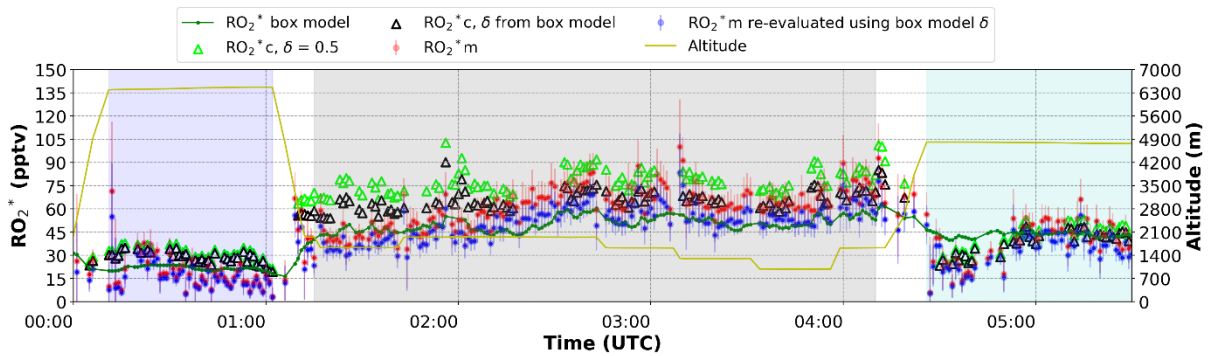
A 33: Time series of the RO_2^* box model (green line), PSS calculation with $\delta = 0.5$ (lime triangle), PSS calculation with δ from box model (black triangle), measurement original (red filled circles), and re-evaluated measurement using δ from box model (blue filled circles) for E-AS-10. The regions highlighted in blue, grey, and cyan mark sections 1), 2), and 3) of this flight, respectively.
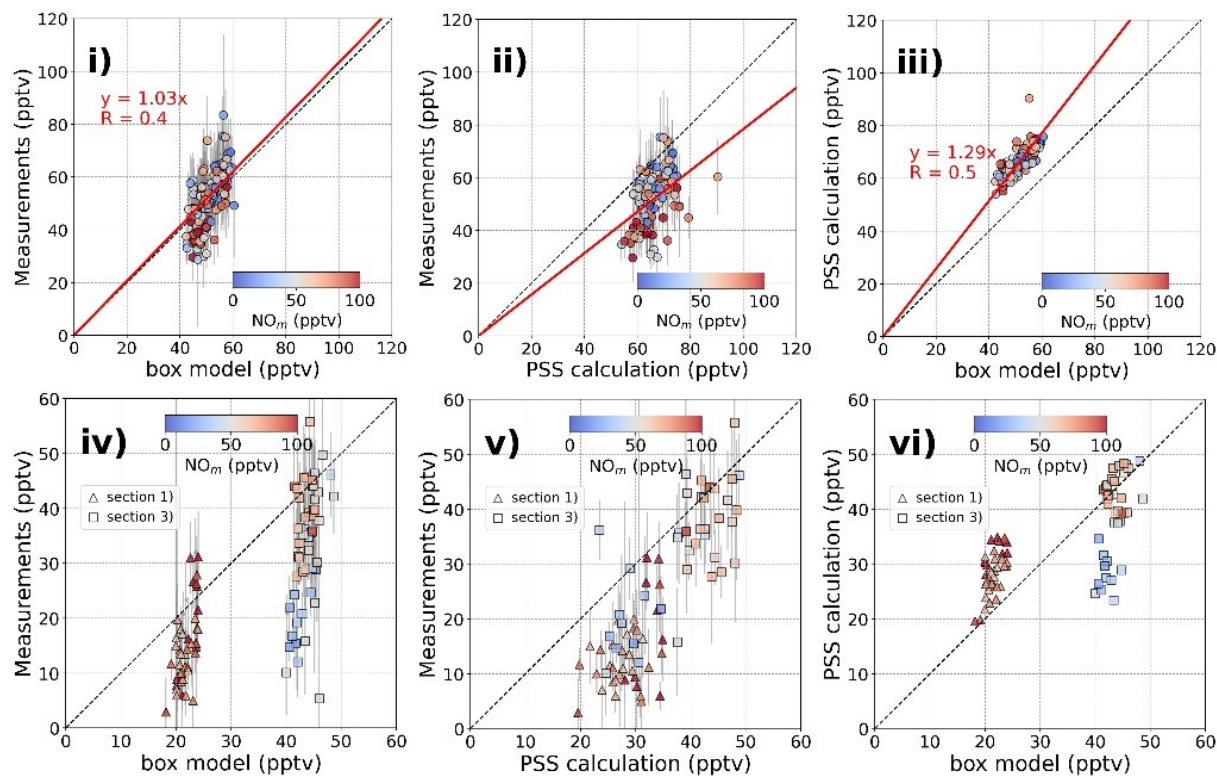
A 34: Correlation scatter plots for E-AS-10 i) box model vs. re-evaluated measurement RO_2^*; ii) PSS re-calculated RO_2^* vs. re-evaluated measurement RO_2^*; iii) box model vs. PSS re-calculated RO_2^* for section 2). iv) - vi) are the same correlations for sections 1) as triangles and 3) as squares. All the plots are colour-coded with measurements of NO. δ adapted from the box model. The 1:1 line is represented by black dashed lines, while the linear fit is denoted by red solid lines. All the correlations are forced through the origin. Slopes and correlation coefficients are not depicted when the correlation coefficient is less than 0.4.
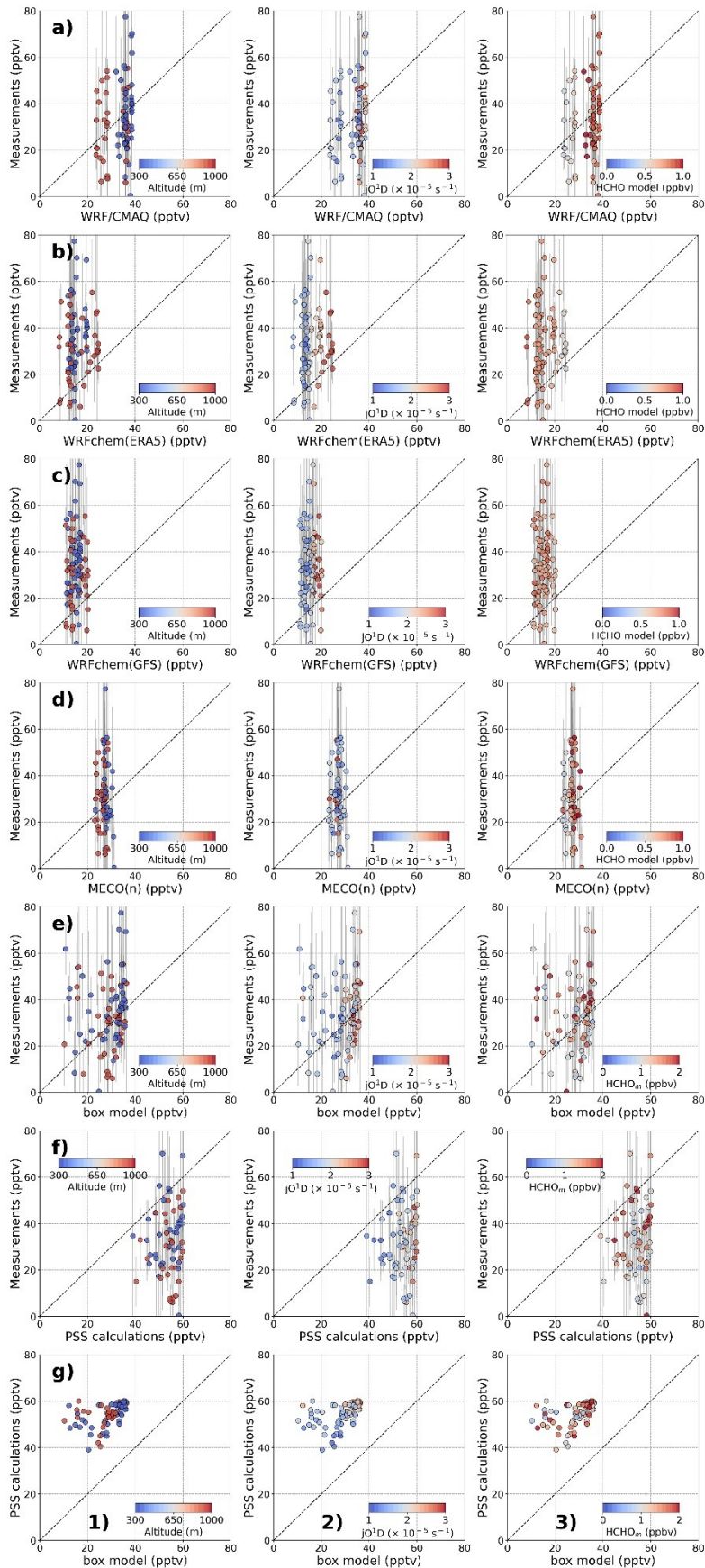
A 35: Relationship between RO_2^* PeRCEAS measurements and the modelling results from a) WRF/CMAQ, b) WRFchem(ERA5), c) WRFchem(GFS), d) MECO(n), e) box model, and f) PSS calculation for E-AS-08 over the East China Sea. In g), the RO_2^* simulated by the box model and the PSS expression are compared. All the plots are colour-coded with measured or modelled 1) altitude, 2) jO^1D, and 3) HCHO mixing ratio. The black dasehd line is the 1:1 line in the scatter plot. The temporal resolution for the plotted data is normalised to 60 s.
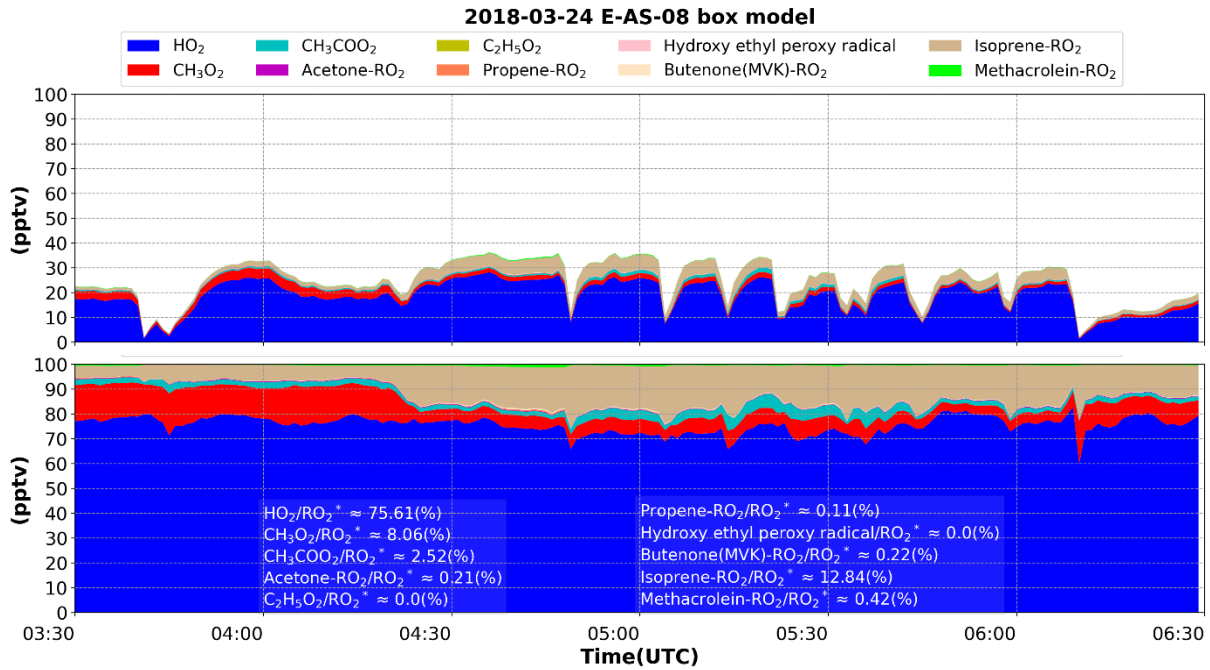
A 36: Time series of differentiation of peroxy radicals using the box model for the E-AS-08 flight. The top panel displays stacked results of peroxy radicals with outputs exceeding 0.1 pptv. The bottom panel illustrates specific radicals contributing more than 0.1 pptv to the total radical composition, expressed as a percentage. Percentages represent the average contribution of each specific radical to the total radical count.
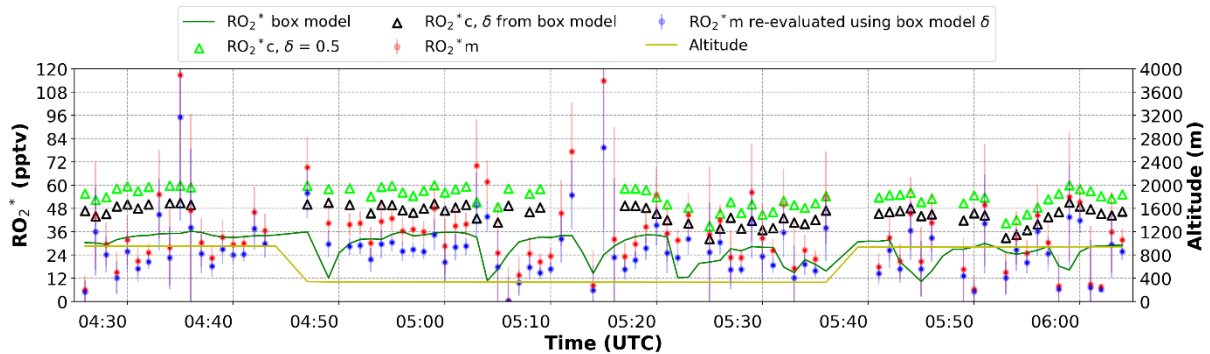
A 37: Time series of the RO_2^* box model (green line), PSS calculation with $\delta = 0.5$ (lime triangle), PSS calculation with δ from box model (black triangle), measurement original (red filled circles), and re-evaluated measurement using δ from box model (blue filled circles) for E-AS-08.
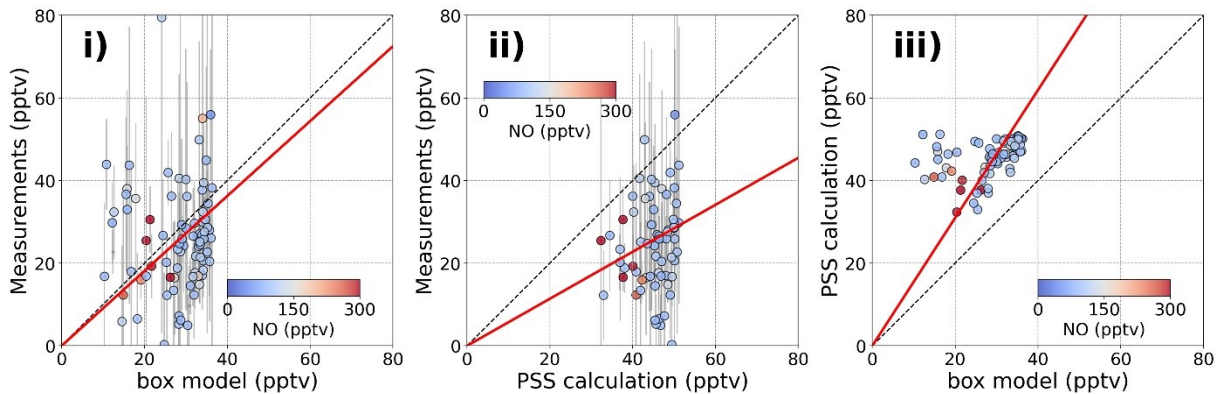
A 38: Correlation scatter plots for E-AS-08 i) box model vs. re-evaluated measurement RO_2^*; ii) PSS re-calculated RO_2^* vs. re-evaluated measurement RO_2^*; iii) box model vs. PSS re-calculated RO_2^*. All the plots are colour-coded with measurements of NO. δ adapted from the box model. The 1:1 line is represented by black dashed lines, while the linear fit is denoted by red solid lines. All the correlations are forced through the origin. Slopes and correlation coefficients are not depicted when the correlation coefficient is less than 0.4.
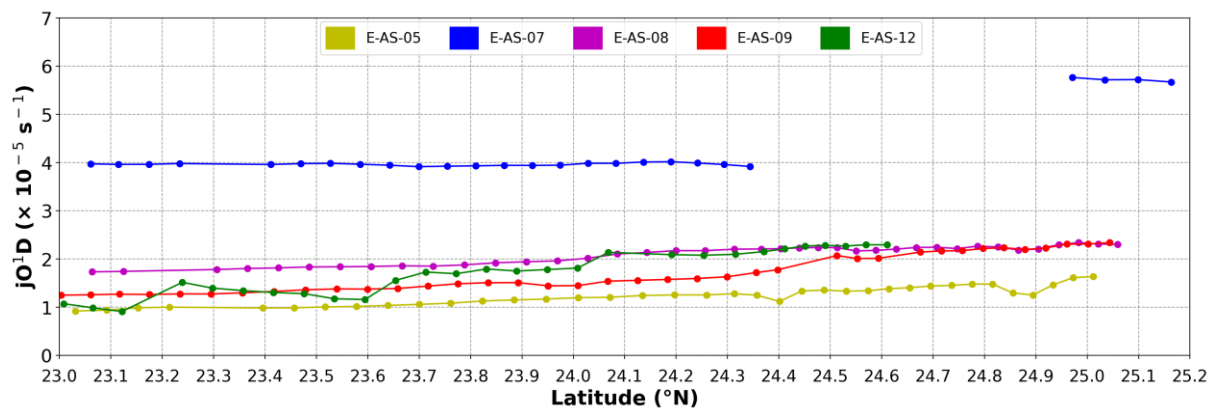
A 39: jO(¹D) measurement by HALO – SR over the latitude for the selected flights over TW1 at 60 s temporal resolution.
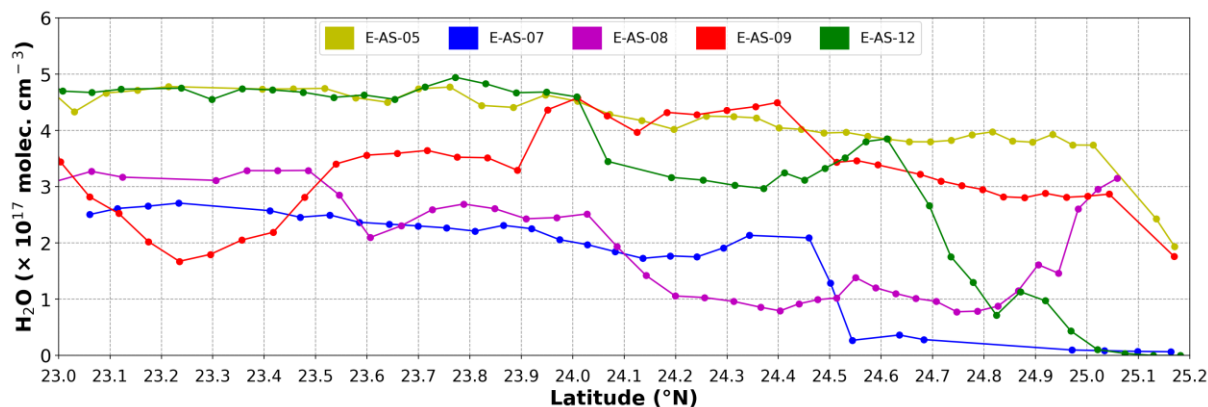
A 40: H₂O measurement over the latitude for the selected flights over TW1 at 60 s temporal resolution.
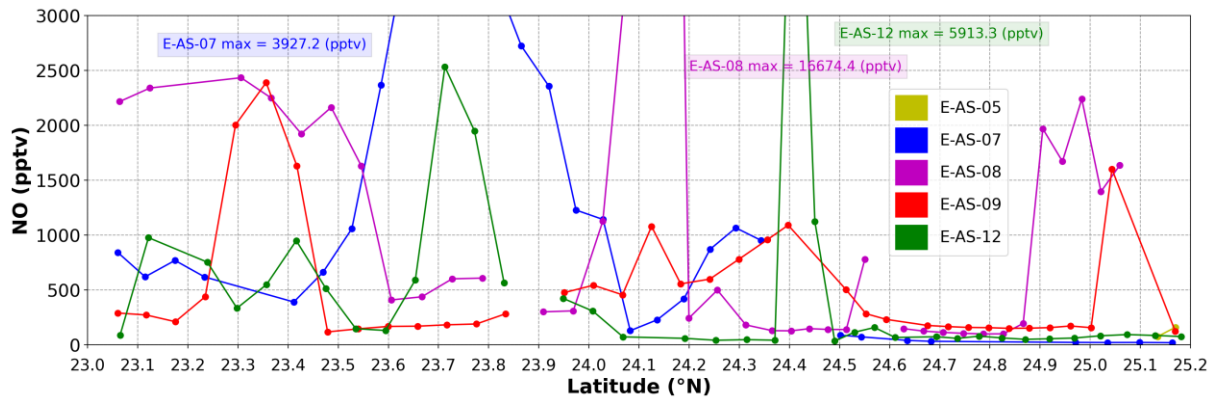
A 41: NO measurement over the latitude for the selected flights over TW1 at 60 s temporal resolution.
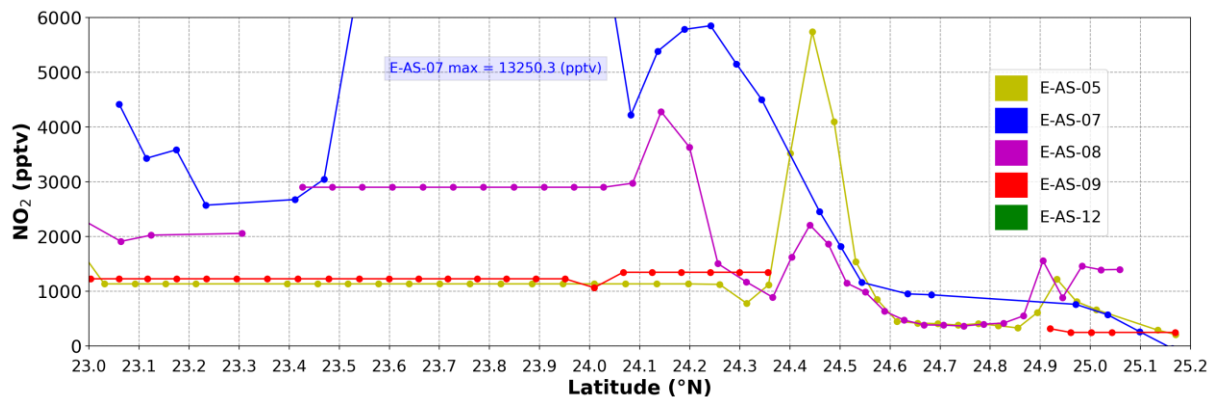
A 42: NO₂ measurement over the latitude for the selected flights over TW1 at 60 s temporal resolution.
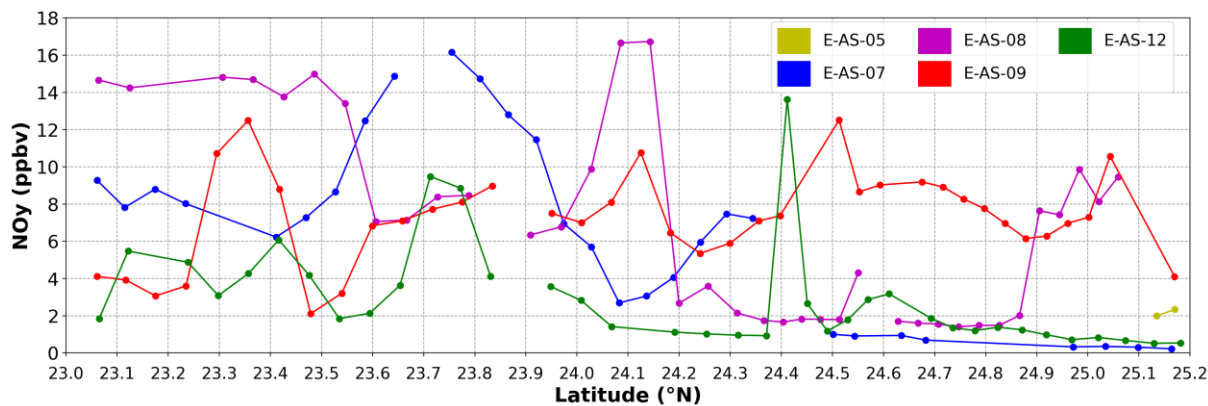
A 43: NOy measurement over the latitude for the selected flights over TW1 at 60 s temporal resolution.
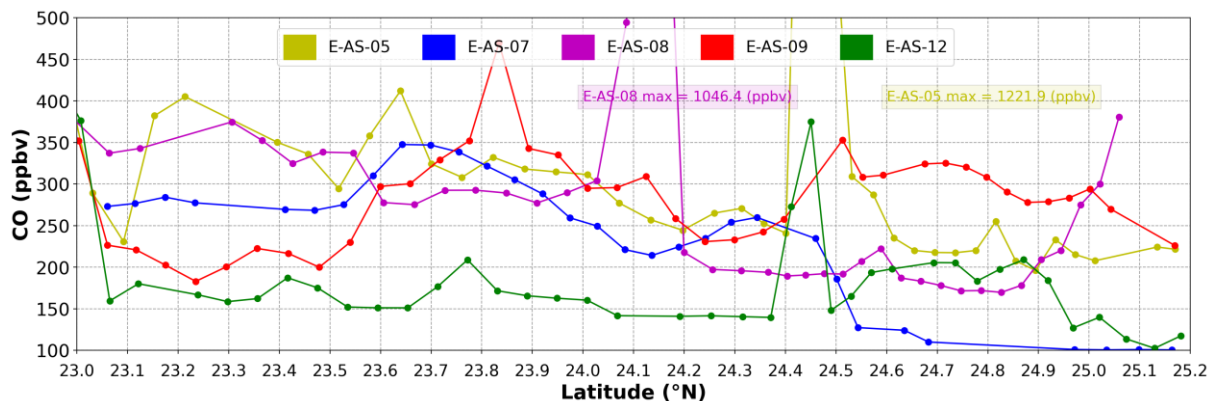
A 44: CO measurement over the latitude for the selected flights over TW1 at 60 s temporal resolution.
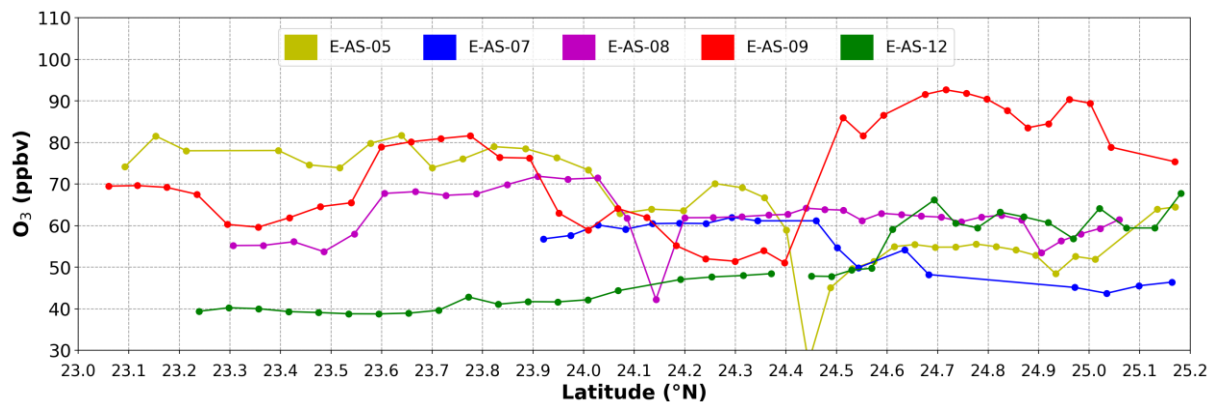
A 45: O₃ measurement over the latitude for the selected flights over TW1 at 60 s temporal resolution.
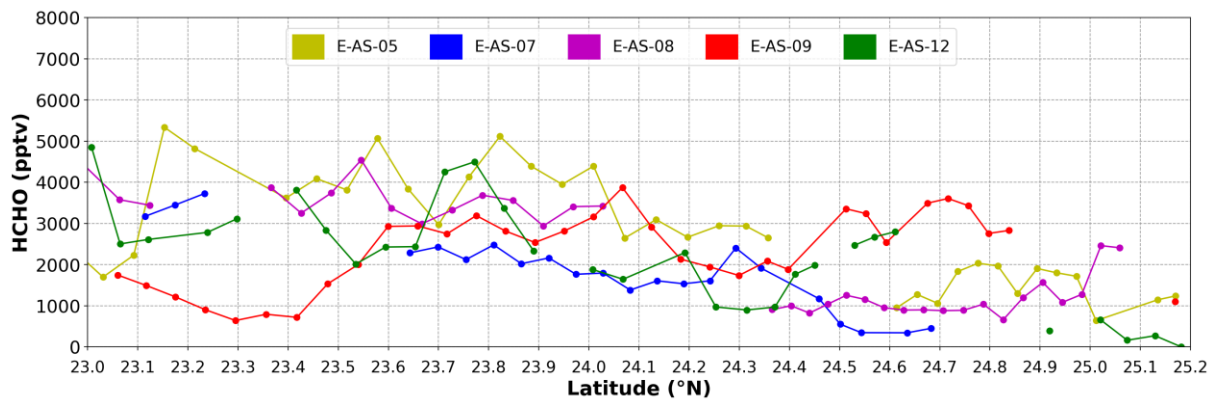
A 46: HCHO measurement over the latitude for the selected flights over TW1 at 60 s temporal resolution.
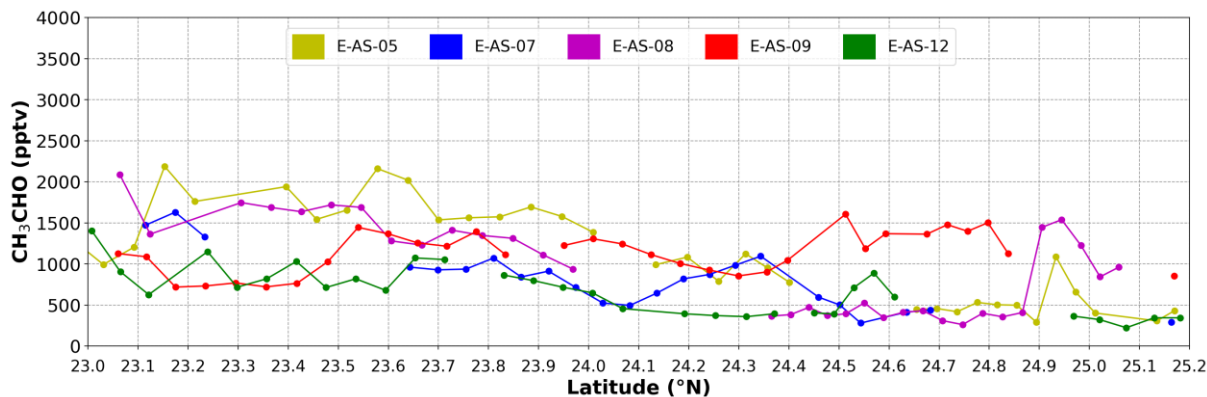
A 47: CH₃CHO measurement over the latitude for the selected flights over TW1 at 60 s temporal resolution.
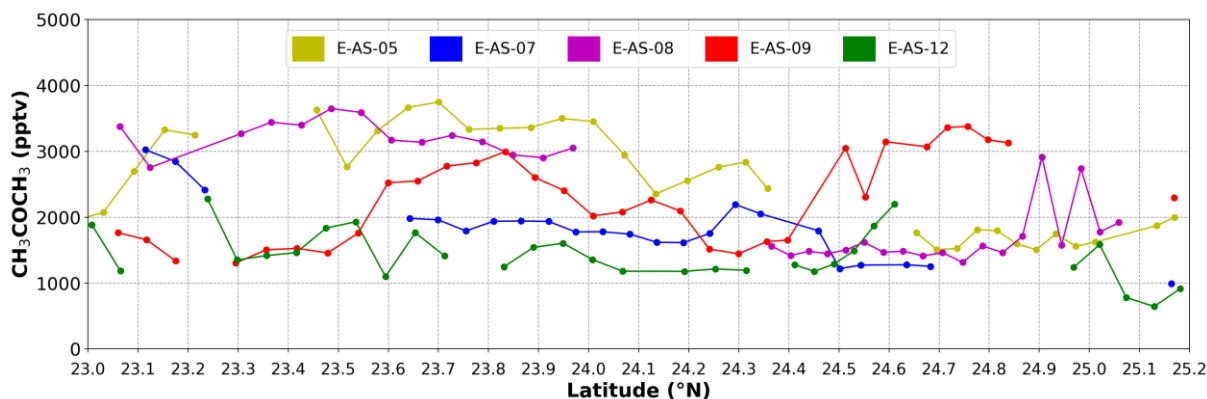
A 48: CH₃COCH₃ measurement over the latitude for the selected flights over TW1 at 60 s temporal resolution.
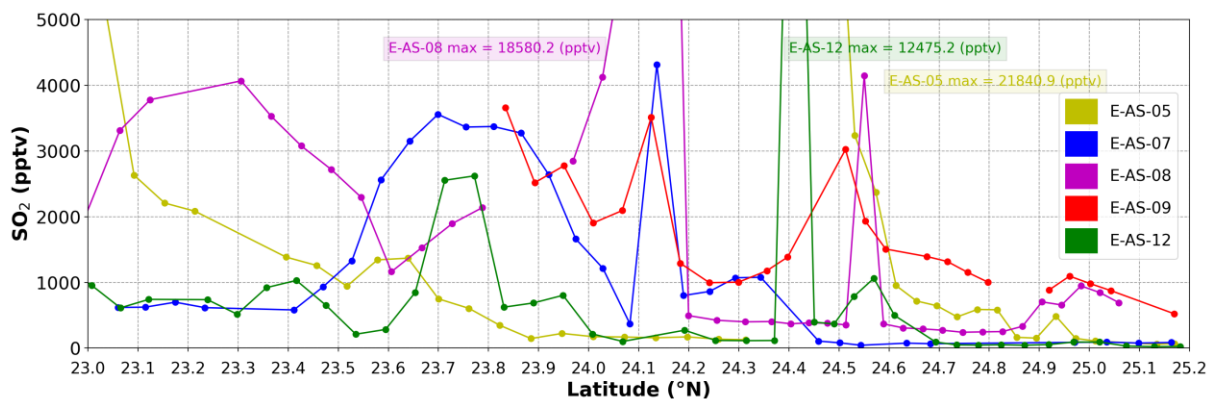
A 49: SO₂ measurement over the latitude for the selected flights over TW1 at 60 s temporal resolution.
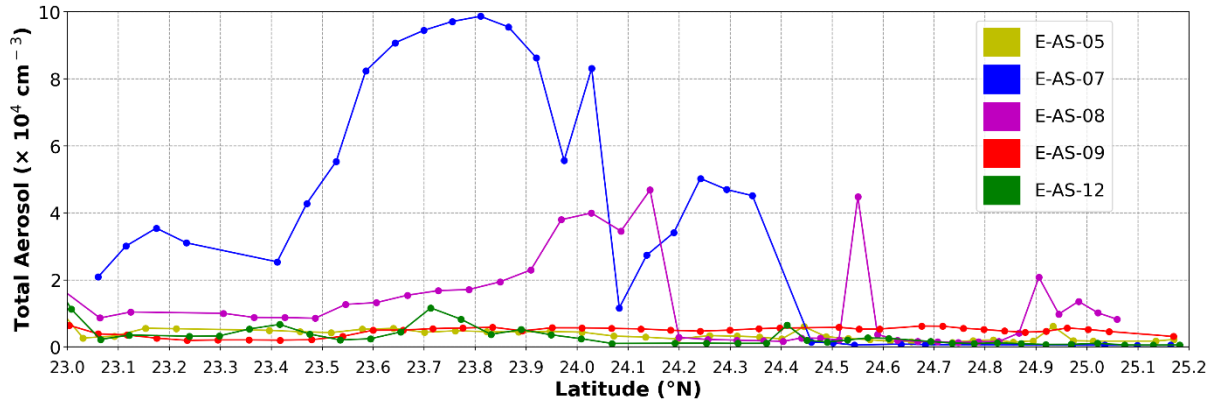
A 50: Totoal aerosol measurement over the latitude for the selected flights over TW1 at 60 s temporal resolution.
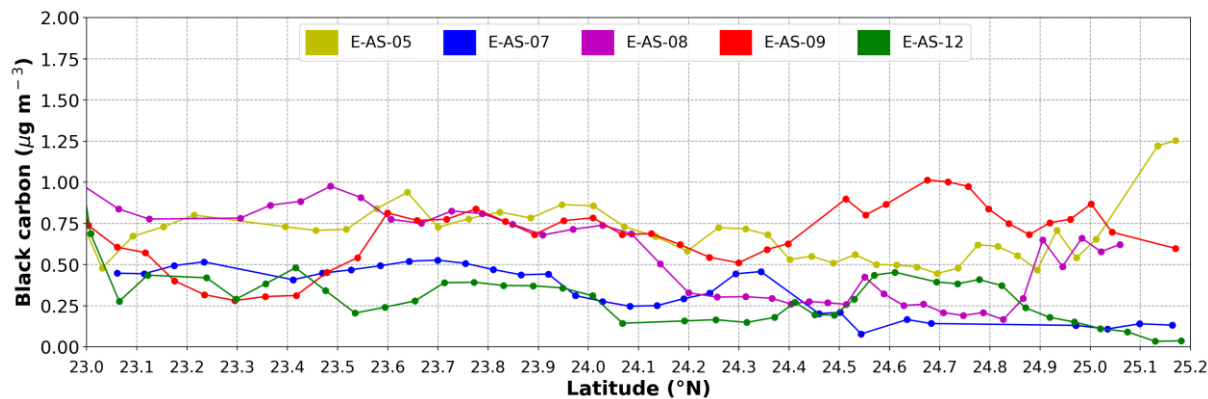
A 51: Black carbon measurement over the latitude for the selected flights over TW1 at 60 s temporal resolution.
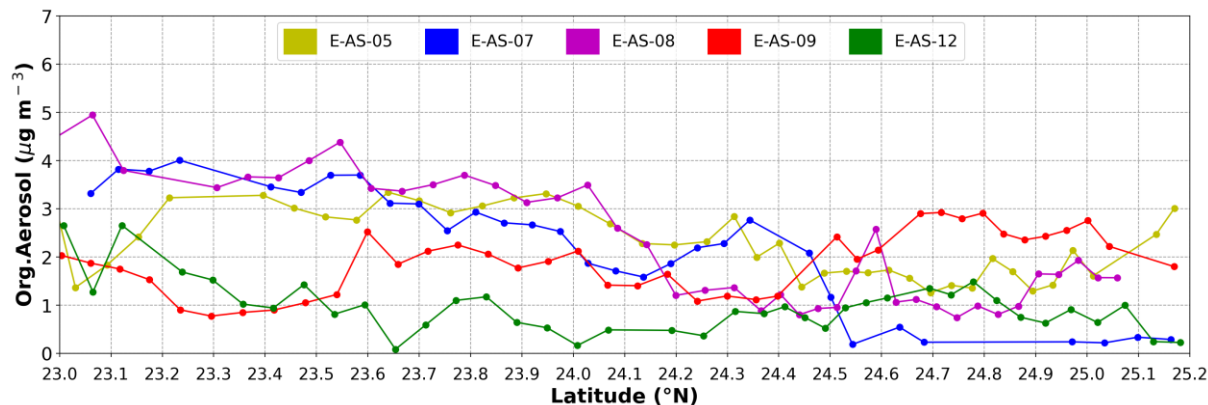
A 52: Organic aerosol measurement over the latitude for the selected flights over TW1 at 60 s temporal resolution.
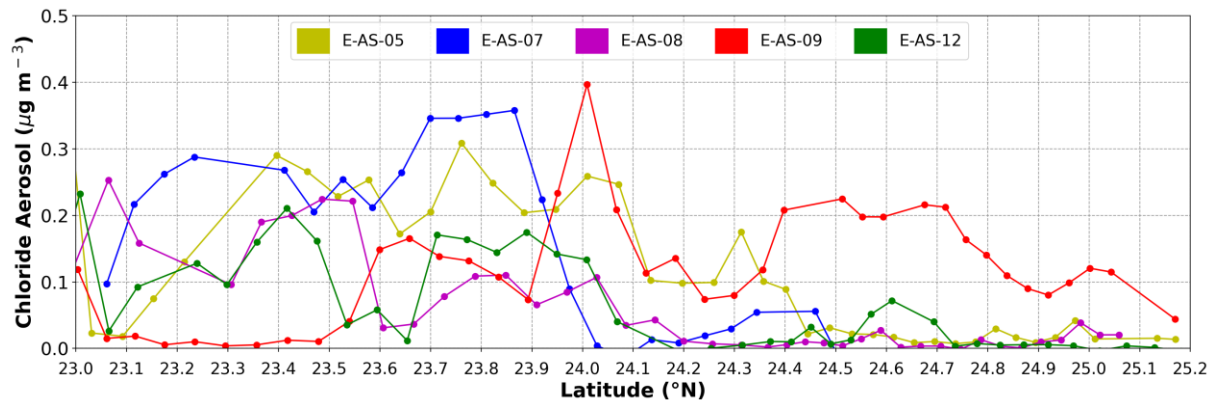
A 53: Chloride aerosol measurement over the latitude for the selected flights over TW1 at 60 s temporal resolution.
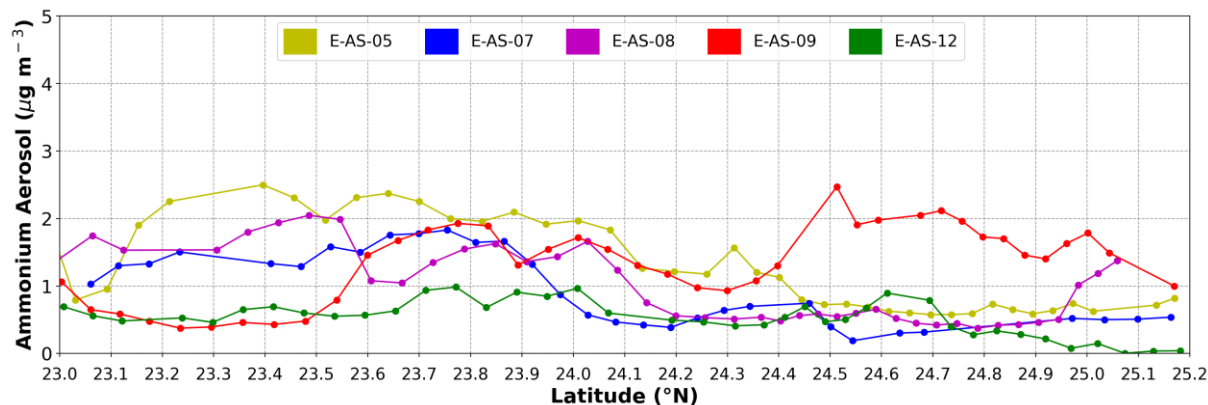
A 54: Ammonium aerosol measurement over the latitude for the selected flights over TW1 at 60 s temporal resolution.
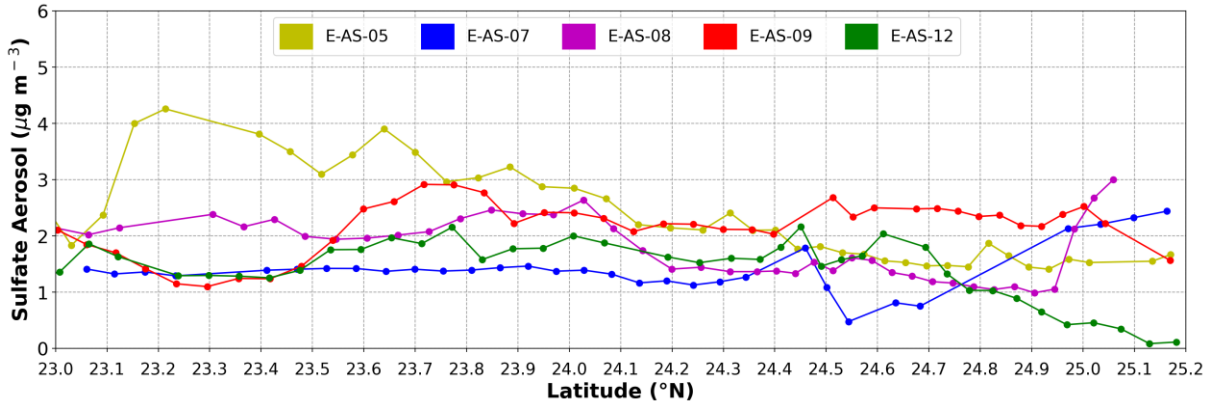
A 55: Sulfate aerosol measurement over the latitude for the selected flights over TW1 at 60 s temporal resolution.
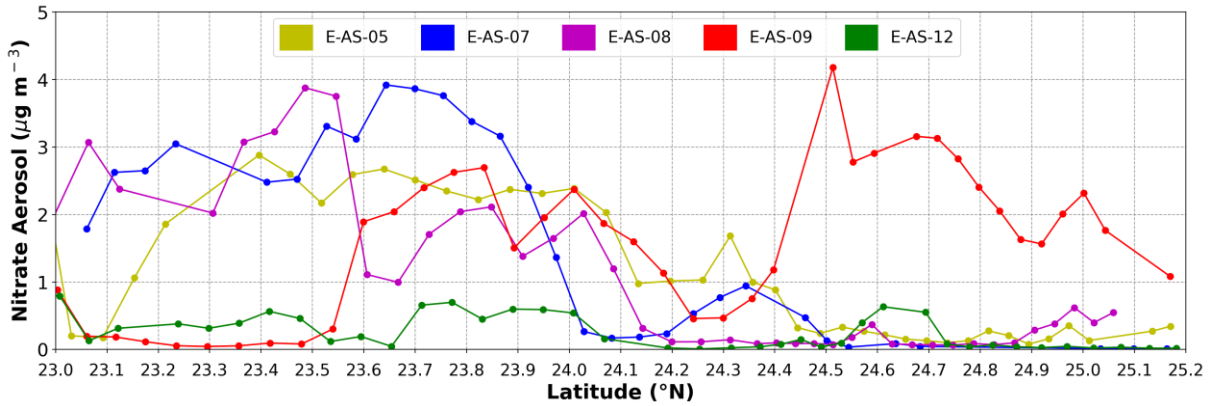
A 56: Nitrate aerosol measurement over the latitude for the selected flights over TW1 at 60 s temporal resolution.
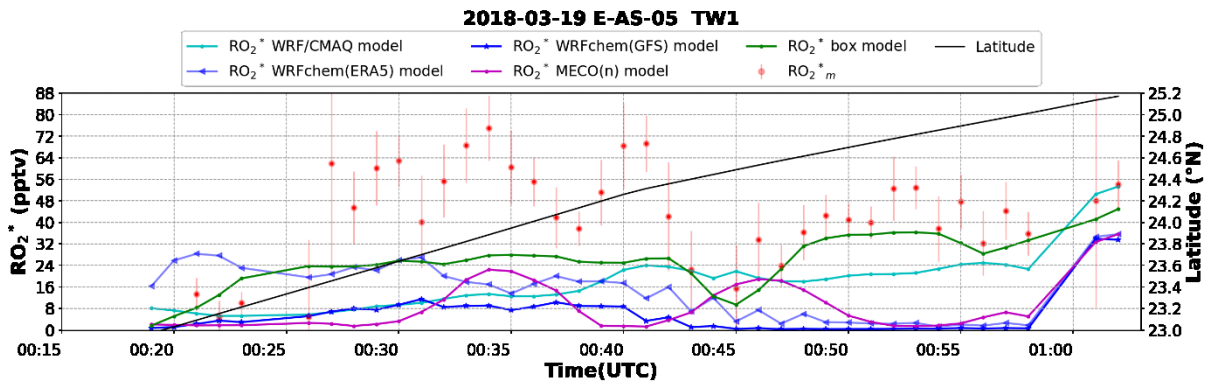
A 57: Temporal distribution of RO_2^* measurement and the corresponding results from available models for E-AS-05 TW1. The corresponding latitudes are provided on the secondary y-axis.
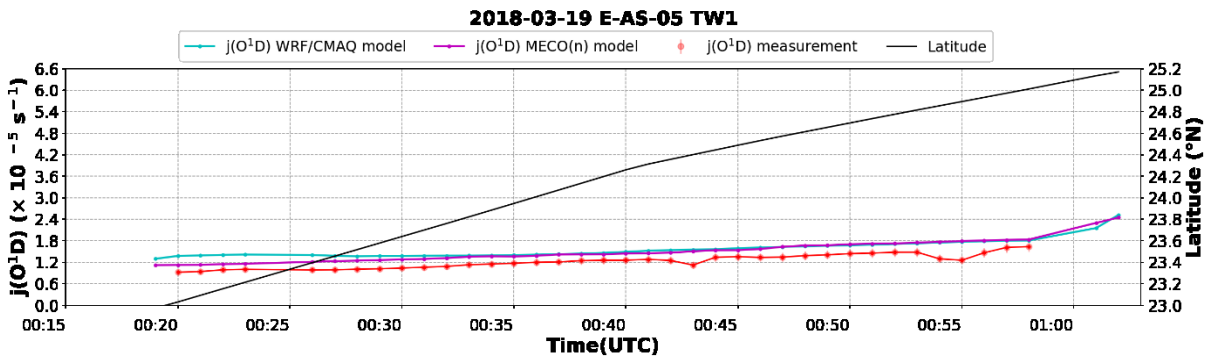
A 58: Temporal distribution of jO^1D measurement and the corresponding results from available models for E-AS-05 TW1. The corresponding latitudes are provided on the secondary y-axis. The box model constrains the measurements, therefore, is not featured in the plots.

144
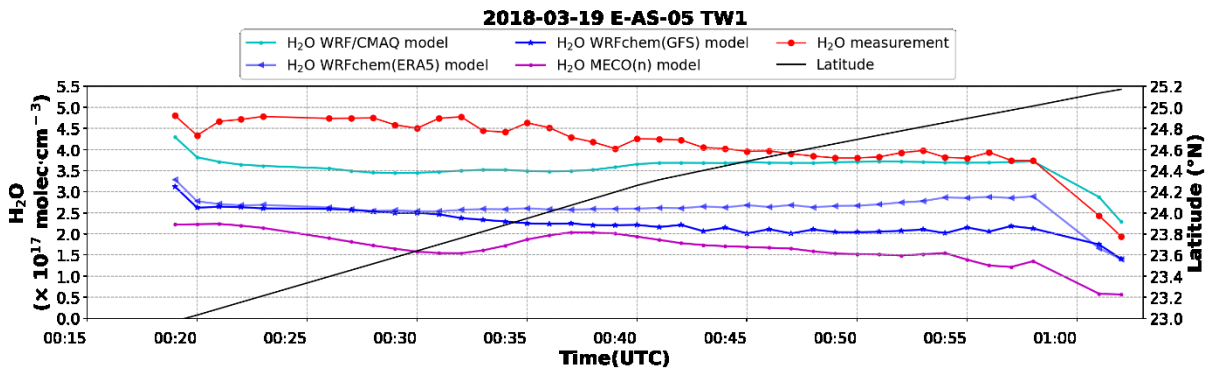
A 59: Temporal distribution of H_2O measurement and the corresponding results from available models for E-AS-05 TW1. The corresponding latitudes are provided on the secondary y-axis. The box model constrains the measurements, therefore, is not featured in the plots.
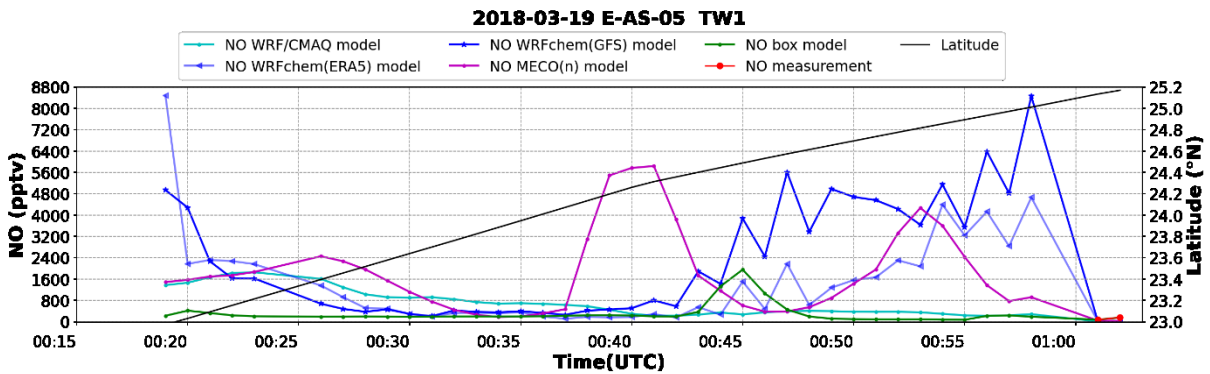
A 60: Temporal distribution of NO measurement and the corresponding results from available models for E-AS-05 TW1. The corresponding latitudes are provided on the secondary y-axis.
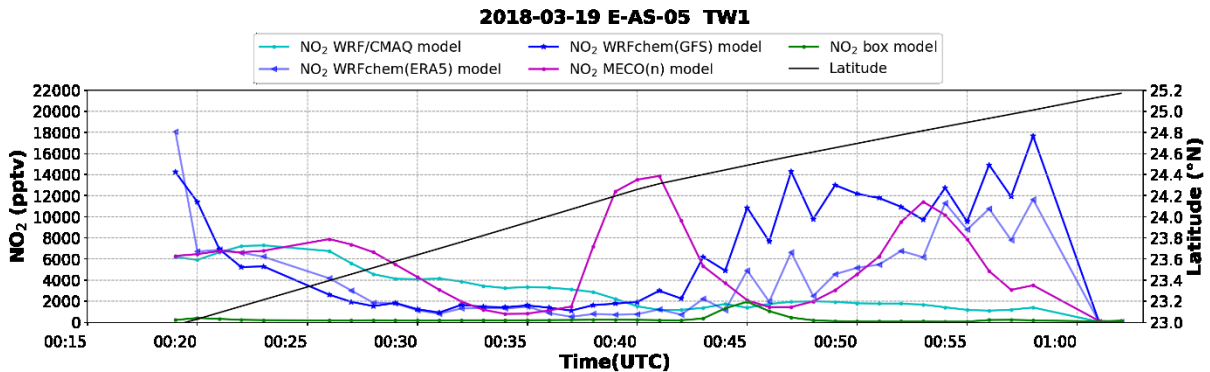
A 61: Temporal distribution of NO₂ results from available models for E-AS-05 TW1. The corresponding latitudes are provided on the secondary y-axis.
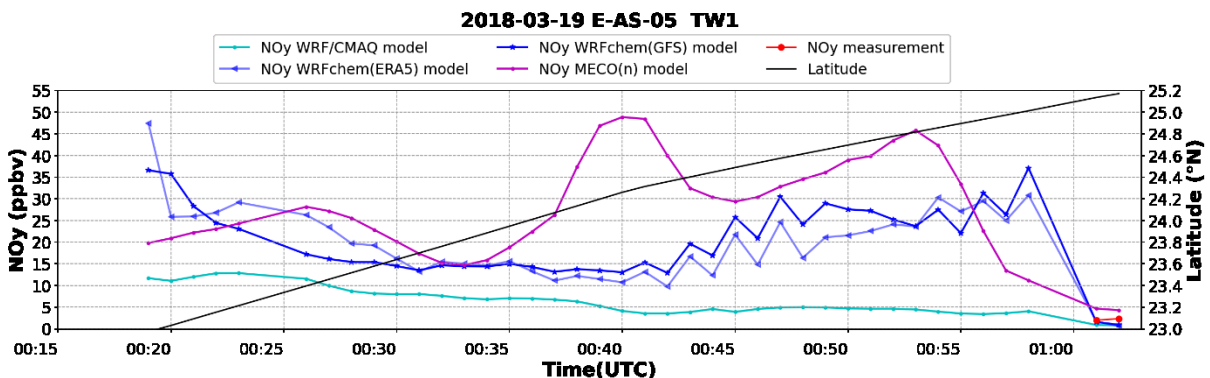
A 62: Temporal distribution of NOy measurement and the corresponding results from available models for E-AS-05 TW1. The corresponding latitudes are provided on the secondary y-axis.
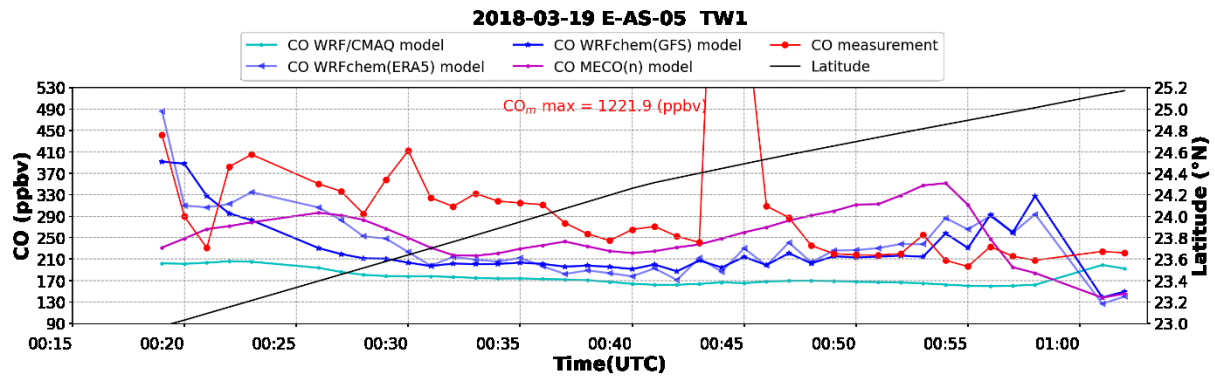
A 63: Temporal distribution of CO measurement and the corresponding results from available models for E-AS-05 TW1. The corresponding latitudes are provided on the secondary y-axis. The box model constrains the measurements, therefore, is not featured in the plots.
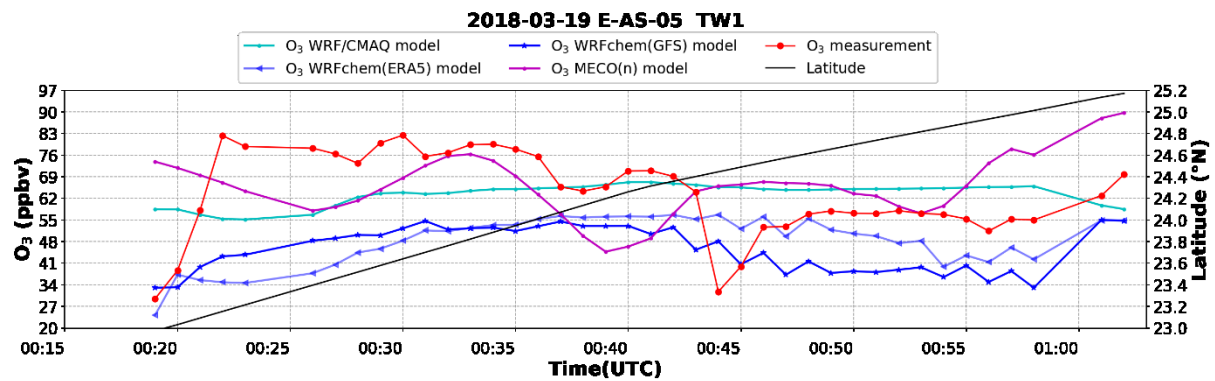
A 64: Temporal distribution of O₃ measurement and the corresponding results from available models for E-AS-05 TW1. The corresponding latitudes are provided on the secondary y-axis. The box model constrains the measurements, therefore, is not featured in the plots.
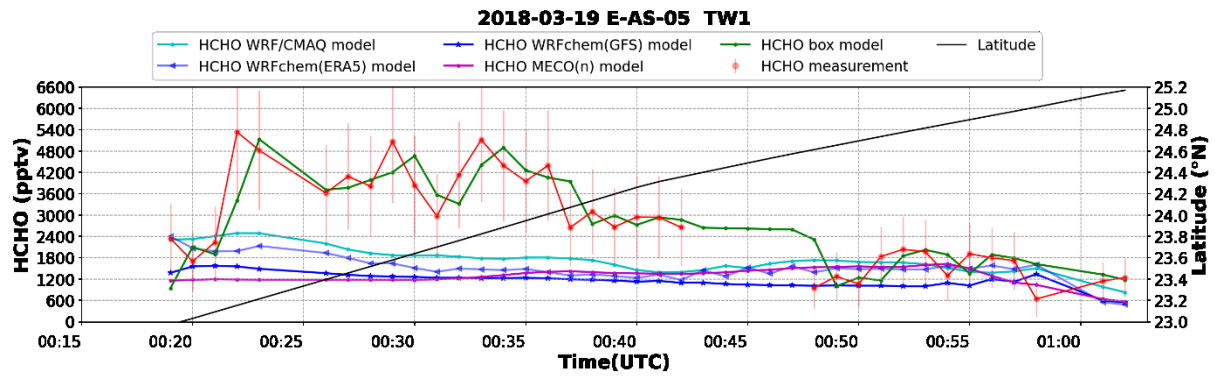
A 65: Temporal distribution of HCHO measurement and the corresponding results from available models for E-AS-05 TW1. The corresponding latitudes are provided on the secondary y-axis.
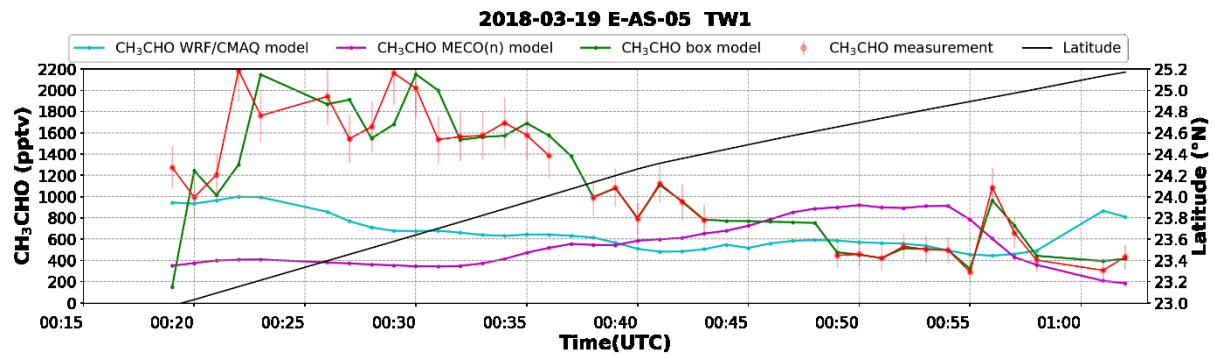
A 66: Temporal distribution of CH₃CHO measurement and the corresponding results from available models for E-AS-05 TW1. The corresponding latitudes are provided on the secondary y-axis.

146
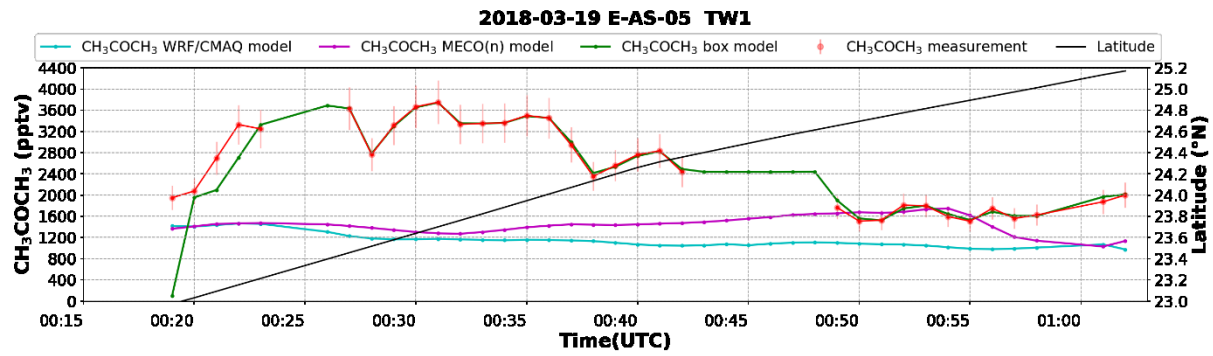
A 67: Temporal distribution of CH₃COCH₃ measurement and the corresponding results from available models for E-AS-05 TW1. The corresponding latitudes are provided on the secondary y-axis.
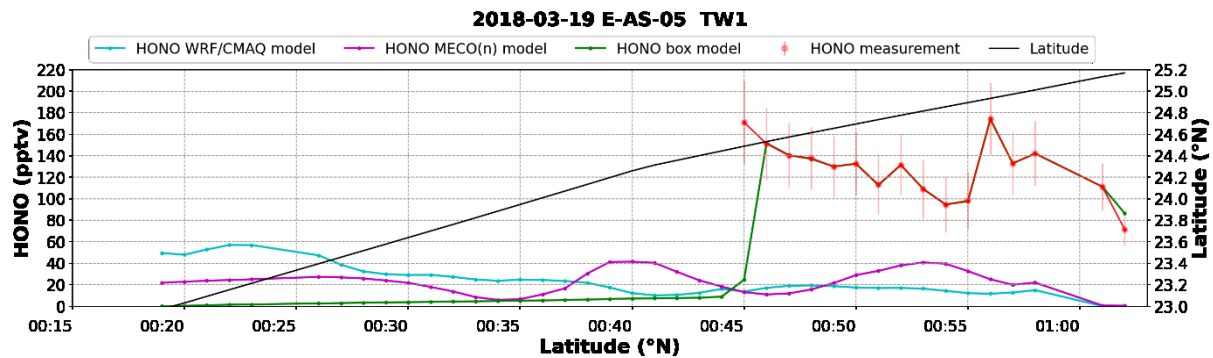
A 68: Temporal distribution of HONO measurement and the corresponding results from available models for E-AS-05 TW1. The corresponding latitudes are provided on the secondary y-axis.
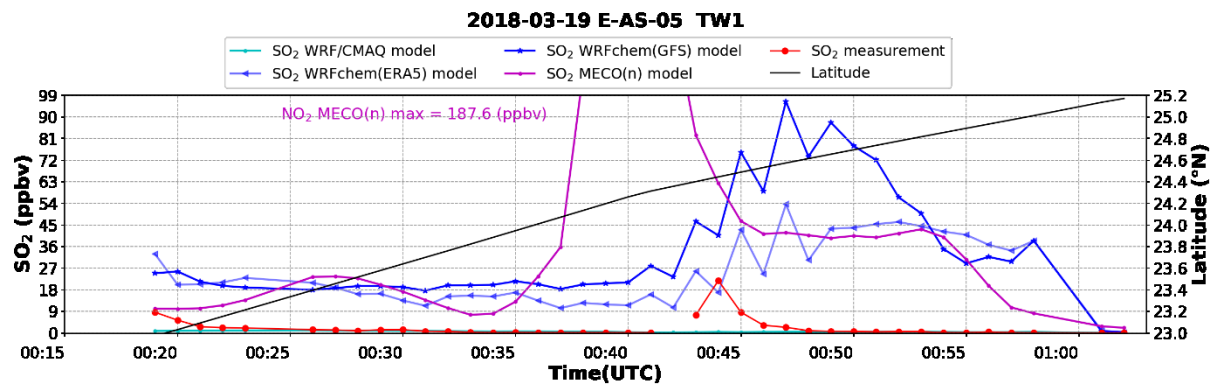
A 69: Temporal distribution of SO₂ measurement and the corresponding results from available models for E-AS-05 TW1. The corresponding latitudes are provided on the secondary y-axis. The box model constrains the measurements, therefore, is not featured in the plots.
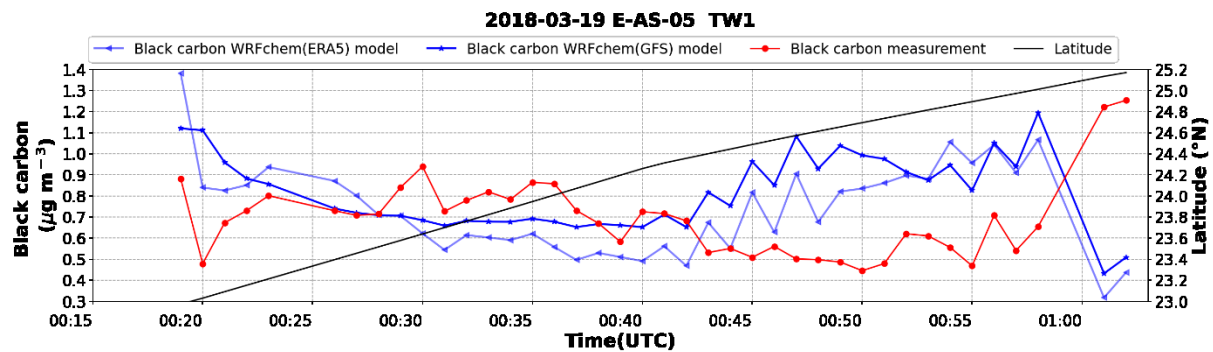
A 70: Temporal distribution of black carbon measurement and the corresponding results from available models for E-AS-05 TW1. The corresponding latitudes are provided on the secondary y-axis. The box model constrains the measurements, therefore, is not featured in the plots.
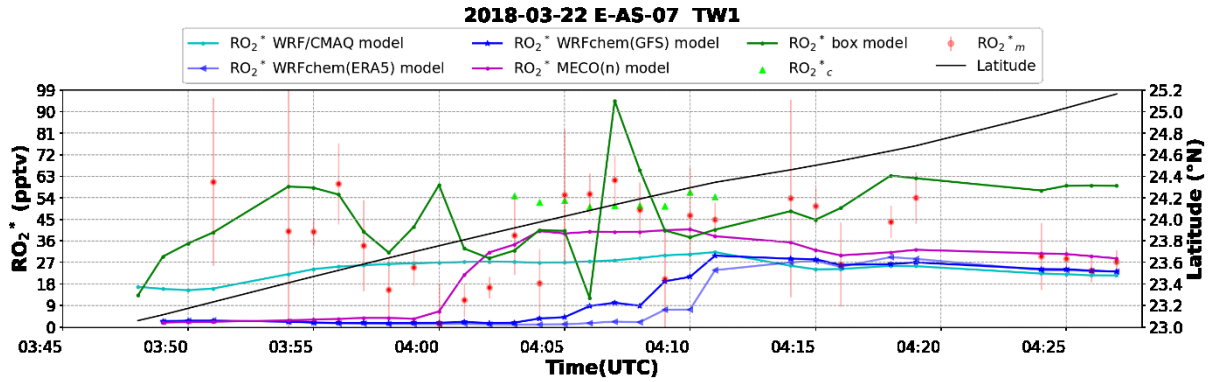
A 71: Temporal distribution of RO_2^* measurement, the corresponding results from available models, and the PSS calculation for E-AS-07 TW1. The corresponding latitudes are provided on the secondary y-axis.
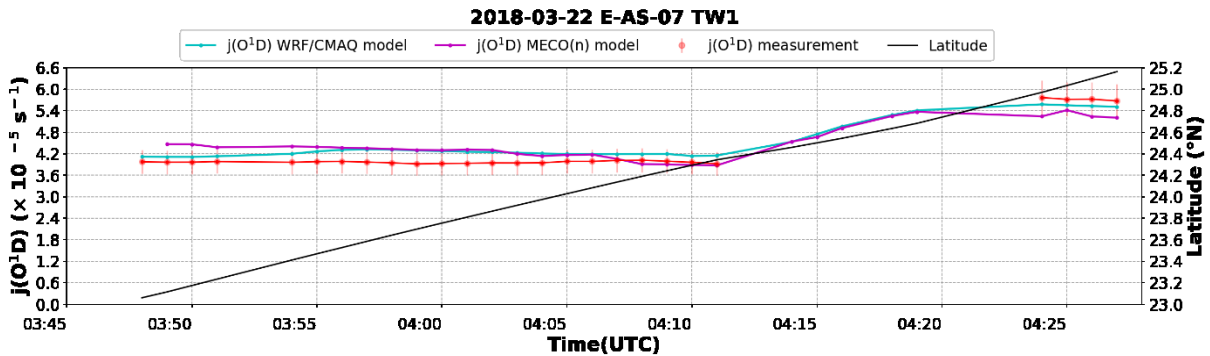
A 72: Temporal distribution of jO^1D measurement and the corresponding results from available models for E-AS-07 TW1. The corresponding latitudes are provided on the secondary y-axis. The box model constrains the measurements, therefore, is not featured in the plots.
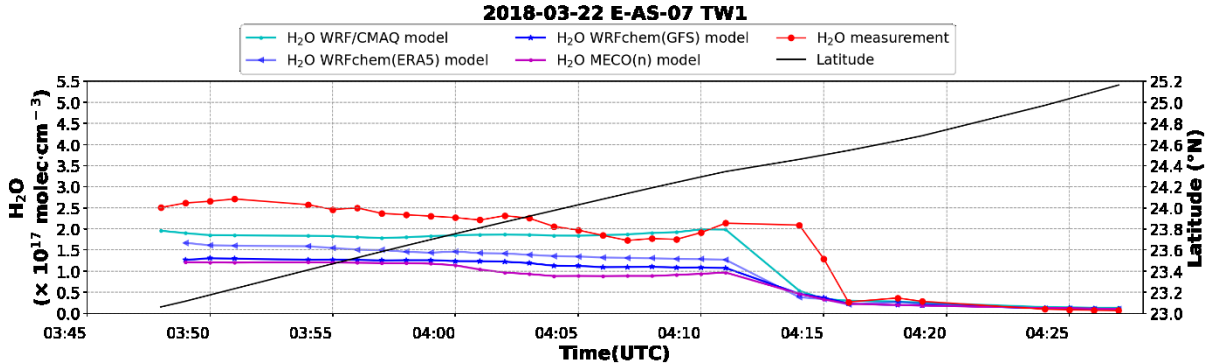
A 73: Temporal distribution of H_2O measurement and the corresponding results from available models for E-AS-07 TW1. The corresponding latitudes are provided on the secondary y-axis. The box model constrains the measurements, therefore, is not featured in the plots.
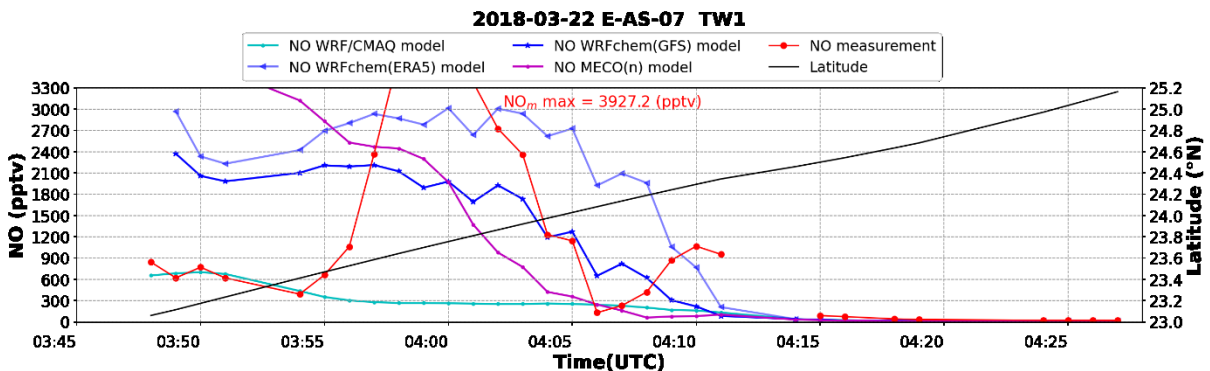
A 74: Temporal distribution of NO measurement and the corresponding results from available models for E-AS-07 TW1. The corresponding latitudes are provided on the secondary y-axis. The box model constrains the measurements, therefore, is not featured in the plots.
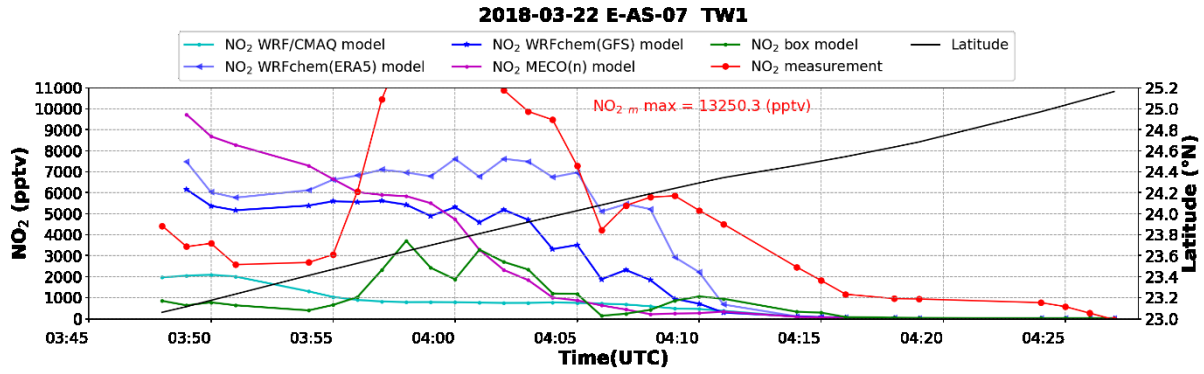
A 75: Temporal distribution of NO₂ measurement and the corresponding results from available models for E-AS-07 TW1. The corresponding latitudes are provided on the secondary y-axis. The NO₂ measurement made by HAIDI.
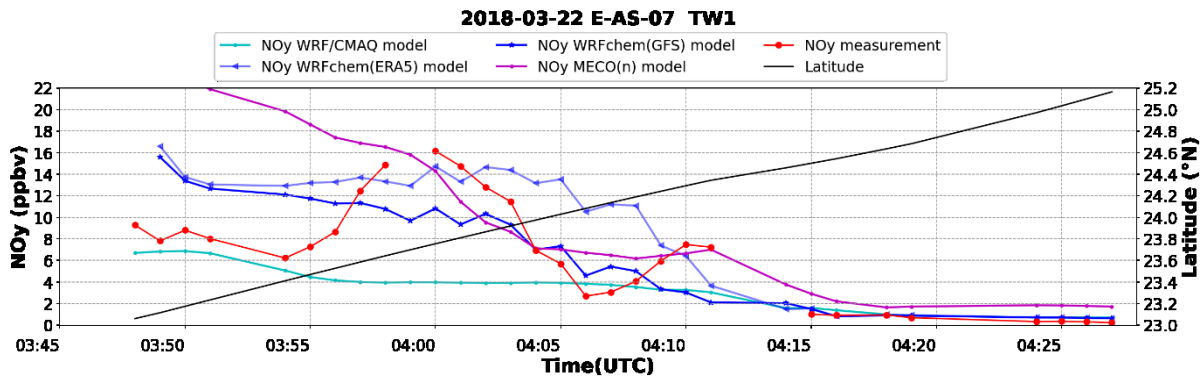
A 76: Temporal distribution of NOy measurement and the corresponding results from available models for E-AS-07 TW1. The corresponding latitudes are provided on the secondary y-axis.
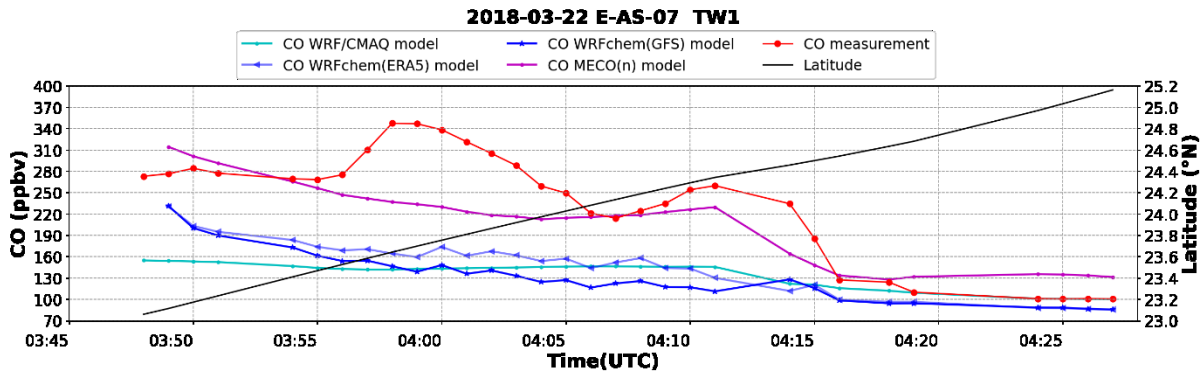
A 77: Temporal distribution of CO measurement and the corresponding results from available models for E-AS-07 TW1. The corresponding latitudes are provided on the secondary y-axis. The box model constrains the measurements, therefore, is not featured in the plots.
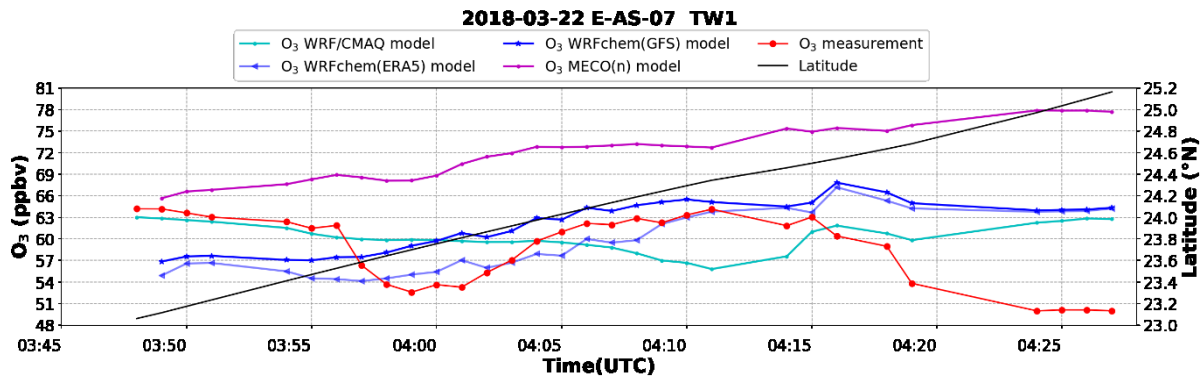
A 78: Temporal distribution of O₃ measurement and the corresponding results from available models for E-AS-07 TW1. The corresponding latitudes are provided on the secondary y-axis. The box model constrains the measurements, therefore, is not featured in the plots.

149
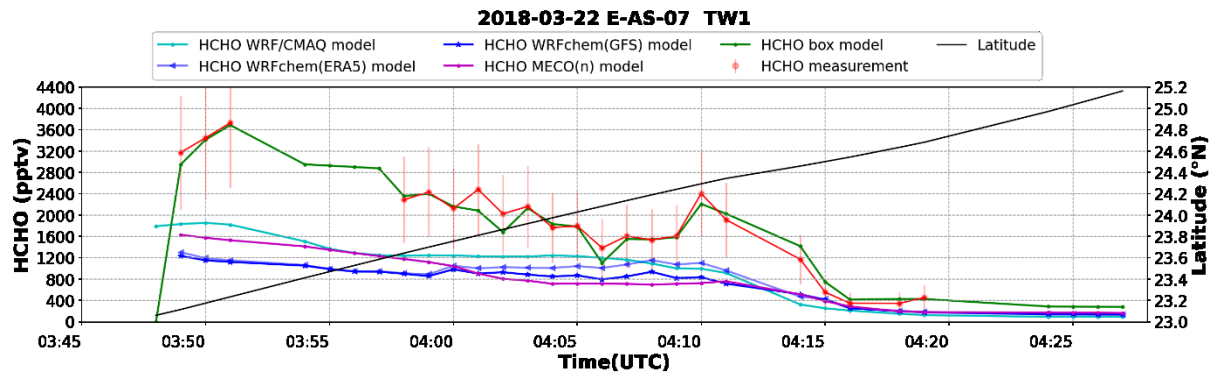
A 79: Temporal distribution of HCHO measurement and the corresponding results from available models for E-AS-07 TW1. The corresponding latitudes are provided on the secondary y-axis.
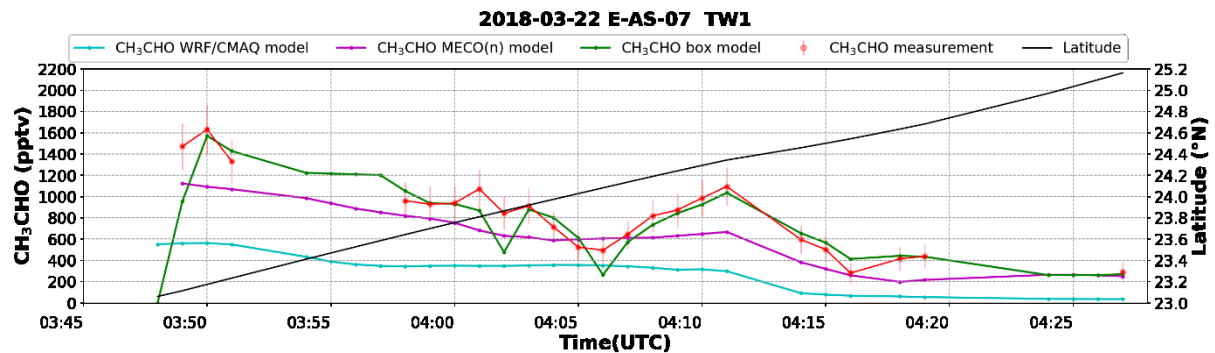
A 80: Temporal distribution of CH₃CHO measurement and the corresponding results from available models for E-AS-07 TW1. The corresponding latitudes are provided on the secondary y-axis.
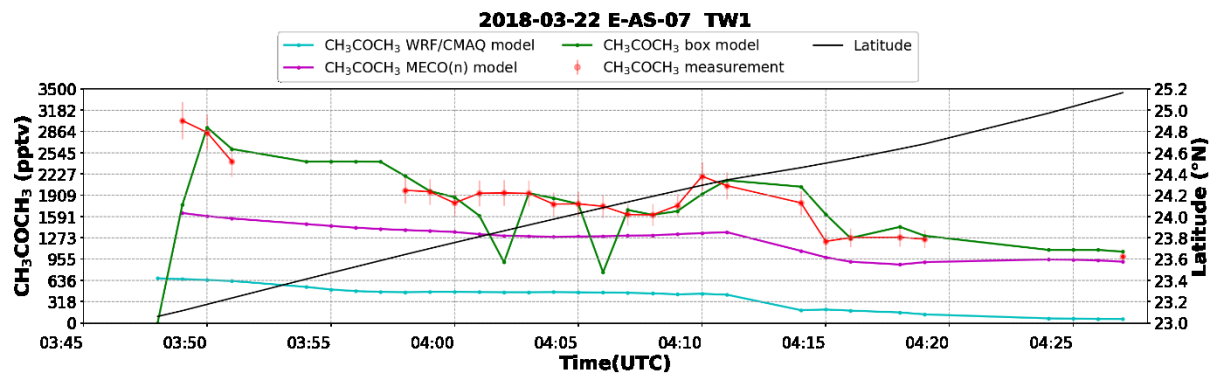
A 81: Temporal distribution of CH₃COCH₃ measurement and the corresponding results from available models for E-AS-07 TW1. The corresponding latitudes are provided on the secondary y-axis.
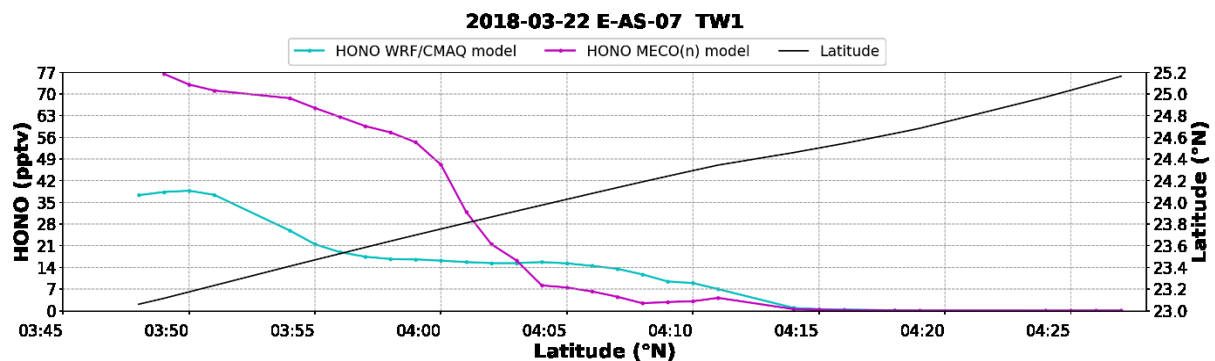
A 82: Temporal distribution of HONO results from available models for E-AS-07 TW1. The corresponding latitudes are provided on the secondary y-axis.
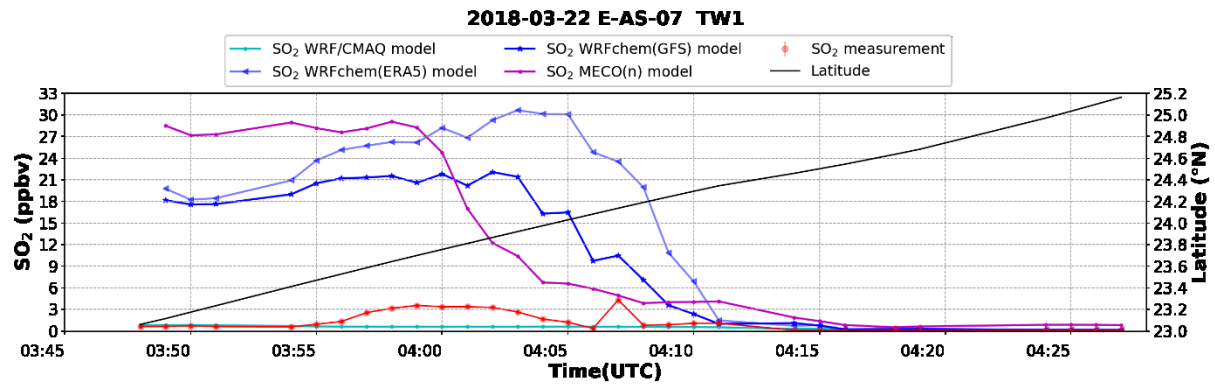
A 83: Temporal distribution of SO₂ measurement and the corresponding results from available models for E-AS-07 TW1. The corresponding latitudes are provided on the secondary y-axis. The box model constrains the measurements, therefore, is not featured in the plots.
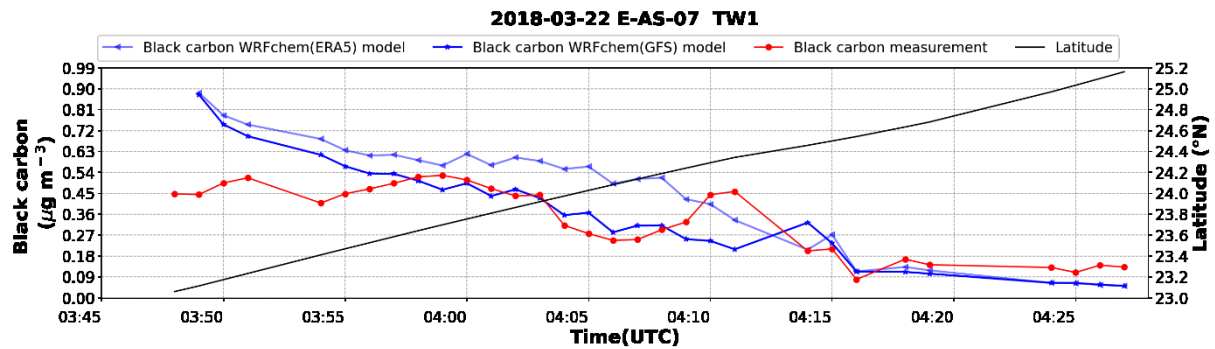
A 84: Temporal distribution of black carbon measurement and the corresponding results from available models for E-AS-07 TW1. The corresponding latitudes are provided on the secondary y-axis. The box model constrains the measurements, therefore, is not featured in the plots.
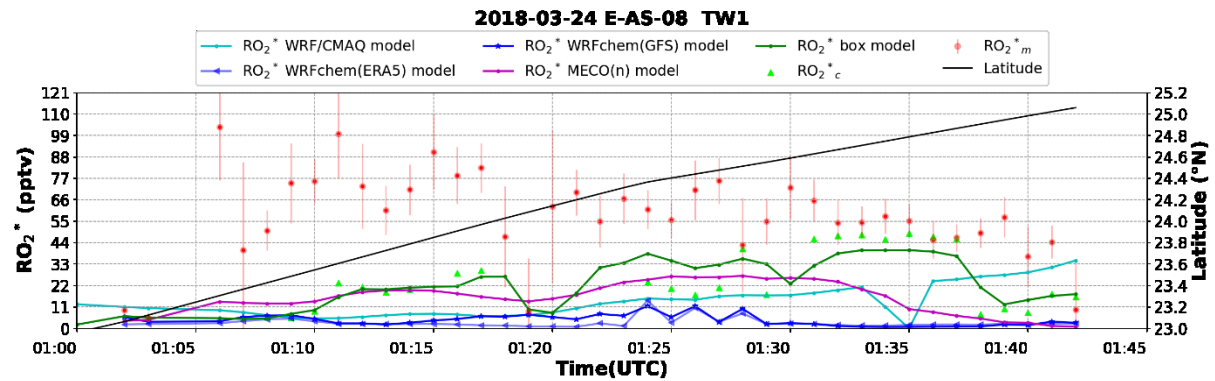
A 85: Temporal distribution of RO_2^* measurement, the corresponding results from available models, and the PSS calculation for E-AS-08 TW1. The corresponding latitudes are provided on the secondary y-axis.
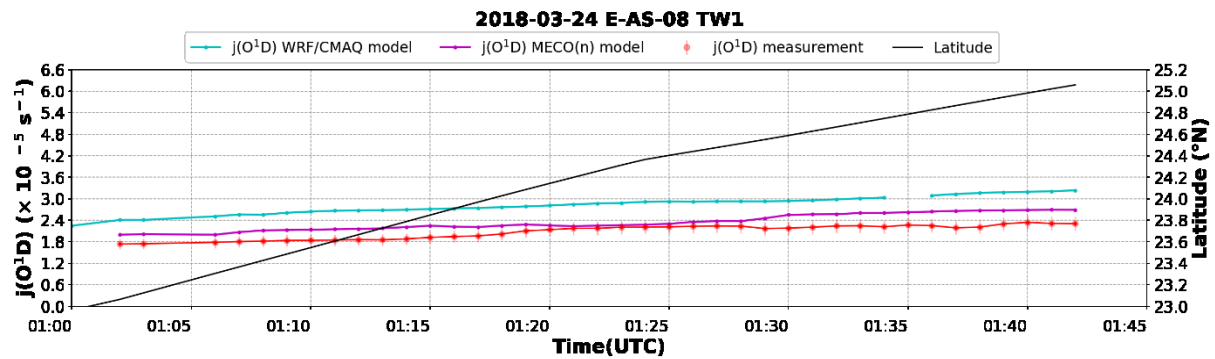
A 86: Temporal distribution of jO^1D measurement and the corresponding results from available models for E-AS-08 TW1. The corresponding latitudes are provided on the secondary y-axis. The box model constrains the measurements, therefore, is not featured in the plots.

151
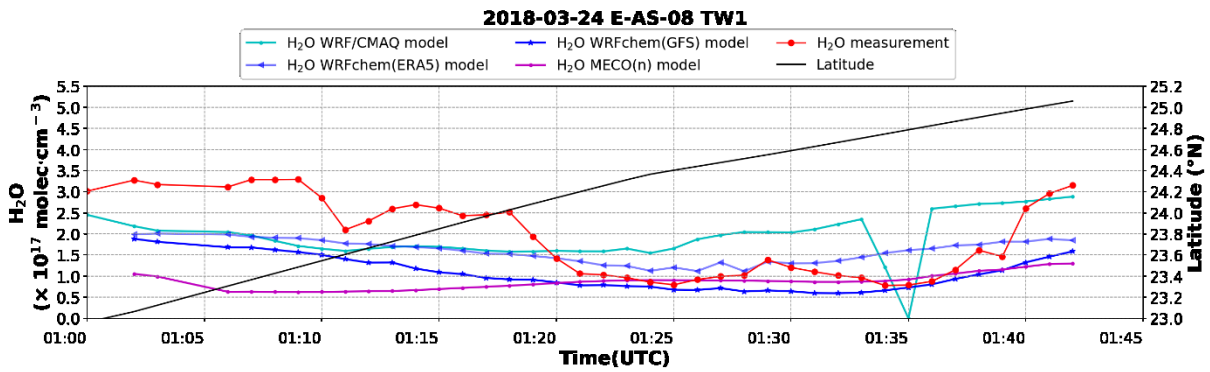
A 87: Temporal distribution of H₂O measurement and the corresponding results from available models for E-AS-08 TW1. The corresponding latitudes are provided on the secondary y-axis. The box model constrains the measurements, therefore, is not featured in the plots.
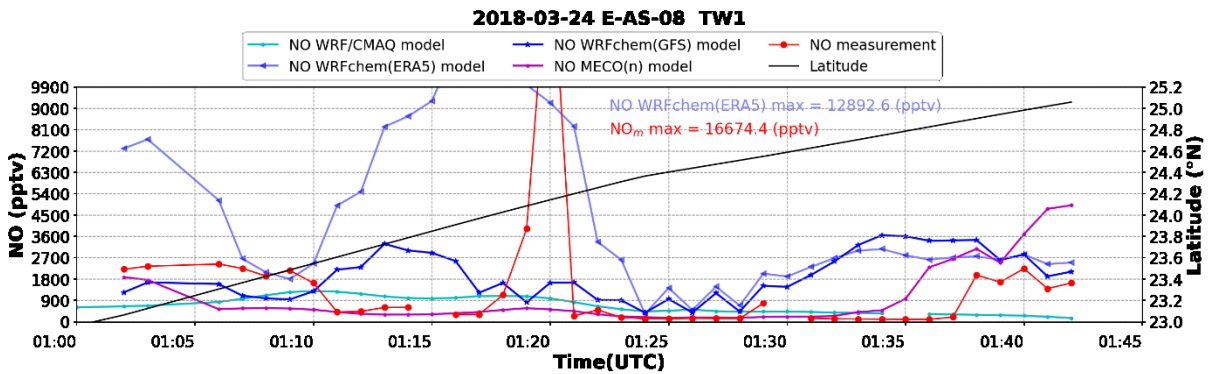
A 88: Temporal distribution of NO measurement and the corresponding results from available models for E-AS-08 TW1. The corresponding latitudes are provided on the secondary y-axis. The box model constrains the measurements, therefore, is not featured in the plots.
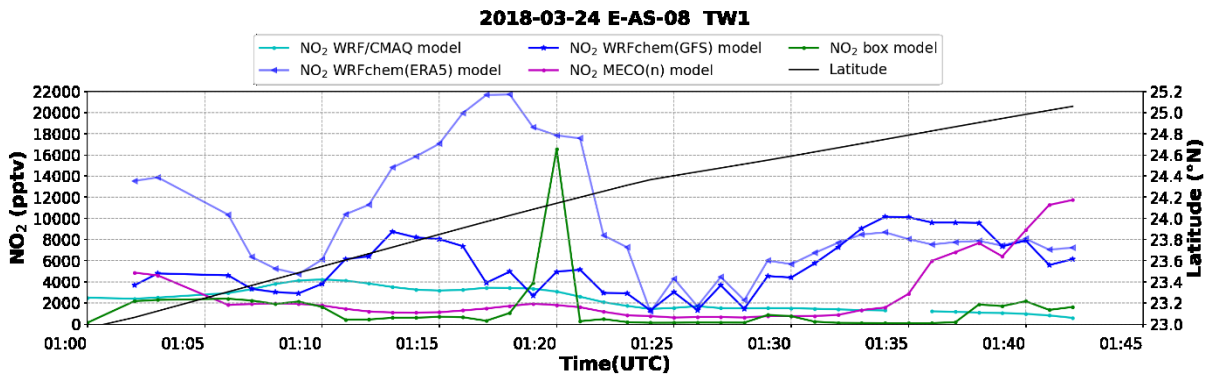
A 89: Temporal distribution of NO₂ results from available models for E-AS-08 TW1. The corresponding latitudes are provided on the secondary y-axis.
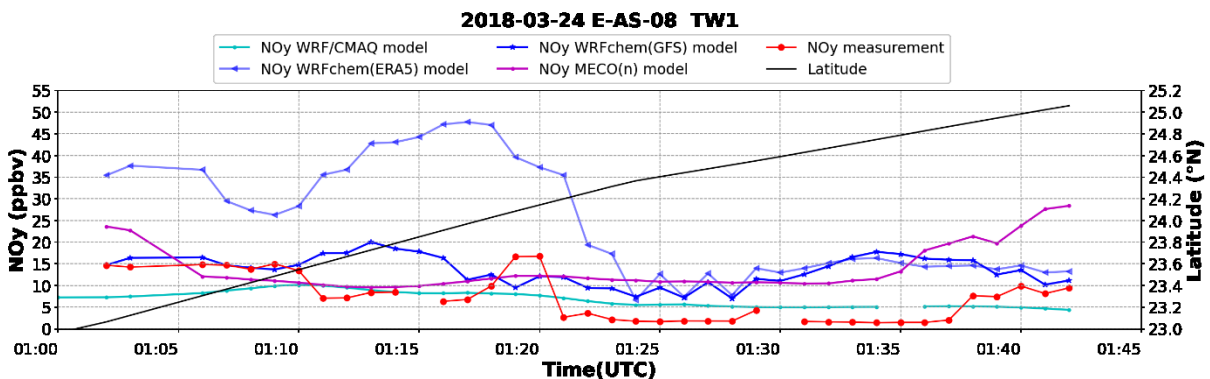
A 90: Temporal distribution of NOy measurement and the corresponding results from available models for E-AS-08 TW1. The corresponding latitudes are provided on the secondary y-axis.

152
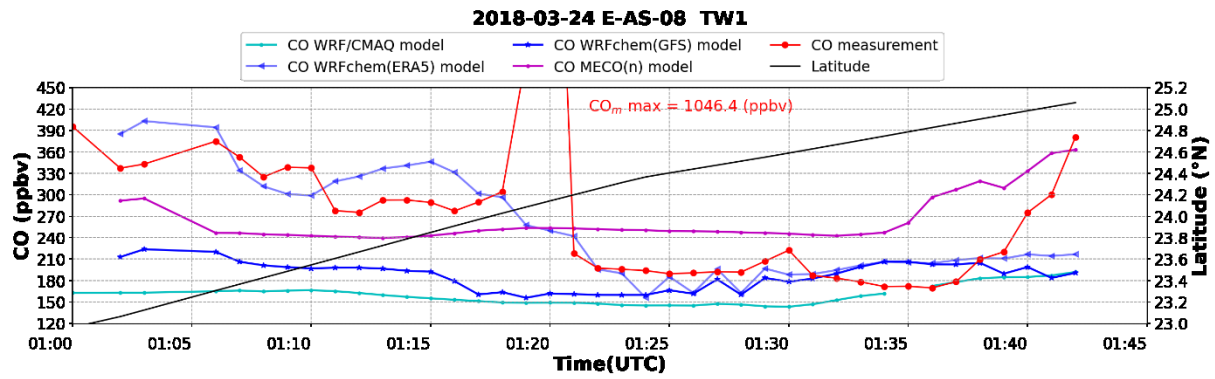
A 91: Temporal distribution of CO measurement and the corresponding results from available models for E-AS-08 TW1. The corresponding latitudes are provided on the secondary y-axis. The box model constrains the measurements, therefore, is not featured in the plots.
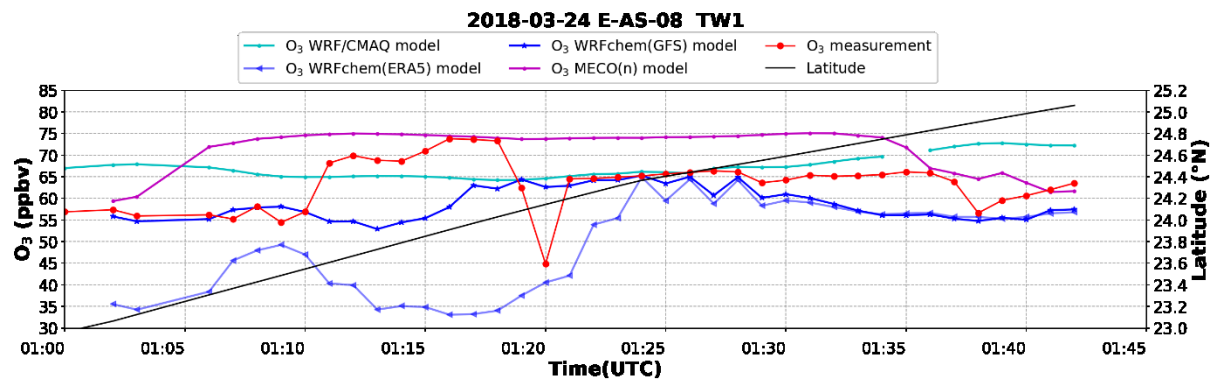
A 92: Temporal distribution of O_3 measurement and the corresponding results from available models for E-AS-08 TW1. The corresponding latitudes are provided on the secondary y-axis. The box model constrains the measurements, therefore, is not featured in the plots.
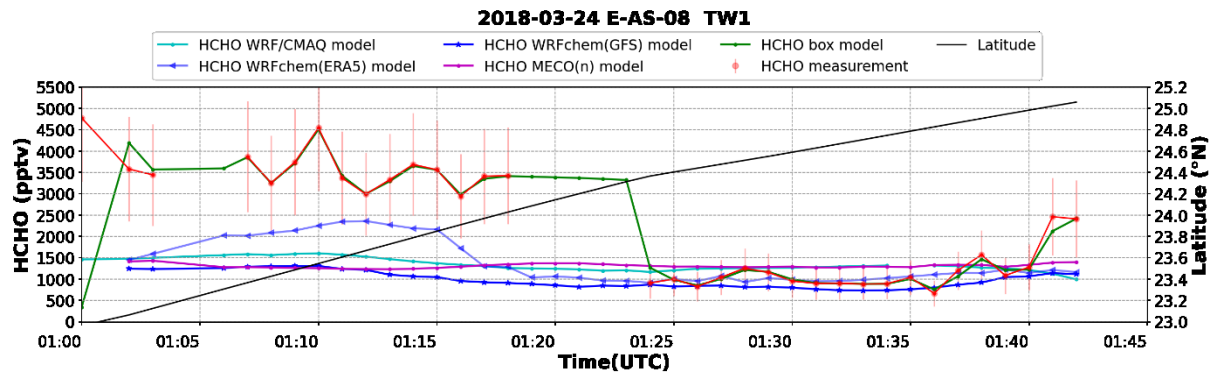
A 93: Temporal distribution of HCHO measurement and the corresponding results from available models for E-AS-08 TW1. The corresponding latitudes are provided on the secondary y-axis.
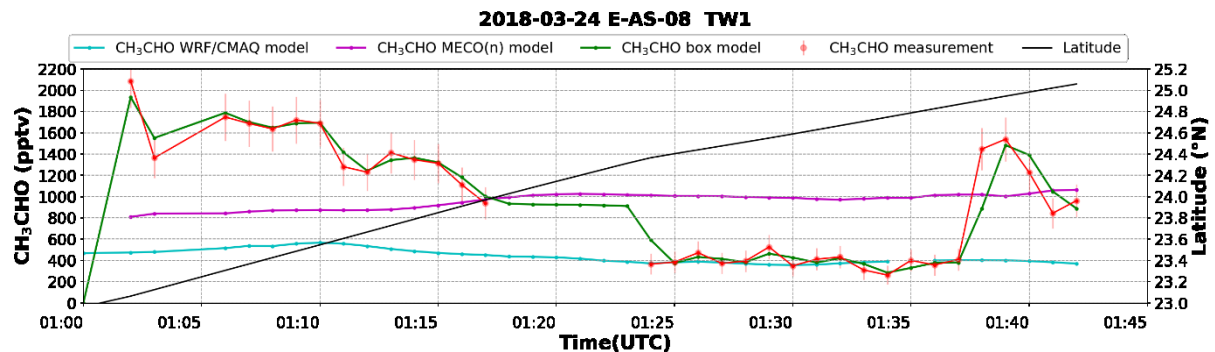
A 94: Temporal distribution of CH_3CHO measurement and the corresponding results from available models for E-AS-08 TW1. The corresponding latitudes are provided on the secondary y-axis.
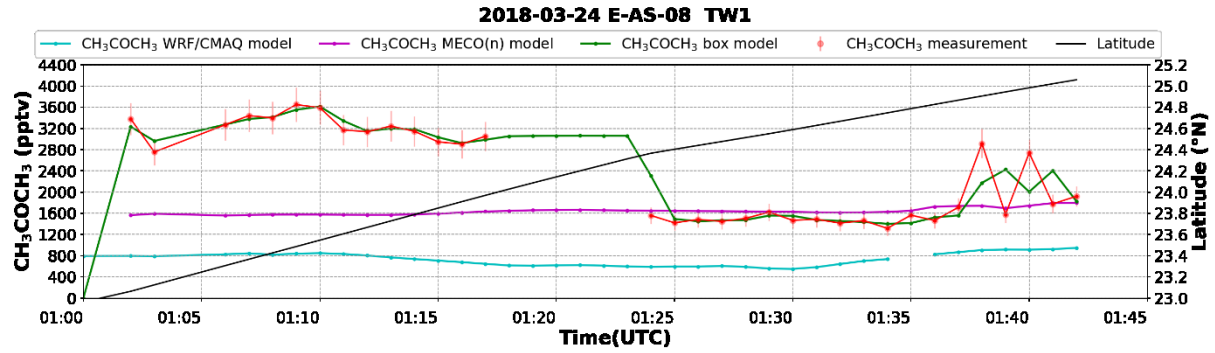
A 95: Temporal distribution of CH₃COCH₃ measurement and the corresponding results from available models for E-AS-08 TW1. The corresponding latitudes are provided on the secondary y-axis.
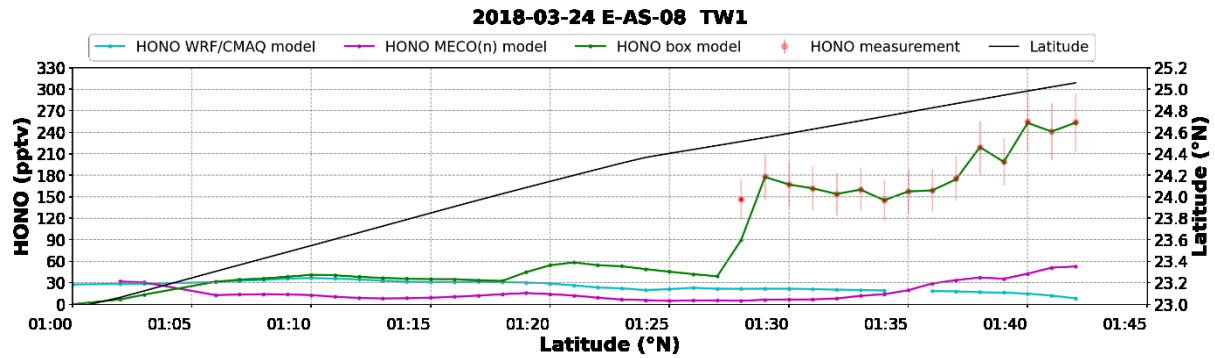
A 96: Temporal distribution of HONO measurement and the corresponding results from available models for E-AS-08 TW1. The corresponding latitudes are provided on the secondary y-axis.
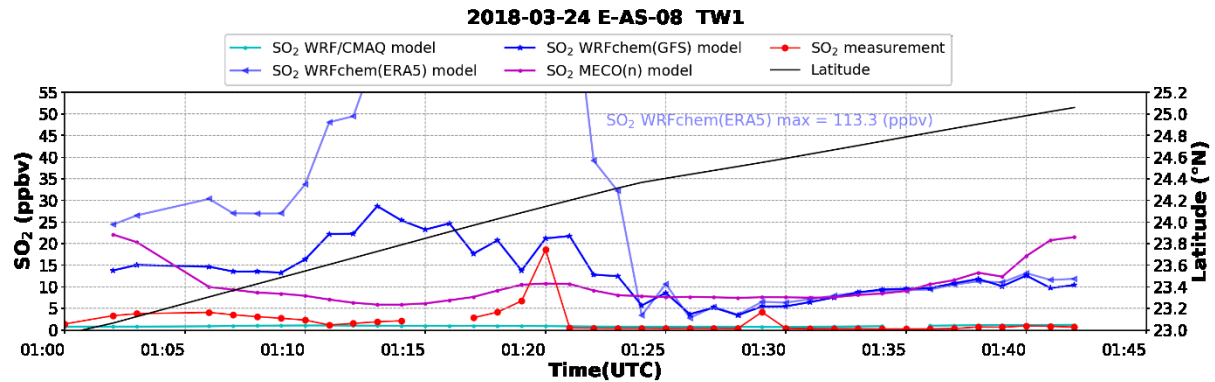
A 97: Temporal distribution of SO₂ measurement and the corresponding results from available models for E-AS-08 TW1. The corresponding latitudes are provided on the secondary y-axis. The box model constrains the measurements, therefore, is not featured in the plots.
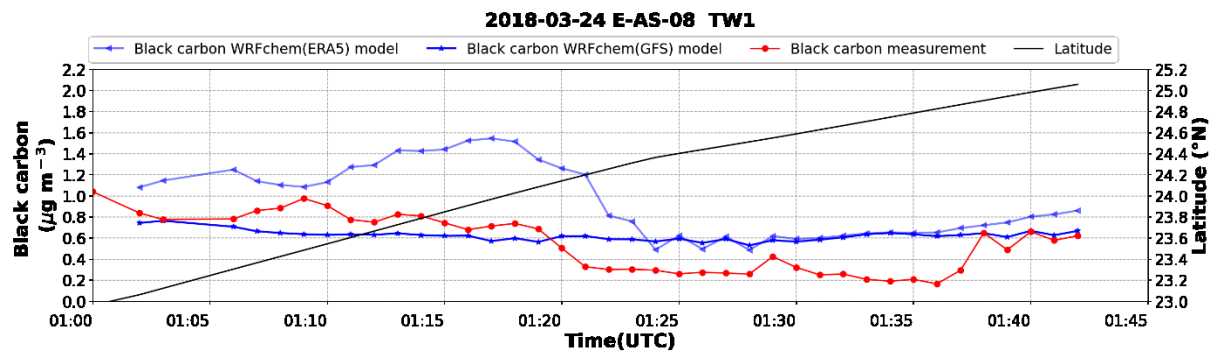
A 98: Temporal distribution of black carbon measurement and the corresponding results from available models for E-AS-08 TW1. The corresponding latitudes are provided on the secondary y-axis. The box model constrains the measurements, therefore, is not featured in the plots.

154
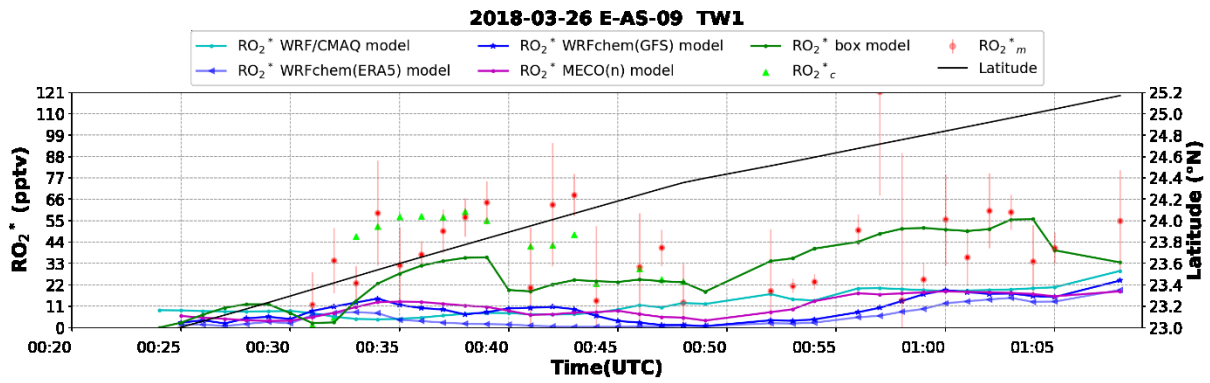
A 99: Temporal distribution of RO_2^* measurement, the corresponding results from available models, and the PSS calculation for E-AS-09 TW1. The corresponding latitudes are provided on the secondary y-axis.
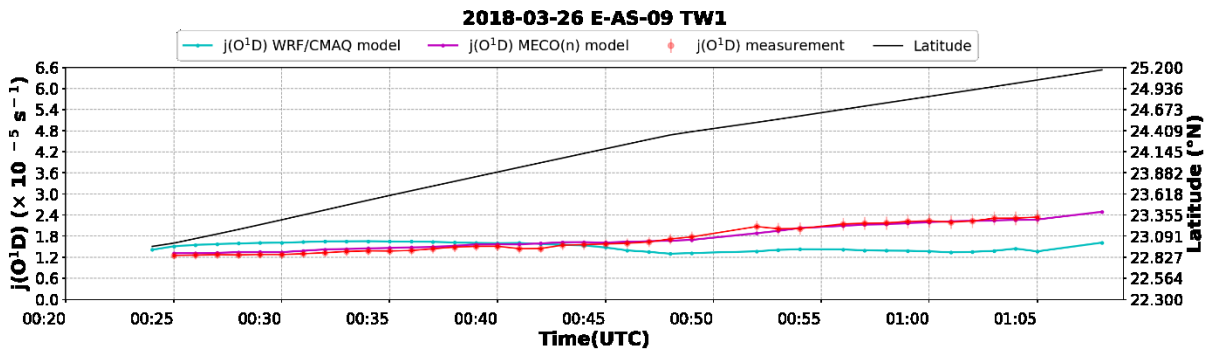
A 100: Temporal distribution of jO^1D measurement and the corresponding results from available models for E-AS-09 TW1. The corresponding latitudes are provided on the secondary y-axis. The box model constrains the measurements, therefore, is not featured in the plots.
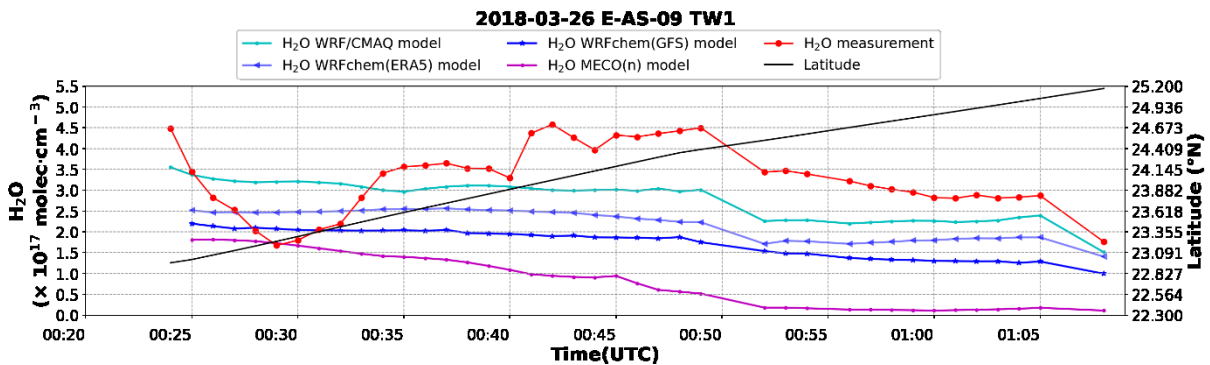
A 101: Temporal distribution of H_2O measurement and the corresponding results from available models for E-AS-09 TW1. The corresponding latitudes are provided on the secondary y-axis. The box model constrains the measurements, therefore, is not featured in the plots.
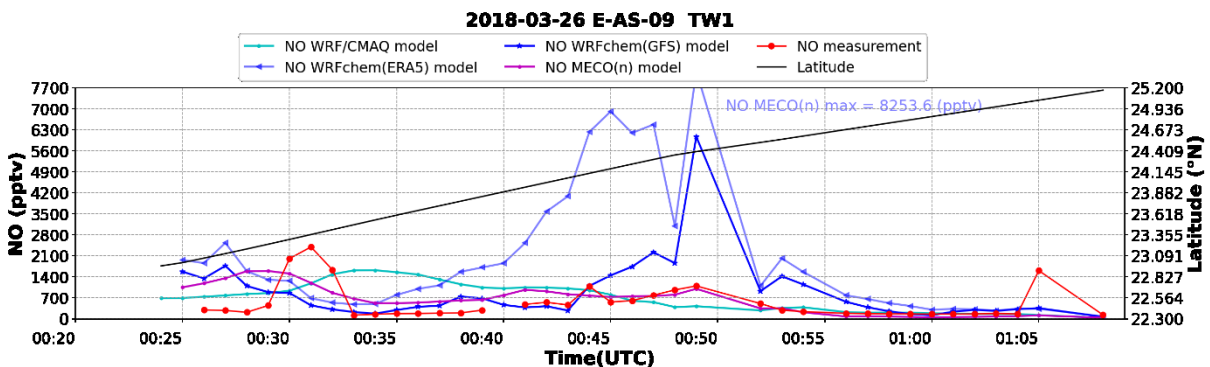
A 102: Temporal distribution of NO measurement and the corresponding results from available models for E-AS-09 TW1. The corresponding latitudes are provided on the secondary y-axis. The box model constrains the measurements, therefore, is not featured in the plots.
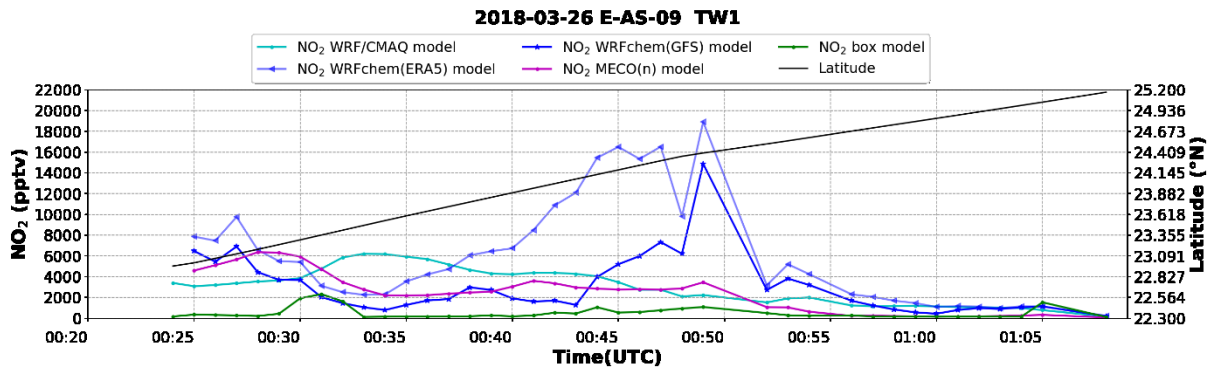
A 103: Temporal distribution of NO₂ results from available models for E-AS-09 TW1. The corresponding latitudes are provided on the secondary y-axis.
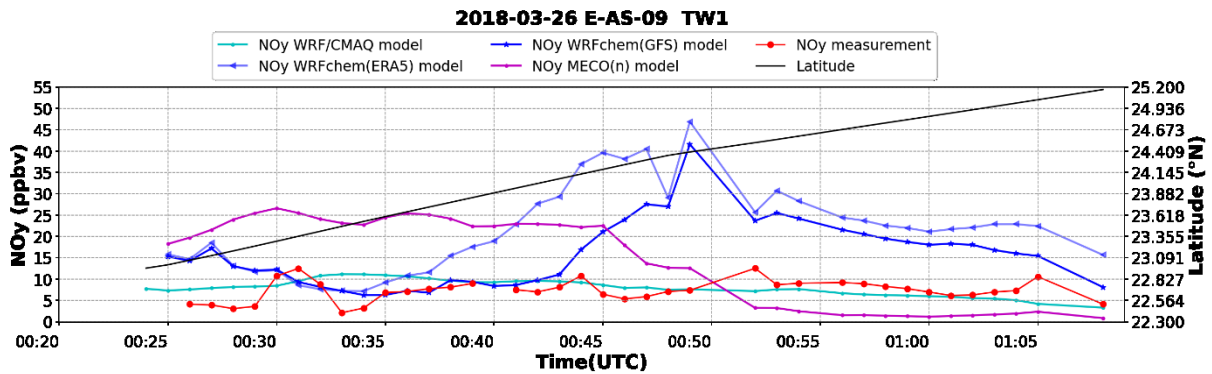
A 104: Temporal distribution of NOy measurement and the corresponding results from available models for E-AS-09 TW1. The corresponding latitudes are provided on the secondary y-axis.
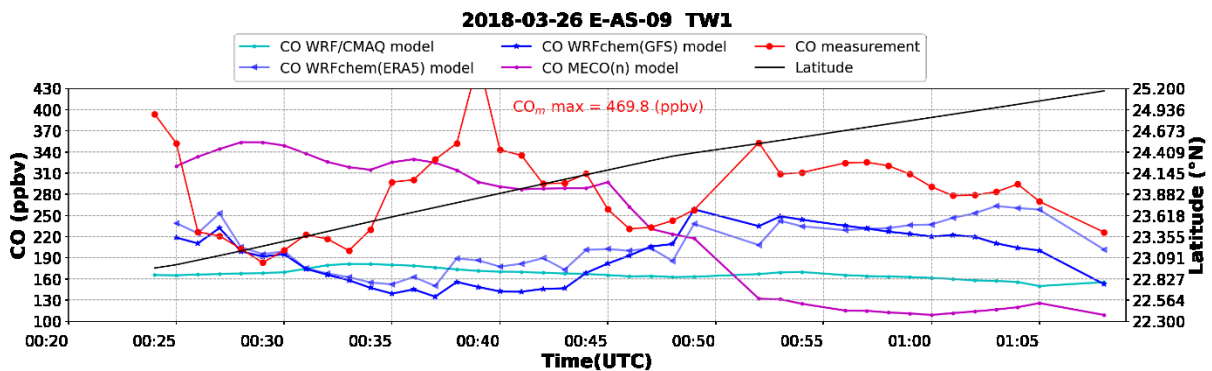
A 105: Temporal distribution of CO measurement and the corresponding results from available models for E-AS-09 TW1. The corresponding latitudes are provided on the secondary y-axis. The box model constrains the measurements, therefore, is not featured in the plots.
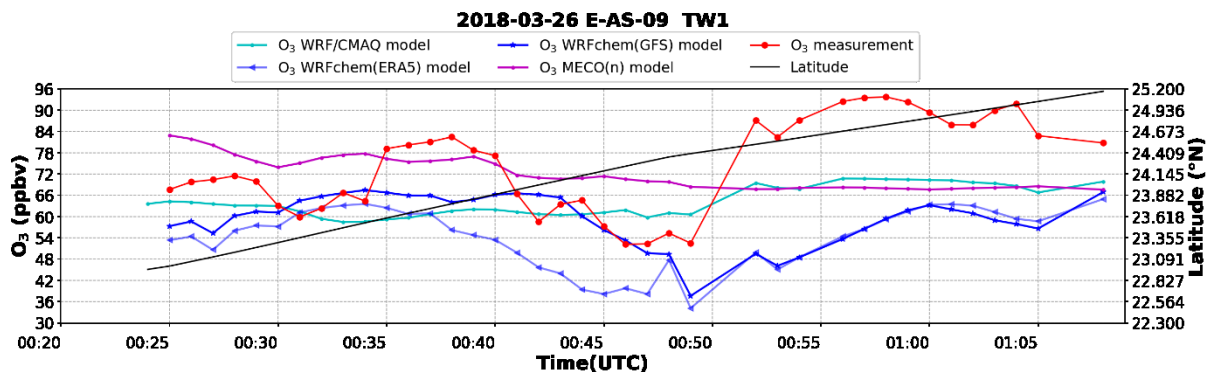
A 106: Temporal distribution of O₃ measurement and the corresponding results from available models for E-AS-09 TW1. The corresponding latitudes are provided on the secondary y-axis. The box model constrains the measurements, therefore, is not featured in the plots.
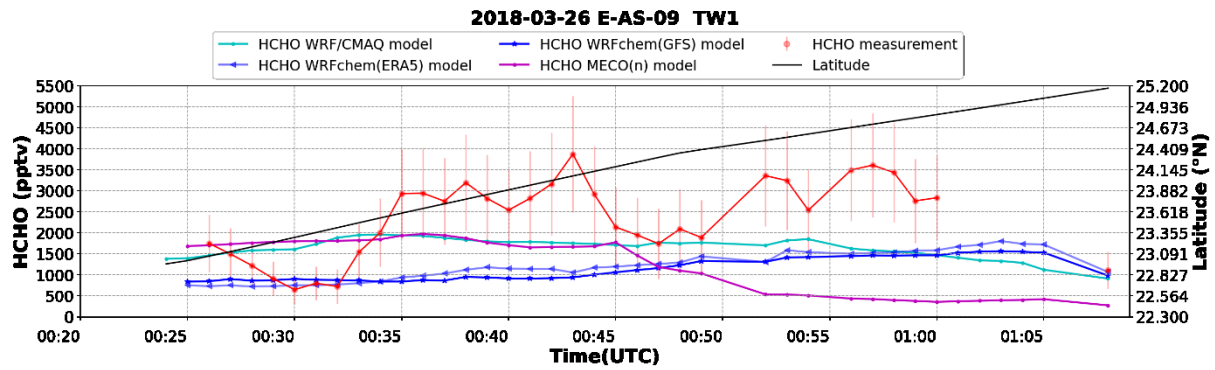
A 107: Temporal distribution of HCHO measurement and the corresponding results from available models for E-AS-09 TW1. The corresponding latitudes are provided on the secondary y-axis. The box model constrains the measurements, therefore, is not featured in the plots.
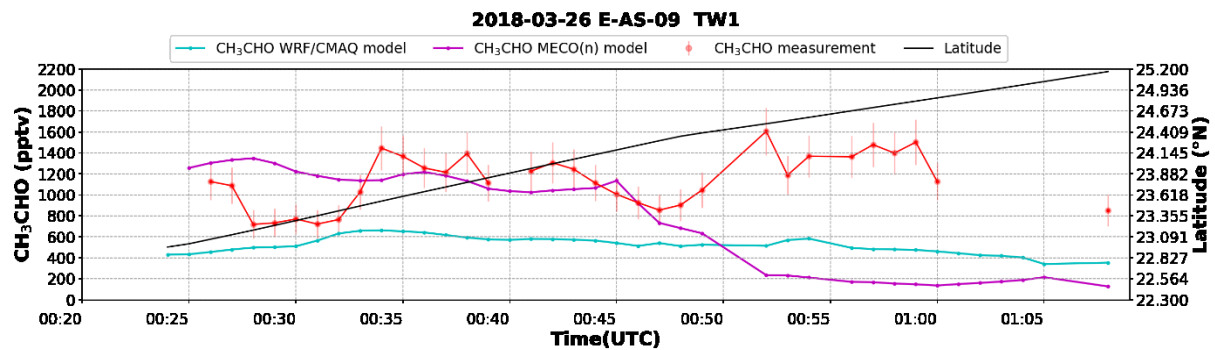
A 108: Temporal distribution of CH₃CHO measurement and the corresponding results from available models for E-AS-09 TW1. The corresponding latitudes are provided on the secondary y-axis. The box model constrains the measurements, therefore, is not featured in the plots.
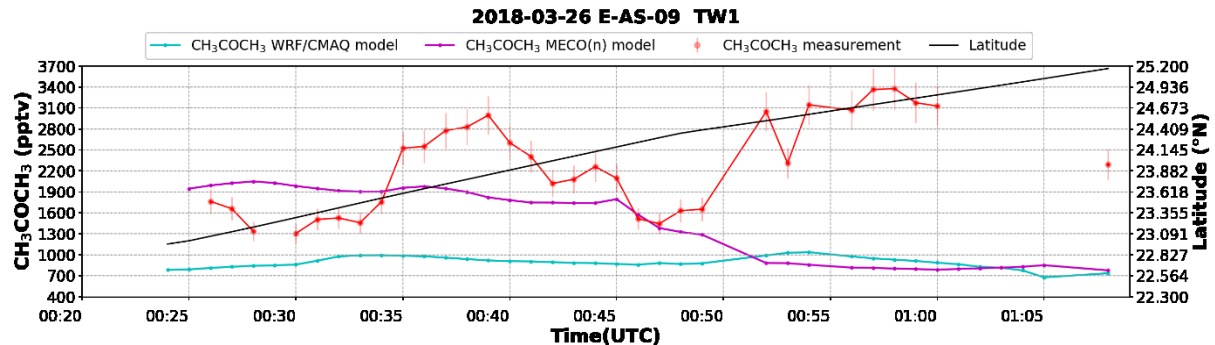
A 109: Temporal distribution of CH₃COCH₃ measurement and the corresponding results from available models for E-AS-09 TW1. The corresponding latitudes are provided on the secondary y-axis. The box model constrains the measurements, therefore, is not featured in the plots.
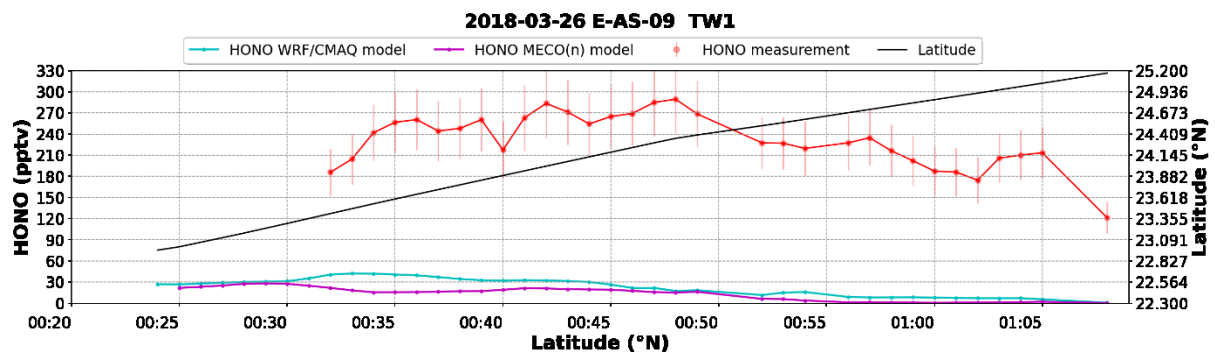
A 110: Temporal distribution of HONO measurement and the corresponding results from available models for E-AS-09 TW1. The corresponding latitudes are provided on the secondary y-axis. The box model constrains the measurements, therefore, is not featured in the plots.
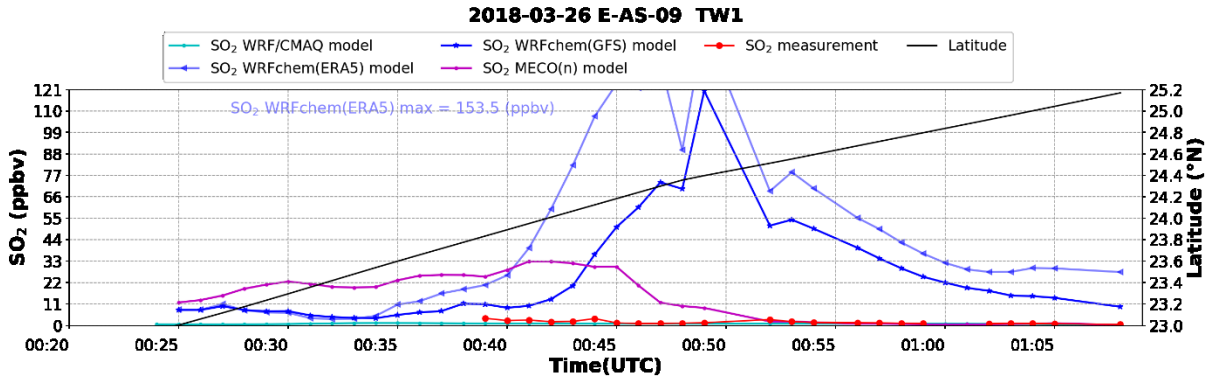
A 111: Temporal distribution of SO₂ measurement and the corresponding results from available models for E-AS-09 TW1. The corresponding latitudes are provided on the secondary y-axis. The box model constrains the measurements, therefore, is not featured in the plots.
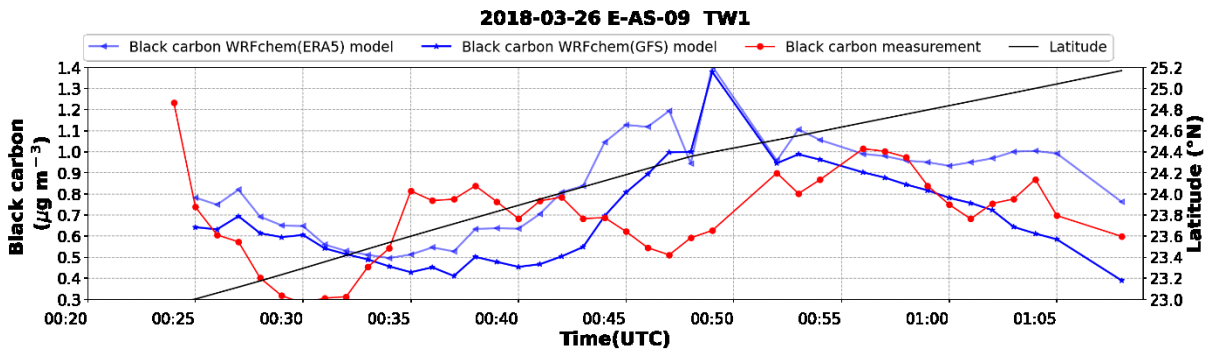
A 112: Temporal distribution of black carbon measurement and the corresponding results from available models for E-AS-09 TW1. The corresponding latitudes are provided on the secondary y-axis. The box model constrains the measurements, therefore, is not featured in the plots.
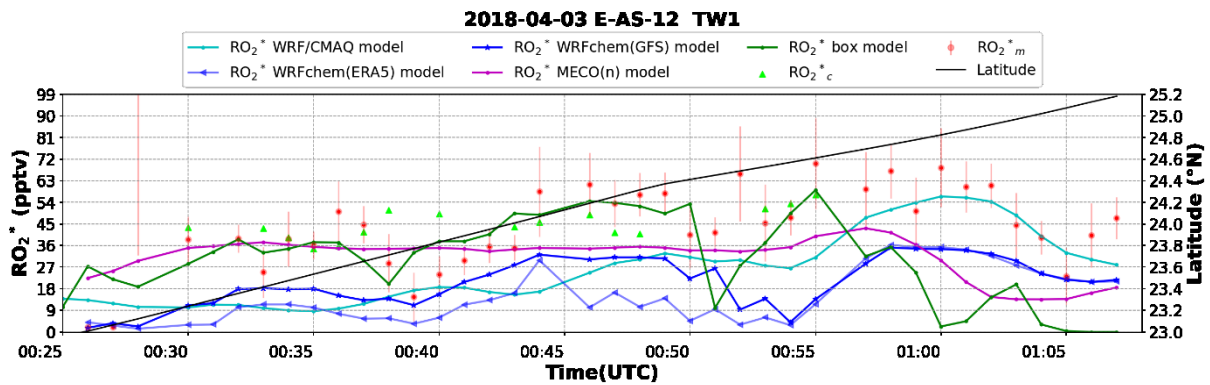
A 113: Temporal distribution of RO_2^* measurement, the corresponding results from available models, and the PSS calculation for E-AS-12 TW1. The corresponding latitudes are provided on the secondary y-axis.
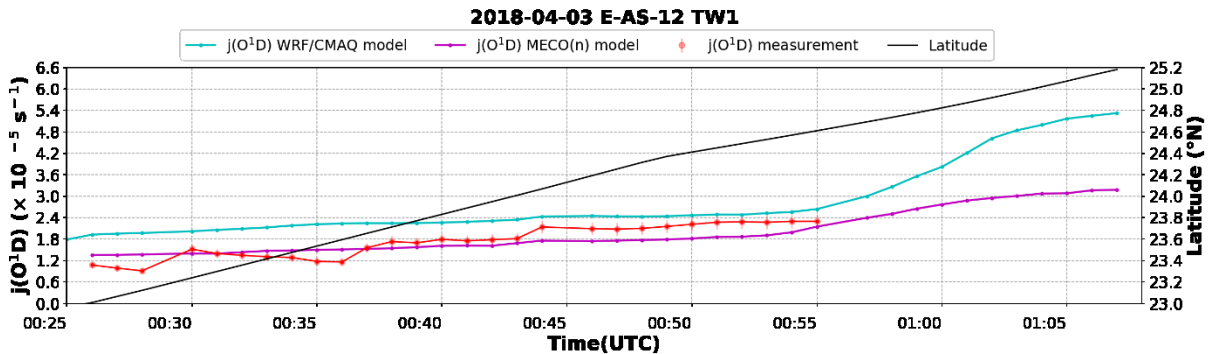
A 114: Temporal distribution of jO^1D measurement and the corresponding results from available models for E-AS-12 TW1. The corresponding latitudes are provided on the secondary y-axis. The box model constrains the measurements, therefore, is not featured in the plots.

158
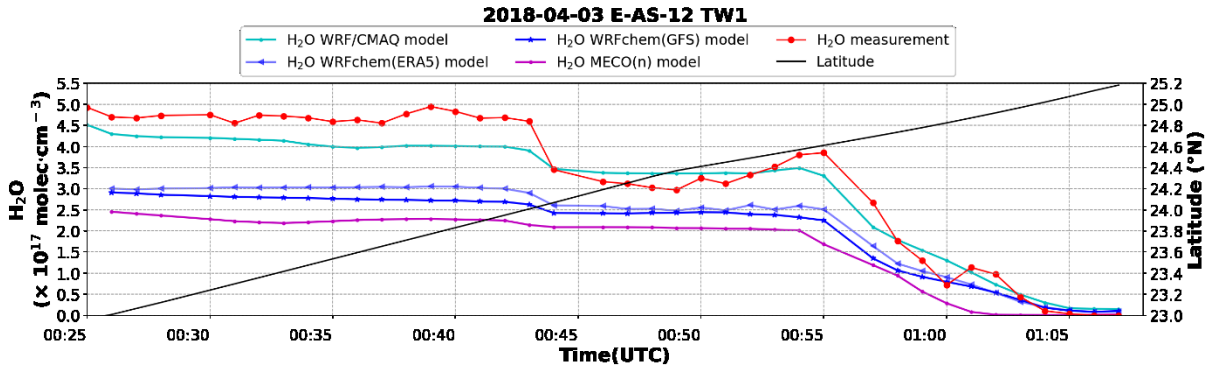
A 115: Temporal distribution of H_2O measurement and the corresponding results from available models for E-AS-12 TW1. The corresponding latitudes are provided on the secondary y-axis. The box model constrains the measurements, therefore, is not featured in the plots.
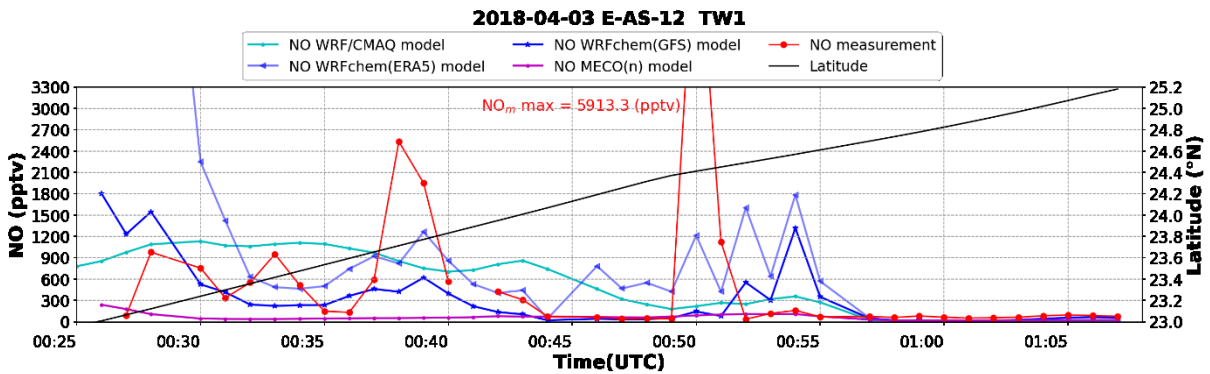
A 116: Temporal distribution of NO measurement and the corresponding results from available models for E-AS-12 TW1. The corresponding latitudes are provided on the secondary y-axis. The box model constrains the measurements, therefore, is not featured in the plots.
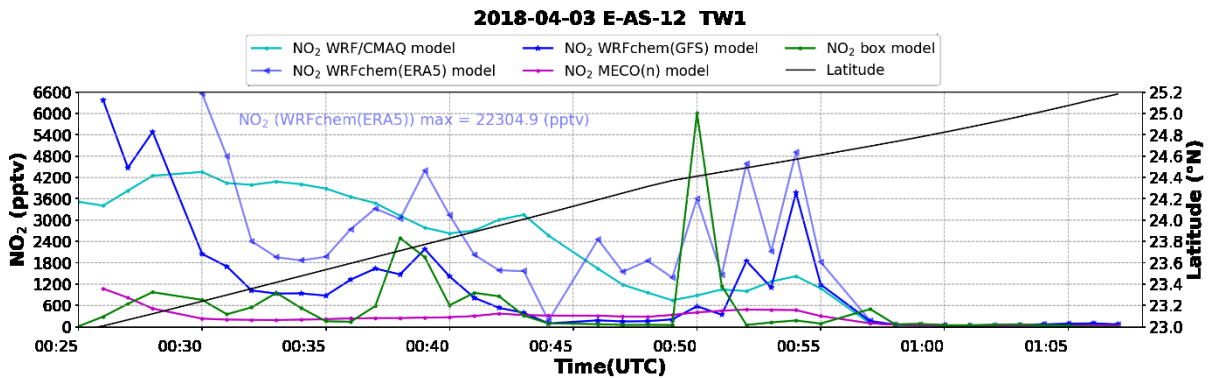
A 117: Temporal distribution of NO_2 results from available models for E-AS-12 TW1. The corresponding latitudes are provided on the secondary y-axis.
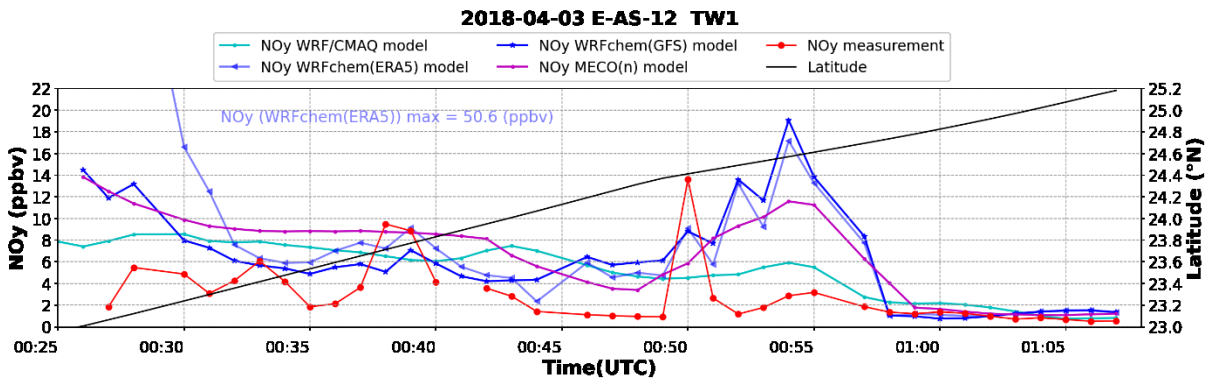
A 118: Temporal distribution of NOy measurement and the corresponding results from available models for E-AS-12 TW1. The corresponding latitudes are provided on the secondary y-axis

159
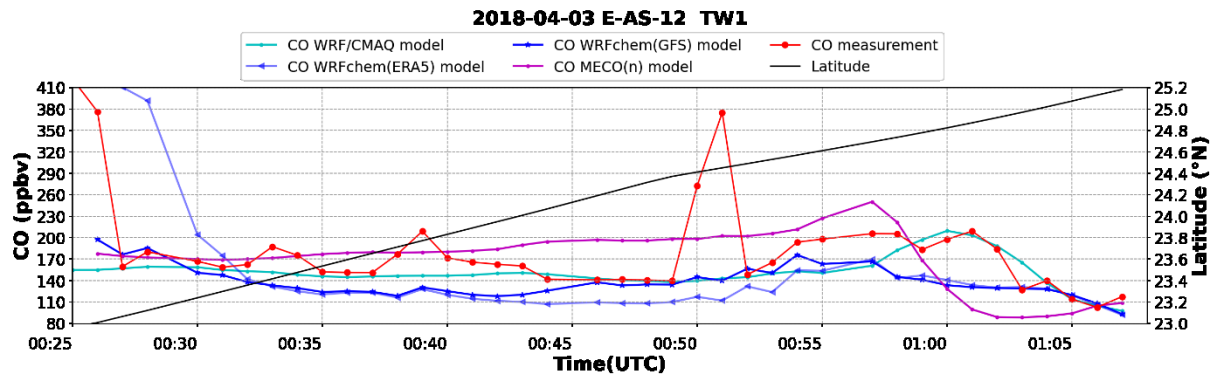
A 119: Temporal distribution of CO measurement and the corresponding results from available models for E-AS-12 TW1. The corresponding latitudes are provided on the secondary y-axis. The box model constrains the measurements, therefore, is not featured in the plots.
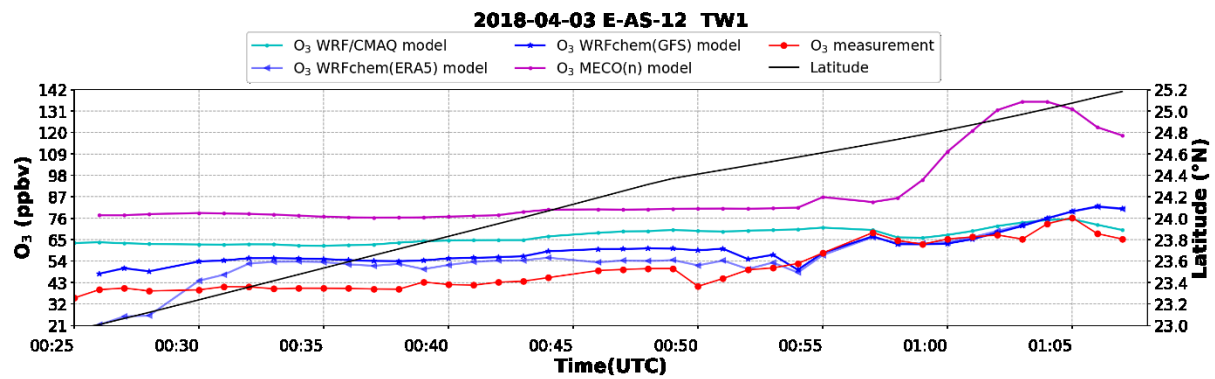
A 120: Temporal distribution of O₃ measurement and the corresponding results from available models for E-AS-12 TW1. The corresponding latitudes are provided on the secondary y-axis. The box model constrains the measurements, therefore, is not featured in the plots.
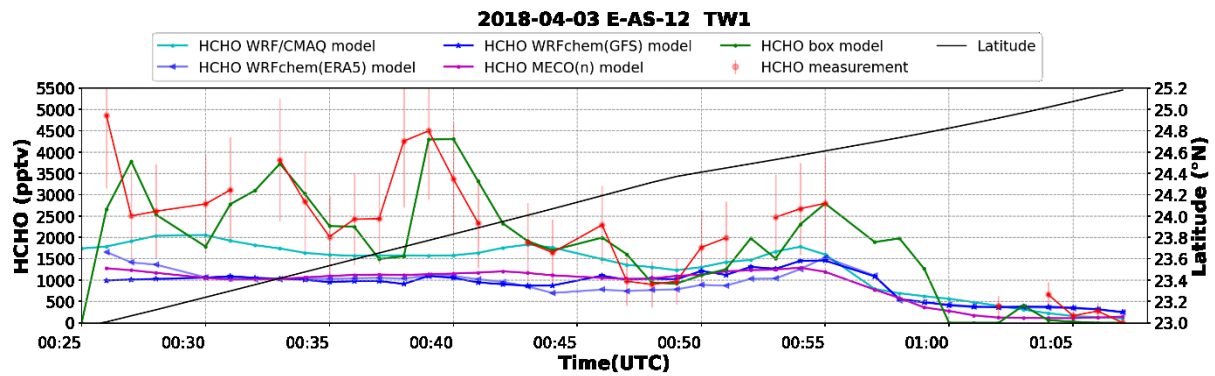
A 121: Temporal distribution of HCHO measurement and the corresponding results from available models for E-AS-12 TW1. The corresponding latitudes are provided on the secondary y-axis.
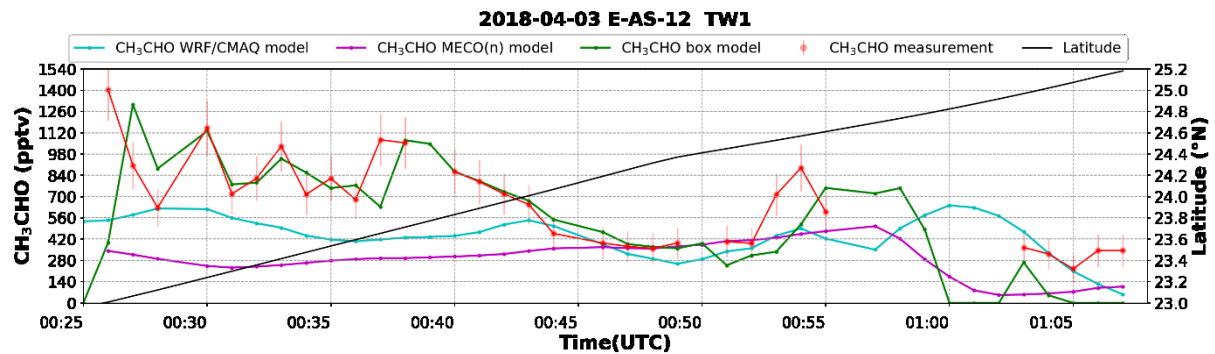
A 122: Temporal distribution of CH₃CHO measurement and the corresponding results from available models for E-AS-12 TW1. The corresponding latitudes are provided on the secondary y-axis.
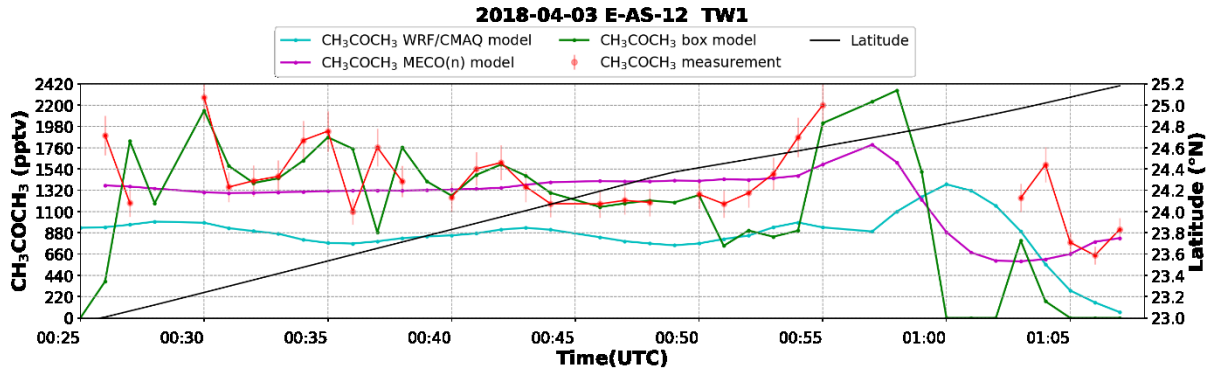
A 123Temporal distribution of CH₃COCH₃ measurement and the corresponding results from available models for E-AS-12 TW1. The corresponding latitudes are provided on the secondary y-axis.
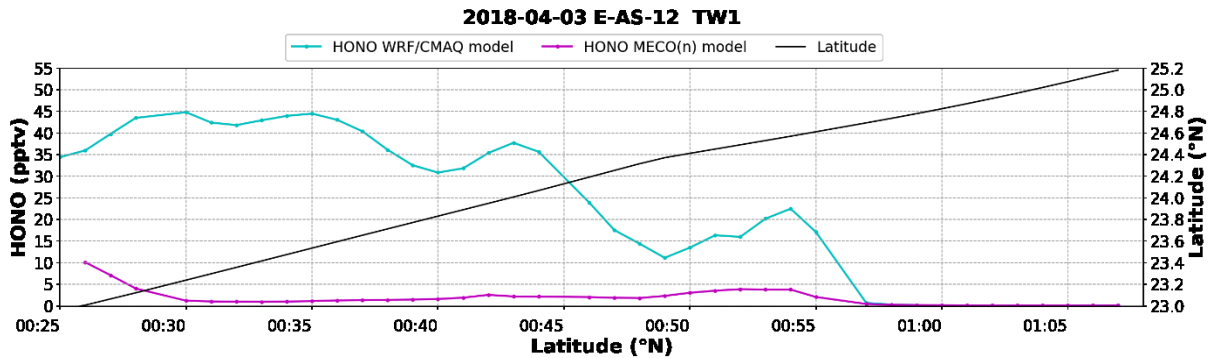
A 124: Temporal distribution of HONO measurement and the corresponding results from available models for E-AS-12 TW1. The corresponding latitudes are provided on the secondary y-axis.
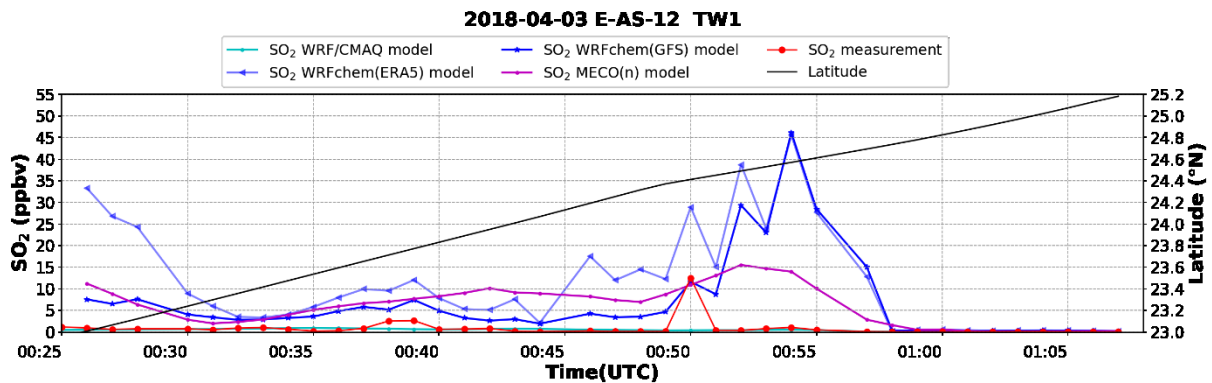
A 125: Temporal distribution of SO₂ measurement and the corresponding results from available models for E-AS-12 TW1. The corresponding latitudes are provided on the secondary y-axis. The box model constrains the measurements, therefore, is not featured in the plots.
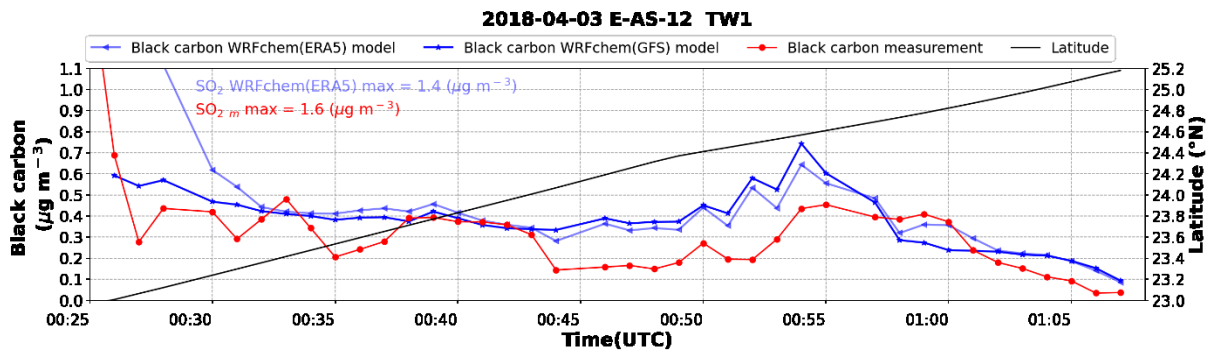
A 126: Temporal distribution of black carbon measurement and the corresponding results from available models for E-AS-12 TW1. The corresponding latitudes are provided on the secondary y-axis. The box model constrains the measurements, therefore, is not featured in the plots.
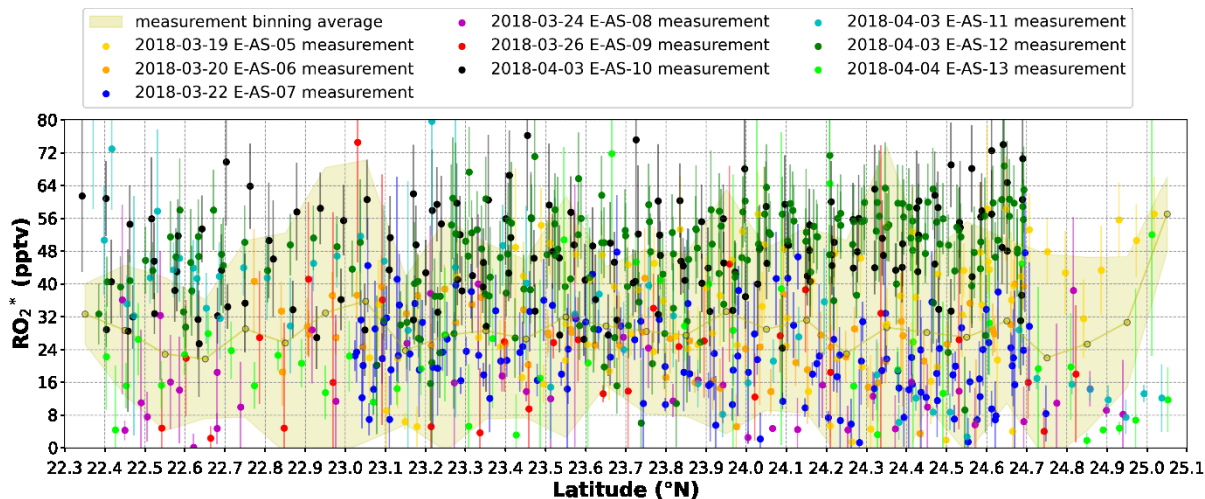
A 127: Latitudinal distribution of RO_2^* mixing ratios observed of the five selected flights for TW2. The yellow filled circles and line are the mean value of five flights within the same 0.1° binning range, and the yellow envelopes are the 1σ standard deviation of the average including each measurement error propagation.
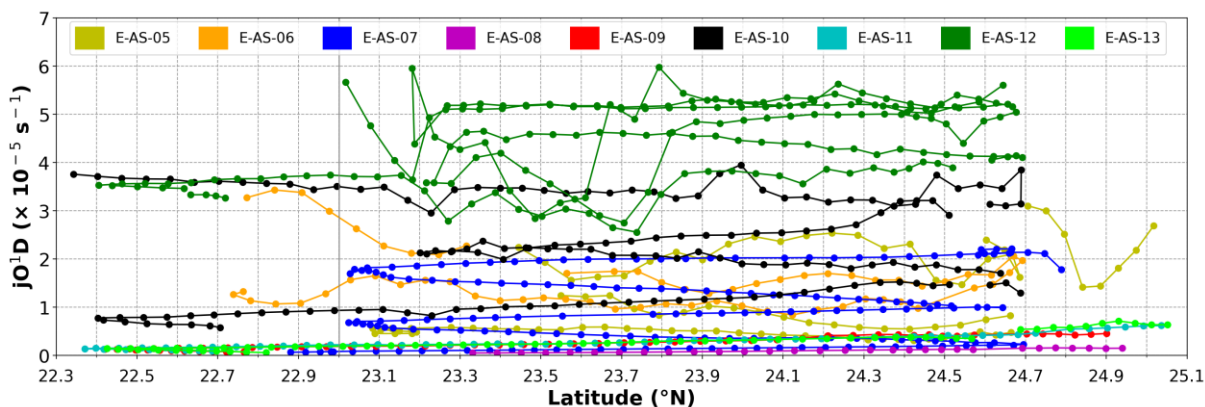
A 128: jO(^{1}D) measurement by HALO – SR over the latitude for the selected flights over TW2 at 60 s temporal resolution.
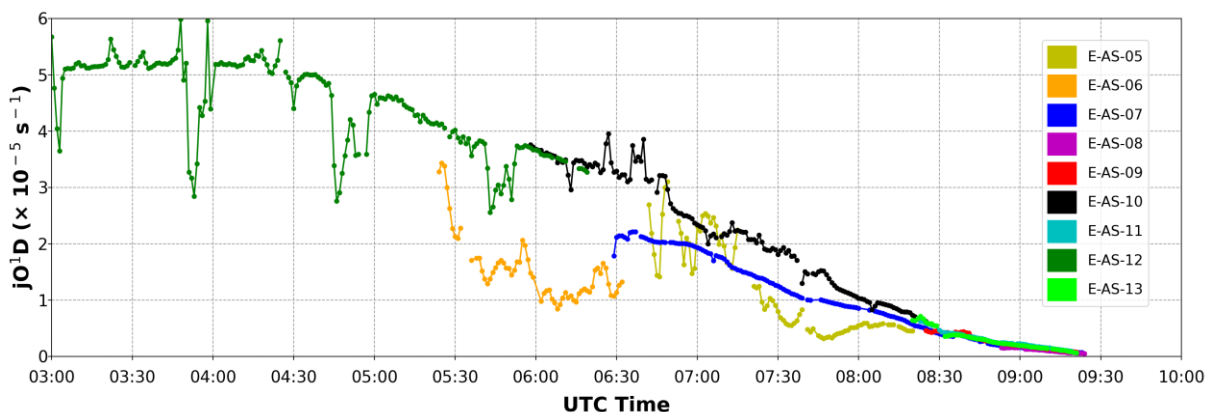
A 129: Time series of jO(^{1}D) measurement by HALO – SR for the selected flights over TW2 at 60 s temporal resolution.
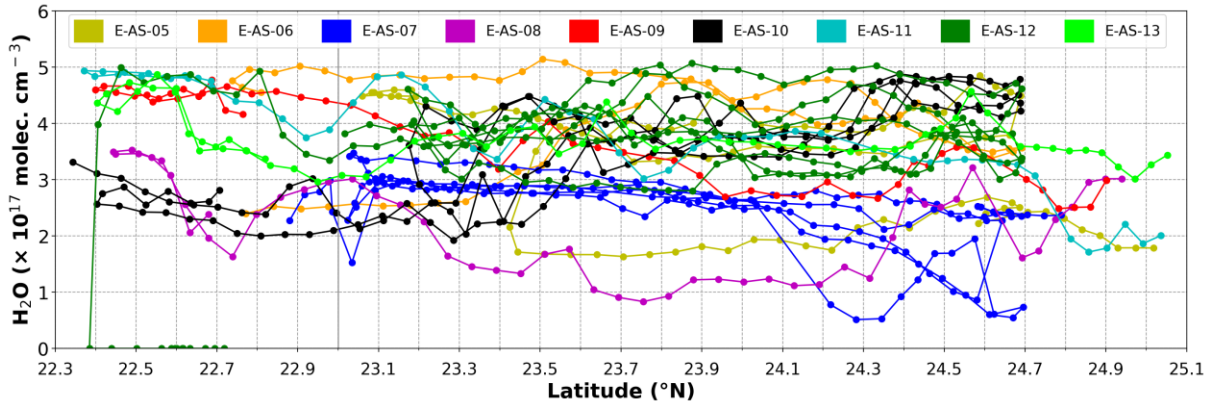
A 130: H₂O measurement over the latitude for the selected flights over TW2 at 60 s temporal resolution.
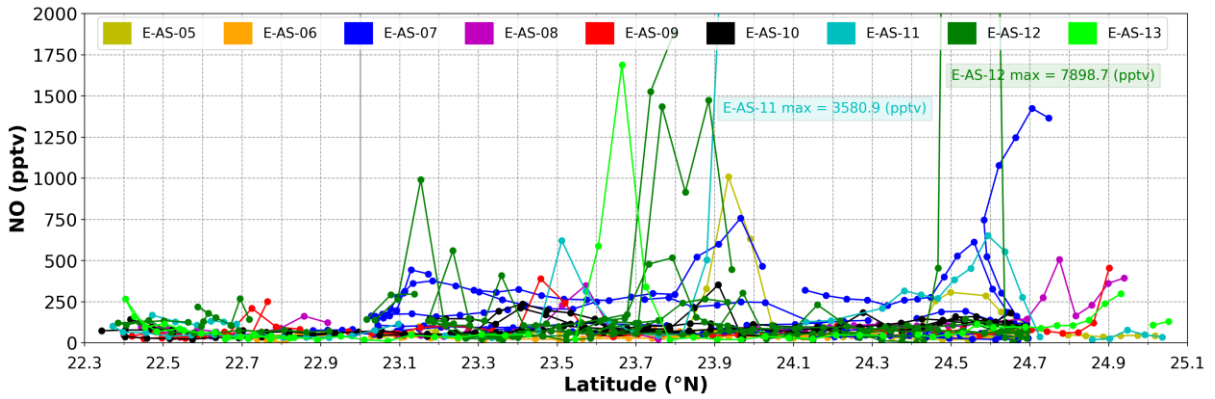
A 131: NO measurement over the latitude for the selected flights over TW2 at 60 s temporal resolution.
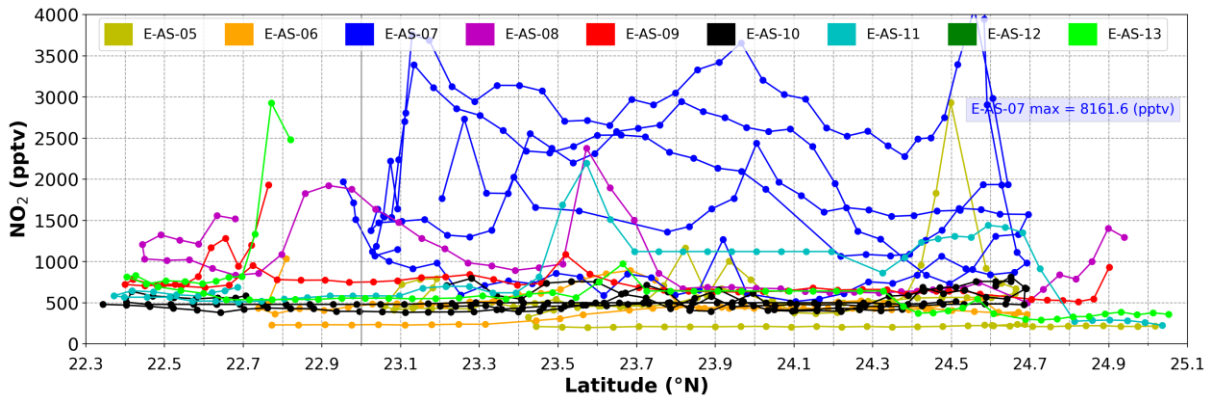
A 132: NO₂ measurement over the latitude for the selected flights over TW2 at 60 s temporal resolution.
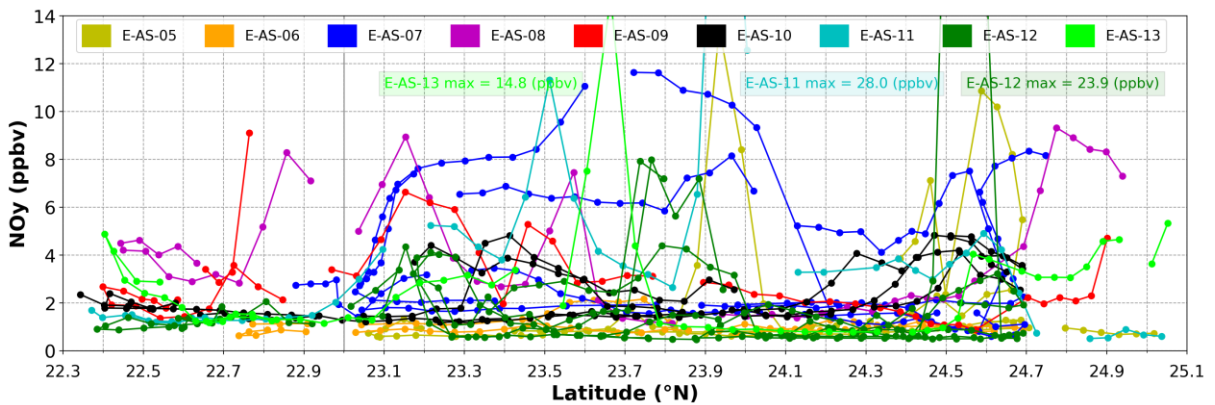
A 133: NOy measurement over the latitude for the selected flights over TW2 at 60 s temporal resolution.
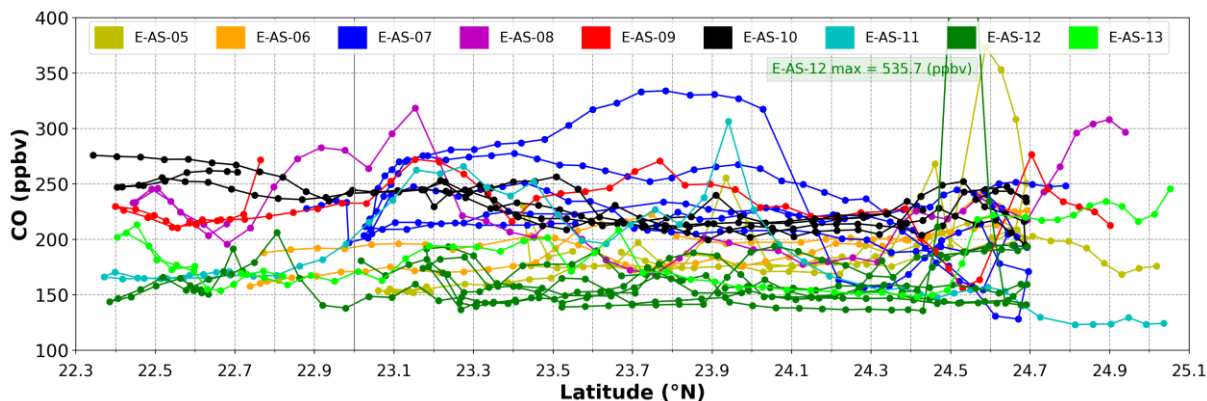
A 134: CO measurement over the latitude for the selected flights over TW2 at 60 s temporal resolution.
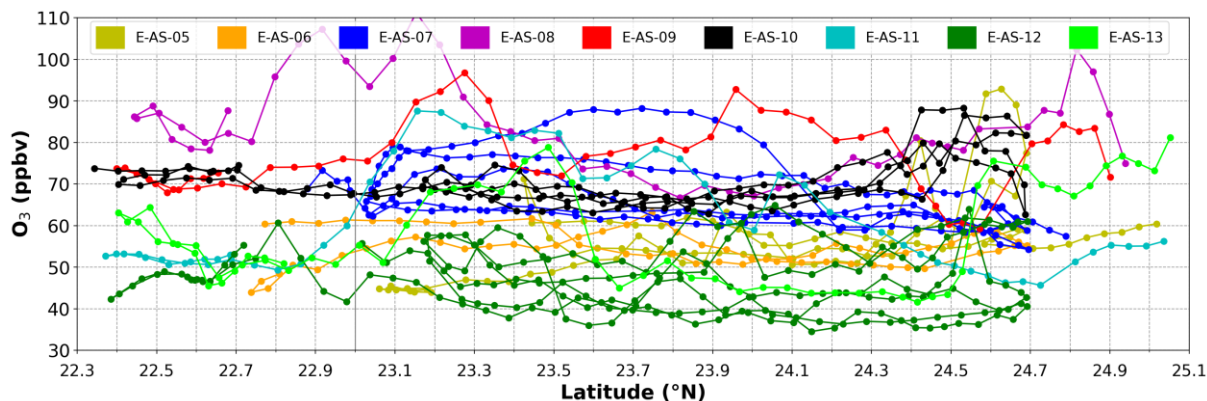
A 135: O₃ measurement over the latitude for the selected flights over TW2 at 60 s temporal resolution.
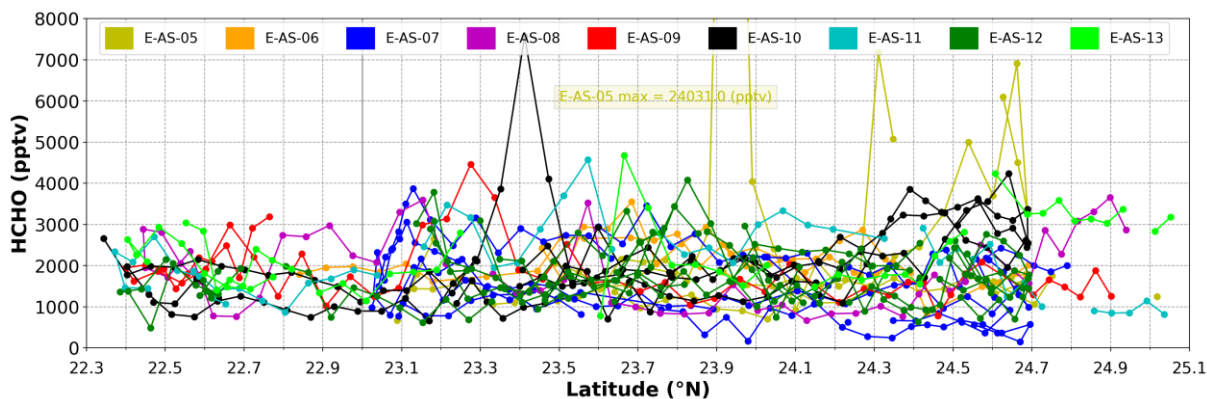
A 136: HCHO measurement over the latitude for the selected flights over TW2 at 60 s temporal resolution.
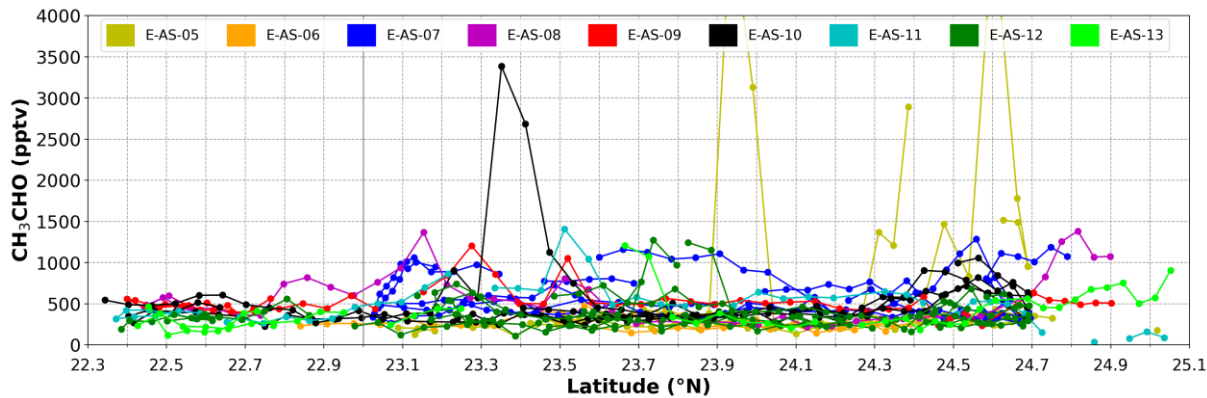
A 137:CH₃CHO measurement over the latitude for the selected flights over TW2 at 60 s temporal resolution.
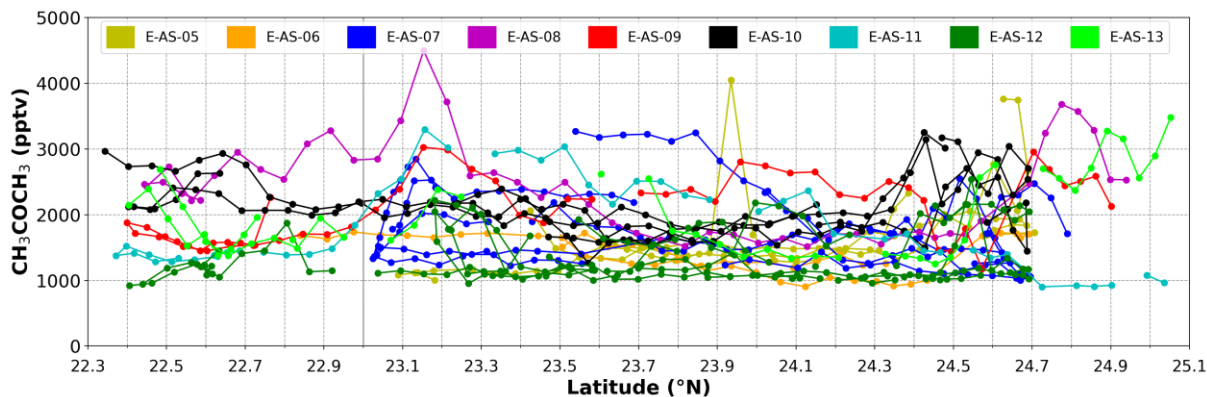
A 138: CH₃COCH₃ measurement over the latitude for the selected flights over TW2 at 60 s temporal resolution.
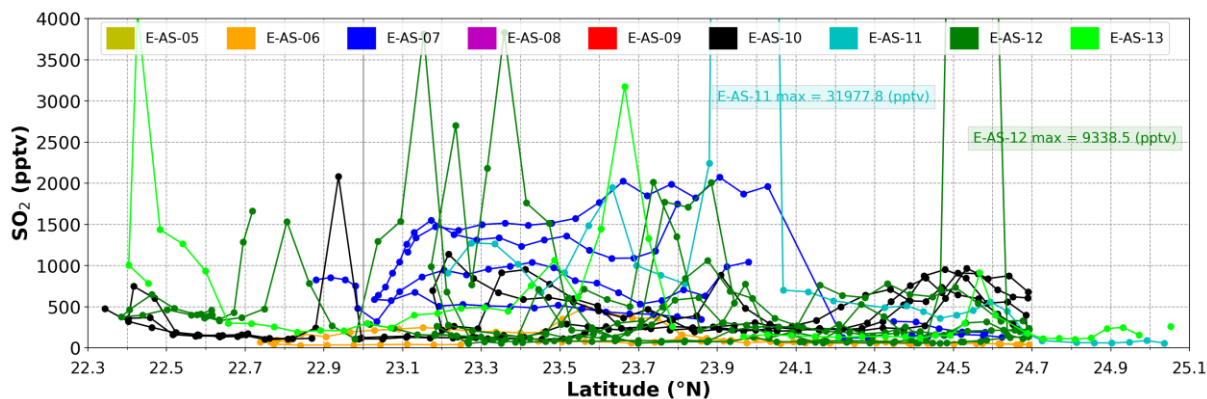
A 139: SO₂ measurement over the latitude for the selected flights over TW2 at 60 s temporal resolution.
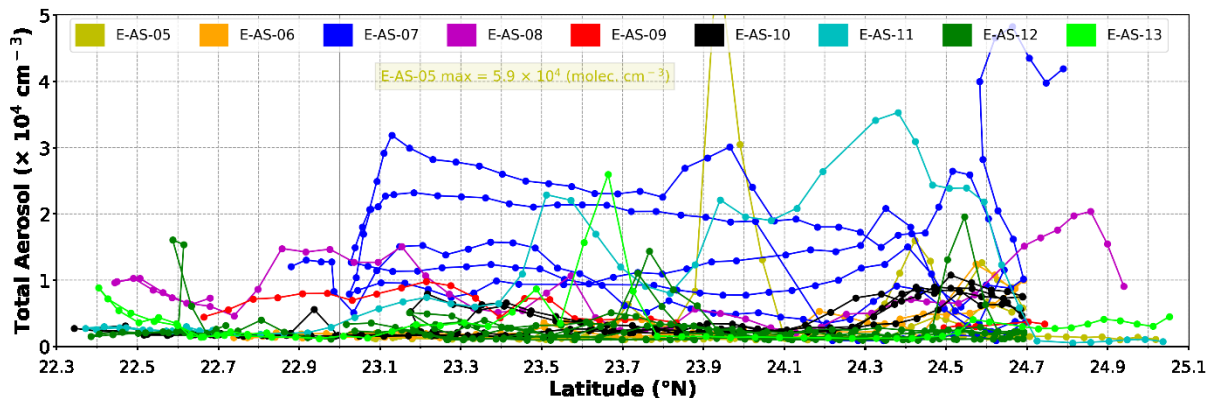
A 140: Total aerosol measurement over the latitude for the selected flights over TW2 at 60 s temporal resolution.
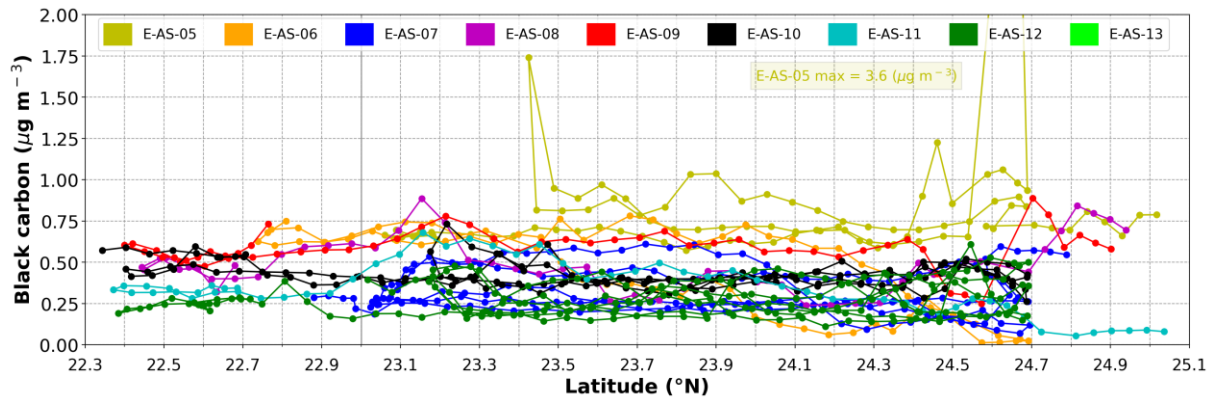
A 141: Black carbon measurement over the latitude for the selected flights over TW2 at 60 s temporal resolution.
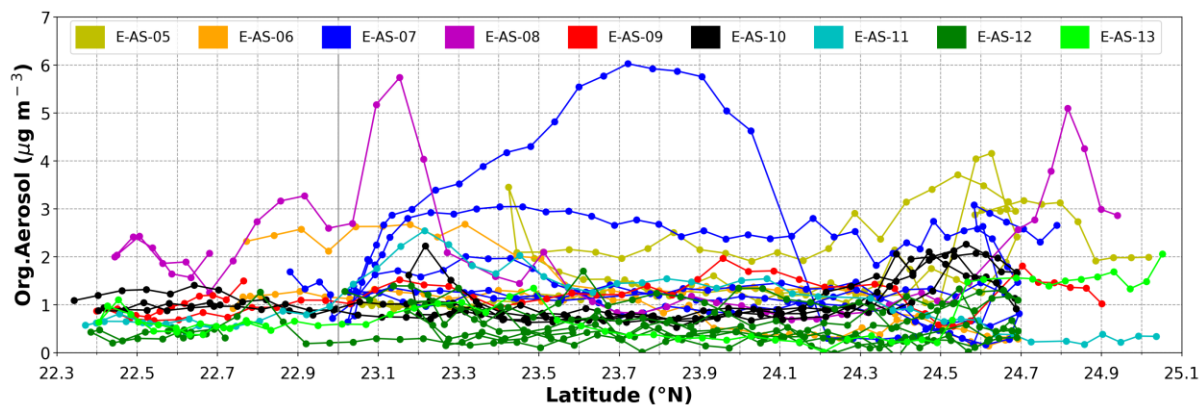
A 142: Organic aerosol measurement over the latitude for the selected flights over TW2 at 60 s temporal resolution.
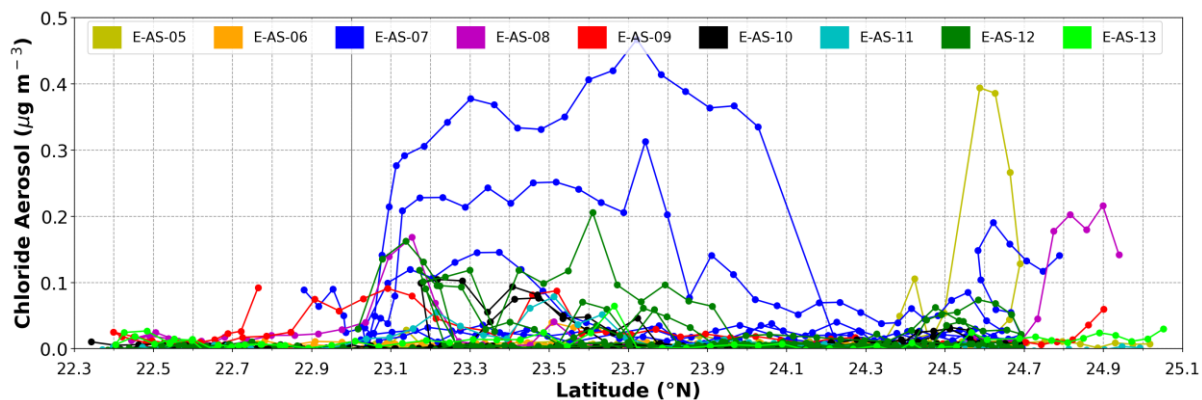
A 143: Chloride aerosol measurement over the latitude for the selected flights over TW2 at 60 s temporal resolution.
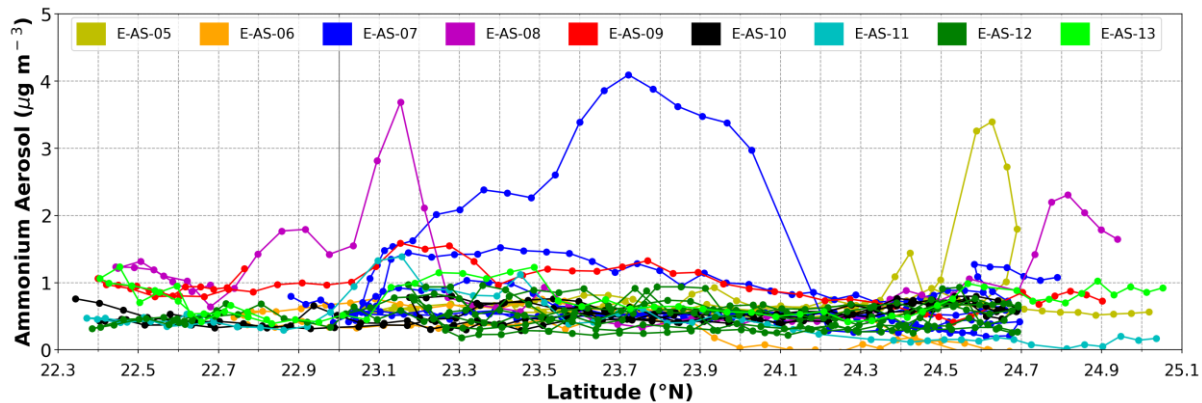
A 144: Ammonium aerosol measurement over the latitude for the selected flights over TW2 at 60 s temporal resolution.
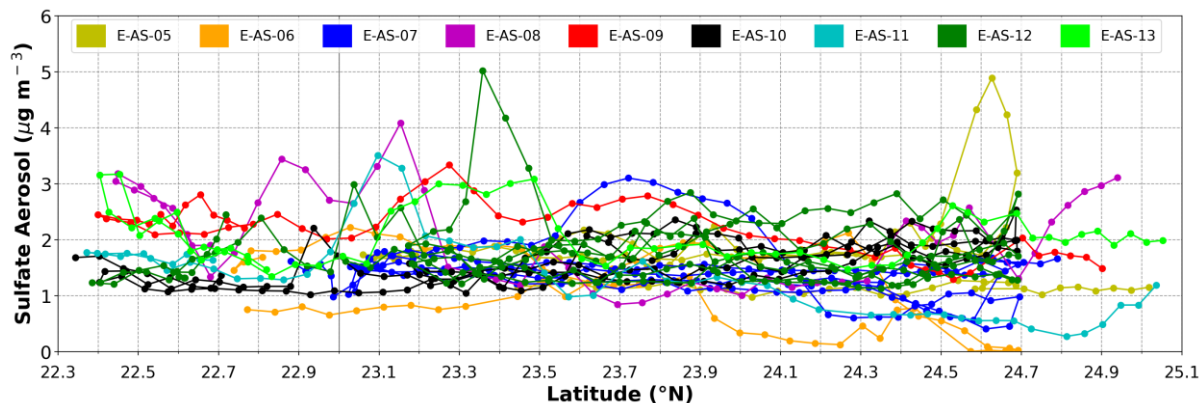
A 145: Sulfate aerosol measurement over the latitude for the selected flights over TW2 at 60 s temporal resolution.
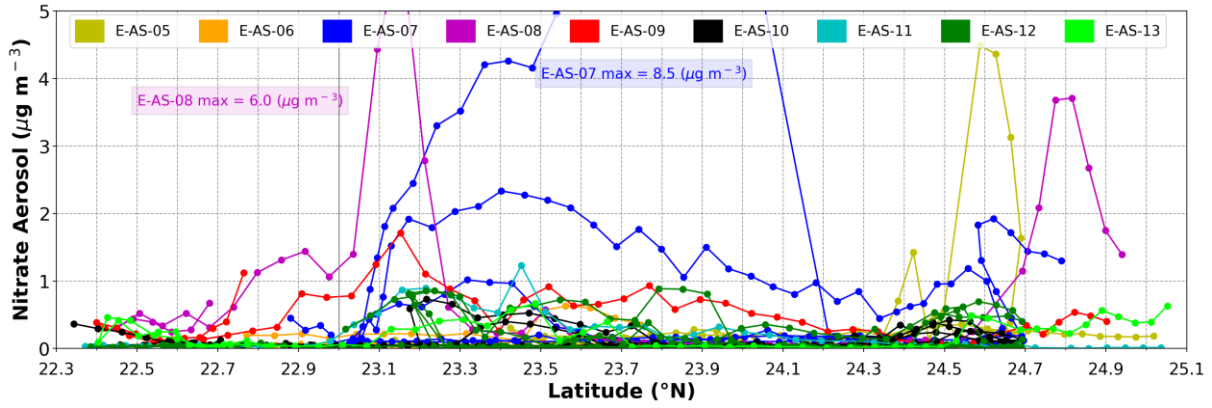
A 146: Nitrate aerosol measurement over the latitude for the selected flights over TW2 at 60 s temporal resolution.
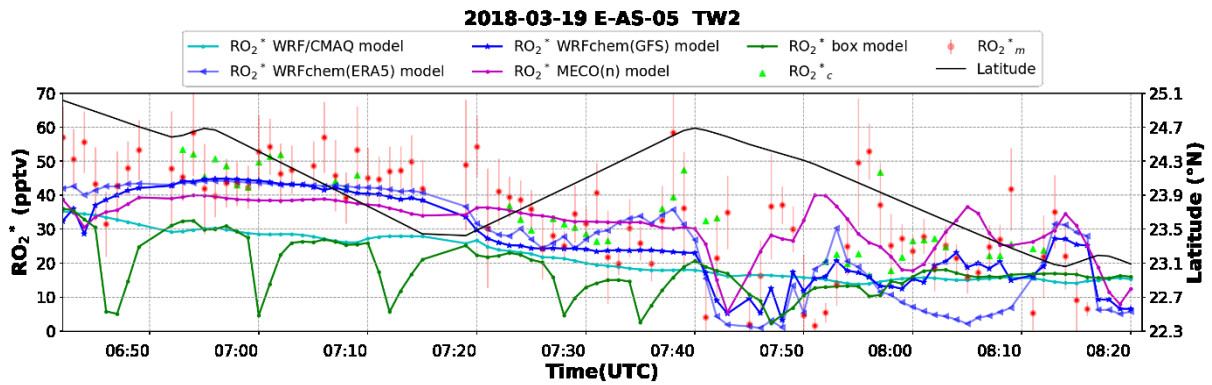
A 147: Temporal distribution of RO_2^* measurement, the corresponding results from available models, and the PSS calculations for E-AS-05 TW2. The corresponding latitudes are provided on the secondary y-axis.
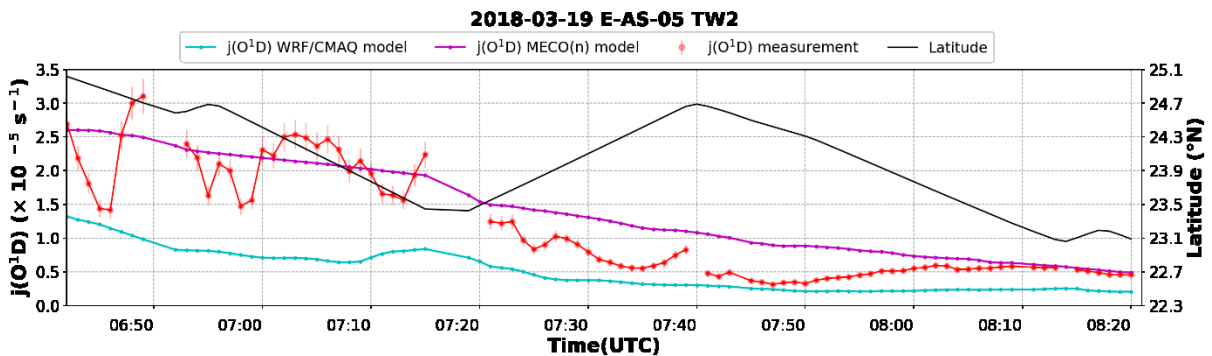
A 148: Temporal distribution of jO^1D measurement and the corresponding results from available models for E-AS-05 TW2. The corresponding latitudes are provided on the secondary y-axis. The box model constrains the measurements, therefore, is not featured in the plots.
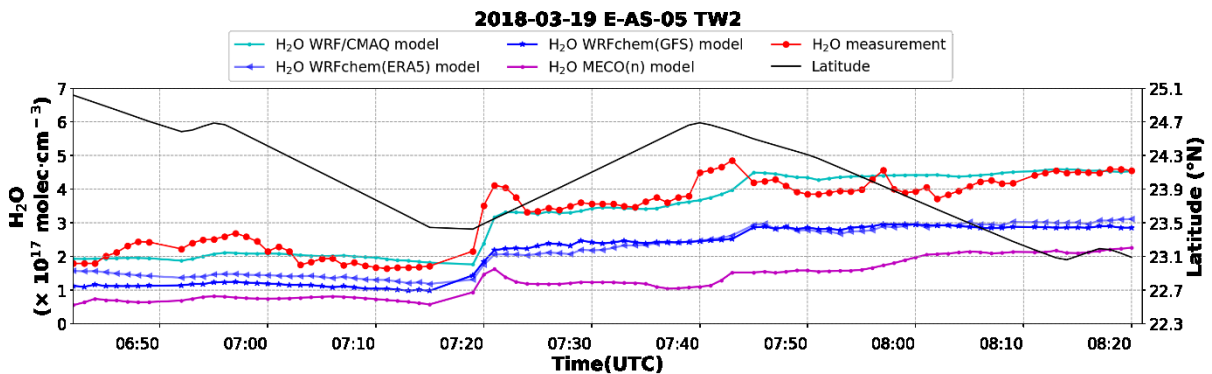
A 149: Temporal distribution of H_2O measurement and the corresponding results from available models for E-AS-05 TW2. The corresponding latitudes are provided on the secondary y-axis. The box model constrains the measurements, therefore, is not featured in the plots.

167
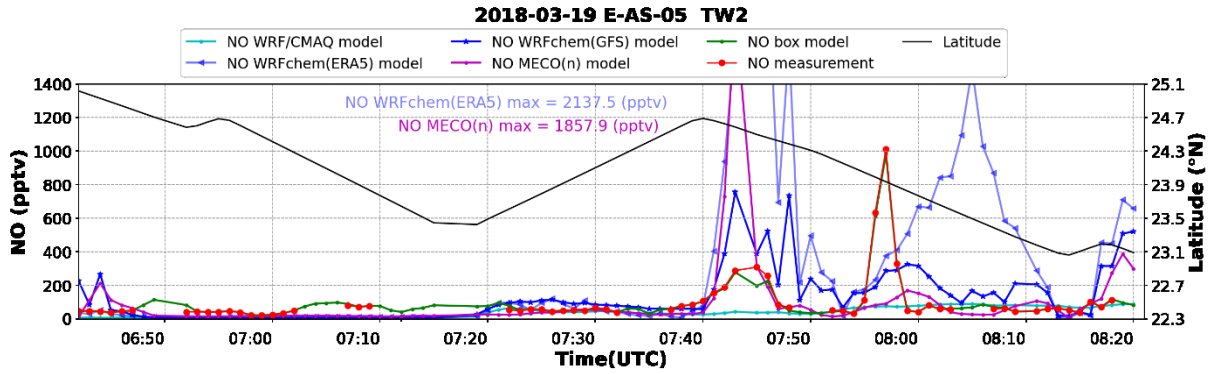
A 150: Temporal distribution of NO measurement and the corresponding results from available models for E-AS-05 TW2. The corresponding latitudes are provided on the secondary y-axis.
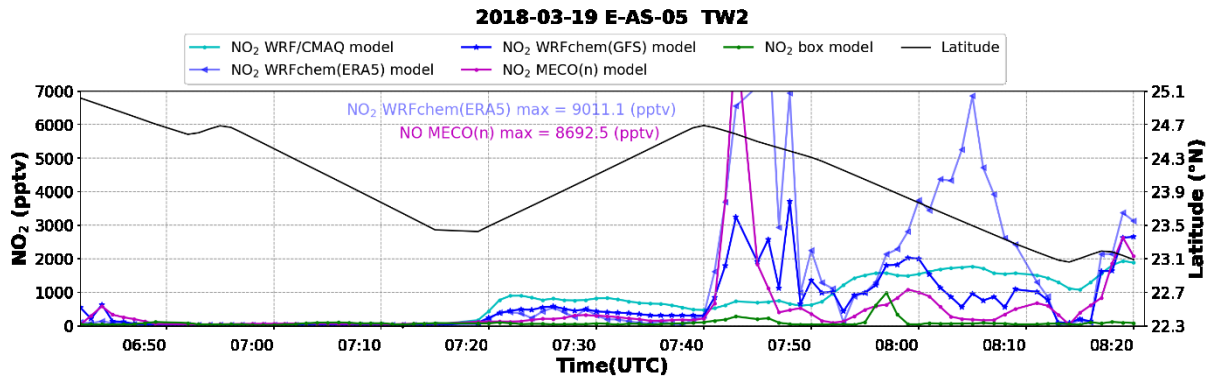
A 151: Temporal distribution of NO₂ results from available models for E-AS-05 TW2. The corresponding latitudes are provided on the secondary y-axis.
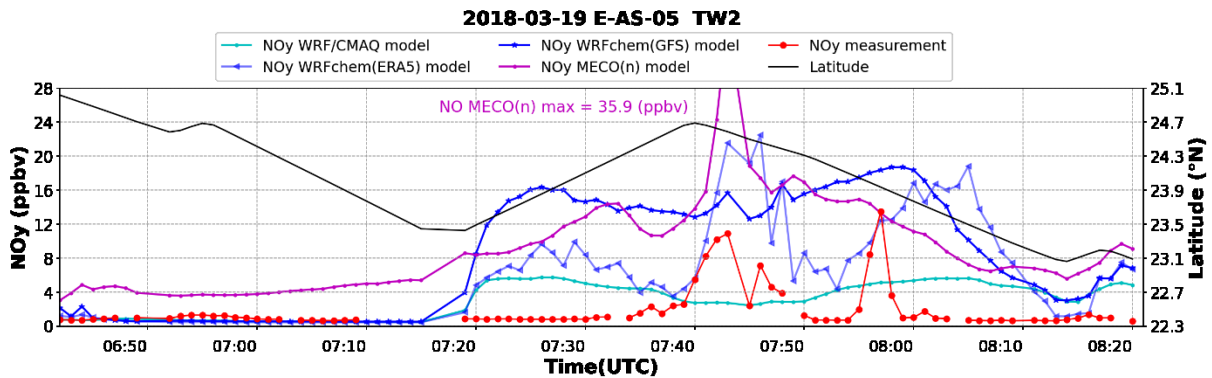
A 152: Temporal distribution of NOy measurement and the corresponding results from available models for E-AS-05 TW2. The corresponding latitudes are provided on the secondary y-axis.
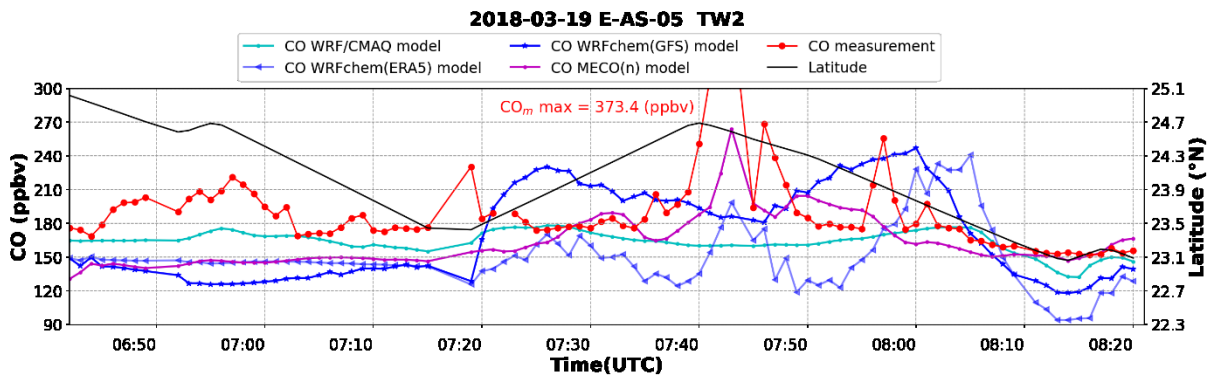
A 153: Temporal distribution of CO measurement and the corresponding results from available models for E-AS-05 TW2. The corresponding latitudes are provided on the secondary y-axis. The box model constrains the measurements, therefore, is not featured in the plots.
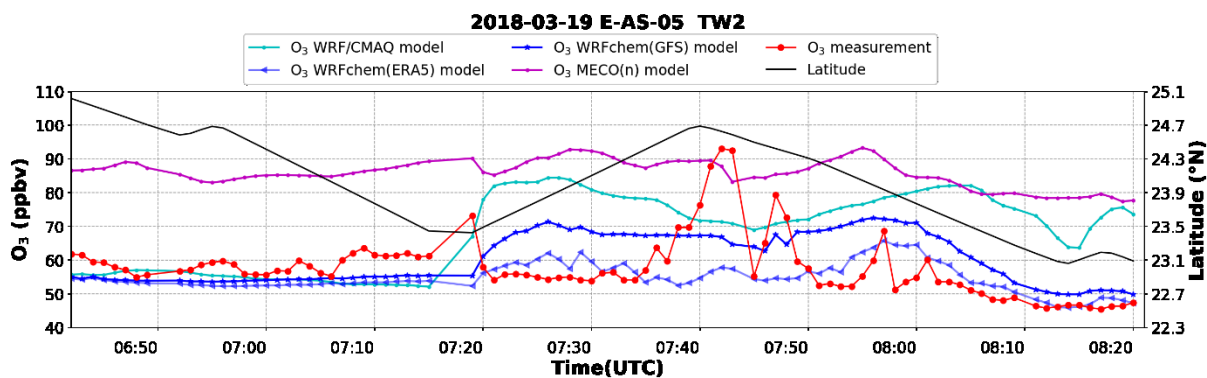
A 154: Temporal distribution of O₃ measurement and the corresponding results from available models for E-AS-05 TW2. The corresponding latitudes are provided on the secondary y-axis. The box model constrains the measurements, therefore, is not featured in the plots.
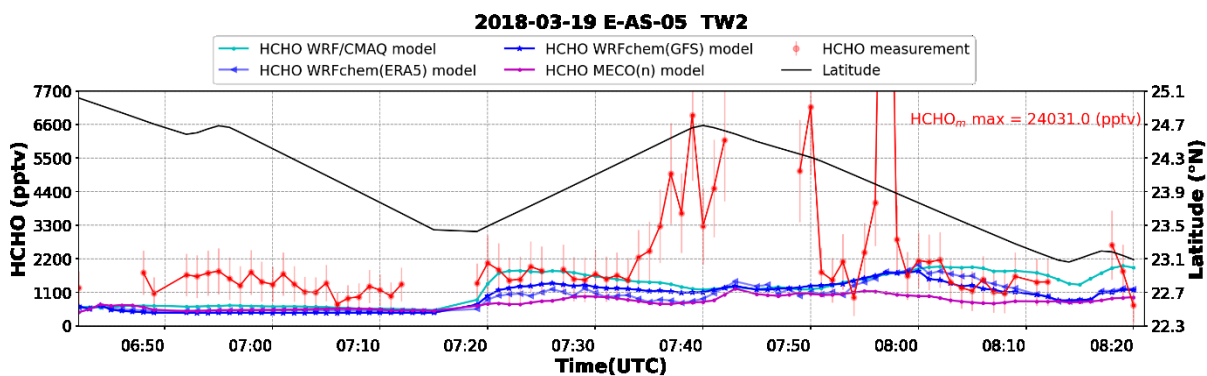
A 155: Temporal distribution of HCHO measurement and the corresponding results from available models for E-AS-05 TW2. The corresponding latitudes are provided on the secondary y-axis. The box model constrains the measurements, therefore, is not featured in the plots.
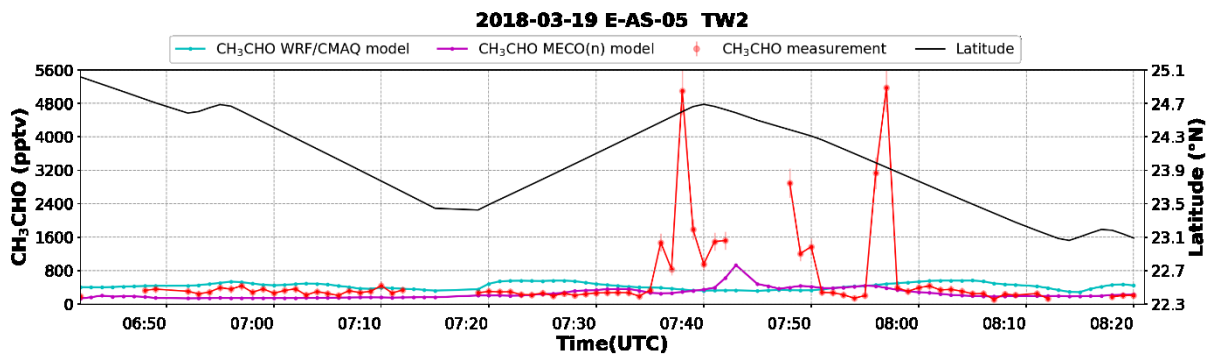
A 156: Temporal distribution of CH₃CHO measurement and the corresponding results from available models for E-AS-05 TW2. The corresponding latitudes are provided on the secondary y-axis. The box model constrains the measurements, therefore, is not featured in the plots.
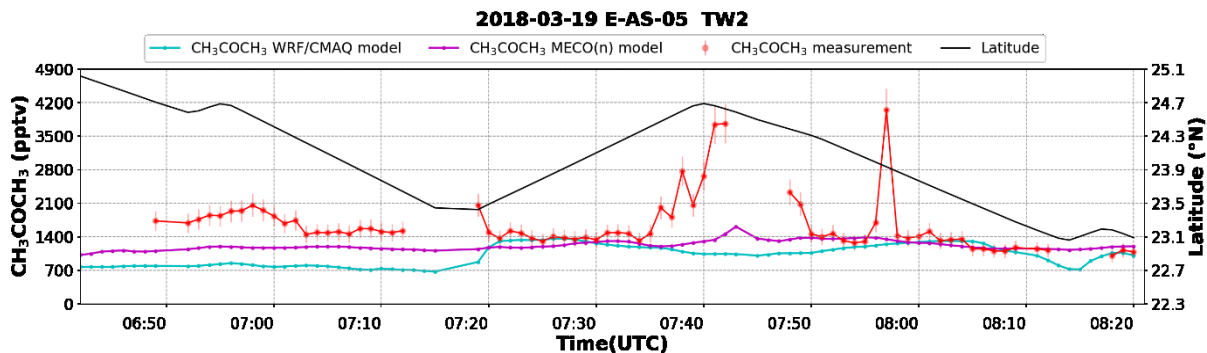
A 157: Temporal distribution of CH₃COCH₃ measurement and the corresponding results from available models for E-AS-05 TW2. The corresponding latitudes are provided on the secondary y-axis. The box model constrains the measurements, therefore, is not featured in the plots.
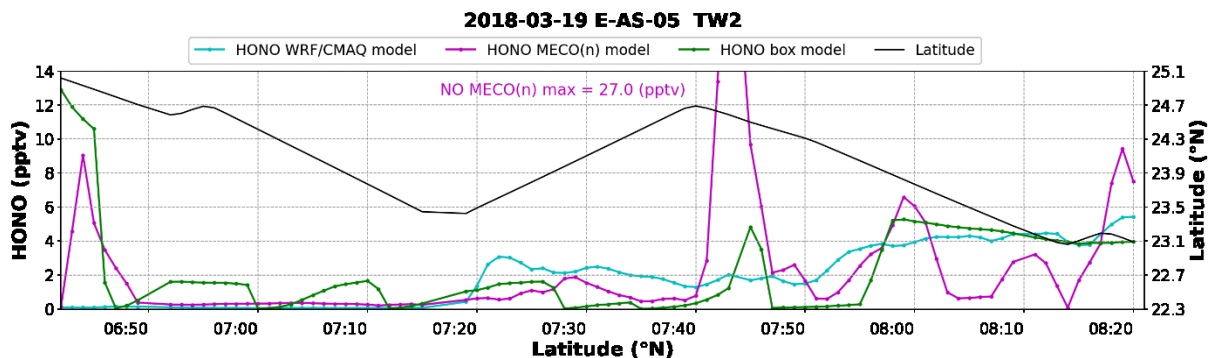
A 158: *Temporal distribution of HONO results from available models for E-AS-05 TW2. The corresponding latitudes are provided on the secondary y-axis.*
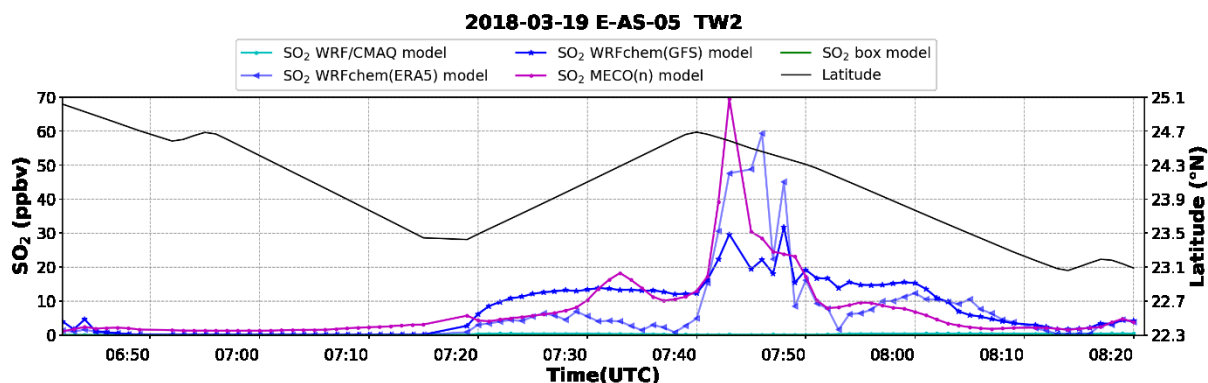
A 159: *Temporal distribution of SO₂ results from available models for E-AS-05 TW2. The corresponding latitudes are provided on the secondary y-axis.*
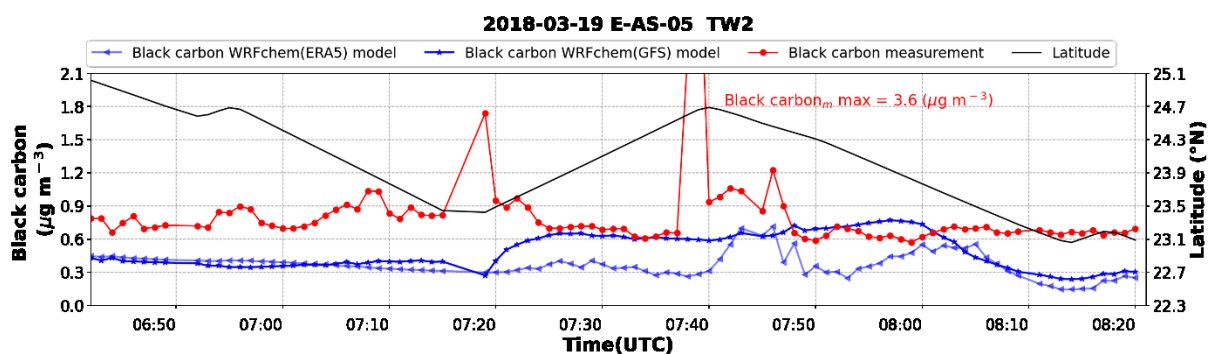
A 160: *Temporal distribution of black carbon measurement and the corresponding results from available models for E-AS-05 TW2. The corresponding latitudes are provided on the secondary y-axis. The box model constrains the measurements, therefore, is not featured in the plots.*
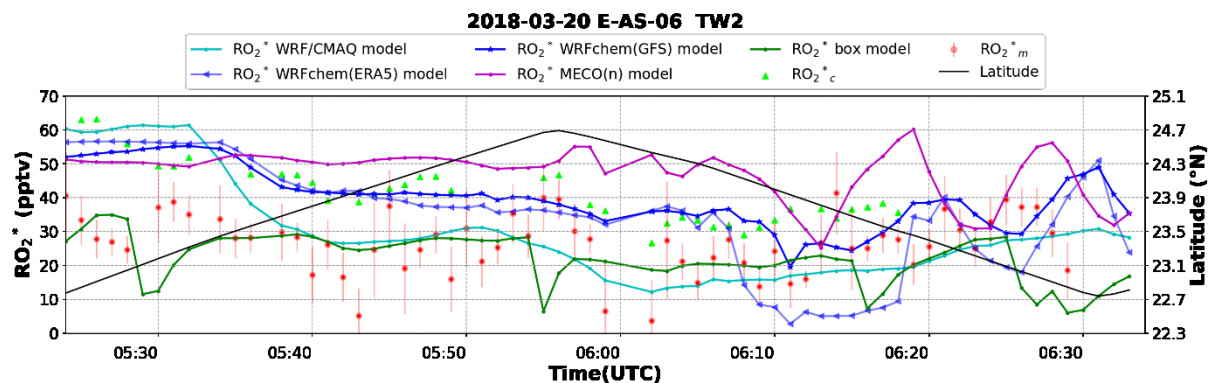
A 161: *Temporal distribution of RO_2^* measurement, the corresponding results from available models, and the PSS calculations for E-AS-06 TW2. The corresponding latitudes are provided on the secondary y-axis*

170
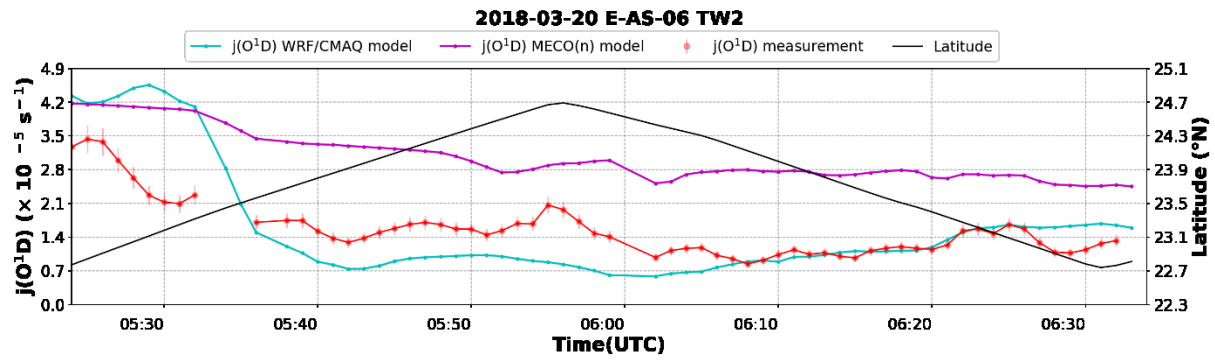
A 162: Temporal distribution of jO^1D measurement and the corresponding results from available models for E-AS-06 TW2. The corresponding latitudes are provided on the secondary y-axis. The box model constrains the measurements, therefore, is not featured in the plots.
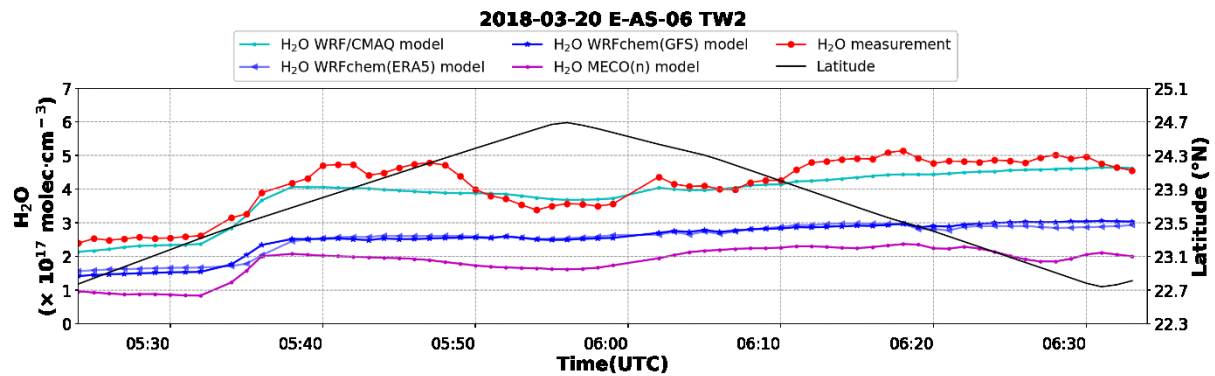
A 163: Temporal distribution of H_2O measurement and the corresponding results from available models for E-AS-06 TW2. The corresponding latitudes are provided on the secondary y-axis. The box model constrains the measurements, therefore, is not featured in the plots.
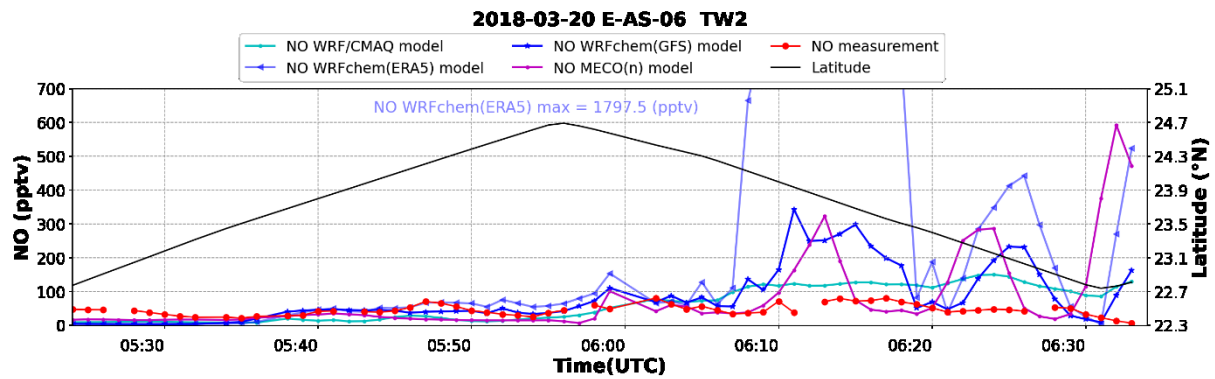
A 164: Temporal distribution of NO measurement and the corresponding results from available models for E-AS-06 TW2. The corresponding latitudes are provided on the secondary y-axis. The box model constrains the measurements, therefore, is not featured in the plots.
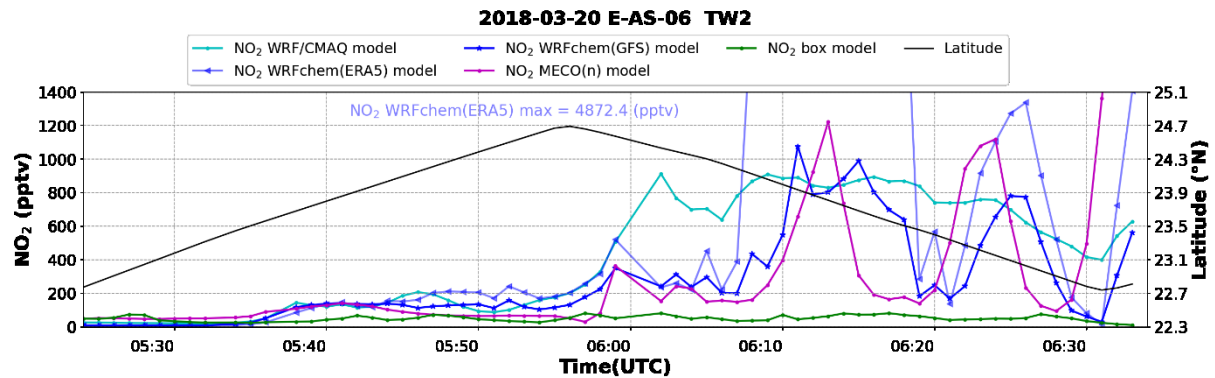
A 165: Temporal distribution of NO_2 results from available models for E-AS-06 TW2. The corresponding latitudes are provided on the secondary y-axis.
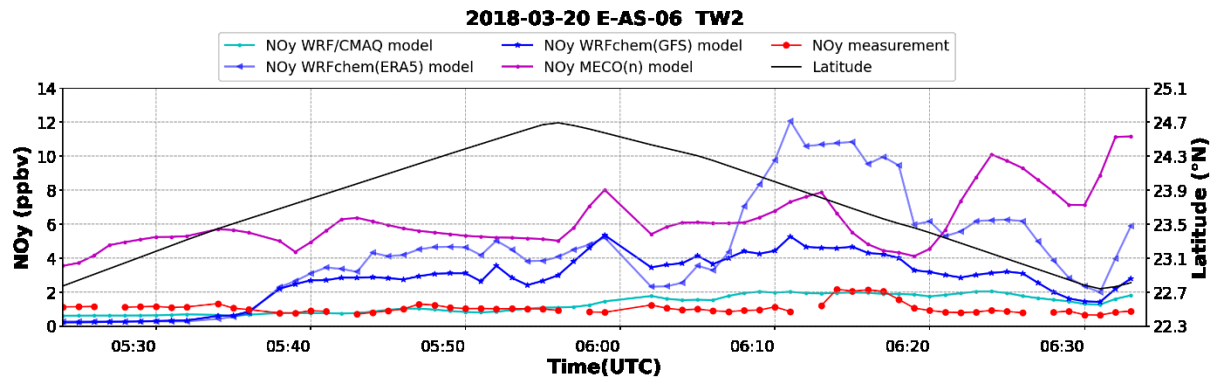
A 166: Temporal distribution of NOy measurement and the corresponding results from available models for E-AS-06 TW2. The corresponding latitudes are provided on the secondary y-axis.
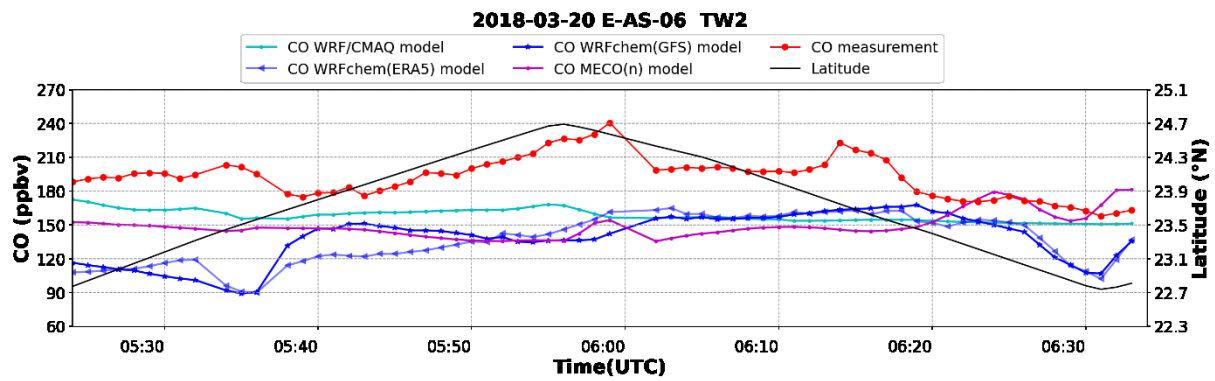
A 167: Temporal distribution of CO measurement and the corresponding results from available models for E-AS-06 TW2. The corresponding latitudes are provided on the secondary y-axis. The box model constrains the measurements, therefore, is not featured in the plots.
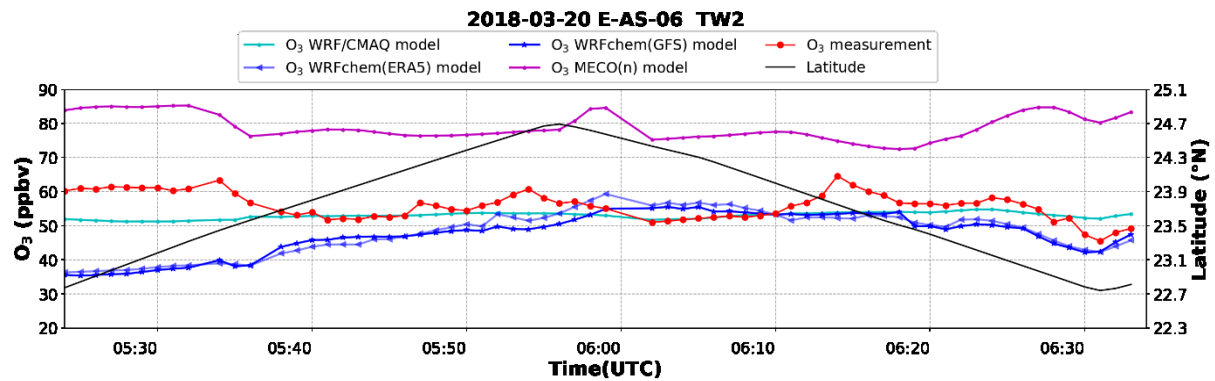
A 168: Temporal distribution of O₃ measurement and the corresponding results from available models for E-AS-06 TW2. The corresponding latitudes are provided on the secondary y-axis. The box model constrains the measurements, therefore, is not featured in the plots.
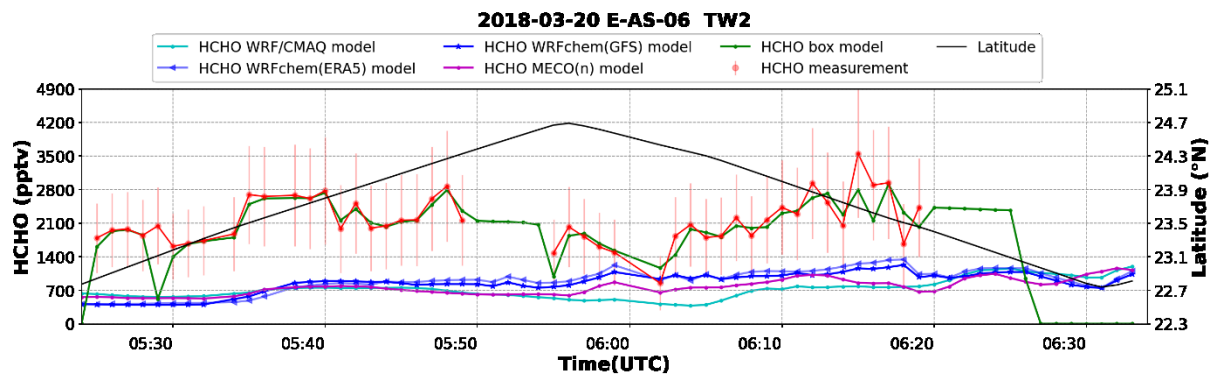
A 169: Temporal distribution of HCHO measurement and the corresponding results from available models for E-AS-06 TW2. The corresponding latitudes are provided on the secondary y-axis.
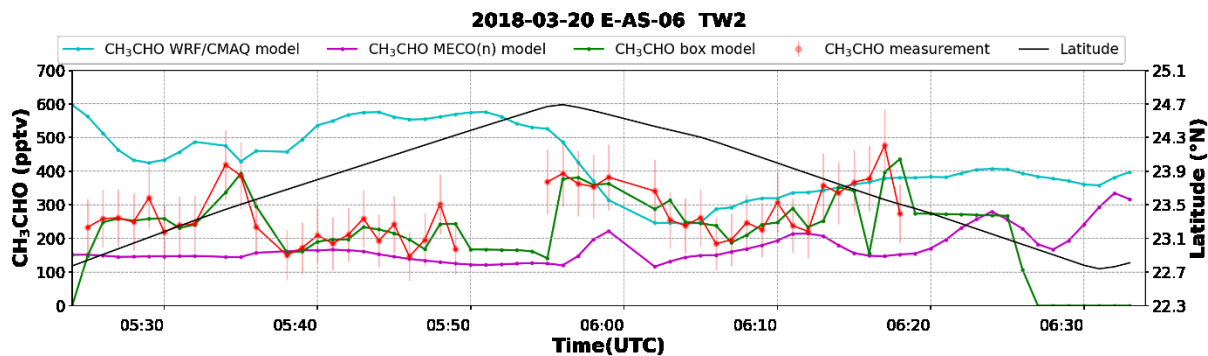
A 170: Temporal distribution of CH₃CHO measurement and the corresponding results from available models for E-AS-06 TW2. The corresponding latitudes are provided on the secondary y-axis.
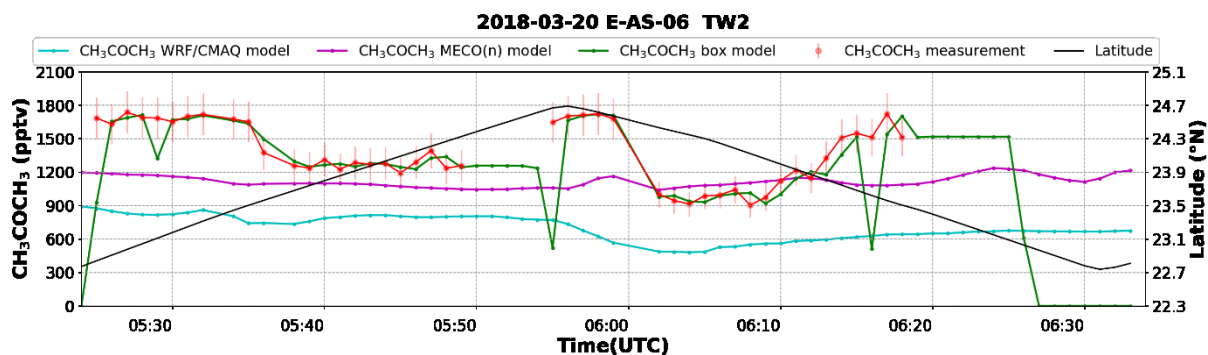
A 171: Temporal distribution of CH₃COCH₃ measurement and the corresponding results from available models for E-AS-06 TW2. The corresponding latitudes are provided on the secondary y-axis.
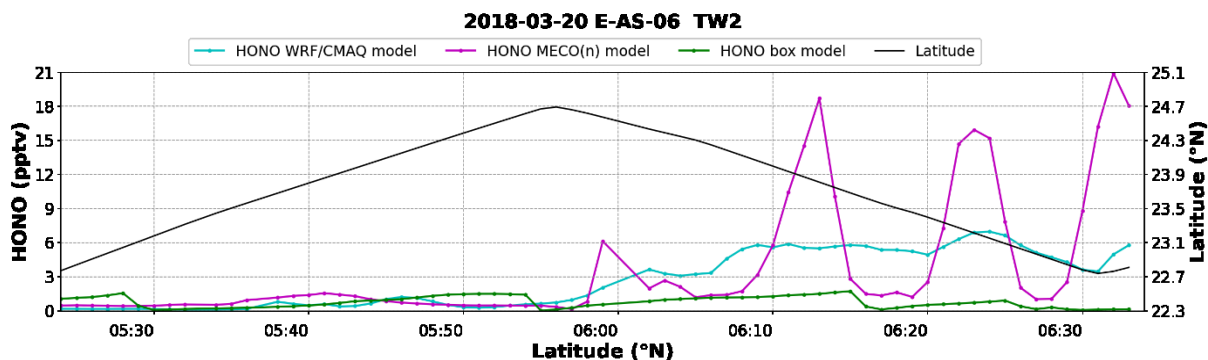
A 172: Temporal distribution of HONO results from available models for E-AS-06 TW2. The corresponding latitudes are provided on the secondary y-axis.
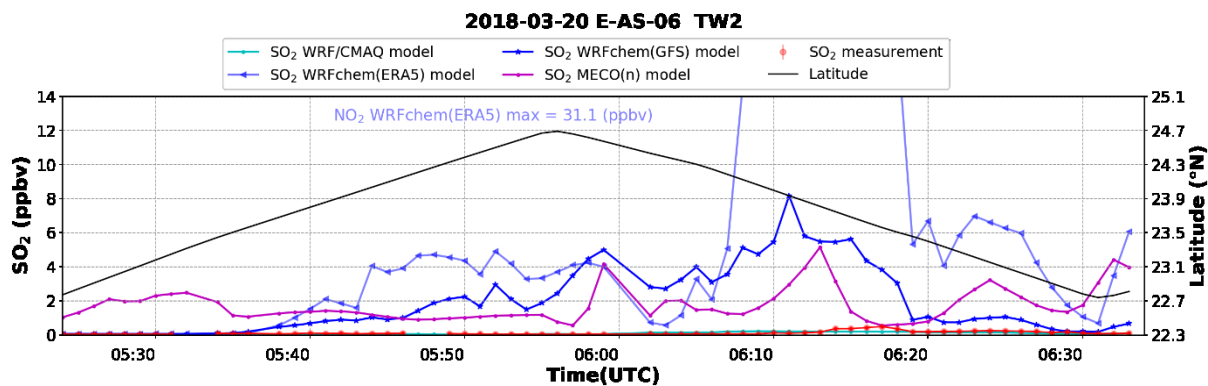
A 173: Temporal distribution of SO₂ measurement and the corresponding results from available models for E-AS-06 TW2. The corresponding latitudes are provided on the secondary y-axis. The box model constrains the measurements, therefore, is not featured in the plots.
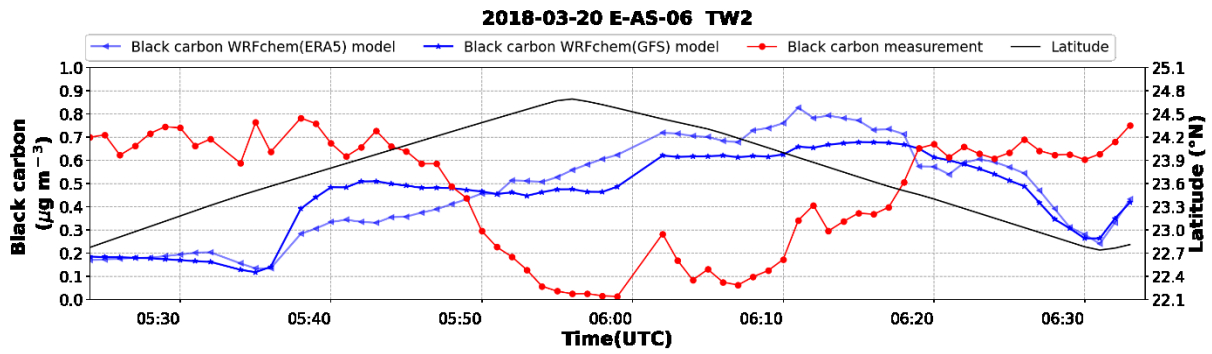
A 174: Temporal distribution of black carbon measurement and the corresponding results from available models for E-AS-06 TW2. The corresponding latitudes are provided on the secondary y-axis. The box model constrains the measurements, therefore, is not featured in the plots.
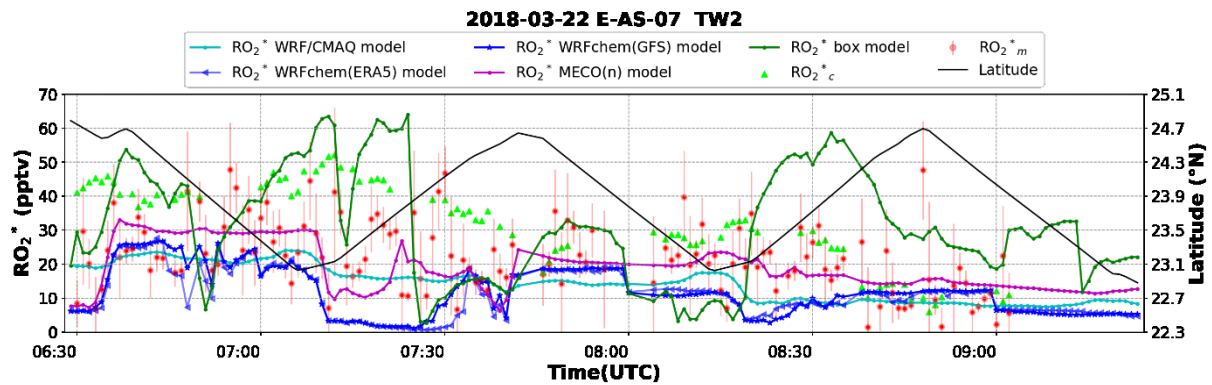
A 175: Temporal distribution of RO_2^* measurement, the corresponding results from available models, and the PSS calculations for E-AS-07 TW2. The corresponding latitudes are provided on the secondary y-axis.
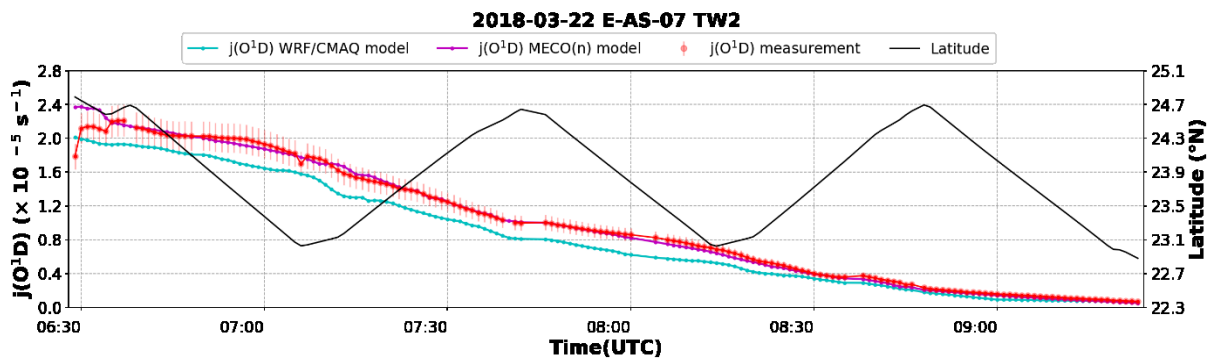
A 176: Temporal distribution of jO^1D measurement and the corresponding results from available models for E-AS-07 TW2. The corresponding latitudes are provided on the secondary y-axis. The box model constrains the measurements, therefore, is not featured in the plots.
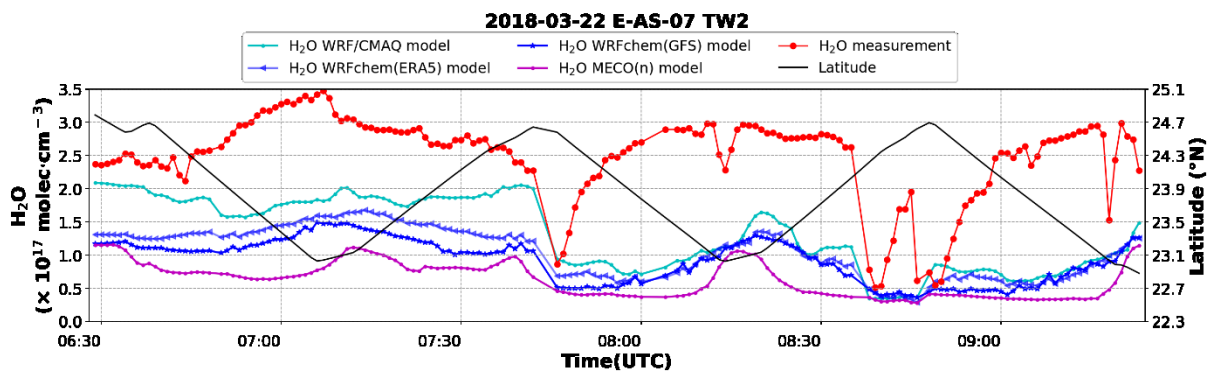
A 177: Temporal distribution of H_2O measurement and the corresponding results from available models for E-AS-07 TW2. The corresponding latitudes are provided on the secondary y-axis. The box model constrains the measurements, therefore, is not featured in the plots.
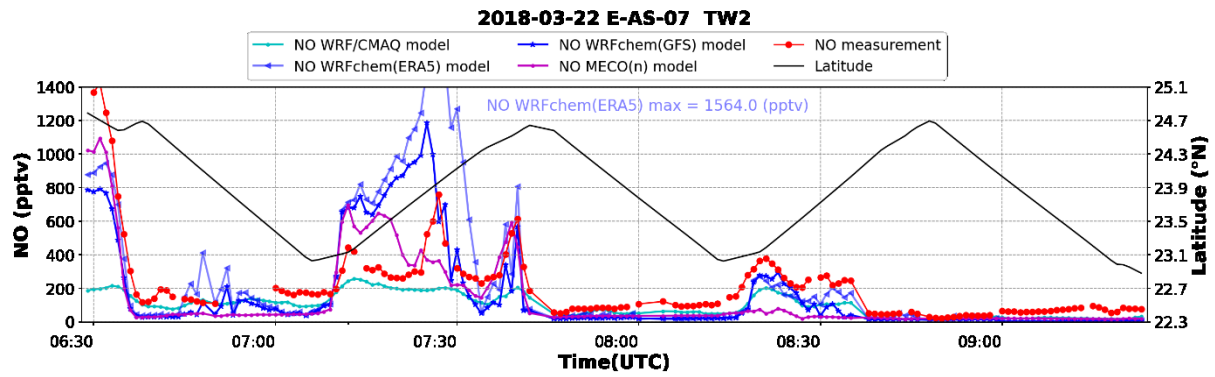
A 178: Temporal distribution of NO measurement and the corresponding results from available models for E-AS-07 TW2. The corresponding latitudes are provided on the secondary y-axis. The box model constrains the measurements, therefore, is not featured in the plots.
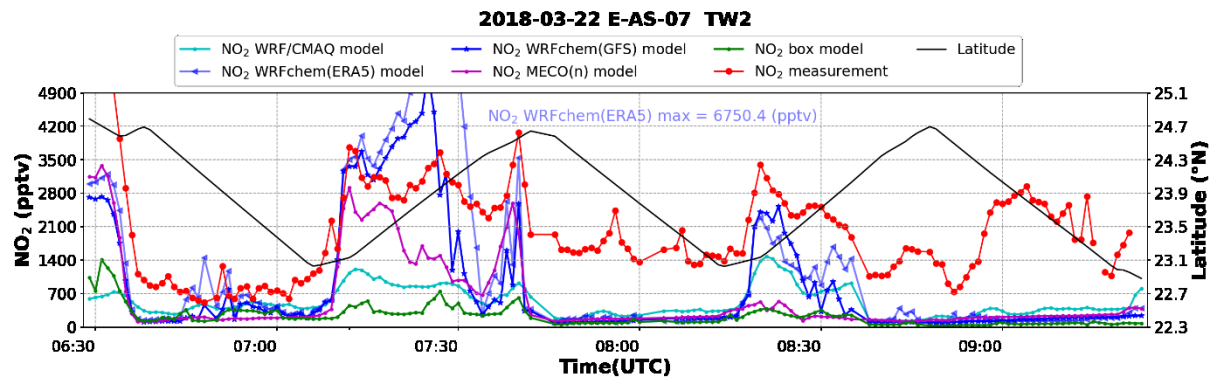
A 179: Temporal distribution of NO₂ measurement and the corresponding results from available models for E-AS-07 TW2. The corresponding latitudes are provided on the secondary y-axis. NO₂ measurement made by HAIDI.
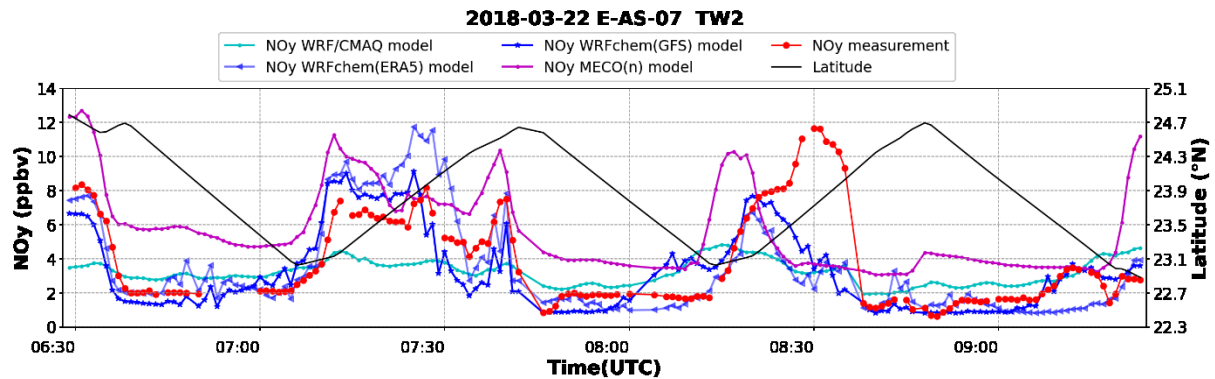
A 180: Temporal distribution of NOy measurement and the corresponding results from available models for E-AS-07 TW2. The corresponding latitudes are provided on the secondary y-axis.
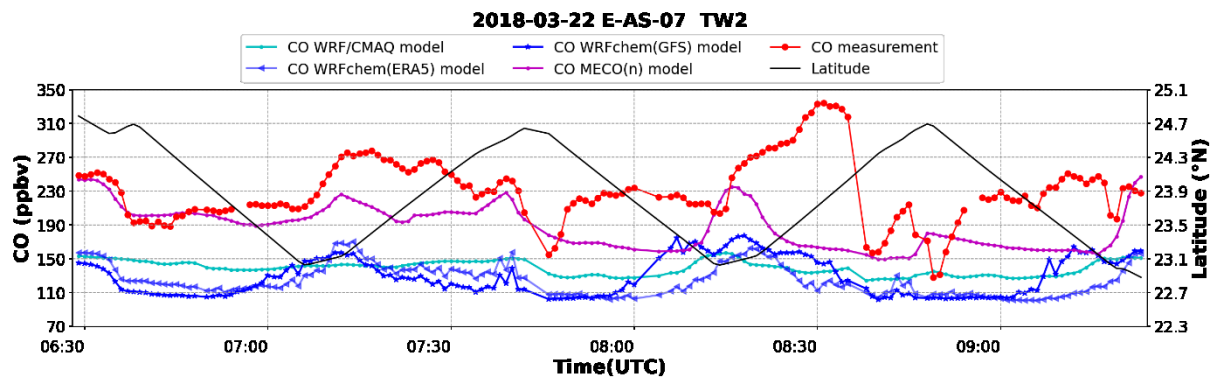
A 181: Temporal distribution of CO measurement and the corresponding results from available models for E-AS-07 TW2. The corresponding latitudes are provided on the secondary y-axis. The box model constrains the measurements, therefore, is not featured in the plots.

175
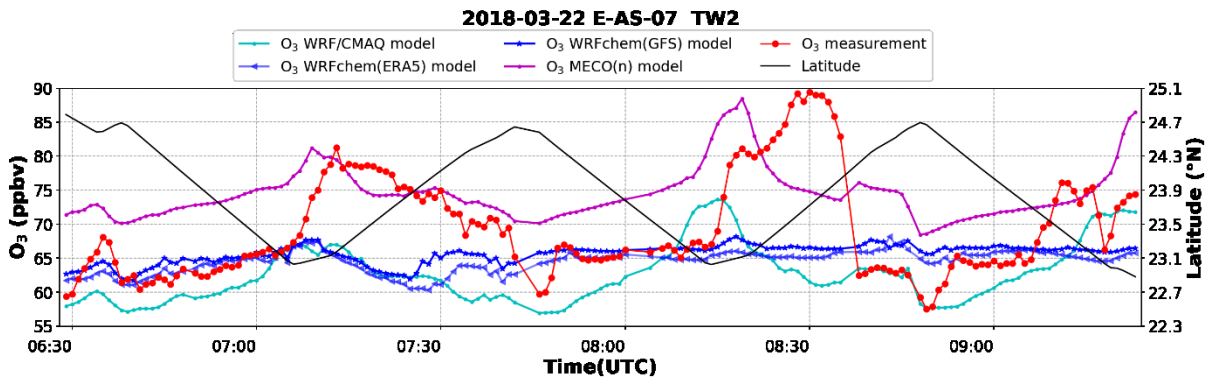
A 182: Temporal distribution of O₃ measurement and the corresponding results from available models for E-AS-07 TW2. The corresponding latitudes are provided on the secondary y-axis. The box model constrains the measurements, therefore, is not featured in the plots.
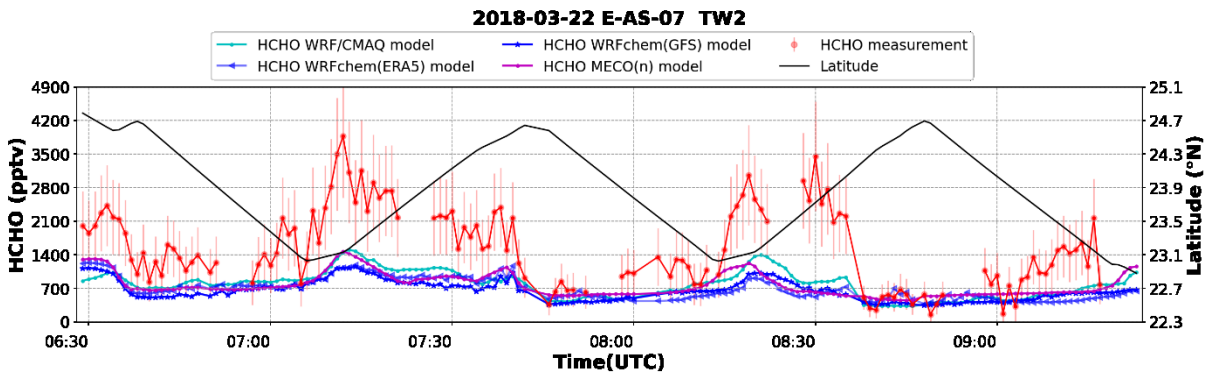
A 183: Temporal distribution of HCHO measurement and the corresponding results from available models for E-AS-07 TW2. The corresponding latitudes are provided on the secondary y-axis. The box model constrains the measurements, therefore, is not featured in the plots.
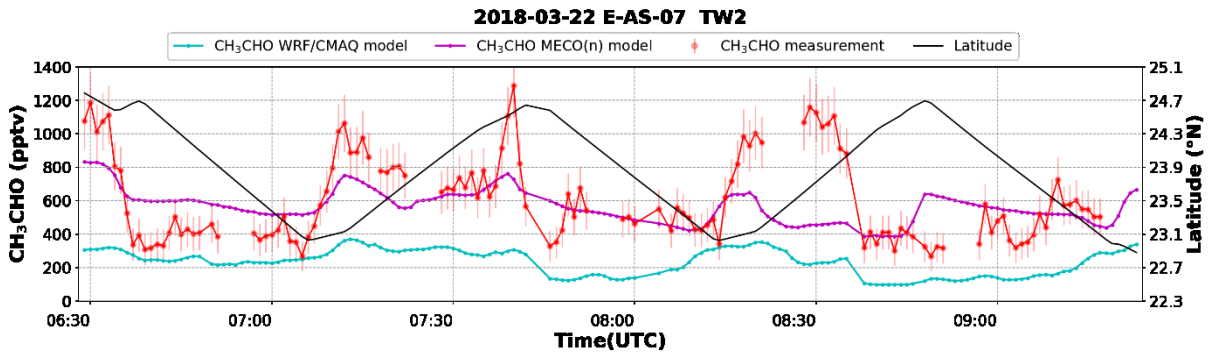
A 184: Temporal distribution of CH₃CHO measurement and the corresponding results from available models for E-AS-07 TW2. The corresponding latitudes are provided on the secondary y-axis. The box model constrains the measurements, therefore, is not featured in the plots.
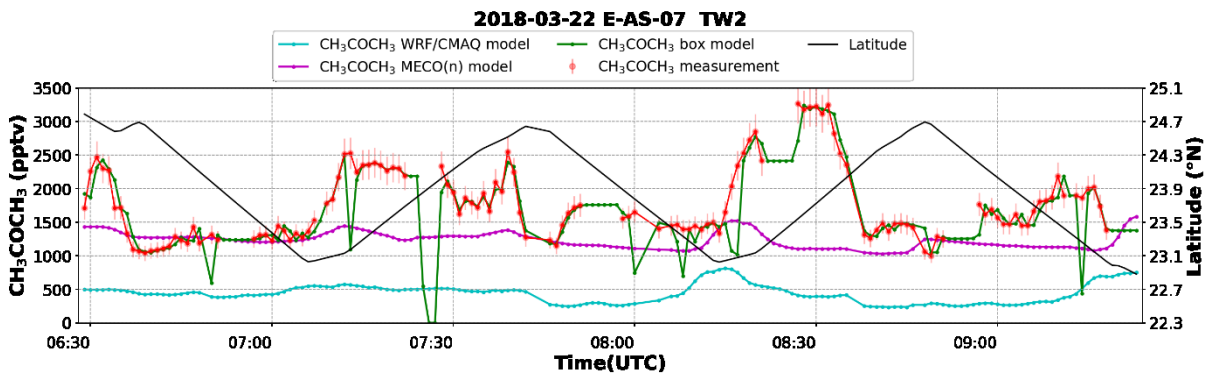
A 185: Temporal distribution of CH₃COCH₃ measurement and the corresponding results from available models for E-AS-07 TW2. The corresponding latitudes are provided on the secondary y-axis.

176
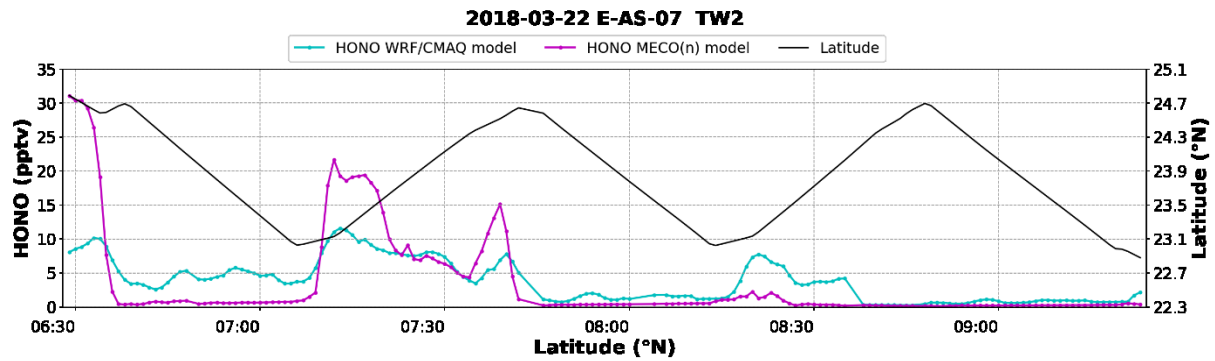
A 186: Temporal distribution of HONO results from available models for E-AS-07 TW2. The corresponding latitudes are provided on the secondary y-axis.
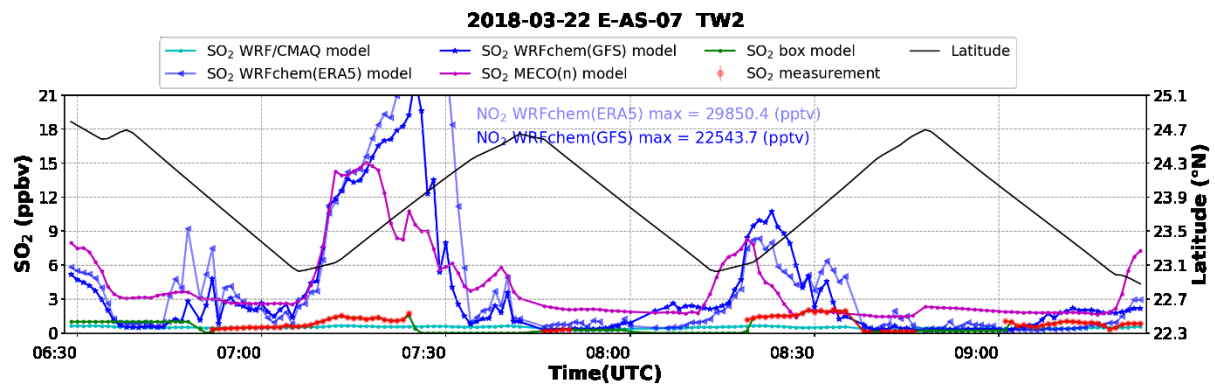
A 187: Temporal distribution of SO₂ measurement and the corresponding results from available models for E-AS-07 TW2. The corresponding latitudes are provided on the secondary y-axis.
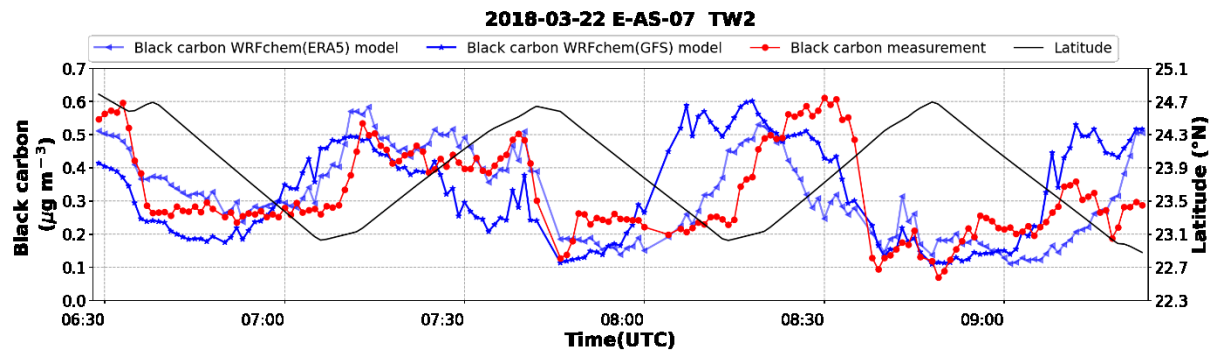
A 188: Temporal distribution of black carbon measurement and the corresponding results from available models for E-AS-07 TW2. The corresponding latitudes are provided on the secondary y-axis. The box model constrains the measurements, therefore, is not featured in the plots.
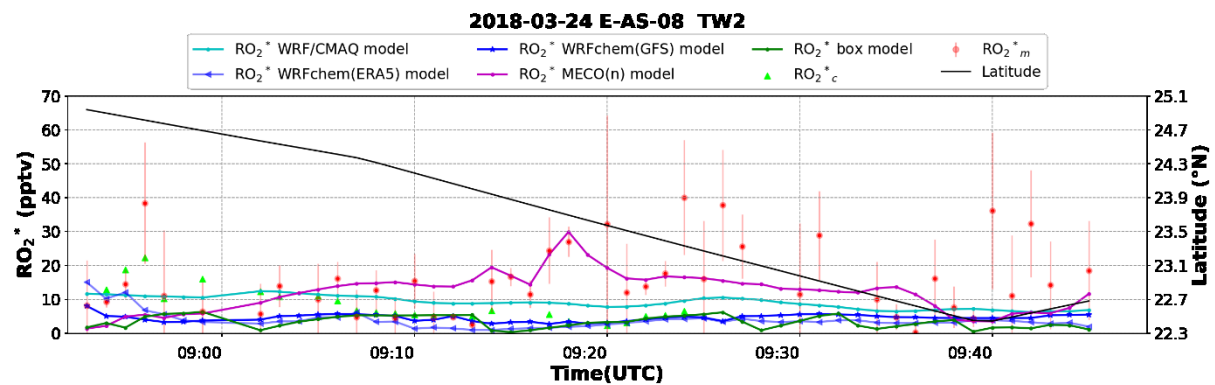
A 189: Temporal distribution of RO_2^* measurement, the corresponding results from available models, and the PSS calculations for E-AS-08 TW2. The corresponding latitudes are provided on the secondary y-axis.
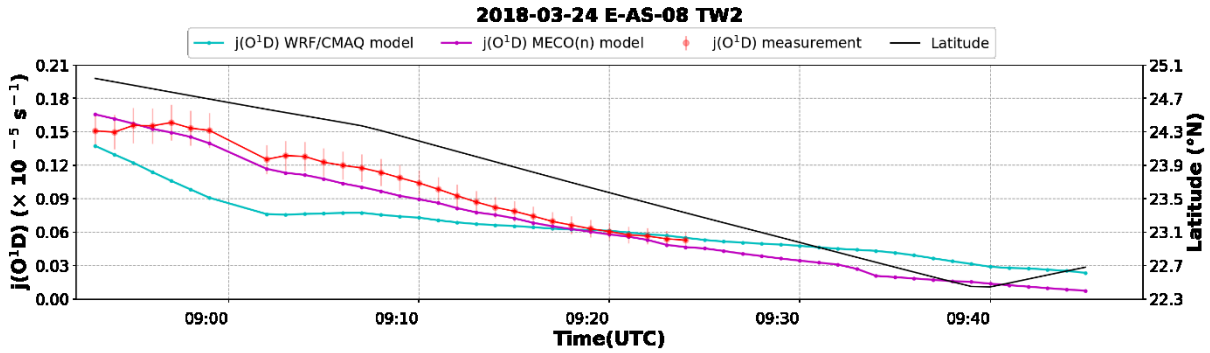
A 190: Temporal distribution of jO^1D measurement and the corresponding results from available models for E-AS-08 TW2. The corresponding latitudes are provided on the secondary y-axis. The box model constrains the measurements, therefore, is not featured in the plots.
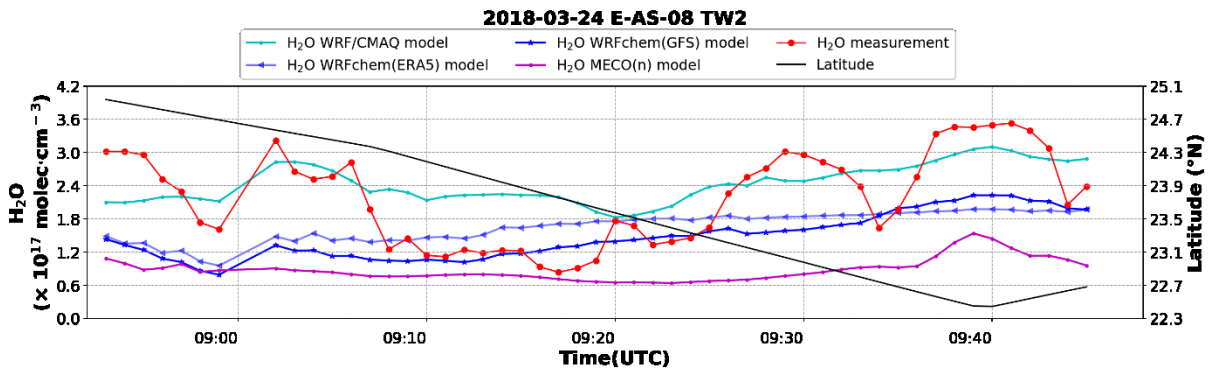
A 191: Temporal distribution of H_2O measurement and the corresponding results from available models for E-AS-08 TW2. The corresponding latitudes are provided on the secondary y-axis. The box model constrains the measurements, therefore, is not featured in the plots.
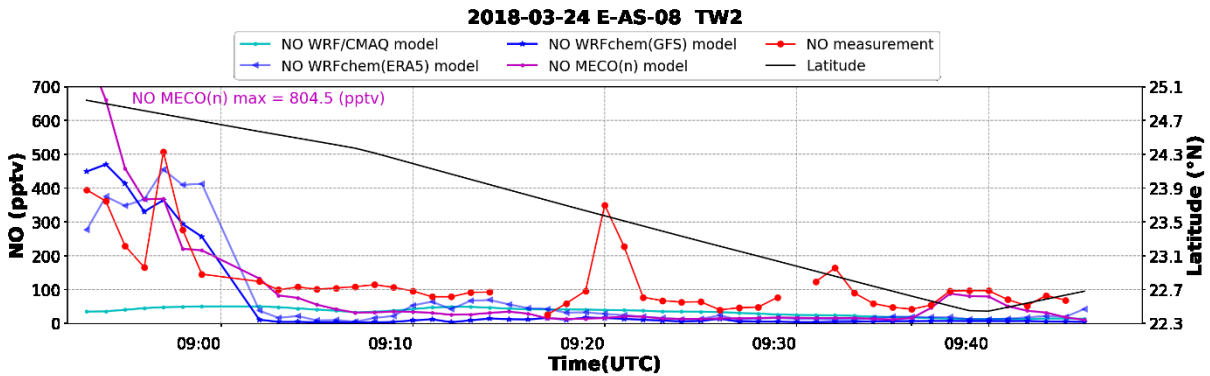
A 192: Temporal distribution of NO measurement and the corresponding results from available models for E-AS-08 TW2. The corresponding latitudes are provided on the secondary y-axis. The box model constrains the measurements, therefore, is not featured in the plots.

A 193: Temporal distribution of NO_2 results from available models for E-AS-08 TW2. The corresponding latitudes are provided on the secondary y-axis.

2018-03-24 E-AS-08 TW2
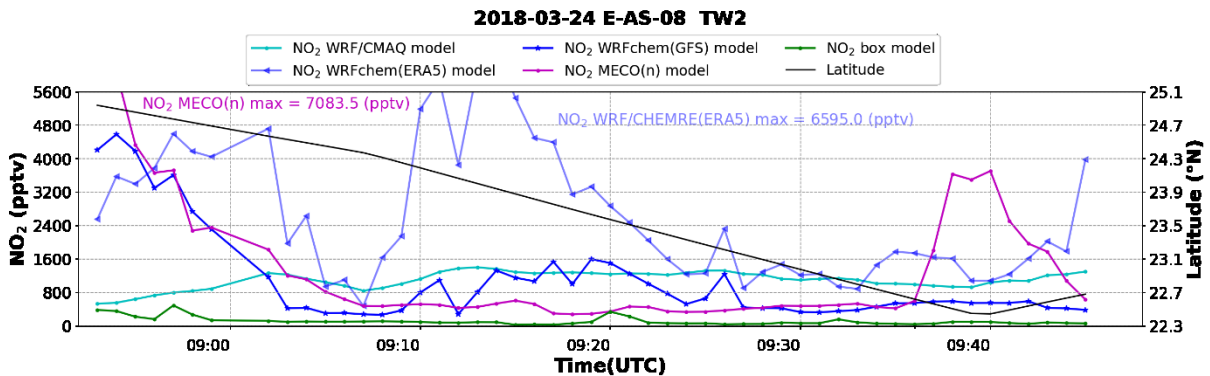
A 194: Temporal distribution of NOy measurement and the corresponding results from available models for E-AS-08 TW2. The corresponding latitudes are provided on the secondary y-axis.

2018-03-24 E-AS-08 TW2
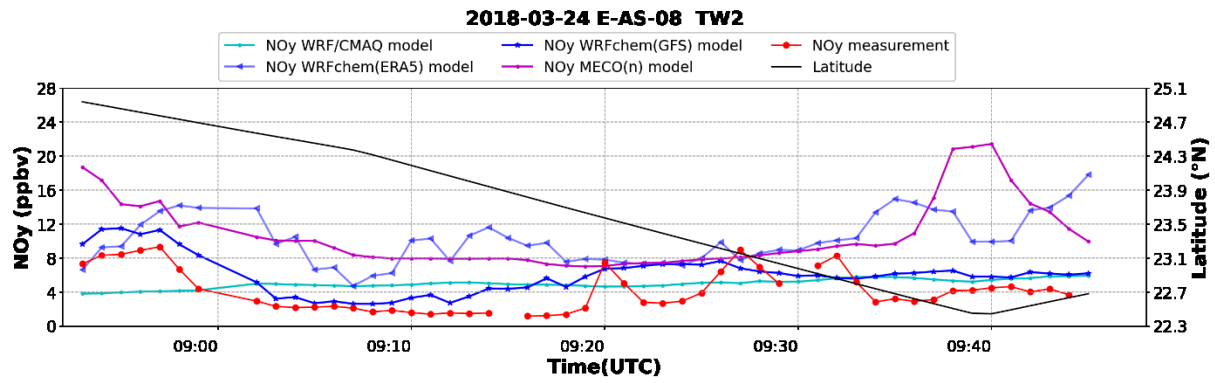
A 195: Temporal distribution of CO measurement and the corresponding results from available models for E-AS-08 TW2. The corresponding latitudes are provided on the secondary y-axis. The box model constrains the measurements, therefore, is not featured in the plots.

2018-03-24 E-AS-08 TW2
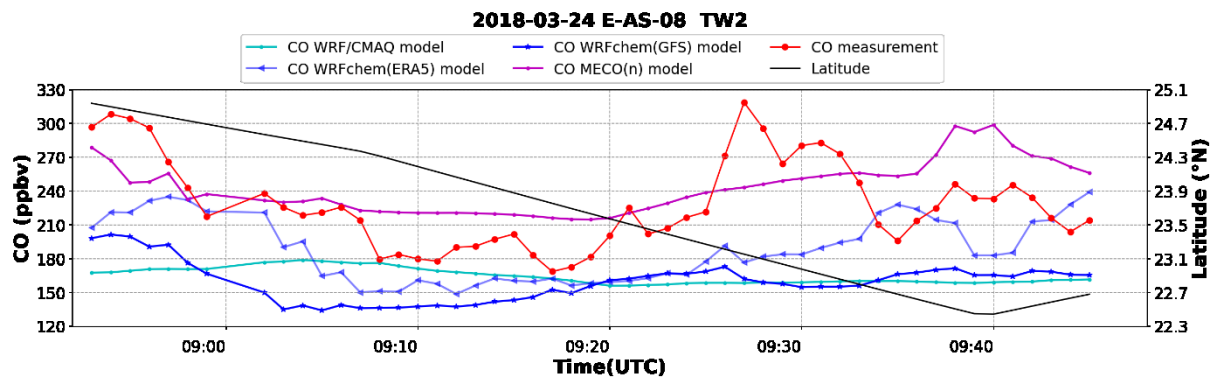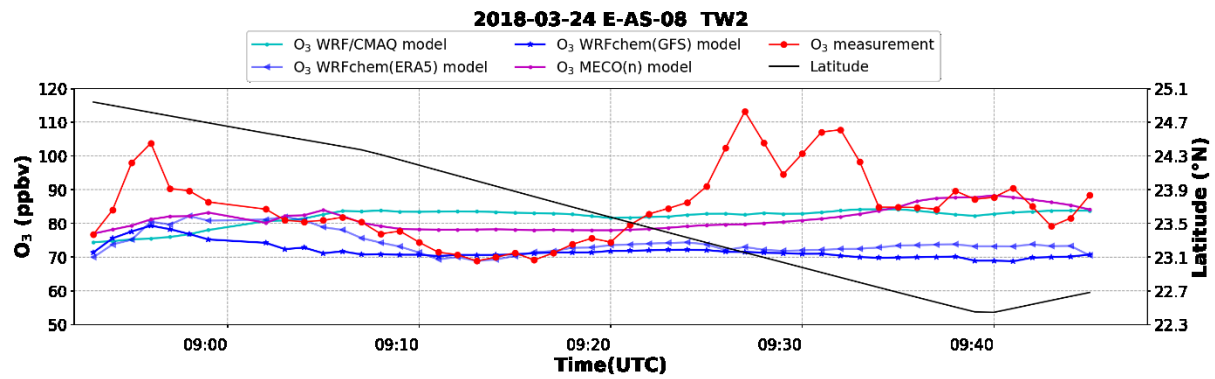
A 196: Temporal distribution of O₃ measurement and the corresponding results from available models for E-AS-08 TW2. The corresponding latitudes are provided on the secondary y-axis. The box model constrains the measurements, therefore, is not featured in the plots.

2018-03-24 E-AS-08 TW2

A 197: Temporal distribution of HCHO measurement and the corresponding results from available models for E-AS-08 TW2. The corresponding latitudes are provided on the secondary y-axis. The box model constrains the measurements, therefore, is not featured in the plots

179

A 198: Temporal distribution of CH₃CHO measurement and the corresponding results from available models for E-AS-08 TW2. The corresponding latitudes are provided on the secondary y-axis. The box model constrains the measurements, therefore, is not featured in the plots.

A 199: Temporal distribution of CH₃COCH₃ measurement and the corresponding results from available models for E-AS-08 TW2. The corresponding latitudes are provided on the secondary y-axis. The box model constrains the measurements, therefore, is not featured in the plots.
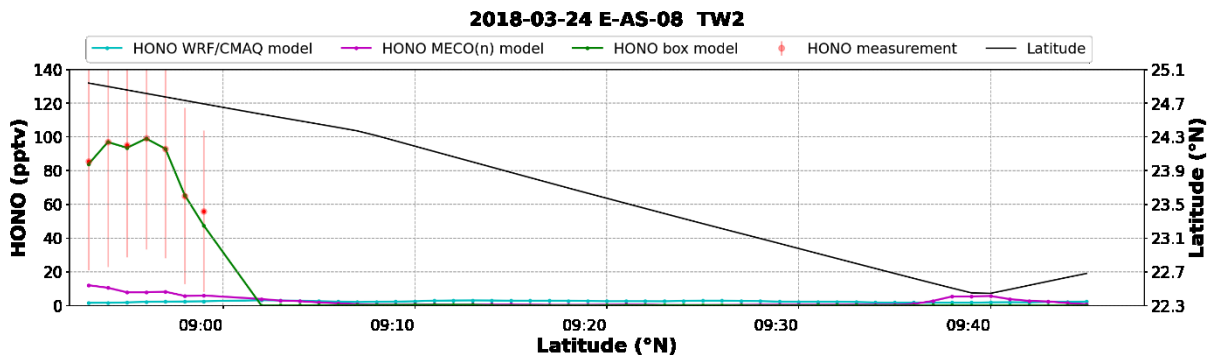
A 200: Temporal distribution of HONO measurement and the corresponding results from available models for E-AS-08 TW2. The corresponding latitudes are provided on the secondary y-axis.
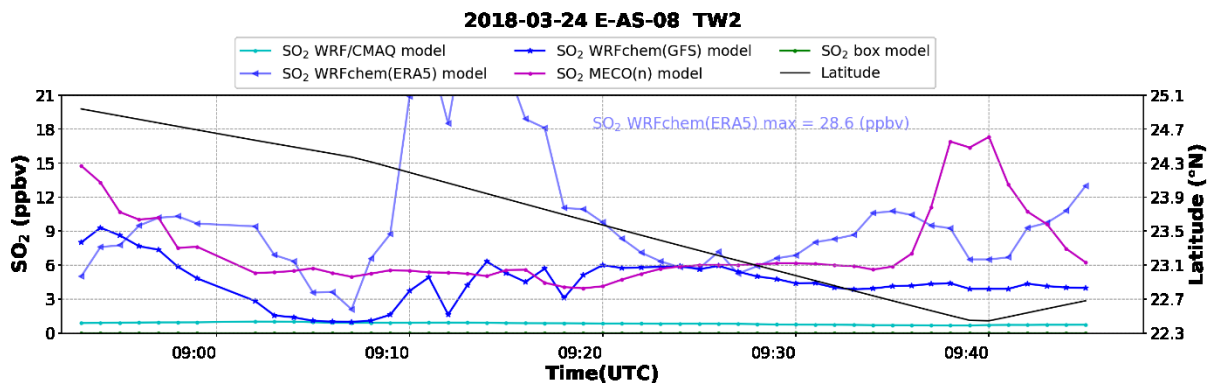
A 201: Temporal distribution of SO₂ results from available models for E-AS-08 TW2. The corresponding latitudes are provided on the secondary y-axis.
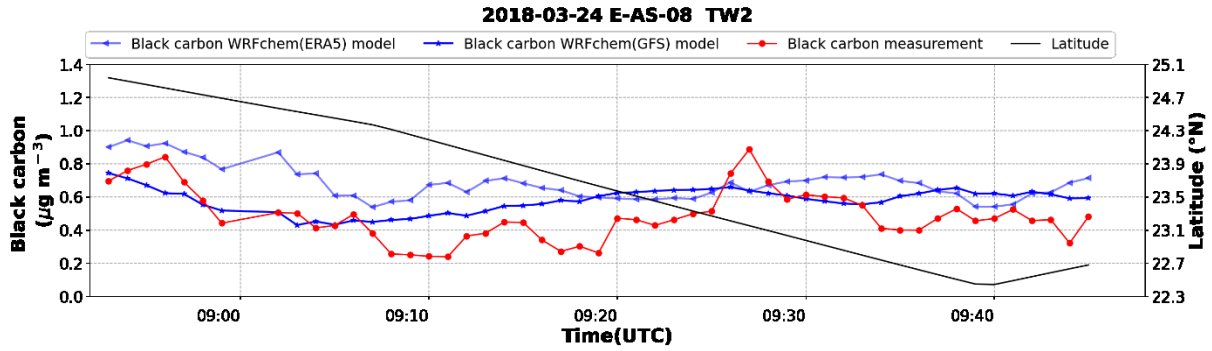
A 202: Temporal distribution of black carbon measurement and the corresponding results from available models for E-AS-08 TW2. The corresponding latitudes are provided on the secondary y-axis. The box model constrains the measurements, therefore, is not featured in the plots.
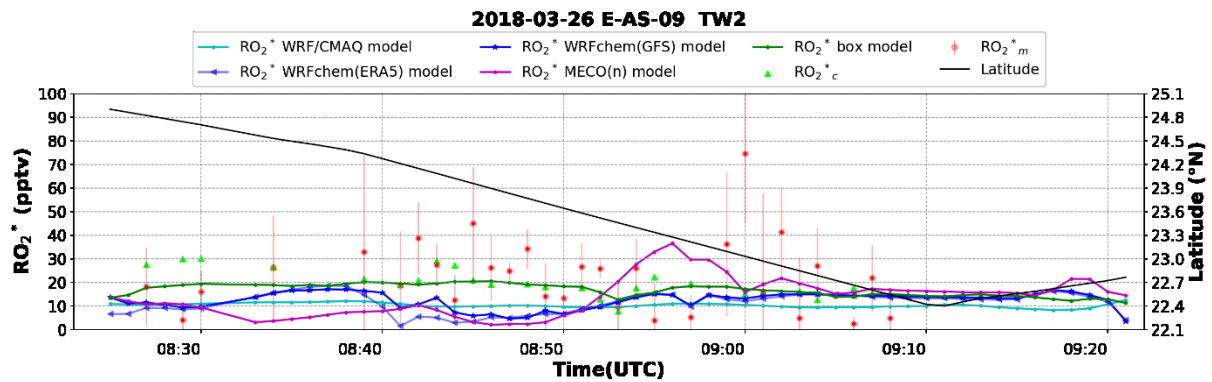
A 203: Temporal distribution of RO_2^* measurement, the corresponding results from available models, and the PSS calculations for E-AS-09 TW2. The corresponding latitudes are provided on the secondary y-axis.
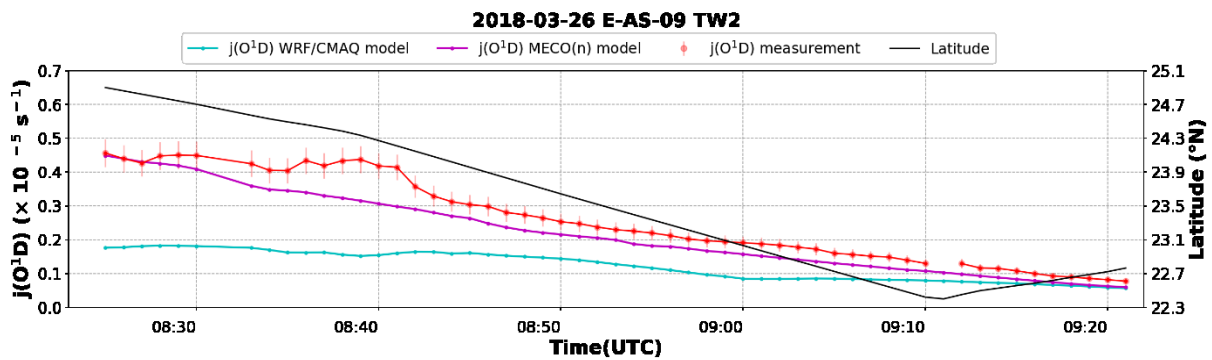
A 204: Temporal distribution of jO^1D measurement and the corresponding results from available models for E-AS-09 TW2. The corresponding latitudes are provided on the secondary y-axis. The box model constrains the measurements, therefore, is not featured in the plots.
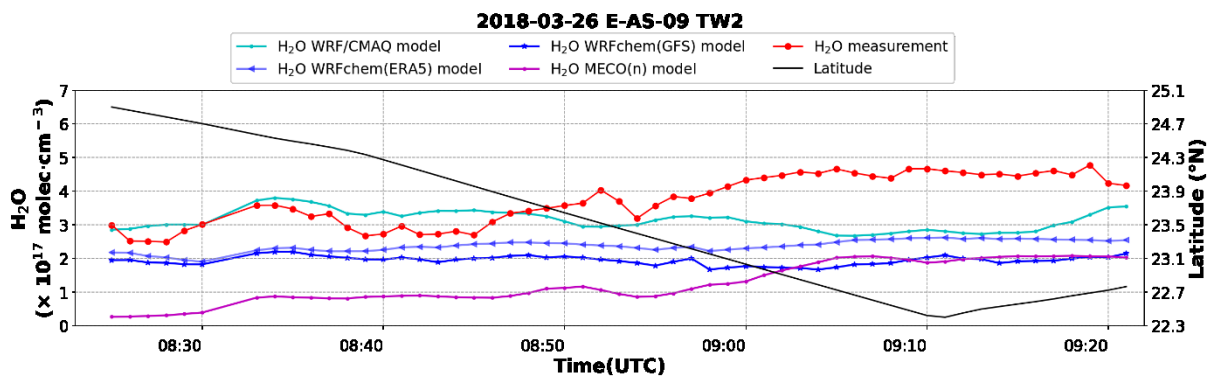
A 205: Temporal distribution of H_2O measurement and the corresponding results from available models for E-AS-09 TW2. The corresponding latitudes are provided on the secondary y-axis. The box model constrains the measurements, therefore, is not featured in the plots.

181
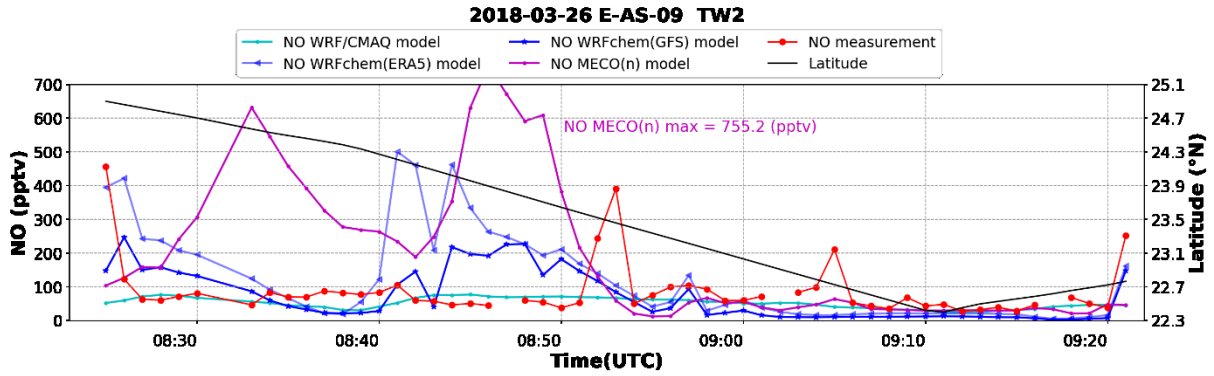
A 206: Temporal distribution of NO measurement and the corresponding results from available models for E-AS-09 TW2. The corresponding latitudes are provided on the secondary y-axis. The box model constrains the measurements, therefore, is not featured in the plots.
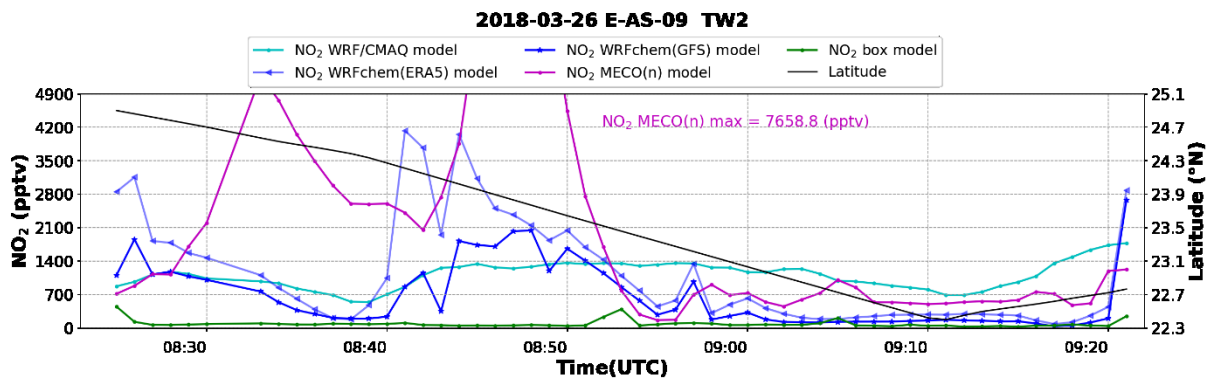
A 207: Temporal distribution of NO₂ results from available models for E-AS-09 TW2. The corresponding latitudes are provided on the secondary y-axis.
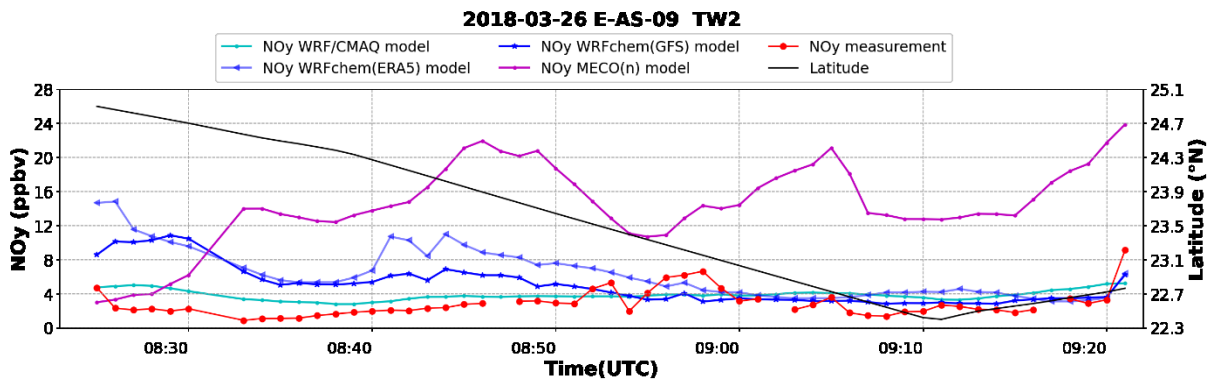
A 208: Temporal distribution of NOy measurement and the corresponding results from available models for E-AS-09 TW2. The corresponding latitudes are provided on the secondary y-axis.
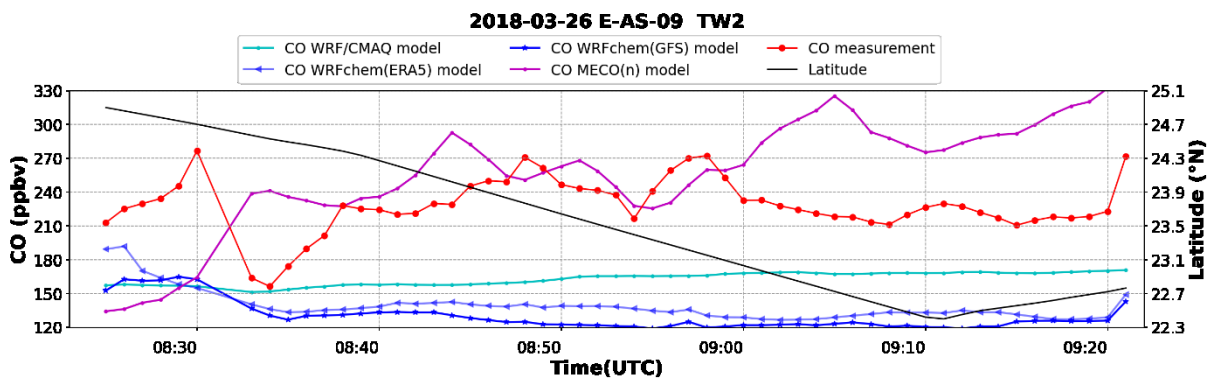
A 209: Temporal distribution of CO measurement and the corresponding results from available models for E-AS-09 TW2. The corresponding latitudes are provided on the secondary y-axis. The box model constrains the measurements, therefore, is not featured in the plots.

182
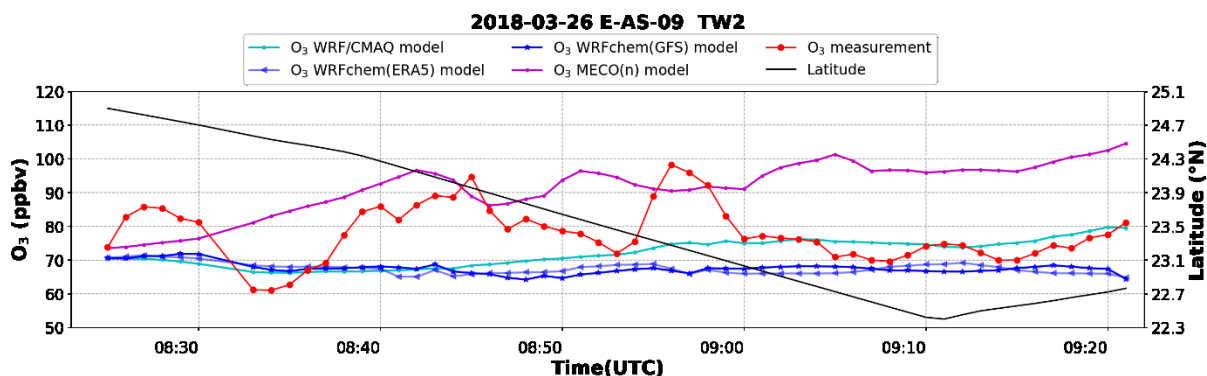
A 210: Temporal distribution of O₃ measurement and the corresponding results from available models for E-AS-09 TW2. The corresponding latitudes are provided on the secondary y-axis. The box model constrains the measurements, therefore, is not featured in the plots.
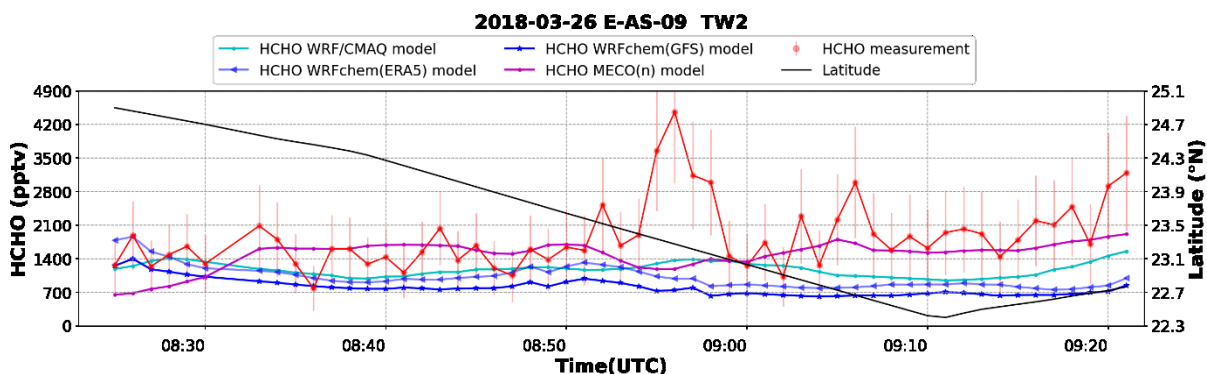
A 211: Temporal distribution of HCHO measurement and the corresponding results from available models for E-AS-09 TW2. The corresponding latitudes are provided on the secondary y-axis. The box model constrains the measurements, therefore, is not featured in the plots.
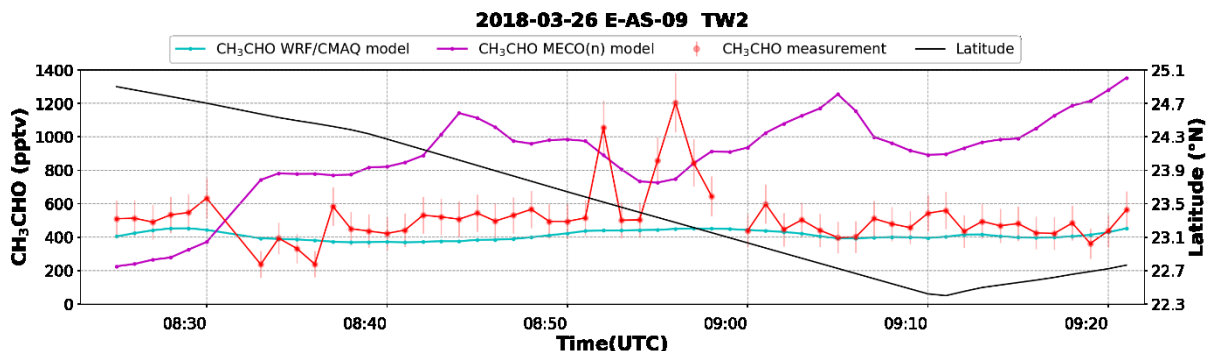
A 212: Temporal distribution of CH₃CHO measurement and the corresponding results from available models for E-AS-09 TW2. The corresponding latitudes are provided on the secondary y-axis. The box model constrains the measurements, therefore, is not featured in the plots.
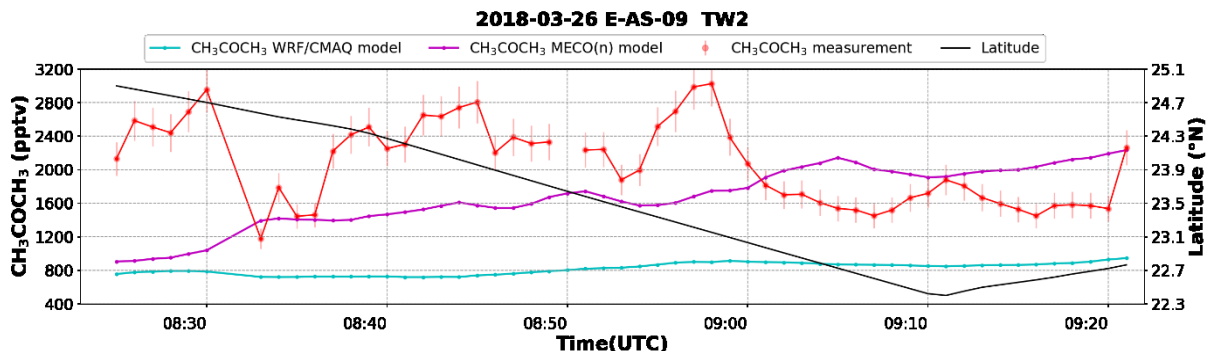
A 213: Temporal distribution of CH₃COCH₃ measurement and the corresponding results from available models for E-AS-09 TW2. The corresponding latitudes are provided on the secondary y-axis. The box model constrains the measurements, therefore, is not featured in the plots.
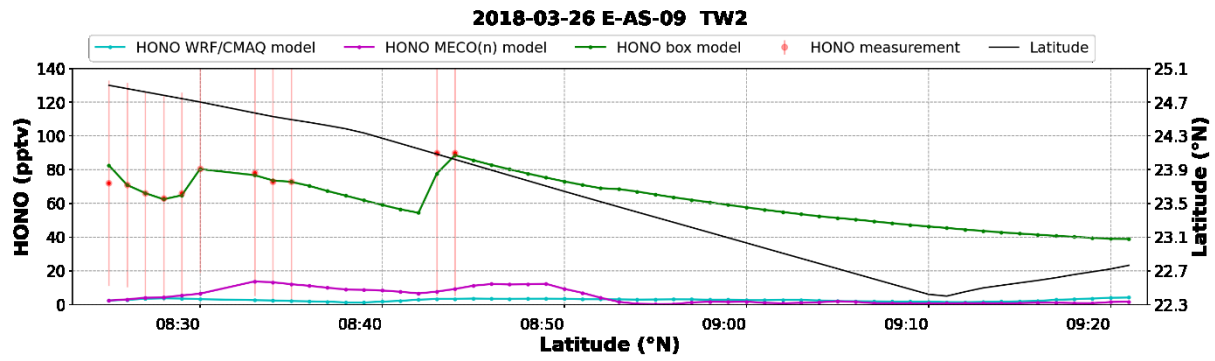
A 214: Temporal distribution of HONO measurement and the corresponding results from available models for E-AS-09 TW2. The corresponding latitudes are provided on the secondary y-axis.
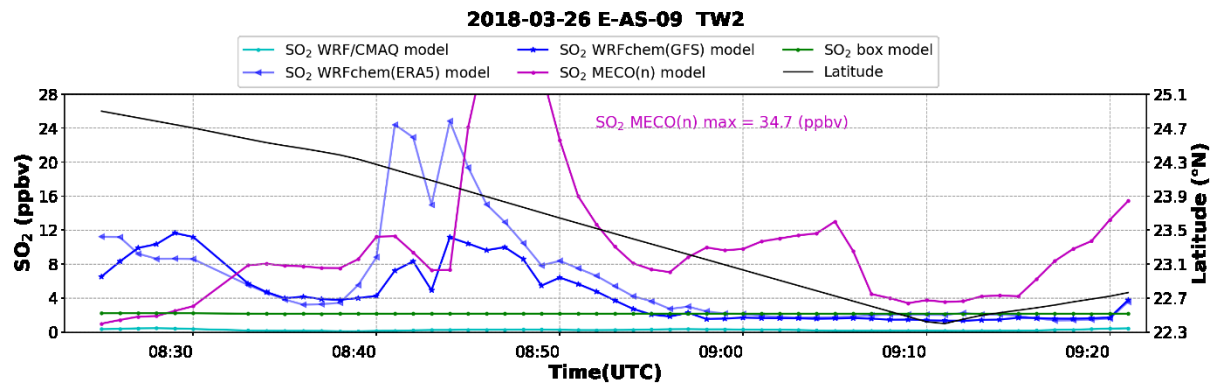
A 215: Temporal distribution of SO_2 results from available models for E-AS-09 TW2. The corresponding latitudes are provided on the secondary y-axis.
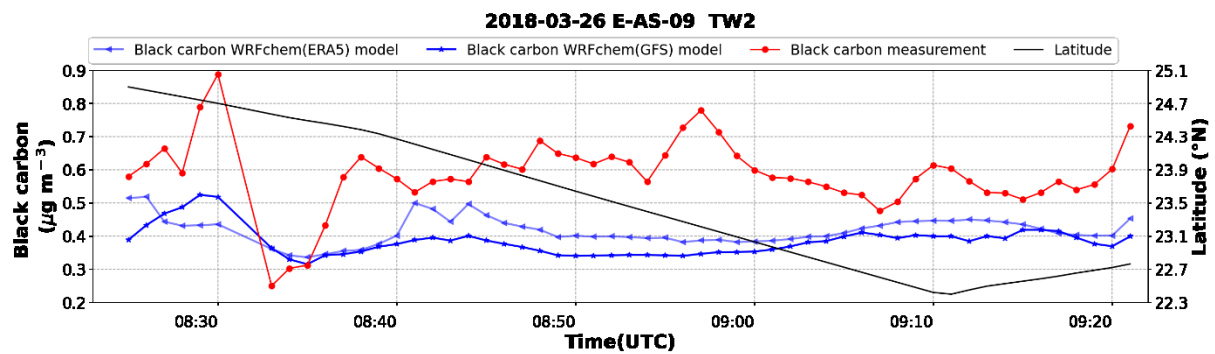
A 216: Temporal distribution of black carbon measurement and the corresponding results from available models for E-AS-09 TW2. The corresponding latitudes are provided on the secondary y-axis. The box model constrains the measurements, therefore, is not featured in the plots.
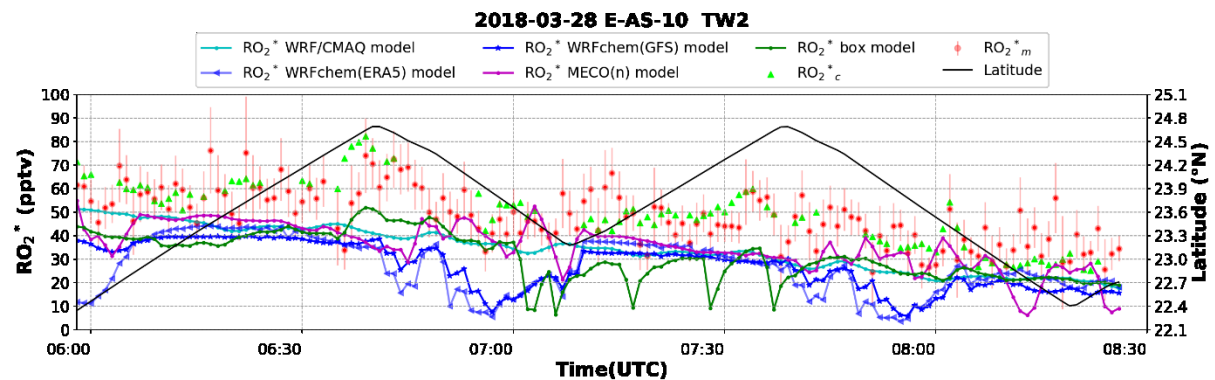
A 217: Temporal distribution of RO_2^* measurement, the corresponding results from available models, and the PSS calculations for E-AS-10 TW2. The corresponding latitudes are provided on the secondary y-axis.
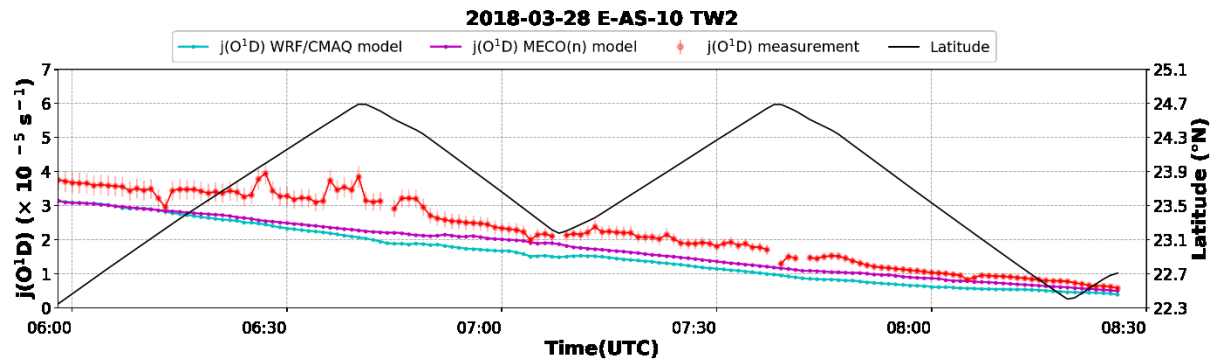
A 218: Temporal distribution of jO^{1}D measurement and the corresponding results from available models for E-AS-10 TW2. The corresponding latitudes are provided on the secondary y-axis. The box model constrains the measurements, therefore, is not featured in the plots.
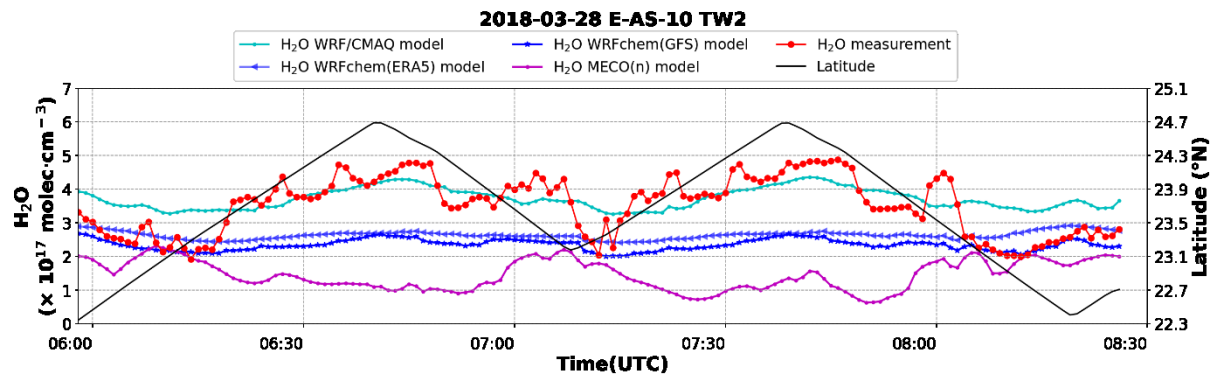
A 219: Temporal distribution of H$_2$O measurement and the corresponding results from available models for E-AS-10 TW2. The corresponding latitudes are provided on the secondary y-axis. The box model constrains the measurements, therefore, is not featured in the plots.
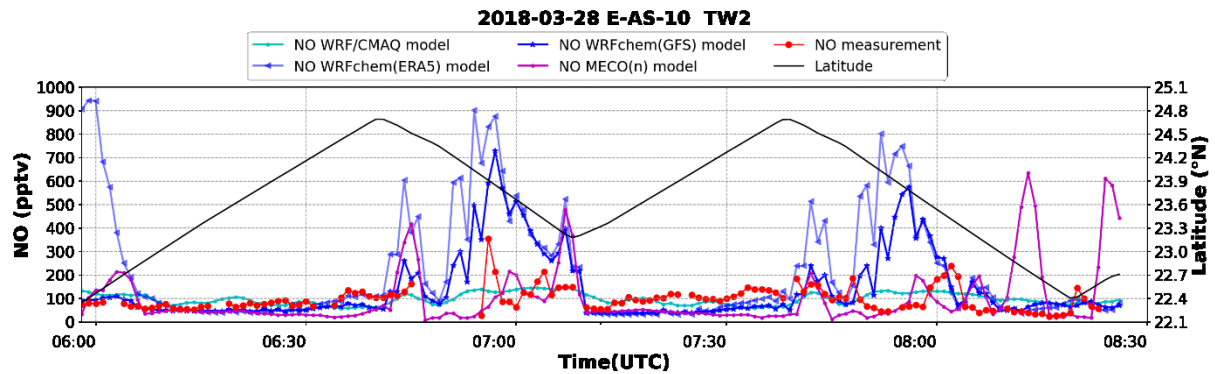
A 220: Temporal distribution of NO measurement and the corresponding results from available models for E-AS-10 TW2. The corresponding latitudes are provided on the secondary y-axis. The box model constrains the measurements, therefore, is not featured in the plots.
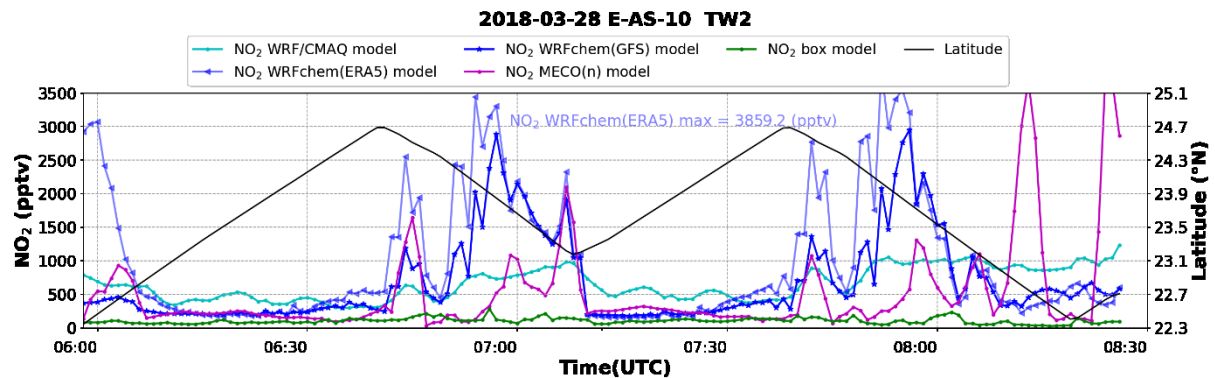
A 221: Temporal distribution of NO$_2$ results from available models for E-AS-10 TW2. The corresponding latitudes are provided on the secondary y-axis.

185
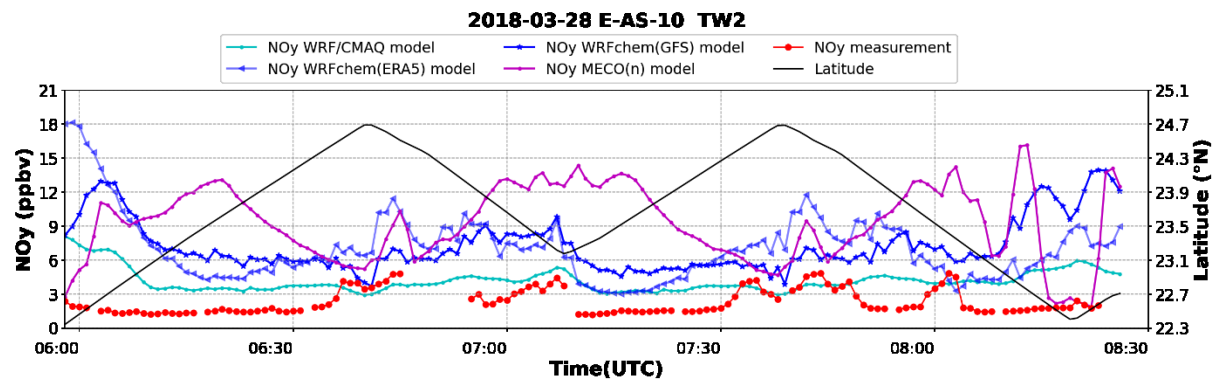
A 222: Temporal distribution of NOy measurement and the corresponding results from available models for E-AS-10 TW2. The corresponding latitudes are provided on the secondary y-axis.
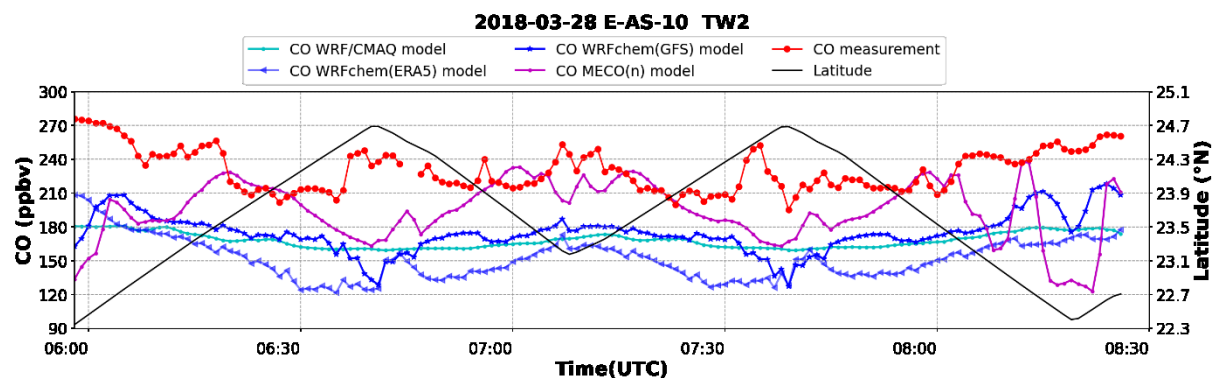
A 223: Temporal distribution of CO measurement and the corresponding results from available models for E-AS-10 TW2. The corresponding latitudes are provided on the secondary y-axis. The box model constrains the measurements, therefore, is not featured in the plots.
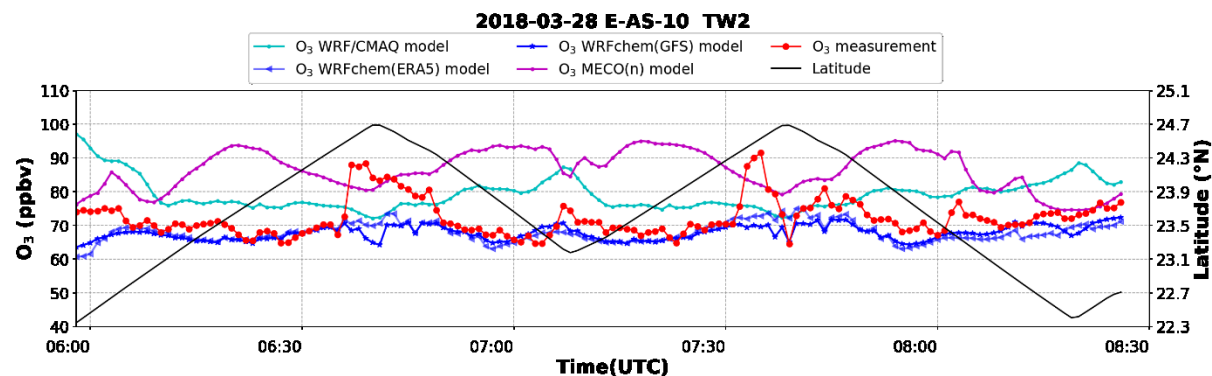
A 224: Temporal distribution of O₃ measurement and the corresponding results from available models for E-AS-10 TW2. The corresponding latitudes are provided on the secondary y-axis. The box model constrains the measurements, therefore, is not featured in the plots.
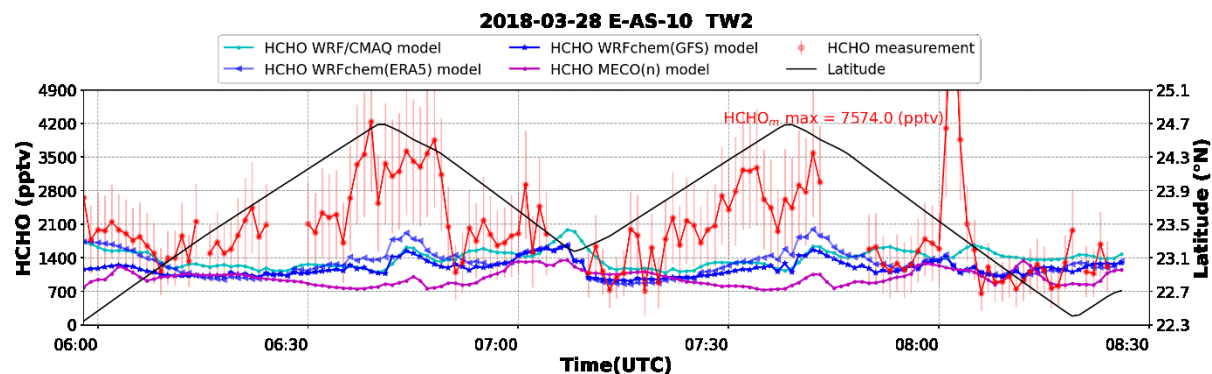
A 225: Temporal distribution of HCHO measurement and the corresponding results from available models for E-AS-10 TW2. The corresponding latitudes are provided on the secondary y-axis. The box model constrains the measurements, therefore, is not featured in the plots.
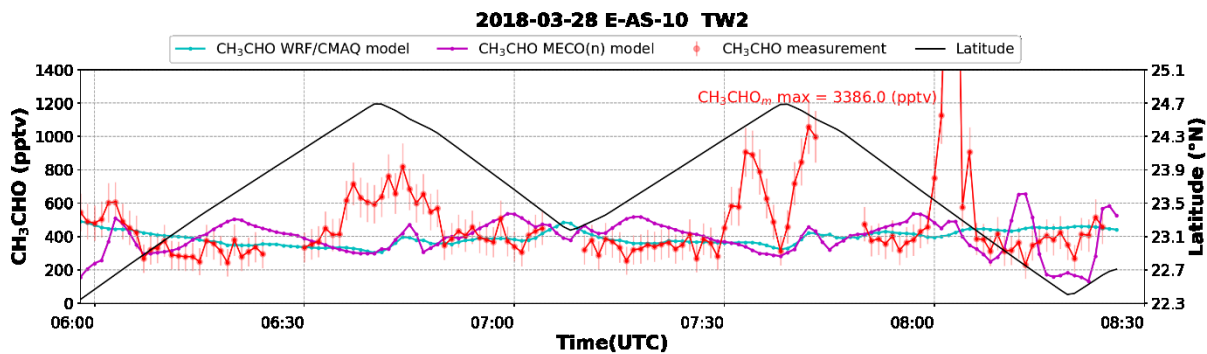
A 226: Temporal distribution of CH₃CHO measurement and the corresponding results from available models for E-AS-10 TW2. The corresponding latitudes are provided on the secondary y-axis. The box model constrains the measurements, therefore, is not featured in the plots.
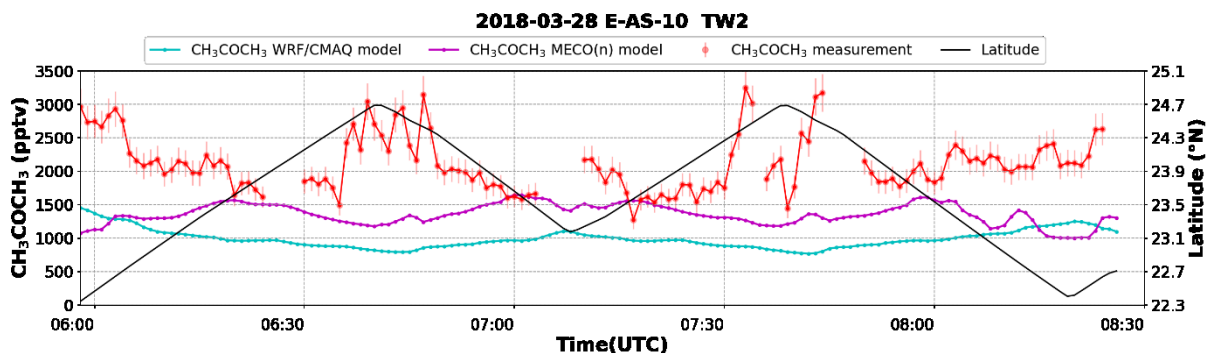
A 227: Temporal distribution of CH₃COCH₃ measurement and the corresponding results from available models for E-AS-10 TW2. The corresponding latitudes are provided on the secondary y-axis. The box model constrains the measurements, therefore, is not featured in the plots.
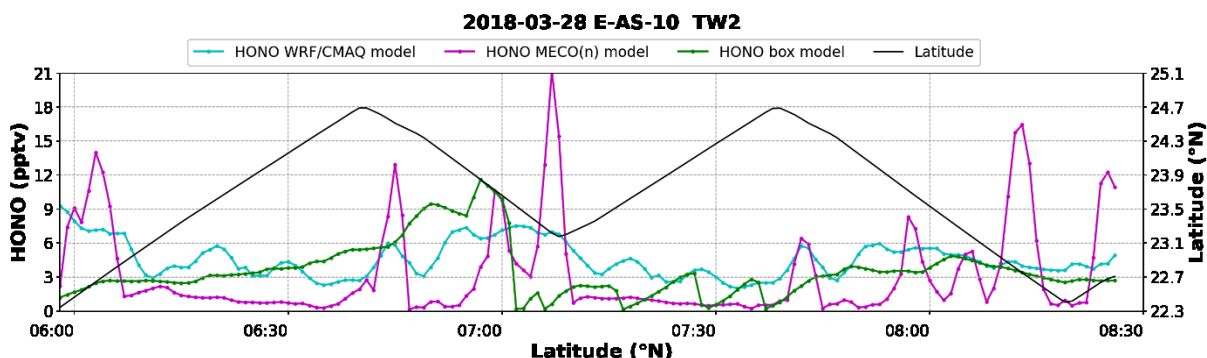
A 228: Temporal distribution of HONO results from available models for E-AS-10 TW2. The corresponding latitudes are provided on the secondary y-axis.
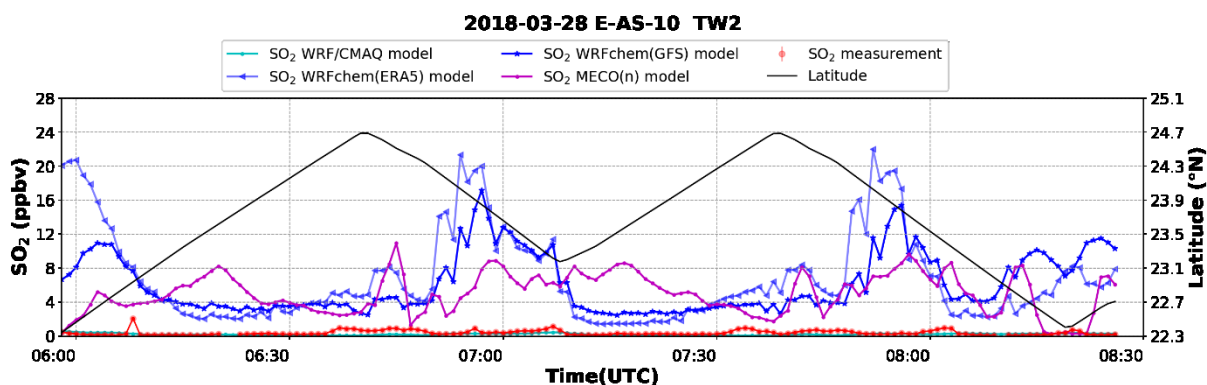
A 229: Temporal distribution of SO₂ measurement and the corresponding results from available models for E-AS-10 TW2. The corresponding latitudes are provided on the secondary y-axis. The box model constrains the measurements, therefore, is not featured in the plots.
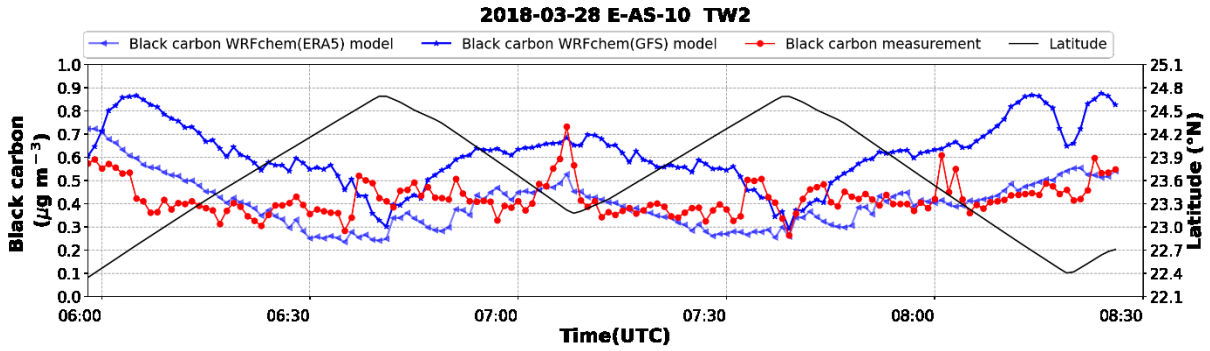
A 230: Temporal distribution of black carbon measurement and the corresponding results from available models for E-AS-10 TW2. The corresponding latitudes are provided on the secondary y-axis. The box model constrains the measurements, therefore, is not featured in the plots.
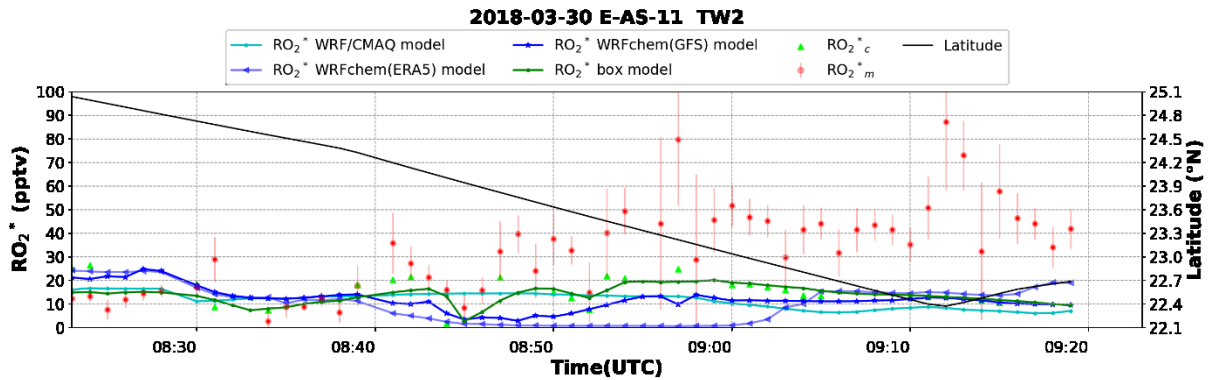
A 231: Temporal distribution of RO_2^* measurement, the corresponding results from available models, and the PSS calculations for E-AS-11 TW2. The corresponding latitudes are provided on the secondary y-axis.
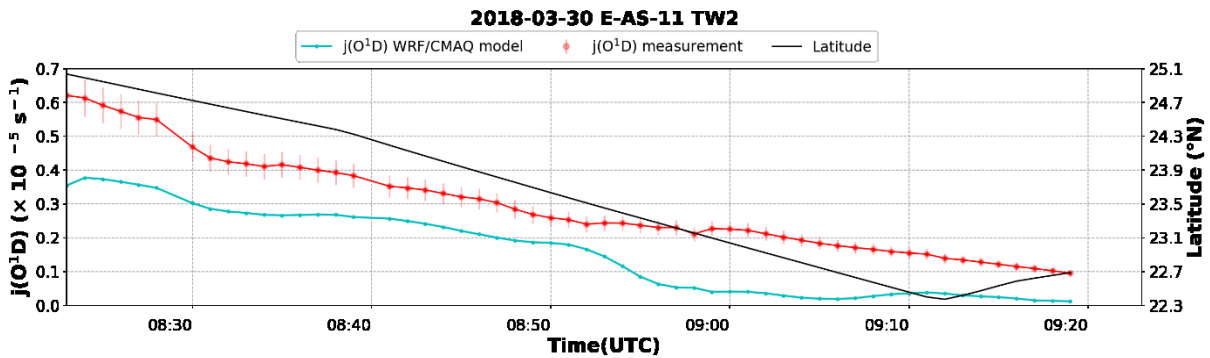
A 232: Temporal distribution of jO^1D measurement and the corresponding results from available models for E-AS-11 TW2. The corresponding latitudes are provided on the secondary y-axis. The box model constrains the measurements, therefore, is not featured in the plots.
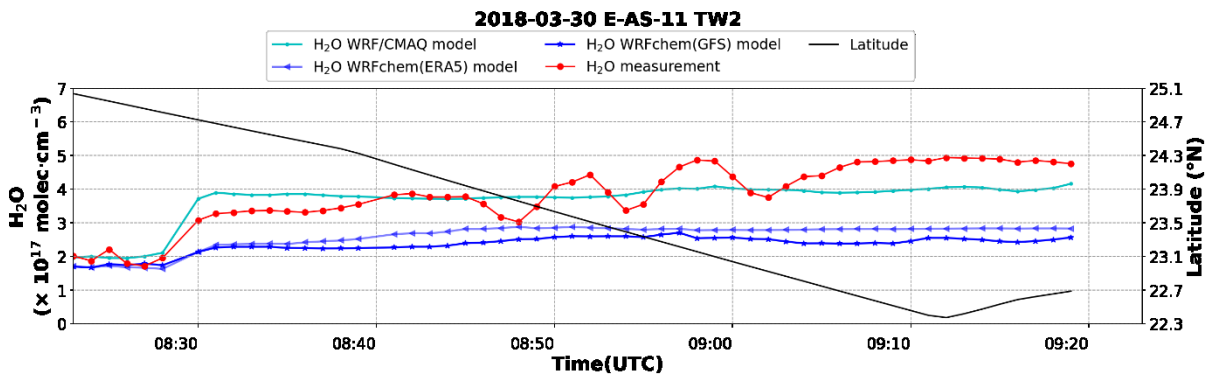
A 233: Temporal distribution of H_2O measurement and the corresponding results from available models for E-AS-11 TW2. The corresponding latitudes are provided on the secondary y-axis. The box model constrains the measurements, therefore, is not featured in the plots.
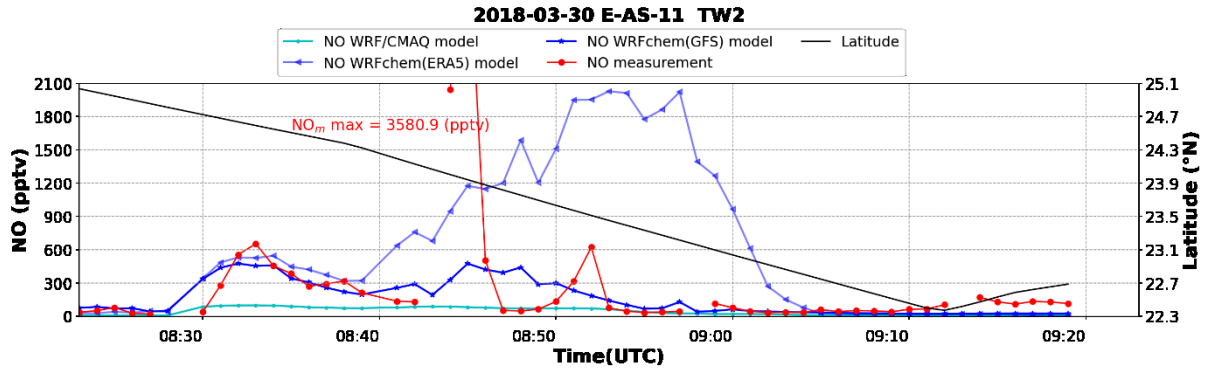
A 234: Temporal distribution of NO measurement and the corresponding results from available models for E-AS-11 TW2. The corresponding latitudes are provided on the secondary y-axis. The box model constrains the measurements, therefore, is not featured in the plots.
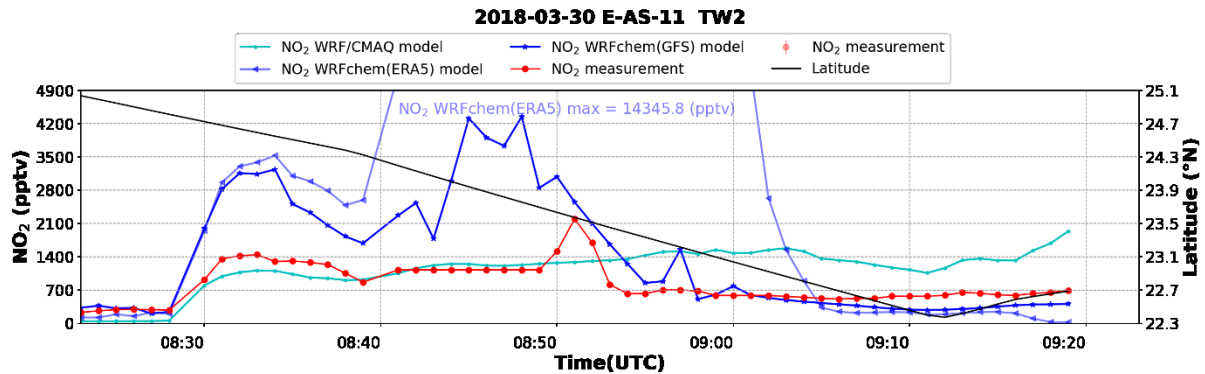
A 235: Temporal distribution of NO₂ measurement and the corresponding results from available models for E-AS-11 TW2. The corresponding latitudes are provided on the secondary y-axis. The box model constrains the measurements, therefore, is not featured in the plots.
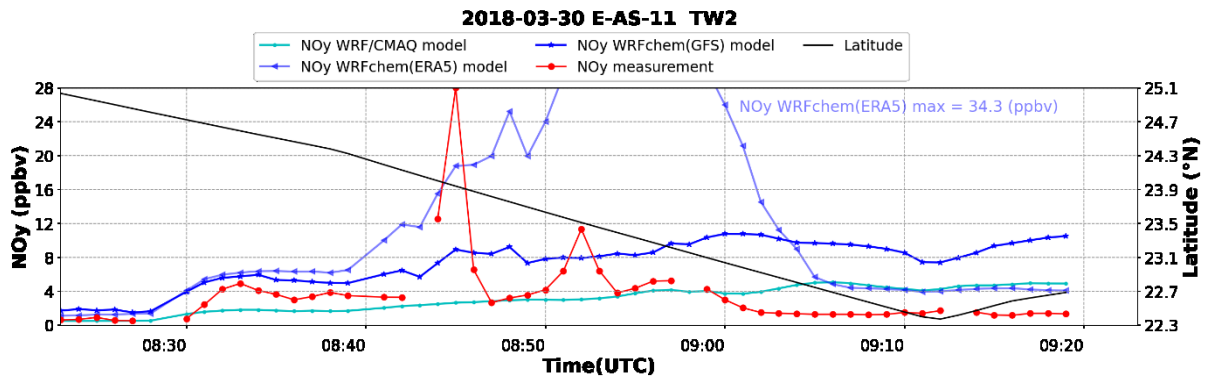
A 236: Temporal distribution of NOy measurement and the corresponding results from available models for E-AS-11 TW2. The corresponding latitudes are provided on the secondary y-axis.
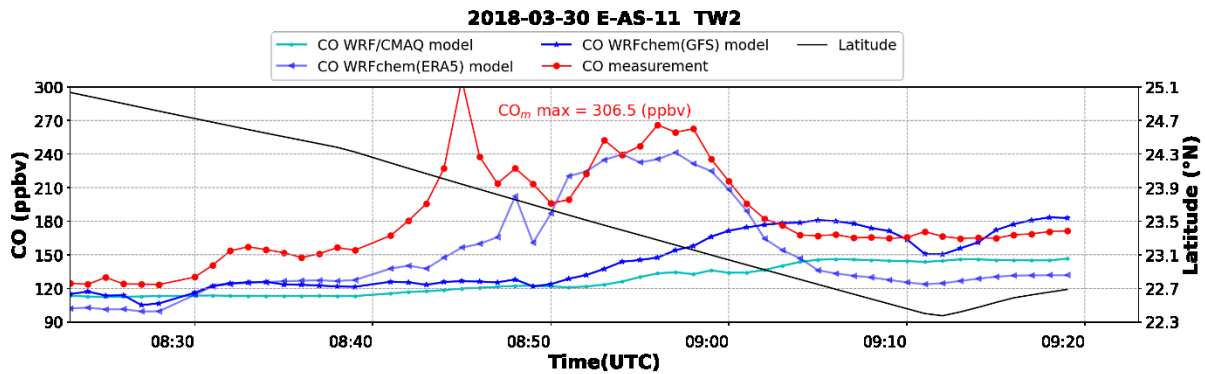
A 237: Temporal distribution of CO measurement and the corresponding results from available models for E-AS-11 TW2. The corresponding latitudes are provided on the secondary y-axis. The box model constrains the measurements, therefore, is not featured in the plots.

189
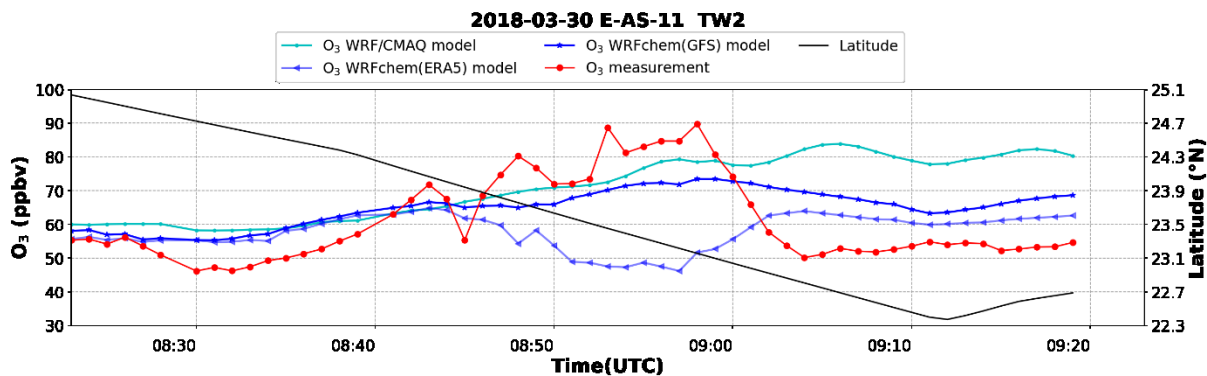
A 238: Temporal distribution of O₃ measurement and the corresponding results from available models for E-AS-11 TW2. The corresponding latitudes are provided on the secondary y-axis. The box model constrains the measurements, therefore, is not featured in the plots.
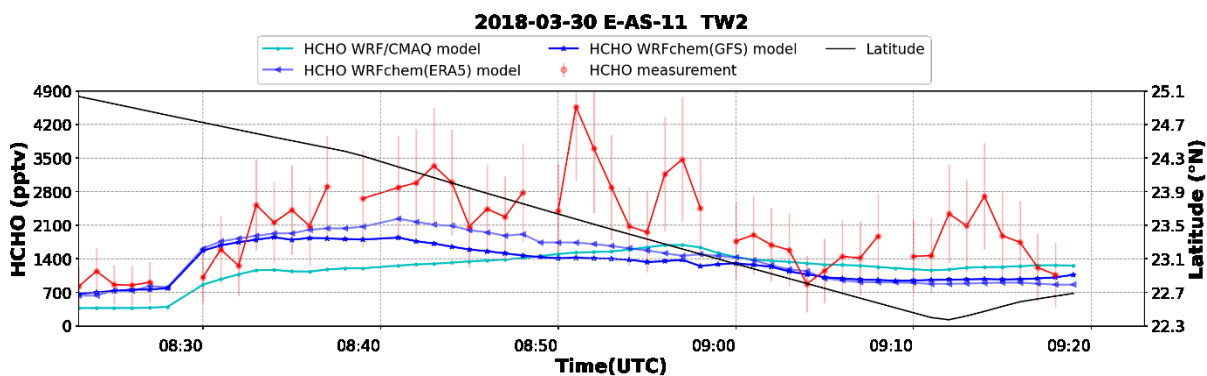
A 239: Temporal distribution of HCHO measurement and the corresponding results from available models for E-AS-11 TW2. The corresponding latitudes are provided on the secondary y-axis. The box model constrains the measurements, therefore, is not featured in the plots.
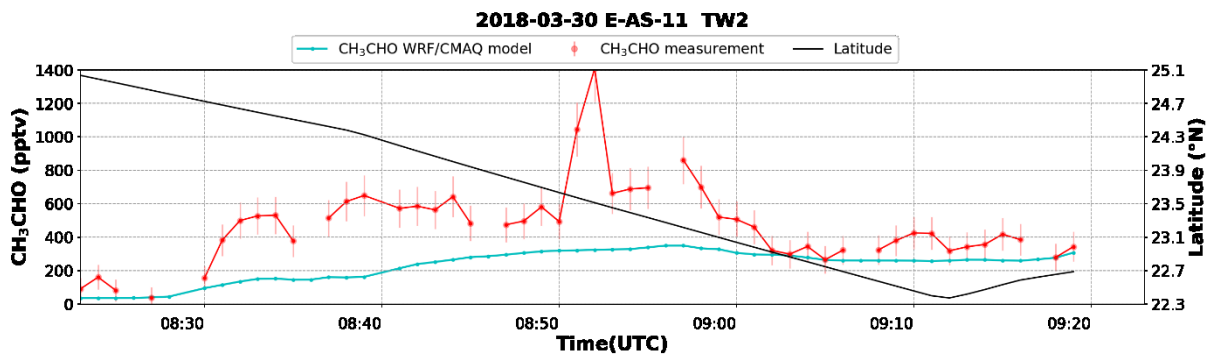
A 240: Temporal distribution of CH₃CHO measurement and the corresponding results from available models for E-AS-11 TW2. The corresponding latitudes are provided on the secondary y-axis. The box model constrains the measurements, therefore, is not featured in the plots.
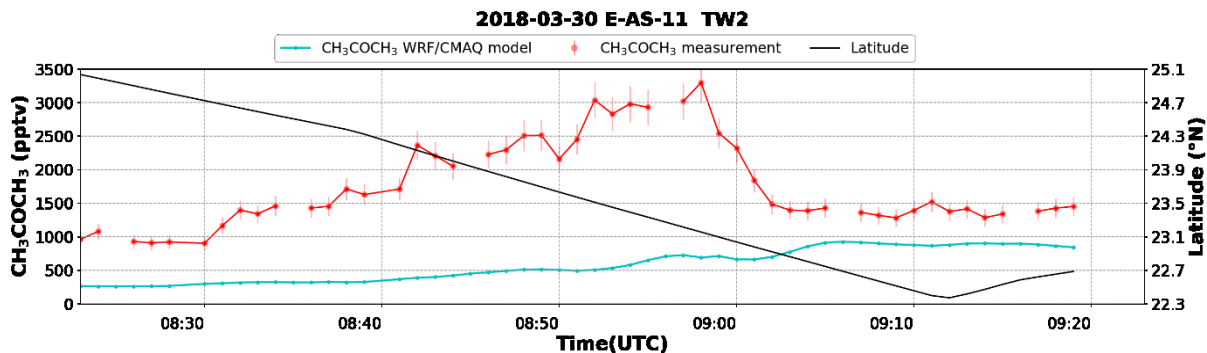
A 241: Temporal distribution of CH₃COCH₃ measurement and the corresponding results from available models for E-AS-11 TW2. The corresponding latitudes are provided on the secondary y-axis. The box model constrains the measurements, therefore, is not featured in the plots.
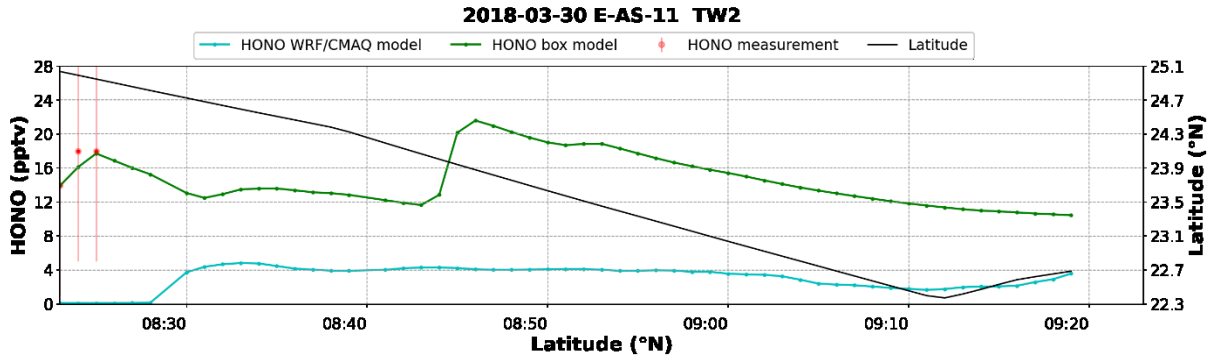
A 242: Temporal distribution of HONO measurements and the corresponding results from available models for E-AS-11 TW2. The corresponding latitudes are provided on the secondary y-axis.
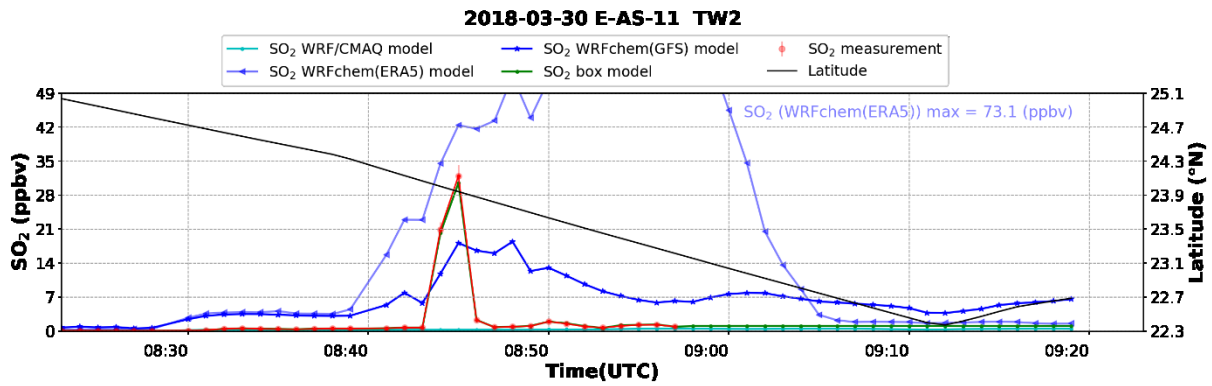
A 243: Temporal distribution of SO₂ measurement and the corresponding results from available models for E-AS-11 TW2. The corresponding latitudes are provided on the secondary y-axis.
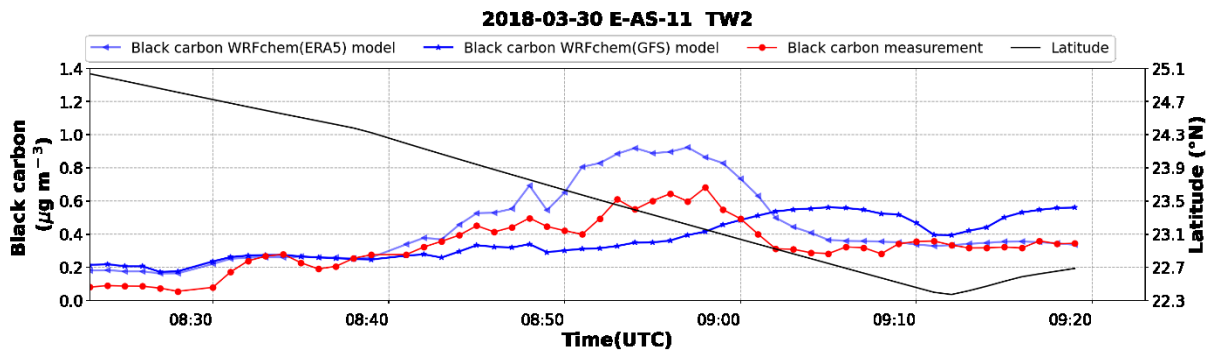
A 244: Temporal distribution of black carbon measurement and the corresponding results from available models for E-AS-11 TW2. The corresponding latitudes are provided on the secondary y-axis. The box model constrains the measurements, therefore, is not featured in the plots.
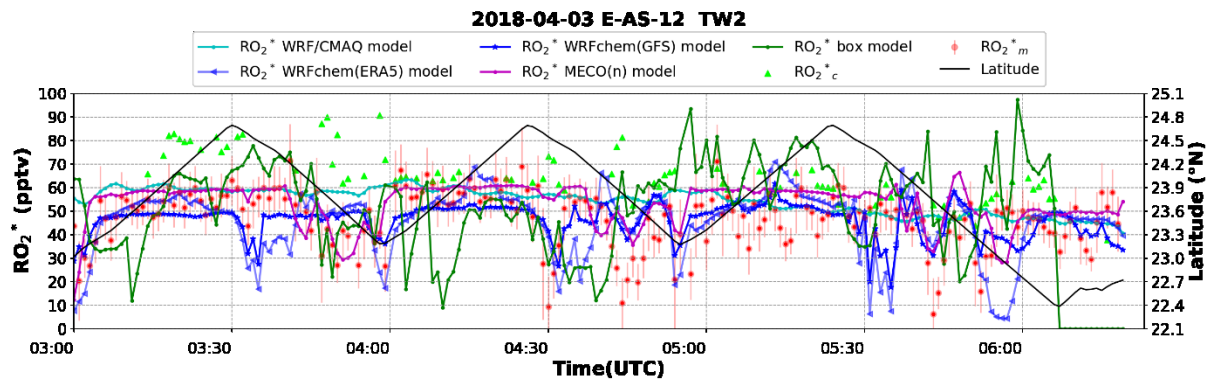
A 245: Temporal distribution of RO_2^* measurement, the corresponding results from available models, and the PSS calculations for E-AS-12 TW2. The corresponding latitudes are provided on the secondary y-axis.
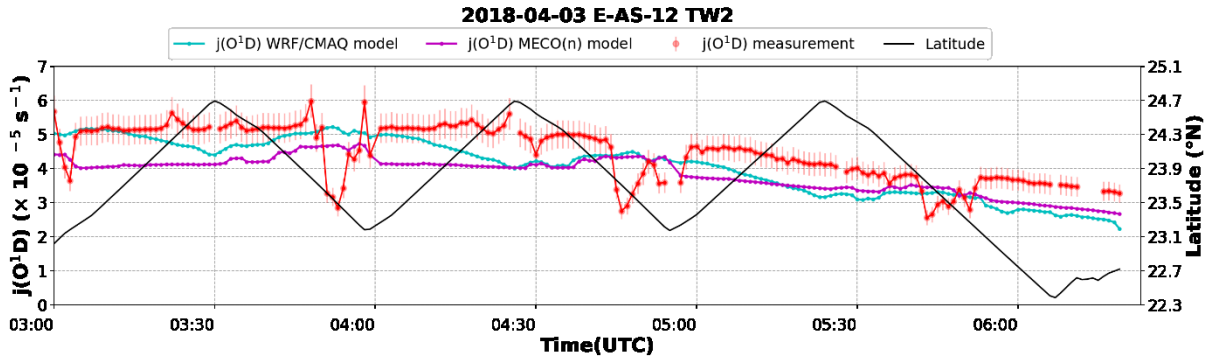
A 246: Temporal distribution of jO^1D measurement and the corresponding results from available models for E-AS-12 TW2. The corresponding latitudes are provided on the secondary y-axis. The box model constrains the measurements, therefore, is not featured in the plots.
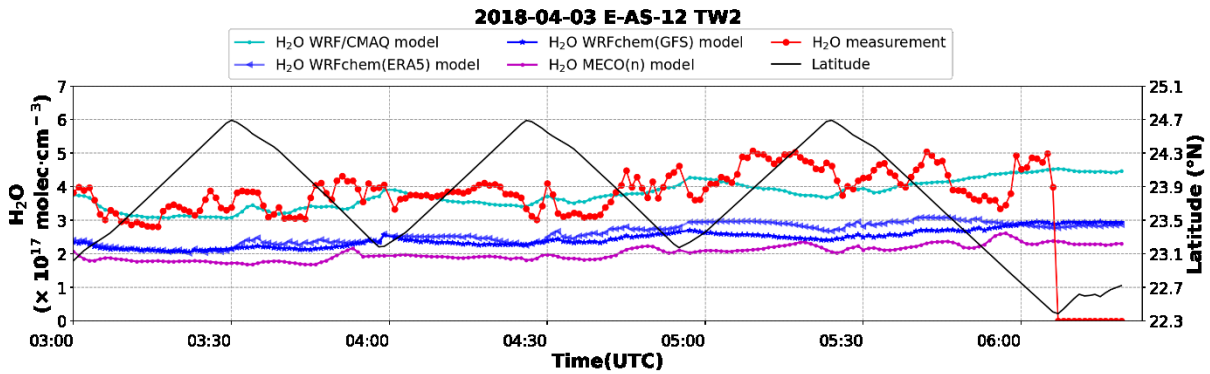
A 247: Temporal distribution of H_2O measurement and the corresponding results from available models for E-AS-12 TW2. The corresponding latitudes are provided on the secondary y-axis. The box model constrains the measurements, therefore, is not featured in the plots.
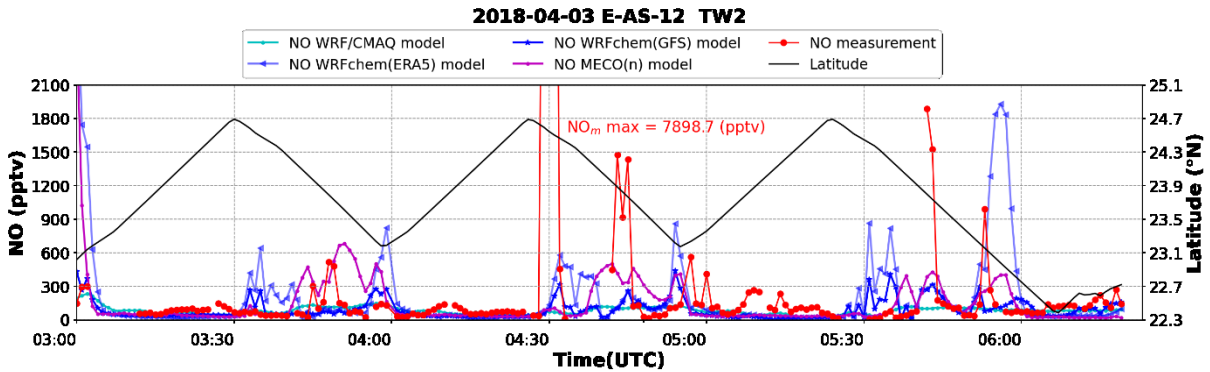
A 248: Temporal distribution of NO measurement and the corresponding results from available models for E-AS-12 TW2. The corresponding latitudes are provided on the secondary y-axis. The box model constrains the measurements, therefore, is not featured in the plots.
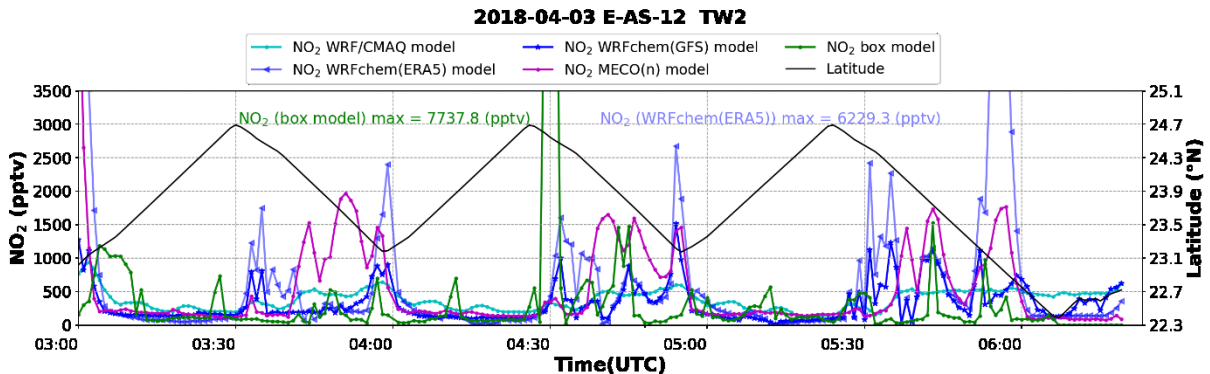
A 249: Temporal distribution of NO₂ results from available models for E-AS-12 TW2. The corresponding latitudes are provided on the secondary y-axis.
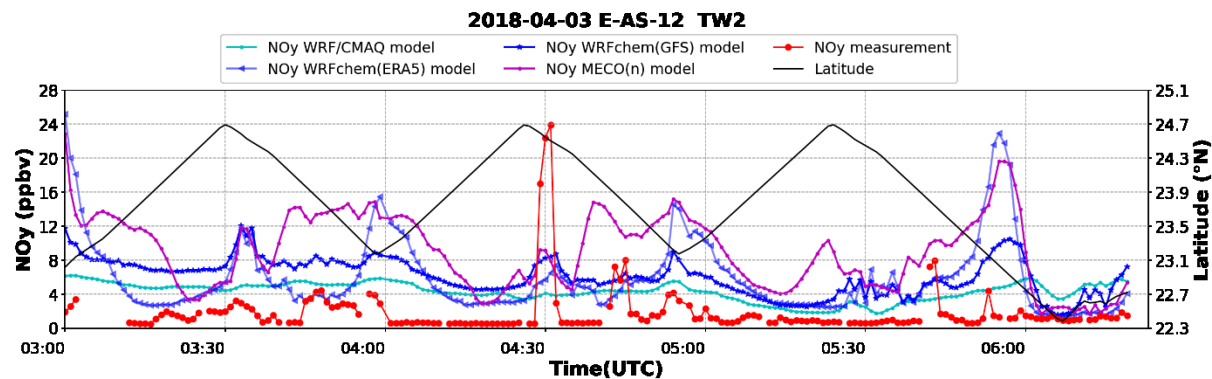
A 250: Temporal distribution of NOy measurement and the corresponding results from available models for E-AS-12 TW2. The corresponding latitudes are provided on the secondary y-axis.
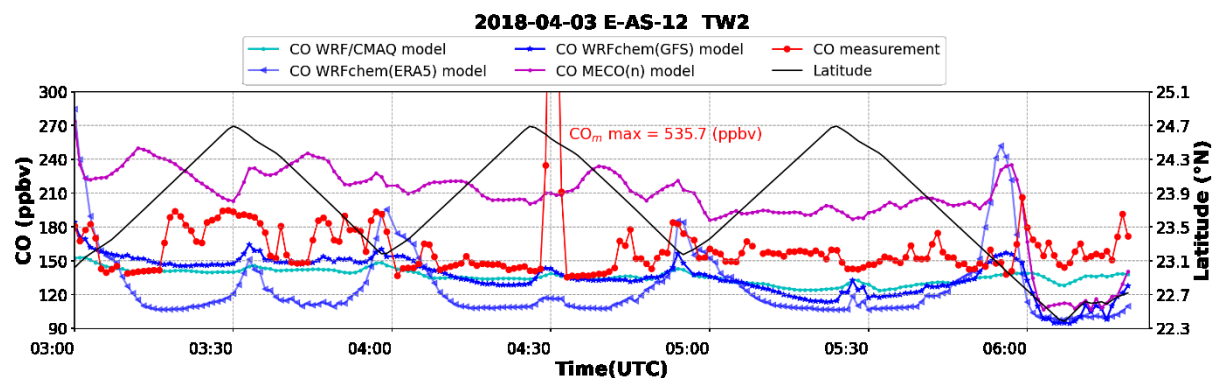
A 251: Temporal distribution of CO measurement and the corresponding results from available models for E-AS-12 TW2. The corresponding latitudes are provided on the secondary y-axis. The box model constrains the measurements, therefore, is not featured in the plots.
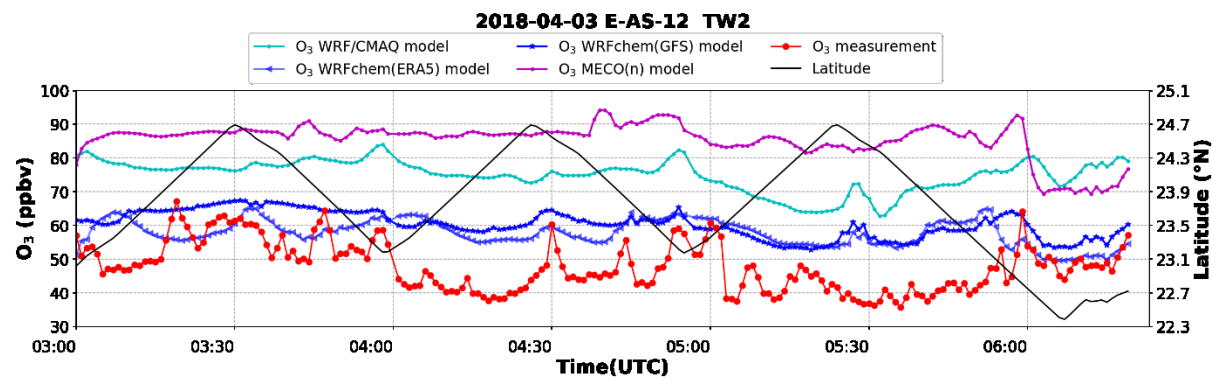
A 252: Temporal distribution of O₃ measurement and the corresponding results from available models for E-AS-12 TW2. The corresponding latitudes are provided on the secondary y-axis. The box model constrains the measurements, therefore, is not featured in the plots.

A 253: Temporal distribution of HCHO measurement and the corresponding results from available models for E-AS-12 TW2. The corresponding latitudes are provided on the secondary y-axis. The box model constrains the measurements, therefore, is not featured in the plots.

2018-04-03 E-AS-12 TW2
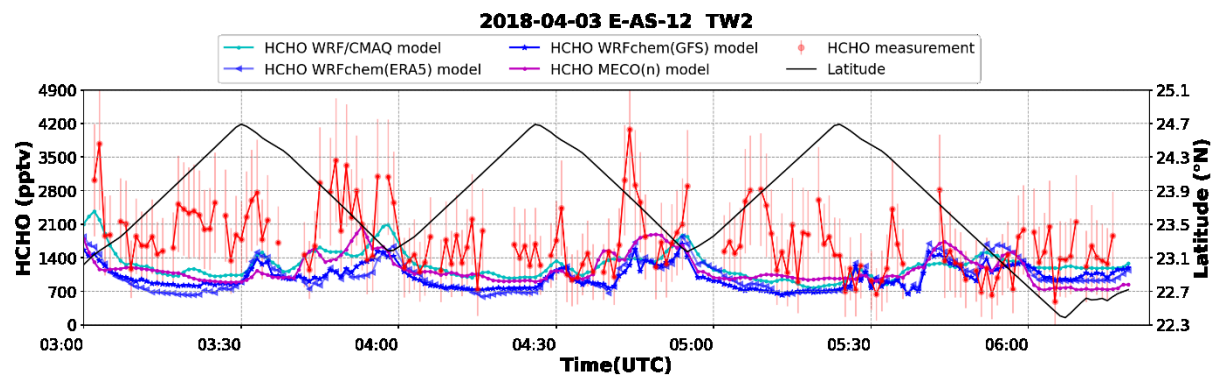
A 254: Temporal distribution of CH₃CHO measurement and the corresponding results from available models for E-AS-12 TW2. The corresponding latitudes are provided on the secondary y-axis. The box model constrains the measurements, therefore, is not featured in the plots.

2018-04-03 E-AS-12 TW2
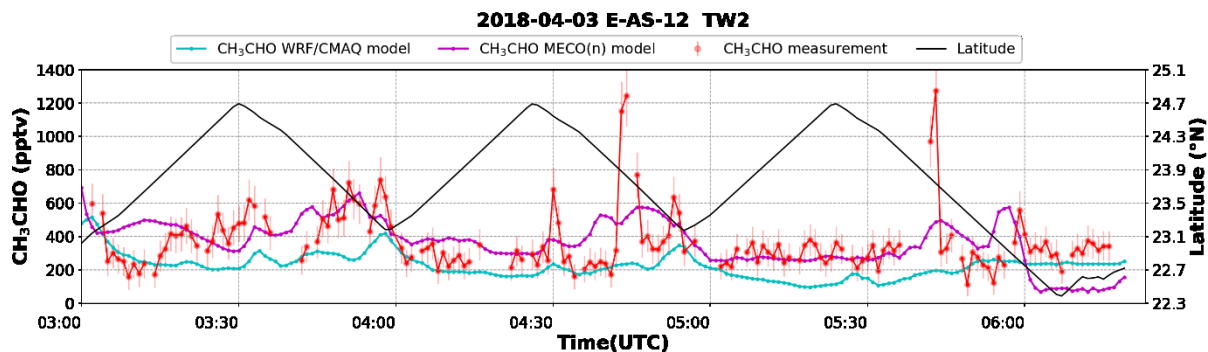
A 255: Temporal distribution of CH₃COCH₃ measurement and the corresponding results from available models for E-AS-12 TW2. The corresponding latitudes are provided on the secondary y-axis.

2018-04-03 E-AS-12 TW2
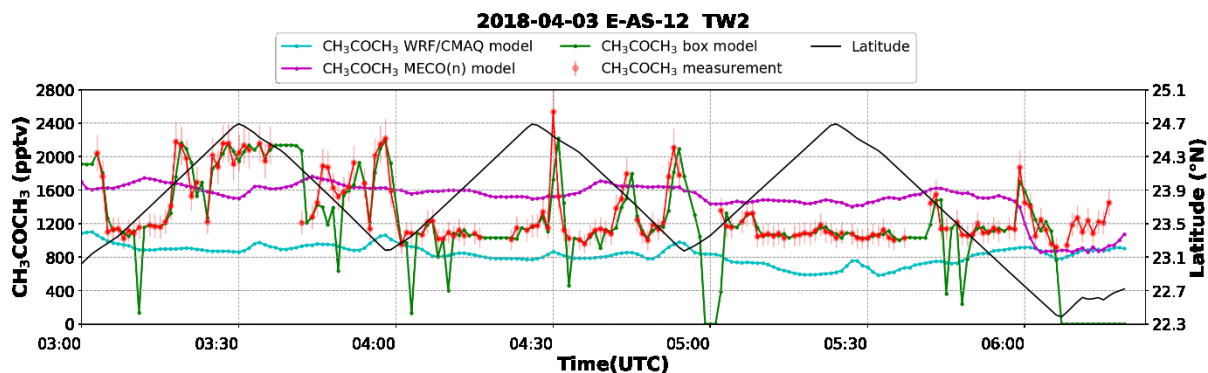
A 256: Temporal distribution of HONO results from available models for E-AS-12 TW2. The corresponding latitudes are provided on the secondary y-axis.

2018-04-03 E-AS-12 TW2
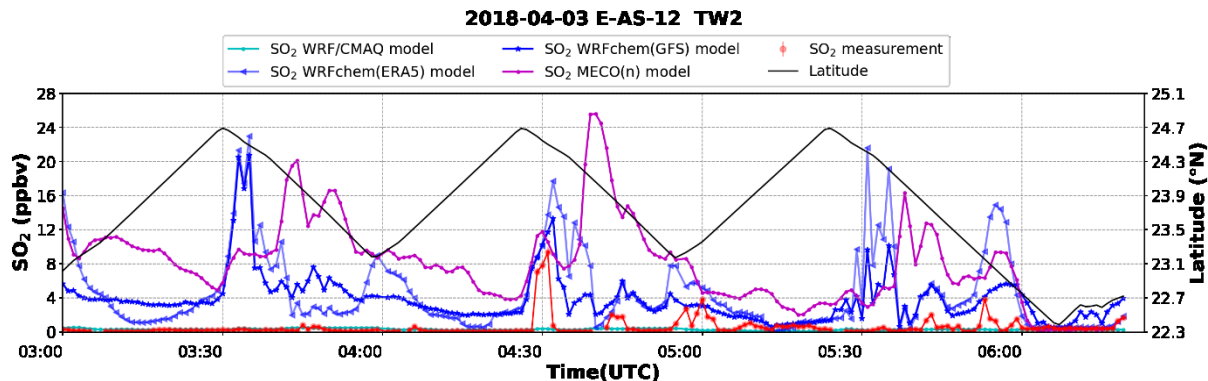
A 257: Temporal distribution of SO₂ measurement and the corresponding results from available models for E-AS-12 TW2. The corresponding latitudes are provided on the secondary y-axis. The box model constrains the measurements, therefore, is not featured in the plots.
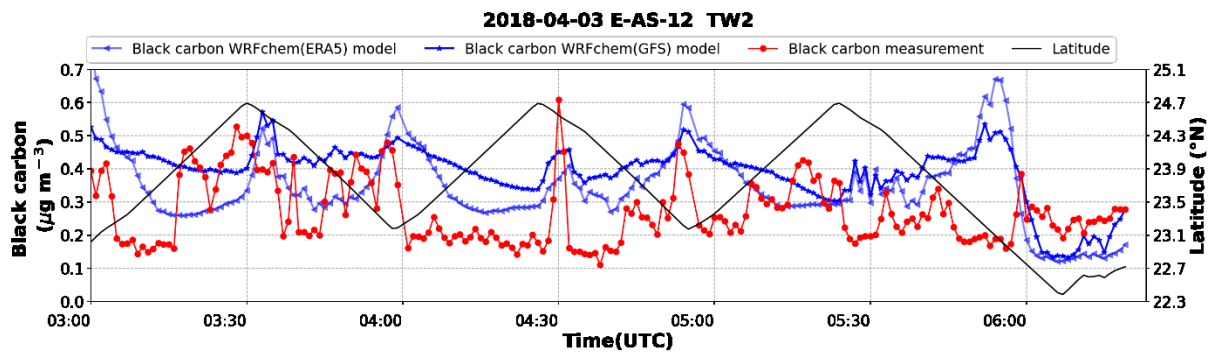
A 258: Temporal distribution of black carbon measurement and the corresponding results from available models for E-AS-12 TW2. The corresponding latitudes are provided on the secondary y-axis. The box model constrains the measurements, therefore, is not featured in the plots.

A 259: Temporal distribution of RO_2^* measurement, the corresponding results from available models, and the PSS calculations for E-AS-13 TW2. The corresponding latitudes are provided on the secondary y-axis.
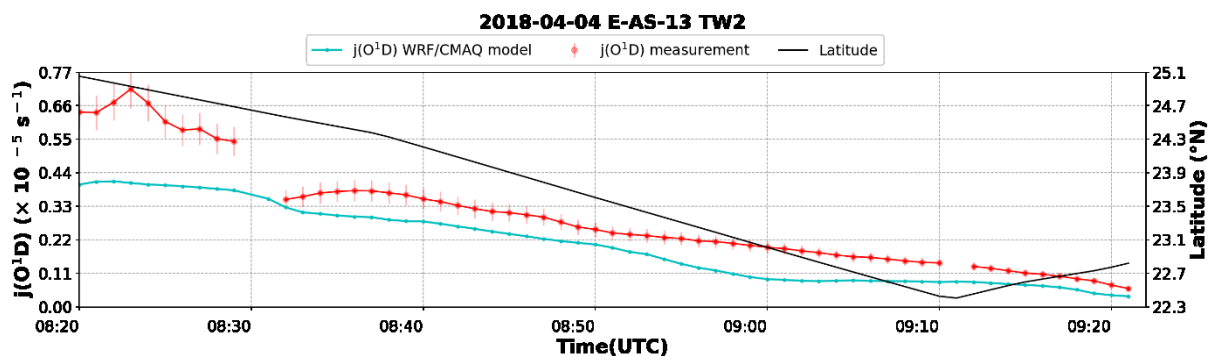
A 260: Temporal distribution of jO^1D measurement and the corresponding results from available models for E-AS-13 TW2. The corresponding latitudes are provided on the secondary y-axis. The box model constrains the measurements, therefore, is not featured in the plots.
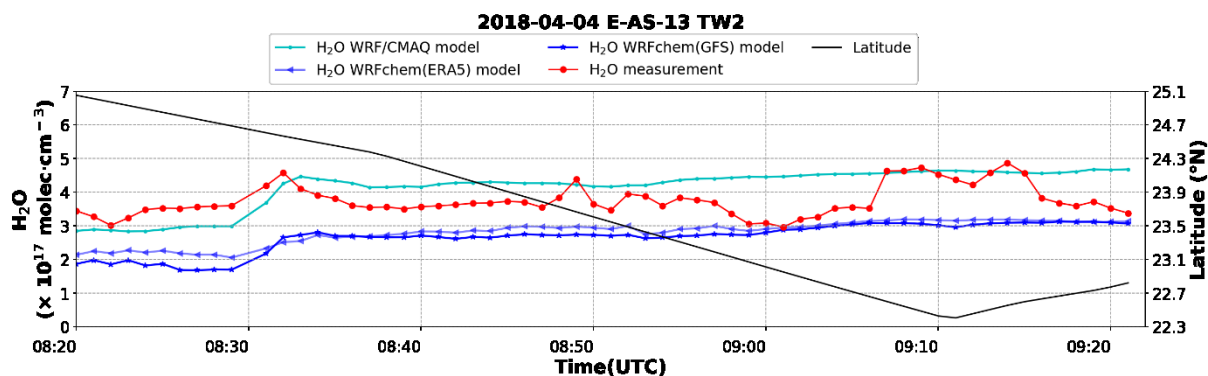
A 261: Temporal distribution of H_2O measurement and the corresponding results from available models for E-AS-13 TW2. The corresponding latitudes are provided on the secondary y-axis. The box model constrains the measurements, therefore, is not featured in the plots.
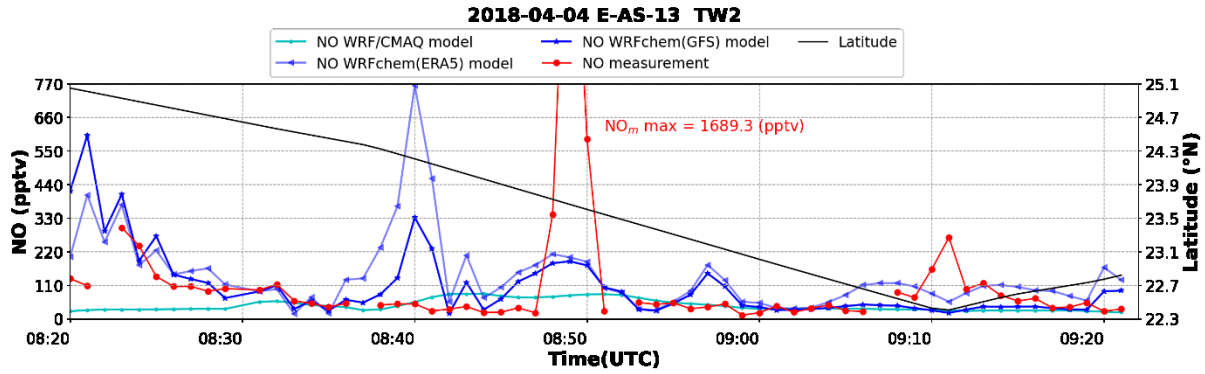
A 262: Temporal distribution of NO measurement and the corresponding results from available models for E-AS-13 TW2. The corresponding latitudes are provided on the secondary y-axis. The box model constrains the measurements, therefore, is not featured in the plots.
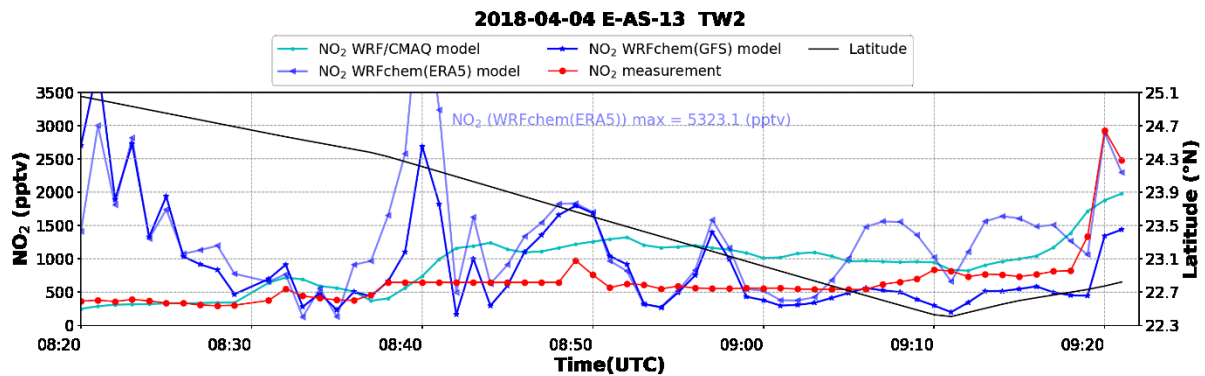
A 263: Temporal distribution of NO₂ measurement and the corresponding results from available models for E-AS-13 TW2. The corresponding latitudes are provided on the secondary y-axis. The box model constrains the measurements, therefore, is not featured in the plots.
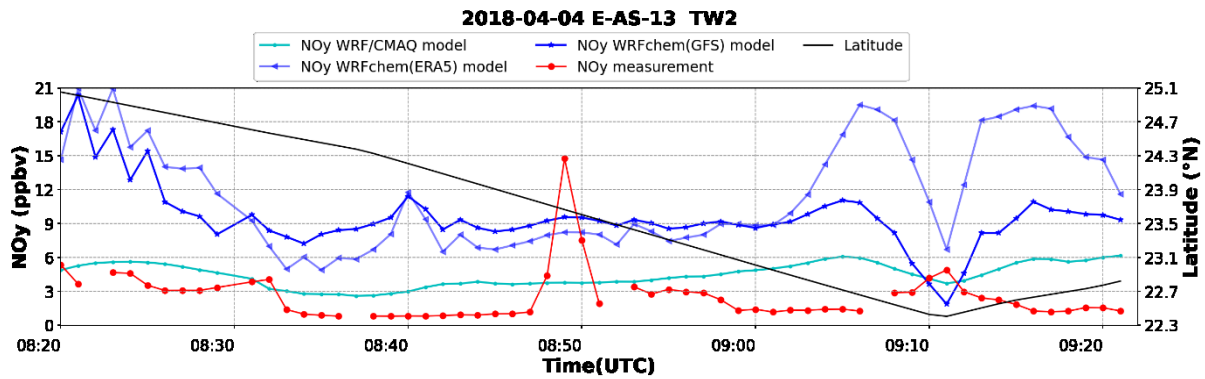
A 264: Temporal distribution of NOy measurement and the corresponding results from available models for E-AS-13 TW2. The corresponding latitudes are provided on the secondary y-axis.
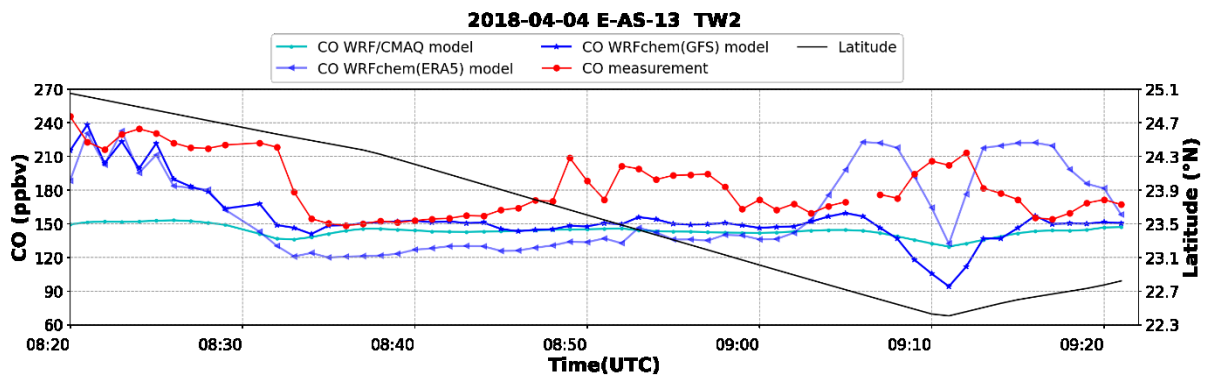
A 265: Temporal distribution of CO measurement and the corresponding results from available models for E-AS-13 TW2. The corresponding latitudes are provided on the secondary y-axis. The box model constrains the measurements, therefore, is not featured in the plots.
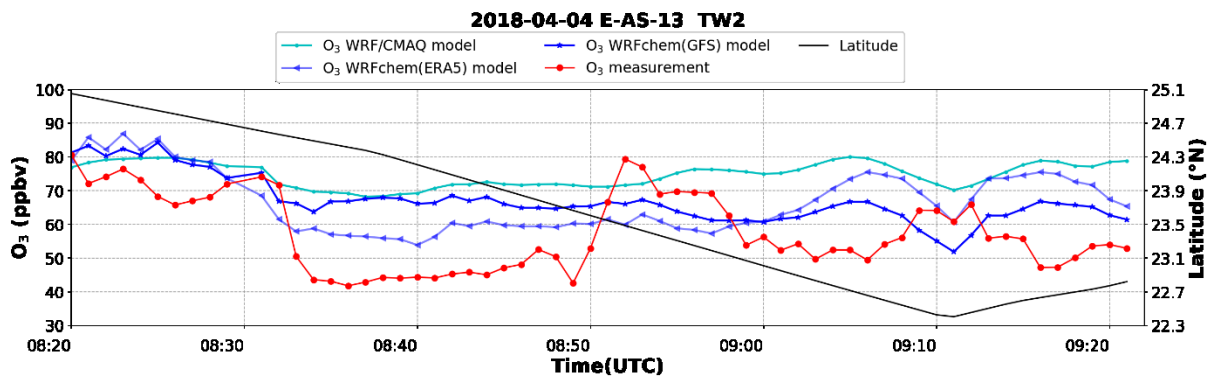
A 266: Temporal distribution of O₃ measurement and the corresponding results from available models for E-AS-13 TW2. The corresponding latitudes are provided on the secondary y-axis. The box model constrains the measurements, therefore, is not featured in the plots.
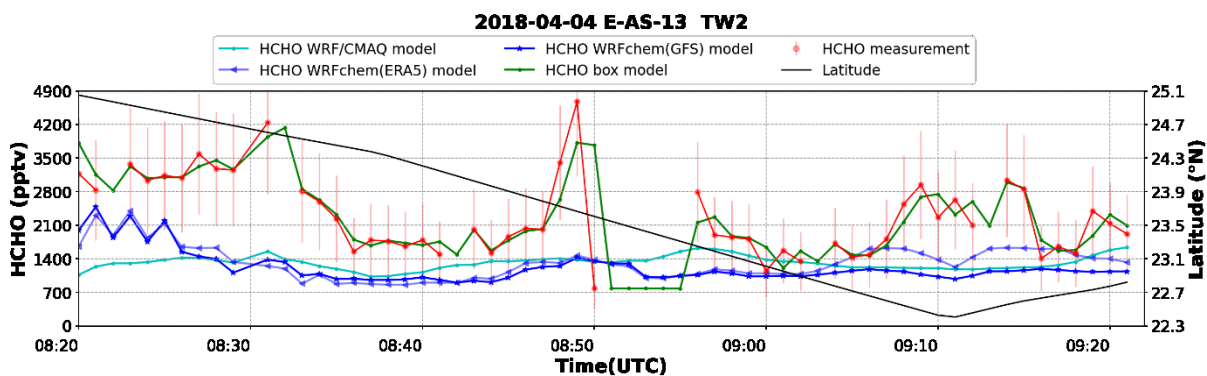
A 267: Temporal distribution of HCHO measurement and the corresponding results from available models for E-AS-13 TW2. The corresponding latitudes are provided on the secondary y-axis.
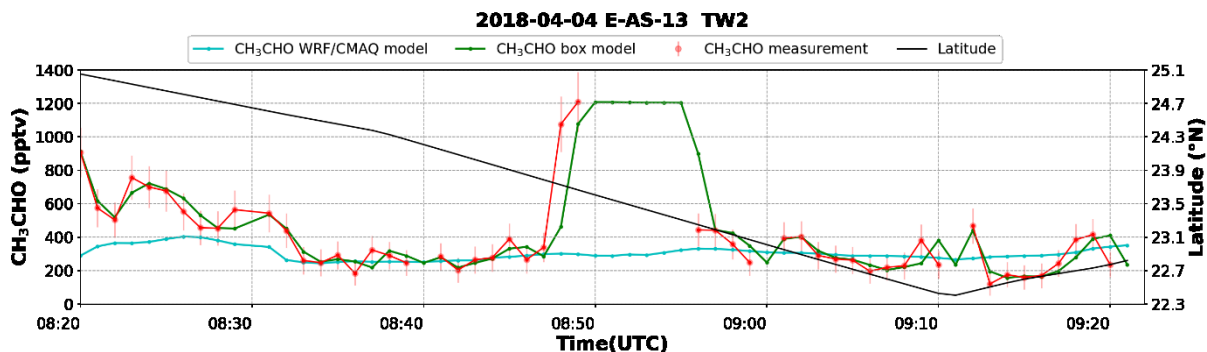
A 268: Temporal distribution of CH₃CHO measurement and the corresponding results from available models for E-AS-13 TW2. The corresponding latitudes are provided on the secondary y-axis.
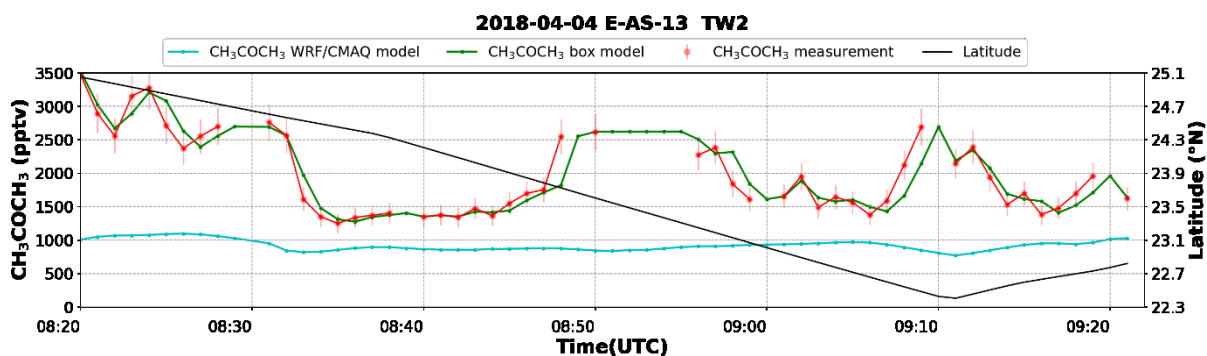
A 269: Temporal distribution of CH₃COCH₃ measurement and the corresponding results from available models for E-AS-13 TW2. The corresponding latitudes are provided on the secondary y-axis.
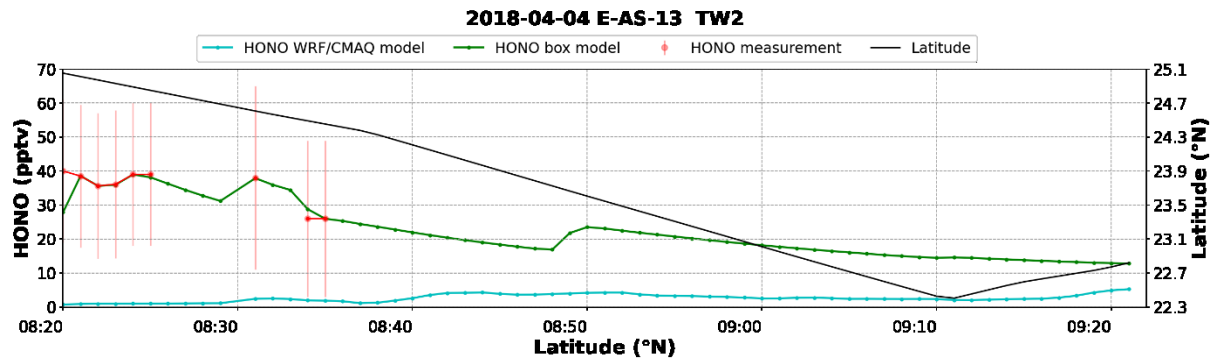
A 270: Temporal distribution of HONO measurement and the corresponding results from available models for E-AS-13 TW2. The corresponding latitudes are provided on the secondary y-axis.
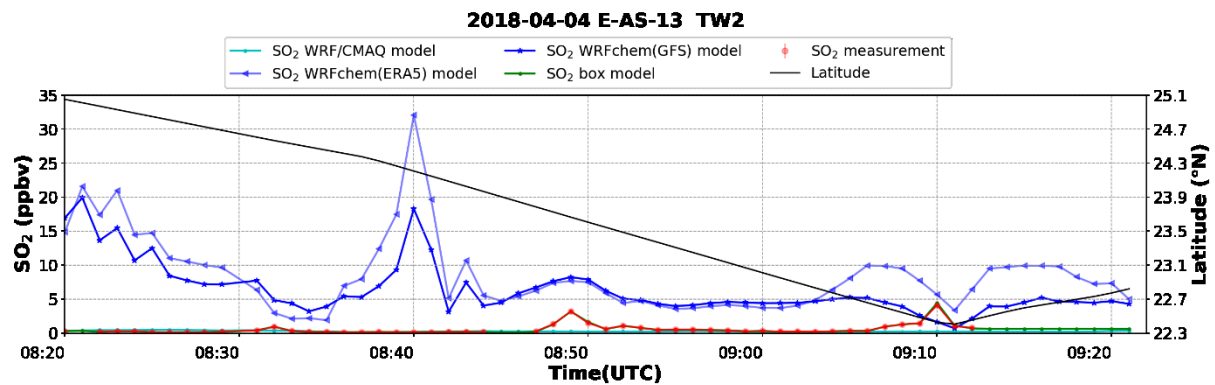
A 271: Temporal distribution of SO₂ measurement and the corresponding results from available models for E-AS-13 TW2. The corresponding latitudes are provided on the secondary y-axis.
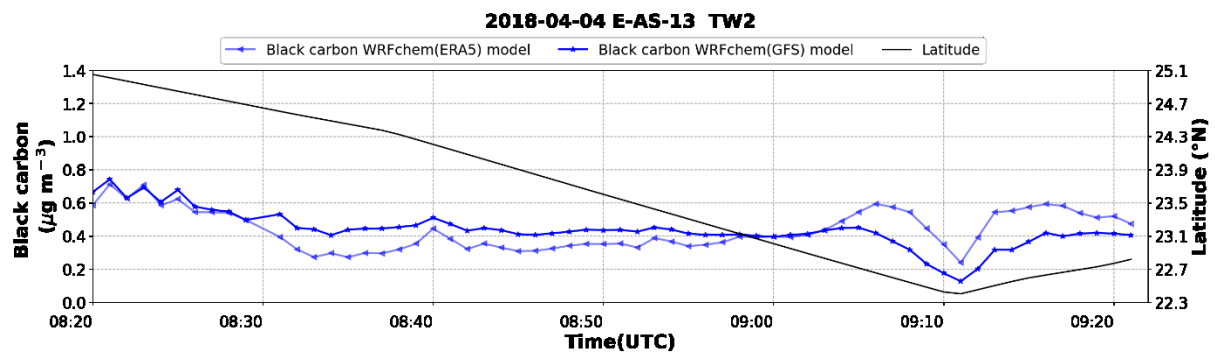
A 272: Temporal distribution of black carbon measurement and the corresponding results from available models for E-AS-13 TW2. The corresponding latitudes are provided on the secondary y-axis.
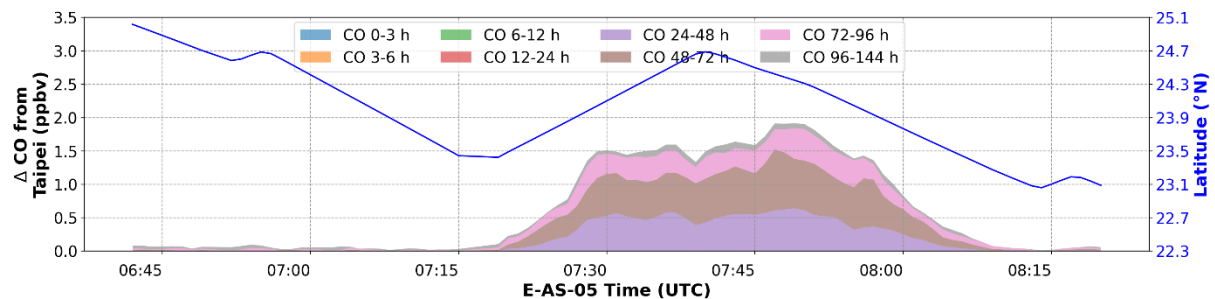
A 273: Stacked time series of CO enhancements from Taipei outflows modelled by HYSPLIT for E-AS-05 TW2 colour-coded with 8 aged period groups. The corresponding latitudes are provided on the secondary y-asix.
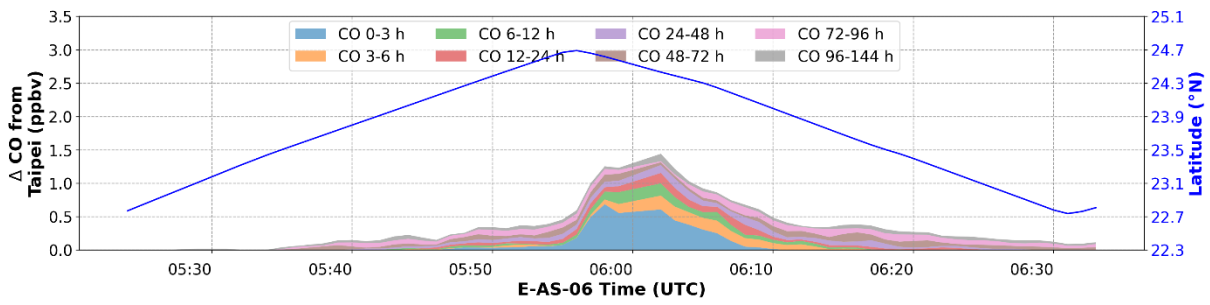
A 274: Stacked time series of CO enhancements from Taipei outflows modelled by HYSPLIT for E-AS-06 TW2 colour-coded with 8 aged period groups. The corresponding latitudes are provided on the secondary y-asix.
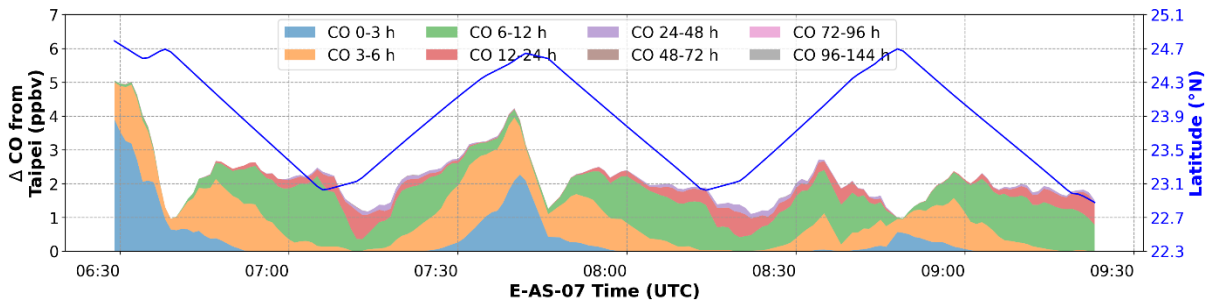
A 275: Stacked time series of CO enhancements from Taipei outflows modelled by HYSPLIT for E-AS-07 TW2 colour-coded with 8 aged period groups. The corresponding latitudes are provided on the secondary y-asix.
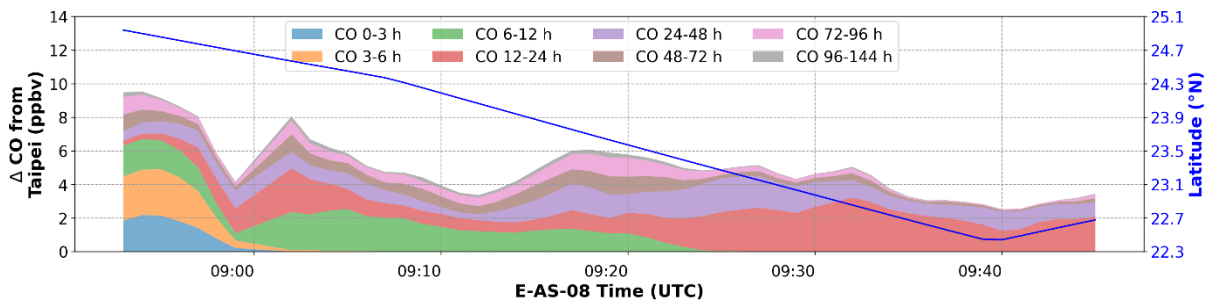
A 276: Stacked time series of CO enhancements from Taipei outflows modelled by HYSPLIT for E-AS-08 TW2 colour-coded with 8 aged period groups. The corresponding latitudes are provided on the secondary y-asix.
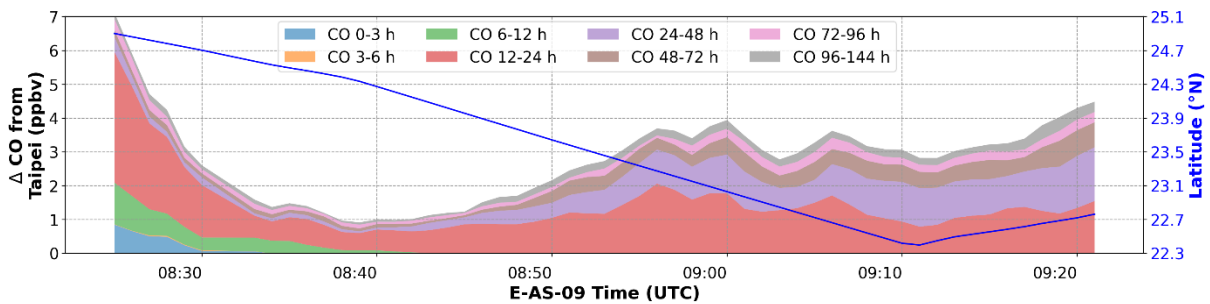
A 277: Stacked time series of CO enhancements from Taipei outflows modelled by HYSPLIT for E-AS-09 TW2 colour-coded with 8 aged period groups. The corresponding latitudes are provided on the secondary y-asix.
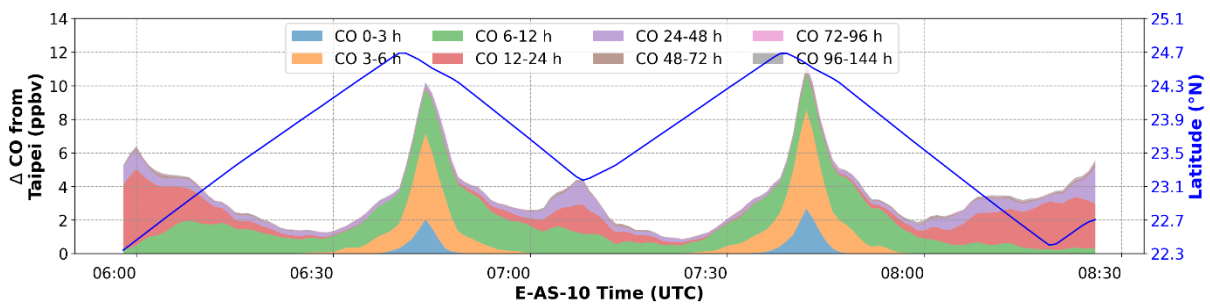
A 278: Stacked time series of CO enhancements from Taipei outflows modelled by HYSPLIT for E-AS-10 TW2 colour-coded with 8 aged period groups. The corresponding latitudes are provided on the secondary y-asix.
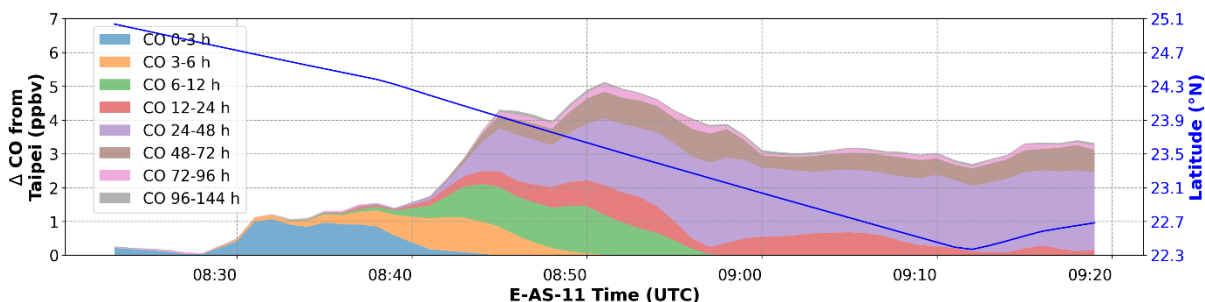
A 279: Stacked time series of CO enhancements from Taipei outflows modelled by HYSPLIT for E-AS-11 TW2 colour-coded with 8 aged period groups. The corresponding latitudes are provided on the secondary y-asix.
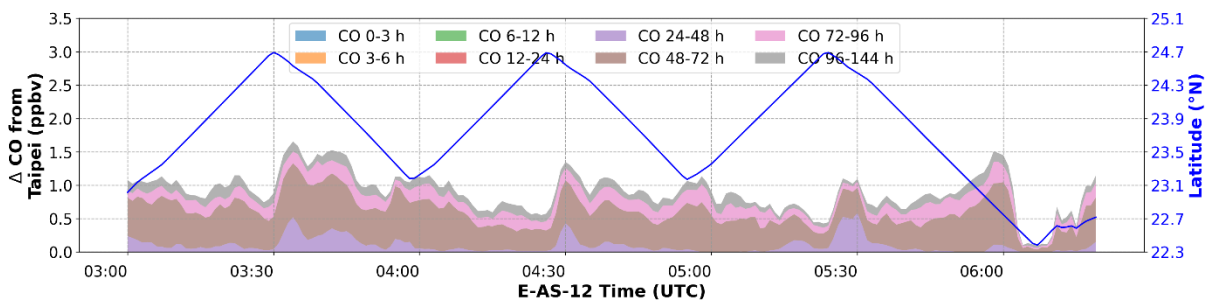
A 280: Stacked time series of CO enhancements from Taipei outflows modelled by HYSPLIT for E-AS-12 TW2 colour-coded with 8 aged period groups. The corresponding latitudes are provided on the secondary y-asix.
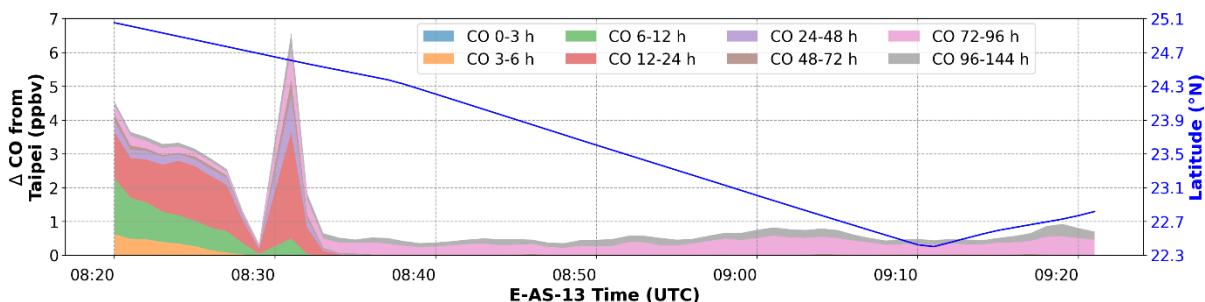
A 281: Stacked time series of CO enhancements from Taipei outflows modelled by HYSPLIT for E-AS-13 TW2 colour-coded with 8 aged period groups. The corresponding latitudes are provided on the secondary y-asix.

References

Abjean: Mesure interfromtrique des indices de rfraction de l'azote et de l'argon dans l'ultraviolet, C R Acad Sci Paris, 271, 411, 1970.

Alms, G. R., Burnham, A. K., and Flygare, W. H.: Measurement of the dispersion in polarizability anisotropies, The Journal of Chemical Physics, 63, 3321–3326, https://doi.org/10.1063/1.431821, 1975.

Andreae, M. O., Afchine, A., Albrecht, R., Holanda, B. A., Artaxo, P., Barbosa, H. M. J., Borrmann, S., Cecchini, M. A., Costa, A., Dollner, M., Fütterer, D., Järvinen, E., Jurkat, T., Klimach, T., Konemann, T., Knote, C., Krämer, M., Krisna, T., Machado, L. A. T., Mertes, S., Minikin, A., Pöhlker, C., Pöhlker, M. L., Pöschl, U., Rosenfeld, D., Sauer, D., Schlager, H., Schnaiter, M., Schneider, J., Schulz, C., Spanu, A., Sperling, V. B., Voigt, C., Walser, A., Wang, J., Weinzierl, B., Wendisch, M., and Ziereis, H.: Aerosol characteristics and particle production in the upper troposphere over the Amazon Basin, Atmos. Chem. Phys., 18, 921–961, https://doi.org/10.5194/acp-18-921-2018, 2018.

Andrés Hernández, M. D., Hilboll, A., Ziereis, H., Förster, E., Krüger, O. O., Kaiser, K., Schneider, J., Barnaba, F., Vrekoussis, M., Schmidt, J., Huntrieser, H., Blechschmidt, A.-M., George, M., Nenakhov, V., Harlass, T., Holanda, B. A., Wolf, J., Eirenschmalz, L., Krebsbach, M., Pöhlker, M. L., Kalisz Hedegaard, A. B., Mei, L., Pfeilsticker, K., Liu, Y., Koppmann, R., Schlager, H., Bohn, B., Schumann, U., Richter, A., Schreiner, B., Sauer, D., Baumann, R., Mertens, M., Jöckel, P., Kilian, M., Stratmann, G., Pöhlker, C., Campanelli, M., Pandolfi, M., Sicard, M., Gómez-Amo, J. L., Pujadas, M., Bigge, K., Kluge, F., Schwarz, A., Daskalakis, N., Walter, D., Zahn, A., Pöschl, U., Bönisch, H., Borrmann, S., Platt, U., and Burrows, J. P.: Overview: On the transport and transformation of pollutants in the outflow of major population centres – observational data from the EMeRGe European intensive operational period in summer 2017, Atmos. Chem. Phys., 22, 5877–5924, https://doi.org/10.5194/acp-22-5877-2022, 2022.

Atkinson, R. and Aschmann, S. M.: Hydroxyl radical production from the gas-phase reactions of ozone with a series of alkenes under atmospheric conditions, Environmental Science & Technology, 27, 1357–1363, https://doi.org/10.1021/es00044a010, 1993.

Bates, D. R.: Rayleigh scattering by air, Planetary and Space Science, 32, 785–790, https://doi.org/10.1016/0032-0633(84)90102-8, 1984.

Bedjanian, Y., Lelièvre, S., and Le Bras, G.: Experimental study of the interaction of HO2 radicals with soot surface, Phys. Chem. Chem. Phys., 7, 334–341, https://doi.org/10.1039/B414217A, 2005.

Berden, G., Peeters, R., and Meijer, G.: Cavity ring-down spectroscopy: Experimental schemes and applications, International Reviews in Physical Chemistry, 19, 565–607, https://doi.org/10.1080/014423500750040627, 2000.

Bideau-Mehu, A., Guern, Y., Abjean, R., and Johannin-Gilles, A.: Interferometric determination of the refractive index of carbon dioxide in the ultraviolet region, Optics Communications, 9, 432–434, https://doi.org/10.1016/0030-4018(73)90289-7, 1973.

Bogaard, M. P., Buckingham, A. D., Pierens, R. K., and White, A. H.: Rayleigh scattering depolarization ratio and molecular polarizability anisotropy for gases, J. Chem. Soc., Faraday Trans. 1, 74, 3008, https://doi.org/10.1039/f19787403008, 1978.

Boggs, P. T. and Donaldson, J. R.: Orthogonal distance regression, Gaithersburg, MD, 1989.

References

Bohn, B. and Lohse, I.: Calibration and evaluation of CCD spectroradiometers for ground-based and airborne measurements of spectral actinic flux densities, Atmospheric Measurement Techniques, 10, 3151–3174, https://doi.org/10.5194/amt-10-3151-2017, 2017.

Boyd, R. W.: Nonlinear optics, 3rd ed., Academic Press, Place of publication not identified, 2008.

Bregman, B., Segers, A., Krol, M., Meijer, E., and van Velthoven, P.: On the use of mass-conserving wind fields in chemistry-transport models, Atmos. Chem. Phys., 3, 447–457, https://doi.org/10.5194/acp-3-447-2003, 2003.

Bridge, N. J. and Buckingham, A. D.: The polarization of laser light scattered by gases, Proceedings of the Royal Society of London. Series A. Mathematical and Physical Sciences, 295, 334–349, https://doi.org/10.1098/rspa.1966.0244, 1966.

Brito, J. and Zahn, A.: An unheated permeation device for calibrating atmospheric VOC measurements, Atmospheric Measurement Techniques, 4, 2143–2152, https://doi.org/10.5194/amt-4-2143-2011, 2011.

Bucholtz, A.: Rayleigh-scattering calculations for the terrestrial atmosphere, Applied optics, 34, 2765–2773, https://doi.org/10.1364/AO.34.002765, 1995.

Burns, K., Adams, K. B., and Longwell, J.: Interference Measurements in the Spectra of Neon and Natural Mercury, J. Opt. Soc. Am., 40, 339, https://doi.org/10.1364/JOSA.40.000339, 1950.

Byun, D. and Schere, K. L.: Review of the Governing Equations, Computational Algorithms, and Other Components of the Models-3 Community Multiscale Air Quality (CMAQ) Modeling System, Applied Mechanics Reviews, 59, 51–77, https://doi.org/10.1115/1.2128636, 2006.

Cantrell, C. A. and Stedman, D. H.: A possible technique for the measurement of atmospheric peroxy radicals, Geophys. Res. Lett., 9, 846–849, https://doi.org/10.1029/GL009i008p00846, 1982.

Carter, W. P.: Development of the SAPRC-07 chemical mechanism, Atmospheric Environment, 44, 5324–5335, https://doi.org/10.1016/j.atmosenv.2010.01.026, available at: https://www.sciencedirect.com/science/article/pii/S1352231010000646, 2010.

Center of Japan, Ministry of the Environment Natural Environment Bureau Biodiversity: Biodiversity Center of Japan, https://www.biodic.go.jp/index_e.html, last access: 12 April 2023, 2023.

Chatani, S., Yamaji, K., Sakurai, T., Itahashi, S., Shimadera, H., Kitayama, K., and Hayami, H.: Overview of Model Inter-Comparison in Japan's Study for Reference Air Quality Modeling (J-STREAM), Atmosphere, 9, 19, https://doi.org/10.3390/atmos9010019, 2018.

Chen, H., Winderlich, J., Gerbig, C., Hoefer, A., Rella, C. W., Crosson, E. R., van Pelt, A. D., Steinbach, J., Kolle, O., Beck, V., Daube, B. C., Gottlieb, E. W., Chow, V. Y., Santoni, G. W., and Wofsy, S. C.: High-accuracy continuous airborne measurements of greenhouse gases (CO_2 and CH_4) using the cavity ring-down spectroscopy (CRDS) technique, Atmospheric Measurement Techniques, 3, 375–386, https://doi.org/10.5194/amt-3-375-2010, 2010.

References

Chin, M., Rood, R. B., Lin, S.-J., Müller, J.-F., and Thompson, A. M.: Atmospheric sulfur cycle simulated in the global model GOCART: Model description and global properties, J. Geophys. Res., 105, 24671–24687, https://doi.org/10.1029/2000JD900384, 2000.

de-Bruine, M., Krol, M., van Noije, T., Le Sager, P., and Röckmann, T.: The impact of precipitation evaporation on the atmospheric aerosol distribution in EC-Earth v3.2.0, Geosci. Model Dev., 11, 1443–1465, https://doi.org/10.5194/gmd-11-1443-2018, available at: https://gmd.copernicus.org/articles/11/1443/2018/, 2018.

Dee, D. P., Uppala, S. M., Simmons, A. J., Berrisford, P., Poli, P., Kobayashi, S., Andrae, U., Balmaseda, M. A., Balsamo, G., Bauer, P., Bechtold, P., Beljaars, A. C. M., van de Berg, L., Bidlot, J., Bormann, N., Delsol, C., Dragani, R., Fuentes, M., Geer, A. J., Haimberger, L., Healy, S. B., Hersbach, H., Hólm, E. V., Isaksen, L., Kållberg, P., Köhler, M., Matricardi, M., McNally, A. P., Monge-Sanz, B. M., Morcrette, J.-J., Park, B.-K., Peubey, C., Rosnay, P. de, Tavolato, C., Thépaut, J.-N., and Vitart, F.: The ERA-Interim reanalysis: configuration and performance of the data assimilation system, Q.J.R. Meteorol. Soc., 137, 553–597, https://doi.org/10.1002/qj.828, 2011.

Demore, W. B.: Rate constant for the OH + CO reaction: Pressure dependence and the effect of oxygen, Int J of Chemical Kinetics, 16, 1187–1200, https://doi.org/10.1002/kin.550161003, 1984.

Demtröder, W.: Laser Spectroscopy 1: Basic Principles, 5th Edition, Springer Berlin Heidelberg, Berlin, Heidelberg, 496 pp., 2014.

Deroubaix, A., Menut, L., Flamant, C., Knippertz, P., Fink, A. H., Batenburg, A., Brito, J., Denjean, C., Dione, C., Dupuy, R., Hahn, V., Kalthoff, N., Lohou, F., Schwarzenboeck, A., Siour, G., Tuccella, P., and Voigt, C.: Sensitivity of low-level clouds and precipitation to anthropogenic aerosol emission in southern West Africa: a DACCIWA case study, Atmos. Chem. Phys., 22, 3251–3273, https://doi.org/10.5194/acp-22-3251-2022, 2022.

Doms, G. and Baldauf, M.: COSMO-Model Version 5.00: A Description of the Nonhydrostatic Regional COSMO-Model - Part I: Dynamics and Numerics, 2013.

EEA Glossary: long-range transport of air pollutants, available at: https://www.eea.europa.eu/help/glossary/eea-glossary/long-range-transport-of-air-pollutants, last access: 30 November 2023.

Ek, M. B., Mitchell, K. E., Lin, Y., Rogers, E., Grunmann, P., Koren, V., Gayno, G., and Tarpley, J. D.: Implementation of Noah land surface model advances in the National Centers for Environmental Prediction operational mesoscale Eta model, J. Geophys. Res., 108, https://doi.org/10.1029/2002JD003296, 2003.

Emmons, L. K., Walters, S., Hess, P. G., Lamarque, J.-F., Pfister, G. G., Fillmore, D., Granier, C., Guenther, A., Kinnison, D., Laepple, T., Orlando, J., Tie, X., Tyndall, G., Wiedinmyer, C., Baughcum, S. L., and Kloster, S.: Description and evaluation of the Model for Ozone and Related chemical Tracers, version 4 (MOZART-4), Geosci. Model Dev., 3, 43–67, https://doi.org/10.5194/gmd-3-43-2010, 2010.

Eyring, V., Bony, S., Meehl, G. A., Senior, C. A., Stevens, B., Stouffer, R. J., and Taylor, K. E.: Overview of the Coupled Model Intercomparison Project Phase 6 (CMIP6) experimental design and organization, Geosci. Model Dev., 9, 1937–1958, https://doi.org/10.5194/gmd-9-1937-2016, 2016.

FAAM: Home - FAAM, https://www.faam.ac.uk/, last access: 25 April 2023, 2022.

References

Fast, J. D., Gustafson, W. I., Easter, R. C., Zaveri, R. A., Barnard, J. C., Chapman, E. G., Grell, G. A., and Peckham, S. E.: Evolution of ozone, particulates, and aerosol direct radiative forcing in the vicinity of Houston using a fully coupled meteorology‐chemistry‐aerosol model, J. Geophys. Res., 111, https://doi.org/10.1029/2005JD006721, available at: https://agupubs.onlinelibrary.wiley.com/doi/10.1029/2005JD006721, 2006.

Fisher, R., Lowry, D., Wilkin, O., Sriskantharajah, S., and Nisbet, E. G.: High-precision, automated stable isotope analysis of atmospheric methane and carbon dioxide using continuous-flow isotope-ratio mass spectrometry, Rapid communications in mass spectrometry RCM, 20, 200–208, https://doi.org/10.1002/rcm.2300, 2006.

Gemmill, W., Katz, B., and Li, X.: The Daily Real-Time, Global Sea Surface Temperature—High Resolution Analysis: RTG_SST_HR, MMAB 260, available at: https://polar.ncep.noaa.gov/mmab/papers/tn260/MMAB260.pdf, 2007.

General, S., Pöhler, D., Sihler, H., Bobrowski, N., Frieß, U., Zielcke, J., Horbanski, M., Shepson, P. B., Stirm, B. H., Simpson, W. R., Weber, K., Fischer, C., and Platt, U.: The Heidelberg Airborne Imaging DOAS Instrument (HAIDI) – a novel imaging DOAS device for 2-D and 3-D imaging of trace gases and aerosols, Atmospheric Measurement Techniques, 7, 3459–3485, https://doi.org/10.5194/amt-7-3459-2014, 2014.

George, M.: Airborne measurement and interpretation of peroxy radical concentrations with a focus on the oxidation mechanisms in the Asian free troposphere, 2022.

George, M., Andrés Hernández, M. D., Nenakhov, V., Liu, Y., Burrows, J. P., Bohn, B., Förster, E., Obersteiner, F., Zahn, A., Harlaß, T., Ziereis, H., Schlager, H., Schreiner, B., Kluge, F., Bigge, K., and Pfeilsticker, K.: Airborne observations of peroxy radicals during the EMeRGe campaign in Europe, Atmos. Chem. Phys., 23, 7799–7822, https://doi.org/10.5194/acp-23-7799-2023, 2023.

George, M., Andrés Hernández, M. D., Nenakhov, V., Liu, Y., and Burrows, J. P.: Airborne measurement of peroxy radicals using chemical amplification coupled with cavity ring-down spectroscopy: the PeRCEAS instrument, Atmospheric Measurement Techniques, 13, 2577–2600, https://doi.org/10.5194/amt-13-2577-2020, 2020.

Gerbig, C., Kley, D., Volz-Thomas, A., Kent, J., Dewey, K., and McKenna, D. S.: Fast response resonance fluorescence CO measurements aboard the C-130: Instrument characterization and measurements made during North Atlantic Regional Experiment 1993, J. Geophys. Res., 101, 29229–29238, https://doi.org/10.1029/95JD03272, 1996.

Gershenzon, Y. M., Grigorieva, V. M., Ivanov, A. V., and Remorov, R. G.: O3 and OH Sensitivity to heterogeneous sinks of HO x and CH3O2 on aerosol particles, Faraday Disc., 100, 83, https://doi.org/10.1039/FD9950000083, 1995.

Geyer, A., Bächmann, K., Hofzumahaus, A., Holland, F., Konrad, S., Klüpfel, T., Pätz, H.-W., Perner, D., Mihelcic, D., Schäfer, H.-J., Volz‐Thomas, A., and Platt, U.: Nighttime formation of peroxy and hydroxyl radicals during the BERLIOZ campaign: Observations and modeling studies, J. Geophys. Res., 108, https://doi.org/10.1029/2001JD000656, 2003.

Geyer, A., Alicke, B., Konrad, S., Schmitz, T., Stutz, J., and Platt, U.: Chemistry and oxidation capacity of the nitrate radical in the continental boundary layer near Berlin, J. Geophys. Res., 106, 8013–8025, https://doi.org/10.1029/2000JD900681, 2001.

References

Gold, V. (Ed.): The IUPAC Compendium of Chemical Terminology, International Union of Pure and Applied Chemistry (IUPAC), Research Triangle Park, NC, 2019.

Grell, G. A. and Dévényi, D.: A generalized approach to parameterizing convection combining ensemble and data assimilation techniques, Geophys. Res. Lett., 29, 38-1-38-4, https://doi.org/10.1029/2002GL015311, 2002.

Grell, G. A., Peckham, S. E., Schmitz, R., McKeen, S. A., Frost, G., Skamarock, W. C., and Eder, B.: Fully coupled "online" chemistry within the WRF model, Atmospheric Environment, 39, 6957–6975, https://doi.org/10.1016/j.atmosenv.2005.04.027, available at: https://www.sciencedirect.com/science/article/pii/S1352231005003560, 2005.

Guenther, A. B., Jiang, X., Heald, C. L., Sakulyanontvittaya, T., Duhl, T., Emmons, L. K., and Wang, X.: The Model of Emissions of Gases and Aerosols from Nature version 2.1 (MEGAN2.1): an extended and updated framework for modeling biogenic emissions, Geosci. Model Dev., 5, 1471–1492, https://doi.org/10.5194/gmd-5-1471-2012, 2012.

Guenther, A., Hewitt, C. N., Erickson, D., Fall, R., Geron, C., Graedel, T., Harley, P., Klinger, L., Lerdau, M., Mckay, W. A., Pierce, T., Scholes, B., Steinbrecher, R., Tallamraju, R., Taylor, J., and Zimmerman, P.: A global model of natural volatile organic compound emissions, J. Geophys. Res., 100, 8873, https://doi.org/10.1029/94JD02950, 1995.

HALO-SPP, https://www.halo-spp.de/, last access: 24 April 2023, 2023.

Hansch, T., Schawlow, A., and Toschek, P.: Ultrasensitive response of a CW dye laser to selective extinction, IEEE J. Quantum Electron., 8, 802–804, https://doi.org/10.1109/JQE.1972.1076854, 1972.

Hanson, D. R., Burkholder, J. B., Howard, C. J., and Ravishankara, A. R.: Measurement of hydroxyl and hydroperoxy radical uptake coefficients on water and sulfuric acid surfaces, J. Phys. Chem., 96, 4979–4985, https://doi.org/10.1021/j100191a046, 1992.

He, Q., Fang, Z., Shoshanim, O., Brown, S. S., and Rudich, Y.: Scattering and absorption cross sections of atmospheric gases in the ultraviolet–visible wavelength range (307–725 nm), Atmos. Chem. Phys., 21, 14927–14940, https://doi.org/10.5194/acp-21-14927-2021, 2021.

Hecht, E.: Optics, 5 edition. Global edition, Pearson Education, Boston, 2017.

Heikes, B. G. and Thompson, A. M.: Effects of heterogeneous processes on NO 3 HONO, and HNO 3 chemistry in the troposphere, J. Geophys. Res., 88, 10883–10895, https://doi.org/10.1029/JC088iC15p10883, 1983.

Heil, A., Kaiser, J., van der Werf, G. R., Wooster, M. J., Schultz, M. G., and van der Gon, H. D.: Assessment of the real-time fire emissions (GFASv0) by MACC, 2010.

Heintz, F., Platt, U., Flentje, H., and Dubois, R.: Long‐term observation of nitrate radicals at the Tor Station, Kap Arkona (Rügen), J. Geophys. Res., 101, 22891–22910, https://doi.org/10.1029/96JD01549, 1996.

Herbelin, J. M., McKay, J. A., Kwok, M. A., Ueunten, R. H., Urevig, D. S., Spencer, D. J., and Benard, D. J.: Sensitive measurement of photon lifetime and true reflectances in an optical cavity by a phase-shift method, Applied optics, 19, 144–147, https://doi.org/10.1364/AO.19.000144, 1980.

References

Hersbach, H., Bell, B., Berrisford, P., Hirahara, S., Horányi, A., Muñoz‑Sabater, J., Nicolas, J., Peubey, C., Radu, R., Schepers, D., Simmons, A., Soci, C., Abdalla, S., Abellan, X., Balsamo, G., Bechtold, P., Biavati, G., Bidlot, J., Bonavita, M., Chiara, G. de, Dahlgren, P., Dee, D., Diamantakis, M., Dragani, R., Flemming, J., Forbes, R., Fuentes, M., Geer, A., Haimberger, L., Healy, S., Hogan, R. J., Hólm, E., Janisková, M., Keeley, S., Laloyaux, P., Lopez, P., Lupu, C., Radnoti, G., Rosnay, P. de, Rozum, I., Vamborg, F., Villaume, S., and Thépaut, J.-N.: The ERA5 global reanalysis, Q.J.R. Meteorol. Soc., 146, 1999–2049, https://doi.org/10.1002/qj.3803, 2020.

Hodges, J. T., Looney, J. P., and van Zee, R. D.: Laser bandwidth effects in quantitative cavity ring-down spectroscopy, Applied optics, 35, 4112–4116, https://doi.org/10.1364/AO.35.004112, 1996.

Hoesly, R. M., Smith, S. J., Feng, L., Klimont, Z., Janssens-Maenhout, G., Pitkanen, T., Seibert, J. J., Vu, L., Andres, R. J., Bolt, R. M., Bond, T. C., Dawidowski, L., Kholod, N., Kurokawa, J., Li, M., Liu, L., Lu, Z., Moura, M. C. P., O'Rourke, P. R., and Zhang, Q.: Historical (1750–2014) anthropogenic emissions of reactive gases and aerosols from the Community Emissions Data System (CEDS), Geosci. Model Dev., 11, 369–408, https://doi.org/10.5194/gmd-11-369-2018, 2018.

Hofmann, C., Kerkweg, A., Wernli, H., and Jöckel, P.: The 1-way on-line coupled atmospheric chemistry model system MECO(n) – Part 3: Meteorological evaluation of the on-line coupled system, Geosci. Model Dev., 5, 129–147, https://doi.org/10.5194/gmd-5-129-2012, 2012.

Hohm, U.: Experimental determination of the dispersion in the mean linear dipole polarizability $\alpha(\omega)$ of small hydrocarbons and evaluation of Cauchy moments between 325 nm and 633 nm, Molecular Physics, 78, 929–941, https://doi.org/10.1080/00268979300100621, 1993.

Hohm, U. and Kerl, K.: Interferometric measurements of the dipole polarizability α of molecules between 300 K and 1100 K, Molecular Physics, 69, 803–817, https://doi.org/10.1080/00268979000100611, 1990.

Holanda, B. A., Pöhlker, M. L., Walter, D., Saturno, J., Sörgel, M., Ditas, J., Ditas, F., Schulz, C., Franco, M. A., Wang, Q., Donth, T., Artaxo, P., Barbosa, H. M. J., Borrmann, S., Braga, R., Brito, J., Cheng, Y., Dollner, M., Kaiser, J. W., Klimach, T., Knote, C., Krüger, O. O., Fütterer, D., Lavrič, J. V., Ma, N., Machado, L. A. T., Ming, J., Morais, F. G., Paulsen, H., Sauer, D., Schlager, H., Schneider, J., Su, H., Weinzierl, B., Walser, A., Wendisch, M., Ziereis, H., Zöger, M., Pöschl, U., Andreae, M. O., and Pöhlker, C.: Influx of African biomass burning aerosol during the Amazonian dry season through layered transatlantic transport of black carbon-rich smoke, Atmos. Chem. Phys., 20, 4757–4785, https://doi.org/10.5194/acp-20-4757-2020, 2020.

Hong, S. Y. and Lim, J.-O. J.: The WRF Single-Moment 6-Class Microphysics Scheme (WSM6), Asia-Pacific Journal of Atmospheric Sciences, 42, 129–151, available at: https://www.kci.go.kr/kciportal/ci/sereArticleSearch/ciSereArtiView.kci?sereArticleSearchBean.artiId=ART001017491, 2006.

Hong, S.-Y., Noh, Y., and Dudhia, J.: A New Vertical Diffusion Package with an Explicit Treatment of Entrainment Processes, Monthly Weather Review, 134, 2318–2341, https://doi.org/10.1175/MWR3199.1, 2006.

Horstjann, M., Andrés Hernández, M. D., Nenakhov, V., Chrobry, A., and Burrows, J. P.: Peroxy radical detection for airborne atmospheric measurements using absorption

spectroscopy of NO$_2$, Atmos. Meas. Tech., 7, 1245–1257, https://doi.org/10.5194/amt-7-1245-2014, 2014.

Hüneke, T., Aderhold, O.-A., Bounin, J., Dorf, M., Gentry, E., Grossmann, K., Grooß, J.-U., Hoor, P., Jöckel, P., Kenntner, M., Knapp, M., Knecht, M., Lörks, D., Ludmann, S., Matthes, S., Raecke, R., Reichert, M., Weimar, J., Werner, B., Zahn, A., Ziereis, H., and Pfeilsticker, K.: The novel HALO mini-DOAS instrument: inferring trace gas concentrations from airborne UV/visible limb spectroscopy under all skies using the scaling method, Atmospheric Measurement Techniques, 10, 4209–4234, https://doi.org/10.5194/amt-10-4209-2017, 2017.

Inness, A., Ades, M., Agustí-Panareda, A., Barré, J., Benedictow, A., Blechschmidt, A.-M., Dominguez, J. J., Engelen, R., Eskes, H., Flemming, J., Huijnen, V., Jones, L., Kipling, Z., Massart, S., Parrington, M., Peuch, V.-H., Razinger, M., Remy, S., Schulz, M., and Suttie, M.: The CAMS reanalysis of atmospheric composition, Atmos. Chem. Phys., 19, 3515–3556, https://doi.org/10.5194/acp-19-3515-2019, 2019.

IPCC: Climate Change 2023: Synthesis Report. Contribution of Working Groups I, II and III to the Sixth Assessment Report of the Intergovernmental Panel on Climate Change [Core Writing Team, H. Lee and J. Romero (eds.)]. IPCC, Geneva, Switzerland, pp. 35-115, doi:10.59327/IPCC/AR6-9789291691647, 2023.

Ityaksov, D., Linnartz, H., and Ubachs, W.: Deep-UV Rayleigh scattering of N2, CH4 and SF6, Molecular Physics, 106, 2471–2479, https://doi.org/10.1080/00268970802570334, 2008.

Jackson, J. D.: Classical electrodynamics, 3rd ed., Wiley, New York, Chichester, 1998.

Janssens-Maenhout, G., Crippa, M., Guizzardi, D., Dentener, F., Muntean, M., Pouliot, G., Keating, T., Zhang, Q., Kurokawa, J., Wankmüller, R., van der Denier Gon, H., Kuenen, J. J. P., Klimont, Z., Frost, G., Darras, S., Koffi, B., and Li, M.: HTAP_v2.2: a mosaic of regional and global emission grid maps for 2008 and 2010 to study hemispheric transport of air pollution, Atmos. Chem. Phys., 15, 11411–11432, https://doi.org/10.5194/acp-15-11411-2015, available at: https://acp.copernicus.org/articles/15/11411/2015/, 2015.

Janssens-Maenhout, G., Crippa, M., Guizzardi, D., Muntean, M., Schaaf, E., Dentener, F., Bergamaschi, P., Pagliari, V., Olivier, J. G. J., Peters, J. A. H. W., van Aardenne, J. A., Monni, S., Doering, U., Petrescu, A. M. R., Solazzo, E., and Oreggioni, G. D.: EDGAR v4.3.2 Global Atlas of the three major greenhouse gas emissions for the period 1970–2012, Earth Syst. Sci. Data, 11, 959–1002, https://doi.org/10.5194/essd-11-959-2019, 2019.

Jöckel, P., Sander, R., Kerkweg, A., Tost, H., and Lelieveld, J.: Technical Note: The Modular Earth Submodel System (MESSy) - a new approach towards Earth System Modeling, Atmos. Chem. Phys., 5, 433–444, https://doi.org/10.5194/acp-5-433-2005, 2005.

Jongma, R. T., Boogaarts, M. G. H., Holleman, I., and Meijer, G.: Trace gas detection with cavity ring down spectroscopy, Review of Scientific Instruments, 66, 2821–2828, https://doi.org/10.1063/1.1145562, 1995.

Kain, J. S. and Fritsch, J. M.: Convective Parameterization for Mesoscale Models: The Kain-Fritsch Scheme, in: The Representation of Cumulus Convection in Numerical Models, edited by: Emanuel, K. A. and Raymond, D. J., American Meteorological Society, Boston, MA, 165–170, https://doi.org/10.1007/978-1-935704-13-3_16, 1993.

References

Kan, C. S., Su, F., Calvert, J. G., and Shaw, J. H.: Mechanism of the ozone-ethene reaction in dilute N2/O2 mixtures near 1-atm pressure, J. Phys. Chem., 85, 2359–2363, https://doi.org/10.1021/j150616a013, 1981.

Kanakidou, M. and Crutzen, P. J.: The photochemical source of carbon monoxide: Importance, uncertainties and feedbacks, Chemosphere - Global Change Science, 1, 91–109, https://doi.org/10.1016/S1465-9972(99)00022-7, 1999.

Karkoschka, E.: Spectrophotometry of the Jovian Planets and Titan at 300- to 1000-nm Wavelength: The Methane Spectrum, Icarus, 111, 174–192, https://doi.org/10.1006/icar.1994.1139, 1994.

Kartal, D., Andrés-Hernández, M. D., Reichert, L., Schlager, H., and Burrows, J. P.: Technical Note: Characterisation of a DUALER instrument for the airborne measurement of peroxy radicals during AMMA 2006, Atmos. Chem. Phys., 10, 3047–3062, https://doi.org/10.5194/acp-10-3047-2010, 2010.

Kastler, A.: Atomes à l'Intérieur d'un Interféromètre Perot-Fabry, Appl. Opt., 1, 67, https://doi.org/10.1364/AO.1.S1.000067, 1962.

Keller-Rudek, H., Moortgat, G. K., Sander, R., and Sörensen, R.: The MPI-Mainz UV/VIS Spectral Atlas of Gaseous Molecules of Atmospheric Interest, https://www.uv-vis-spectral-atlas-mainz.org/, last access: 27 April 2023, 2023.

Keller-Rudek, H., Moortgat, G. K., Sander, R., and Sörensen, R.: The MPI-Mainz UV/VIS Spectral Atlas of Gaseous Molecules of Atmospheric Interest, Earth Syst. Sci. Data, 5, 365–373, https://doi.org/10.5194/essd-5-365-2013, 2013.

Kerkweg, A. and Jöckel, P.: The 1-way on-line coupled atmospheric chemistry model system MECO(n) – Part 1: Description of the limited-area atmospheric chemistry model COSMO/MESSy, Geosci. Model Dev., 5, 87–110, https://doi.org/10.5194/gmd-5-87-2012, 2012a.

Kerkweg, A. and Jöckel, P.: The 1-way on-line coupled atmospheric chemistry model system MECO(n) – Part 2: On-line coupling with the Multi-Model-Driver (MMD), Geosci. Model Dev., 5, 111–128, https://doi.org/10.5194/gmd-5-111-2012, 2012b.

Kerkweg, A., Hofmann, C., Jöckel, P., Mertens, M., and Pante, G.: The on-line coupled atmospheric chemistry model system MECO(n) – Part 5: Expanding the Multi-Model-Driver (MMD v2.0) for 2-way data exchange including data interpolation via GRID (v1.0), Geosci. Model Dev., 11, 1059–1076, https://doi.org/10.5194/gmd-11-1059-2018, 2018.

King, L. V.: On the complex anisotropic molecule in relation to the dispersion and scattering of light, Proc. R. Soc. Lond. A, 104, 333–357, https://doi.org/10.1098/rspa.1923.0113, 1923.

Kogelnik, H. and Li, T.: Laser beams and resonators, Applied optics, 5, 1550–1567, https://doi.org/10.1364/AO.5.001550, 1966.

Krol, M., Houweling, S., Bregman, B., van den Broek, M., Segers, A., van Velthoven, P., Peters, W., Dentener, F., and Bergamaschi, P.: The two-way nested global chemistry-transport zoom model TM5: algorithm and applications, Atmos. Chem. Phys., 5, 417–432, https://doi.org/10.5194/acp-5-417-2005, 2005.

Lelieveld, J., Bourtsoukidis, E., Brühl, C., Fischer, H., Fuchs, H., Harder, H., Hofzumahaus, A., Holland, F., Marno, D., Neumaier, M., Pozzer, A., Schlager, H., Williams, J., Zahn,

References

A., and Ziereis, H.: The South Asian monsoon-pollution pump and purifier, Science, 361, 270–273, https://doi.org/10.1126/science.aar2501, 2018.

Liu, Y., Andrés Hernández, M. D., George, M., and Burrows, J. P.: Experimental determination of Rayleigh scattering cross-sections at 408 nm, Applied Physics B, 129, https://doi.org/10.1007/s00340-023-08025-8, 2023.

Lorentz, H. A.: Over het verband tusschen de voortplantings sneldheit en samestelling der midden stofen, Koninklijke Akademie van Wetenschappen, Amsterdam, Verslagen, 1934–1936, 1878.

Lorenz, L. V.: Experimentale og theoretiske Undersøgelser: over Legmernes Brydningsforhold, Det kongelige danske Videnskabernes Selskabs Skrifter, 5, 203–248, 1869.

Mallaun, C., Giez, A., and Baumann, R.: Calibration of 3-D wind measurements on a single-engine research aircraft, Atmospheric Measurement Techniques, 8, 3177–3196, https://doi.org/10.5194/amt-8-3177-2015, 2015.

Manisalidis, I., Stavropoulou, E., Stavropoulos, A., and Bezirtzoglou, E.: Environmental and Health Impacts of Air Pollution: A Review, Frontiers in public health, 8, 14, https://doi.org/10.3389/fpubh.2020.00014, 2020.

Matsumi, Y. and Kawasaki, M.: Photolysis of atmospheric ozone in the ultraviolet region, Chemical reviews, 103, 4767–4782, https://doi.org/10.1021/cr0205255, 2003.

Mertens, M., Kerkweg, A., Jöckel, P., Tost, H., and Hofmann, C.: The 1-way on-line coupled model system MECO(n) – Part 4: Chemical evaluation (based on MESSy v2.52), Geosci. Model Dev., 9, 3545–3567, https://doi.org/10.5194/gmd-9-3545-2016, 2016.

Miyoshi, A., Matsui, H., and Washida, N.: Detection and reactions of the HOCO radical in gas phase, The Journal of Chemical Physics, 100, 3532–3539, https://doi.org/10.1063/1.466395, 1994.

Mlawer, E. J., Taubman, S. J., Brown, P. D., Iacono, M. J., and Clough, S. A.: Radiative transfer for inhomogeneous atmospheres: RRTM, a validated correlated-k model for the longwave, J. Geophys. Res., 102, 16663–16682, https://doi.org/10.1029/97JD00237, 1997.

Monks, P. S.: Gas-phase radical chemistry in the troposphere, Chemical Society Reviews, 34, 376–395, https://doi.org/10.1039/b307982c, 2005.

Moss, R. H., Edmonds, J. A., Hibbard, K. A., Manning, M. R., Rose, S. K., van Vuuren, D. P., Carter, T. R., Emori, S., Kainuma, M., Kram, T., Meehl, G. A., Mitchell, J. F. B., Nakicenovic, N., Riahi, K., Smith, S. J., Stouffer, R. J., Thomson, A. M., Weyant, J. P., and Wilbanks, T. J.: The next generation of scenarios for climate change research and assessment, Nature, 463, 747–756, https://doi.org/10.1038/nature08823, available at: https://www.nature.com/articles/nature08823, 2010.

Mozurkewich, M., McMurry, P. H., Gupta, A., and Calvert, J. G.: Mass accommodation coefficient for HO 2 radicals on aqueous particles, J. Geophys. Res., 92, 4163–4170, https://doi.org/10.1029/JD092iD04p04163, 1987.

Myriokefalitakis, S., Vrekoussis, M., Tsigaridis, K., Wittrock, F., Richter, A., Brühl, C., Volkamer, R., Burrows, J. P., and Kanakidou, M.: The influence of natural and anthropogenic secondary sources on the glyoxal global distribution, Atmos. Chem. Phys., 8, 4965–4981, https://doi.org/10.5194/acp-8-4965-2008, 2008.

References

Myriokefalitakis, S., Daskalakis, N., Gkouvousis, A., Hilboll, A., van Noije, T., Williams, J. E., Le Sager, P., Huijnen, V., Houweling, S., Bergman, T., Nüß, J. R., Vrekoussis, M., Kanakidou, M., and Krol, M. C.: Description and evaluation of a detailed gas-phase chemistry scheme in the TM5-MP global chemistry transport model (r112), Geosci. Model Dev., 13, 5507–5548, https://doi.org/10.5194/gmd-13-5507-2020, 2020.

Nakanishi, M. and Niino, H.: An Improved Mellor–Yamada Level-3 Model: Its Numerical Stability and Application to a Regional Prediction of Advection Fog, Boundary-Layer Meteorol, 119, 397–407, https://doi.org/10.1007/s10546-005-9030-8, available at: https://link.springer.com/article/10.1007/s10546-005-9030-8, 2006.

National Centers for Environmental Prediction/National Weather Service/NOAA/U.S. Department of Commerce: NCEP GDAS/FNL 0.25 Degree Global Tropospheric Analyses and Forecast Grids, 2015.

National Oceanic and Atmospheric Administration: The Global Forecaset System (GFS), https://www.emc.ncep.noaa.gov/emc/pages/numerical_forecast_systems/gfs/documentation.php, last access: 14 April 2023, 2023.

Naus, H. and Ubachs, W.: Experimental verification of Rayleigh scattering cross sections, Optics letters, 25, 347–349, https://doi.org/10.1364/ol.25.000347, 2000.

Naus, H., Lange, A. de, and Ubachs, W.: b1Σg+–X3Σg− (0,0) band of oxygen isotopomers in relation to tests of the symmetrization postulate in 16O2, Phys. Rev. A, 56, 4755–4763, https://doi.org/10.1103/PhysRevA.56.4755, 1997.

O′Keefe, A. and Deacon, D. A. G.: Cavity ring‐down optical spectrometer for absorption measurements using pulsed laser sources, Review of Scientific Instruments, 59, 2544–2551, https://doi.org/10.1063/1.1139895, 1988.

Oddershede, J. and Svendsen, E.: Dynamic polarizabilities and raman intensities of CO, N2, HCl and Cl2, Chemical Physics, 64, 359–369, https://doi.org/10.1016/0301-0104(82)80004-9, 1982.

Olson, J. B.: A Description of the MYNN Surface-Layer Scheme, Global Systems Laboratory (U.S.), 2021.

Owens, J. C.: Optical refractive index of air: dependence on pressure, temperature and composition, Applied optics, 6, 51–59, https://doi.org/10.1364/AO.6.000051, 1967.

Paulson, S. E. and Orlando, J. J.: The reactions of ozone with alkenes: An important source of HO x in the boundary layer, Geophys. Res. Lett., 23, 3727–3730, https://doi.org/10.1029/96GL03477, 1996.

Peck, E. R. and Khanna, B. N.: Dispersion of Nitrogen*, J. Opt. Soc. Am., 56, 1059, https://doi.org/10.1364/JOSA.56.001059, 1966.

Peck, E. R. and Fisher, D. J.: Dispersion of Argon, J. Opt. Soc. Am., 54, 1362, https://doi.org/10.1364/JOSA.54.001362, 1964.

Pincus, R., Mlawer, E. J., Oreopoulos, L., Ackerman, A. S., Baek, S., Brath, M., Buehler, S. A., Cady-Pereira, K. E., Cole, J. N. S., Dufresne, J.-L., Kelley, M., Li, J., Manners, J., Paynter, D. J., Roehrig, R., Sekiguchi, M., and Schwarzkopf, D. M.: Radiative flux and forcing parameterization error in aerosol-free clear skies, Geophys. Res. Lett., 42, 5485–5492, https://doi.org/10.1002/2015GL064291, available at: https://agupubs.onlinelibrary.wiley.com/doi/full/10.1002/2015GL064291, 2015.

References

Piolle, J.-F.: GHRSST R/G TS System Architecture GSA, Zenodo, 2020.

Platt, U., Perner, D., Schröder, J., Kessler, C., and Toennissen, A.: The diurnal variation of NO 3, J. Geophys. Res., 86, 11965–11970, https://doi.org/10.1029/JC086iC12p11965, 1981.

Poisson, N., Kanakidou, M., Bonsang, B., Behmann, T., Burrows, J. P., Fischer, H., Gölz, C., Harder, H., Lewis, A., Moortgat, G. K., Nunes, T., Pio, C. A., Platt, U., Sauer, F., Schuster, G., Seakins, P., Senzig, J., Seuwen, R., Trapp, D., Volz-Thomas, A., Zenker, T., and Zitzelberger, R.: The impact of natural non-methane hydrocarbon oxidation on the free radical and ozone budgets above a eucalyptus forest, Chemosphere - Global Change Science, 3, 353–366, https://doi.org/10.1016/S1465-9972(01)00016-2, 2001.

Poisson, N., Kanakidou, M., and Crutzen, P. J.: Impact of Non-Methane Hydrocarbons on Tropospheric Chemistry and the Oxidizing Power of the Global Troposphere: 3-Dimensional Modelling Results, J Atmos Chem, 36, 157–230, https://doi.org/10.1023/A:1006300616544, 2000.

Pöschl, U., Kuhlmann, R. von, Poisson, N., and Crutzen, P. J.: Development and Intercomparison of Condensed Isoprene Oxidation Mechanisms for Global Atmospheric Modeling, J Atmos Chem, 37, 29–52, https://doi.org/10.1023/A:1006391009798, available at: https://link.springer.com/article/10.1023/A:1006391009798, 2000.

Powers, J. G., Klemp, J. B., Skamarock, W. C., Davis, C. A., Dudhia, J., Gill, D. O., Coen, J. L., Gochis, D. J., Ahmadov, R., Peckham, S. E., Grell, G. A., Michalakes, J., Trahan, S., Benjamin, S. G., Alexander, C. R., Dimego, G. J., Wang, W., Schwartz, C. S., Romine, G. S., Liu, Z., Snyder, C., Chen, F., Barlage, M. J., Yu, W., and Duda, M. G.: The Weather Research and Forecasting Model: Overview, System Efforts, and Future Directions, Bulletin of the American Meteorological Society, 98, 1717–1737, https://doi.org/10.1175/BAMS-D-15-00308.1, 2017.

Price, C. and Rind, D.: Modeling Global Lightning Distributions in a General Circulation Model, Mon. Wea. Rev., 122, 1930–1939, https://doi.org/10.1175/1520-0493(1994)122<1930:MGLDIA>2.0.CO;2, 1994.

Rayleigh: XXXIV. On the transmission of light through an atmosphere containing small particles in suspension, and on the origin of the blue of the sky, The London, Edinburgh, and Dublin Philosophical Magazine and Journal of Science, 47, 375–384, https://doi.org/10.1080/14786449908621276, 1899.

Remorov, R. G., Gershenzon, Y. M., Molina, L. T., and Molina, M. J.: Kinetics and Mechanism of HO 2 Uptake on Solid NaCl, The Journal of Physical Chemistry A, 106, 4558–4565, https://doi.org/10.1021/jp013179o, 2002.

Ren, Y., Baumann, R., and Schlager, H.: An airborne perfluorocarbon tracer system and its first application for a Lagrangian experiment, Atmospheric Measurement Techniques, 8, 69–80, https://doi.org/10.5194/amt-8-69-2015, 2015.

Rockel, B. and Geyer, B.: The performance of the regional climate model CLM in different climate region, based on the example of precipitation, Meteorologische Zeitschrift, 17, 487–498, 2008.

Roeckner, E., Brokopf, R., Esch, M., Giorgetta, M., Hagemann, S., Kornblueh, L., Manzini, E., Schlese, U., and Schulzweida, U.: The atmospheric general circulation model ECHAM5 Part II: Sensitivity of simulated climate to horizontal and vertical resolution, Max Planck Institut für Meteorologie, 2004.

References

Roeckner, E., Bäuml, G., Bonaventura, L., Brokopf, R., Esch, M., Giorgetta, M., Hagemann, S., Kirchner, I., Kornblueh, L., Manzini, E., Rhodin, A., Schlese, U., Schulzweida, U., and Tompkins, A.: The atmospheric general circulation model ECHAM 5. PART I: Model description, (:unas), 2003.

Russell, G. L. and Lerner, J. A.: A New Finite-Differencing Scheme for the Tracer Transport Equation, J. Appl. Meteor., 20, 1483–1498, https://doi.org/10.1175/1520-0450(1981)020%3C1483:ANFDSF%3E2.0.CO;2, 1981.

Sander, R., Baumgaertner, A., Gromov, S., Harder, H., Jöckel, P., Kerkweg, A., Kubistin, D., Regelin, E., Riede, H., Sandu, A., Taraborrelli, D., Tost, H., and Xie, Z.-Q.: The atmospheric chemistry box model CAABA/MECCA-3.0, Geosci. Model Dev., 4, 373–380, https://doi.org/10.5194/gmd-4-373-2011, 2011.

Schulz, C., Schneider, J., Amorim Holanda, B., Appel, O., Costa, A., Sá, S. S. de, Dreiling, V., Fütterer, D., Jurkat-Witschas, T., Klimach, T., Knote, C., Krämer, M., Martin, S. T., Mertes, S., Pöhlker, M. L., Sauer, D., Voigt, C., Walser, A., Weinzierl, B., Ziereis, H., Zöger, M., Andreae, M. O., Artaxo, P., Machado, L. A. T., Pöschl, U., Wendisch, M., and Borrmann, S.: Aircraft-based observations of isoprene-epoxydiol-derived secondary organic aerosol (IEPOX-SOA) in the tropical upper troposphere over the Amazon region, Atmos. Chem. Phys., 18, 14979–15001, https://doi.org/10.5194/acp-18-14979-2018, 2018.

Schumann, U.: Measurement and model data comparisons for the HALO-FAAM formation flight during EMeRGe on 17 July 2017, 2021.

Simon, H. and Bhave, P. V.: Simulating the degree of oxidation in atmospheric organic particles, Environmental Science & Technology, 46, 331–339, https://doi.org/10.1021/es202361w, 2012.

Simpson, W. R., Brown, S. S., Saiz-Lopez, A., Thornton, J. A., and Glasow, R. von: Tropospheric halogen chemistry: sources, cycling, and impacts, Chemical reviews, 115, 4035–4062, https://doi.org/10.1021/cr5006638, 2015.

Skamarock, W., Klemp, J., Dudhia, J., Gill, D., Barker, D., Wang, W., Huang, X., and Duda, M.: A Description of the Advanced Research WRF Version 3, 2008.

Smith, P. L., Huber, M. C. E., and Parkinson, W. H.: Refractivities of H2 He, O2 CO, and Kr for 168≤λ≤288 nm, Phys. Rev. A, 13, 1422–1434, https://doi.org/10.1103/PhysRevA.13.1422, 1976.

Sneep, M. and Ubachs, W.: Direct measurement of the Rayleigh scattering cross section in various gases, Journal of Quantitative Spectroscopy and Radiative Transfer, 92, 293–310, https://doi.org/10.1016/j.jqsrt.2004.07.025, 2005.

Speidel, M., Nau, R., Arnold, F., Schlager, H., and Stohl, A.: Sulfur dioxide measurements in the lower, middle and upper troposphere: Deployment of an aircraft-based chemical ionization mass spectrometer with permanent in-flight calibration, Atmospheric Environment, 41, 2427–2437, https://doi.org/10.1016/j.atmosenv.2006.07.047, 2007.

Stein, A. F., Draxler, R. R., Rolph, G. D., Stunder, B. J. B., Cohen, M. D., and Ngan, F.: NOAA's HYSPLIT Atmospheric Transport and Dispersion Modeling System, Bulletin of the American Meteorological Society, 96, 2059–2077, https://doi.org/10.1175/BAMS-D-14-00110.1, 2015.

Stohl, A., Haimberger, L., Scheele, M. P., and Wernli, H.: An intercomparison of results from three trajectory models, Meteorol. Appl, 8, 127–135, https://doi.org/10.1017/S1350482701002018, 2001.

References

Stohl, A., Wotawa, G., Seibert, P., and Kromp-Kolb, H.: Interpolation Errors in Wind Fields as a Function of Spatial and Temporal Resolution and Their Impact on Different Types of Kinematic Trajectories, Journal of Applied Meteorology (1988-2005), 34, 2149–2165, available at: http://www.jstor.org/stable/26187926, 1995.

Strutt R.J.: A re-examination of the light scattered by gases in respect of polarisation. I.—Experiments on the common gases, Proc. R. Soc. Lond. A, 97, 435–450, https://doi.org/10.1098/rspa.1920.0044, 1920.

Strutt R.J.: The light scattered by gases: its polarisation and intensity, Proc. R. Soc. Lond. A, 95, 155–176, https://doi.org/10.1098/rspa.1918.0057, 1918.

Taketani, F., Kanaya, Y., and Akimoto, H.: Kinetics of HO 2 Uptake in Levoglucosan and Polystyrene Latex Particles, J. Phys. Chem. Lett., 1, 1701–1704, https://doi.org/10.1021/jz100478s, 2010.

Taketani, F., Kanaya, Y., and Akimoto, H.: Heterogeneous loss of HO2 by KCl, synthetic sea salt, and natural seawater aerosol particles, Atmospheric Environment, 43, 1660–1665, https://doi.org/10.1016/j.atmosenv.2008.12.010, 2009.

Taketani, F., Kanaya, Y., and Akimoto, H.: Kinetics of heterogeneous reactions of HO2 radical at ambient concentration levels with (NH4)2SO4 and NaCl aerosol particles, The Journal of Physical Chemistry A, 112, 2370–2377, https://doi.org/10.1021/jp0769936, 2008.

Thalman, R., Zarzana, K. J., Tolbert, M. A., and Volkamer, R.: Erratum to "Rayleigh scattering cross-section measurements of nitrogen, argon, oxygen and air" J Quant Spectrosc Radiat Transf 147 (2014) 171–177, Journal of quantitative spectroscopy & radiative transfer, 189, 281–282, https://doi.org/10.1016/j.jqsrt.2016.12.014, available at: https://www.sciencedirect.com/science/article/pii/S0022407316308457, 2017.

Thalman, R., Zarzana, K. J., Tolbert, M. A., and Volkamer, R.: Rayleigh scattering cross-section measurements of nitrogen, argon, oxygen and air, Journal of Quantitative Spectroscopy and Radiative Transfer, 147, 171–177, https://doi.org/10.1016/j.jqsrt.2014.05.030, available at: https://www.sciencedirect.com/science/article/pii/S0022407314002453, 2014.

Thompson, G., Field, P. R., Rasmussen, R. M., and Hall, W. D.: Explicit Forecasts of Winter Precipitation Using an Improved Bulk Microphysics Scheme. Part II: Implementation of a New Snow Parameterization, Monthly Weather Review, 136, 5095–5115, https://doi.org/10.1175/2008MWR2387.1, 2008.

Thornton, J. and Abbatt, J. P. D.: Measurements of HO 2 uptake to aqueous aerosol: Mass accommodation coefficients and net reactive loss, J. Geophys. Res., 110, https://doi.org/10.1029/2004jd005402, 2005.

Tiedtke, M.: A Comprehensive Mass Flux Scheme for Cumulus Parameterization in Large-Scale Models, Mon. Wea. Rev., 117, 1779–1800, https://doi.org/10.1175/1520-0493(1989)117%3C1779:ACMFSF%3E2.0.CO;2, 1989.

Tost, H., Lawrence, M. G., Brühl, C., and Jöckel, P.: Uncertainties in atmospheric chemistry modelling due to convection parameterisations and subsequent scavenging, Atmos. Chem. Phys., 10, 1931–1951, https://doi.org/10.5194/acp-10-1931-2010, 2010.

Tost, H., Jöckel, P., Kerkweg, A., Pozzer, A., Sander, R., and Lelieveld, J.: Global cloud and precipitation chemistry and wet deposition: tropospheric model simulations with

References

ECHAM5/MESSy1, Atmos. Chem. Phys., 7, 2733–2757, https://doi.org/10.5194/acp-7-2733-2007, 2007.

Tost, H., Jöckel, P., Kerkweg, A., Sander, R., and Lelieveld, J.: Technical note: A new comprehensive SCAVenging submodel for global atmospheric chemistry modelling, Atmos. Chem. Phys., 6, 565–574, https://doi.org/10.5194/acp-6-565-2006, 2006.

US EPA Office of Research and Development: Cmaqv5.0.2, Zenodo, 2014.

van der Werf, G. R., Randerson, J. T., Giglio, L., van Leeuwen, T. T., Chen, Y., Rogers, B. M., Mu, M., van Marle, M. J. E., Morton, D. C., Collatz, G. J., Yokelson, R. J., and Kasibhatla, P. S.: Global fire emissions estimates during 1997–2016, Earth Syst. Sci. Data, 9, 697–720, https://doi.org/10.5194/essd-9-697-2017, 2017.

van Marle, M. J. E., Kloster, S., Magi, B. I., Marlon, J. R., Daniau, A.-L., Field, R. D., Arneth, A., Forrest, M., Hantson, S., Kehrwald, N. M., Knorr, W., Lasslop, G., Li, F., Mangeon, S., Yue, C., Kaiser, J. W., and van der Werf, G. R.: Historic global biomass burning emissions for CMIP6 (BB4CMIP) based on merging satellite observations with proxies and fire models (1750–2015), Geosci. Model Dev., 10, 3329–3357, https://doi.org/10.5194/gmd-10-3329-2017, 2017.

van Zee, R. D., Hodges, J. T., and Looney, J. P.: Pulsed, single-mode cavity ringdown spectroscopy, Applied optics, 38, 3951–3960, https://doi.org/10.1364/ao.38.003951, 1999.

van Zee, R. D. and Looney, J. P.: Cavity-enhanced spectroscopies, Experimental methods in the physical sciences, 1079-4042, v. 40, London Academic, Amsterdam, 2002.

Vandaele, A. C.: High-resolution Fourier transform measurement of the NO 2 visible and near-infrared absorption cross sections: Temperature and pressure effects, J. Geophys. Res., 107, https://doi.org/10.1029/2001JD000971, 2002.

Volz-Thomas, A., Xueref, I., and Schmitt, R.: Automatic gas chromatograph and calibration system for ambient measurements of PAN and PPN, Environmental science and pollution research, 9, available at: https://juser.fz-juelich.de/record/34322?ln=en, 2002.

Wayne, R., Barnes, I., Biggs, P., Burrows, J., Canosa-Mas, C., Hjorth, J., Le Bras, G., Moortgat, G., Perner, D., Poulet, G., Restelli, G., and Sidebottom, H.: The nitrate radical: Physics, chemistry, and the atmosphere, Atmospheric Environment. Part A. General Topics, 25, 1–203, https://doi.org/10.1016/0960-1686(91)90192-A, available at: https://www.sciencedirect.com/science/article/pii/096016869190192A, 1991.

Wendisch, M., Pöschl, U., Andreae, M. O., Machado, L. A. T., Albrecht, R., Schlager, H., Rosenfeld, D., Martin, S. T., Abdelmonem, A., Afchine, A., Araùjo, A. C., Artaxo, P., Aufmhoff, H., Barbosa, H. M. J., Borrmann, S., Braga, R., Buchholz, B., Cecchini, M. A., Costa, A., Curtius, J., Dollner, M., Dorf, M., Dreiling, V., Ebert, V., Ehrlich, A., Ewald, F., Fisch, G., Fix, A., Frank, F., Fütterer, D., Heckl, C., Heidelberg, F., Hüneke, T., Jäkel, E., Järvinen, E., Jurkat, T., Kanter, S., Kästner, U., Kenntner, M., Kesselmeier, J., Klimach, T., Knecht, M., Kohl, R., Kölling, T., Krämer, M., Krüger, M., Krisna, T. C., Lavric, J. V., Longo, K., Mahnke, C., Manzi, A. O., Mayer, B., Mertes, S., Minikin, A., Molleker, S., Münch, S., Nillius, B., Pfeilsticker, K., Pöhlker, C., Roiger, A., Rose, D., Rosenow, D., Sauer, D., Schnaiter, M., Schneider, J., Schulz, C., Souza, R. A. F. de, Spanu, A., Stock, P., Vila, D., Voigt, C., Walser, A., Walter, D., Weigel, R., Weinzierl, B., Werner, F., Yamasoe, M. A., Ziereis, H., Zinner, T., and Zöger, M.: ACRIDICON–CHUVA Campaign: Studying Tropical Deep Convective Clouds and Precipitation over Amazonia Using the New German Research Aircraft HALO, Bulletin of the American

<u>References</u>

Meteorological Society, 97, 1885–1908, https://doi.org/10.1175/BAMS-D-14-00255.1, 2016.

Wesely, M. L.: Parameterization of surface resistances to gaseous dry deposition in regional-scale numerical models, Atmospheric Environment (1967), 23, 1293–1304, https://doi.org/10.1016/0004-6981(89)90153-4, 1989.

Wheeler, M. D., Newman, S. M., Orr-Ewing, A. J., and Ashfold, M. N. R.: Cavity ring-down spectroscopy, Faraday Trans., 94, 337–351, https://doi.org/10.1039/a707686j, 1998.

Williams, J. E., Boersma, K. F., Le Sager, P., and Verstraeten, W. W.: The high-resolution version of TM5-MP for optimized satellite retrievals: description and validation, Geosci. Model Dev., 10, 721–750, https://doi.org/10.5194/gmd-10-721-2017, 2017.

Wilmouth, D. M. and Sayres, D. S.: Determination of Rayleigh scattering cross sections and indices of refraction for Ar, CO2, SF6, and CH4 using BBCES in the ultraviolet, Journal of Quantitative Spectroscopy and Radiative Transfer, 255, 107224, https://doi.org/10.1016/j.jqsrt.2020.107224, available at: https://www.sciencedirect.com/science/article/pii/S002240732030474X, 2020.

Wilmouth, D. M. and Sayres, D. S.: Rayleigh scattering cross sections of argon, carbon dioxide, sulfur hexafluoride, and methane in the UV-A region using Broadband Cavity Enhanced Spectroscopy, Journal of quantitative spectroscopy & radiative transfer, 234, 32–39, https://doi.org/10.1016/j.jqsrt.2019.05.031, 2019.

Wintel, J., Hösen, E., Koppmann, R., Krebsbach, M., Hofzumahaus, A., and Rohrer, F.: Stable carbon isotope ratios of toluene in the boundary layer and the lower free troposphere, Atmos. Chem. Phys., 13, 11059–11071, https://doi.org/10.5194/acp-13-11059-2013, 2013.

World Meteorological Organization: Executive Summary: Scientific assessment of ozone depletion: 2022, Global Atmosphere Watch report series, No. 278, World Meteorological Organization, Geneva, Switzerland, 56 pp., 2022.

Yienger, J. J. and Levy, H.: Empirical model of global soil-biogenic NO χ emissions, J. Geophys. Res., 100, 11447, https://doi.org/10.1029/95JD00370, 1995.

Zahn, A., Weppner, J., Widmann, H., Schlote-Holubek, K., Burger, B., Kühner, T., and Franke, H.: A fast and precise chemiluminescence ozone detector for eddy flux and airborne application, Atmospheric Measurement Techniques, 5, 363–375, https://doi.org/10.5194/amt-5-363-2012, 2012.

Zalicki, P. and Zare, R. N.: Cavity ring‐down spectroscopy for quantitative absorption measurements, The Journal of Chemical Physics, 102, 2708–2717, https://doi.org/10.1063/1.468647, 1995.

Ziereis, H., Minikin, A., Schlager, H., Gayet, J. F., Auriol, F., Stock, P., Baehr, J., Petzold, A., Schumann, U., Weinheimer, A., Ridley, B., and Ström, J.: Uptake of reactive nitrogen on cirrus cloud particles during INCA, Geophys. Res. Lett., 31, n/a-n/a, https://doi.org/10.1029/2003GL018794, 2004.

Zimmermann, P. H.: MOGUNTIA: A handy global tracer, in: Air Pollution Modeling and its Applications VI, edited by: van Dop, H., NATO/CCMS, New York, 593–608, 1988.

References

217

Acknowledgements

Sometimes it can be complicated to write the last chapter of any work, here, for instance, the acknowledgements. On one side people start to be excited and feel fulfilled about the finish of the work, on the other side, you may miss the very last experience and continue to your next challenge. Like Lola's catch phase, but in a very good way: "It is the beginning of the end."

I would like to express my sincere gratitude to my supervisor, Prof. Dr. John P. Burrows, a distinguished scientist, highly knowledgeable professor, and a respected mentor whom I have known for over a decade. Whether within the university or during field campaigns, he consistently exhibits enthusiasm and provides me with limitless, selfless assistance and guidance. He is a true role model for a scientist.

My heartfelt appreciation goes to my most respectful and grateful colleague, our group leader, my mentor, and my office roommate, Dr. M. D. Andrés Hernández, aka. Lola. She believed me in the very beginning, providing me the opportunity to start my PhD. Throughout the journey, she dedicated considerable efforts to helping me navigate numerous challenges. As one of the finest experimental scientists, she serves as a role model for women in science.

I express my gratitude to my former colleagues and friends, Vlad and Midhun. Their assistance with lab work, scientific topics, programming, and more was invaluable. We worked tirelessly and created numerous wonderful memories during many campaigns. Their presence made my PhD journey much more manageable. A special acknowledgement to Wilke, the exceptional electrical technician who consistently played a supporting role that we all relied on.

Special thanks to the EMeRGe teams with whom I have collaborated closely during the campaigns, offering invaluable assistance in numerous ways. Special thanks to the modelling groups, who generously shared insights, exchanged ideas, and patiently addressed my numerous questions.

I extend my deepest gratitude to my parents, Xiaojun and Jun, for their unwavering mental support and unfaltering belief in me. Special thanks to my family in Bremen, the Chan family, for their tremendous help during the pandemic and for treating me as one of their own. My appreciation also goes to all the families and friends who have taken care of me and offered countless acts of kindness.

The acknowledgement could be endless, but the life will go on. The finishing of PhD might be a summary of the current, the future will be forever and sometimes.